Lecture Notes in Electrical Engineering 86

Dehuai Zeng
Editor

Future Intelligent Information Systems

Volume 1

Springer

Lecture Notes in Electrical Engineering

Volume 86

Dehuai Zeng (Ed.)

Future Intelligent Information Systems

Volume 1

Springer

Prof. Dehuai Zeng
Shenzhen University
Nanhai Ave 3688
Guangdong
Shenzhen 518060
P.R. China
E-mail: zengdh2008@gmail.com

ISBN 978-3-642-19705-5 e-ISBN 978-3-642-19706-2

DOI 10.1007/978-3-642-19706-2

Lecture Notes in Electrical Engineering ISSN 1876-1100

Library of Congress Control Number: 2011923799

© 2011 Springer-Verlag Berlin Heidelberg

This work is subject to copyright. All rights are reserved, whether the whole or part of the material is concerned, specifically the rights of translation, reprinting, reuse of illustrations, recitation, broadcasting, reproduction on microfilm or in any other way, and storage in data banks. Duplication of this publication or parts thereof is permitted only under the provisions of the German Copyright Law of September 9, 1965, in its current version, and permission for use must always be obtained from Springer. Violations are liable to prosecution under the German Copyright Law.

The use of general descriptive names, registered names, trademarks, etc. in this publication does not imply, even in the absence of a specific statement, that such names are exempt from the relevant protective laws and regulations and therefore free for general use.

Typeset & Coverdesign: Scientific Publishing Services Pvt. Ltd., Chennai, India.

Printed on acid-free paper

9 8 7 6 5 4 3 2 1

springer.com

Preface

We are delighted to invite you to participate in 2010 International conference on Electrical and Electronics Engineering (ICEEE 2010) in Wuhan, China, and December 4–5, 2010. The objective of ICEEE 2010 is to provide a forum for researchers, educators, engineers, and government officials involved in the general areas of Electrical and Electronics Engineering to disseminate their latest research results and exchange views on the future research directions of these fields.

This year, 2010 International conference on Electrical and Electronics Engineering (ICEEE 2010) invites high-quality recent research results in the areas of Electrical and Electronics Engineering.

The main goal of the Conference is to bring together scientists and engineers who work on Electrical and Electronics Engineering. The ICEEE conference will provide an opportunity for academic and industry professionals to discuss the latest issues and progress in the area of Electrical and Electronics Engineering. Furthermore, we expect that the conference and its publications will be a trigger for further related research and technology improvements in this important subject.

ICEEE 2010 will also include presentations of contributed papers and state-of-the-art lectures by invited keynote speakers. The conference will bring together leading researchers, engineers and scientists in the domain of interest from around the world. We would like to thank the program chairs, organization staff, and the members of the program committees for their hard work. Special thanks go to Springer Publisher.

We hope that ICEEE 2010 will be successful and enjoyable to all participants. We look forward to seeing all of you next year at the ICEEE 2011.

Jian Lee
Hubei University of Education, China

ICEEE 2010 Organizing Committee

ICEEE 2011 Keynote Speakers

Chin-Chen Chang, IEEE Fellow	Feng Chia University, Taiwan
Jun Wang	The Chinese University of Hong Kong, Hong Kong

General Chairs

Jian Li	Nanchang University, China
Mark Zhou	International Industrial Electronics Center, Hong Kong

Program Chairs

Dehuai Zeng	Shenzhen University, China
Jian Lee	Hubei University of Education, China

Program Committee

Zhu Min	Nanchang University, China
Peide Liu	Shangdong Economic University, China
Ying Zhang	Wuhan Universtiy, China
Changhui Liu	Huazhong University of Science and Technology, China
Ping He	Liaoning Police Academy, China
Minli Dai	Suzhou University, China
Zhenghong Wu	East China Normal University, China
Qingyuan Zhou	Jiangsu Teachers University of Technology, China
Wei Li	Asia Pacific Human-Computer Interaction Research Center, Hong Kong

Contents

Design of Intelligent Supersonic Rangefinders

Wang Wen-cheng and Guan Feng-nian

College of Information and Control Engineering, Weifang University,
261061Weifang, China
wwcwfu@126.com

Abstract. The overall framework of intelligent supersonic rangefinder is presented in this paper, which is designed on the basis of measuring the width of pulses. The working principle of supersonic ranging is analyzed firstly. Then, the system structure and unit circuits are given and the flowchart of control program is presented. Finally, the main factors which impact measurement accuracy are analyzed in detail, and the strategies of improving the accuracy and specific circuits are introduced correspondingly. This system is tested in our laboratory, experiment shows that the system has the advantages of simply structure, easy to use and high accuracy.

Keywords: supersonic rangefinder; DS18B20; RS232; transmitter.

1 Introduction

Automatic ranging technology has been widely used in many fields such as navigation systems, industrial robots, machining and other applications [1]. The common methods include infrared ranging, laser ranging, eddy ranging and radio ranging, etc.. They are applied in different occasions according to their working characteristics [2][3]. Compared with the common methods, supersonic ranging has the advantages of less transmission attenuation, strong reflectivity, insensitive to light and electromagnetic. Especially with the rising of intelligent machines which take micro controller as the core, the supersonic detection device has been greatly improved in its detection accuracy, method and application range, and it has become an important part in the intelligent detection field [4]. However, because of the effect of temperature on ultrasound propagation velocity, the accuracy will be declined to some extent accordingly; which will result in the limitation of application in high accuracy occasions to supersonic ranging system. For such problems, a designed method of intelligent supersonic rangefinder with low-cost and high-precision is introduced in this paper; the hardware and software are described in details.

This paper is organized as follows. Section 2 introduced the principle of supersonic ranging. The next section described the overall structure of the system, and unit circuits are given. In section 4, the flowchart of control program is presented. After that, some methods for improving the accuracy of system are proposed, it is followed by a discussion of the experiments in section 5, and the experimental results are analyzed. Finally, in section 6, some conclusions are presented.

D. Zeng (Ed.): Future Intelligent Information Systems, LNEE 86, pp. 1–6.
springerlink.com © Springer-Verlag Berlin Heidelberg 2011

2 The Principle of Supersonic Ranging

The supersonic wave used for ranging is usually generated from the piezoelectric effect of piezoelectric ceramic, which is composed of two piezoelectric patches and one resonant plate. When the pulse signal is applied to the poles and its frequency is equal to the natural oscillation frequency of the piezoelectric chip. Supersonic wave spreads in a straight line, the higher the frequency, the stronger the reflectivity. Such feature is often used for ranging with a "timing method". Its working principle is as follows: The supersonic generator transmits the signal at a given moment, when the ultrasound wave meets the measured object; it will be reflected back and received by the supersonic receivers [5][6]. As long as we compute the echo time from supersonic transmitting to receiving and know the propagation speed in the medium. Then, the distance from measured object can be calculated. The formula is as follows:

$$d = s/2 = (v \times t)/2 \tag{1}$$

where d is the distance from the device to object, s is the round trip of supersonic wave, v is the spread speed in the medium, t is the time from supersonic transmitting to receiving.

3 Hardware of System

The Intelligent supersonic ranging system is composed of microcontroller, supersonic transmitter, supersonic receiver modules, temperature measurement module, display module and data communication, et al.. The overall structure of the system is shown in Fig.1.

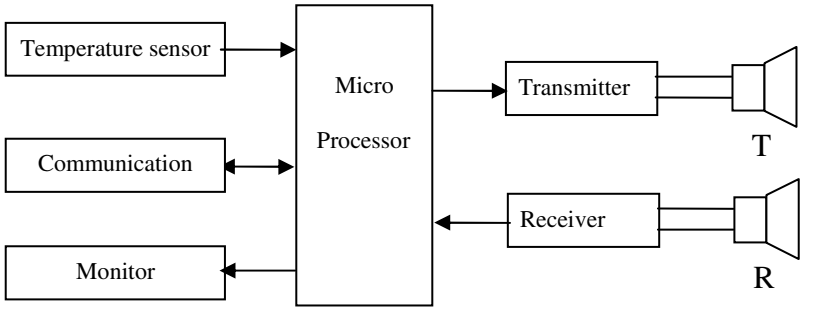

Fig. 1. The overall structure of system

The microprocessor is the control core of system, which is responsible for coordinating the work of the various modules. When the system is power on, the processor will generate 40KHZ pulse. After passing by the amplification-driven emission sensor, the signal will become the supersonic wave with the same frequency. When

the first pulse is transmitted, the counter started counting. The supersonic wave is reflected back and converted to electrical signals via the receiver transducer, which is send to microprocessor after filtering, amplifying and rectifying. Once the processor detects the echo signals, the counter will stop counting. Then, the microprocessor computes the distance according to the counting number and the temperature collected in the scene, and display it on the LCD immediately.

3.1 Supersonic Transmitter

The circuit of supersonic transmitter is composed of power amplifier circuit and supersonic emission sensors. The amplifier terminal gets a pulse signal with the frequency of 40 KHz from controller. Then, it is amplified to a large enough energy by power amplifier circuit and added to the supersonic emission sensor, which drivers the probe to launch pulse outside through the space. Where the amplifier is LM386, it is an audio integrated amplifier with the performances of low power consumption, voltage gain adjustable, total harmonic distortion etc., It is widely used in amplification circuit, and only needs very simple hardware circuit to complete the function. TCT is the launch probe of supersonic.

3.2 Supersonic Receiver

The Receiver module is composed of the signal amplification circuit and comparison circuit. When the echo signal is back, it will be proceed to standard square wave signal after amplification and shaping treatment. Then, the square wave is sent to the external interrupt controller ports and converted to time by counting the numbers. Calling the distance calculation module, the distance will obtain.

The receiving circuit is a two-cascade signal amplification circuit composed of two high-speed operational amplifiers. Its magnification can be adjusted from10 to 50, and its role is to amplify the weak signal reflected back from the goal to meet the requirements of gain bandwidth and slew rate. The task of comparison circuit is mainly to send the signals from conditioning circuit to microprocessor in order to cause disruption, and convert the echo signal into high or low levels which the CPU can recognize. It is constituted by the voltage comparator and the signal amplified is imported from the first two pins. The opposite reference voltage should be less than the peak value of the effective signal, and greater than the peak noise signal.

3.3 Temperature Measuring Circuit

Since the propagation velocity of supersonic wave is particularly affected by temperature. Therefore, in high precision occasions, it is necessary to conduct temperature compensation and correction for the supersonic transmission speed in order to improve the measurement accuracy and reduce errors. DS18B20 is used for the temperature measuring in this system, which is a digital thermometer provides 9-bit to 12-bit Celsius temperature measurements and has an alarm function with nonvolatile user-programmable upper and lower trigger points. Temperature detection module circuit is shown in Fig.2.

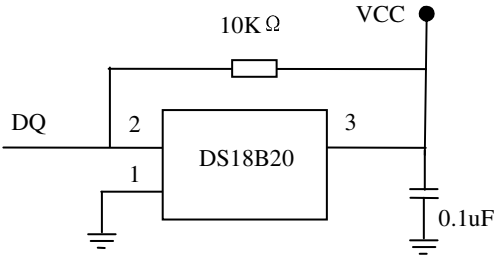

Fig. 2. Temperature measurement circuit

3.4 Communication Module

The system uses the RS-232 bus to achieve communications between the computer and supersonic rangefinder. As the microprocessor signal is TTL level, in order to realize level conversion, it is needed the conversion module MAX232. MAX232 is designed for RS-232 and V.28communications in harsh environments. Each transmitter output and receiver input is protected against ±15kV electrostatic discharge (ESD) shocks, without latch up. Through serial communication, the measured distance information can be send to the host computer. The application circuit is shown in Fig.3.

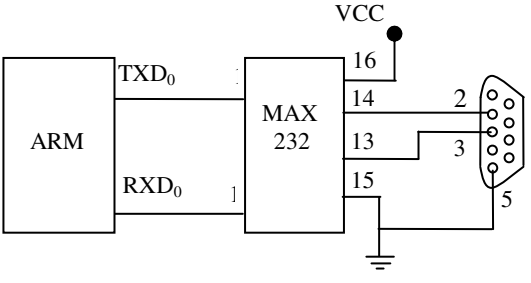

Fig. 3. Level converter of RS232

3.5 Displaying Module

In order to facilitate the observation and debugging of the precision location device, the liquid crystal display is used for showing the measured values in the system, and the data unit is in millimeters. To simplify the circuit and give full play to the performance of ARM, it used the 320 × 240 16-level gray LCD as the monitor. As the LCD signal frequency is high and LCD cable is longer, the signal line is increased 74HC244 to enhance the driving capability.

4 Software Design

The system software is designed in modular, and the supersonic transceiver control, data processing and communication are all completed by the microprocessor. The software is prepared using C51, which is composed of the subroutines such as the pulse launching program, echo reception program, data processing program, display program, and time delay program, et al.

When the control system is power on, it first initializes a series of initial value for the system settings; which including the number of supersonic emission interval, distance calculation parameters, and initializes the DS18B20. Then, it controls the port to transmit square wave signals. After a time delay, it starts receiving echo procedures to waiting for echo. If it is time out, then the supersonic wave is prompted to re-launch. Otherwise, it stops timing, reads the time difference to generate interrupt and stop counting, It is repeats the measurements according to the settings, considers the impact of temperate on the supersonic wave velocity and to obtain the corrected data trough speed compensation method. After analyzing and processing the data, the distance value will be outputted on the LCD and conducted voice broadcasting. If the data is exceeding the threshold, the buzzer will start alarming. When we need the data storage, the system will judge whether the keyboard is pressed through external interrupt, and lock the data by showing the previous measurements repeatedly.

5 Experiment Analysis

After the accomplishment of supersonic range finder, in order to verify its accuracy, the experiment is designed on the smooth hard surface in the laboratory with the measuring range 5~300cm. The experimental results are shown in Fig.4.

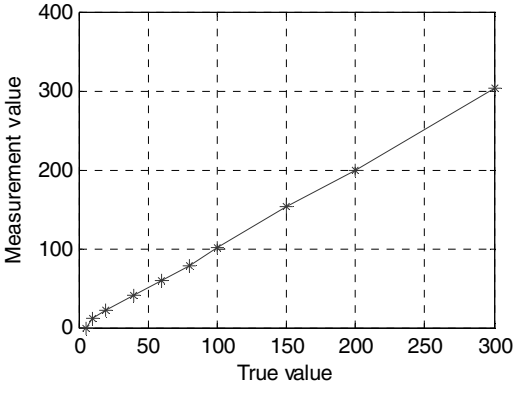

Fig. 4. Experimental data curve

The measurement results show that the blind area of this system is relatively small. In the other measurements, the absolute errors are all within 3cm, and with the increase of the distance, the relative errors become smaller and smaller. Thus, the

experiment shows that the rangefinder has high measurement accuracy, and can meet the needs of measuring most obstacles with practical applications.

6 Conclusion

The intelligent supersonic range finder has the advantages of simple structure, small size, and high accuracy. The system has used microprocessor to counting time, considered the impact of temperature on the speed of sound, and realized the error correction by adopting temperature compensation circuitry. The experiment is conducted in the laboratory environment, and the measured data has little difference with the actual measurements. The accuracy of the system can achieve the practical acquirements of industry, not only for the parking sensor, object position measurement, logging and other common situations, but also can be widely used in mobile robot research, and it will have broad application prospects.

Acknowledgments

This work has been supported partly by Natural Science Foundation of Weifang University (2008K17) and Shandong Provincial Natural Science Foundation (Z2007F08).

References

1. Song, J.G., Li, Y.Z., Xu, Y.H.: Application of PIC16F877 in Supersonic Measuring System. Mechanical Engineering &Automatic (4), 118–120 (2007)
2. Perov, D.V., Rinkevich, A.B., Nemytova, O.V.: Interaction of pulse supersonic signals with reflectors of different types. Acoustic Methods 43(6), 25–35 (2007)
3. Wu, C., Dai, Y.W.: The Design of Supersonic Ranging System Based on AT89S52MCU. Journal of Zhongyuan University of Technology 19(5), 65–68 (2008)
4. Liu, Y.M., Zhang, Q.Z.: Design of Distance Measurement System Based on Supersonic Sensor. Instrument Technique and Sensor 2, 109–110 (2009)
5. Zhang, C.G.: Design of Supersonic Distance Measurement System Based on Microprocessor. Machine Tool & Hydraulics 36(7), 208–211 (2008)
6. Xiao, J., Niu, W., Mo, Y.M.: Design of supersonic distance measuring system with transmitting-receipting sensor. Journal of Transducer Technology (8), 32–34 (2003)

A System Design Method for Gear Parameters Analyzing

Wang Wen-cheng and Ji Tao

College of Information and Control Engineering, Weifang University,
261061 Weifang, China
wwcwfu@126.com, jtsdu@126.com

Abstract. To the problem of gear parameters measurement, this paper has presented a system design method based on machine version. Firstly, gear image was captured by CCD and input into computer for processing. Then, a kind of gray image processing methods such as denoising, binary conversion, mathematical morphology have been conducted. After that, a method for gear center location and gear teeth number counting is proposed and the other parameters can be obtained by calculating. The method is simple and does not need edge detecting. Experiment shows that the system is stable and fast, and it will have widely application in the future.

Keywords: gear parameters; computer version; image preprocessing; binarization.

1 Introduction

With the development of science and technology, the gear has played a very important role as one of the basic components in force and motion transferring. Its quality has a direct impact on the performance of machine products. So, the measurement on every parameter of gear has become an indispensable step in the course of instrument production [1]. Because the gear shape is complex and has a lot of parameters, therefore, gear geometry measurement is difficulty and has high requirement to the test staffs. In recent years, computer vision technology acts as a new nondestructive testing method and shows great vitality in gear measurement techniques [2][3]. Compared with traditional methods, it has irreplaceable advantages such as reducing the labor intensity of testers, avoiding the subjective errors, and can improve the efficiency.

To those methods based on computer version, they need to determine the center of the gear as a benchmark firstly, and the detection accuracy of gear center affects the measurement of other parameters directly. The traditional center detection methods usually take the edge detection method to determine the edge of gear. Then, the center of gravity method, the median value method or the Hough transform method is adopted to determine center of the circle. The first two algorithms require the image distributed more evenly, otherwise it will lead to considerable error [4][5]. The latter algorithm needs to point by point voting record, the use of more time but the precision is not high enough. In response to such a question, the design of gear parameters automatic counting system based on image processing is proposed after the

D. Zeng (Ed.): Future Intelligent Information Systems, LNEE 86, pp. 7–13.
springerlink.com © Springer-Verlag Berlin Heidelberg 2011

combination of morphology technology, which inputs the gear image to computer, conducts the feature extraction using image processing algorithm, isolates the pure gear from complex background and realizes automatic analyzing. It will achieve good results in production and applications.

The rest of this paper is organized as follows. Section 2 introduces the framework of hardware and the flow chart of software. The next section describes the course of realizing gear image preprocessing by using digital image processing methods, it has obtain a good quality binary image through a series of operations. After that, gear parameters analyzing method has been described in details. Finally, the last section gives some concluding remarks.

2 The Structure of System

The overall structure of system is composed of physical hardware and logical software which including image processing and target recognition.

2.1 Hardware

The physical hardware is mainly composed of working platform, light source, CCD camera, image acquisition card and computer, which is shown in Fig.1. Its working principle is as follows: the gear is placed on the platform, the digital camera acquires image, translates the signals to digital information and sends them to computer by image acquisition card. In addition to this, the printer is sometime used as the outputting device.

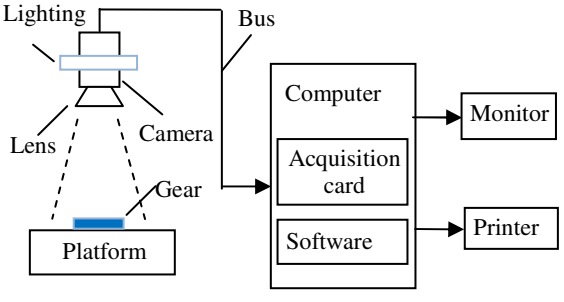

Fig. 1. The overall structure of system

Because of the uncertainty illumination in gear image acquisition, so the light source is often used for obtain the better performance. The LED light source is at the top, so that each gear is able to obtain uniform illumination. Before the image acquisition, the regulation of environmental parameters should be done according to lighting conditions. The CCD camera is installed with lighting; it has auto-focus function which is able to improve the image quality. Image acquisition card is installed in the computer's motherboard expansion slot; it translates the signals to

digital information and sends them to computer. The software of operating system is Windows XP , application program includes controlling program for image acquisition and image processing program.

2.2 Application Software

In general, this software flow chart can be described as the course of image processing and target recognition. As is shown in Fig.2, it is composed of image preprocessing, binarization, morphological processing, number counting, and parameter analyzing, et al.. They are described in the following section in detail.

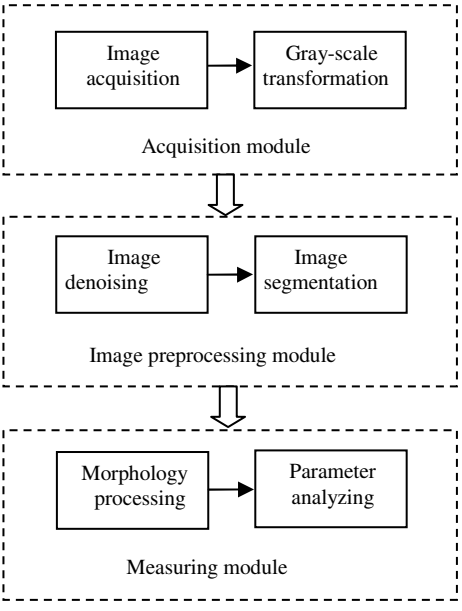

Fig. 2. Measuring flowchart of gear parameters

3 Parameter Analyzing

3.1 Image Binarization

Image binarization is to separate the object from background completely using the grey level. Therefore, the key is how to selecting a segmentation threshold. When a pixel's gray value is above this threshold, we can say that the pixel belongs to the objectives of interest; otherwise it is treated as the part of the background. This paper adopts iterative threshold method. Firstly it chooses an approximate threshold value as the initial estimate value, and then continuously improves this estimate value,

which is named the use of the initial value for sub-image generation. According to the characteristics of sub-image, it selects a new threshold uses the new threshold to segment images, the segmentation result is better than that with the initial threshold.

Suppose original image is $f(x, y)$, binary image is $g(x, y)$, threshold is T, then :

$$g(x, y) = \begin{cases} 1 & f(x, y) \geq T \\ 0 & f(x, y) < T \end{cases}. \tag{1}$$

The source image and binary image are shown in Fig.3(a) and Fig.3(b), respectively.

3.2 Morphological Processing

After the image binarization, the gear and background will be separated. As shown in Fig.3(b), the white represents the gear and the black represents the background. According to the analysis of binary image, because of the holes in gear, it needs to fill in the holes by using filling algorithm.

A seed fill is an image processing operation where pixels in some region of an image are assigned a label. Often this is described as having the pixels change "color." As we will be filling on binary images, the color change is from black to white. A seed is a single pixel or a collection of pixels where the change is selected to begin. The seed is allowed to grow, under the constraint of a mask that limits the growth. The seed fill process ends when the seed has grown under the mask as far as possible. First of all, the binary image is read in and finished parameter initialization. From an inner point within the polygon region, in all cases that we consider, seed fill works by a growing process that is constrained by a mask image. These are called 4-connected and 8-connected seed filling, and they fill into 4-connected and 8-connected regions of the mask, respectively. So doing it repeatedly until the scan is completed on the whole image. The image after that is shown in Fig.3(c).

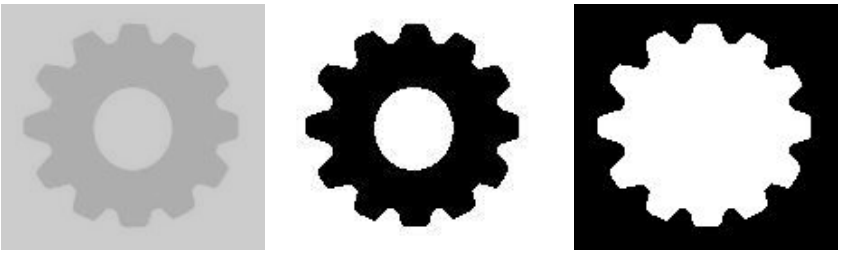

(a) Source image (b) Binary image (c) Holes filled image

Fig. 3. Morphological processing

3.3 Determination of Gear Center

As a benchmark of other gear parameters, the accuracy of gear center is directly related to measurement accuracy. The method used in this paper is:

(1) Read in the binary image.
(2) Take the gear in binary image as the target, record the coordinates on gear.
(3) Obtain the coordinates of minimum polygon which containing the gear.
(4) Draw the convex polygon according to coordinates and display it.
(5) To the coordinates, using the least squares curve fitting method for a circular.
(6) Determine the circle center(x_0, y_0) and radius r.

As shown in following figures, Fig.4(a) is the minimum polygon which contains the gear, and the fitting circle is shown in Fig4.(b).

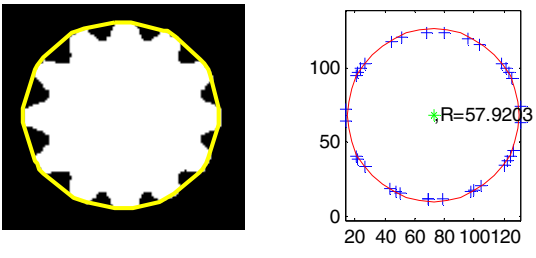

(a) Polygon (b) Fitted circle

Fig. 4. The determination of gear center

3.4 Gear Teeth Measurement

After the gear center is established, another very important parameter is the gear teeth. The measurement methods can be described as:

(1) Read in image and finish initialization.
(2) Set morphology structure element.
(3) Conduct erosion operation and obtain a new image.
(4) Subtract the source image from erosion image and obtain the gear teeth image.
(5)Analyze the teeth image, and the region number will be the gear teeth number.

The gear teeth image is show in Fig.5.

(a) Eroded image (b) Gear teeth image

Fig. 5. The acquisition of gear teeth image

3.5 Calculation of Rest Parameters

After determining the gear center, the other parameters can obtain based on the geometry relationships.

Root circle radius r_f : We take the maximum size of center hole as radius, then seek for the distance which is the nearest to gear center. The tooth root radius can be defined as r_f .

Modulus m : According to the formula:

$$m = (d_a + d_f) / 2Z \tag{2}$$

Then, we compared the calculated modulus with the standard modulus table, by using the nearest method to judge the final modulus of this gear.

4 Experiment Analysis

In order to verify the effectiveness of the algorithm, we have developed a system according to what have been discussed above. The tested images are all collected from scene. After calibration, Tab.1 shows some experimental results by using mechanical caliper.

Table 1. Experiment results

Parameters	number	Top circle radius (mm)	Root circle radius(mm)	Modulus
Artificial	12	7.01	5.02	1
Computer	12	6.94	5.04	1

From the experimental results above, it can be seen that this method has good performance; it can separate the gear from the background and is able to realize accurate parameter analyzing.

5 Conclusion

This paper has designed a gear parameters measurement system based on machine vision, which described the working principle and methods in detail. It acquires the gear image through the digital camera, translates the signals to digital information and sends them to computer by image acquisition card. The computer can realize the parameters analyzing based on image processing. A significant advantage of this method is non-contact. Experiments show that this method is easy to implement and has importance in production. It not only can be applied in the gear analyzing but also can be used in the fields of biology. Meanwhile, it provides a reference to other research fields.

Acknowledgments

This work has been supported partly by Natural Science Foundation of Weifang University (2008K17) and Shandong Provincial Natural Science Foundation (Z2007F08).

References

1. Hong, H.T., Zhao, H.: Study on the Imaging Technology for Object Measuring. Chinese Journal of Scientific Instrument 22(3), 213–218 (2001)
2. Zhang, S.J., Gou, Z.K., Li, Q.L., et al.: Digital image processing technology for spur gear measurement. Optics and Precision Engineering 12(6), 621–623 (2004)
3. Ni, Z.S., Xing, J.S.: Computer vision technology in gear measurement applied research. Microcomputer Information 23(3), 123–125 (2007)
4. Zhao, X., Mao, J.D.: Measurement of the Gear Involute-error Based on Image Processing Method. Machine Tool & Ydraul Ics 37(6), 124–128 (2009)
5. Chen, X.W., Wang, L.S., Liu, Q.M., et al.: Research on Measuring System for Gear Parameters based on CCD. Tool Engineering 38(5), 44–46 (2004)

Research on Audio-Visual Asynchronous Correlation for Speaker Identification Based on DBN

Yanxiang Chen

School of Computer Science & Information, Hefei University of Technology,
Hefei, Anhui, 230009, China
hfutchenyx716@hotmail.com

Abstract. In noisy or other adverse conditions, consistently high speaker identification accuracy is difficult to attain via speech signal, hence visual component which can complement audio information is of particular interest. In this paper, we capture the asynchronous correlation instead of tight synchrony between audio and visual modalities. Furthermore, the apparent asynchrony between the two modalities is effectively modeled based on Dynamic Bayesian Network (DBN) with asynchronous articulatory feature in three ways: (1) there are three hidden state variables, each representing one articulatory feature, (2) the degree of asynchrony among articulatory features is controlled by probability distribution, (3) the audio and video observations depend on all three hidden state variables. Then a multi-level hybrid fusion is explored to combine model-level and decision-level fusion. The experiment results for audio-visual bimodal corpus show that the effectiveness of the method.

Keywords: Asynchronous correlation, speaker identification, Dynamic Bayesian Network.

1 Introduction

While the audio is a major source of speech information, the visual component is considered to be a valuable supplementary information source in noisy environments because it remains unaffected by acoustic noise. Motivated by the audio-visual correlation, many models have been proposed such as multi-stream hidden Markov model which assumes the audio and video sequences are state synchronous [1]. However, the audible and visible correlates may be asynchronous, e.g., the visual speech usually leads the audio speech by duration about 120ms. For this reason, the system allowing the observed audio-visual asynchrony outperforms that allowing no such asynchrony. The most common model is coupled hidden Markov model (CHMM) [2] in which the audio and video observations are separately recognized by audio and video HMMs with coupled transition probability matrices.

In the articulatory phonology representation, it is not the audio and video streams that are asynchronous; rather, asynchrony exists among the different articulators [3]. Karen Livescu's group has applied articulatory feature-based model in speech recognition and achieved considerable results [4]. No literature has been found using asynchrony among the different articulators for speaker identification, whose task is to

D. Zeng (Ed.): Future Intelligent Information Systems, LNEE 86, pp. 15–21.
springerlink.com © Springer-Verlag Berlin Heidelberg 2011

determine the identity of a speaker given his/her utterances. In this paper we propose an articulatory feature-based audio-visual model (AFAVM) for speaker identification, which is realized by the Dynamic Bayesian Network (DBN). We also explore the fusion of audio and visual evidences through a multi-level hybrid fusion based on DBN, which combines model-level and decision-level fusion to achieve higher performance.

In the next section, the correlation based on the asynchronous articulatory feature is proposed. The multi-level fusion scheme for combining the advantages of model fusion and decision fusion is then presented in Section 3, followed by experiments and results in Section 4. This paper is concluded in Section 5.

2 Correlation Based on Asynchronous Articulatory Feature

The theory of articulatory phonology provides a new way of thinking about asynchrony. Specifically, we propose that the apparent asynchrony between acoustic and visual modalities may be caused by the inter-articulator asynchrony.

2.1 Articulatory Feature Sets

In the theory of Articulatory Phonology, the following 8 tract variables are independently and asynchronously controlled: LIP-LOC (lip location), LIP-OP (lip opening), TT (Tongue Tip) -LOC, TT-OP, TB (Tongue Body) -LOC, TB-OP, GLOTTIS, VELUM [3]. The lexical entry for each word is composed of loosely ordered, indivisible mental constructs called "gestures". Karen Livescu's group has described the tract variables and corresponding gestures in detail [4]. Under some simplifying assumptions (e.g. LIP-LOC and LIP-OP are always synchronized), we collapse these into 3 articulatory feature sets: lips, tongue, and glottis.

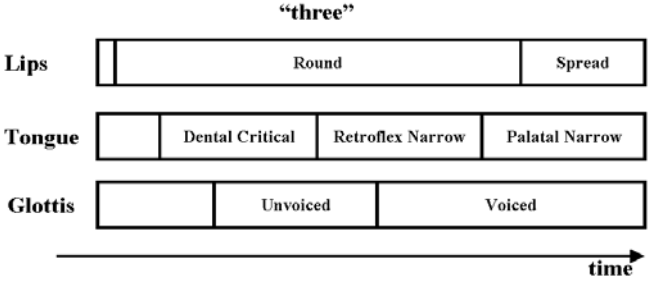

Fig. 1. Articulatory phonology-based interpretation of word three

Fig. 1 depicts an articulatory phonology-based interpretation of the production of word "three." At one instant excised from the silence preceding the word "three", the talker's tongue tip is already in position for the first phone /θ/ (the gesture of tongue corresponds to "Dental Critical"), but the audio signal is still silent, because her lungs have not yet started to push air through the vocal tract (the gesture of glottis corresponds to "Silent"). The phone /θ/ has no required lip position, so the lips have

already rounded in anticipation of the second phone /r/ (the gesture of lips corresponds to "Round").

At this instant, the audio and video modalities may be said to be "asynchronous:" the audio observation is still characteristic of silence, but the video modality exhibits a blend of the phones /θ/ and /r/. In the articulatory phonology representation, the audio-visual asynchrony may be the result of asynchrony among the gestures implemented by different articulators, such that the most visibly salient articulator (e.g., the lips) and the most audibly salient articulator (e.g., the glottis) may, at any given time, be dominated by gestures associated with different phones.

2.2 Articulatory Feature-Based Audio-Visual Model (AFAVM)

Dynamic Bayesian networks are a class of Bayesian networks designed to model temporal processes as stochastic evolution of a set of random variables over time [5]. A DBN is a directed acyclic graph whose topology structure can be easily configured to describe various relations among variables. Tailored to our needs of speaker identification, we propose the AFAVM (articulatory feature-based audio-visual model) based on DBN as depicted in Fig. 2.

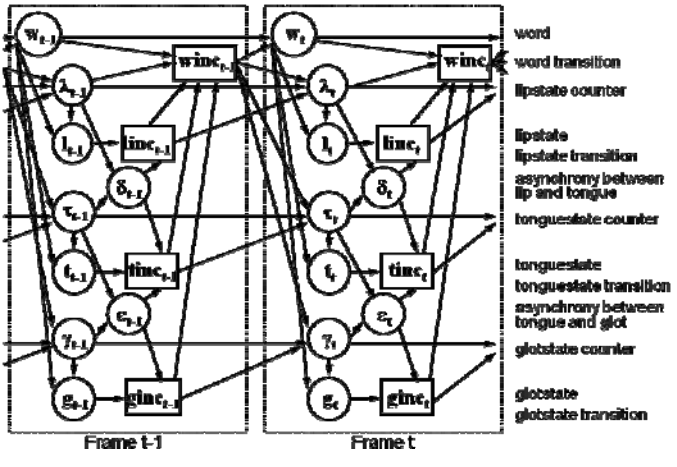

Fig. 2. Articulatory feature-based audio-visual model (AFAVM) based on DBN

First, there are three phone-like hidden variables: l_t, the lipstate, specifies the current lip configuration, and depends on the lipstate counter λ_t. t_t, the tonguestate, specifies the current tongue configuration, and depends on the tonguestate counter τ_t. g_t, the glotstate, specifies the current state of the glottis, velum, and lungs, and depends on the glotstate counter γ_t. In Fig. 2, $\lambda_t, \tau_t, \gamma_t$ are counters indexing how far along we are in the current word. For example, γ_t is the position of glotstate g_t in word w_t. The probability distribution $P(\gamma_t \mid \gamma_{t-1}, ginc_{t-1}, winc_{t-1})$ has an extremely limited form. γ_t is always equal to γ_{t-1} unless there is a glotstate transition or a word

transition. If there is a word transition ($winc_{t-1}=1$), γ_t is reset to $\gamma_t=1$. If there is a glotstate transition but no word transition ($winc_{t-1}=0, ginc_{t-1}=1$), then $\gamma_t=\gamma_{t-1}+1$.

Second, asynchrony between the counters is measured using three asynchrony variables, of which two are shown in the figure: $\delta_t=|\lambda_t-\tau_t|$, and $\varepsilon_t=|\tau_t-\gamma_t|$. For example, δ_t is a variable whose value corresponds to the current "degree of asynchrony" between the lip and tongue, defined as the absolute difference between lipstate counter and tonguestate counter. Its distribution encodes the probability of the lip and tongue desynchronizing by a given amount. A maximum degree of allowed asynchrony δ_{max} is imposed by setting 0 to the probability of $\delta_t=a$ for any $a>\delta_{max}$, i.e. $P(\delta_t=a\mid a>\delta_{max})=0$. In our experiments, we allowed $\delta_{max}=2$ and δ_t had non-zero probability only for the values 0, 1 and 2. Then δ_t enforces constraints on lipstate transition $linc_t$ ($linc_{t-1}=1$, if the current frame ends the current lipstate) and tonguestate transition $tinc_t$ to control the degree of asynchrony between the lip and tongue.

Third, the audio and video observations, $\boldsymbol{x}_t$ and $\boldsymbol{y}_t$ depend on all three hidden state variables. Fig. 2 does not show $\boldsymbol{x}_t$ and $\boldsymbol{y}_t$ because space is limited, but the forms of their probability density functions are as follows. $\boldsymbol{x}_t$ depends on all three articulators, $P(\boldsymbol{x}_t\mid l_t,t_t,g_t)$ is modeled using a mixture Gaussian PDF. $\boldsymbol{y}_t$ depends on the states of the lips and tongue, and $P(\boldsymbol{y}_t\mid l_t,t_t)$ is modeled using a mixture Gaussian, the glottis/velum state variable g_t is assumed to have no visual correlates.

3 Multi-level Audio Visual Fusion

In view of the advantages of model fusion and decision fusion, we proposed a multi-level fusion strategy via DBN. There are three models altogether: the audio-only model, the video-only model and the AFAVM model that performs model-based audio-video fusion. These three models are further combined by means of decision-level fusion to deliver the final speaker identification result. Decision-level fusion for the three models is also achieved through the use of DBN, by virtue of its extensibility.

Equation 1 shows the mathematical formula we use for multi-level fusion:

$$P(\boldsymbol{O}_A,\boldsymbol{O}_V\mid M_A,M_V,M_{AV})=[P(\boldsymbol{O}_A\mid M_A)]^{\lambda_A}\cdot[P(\boldsymbol{O}_V\mid M_V)]^{\lambda_V}\cdot[P(\boldsymbol{O}_A,\boldsymbol{O}_V\mid M_{AV})]^{\lambda_{AV}} \quad (1)$$

where $P(\boldsymbol{O}_A\mid M_A)$ is the recognition formula for audio-only model M_A of audio observation $\boldsymbol{O}_A$, and $P(\boldsymbol{O}_V\mid M_V)$ is the formula for video-only model M_V of video observation $\boldsymbol{O}_V$, and $P(\boldsymbol{O}_A,\boldsymbol{O}_V\mid M_{AV})$ is the formula for model M_{AV} .

λ_A , λ_V and λ_{AV} are stream exponents (fusion weights) for audio-only, video-only and AFAVM model, which encode the relative reliability of the models and can be

varied according to ambient noise conditions (i.e. SNR). For example, when SNR is low, the reliability of the audio-only and AFAVM models degrade, hence the video-only model should carry the highest weight. We enforce the parameter constraints of $\lambda_A + \lambda_V + \lambda_{AV} = 1$, $\lambda_A = \lambda_{AV}$, and $\lambda_A, \lambda_V, \lambda_{AV} \geq 0$, then we use the method of support vector regression (SVR) to estimate the fusion weights. The proposed multi-level fusion strategy combines the advantages of model fusion and decision fusion and has the potential of achieving performance improvement.

4 Experiments

The experiments are conducted on the audio-visual bimodal database from Carnegie Mellon University (CMU database) [6]. It includes 10 subjects (7 males and 3 females) speaking 78 isolated words repeated 10 times.

The acoustic front-end includes 13 Mel frequency cepstral coefficients (MFCCs) and 1 energy parameter (with frame window size of 25ms and frame shift of 11ms) together with their delta parameters. Hence the audio feature vector has 28 dimensions. The visual front-end includes mouth width, upper lip height, lower lip height and their delta parameters. Thus the visual feature vector has 6 dimensions. The video frame rate is 30 frames per second (fps), which is up-sampled to 90fps (11ms) by copying and inserting two frames between each two original video frames.

We perform the text-prompted speaker identification experiments to evaluate the performance of various models including audio-only, video-only, coupled HMM (CHMM), AFAVM and multi-level fusion. The CHMM-based system uses 5 states to model the audio channel and 3 states for the visual channel, each state using a 3-mixture Gaussian PDF. In the AFAVM-based system, each of the three variables (lipstate, tonguestate and glotstate) is modeled with 3 states and each state uses a 2-mixture Gaussian PDF. During speaker identification, a DBN is developed for each word and the DBNs of words are connected to form a whole sentence model, which is used to identify the speakers. The DBNs are implemented using the graphical modeling toolkit (GMTK) [7].

Artificial white Gaussian noise was added to the original audio data (SNR=30dB) to simulate various SNR levels. The models were trained at 30dB SNR and tested under SNR levels ranging from 0dB to 30dB at 10dB intervals. A cross-validation scheme was used, i.e. 90% of all the data are used as training set, and the remaining 10% as testing set. This process was repeated until all data had been covered in testing.

Table 1. Accuracies (%) of speaker identification under different SNR

Audio signal-noise-ratio (SNR)	30dB	20dB	10dB	0dB
Audio-only	100	64	22	17
Video-only	77	77	77	77
CHMM	100	90	78	60
AFAVM	100	92	80	65
Multi-level fusion	100	93	82	79

The identification accuracies from all the testing data are averaged and reported as the final result. The results on CMU database are summarized in Table 1. Main observations include:

(1) The accuracy of audio-only system is very low when SNR≤10dB. The accuracy of visual-only system is not affected by any additional noise during testing. Both of the bimodal systems demonstrate improved noise robustness in comparison to audio-only system.

(2) The AFAVM model proposed in this paper has higher accuracy than CHMM, especially in low SNR level, because it effectively describes the apparent asynchrony between acoustic and visual modalities as asynchrony among the articulatory gestures implemented by the lips, tongue, and glottis.

(3) Because of the misalignment during model training, when SNR<10dB, the performance of the AFAVM and CHMM degrades and the accuracy is even lower than the video-only model.

(4) The audio-visual multi-level fusion strategy has solved the problem in (3) well. Best identification performance is obtained even when SNR=0dB. It can also be seen that better results are also obtained when SNR is 10dB and 20dB than the AFAVM model. This is because that the multi-level fusion strategy combines the results from audio-only, video-only and AFAVM model, and the results of audio and video model are supplementary to that of AFAVM.

5 Conclusion

Asynchrony among different articulators provides a powerful method for representing the audio-visual asynchrony and the multi-level fusion combines the advantages of model fusion and decision fusion to achieve performance improvement. We have presented a framework using articulatory feature-based audio-visual model (AFAVM) based on DBN for speaker identification and have achieved considerable results in the experiments on the audio-visual bimodal CMU database.

Acknowledgments

We wish to acknowledge support by the National Programs for Fundamental Research and Development (973) of China (No. 2009CB326203).

References

1. Neti, C., Potamianos, G.: Audio visual speech recognition. In: Final report: JHU 2000 Summer Workshop (2000)
2. Chu, S.M., Huang, T.S.: Multi-model sensory fusion with application to audio-visual speech recognition. In: Proceedings of European Conference on Speech Communication and Technology (Eurospeech), Aalborg, Denmark (2001)
3. Browman, C.P., Goldstein, L.: Articulatory phonology: An overview. Phonetica 49, 155–180 (1992)

4. Livescu, K., Cetin, O.: Articulatory Feature-based methods for acoustic and audio-visual speech recognition. In: Final report: JHU 2006 Summer Workshop (2006)
5. Zhang, Y., Diao, Q.: DBN based multi-stream models for speech. In: Proceedings of the International Conference on Acoustic, Speech and Signal Processing (ICASSP), Hong Kong, China, pp. 836–839 (2003)
6. Chen, T.: Audiovisual speech processing. IEEE Transactions on Signal Processing 18(1), 9–21 (2001)
7. Bilmes, J., Zweig, G.: The graphical models toolkit: An open source software system for speech and time-series processing. In: Proceedings of the International Conference on Acoustic, Speech and Signal Processing (ICASSP), Florida, USA, pp. 3916–3919 (2002)

High Radix Montgomery Multipliers for Residue Arithmetic Channels on FPGAs

Yinan Kong

Department of Electronic Engineering, Macquarie University
North Ryde, NSW 2109, Australia
yinan.kong@mq.edu.au

Abstract. This work targets an efficient Montgomery Modular Multiplier for use in the channels of a Residue Number System (RNS). It is implemented on FPGA and optimized by attempting and evaluating the high radix techniques of the Montgomery Algorithm. The usual correction shift step at the end is proved to be infeasible. The resulting multiplier achieves 15ns for a modular multiplication using high radix without correction shift.

Keywords: Montgomery Modular Multiplication, the Residue Number System, FPGA, Digital Arithmetic, Public-Key Cryptosystems.

1 Introduction

The demand for high-speed computing continues to increase for Digital Signal Processing (DSP), multimedia applications and cryptosystems, and appropriate research activity grows at a similar rate. Residue Number System (RNS), as one of the efficient tools in meeting the demand, has long been a topic of interest to the DSP and Crypto community due to its applicability to Very Large Scale Integration (VLSI) System design [1, 2, 3].

It has been confirmed that speed and simplicity are the primary advantages of residue arithmetic [4]. This is because all arithmetic operations are performed on smaller residues instead simultaneously in all the modulo channels. Thus, speeding up the residue arithmetic is equivalent to speeding up the modular operations within the RNS channels.

The aim of this work is to produce a Montgomery Multiplier most suitable for a channel within a large RNS system with a dynamic range of 1024 bits, which is to be applied for a RSA cryptosystem [5]. The multiplier is implemented implementation on the FPGA technology by applying and testing the high radix techniques.

Different combinations of the radices and the final correction methods lead to various kinds of Montgomery Modular Multipliers and at least 20 versions of implementations can be obtained for comparison. Actually, some of them are obviously unsuitable for implementation on FPGA or use in a RNS channel and so can be ignored. The others need to be analyzed and compared thoroughly. This paper will discuss these in detail.

D. Zeng (Eds.): Future Intelligent Information Systems, LNEE 86, pp. 23–30.
springerlink.com © Springer-Verlag Berlin Heidelberg 2011

2 FPGA Specification

Target FPGA:	Virtex2 XC2V1000 with a -6 speed grade, 1M gates, 5120 slices and 40 embedded 18×18 multipliers
Xilinx 6.1i:	XST – Synthesis ISE – Place and Route
Optimization Goal:	Speed
Language:	VHDL

Virtex2 is an advanced version of the Xilinx FPGA and is remarkable for its incorporation of embedded hardware multipliers. Indeed, for this project, both VirtexE and Virtex2 were tried and the latter has obvious speed advantage over the former for our application.

The XC2V1000 version was chosen because it has 5120 slices and 40 18×18 multipliers and this is more than enough to implement a modular multiplier for a RNS channel.

Both high and normal optimization effort were used for all the implementations. No significant difference was found in the results.

Pure delays of the combinatorial circuit were measured excluding those between pads and pins. They were generated from the Post-Place & Route Static Timing Analyzer with a standard place & route effort level. This is because all the three Place & Route Effort Level options – "Standard", "Medium" and "High" – were tried for some cases and the results showed that the circuits generated with the "Standard" option exhibited less delay than circuits generated with the other two options.

3 The Residue Number System (RNS)

A Residue Number System [4] is characterized by a set of N co-prime moduli $\{m_1,\ldots,m_N\}$. In the RNS a non-negative integer X is represented in N channels: $X = \{x_1, x_2, \ldots, x_N\}$, where x_i is the residue of X with respect to m_i, i.e. $x_i = \langle X \rangle_{m_i} = X \bmod m_i$. n, the length of m_i, is denoted as the channel width of the RNS. Within the RNS there is a unique representation of all integers in the range $0 \le X < D$ where $D = m_1 m_2 \ldots m_N$. D is therefore known as the dynamic range of the RNS.

3.1 The Advantages of RNS

If A, B and C have RNS representations given by $A = \{a_1, a_2, \ldots, a_N\}$, $B = \{b_1, b_2, \ldots, b_N\}$ and $C = \{c_1, c_2, \ldots, c_N\}$, then denoting * to represent the operations +, – or ×, the RNS version of $C = A * B$ satisfies

$$C = \{\langle a_1 * b_1 \rangle_{m_1}, \langle a_2 * b_2 \rangle_{m_2}, \ldots, \langle a_N * b_N \rangle_{m_N}\}. \quad (1)$$

Thus addition, subtraction and multiplication can be concurrently performed on the N residues within N parallel channels, and it is this high speed parallel operation that makes RNS attractive [4], [6]. This paper is also trying to improve this operation to speed further up a RNS.

3.2 RNS Channel Width

RNS is being used to construct a 1024-bit RSA cryptosystem, whose encryption and decryption equations are in the same form, $X = A^B \bmod M$ [7]. This means that A, B and M are all 1024 bits. Because the product of two 1024-bit numbers is 2048 bits long, the dynamic range, D, of the RNS should be no smaller than 2048 bits to be wide enough to contain the product of 1024-bit multiplicands before modular reduction.

The smaller the RNS channel width n, the faster the computation within RNS and the more remarkably the advantage of RNS can be shown. Therefore, we want n as small as possible. On the other hand, suppose the N RNS moduli are $m_1, m_2, \ldots m_N$. If m_1 is 16 bits and m_2 is 64 bits long, the computation in the m_2 channel will be much slower than in the m_1 channel. Thus, it is better if the N moduli are of the same wordlength. This means the dynamic range D of the RNS system is evenly distributed into the N moduli. The remaining work is to make sure N coprime n-bit moduli exist.

For example, suppose $n = 8$. Then there should be $N = \lceil 2048/8 \rceil = 256$ channels, i.e. 256 coprime numbers have to be found within the range from $2^7 = 128$ to $2^8\text{-}1 = 255$, inclusive. This is obviously impossible since there are only 128 integers from 128 to 255. Then, if $n = 9$, $N = \lceil 2048/9 \rceil = 228$, i.e. 228 coprime moduli must be found within the range from $2^8 = 256$ to $2^9\text{-}1 = 511$, inclusive. Because there are only 128 odd integers from 256 to 511, it is impossible to find 228 coprime numbers. Now, $n = 10$. $N = \lceil 2048/10 \rceil = 205$ channels and these 205 coprime moduli should be within the range from $2^9 = 512$ to $2^{10}\text{-}1 = 1023$, inclusive. However, according to our search algorithm, there are only 79 coprime numbers among the 256 odd numbers within [512, 1023], so $n = 10$ is invalid. Similarly when $n = 11$. For the case of $n = 12$, a set of 259 coprime numbers have been found within $[2^{11}, 2^{12}\text{-}1] = [2048, 4095]$. This is enough for the requirement of the number of moduli, $N = \lceil 2048/12 \rceil = 171$.

Consequently, to construct a RNS system with 2048-bit dynamic range D and moduli of equal wordlength, the channel width n should be at least 12 bits.

4 The Montgomery Modular Multiplication Algorithm

The Montgomery Modular Multiplication uses Montgomery Algorithm [8] for modular reduction. Suppose C is the $2n$-bit product of $A \times B$, the Montgomery Modular Reduction algorithm MR(C) calculates $MR(C) = C \times 2^{-n} \bmod M$.

In a higher radix version [9], $C \times r^{-l} \bmod M$ is first calculated as

$$\begin{aligned} & C \times r^{-l} \bmod M \\ &= (.....((Cr^{-1})r^{-1})r^{-1}.....)r^{-1} \bmod M \\ &= (.....((C + q_0 M)/r) + q_1 M)/r) + q_2 M)/r + ... + q_{l-1} M)/r \bmod M \end{aligned}$$

Then, the Correct(C_l) is used to adjust it to $C \times 2^{-n} \bmod M$.

The algorithm is listed as the following pseudo code:

$C_0 = A \times B$;
for $i = 0$ to l-1
$q_i = C_i \times (-M_0^{-1}) \bmod r$
$C_{i+1} = (C_i + q_i M)/r$
next i
Correct(C_l)

Fig. 1. The Montgomery Modular Multiplication Algorithm

5 Radix Selection and Additional Correction for Higher Radix

Radix can be selected as 2 or a power of 2. We use r to denote the radix, and $r = 2^k$, $k = 0, 1, 2, \ldots$. Consider the Montgomery Modular Multiplier in Figure 1. The product C yet to be reduced modular M is $2n$ bits and M is n bits long.

5.1 Radix-2

If $k = 1$, i.e. $r = 2$, then there are $l = n$ iterations. Exactly one bit is reduced in each iteration since the least significant bit of the current C_i is made 0 by adding $q_i M$. Finally n bits of C are reduced, and $C \times 2^{-n} \bmod M$ is generated at the end as C_n. Figure 2 illustrates the process for the case of $n = 8$. To show the reducing process more clearly, assume there is no wordlength growth on the partially reduced results C_i. However, this is impossible and the boundary of the growth will be calculated in next section.

5.2 Higher Radix

If $k > 1$, i.e. $r > 2$, then there is 1 digit, i.e. k bits to be reduced in each iteration. For example, if $k = 2$, i.e. radix-4, according to the Montgomery Modular Reduction Algorithm in Figure 1, 2 bits will be reduced in one iteration [10], and there will be $l = 8/2 = 4$ iterations in the case of $n = 8$. This reduction process is illustrated in Figure 3 with the assumption that no wordlength grows during it. However, if n is not divisible by k in some cases, the number of iterations l can be $\lceil n/k \rceil$ or $\lfloor n/k \rfloor$ with some additional correction steps after l iterations. This is just what the function Correct(C_l) does in Figure 1. Take $n = 8$ and $k = 3$ as an example, where 1 digit equals 3 bits and hence, 3 bits are reduced in each iteration.

If $l = \lceil n/k \rceil = \lceil 8/3 \rceil = 3$, 9 bits will be reduced and the result is $C \times 2^{-9} \bmod M$ instead of $C \times 2^{-8} \bmod M$. Then $C \times 2^{-9} \bmod M$ is multiplied by 2 in the correction step to obtain the correct answer. This is shown in Figure 4.

If $l = \lfloor n/k \rfloor = \lfloor 8/3 \rfloor = 2$, 6 bits will be reduced and the result is $C \times 2^{-6} \bmod M$. Then $C \times 2^{-6} \bmod M$ is further reduced to $C \times 2^{-8} \bmod M$ either by two additional radix-2 iterations or one radix-4 iteration. This is shown in Figure 5 with one radix-4 iteration added at the end as a correction step.

Bits	16	15	14	13	12	11	10	9	8	7	6	5	4	3	2	1	0
C_0		*	*	*	*	*	*	*	*	*	*	*	*	*	*	*	*
q_0M										*	*	*	*	*	*	*	*
$C_0 + q_0M$		*	*	*	*	*	*	*	*	*	*	*	*	*	*	*	0
C_1			*	*	*	*	*	*	*	*	*	*	*	*	*	*	*
q_1M										*	*	*	*	*	*	*	*
$C_1 + q_1M$			*	*	*	*	*	*	*	*	*	*	*	*	*	*	0
C_2				*	*	*	*	*	*	*	*	*	*	*	*	*	*
q_2M										*	*	*	*	*	*	*	*
$C_2 + q_2M$				*	*	*	*	*	*	*	*	*	*	*	*	*	0
C_3					*	*	*	*	*	*	*	*	*	*	*	*	*
q_3M										*	*	*	*	*	*	*	*
$C_3 + q_3M$					*	*	*	*	*	*	*	*	*	*	*	*	0
C_4						*	*	*	*	*	*	*	*	*	*	*	*
q_4M										*	*	*	*	*	*	*	*
$C_4 + q_4M$						*	*	*	*	*	*	*	*	*	*	*	0
C_5							*	*	*	*	*	*	*	*	*	*	*
q_5M										*	*	*	*	*	*	*	*
$C_5 + q_5M$							*	*	*	*	*	*	*	*	*	*	0
C_6								*	*	*	*	*	*	*	*	*	*
q_6M										*	*	*	*	*	*	*	*
$C_6 + q_6M$								*	*	*	*	*	*	*	*	*	0
C_7									*	*	*	*	*	*	*	*	*
q_7M										*	*	*	*	*	*	*	*
$C_7 + q_7M$									*	*	*	*	*	*	*	*	0
$C_8 = C_0 \times 2^{-8} \bmod M$										*	*	*	*	*	*	*	*

Fig. 2. Montgomery Modular Reduction Process at Radix-2

If $l = \lfloor n/k \rfloor = \lfloor 8/3 \rfloor = 2$, 6 bits will be reduced and the result is $C \times 2^{-6} \bmod M$. Then $C \times 2^{-6} \bmod M$ is further reduced to $C \times 2^{-8} \bmod M$ either by two additional radix-2 iterations or one radix-4 iteration. This is shown in Figure 5 with one radix-4 iteration added at the end as a correction step.

Bits	16	15	14	13	12	11	10	9	8	7	6	5	4	3	2	1	0
C_0		*	*	*	*	*	*	*	*	*	*	*	*	*	*	*	*
q_0M											*	*	*	*	*	*	*
$C_0 + q_0M$		*	*	*	*	*	*	*	*	*	*	*	*	*	*	0	0
C_1				*	*	*	*	*	*	*	*	*	*	*	*	*	*
q_1M											*	*	*	*	*	*	*
$C_1 + q_1M$				*	*	*	*	*	*	*	*	*	*	*	*	0	0
C_2						*	*	*	*	*	*	*	*	*	*	*	*
q_2M											*	*	*	*	*	*	*
$C_2 + q_2M$						*	*	*	*	*	*	*	*	*	*	0	0
C_3								*	*	*	*	*	*	*	*	*	*
q_3M											*	*	*	*	*	*	*
$C_3 + q_3M$								*	*	*	*	*	*	*	*	0	0
$C_4 = C_0 \times r^{-4} \bmod M$											*	*	*	*	*	*	*
$= C_0 \times 2^{-8} \bmod M$																	

Fig. 3. Montgomery Modular Reduction Process at Radix-4

Bits	16	15	14	13	12	11	10	9	8	7	6	5	4	3	2	1	0
C_0		*	*	*	*	*	*	*	*	*	*	*	*	*	*	*	*
q_0M											*	*	*	*	*	*	*
$C_0 + q_0M$		*	*	*	*	*	*	*	*	*	*	*	*	*	0	0	0
C_1					*	*	*	*	*	*	*	*	*	*	*	*	*
q_1M											*	*	*	*	*	*	*
$C_1 + q_1M$					*	*	*	*	*	*	*	*	*	*	0	0	0
C_2								*	*	*	*	*	*	*	*	*	*
q_2M											*	*	*	*	*	*	*
$C_2 + q_2M$								*	*	*	*	*	*	*	0	0	0
$C_3 = C_0 \times r^{-3} \bmod M$												*	*	*	*	*	*
$= C_0 \times 2^{-9} \bmod M$																	
Corrected $C_3 = 2 \times C_0 \times 2^{-9} \bmod M$											*	*	*	*	*	*	0
$= C_0 \times 2^{-8} \bmod M$																	

Fig. 4. Montgomery Modular Reduction Process at Radix-8 ($l = \lceil n/k \rceil$)

For these two methods, $l = \lfloor n/k \rfloor$ is better because the result from $l = \lceil n/k \rceil$ is likely not to be fully reduced. Therefore, the version of $l = \lfloor n/k \rfloor$ iterations is adopted in the final algorithm with one n mod k correction step added at the end when n is not divisible by k.

Bits	16	15	14	13	12	11	10	9	8	7	6	5	4	3	2	1	0
C_0		*	*	*	*	*	*	*	*	*	*	*	*	*	*	*	*
q_0M										*	*	*	*	*	*	*	*
$C_0 + q_0M$	*	*	*	*	*	*	*	*	*	*	*	*	*	*	0	0	0
C_1				*	*	*	*	*	*	*	*	*	*	*	*	*	*
q_1M										*	*	*	*	*	*	*	*
$C_1 + q_1M$				*	*	*	*	*	*	*	*	*	*	*	0	0	0
C_2								*	*	*	*	*	*	*	*	*	*
q_2M										*	*	*	*	*	*	*	*
$C_2 + q_2M$								*	*	*	*	*	*	*	*	0	0
Corrected $C_2 = C_0 \times 2^{-8} \bmod M$										*	*	*	*	*	*	*	*

Fig. 5. Montgomery Modular Reduction Process at Radix-8 ($l = \lfloor n/k \rfloor$)

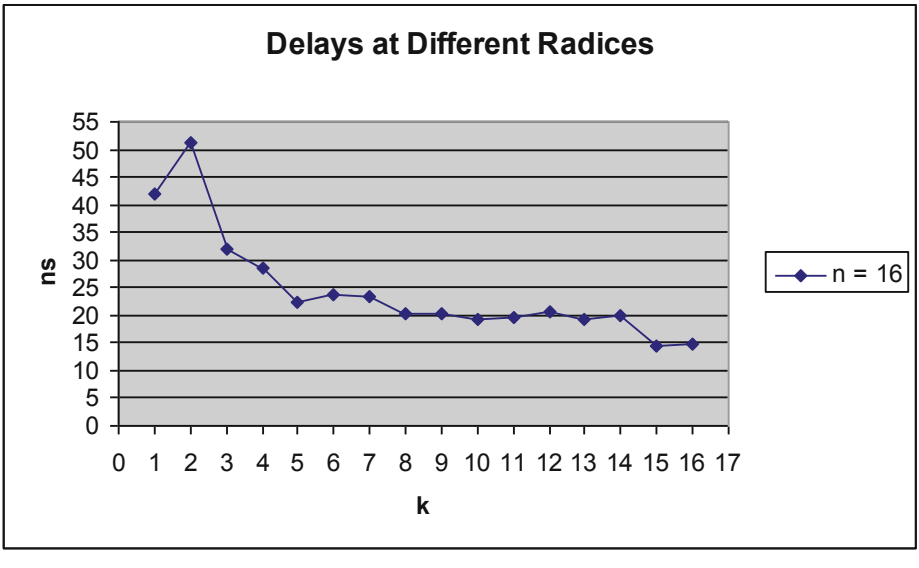

Fig. 6. Delays of Montgomery Modular Multipliers at Different Radices

Now the performance of the multipliers using different radices are compared in Figure 6. $n = 16$ is chosen here, which is greater than 12 bits, the lower bound of n derived above. The version of $l = \lfloor n/k \rfloor$ iterations is used with one correction step of n mod k added at the end when n is not divisible by k.

As can be seen from Figure 6, the higher the radix $r = 2^k$, the faster the modular multiplier runs, especially when k becomes close to the wordlength n. Therefore, the radix is often selected to be as high as possible under the condition of real applications. Note that this is consistent with the results from the literature which used different methods to arrive at similar conclusions [11, 12].

7 Conclusions and Future Work

All the discussions above are to find a fast high radix Montgomery Modular Multiplier. Finally, we recommended a Montgomery Modular Multiplier using high radix without correction shift.

For future work, more techniques on Montgomery algorithm, e.g. Trivial Quotient Digit Selection, Quotient Pipelining and Interleaved Structures are to be investigated. The bounds of inputs and outputs are to be determined. Also, the constraints of very high radix will be further studied.

References

1. Omondi, A., Premkumar, B.: Residue Number Systems – Theory and Implementation, ser. Advances in Computer Science and Engineering: Texts, vol. 2. Imperial College Press, UK (2007)
2. Barraclough, S.R.: The Design and Implementation of the IMS A110 Image and Signal Processor. In: Proc. IEEE CICC, San Diego, pp. 24.5/1-4 (1989)
3. Bajard, J.C., Imbert, L.: A full RNS implementation of RSA. IEEE Trans. Comput. 53(6) (June 2004)
4. Parhami, B.: Computer Arithmetic – Algorithms and Hard-ware Designs. Oxford University Press, Oxford (2000)
5. Rivest, R.L., Shamir, A., Adleman, L.M.: A method for obtaining digital signatures and public-key cryptosystems. Communications of the ACM 21(2), 120–126 (1978)
6. Soderstrand, M.A., Jenkins, W., Jullien, G.: Residue number system arithmetic: Modern applications. Digital Signal Processing (1986)
7. Shand, M., Vuillemin, J.: Fast Implementations of RSA Cryptography. In: Proceedings 11th IEEE Symposium on Computer Arithmetic, pp. 252–259. IEEE Computer Society Press, Los Alamitos (1993)
8. Montgomery, P.L.: Modular multiplication without trial division. Mathematics of Computation 44(170), 519–521 (1985)
9. Walter, C.D.: Still faster modular multiplication. Electronics Letters 31(4), 263–264 (1995)
10. Takagi, N.: A Radix-4 Modular Multiplication Hardware Algorithm for Modular Exponentiation. IEEE Transactions on Computers 41(8), 949–956 (1992)
11. Kouretas, I., Paliouras, V.: A low-complexity high-radix RNS multiplier. IEEE Transactions on Circuits and Systems Part I 56(11), 2449–2462 (2009)
12. Orup, H.: Simplifying quotient determination in high-radix modular multiplication. In: Proceedings of the 12th IEEE Symposium on Computer Arithmetic, pp. 193–199 (1995)

Dual-Threshold CMOS Technique for Pass-Transistor Adiabatic Logic with PMOS Pull-Up Configuration

Haiyan Ni, Lifang Ye, and Jianping Hu

Faculty of Information Science and Technology, Ningbo University
315211 Ningbo City, China
nbhjp@yahoo.com.cn

Abstract. DTCMOS (Dual-threshold CMOS) has been proven as an effective way to reduce sub-threshold leakage consumption. P-type logic circuits that consist mostly of PMOS transistors can significantly reduce the gate leakage dissipations in nanometer CMOS processes with gate oxide structure. This paper proposes a dual-threshold CMOS scheme for PAL-2P (pass-transistor adiabatic logic with PMOS pull-up configuration) circuits. An s27 benchmark circuit from the ISCAS89 sequential benchmark set is verified using the DTCMOS PAL-2P circuits. All circuits are verified with HSPICE using the 65nm CMOS process with gate oxide materials. The PAL-2P circuits using DTCMOS (dual-threshold CMOS) technique exhibit large energy savings, since both sub-threshold and gate leakage dissipations are reduced effetely.

Keywords: Nano-circuits, DTCMOS, P-type logic, Pass-transistor adiabatic logic with NMOS pull-down configuration, Leakage reduction.

1 Introduction

In the past, dynamic energy loss has always dominated total power dissipation, while leakage power is small and can be ignored [1]. When CMOS scales down into 100nm, leakage consumption increases faster than dynamic power and is becoming a dominated factor in total power consumptions. There are different mechanisms that contribute to leakage power, which include mainly sub-threshold leakage and gate leakage, etc. [2].

If the gate oxide thickness is less than 20˚A, the gate leakage would be an important component in total leakage dissipations. Therefore, in 45-nm generation and beyond, the high-k metal gate silicon technology is applied to reduce the gate leakage current. However, the gate leakage issue still exists in the 90-nm and 65-nm technologies that are currently used in production without the high-k metal gate silicon structure. Based on the basis that PMOS devices exhibit lower gate leakage compared to NMOS devices, P-type logic circuits that consist mostly of PMOS transistors have been proposed to reduce gate leakage dissipations [3].

Dual threshold CMOS (DTCMOS) technique has proved to be a very effective method for reducing sub-threshold leakage [4]. A higher threshold voltage can be assigned to some transistors on non-critical paths to reduce sub-threshold leakage current, while the performance is maintained due to low threshold transistors in the

D. Zeng (Ed.): Future Intelligent Information Systems, LNEE 86, pp. 31–38.
springerlink.com © Springer-Verlag Berlin Heidelberg 2011

critical paths. Therefore, no additional transistors are required, and both high performance and low power can be achieved simultaneously.

Adiabatic logic circuits utilize AC voltage supplies (power-clocks) to recycle the energy of circuits, and thus their dynamitic energy dissipations are reduced effetely [5]. However, there also exist leakage dissipations in nano-scale adiabatic circuits similar to the traditional CMOS circuits. Several DTCMOS techniques for adiabatic circuits have been reported in [6, 7]. In order to reduce gate leakage, P-type schemes for PAL-2N (pass-transistor adiabatic logic with NMOS pull-down configuration) [8], and CPAL (complementary pass-transistor adiabatic logic) [9] have also been addressed.

This paper proposes a dual-threshold CMOS scheme for PAL-2P (pass-transistor adiabatic logic with PMOS pull-up configuration) circuits. An s27 benchmark circuit from the ISCAS89 sequential benchmark set is verified using the DTCMOS PAL-2P scheme. All circuits are verified with HSPICE using the 65nm CMOS process with gate oxide materials. The PAL-2P circuits using DTCMOS technique exhibit large energy savings, since both sub-threshold and gate leakage dissipations are reduced effetely.

2 Leakage of MOS Transistors

Sub-threshold and gate oxide leakage currents are the main sources of leakage dissipations in recent CMOS processes. In current CMOS technologies, the sub-threshold leakage current, I_{SUB}, is larger than the other leakage current components. This is mainly because of the relatively low V_T (threshold voltage) in modern CMOS devices. I_{SUB} is calculated by using the following formula [2]

$$I_{\mathrm{SUB}} = \frac{W}{L}\mu V_{th}^2 C_{sth} \exp\left(\frac{V_{GS} - V_T + \eta V_{DS}}{nV_{\mathrm{th}}}\right)\left(1 - \exp\left(\frac{-V_{DS}}{V_{\mathrm{th}}}\right)\right), \tag{1}$$

where W and L denote the transistor width and length, μ denotes the carrier mobility, $V_{th}=kT/q$ is the thermal voltage at temperature T, $C_{sth}=C_{dep}+C_{it}$ denotes the summation of the depletion region capacitance and the interface trap capacitance both per unit area of the MOS gate, and η is the drain-induced barrier lowering (DIBL) coefficient. $n = 1+ C_{sth} / C_{ox}$ is the slope shape factor, where C_{ox} is the gate input capacitance per unit area of the MOS gate.

Clearly, increasing the threshold voltage can decrease the leakage current exponentially. In fact, increasing the threshold voltage by 100mV decreases the leakage current by a factor of 10 [3]. However, the large threshold voltage would reduce the operation speed of the circuits. Dual threshold CMOS technique uses some transistors with a higher threshold voltage on non-critical paths to reduce sub-threshold leakage currents, while the performance is maintained by using low threshold transistors in the critical paths. Therefore, both high performance and low power can be achieved simultaneously.

For gate leakage currents, a simplification of equations is sufficient to illustrate the key factors

$$I_{OX} = KW\left(\frac{V}{T_{OX}}\right)^2 e^{-\alpha T_{OX}/V}, \tag{2}$$

where V is the voltage of the gate, W is the width of the channel, T_{OX} is oxide thickness, and K and α are experimentally derived.

Reduction of gate oxide thickness results in an increase in the field across the oxide. The high electric field coupled with low oxide thickness results in tunneling of electrons from inverted channel to gate (or vice versa) or from gate to source/drain overlap region (or vice versa) [3]. If the gate oxide thickness is less than 20˚A, the gate leakage would be an important component in total leakage dissipations. Therefore, in 45-nm generation and beyond, the high-k metal gate silicon technology is applied to reduce the gate leakage current. However, the gate leakage issue still exists in the 90-nm and 65-nm technologies that are currently used in production without the high-k metal gate silicon structure.

There are two types of different tunneling, namely direct tunneling and Fowler-Nordheim (FN) tunneling [3]. The gate leakage of micro device comes mostly from direct tunneling. There are three major mechanisms for direct tunneling in MOS devices, namely electron tunneling from the conduction band (ECB), electron tunneling from the valence band (EVB), and hole tunneling from the valance band (HVB). In NMOS, ECB controls the gate to channel tunneling current in inversion, whereas gate to body tunneling is controlled by EVB in depletion-inversion and ECB in accumulation. In PMOS, HVB controls the gate to channel leakage in inversion, whereas gate-to-body leakage is controlled by EVB in depletion-inversion and ECB in accumulation. Since the barrier height for HVB (4.5eV) is considerably higher than the barrier height for ECB (3.1eV), the tunneling current associated with HVB is much less than the current associated with ECB. This results in a lower gate leakage current in PMOS than NMOS with gate oxide structure. Based on the basis that PMOS devices exhibit lower gate leakage compared to NMOS devices, P-type logic circuits that consist mostly of PMOS transistors have been proposed to reduce gate leakage dissipations [3].

3 Dual-Threshold Technique for PAL-2P Circuits

Basic PAL-2P (pass-transistor adiabatic logic with PMOS pull-up configuration) buffer is shown in Fig. 1 [8], which consists mostly of PMOS transistors. The structure and operation of the PAL-2P are complementary to PAL-2N [5]. Compared with traditional PAL-2N, the PAL-2P circuits consume low gate leakage dissipations, because PMOS transistors have an order of magnitude smaller gate leakage than NMOS ones.

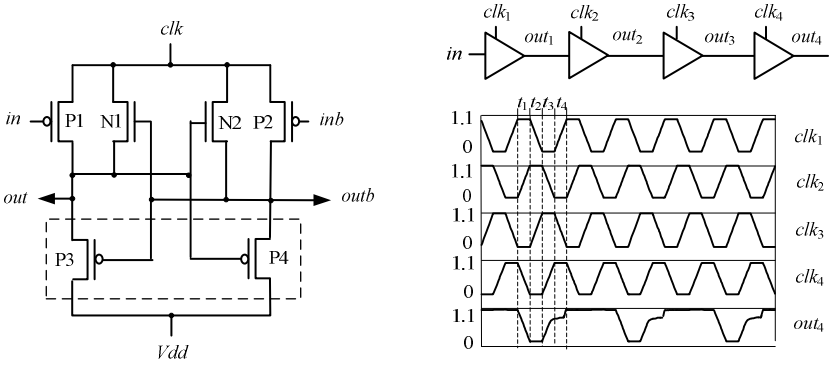

Fig. 1. Basic PAL-2N buffer, buffer chain, and power-clocks and its simulated waveform

The most straightforward application of DTCMOS technique is simply to partition a circuit into critical and non-critical regions, and then to only use fast low-V_t devices in critical paths to meet performance goals. The clamp transistors (P3 and P4) (part enclosed with dotted lines) is the non-critical region, and the other transistors is the critical region in the PAL-2P buffer. So we only replace those two transistors (P3 and P4) with high-V_t CMOS to reduce leakage currents, as shown in Fig. 2.

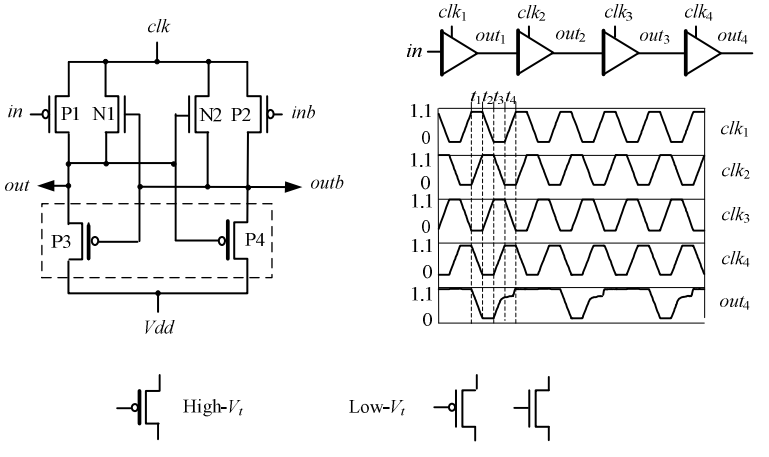

Fig. 2. DTCMOS PAL-2P buffer, buffer chain, and power-clocks and its simulated waveform

For an example, an s27 benchmark circuit from the ISCAS89 sequential benchmark set is verified using the DTCMOS PAL-2P scheme. Traditional s27 benchmark circuits can be obtained by VHDL coding and logic synthesis with Synopsys, and its logic schematic can be founded in [8]. The transition function of the flip-flops can be expressed as

$$
\begin{aligned}
Q_0^{'} &= \overline{\overline{A+\overline{Q}_0}+B} \\
Q_1^{'} &= \overline{\overline{(\overline{A+\overline{Q}_0}+\overline{D}Q_1)(C+\overline{D}Q_1)}+Q_2} \\
Q_2^{'} &= \overline{\overline{(\overline{A+\overline{Q}_0}+\overline{D}Q_1)(C+\overline{D}Q_1)}+Q_2+\overline{D}}\,.
\end{aligned}
\tag{3}
$$

Based on the adiabatic *D* flip-flop, complex sequential circuits can also be realized [10]. The PAL-2P gates can be realized by using PMOS blocks to replace the input PMOS (P1 and P2) of the PAL-2P buffer.

4 Estimation of Active Leakage

Based on the power dissipation models of adiabatic circuits, active leakage dissipations can be estimated by testing total leakage dissipations using SPICE simulations. The estimation technique for basic PAL-2P circuits have been reported in [9], which can also be used for estimating active leakage dissipations of the DTCMOS PAL-2P circuits.

The energy dissipation per cycle of PAL-2P circuits includes adiabatic energy dissipation ($E_{adiabatic}$), non-adiabatic energy loss ($E_{non\text{-}adiabatic}$) and leakage dissipation (E_{Leak}). The total energy dissipation per cycle of the PAL-2P buffer can be expressed as

$$
\begin{aligned}
E_{\mathrm{P,\,total}} &= E_{\mathrm{adiabatic}} + E_{\mathrm{non-adiabatic}} + E_{\mathrm{leak}} \\
&\approx (\frac{R_P C_L}{T}) C_{\mathrm{L}} V_{\mathrm{DD}}^2 + \frac{1}{2} C_L V_{\mathrm{tn}}{}^2 + \frac{1}{2} V_{\mathrm{DD}} I_{P,Leak} T\,,
\end{aligned}
\tag{4}
$$

where C_{L} is additional load capacitance of the PAL-2P buffer, which is introduced for the purpose of estimating leakage dissipations, T is period of the power-clock, R_P is the turn-on resistance of transmission gate P1 and N1 (P2 and N2) in the PAL-2P buffer, V_{th} is threshold voltage of NMOS transistors, V_{DD} is peak-peak voltage of power clocks, and $I_{N,\,Leak}$ is average leakage current of the PAL-2P buffer through the voltage v_{DD}(t) of the power clock.

According Eq. 4, the total energy dissipation per cycle of PAL-2P circuits can also be represented as

$$
E_{\mathrm{P,\,total}} = \frac{k_{P1} C_{\mathrm{L}}{}^2}{T} + k_{P2} C_L + k_{P3} T\,,
\tag{5}
$$

where k_{P1} is $R_N V_{\mathrm{DD}}^2$, k_{P2} is $V_{\mathrm{tn}}^2/2$, and k_{P3} is $V_{DD} I_{\mathrm{P,\,Leak}}/2$. According to Eq. 5, the leakage power dissipation of PAL-2P circuits can be estimated by measuring total

energy dissipations ($E_{P,total1}$, $E_{P,total2}$ and $E_{P,total3}$) in three different capacitances (C_L, $3/2C_L$, and $2C_L$). The leakage energy dissipation of PAL-2N circuits can be given by

$$E_{P,\,leak} = 6E_{P,\,total1} - 8E_{P,\,total2} + 3E_{P,\,total3}\,, \tag{6}$$

5 Simulation Results

HSPICE simulations have been carried out for the s27 benchmark circuits based on DTCMOS PAL-2P circuits using 65nm CMOS process at 20MHz, 100MHz, 200MHz, respectively. The supply voltage is 1.1V. BSIM4 model is adopted to reflect the characteristics of the leakage currents. For comparison, the two other S27 benchmark circuits based on basic PAL-2P, and basic PAL-2N circuits using low-V_T transistors also are simulated. The function verifications, leakage consumption, and total power consumption tests have been carried out.

The estimated leakage power losses of S27 benchmark circuits based on DTCMOS PAL-2P, basic PAL-2P, and basic PAL-2N at 65nm CMOS process are listed in Table 1, where C_L is taken as 10fF. Fig. 3 shows the saving rate of leakage power losses of the s27 benchmark circuit using PAL-2P circuits DTCMOS techniques compared with the basic PAL-2P and PAL-2N ones using low-V_T transistors at 65nm CMOS process.

Table 1. Estimated leakage energy losses per cycle of S27 benchmark circuits based on DTCMOS PAL-2P, baisc PAL-2P, and basic PAL-2N at 65nm CMOS process. C_L=10fF

Operation frequency (MHz)	20	100	200
DTCMOS PAL-2P	8.76fJ	5.95 fJ	4.36 fJ
Basic PAL-2P	11.25 fJ	8.78 fJ	5.7 fJ
Basic PAL-2N	17.52 fJ	15.92 fJ	12.65 fJ

C_L is additional load capacitance introduced for the purpose of estimating leakage dissipations. The load capacitance of the actual circuits is smaller than 10fF. Table 2 shows total power losses of the three s27 benchmark circuits at 65nm CMOS process for C_L=2.5fF.

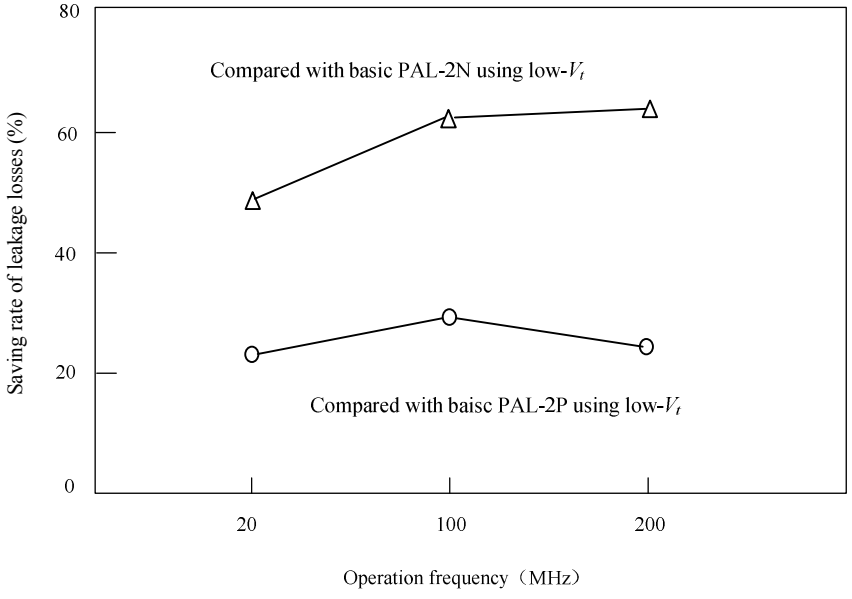

Fig. 3. Saving rate of leakage losses of PAL-2P s27 benchmark circuits using DTCMOS compared with ones using basic PAL-2P and basic PAL-2N using low-V_t in 65nm process

Table 2. Total energygy losses per cycle of S27 benchmark circuits based on DTCMOS PAL-2P, baisc PAL-2P, and basic PAL-2N at 65nm CMOS Process. C_L=2.5fF

Operation frequency (MHz)	20	100	200
DTCMOS PAL-2P	15.09 fJ	12.97 fJ	15.86 fJ
Basic PAL-2P	15.88 fJ	13 fJ	15.94 fJ
Basic PAL-2N	16.25 fJ	14.68 fJ	16.5fJ

6 Conclusion

The dual-threshold CMOS scheme for PAL-2P (pass-transistor adiabatic logic with PMOS pull-up configuration) circuits have been proposed in this paper. The PAL-2P circuits using DTCMOS (dual-threshold CMOS) technique exhibit large energy savings, since both sub-threshold and gate leakage dissipations are reduced effetely. It is found that the s27 benchmark circuit based on the proposed DTCMOS PAL-2P

achieves leakage energy loss savings of about 62% and 23% at 200MHz for 65nm process, respectively, compare with basic PAL-2P and PAL-2N ones, respectively.

Acknowledgments. Project is supported by National Natural Science Foundation of China (No. 60773071), Zhejiang Science and Technology Project of China (No. 2010C31G2070017), Scientific Research Fund of Zhejiang Provincial Education Department (No. Z200908632), and Ningbo Natural Science Foundation (No. 2009A610066), and supported by the Scientific Research Foundation of Graduate School of Ningbo University (No.G10JA005).

References

1. Kim, N.S., Austin, T., et al.: Leakage Current: Moore's Law Meets Static Power. Computer 36(12), 68–75 (2003)
2. Fallah, F., Pedram, M.: Standby and Active Leakage Current Control and Minimization in CMOS VLSI Circuits. IEICE Trans. on Electronics E88-C(4), 509–519 (2005)
3. Hamzaoglu, F., Stan, M.R.: Circuit-Level Techniques to Control Gate Leakage for Sub-100 nm CMOS. In: Proc. Int. Symp. Low Power Electronics and Design, pp. 60–63 (2002)
4. Wei, L., Chen, Z., Johnson, M., Roy, K.: Design and Optimization of Low Voltage High Performance Dual Threshold CMOS Circuits. In: ACM/IEEE DAC, pp. 489–492 (1998)
5. Liu, F., Lau, K.T.: Pass-Transistor Adiabatic Logic with NMOS Pull-Down Configuration. Electronics Letters 34(8), 739–741 (1998)
6. Lu, B.B., Hu, J.P.: Complementary Pass-Transistor Adiabatic Logic using Dual Threshold CMOS Techniques. Submitted to Applied Mechanics and Materials (2010)
7. Hu, J.P. and Zhu, J.G.: An Improved CAL Register File with Dual-Threshold Technique for Leakage Reduction. Submitted to Advanced Materials Research (2010)
8. Hu, J.P., Ye, L.F.: P-Type Complementary Pass-transistor Adiabatic Logic Circuits for Active Leakage Reduction. In: IEEE PACCS 2010 (2010)
9. Jiang, J.T., Ye, L.F.: Leakage Reduction of P-Type Logic Circuits Using Pass-Transistor Adiabatic Logic with PMOS Pull-Up Configuration. Submitted to Applied Mechanics and Materials (2010)

Voltage Scaling for Adiabatic Register File Based on Complementary Pass-Transistor Adiabatic Logic

Haiyan Ni, Xiaolei Sheng, and Jianping Hu

Faculty of Information Science and Technology, Ningbo University
315211 Ningbo City, China
nbhjp@yahoo.com.cn

Abstract. Scaling supply voltage to sub-threshold region can reach minimum energy consumption but only suits for ultra-low operation frequencies. In order to attain more extensive application, scaling supply voltage to medium-voltage region is an attractive approach especially suiting for mid performances. This paper investigates performances of adiabatic register file in near-threshold and super-threshold regions in terms of energy dissipation and max operating frequency. The adiabatic register file is realized with CPAL (complementary pass-transistor adiabatic logic) circuits. All circuits are simulated with HSPICE at a PTM 45nm CMOS technology by supply voltage varies from 0.4V to 1.0V with 0.1V steps. The simulation results demonstrate that the CPAL register file operating on medium-voltage region can not only keep reasonable speed but also reduce greatly energy consumptions.

Keywords: Nanometer CMOS circuits, Medium source voltage, Low power, Register file, Complementary pass-transistor adiabatic logic.

1 Introduction

As CMOS devices approach nanometer processes, energy consumption has become a critical concern. CMOS circuits using the nominal source voltage can operate at high frequency with large energy consumptions. Reduction of the supply voltage (with a fixed threshold voltage) results in a quadratic reduction of dynamic energy at the expense of decreased performance. Therefore, voltage scaling is an effective solution for achieving ultra-low power applications [1].

In conventional CMOS circuits, scaling supply voltage to sub-threshold region can reach minimum energy consumption but only suits for ultra-low operation frequency (f =10KHz to 5MHz) due to the exponential relationship between delay and supply voltage [2]. Moreover, the robustness of sub-threshold logic circuits must carefully be considered.

In order to attain more extensive application, scaling supply voltage to medium-voltage region is an attractive approach especially suiting for mid performances (f =5MHz to 100MHz) [3]. An investigation for full adders based on several logic styles in near-threshold and super-threshold regions has been reported in [4]. The results demonstrate that lowering supply voltage is advantageous, especially in medium-voltage region (700mv-800mv) that yields the best EDP (energy delay product).

D. Zeng (Ed.): Future Intelligent Information Systems, LNEE 86, pp. 39–46.
springerlink.com © Springer-Verlag Berlin Heidelberg 2011

For many applications, the performance penalty of the circuits that operate in medium-voltage region is tolerable [3].

Adiabatic logic utilizes AC power-clock to recover effectively the charge delivered by the clock instead of being dissipated to the ground, so that dynamic power is reduced effetely [5]. However, the previously proposed adiabatic logic families focus mainly on nominal voltage circuits. Presently, performance investigations for the PAL-2N (pass-transistor adiabatic logic with NMOS pull-down configuration) and CPAL (complementary pass-transistor adiabatic logic) circuits operating on near-threshold and super-threshold regions have been reported in [6, 7]. The results show that PAL-2N and CPAL circuits have low EDP (energy delay product) in medium-voltage region (700mv-800mv).

This paper investigates performances of the adiabatic register file based on CPAL circuits in near-threshold and super-threshold regions in terms of energy dissipation and max operating frequency. All circuits are simulated with HSPICE at a PTM 45nm CMOS technology [8] by supply voltage varies from 0.4V to 1.0V with 0.1V steps.

2 Review of Single-Phase Register File Based on CPAL Circuits

2.1 CPAL Buffer and Gates

CPAL circuits using two-phase power-clock scheme have been reported in [5]. The basic structure of the CPAL buffer is shown in Fig. 1 (a).

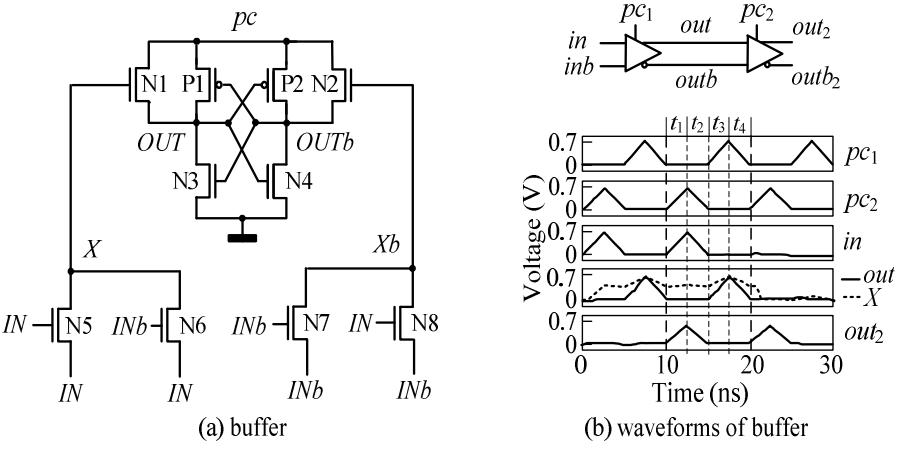

Fig. 1. CPAL buffer using two-phase scheme and its simulated waveforms

The CPAL buffer is composed of two main parts: the logic function circuit and the load driven circuit. The logic circuit consists of four NMOS transistors (N5-N8) with complementary pass-transistor logic (CPL) function block. The load driven circuit

consists of a pair of transmission gates (N1, P1 and N2, P2). The clamp transistors (N3 and N4) ensure stable operation by preventing from floating of output nodes. Its simulated waveforms and two-phase power clocks are also shown in Fig. 1(b). All basic two-input CPAL gates, such as buffer/inverter, AND/NAND gate, OR/NOR gate, XOR/XNOR, and multiplexer, use the same topology, and only inputs are permutated, which can be found in [5].

2.2 The Structure of CPAL Register File

The two-phase CPAL register file is shown in Fig. 2, which consists of a storage-cell array, address decoders, read/write word-line drivers, sense amplifiers, write bit-line and read data-line drivers [5].

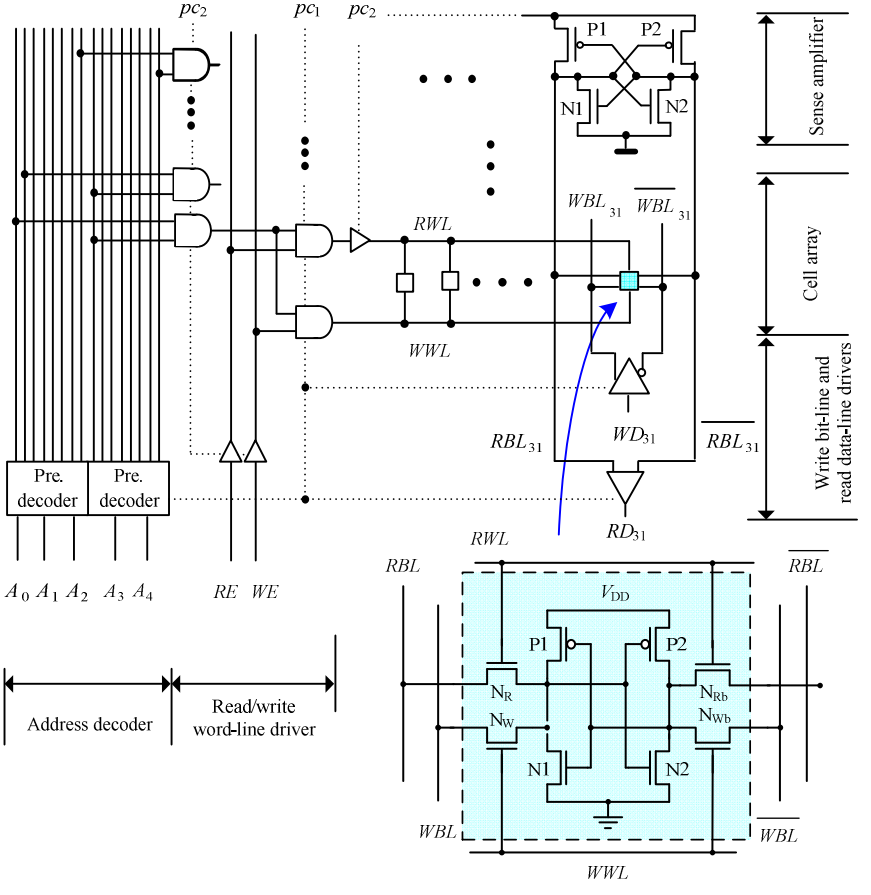

Fig. 2. The structure of the CPAL register file and storage cell

An address decoder is divided into the two-level address decoding that consists of the pre-decoder and two-input NAND gates. The address decoder is used for selecting storage cells by charging the word lines. The word-line signals are produced by using AND gates with the two outputs of the pre-decoding and the read/write enable signals (*RE* and *WE*). *WWL* (write word-line) is charged when pc_1 goes high, and *RWL* (read word-line) is charged when pc_2 goes high.

The sense amplifier consists of the transistors (P1 and P2, N1 and N2). pc_2 charges the read bit-lines (*RBL* and *RBLb*) through P1 (or P2), and the energy of *RBL* (or *RBLb*) is recovered to pc_2 through P1 (or P2). The two-phase CPAL buffers are used to drive write-bit lines (*WBL* and *WBLb*) and read data (*RD* and *RDb*).

The storage-cell structure is the same as a conventional memory cell. The cell consists of a cross-coupled inverter pair (N1, P1, and N2, P2) and two pairs of access transistors (NR and NRb, NW and NWb) that are enabled by *RWL* and *WWL* for read and write operations, respectively. The memory array is composed of a multiplicity of these cells arrayed horizontally and vertically. The *WWL* and *RWL* of a row are connected along the horizontal axis, while the read bit-lines (*RBL* and *RBLb*) and the write bit-lines (*WBL* and *WBLb*) are connected in a column.

3 Simulation Results of Near-Threshold Adiabatic Register File

In order to investigate the performances of the adiabatic register file in near-threshold super-threshold regions, the 32×32 register file based on CPAL circuits are simulated by source voltage ranging from 0.3V to 1.0V with 0.1V step using 45nm PTM CMOS technology.

The non-overlap sinusoidal auxiliary signals (pc_1 and pc_2) are generated with an auxiliary clock generator, as shown in Fig. 3.

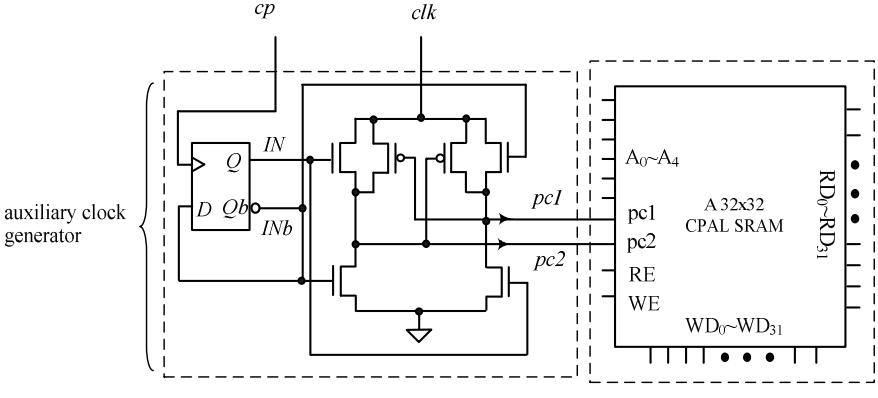

Fig. 3. CPAL register file and single-phase power-clock generator

The rectangle-wave clock *cp* comes from the synchronous single-phase power-clock generator. Its frequency is the same as the power clock *clk*, and the frequency of the auxiliary sinusoidal clocks is half of *clk*, thus a static CMOS logic *D* flip-flop working as mode-2 counter is used. In the CPAL circuits, the charge of the auxiliary clock lines can be well recycled to the power-clock because of using the sinusoidal clock signal.

The 32×32 CPAL register file can well operate based on HSPICE simulation in the supply voltages from 0.4V to 1V. At 0.7V, its simulation waveform is shown in Fig. 4.

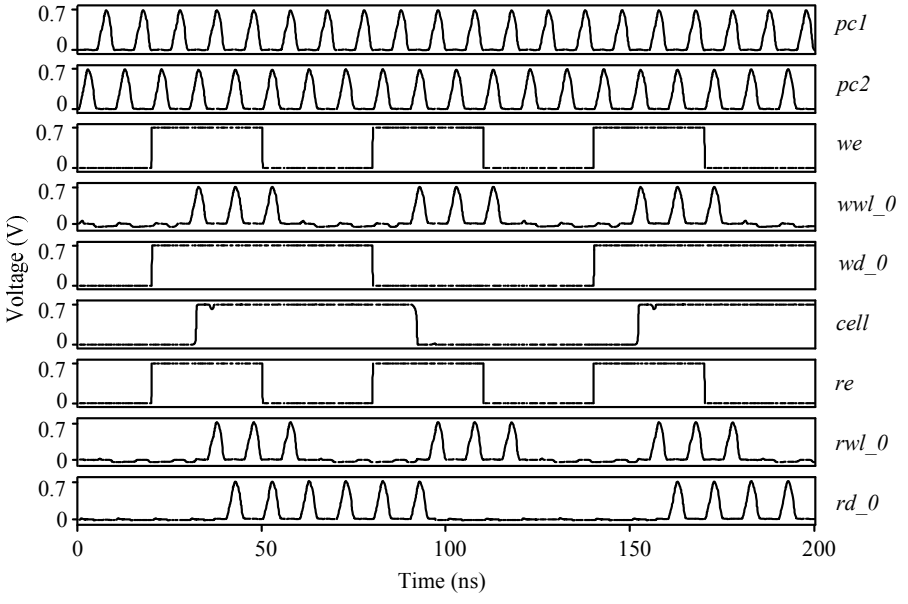

Fig. 4. The simulation waveforms of the 32×32 CPAL register file at V_{DD} = 0.7V

3.1 Energy Consumption for a Given Operation Frequency

Fig. 5 shows the energy consumption of the near-threshold 32×32 CPAL register file with different source voltages (V_{DD}) at 5MHz in active and idle modes, respectively. In this result, the energy dissipation only accounts for the two-phase CPAL register file, witch is powered by pc_1, *pc2* and V_{DD}, but does not include the energy dissipation consumed on the power clock generator. As shown in Fig. 5, both the active and idle energy consumption of the adiabatic register file increases, as the supply voltage rises. For a given frequency, the energy dissipation increases quadratic approximately as the supply voltage is increased. The dissipation at V_{DD}=0.7V is about 19% of the dissipation at V_{DD} =1.0V approximately.

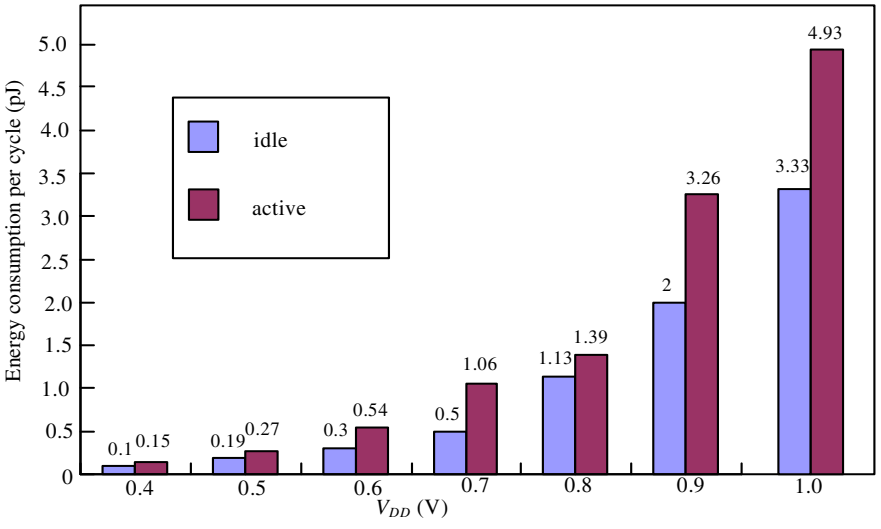

Fig. 5. Energy dissipations of the CPAL register file at 5MHz in active and idle modes

3.2 Max Operating Frequency at Different Source Voltage

The 32×32 CPAL register file has been simulated at different source voltage V_{DD}. At each supply voltage, the maximum operating frequency is obtained, where the CPAL register file has correct logic function. The maximum operating frequency at different source voltage is shown in Fig. 6.

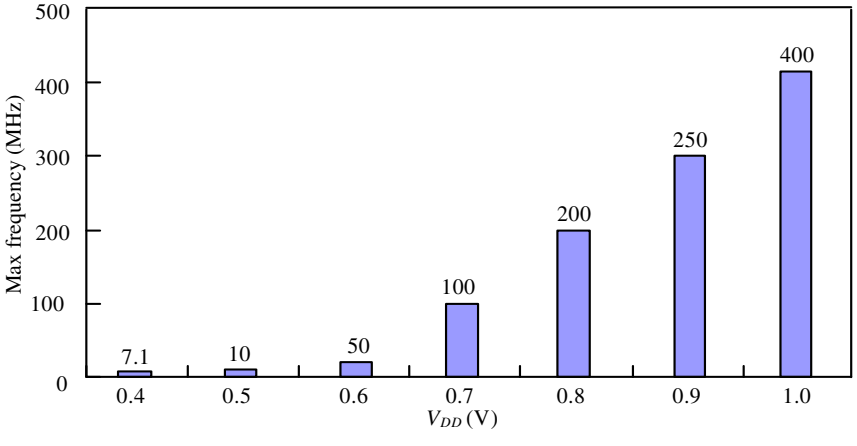

Fig. 6. Max operating frequency at different source voltage (V_{DD})

As shown in this result, the maximum operating frequency reduces from 400MHz to 7.1MHz, as the supply voltage scales down from 1.0V to 0.4V. When the supply voltage is between 0.7V and 0.8V, the maximum operating frequency of the CPAL register file is about 100MHz to 200MHz, which is suitable for mid performances.

3.3 Energy Consumption at Different Period

Fig. 7 shows the energy consumption of the 32×32 CPAL register file in active time with different operation periods at medium source voltage (V_{DD} = 0.7V) and normal source voltage (1.0V), respectively. As shown in Fig. 7, the energy consumption of the adiabatic register increases, as the operation period rises. However, when operation period is between 10ns and 20ns, the change of energy consumption is not obvious. Therefore, if 0.7v is selected as the source voltage of the 32×32 CPAL register file, the frequency of 50MHz maybe a good choice considering of energy dissipation and stability. From the simulation result, the CPAL register operating at low source voltage obtains energy savings of 76% at 100MHz compared with the standard CPAL one operating at the normal source voltage with 1.0V.

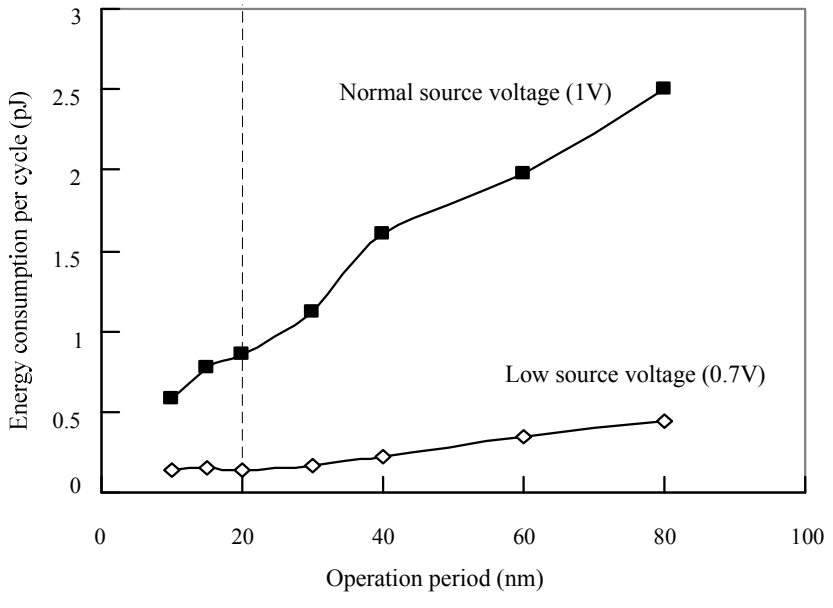

Fig. 7. Energy dissipation of the CPAL register file in different operation period when source voltage (V_{DD}) is 0.7V and 1.0V, respectively

4 Conclusion

The performances of adiabatic register file based on CPAL circuits in near-threshold and super-threshold regions have been addressed in terms of energy dissipation and max operating frequency. The results show that scaling supply voltage to

medium-voltage region can not only keep reasonable speed but also reduce greatly energy consumptions.

Based on the HSPICE simulation results, the energy dissipation increases quadratic approximately for a given frequency, as the supply voltage is increased. The maximum operating frequency of the CPAL register file operating at medium-voltage (0.7V-0.8V) is about 100MHz to 200MHz, which is suitable for mid performances. At 100MHz, the CPAL register operating at medium source voltage (0.7V) obtains energy savings of 76% compared with the standard CPAL one operating at the normal source voltage with 1.0V.

Acknowledgments. Project is supported by National Natural Science Foundation of China (No. 61071049), Zhejiang Science and Technology Project of China (No. 2010C31G2070017), Scientific Research Fund of Zhejiang Provincial Education Department (No. Z200908632), and Ningbo Natural Science Foundation (No. 2009A610066).

References

1. Wang, A., Calhoun, B.H., Chandrakasan, A.P.: Sub-threshold Design for Ultra Low-Power Systems, pp. 12–102. Springer, Heidelberg (2006)
2. Bol, D., Flandre, D., Legat, J.-D.: Technology Flavor Selection and Adaptive Techniques for Timing-Constrained 45nm Subthreshold Circuits. In: Proc. ACM/IEEE Int. Symp. Low-Power Electron, pp. 21–26 (2009)
3. Dreslinski, R., Wieckowski, M., Blaauw, D., Sylvester, D., Mudge, T.L.: Near-Threshold Computing: Reclaiming Moore's Law Through Energy Efficient Integrated Circuits. Proceedings of the IEEE 98, 253–266 (2010)
4. Hu, J.P., Yu, X.Y.: Near-Threshold Full Adders for Ultra Low-Power Applications. In: 2010 Pacific-Asia Conference on Circuits, Communications and System (PACCS 2010),), pp. 300–303 (2010)
5. Hu, J.P., Xu, T.F., Li, H.: A Lower-Power Register File Based on Complementary Pass-Transistor Adiabatic Logic. IEICE Transactions on Information and Systems E88-D, 1479–1485 (2005)
6. Hu, J.P., Yu, X.Y.: Near-Threshold Adiabatic Flip-Flops Based on PAL-2N Circuits in Nanometer CMOS Processes. In: 2010 Pacific-Asia Conference on Circuits, Communications and System (PACCS 2010), pp. 446–449 (2010)
7. Hu, J.P., Liu, B.B.: Energy Efficient Near-threshold Circuits Based on Adiabatic CPL. CCIS. Springer, Heidelberg (2010)
8. Zhao, W., Cao, Y.: New Generation of Predictive Technology Model for Sub-45nm Design Exploration. In: Proc. ISQED, pp. 585–590 (2006)
9. Liu, B.B., Hu, J.P.: Tree Multipliers with Modified Booth Algorithm based on Adiabatic. In: 12th International Symposium on Integrated Circuits (ISIC), pp. 302–305 (2009)

Near-Threshold Flip-Flops for Ultra Low-Power Applications

Xiaoying Yu and Jianping Hu

Faculty of Information Science and Technology, Ningbo University
315211 Ningbo City, China
nbhjp@yahoo.com.cn

Abstract. Scaling supply voltage is an effective technique to reduce energy consumption at the expense of performance degradation. This paper investigates seven representative flip-flops in near-threshold and super-threshold regions in terms of low EDP (Energy Delay Product). All flip-flops are simulated using 45nm CMOS technology by varying supply voltage from 0.4V to 0.9V with 0.1V steps. The simulation results demonstrate that lowering supply voltage is advantageous, especially in medium-voltage region (0.6V-0.8V), which yields the best EDP. In addition, it is shown that the optimum supply voltage of the flip-flops varies slightly with the structure of flip-flops.

Keywords: Near-threshold logic, Ultra low-power, Flip-flop, Nanometer CMOS circuits.

1 Introduction

As flip-flops are critical components in sequential logic circuits, their energy consumption has become a major design concern. The reduction of supply voltage is one of the most effective ways to achieve low-power design. However, scaling supply voltage results a negative effect on the circuit performance, due to the exponential relationship between delay and supply voltage.

EDP (Energy Delay Product) metric provides a good tradeoff between speed and energy consumption. In this work, the EDP characteristics of seven representative flip-flops have been addressed in near-threshold and super-threshold regions. All circuits are simulated with HSPICE at a NCSU PDK 45nm CMOS technology by varying supply voltages from 0.4V to 0.9V with 0.1V steps. The results demonstrate that lowering supply voltage is advantageous, especially in medium-voltage region (0.6V-0.8V), which yields the best EDP. In addition, it is shown that the optimum supply voltage of the flip-flops varies slightly with structure of flip-flop.

2 Delay and Energy of Flip-Flops

There are three important timing parameters associated with a flip-flop: setup time (T_{su}), hold time (T_{hold}) and propagation delay ($T_{C\text{-}Q}$) [1, 2]. T_{su} is the time that the input (D) must valid before the clock triggering edge, which can be written as

D. Zeng (Ed.): Future Intelligent Information Systems, LNEE 86, pp. 47–54.
springerlink.com © Springer-Verlag Berlin Heidelberg 2011

$$T_{\mathrm{su}} = T_{\mathrm{D\text{-}C}} \mid \min(T_{\mathrm{D\text{-}Q}}), \tag{1}$$

where $T_{\mathrm{D\text{-}C}}$ is the time difference between input (D) and *clock*, $T_{\mathrm{D\text{-}Q}}$ is the time difference between input (D) and output (Q). T_{hold} is the time that the input (D) must remain valid after the *clock* edge. $T_{\mathrm{C\text{-}Q}}$ is the time difference between the output (Q) and the *clock* edge. Assuming T_{hold} is met, $T_{\mathrm{D\text{-}Q}}$ can be expressed as

$$T_{\mathrm{D\text{-}Q}} = \max(T_{\mathrm{D\text{-}C\ LH}} + T_{\mathrm{C\text{-}Q\ LH}}, T_{\mathrm{D\text{-}C\ HL}} + T_{\mathrm{C\text{-}Q\ HL}}), \tag{2}$$

where $T_{\mathrm{D\text{-}C\ LH}}$ and $T_{\mathrm{D\text{-}C\ HL}}$ are low-to-high transition and high-to-low transitions time, $T_{\mathrm{C\text{-}Q\ LH}}$ and $T_{\mathrm{C\text{-}Q\ HL}}$ are low-to-high and high-to-low propagation delay [3].

The delay of a flip-flop can be expressed as the minimum time when taken from the input (D) changes to the output (Q) has stabilized.

$$T_{\mathrm{delay}} = \min(T_{\mathrm{D\text{-}Q}}). \tag{3}$$

Assuming symmetrical PMOS and NMOS, the delay of an inverter in super-threshold region is [4]

$$t_d = KC_L V_{DD} / (V_{DD} - V_{th})^{\alpha}, \tag{4}$$

where K is a delay fitting parameter, C_L is the load capacitance, V_{DD} is source voltage, V_{th} is threshold voltage, and a is velocity saturation parameter, respectively. The delay of an inverter in sub-threshold region is given by

$$t_d = KC_L V_{DD} / (I_{o,g} exp(\frac{V_{DD} - V_{th,g}}{nV_T})), \tag{5}$$

where V_{T} is the thermal voltage, n is the sub-threshold slope factor, and $I_{0,\mathrm{g}}$ and $V_{\mathrm{th,g}}$ are fitting parameter. From Eq. (5), the delay increases dramatically in sub-threshold region, because of the exponential relationship between delay and supply voltage. From Eq. (4), the delay is proportional to $V_{DD} / (V_{DD} - V_{th})^{\alpha}$ in super-threshold region.

Another important metric is energy consumption that includes three components: switching energy due to charging and discharging for loads, short energy due to a direct-path from supply voltage to the ground, and static energy dissipation that is

caused by leakage currents of MOS devices. The short energy losses can usually be ignored. The total energy consumption per cycle, E_{total}, is expressed as

$$E_{total} = E_{dyn} + E_{leak} = aC_L V_{DD}^{\ 2} + V_{DD} I_{leak} T \ , \tag{6}$$

where α is switching activity, T is operation cycle, I_{leak} is average leakage current through the power source V_{DD}, which mainly is caused by the leakage currents of MOS transistors. For a given frequency, the E_{total} is quadratically reduced as supply voltage scales down, since E_{dyn} and E_{leak} scales quadratically and linearly with the supply voltage for a given frequency, respectively [5].

The energy dissipation per cycle operating at a maximum frequency, $E_{total,\ max\text{-}freq}$, can be written as

$$E_{total,\ max\text{-}freq} = E_{dyn} + E_{leakage,\ max\text{-}fren} = aC_L V_{DD}^{\ 2} + V_{DD} I_{leak} T_{min} \ , \tag{7}$$

where T_{min} is min operation period. The maximum operation frequency is defined as

$$f_{max} = 1/T_{min} = 1/(m \times t_d) \ , \tag{8}$$

where m is a fitting parameter, where the sequential circuit with the flip-flops has correct timing function.

Plugging (4), (5) and (8) into (7), the energy dissipation per cycle at a max frequency is given by

$$E_{total,max-freq} = \begin{cases} aC_{\text{L}} V_{\text{DD}}^{\ 2} + V_{\text{DD}} I_{\text{leak}} mKC_{\text{L}} V_{\text{DD}} / (V_{\text{DD}} - V_{\text{th}})^{\alpha} & V_{\text{DD}} > V_{\text{th}} \\ aC_L V_{DD}^{\ 2} + V_{DD} I_{leak} mKC_L V_{DD} / I_{o,g} exp\left(\dfrac{V_{DD} - V_{th,g}}{nV_T} \right) & V_{\text{DD}} < V_{\text{th}} \end{cases} . \tag{9}$$

For large source voltages (super-threshold region), the energy dissipation operating at a maximum frequency is reduced quadratically as supply voltage scales down. This is because the leakage dissipation is little with small operation period in super-threshold regions. For a low source voltage ($V_{DD} < V_{th}$), the energy dissipation operating at a maximum frequency is increased exponentially as supply voltage scales down, because of the exponential relationship between delay and supply voltage in sub-threshold region from Eq. (5).

Performance and energy consumption are equally significant in high-performance and low-power applications. The *EDP* (Energy Delay Product) metric provides a good tradeoff between two features. For convenience, the delay is replaced by T_{min}, and thus EDP is written as [5]

$$EDP = E_{total,\max-freq} \times T_{\min} . \tag{10}$$

As is mentioned above, as supply voltage scales down, the energy dissipation operating at a maximum frequency is reduced quadratically for large source voltages, and increased exponentially for a low source voltage. Therefore we can reach the minimum *EDP* in near-threshold regions [5].

3 Review of Flip-Flops

Seven widely used flip-flops are shown in Fig. 1.

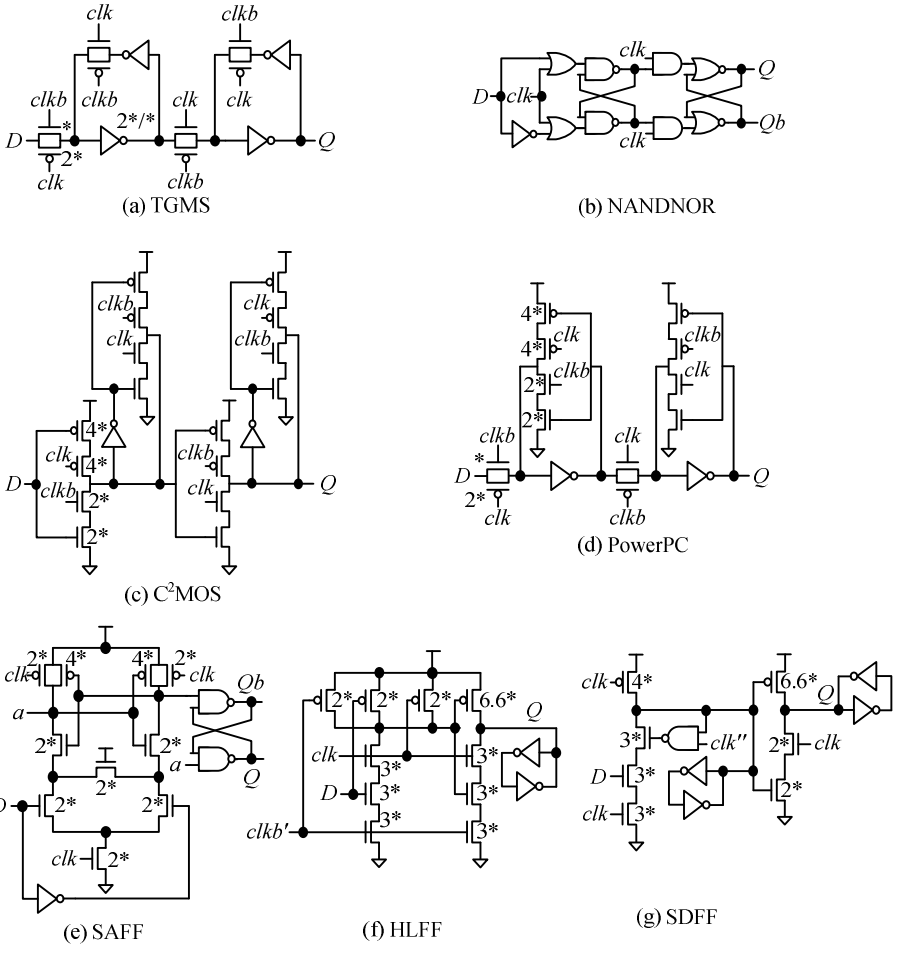

Fig. 1. Seven representative Flip-flops

The transmission-gate Master-Slave flip-flop (TGMS), NAND-NOR Master-Slave flip-flop (NANDNOR) [8], Clocked CMOS Master-Slave flip-flop (C^2MOS) [6], and PowerPC Master-Slave flip-flop (PowerPC) [7] belong to the class of master-slave flip-flops. Sense-amplifier-based flip-flop (SAFF) consists of a sense-amplifier that samples the differential inputs and two coupled NAND gates as the output latch [9]. Hybrid-latch flip flop (HLFF) [10] and Semi-dynamic flip-flop (SDFF) belong to the class of pulse-triggered flip-flops [11], and their input data is latched during a short pulse at the rising edge of the clock.

4 Simulation Results

HSPICE simulations have been carried out for the seven flip-flops. All circuits are simulated with HSPICE at a NCSU PDK 45nm technology by varying supply voltages from 0.4V to 0.9V with 0.1V steps. In order to simulate the work environment of flip-flops, the testing platform is shown in Fig. 2. The energy consumptions of the circuits in the box are tested. In order to assure the fairness of the comparison, the two inverters are paralleled after all outputs to act as load capacitances, and the same input is given to these circuits. In order to make sure efficient pulse length for HLFF and SDFF, additional inverters are inserted into the delayed clock signal.

A size optimization considering delay and power dissipations has been carried out for all the flip-flops. The channel length of all the transistors is taken as L=0.05μm. The channel widths of the transistors are shown in Fig.1, and *=0.075μm.

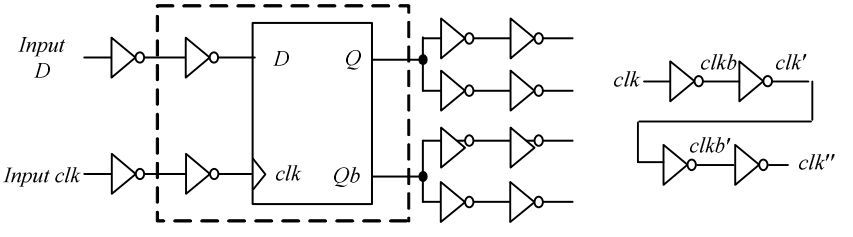

Fig. 2. Testing platform

4.1 Timing Parameters

The timing parameters of the seven flip-flops are shown in Fig. 3. The setup time (T_{su}) has a significant difference for various flip-flops, as shown in Fig. 3 (a). For the master-slave flip-flops, T_{Su} is positive, and it increases as the supply voltage decreases. T_{Su} of SAFF and pulse-triggered flip-flops decreases with decreased supply voltage. SAFF and SDFF have negative T_{Su} at 0.4V supply voltage. Therefore, SAFF and pulse-triggered flip-flops are widely used for high performance application. The $T_{C\text{-}Q}$ and delay of all flip-flops increase as the supply voltage decrease, as shown in Fig. 3 (b) and (c). In this paper, the max operation frequency is defined as $f_{max}=1/(10T_{Delay})$. HLFF achieves the highest operation frequency for all supply voltage, due to its minimal propagation delay and relatively small T_{su}, as shown in Fig. 3 (d).

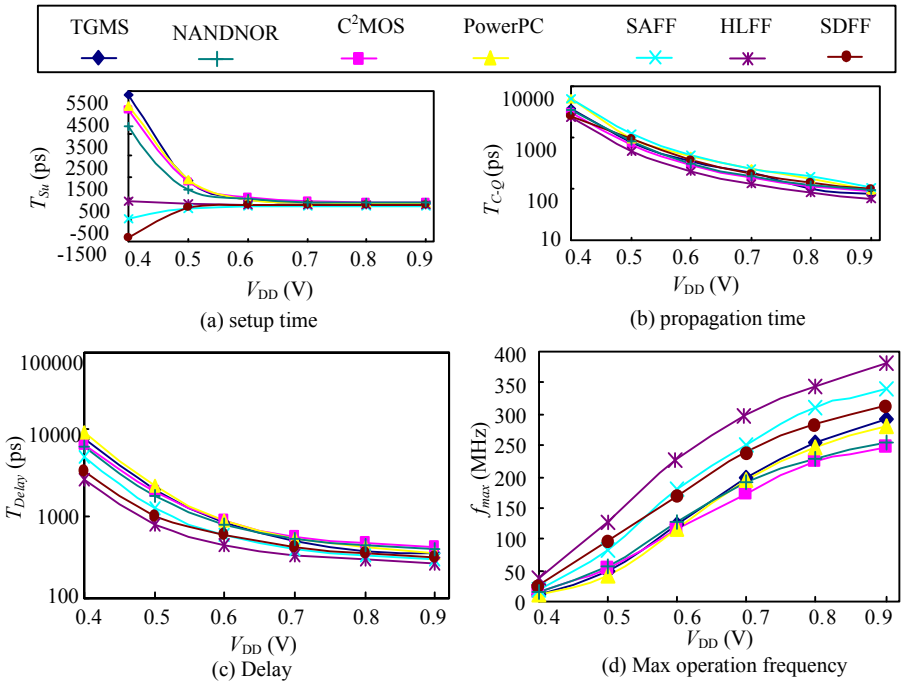

Fig. 3. Timing parameters of seven flip-flops with a varied supply voltage

4.2 Energy Consumption

Fig. 4 (a) shows energy consumption per cycle of the seven flip-flops when V_{DD}=0.7V. The dynamic energy consumption of a flip-flop is directly proportional to the switching activity (α). TGMS consumes the least energy compared to other flip-flops for all switching activities. When the switching activity (α) is zero and the input (D) is high, pulse-triggered flip-flops consume more energy than other flip-flops due to unnecessary transitions of internal node. SDFF has maximum energy consumption when D=1 with the switching activity of 0. The energy consumption of SAFF is not as sensitive to the switching activity.

Fig. 4 (b) shows the energy consumption per cycle of the flip-flops from 0.4 V to 0.9 V with switching activity of 1. Pulse-triggered flip-flops consume a considerably larger power compared with master-slave flip-flops. TGMS is the most energy efficient structure among the master-slave flip-flops. SAFF consumes less energy than other flip-flops when supply voltage. As shown in Fig. 4 (b), one direct solution for reducing energy consumption is to scale supply voltage, since the energy dissipation operating at a maximum frequency is reduced quadratically as supply voltage scales down for super-threshold region from Eq. (9).

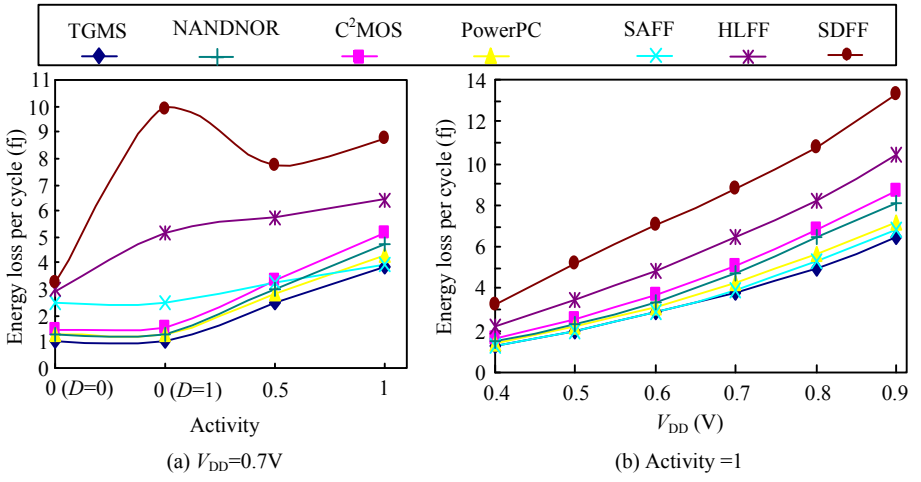

Fig. 4. Energy consumption per cycle for seven flip-flops with a varied supply voltage

4.3 Energy-Delay Product

We can reach the minimum *EDP* in near-threshold region, as shown in Fig. 5.

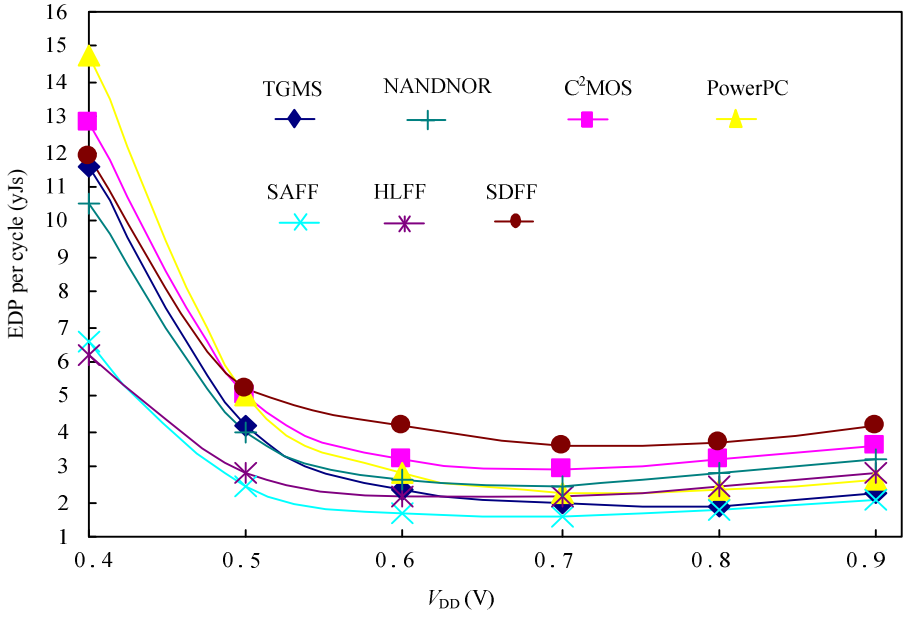

Fig. 5. EDP per cycle when α=1

SAFF show the best energy-performance trade-off among the seven flip-flops, and it shows the lowest EDP (1.62yJs) at 0.7V. TGMS achieves the minimum EDP at the supply voltage of 0.8V, while the EDP of HLFF is minimized at 0.6V and others are minimized at 0.7V. If the high performance is required, the HLFF shows the best delay for all the supply voltage. Scaling supply voltage to medium-voltage region (0.6V-0.8V) can not only but also reduce energy consumptions.

5 Conclusion

Seven typical flip-flops have been investigated in the near-threshold and super-threshold regions using a 45nm process with HSPICE simulations. TGMS and SAFF show low energy consumptions. The simulation results demonstrate that lowering supply voltage is an effective way to achieve low EDP for flip-flop, especially in medium-voltage region (0.6V-0.8V), which yields the best EDP.

Acknowledgments. Project is supported by National Natural Science Foundation of China (No. 61071049), Zhejiang Science and Technology Project of China (No. 2010C31G2070017), Scientific Research Fund of Zhejiang Provincial Education Department (No. Z200908632), and Ningbo Natural Science Foundation (No. 2009A610066).

References

1. Stojanovic, V., Oklobdzija, V.: Comparative Analysis of Master-Slave Latches and Flip-Flops for High-Performance and Low Power System. IEEE JSSC 34, 536–548 (1999)
2. Fu, B., Ampadu, P.: Comparative Analysis of Ultra-Low Voltage Flip-Flops for Energy Efficiency. In: Proc. ISCAS 2007, pp. 1173–1176 (2005)
3. Alstad, H.P., Aunet, S.: Seven Subthreshold Flip-Flops Cells. In: Proc. IEEE NorCHIP, pp. 1–4 (2007)
4. Wang, A., Calhoun, B.H., Chandrakasan, A.P.: Sub-threshold Design for Ultra Low-Power Systems, pp. 12–102. Springer, Heidelberg (2006)
5. Hu, J.P., Zhu, J.G.: Voltage Scaling for SRAM in 45nm CMOS Process. Applied Mechanics and Materials (2010)
6. Suzuki, Y., Odagawa, K., Abe, T.: Clocked CMOS Calculator Circuitry. IEEE JSSC 8, 462–469 (1973)
7. Gerosa, G., et al.: A 2.2W, 80 MHz Superscalar RISC Microprocessor. IEEE JSSC 29, 1440–1454 (1994)
8. Oskuii, S.T.: Comparative Study on Low-Power High-Performance Flip-Flops. Linköping University Press (2004)
9. Nikolić, B., et al.: Sense Amplifier-Based Flip-Flop. In: ISSCC Dig. Tech. Papers, pp. 282–283 (1999)
10. Partovi, H., et al.: Flow-through Latch and Edge-Triggered Flip-Flop Hybrid Elements. In: ISSCC Dig. Tech. Papers, pp. 138–139 (1996)
11. Klass, F.: Semi-dynamic and Dynamic Flip-Flops with Embedded Logic. In: Symp. VLSI Circuits Dig. Tech. Papers, pp. 108–109 (1998)

Proposed of a GIS Cloud (GIS-C) System Architecture in Private Used

Aissatou Diasse[1,2] and Foroski Kone[1,2]

[1] Faculty of Information Engineering, China University of Geosciences, Wuhan, CHINE
diasseastou@yahoo.fr
[2] GIS Software & Application Research Center for Ministry of Education, Wuhan, CHINE
kone69@yahoo.fr

Abstract. This paper discusses a proposed model for designing & implementing cloud computing paradigm in GIS field in a bid to better serve the interest of GIS clients. The system provides efficient resource exchange, performance and highly secured data storage and information, by hosting resource repository within private service oriented environments. By combining GIS and Cloud techniques, we were able to provide a design diagram that describes a GIS-C of a set of Information System. The schema allows the consumer to use On-Demand services such as Storage-as-a-Service, Platform-as-a-Service, and Component-as-a-Service to achieve its goal and optimize its resources. To implement this system, we defined PaaS/CaaS/SaaS-Cloud-Client as IS-Client and Pay-PercentageX-Use-Client as authorized client with X the percentage of utilization. Cloud-Application-Level-X (respectively Component-Level-X) defined the level of complexity or completeness of applications (respectively functions) provides by Own-GIS-Based-Application (respectively Component-Cloud) to clients. The benefits of this GIS-C System architecture to enterprises are undeniable, and vary from a wide range of assets, such as reduction in development cost, easy use and management of data and application, high security, and acquisition of high performance device.

Keywords: GIS-Cloud; Services; SOA; Information System; GIS.

1 Introduction

The introduction of services as new method for serving data over the internet is the major enabling tendency. Nevertheless, internet-based-GIS providers have struck on many difficulties during services genesis. They are facing numerous new challenges toward creating software for millions of consumers to use as a service, rather than to run on their individual computers [1]. Although several challenges had been resolved and the method was undeniably effective, the promise offered by serving software, platform and infrastructure as services (rather than basis services) that has triggered the discovery of a new architectural pattern known as Cloud Computing is overwhelming.

This concept has distinguished itself from the grid computer (GC) by providing the utility computing. For that matter, in this paper, we proposed an architectural design for develop a GIS system based on the Cloud Computing (CC). The first section introduces the CC definition and its characteristics. In the second part, we introduce our system

D. Zeng (Ed.): Future Intelligent Information Systems, LNEE 86, pp. 55–63.
springerlink.com © Springer-Verlag Berlin Heidelberg 2011

architecture by proposing an architecture design and describing its components. The third part is dedicated to the unified model of GIS-C system that is based on implementation of the overall components. At least, the advantages of the designed GIS-C over other GIS models are also given.

2 CC Description and Characteristics

CC is an emerging computing technology that uses the internet and central remote servers to maintain data and applications. It allows consumers to use applications in any computer with internet access to access their personal files without installation. It is an internet-based computing, whereby shared resources are provided to computers and other devices on-demand which is similar to a public utility such as the electricity grid [3]. CC is a general term for anything that involves delivering hosted services over the internet. Service providers are expanding their offerings to include the entire traditional IT stack, ranging from foundational hardware/platforms to application components, software services, and software applications [21]. Services are broadly divided in 3categories: infrastructure-as-a-service, platform-as-a-service, software-as-a-service [2]. In the cloud, the details are abstracted from the users who no longer have need of, expertise in, or control over the technology infrastructure "in the cloud" that supports them [4]. CC describes a new supplement, consumption and delivery model for IT services based on the internet, and it typically involves the provision of dynamically scalable and often virtualized resources as a service over the Internet [5] and [6]. CC users can avoid capital expenditure on hardware, software, and services.

After deep studies, we discover that cloud have three distinct characteristics that differentiate it from traditional hosting such as GC which we call the URE. Utilization: means that the CC is sold on demand. CC involves the utility computing which is paying for what we use on the shared servers for period of time. This characteristic can be compared as the water or gas utilization. Relieved: means that services are fully managed by providers. Consumers need nothing but a personal computer and an internet access. As small as or as big as the client utilization is, the management is completely being done by the provider. It alleviates the consumers' working effort to focus on the business logic of their enterprise. Elasticity: Cloud supplies all type of IS to all type of clients. For instance, a user can purchase as much services as he wants at any given time. Thus Cloud-Client can allocate (dislocate) space to increase (reduce) current space, depending on their needs.

3 System Architecture

3.1 GIS Cloud Architecture (GIS-C)

GIS-C is the use of GIS in CC system which enables applications accessing resource through services rather than a direct access. It offers to users' web-GIS services for uploading, analyzing, editing, creating and publishing geospatial data [19]. Hence, instead of talking to a specific geo-data storage, device or software, the client interacts with service which provides these resources. It main goal is to provide the power of desktop GIS solutions on a web based platform in such way that bring GIS closer to a

wider audience [18] by reducing the expense cost, and high skill requirements. GIS-C system provides web-GIS applications, geo-processing services, storage platform to the GIS-C client. In the following schema, we describe the architecture of our GIS-C, using Amazon EC2 as Cloud infrastructure (Fig.1).

The Client Layer (CL): CL is the GUI directly orientated to users. Like client layer in distributed-GIS, CL in cloud system plays similar roles such as enabling user to manipulate spatial data and information. However in GIS-C the client must purchase one or more services for a matter of time before becoming GIS-C Client. The Component Service Layer (CSL): CSL provides services for geospatial information. It provides sharing and publishing of information using RPC. By using distributed component technology service, consumers purchase desired services in order to integrate them in their applications and reach their goal. The Application Service Layer (ASL): ASL is composed of several applications which client(s) can organize their data in order to form an IS and produce decision making. This layer is supplied to clients who have no need to build their own applications. The Software Service Layer (SFSL): SFSL provides software to client as service. The software is divided into two types which are the platform and the storage software. The Platform Service Layer (PSL): PSL part of SFSL consists of several frameworks to develop, deploy, test, host and maintain applications in the same integrated development environment. It provides different services to support application life cycle. The Storage Service Layer (SSL): SFSL, part of the SSL consists of several spatial database engines (PostgreSQL, proprietary Geodatabase) and large commercial database (SQL, Oracle). It is used to serve client spatial database as services to store, manage and maintain various resources (vector, raster, RS image and temporal data and metadata). The Infrastructure Service Layer (ISL): ISL distributes multi-site physical infrastructure. Most ISL uses server virtualization to better abstract the implementation detail away to users. We used Amazon EC2 as IaaS to provide client highly performing, scalable and secure services with low cost in terms of capital expense and time consuming. Amazon EC2 let users match the software, database environment, and APIs to their need [22].

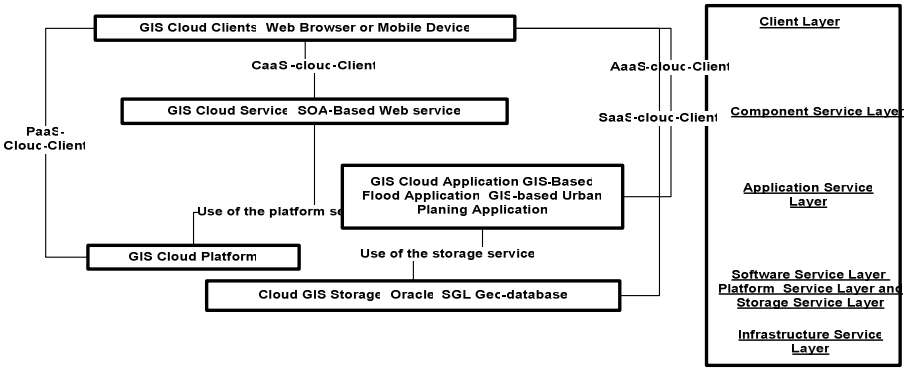

Fig. 1. Designed Architecture of GIS Cloud

In this architectural type, consumers access applications, software, data and information from the GIS-C anywhere in the world on-demand. In other words, GIS-C appears to be a single point of access for all computing needs.

3.2 Diagram Workflow

The aim of the workflow is implemented a private GIS-C host by Amazon EC2. The goal is to purchase an Amazon IaaS; then use it in private sector. By allocating the space from Amazon, we developed GIS-Based-Applications and services, achieved web server and data storage, and hosted them in our OS (Ownership Space). The OS which is an Amazon Cloud is essential for implementing a GIS-C. Having in our disposition the Cloud Infrastructure, we were able to propose a novel model for serving to GIS organization a hosting system for their resources.

In this section, we describe the workflow for implementing GIS-C that serves IS to consumer. The description of work allows client to efficiently select the type of IS they need to purchase. Hence, we used function partition style to provide a set of IS. These services are divided into four groups depending on what they are serving: GIS-Based-SaaS, GIS-based-PaaS, GIS-based-AaaS and GIS-based-CaaS (see Fig.2).

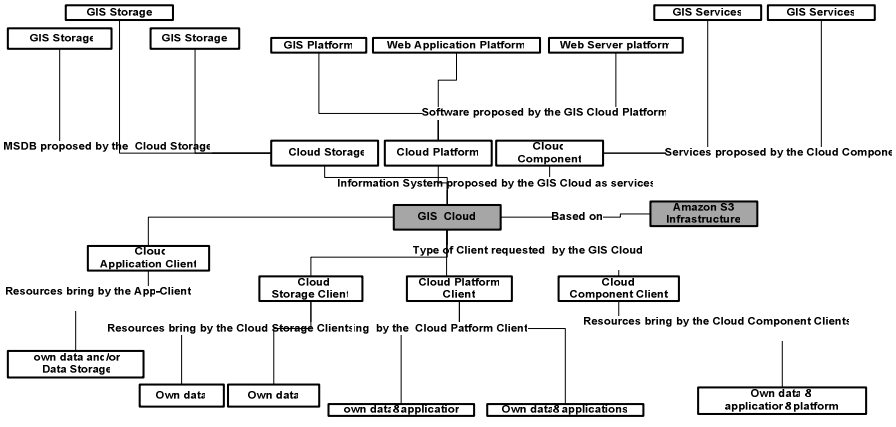

Fig. 2. The Geographic Information System Cloud progressing Workflow

3.3 System Technologies

The emergence of CC and GIS-C raise several questions about the best technologies to use with this new model for on-demand GIS computing. After several studies, we conclude that the techniques are tied up to the services. The important issue for providing services which are abstract away from the implementation is the use for standards. Since the introduction of the web several standards have been provided such as XML, HTTP and XMLHttpRequest, SOA and Web Services.

4 Implementation of GIS-Cloud

The aim of this section is to describe the architecture uses, the type of services provides, and the set of parameters defines in order to efficiently reach the goal. Some parameters, such as the Own-GIS-Based-Application, Cloud-Application-Level-X, Pay-PercentageX-Use-Client and Component-Level-X are proposed.

4.1 GIS-Based-SaaS and GIS-Based-AaaS

GIS-based-SaaS service is an implementation of software-as-a-service in GIS field. We use CC paradigm to provide to Cloud Client a storage space for their data. Cloud-storage-clients are defined as a tier that purchase space disk in a GIS-C system in order to store resources. In our context the system is implemented as a DBMS which provides storage device for the GIS-based-SaaS and as an application platform for the GIS-based-AaaS.

Our GIS-based-SaaS services are composed of a wrapper of legacy software written in a different language and in a completely different architecture. Clients for these types of services are known as SaaS-Client. SaaS-clients consume their resources through a browser, using GIS-based-AaaS which is also an implementation of software-as-a-service. The services are introduced to help enterprises, organizations, and private individuals to better use GIS to fulfill their daily requirements. These latter, mostly do not have any GIS skill to provide and perform advanced GIS tasks. Hence they can use a high efficient GIS-Based-Own-Application by purchasing a GIS-Based-AaaS provided by the Cloud system. GIS-Based-Own-Applications are GIS application which are remodeling toward user's needs. Fig.3 describes the GIS-Based-SaaS model.

Each GIS-Based-Own-Application is defined by levels of complexity. GIS-C-Application-Level-One (GIS-C.A-Level-1) is GIS application hosted in the GIS Cloud with minimum requirement of functions. This kind of application provides to consumers only visualization service. Visualization service is composed of several functions which allow Cloud-storage-clients to display map and perform some tasks such as zoom-in, restore and move.

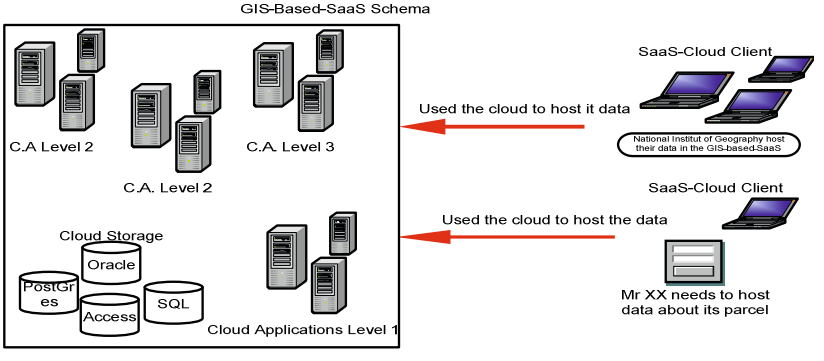

Fig. 3. The GIS-Based Storage as a Service

The Cloud-Application-Level-Two provides, besides the C.A-Level-One functions, some basic GIS analysis functions. Cloud-Application-Level-Three possess the latter entire functions plus some specific functions for a given scientist discipline. GIS-based-SaaS and AaaS are designed to fulfill any request from any client. Therefore, they cover all the consumers' needs from the simplest to more expensive requests.

For the storage of the SaaS, to provide high service availability, the client is supplied with a set of different storages. Data stores and data access software are evaluated for suitability [7]. Therefore, geo-spatial data storage and high scalable data storage are provided, by allowing the SaaS-Cloud-Client to implement evolving applications.

4.2 GIS-Based-CaaS Implementation

SaaS services may be consumed by non-web clients by binding to the service using various API. In the IT community, each SaaS vendor offers these API [8]. In our GIS-C, we propose a type of IS that provides CaaS: hence the name GIS-C Component. In the case of providing service as application component, the GIS-C is implemented using SOA-based via geo-spatial web services. In order to create SOA architecture for the GIS services, we need to create web service correspondences of each GIS service which are be grouped into three categories: data service, processing service and catalog service [10]. The services provided by the CaaS, will be hosted in the GIS Component Cloud, and CaaS-Cloud-Clients can access to them from the discovery repository, by paying what they consume. Services are the architecture components that process business logic for the organization [9]. In recent years, several web service portals or directories have emerged; such as WebServiceList [11] and [12], RemoteMethods in [11] and [14], WSIndex in [13] and [16] and XMethods.net in [11] and [17]. In fact that service must be discovering by any kind of client we propose to use UDDI as hosted services. It allows client to be a Pay-PercentageX-use-Client by searching into the discovery directory and find some functions serve as a service to develop their applications. GIS-based-CaaS provides neither application nor platform to client.

Like the SaaS, the services are defined into levels, depending on their complexity. Component-Level-One (C-L-1) e provides data services which are tightly coupled with specific data sets. The most popular geo-spatial web services implement for this group are the OGC web services such as WMS, WFS and WCS. C-L-Two provides the processing services. These types of services provide operations for processing or transforming data in a manner determined by user-specific parameters [10].

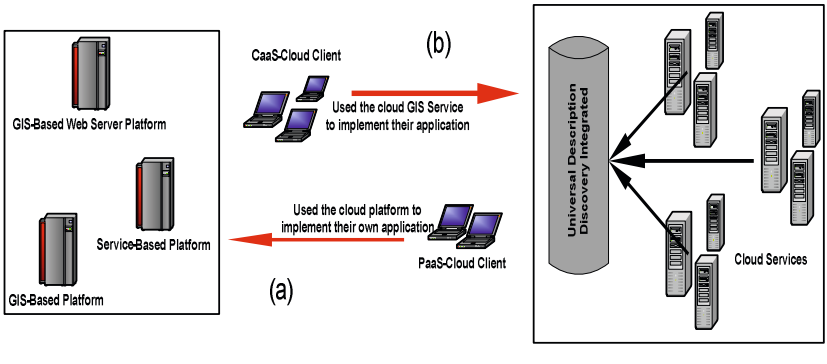

Fig. 4. GIS-based Platform as a Service (b) (a) and GIS-Based Component-as-a-Service

4.3 GIS-Based-PaaS Implementation

PaaS in CC paradigm is a service for delivering operating systems and associated services over the Internet without downloads or installation. PaaS is sometimes called "cloudware" because it moves resources from privately owned computers into the internet "cloud." PaaS is an outgrowth of SaaS [16]. To implement this IS we propose several frameworks in type of IDE and plug-ins. GIS-C Platform provides a set of services. Each service depends on the kind of tasks that the client needs to perform. The services provide frameworks to the PaaS-Cloud-Client and each is composed of plug-ins to enhance the application development. To better supply sophisticated service, we manage to serve to client a unique IDE that provides all services options required for the development life cycle. Nevertheless, most GIS IDEs do not support the entire deployment of applications. So PaaS-Cloud-Client also provided of a set of GIS IDE which do not cover the entire development life cycle.

5 Advantages of GIS Cloud

GIS-C as a system-based-on CC has several advantages over traditional GIS. Easy Setup: GIS-C is available behind few mouse clicks from any point in the world [17]. The same as in web-GIS, clients of the GIS-C only need a browser and an internet connection to get a GIS-C Information System by paying only what they use.

Low Cost: Consumer only pays for what is used. In traditional GIS, even when the client only needs to display, draw and edit features, he is forced to buy the whole GIS desktop license package: paying for more tools than he needs. With the GIS-C, the consumer only needs to purchase the wanted tools, so that results to a low cost for enterprises. Moreover, he doesn't need to have any upfront costs like traditional GIS (hardware) and other components since the entire device is taking care by provider.

Highly-Secure: In centralized systems like GIS-C with encrypted disk partitions and encrypted client connections is in fact much more secure environment for confidential data than in traditional GIS. Because the data is always at one place, on a server which is hidden, highly secured is observed. Server can be physically located in GIS-C data centre or if needed in client's data centre [18], employees have benefit of accessing their data and projects from anywhere without increasing risks of security breaches.

Easy Publishing: with traditional GIS, publishing data is difficult or impossible. Nowadays with the growth of IT, new standards have been introduced to ease the sharing of resources. However, one of the biggest issues that encounter these new standards is maintaining the data. In fact, when data is locally changed and updated, we need to repeat the process to share it on line. With GIS-C as a native web application on line, data sharing is done very easily [17].

Modular Component: GIS-C allows the development modular of GIS components in such a way that system can evolve. Features are packed into modules which can also be used in a pay-per-use model [18]. The SOA-based web service paradigm was used to implement these components. The main aim of this advantage is to allow clients to extend their applications at any time without changing other tiers.

Interoperability & Collaboration: with traditional GIS, the collaboration issue has been a persistent matter for some companies that have many employees in distant

branch offices. Nevertheless in GIS-C, companies' for realization project that is assigned to teams across few branch offices, create a centralized place and assigned to each employee's account by project manager. Hence project is being simultaneously developed by all employees and managing it is very easy because there is no data merging, redundancy and copying. Project is being assembled in real-time [18].

6 Conclusion and Future Work

The aim of this system was to allow organizations to increase their productivity and efficiency in business forces. GIS-C allows customers to abstract away the details of how their applications, component, platform or service are implemented. It provides to these enterprises interoperability among existing technologies without any additional cost. By comparing the benefit of this novel technique, we were able to distinguish the greatest advantages that Cloud techniques can provide for the GIS communities. Only the non-need-device for hosting servers is an enormous gain for the geospatial communities. Hence, we will not be surprise seeing this new model much and much more in the next years. In future we intend to implement this model to supply small and medium sized firms and governments in Africa a GIS-based Cloud applications and services. This GIS-C allows the entities depending of their finance capital, interests and needs, to store their spatial data, purchase services and web-applications, and develop applications with small cost and high quality of service.

References

1. Buyya, R., Yeo, C.S., Venugopal, S.: Market-Oriented Cloud Computing: Vision, Hype, and Reality for Delivering IT Services as Computing Utilities, http://www.buyya.com/papers/hpcc2008_keynote_cloudcomputing.pdf
2. Cloud-computing-Definitions-Cloud-computing-SearchCloudComputing.comDefinition (PoweredbyWhatIs.com)
3. Cloud Computing from Wikipedia, http://en.wikipedia.org/wiki/Cloud_computing
4. Danieal, K.: Distinguishing Cloud Computing from Utility Computing ebiz O, The insider's Guide to Business and IT Ability (March 26, 2008), http://www.ebizq.net/blogs/saasweek/2008/03/distinguishing_cloud_computing/
5. STAMFORD, Conn. Gartner Says Cloud Computing Will Be As Influential As E-business Spacial Report Examines the Realities and Risk of Cloud Computing (June 26, 2008), http://www.gartner.com/it/page.jsp?id=707508
6. Gruman, G.: What cloud computing really means. InfoWorld, http://www.infoworld.com/d/cloud-computing/what-cloud-computing-really-means-031 (retrieved 06-02- 2009)
7. North, K.: Three Steps To Managing Data In The Cloud. Matching the right cloud platform with the right database is critical (July 2009), http://www.drdobbs.com/database/218500177;jsessionid=WG0KFHPSZ2OJNQE1GHPCKHWATMY32JVN

8. Jamil, E.: What really is SOA. A comparison with Cloud Computing, Web 2.0, SaaS, WOA, Web Services, PaaS and others, Soalib Incorporated
9. ESRI White Paper, Geospatial Service-Oriented Architecture (SOA) (June 2007), http://www.esri.com/library/whitepapers/pdfs/geospatial-soa.pdf
10. GIS Service Oriented Architecture
11. Al-Masri, E., Mahmoud, Q.H.: Investigating Web Services on the World Wide Web, WWW 2008 / Refereed Track: Web Engineering - Web Service Deployment, http://www2008.org/papers/pdf/p795-almasriA.pdf
12. WebServiceList, http://www.webservicelist.com (accessed February 2008)
13. RemoteMethods: Home of Web Services (accessed February 2008)
14. WebServices Directory (WSIndex), http://www.wsindex.org (accessed February 2008)
15. XMethods, http://www.xmethods.net (accessed February 2008)
16. SearchCloudComputing.com Definitions, Platform as a Service (PaaS): What is platform as a service (PaaS)?
17. GIS Cloud Beta the new generation of GIS, About GIS Cloud:GIS Cloud vs. Traditional GIS, http://www.giscloud.com/about/gis-cloud-vs-traditional-gis/
18. Omnisdata geo-informatics technologies and services, GIS-Cloud the next Generation of GIS, http://www.riso.ee/et/files/015_omnisdata_giscloud.pdf
19. About GIS cloud, by GIS Cloud Beta, the next generation of GIS

Study on Steam Turbine Fault Diagnosis of Fish-Swarm Optimized Probabilistic Neural Network Algorithm

Jian-jun Xu[1,2], Chao Liu[1], and Quan Zhou[1]

[1] Electricity and Information Engineering College, Northeast Petroleum University, Daqing, 163318, P.R. China
[2] School of Electrical Engineering and Automation, Harbin Institute of Technology, Harbin, 150001, P.R. China

Abstract. This paper investigates that artificial fish-swam algorithm and the probabilistic neural network combination as a hybrid optimization algorithm, of which steps are given and a corresponding network model is built. During the procedure, the study concentrates on that 10 kinds of fault types which are misalignments, unbalance, and rub impact .etc. By using artificial fish-swarm algorithm to train the probabilistic neural network, building the model in which the number of artificial fish is 20, vision range is 2.5, maximum number of iterations is 50, maximum moving step size is 0.3, and crowding factor is 0.618, we can quickly obtain the global optimal solutions. This algorithm is introduced to the steam turbine fault diagnosis applications, according to 100 groups of data, during probabilistic neural network training, the correct diagnosis rate based on steam turbine fault diagnosis is 87%, while the one based on fish-swarm optimized network is 96%.

Keywords: steam turbine unit, fault diagnosis, artificial fish-swarm algorithm, probabilistic neural network.

1 Introduction

With the development of intelligent mechanical equipment, the requirement of higher correct diagnosis rate has become stronger and the applications of intelligent algorithm have become also wider in fault diagnosis. In industrial production, steam turbine plays a decisive role. However, due to the complexity of steam turbine equipment and operating ambient are usually specific, it is prone to malfunction. Besides, reasons for malfunction are diverse. In recent years, the traditional fault diagnosis methods have been gradually replaced by the intelligent ones [1].

Neural network, which is high parallel information processing capability, strong fault tolerance and satisfactory adaptive characteristics, is widely used in many fields [2]. Compared with BP network, it has the advantages of network training: simple, reliable, strong anti-interference. Meanwhile, it still has some shortcomings, for instance, network with low precision. In some respects, the emergence of intelligent algorithms, can remedy the shortcomings of neural networks. Based on analysis of the behavior of fish swarm, artificial fish-swarm algorithm with its parallelism, simplicity, overall, rapidity and tracking is widely applied in many fields [4-8].

D. Zeng (Ed.): Future Intelligent Information Systems, LNEE 86, pp. 65–72.
springerlink.com © Springer-Verlag Berlin Heidelberg 2011

2 Feature Extraction of Steam Turbine Fault Diagnosis

As the complexity of equipment structure, causes which contribute to malfunction of steam turbine are varied. Currently, the researches on steam turbine failure are studies on mostly steam turbine vibration failure; studies objects on steam turbine vibration failure are mainly mechanical failure. There are many types of turbo generators vibrating fault, however, 95% of faults are the common faults which include several faults types as followed. Table 1 shows the 10 common rotating machinery fault types, such as misalignment, unbalance, rubbing, etc. In addition, the misalignment and imbalance are two of the most common turbine faults [8-9].

Table 1. Steam Turbine Vibration and Fault Symptom Table

Fault samples	0	1	2	3	4	5	6	7	8
Band(f=50HZ)	0.01-0.39f	0.40-0.49f	0.50 f	0.51-0.99f	f	2f	3-5f	Odd multiple f	Frequency f
unbalance	0.00	0.00	0.00	0.00	0.90	0.05	0.05	0.00	0.00
Steam power force couple	0.00	0.30	0.10	0.60	0.00	0.00	0.00	0.00	0.10
misalignment	0.00	0.00	0.00	0.00	0.40	0.50	0.10	0.00	0.00
oil film eddy	0.10	0.80	0.00	0.10	0.00	0.00	0.00	0.00	0.00
rotor radial rub	0.10	0.10	0.10	0.10	0.20	0.10	0.10	0.10	0.10
symbiotic looseness	0.00	0.00	0.00	0.00	0.20	0.15	0.40	0.00	0.25
thrust bearing damage	0.00	0.00	0.10	0.90	0.00	0.00	0.00	0.00	0.00
surge	0.00	0.30	0.10	0.60	0.00	0.00	0.00	0.00	0.00
Bearing housing loose	0.90	0.00	0.00	0.00	0.00	0.00	0.00	0.10	0.00
Bearing stiffness ranging	0.00	0.00	0.00	0.00	0.00	0.80	0.20	0.00	0.00

3 Fish-Swarm Algorithm to Optimize Probabilistic Neural Network

Probabilistic neural network has less network parameters. Compared with BP network and RBF network it is much easier to achieve and it has higher stability and the classification which are based on Bayesian (Bayes) classification criteria for minimum risk [6]. However, due to the same smoothing parameters σ of the network, the accuracy of identification would be limited and the final judgment is effected. The artificial fish-swarm algorithm has good global search capability, and can reduce the risk of falling into local extreme point. Furthermore, the requirement of its initial value and

parameters is not high. Consequently, in this paper, a hybrid optimization algorithm has been proposed, which has combined with artificial fish-swarm algorithm and probabilistic neural network. The algorithm which has the advantages of two algorithms has a better application effect. Algorithm training idea is that using artificial fish-swarm algorithm to optimize the probabilistic neural network smoothing factor. The single artificial fish, through foraging behavior, clustering behavior, and rear-end behavior repeated iteration to the extent permitted error, gains the best smoothing factor. Then this smoothing factor value is used to build probabilistic neural network, the PNN network which has optimal smoothing factor.

Construction of the single artificial fish model is the key of hybrid optimization algorithm. Setting the size of artificial fish is N, each single artificial fish can be seen as a smoothing factor set $\sigma = \{\sigma_1, \sigma_2, \cdots \sigma_n\}$, and selecting the error function E_p as the objective function of artificial fish-swarm algorithm.

$$E_P = \frac{1}{2}\sum_{i=1}^{P}\left\| d\left(x_j\right) - y\left(x_j\right)\right\| \tag{1}$$

The steps of the training of fish-swarm algorithm optimizes probabilistic neural network are as follows:

Step 1: According to the training samples to determine the probabilistic neural network input and output. To assign a random value to the probabilistic neural network smoothing factor in the range interval.

$$\sigma = g \cdot \bar{d}_{\min}[k] \tag{2}$$

$\bar{d}_{\min}[k]$ means that it is the minimum distance average in the same samples, g is the coefficient [7] (generally is among 1.1-2.0).

Step 2: According to the structure of probabilistic neural network algorithm, we determine the relevant parameters of fish-swarm algorithm. To input the number of artificial fish is 'N', the vision range of artificial fish is 'Visual', the maximum number of iterations is 'Number', the maximum moving step size is 'Step', the crowding factor is 'δ', and define the distance between the two artificial fish is:

$$d_{pq} = \sum_{i=1}^{n}\left(\sigma_i(p) - \sigma_i(q)\right)^2 \tag{3}$$

$\sigma_i(p)$ means the parameter of artificial fish X_p, and $\sigma_i(q)$ means the parameter of artificial fish X_q.

Step 3: The artificial fish-swarm algorithm is initialized. Setting the initial number of iterations Num is 0, random generate N artificial fishes in the interval [0,1] in order to construction initial fish, that is, to generate N groups of smoothing factor sets { σ_i }.

Step 4: To calculate the food concentration (FC) where each artificial fish positioned, then compared each value of food concentration and assigned bulletin board with the lower FC and condition in the fish group.

Step 5: Each artificial fish simulates implementation clustering behavior. That is searching for the partner X_q who is in the scope of the current view. The number of the searching partner named n_f, and the set of n_f named U_p, its mathematical expression is that:

$$U_p = \left\{ X_q \middle| d_{pq} \le Visual \right\} \tag{4}$$

If $U_q \neq \phi$ (ϕ is null set), then it can say that the area near X_p have other partners, and we can find the center position X_c according to expression (4) in the set.

$$\sigma_i(c) = \left(\sum_{q=1}^{n_f} \sigma_i(q) \right) \Big/ n_f \tag{5}$$

In the expression, $\sigma_i(q)$ means the variable which the partner X_q owned around X_p. Computing the location of food concentration FC_c, if FC_c meets the expression as follows:

$$FC_c / n_f < \delta FC_p \qquad \delta > 1 \tag{6}$$

Then we can say that the center position of the partner is in a good condition and the crowding of that is not high, the artificial fish will go a step forward to this location, executes the expression (7), otherwise, does foraging behavior.

$$\sigma_i(p+1) = \sigma_i(p) + (Step)(\sigma_i(c) - \sigma_i(p)) / d_{p,c} \tag{7}$$

If $U_q = \phi$, means that there is not has other partners in the scope of the view, the artificial fish executes foraging behavior.

The learning methods of foraging behavior can be divided into two ways. When artificial fish meets the expression of $FC_q < FC_p$, executes (8); When meets $FC_q \ge FC_p$, executes (9).

$$\sigma_i(p+1) = \sigma_i(p) + (Step)(\sigma_i(p) - \sigma_i(q)) / d_{pq} \tag{8}$$

$$\sigma_i(p+1) = \sigma_i(p) + (Step) \tag{9}$$

Step 6: Each artificial fish simulates implementation rear-end behavior, which is searching for the partner $X_{\min}$ who is the lowest food concentrationin the scope of the current view. If it can meet the expression as follows:

$$FC_{\min} < \delta FC_p \qquad \delta > 1 \tag{10}$$

Then we can say that the position of the partner $X_{\min}$ is in a good condition and the crowding of that is not high, execute the expression (11), otherwise, execute foraging behavior.

$$\sigma_i(p+1) = \sigma_i(p) + (Step)(\sigma_i(\mathrm{m}) - \sigma_i(p))/d_{p,\mathrm{m}} \tag{11}$$

If the current view of artificial fish does not exist other partners, execute the expression (11).

Step 7: Compared the food concentrations of step5 and step6, choosing the behavior to execute which is lower food concentration, the default behavior is foraging behavior, that is, according to the condition to execute (8) or (9).

Step 8: After an individual action of each artificial fish, compared with the food concentrations of itself and the bulletin board, if the value of food concentration is better than that of the bulletin board, assigned the value and the condition to the bulletin board, updates the value of bulletin board.

Step 9: To judge whether the 'Num' has reached the predefined maximum iterations 'Number' or to judge whether the result has achieved the required range of admissible error. And if so, put the value of food concentration in bulletin board as calculated output, execute step 10; if not, $Num = Num + 1$, turn to step 5 to continue iteration.

Step 10: To determine the probabilistic neural network model through the optimal smoothing factor δ.

4 The Establishment and Simulation of Steam Turbine Fault Diagnosis Model Based on Fish-Swarm Optimization Algorithm

4.1 Fault Diagnosis Model

In this paper, the table 1 which has given 10 kinds of fault types of steam turbine set as the network output, and the vibration signal spectrum of 9 different frequency bands on the spectrum peak energy has been selected as the eigenvector. A probabilistic neural network which has 9-input and 10-output has been constructed by them. Use the training method which is fish-swarm optimized probabilistic neural network algorithm previously described to determine the smoothing factor σ, and create a probabilistic neural network. Then, experimental data on the network is trained to construct fault diagnosis model.

4.2 Simulation of Fault Diagnosis

Using MATLAB encode the model above, setting the number of artificial fish N is 20, artificial fish vision range $Visual$ is 2.5, the maximum number of

iterations *Number* is 50, maximum moving step size *Step* is 0.3, and crowding factor δ is 0.618. For 100 groups of fault data, using two methods to train the network which are based on the PNN neural network and fish-swarm optimized neural network algorithm. The simulation results are as follows.

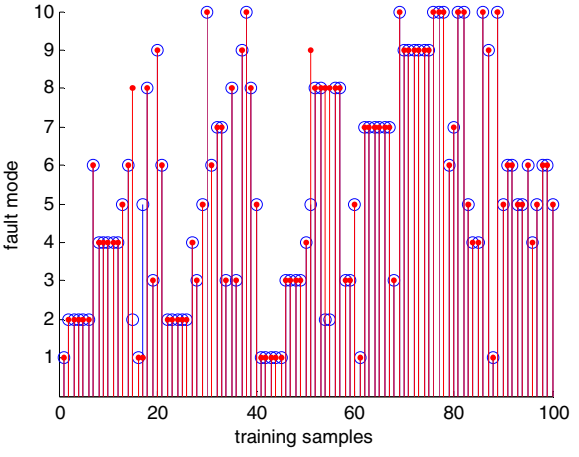

Fig. 1. "○" means the type of network training failure result, "·" means the type of actual failure result. If "○" and "·" are in the same place, it means that the training result is right; otherwise, it is wrong. This figure is the result which training by fish-swarm optimized neural network algorithm

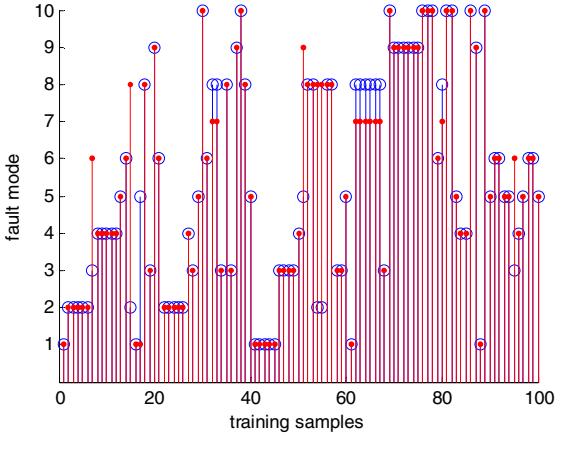

Fig. 2. "○" means the type of network training failure result, "·" means the type of actual failure result. If "○" and "·" are in the same place, it means that the training result is right; otherwise, it is wrong. This figure is the result which training by PNN neural network.

From figures, it can be seen that the simulation result that the error rate which of the PNN network training is higher, but the accuracy rate which training by the fish-swarm optimized probabilistic neural network is better, about 95%.

We diagnose 50 groups of testing data through two networks which have been trained by PNN and fish-swarm optimized probabilistic neural network respectively. The diagnostic result has shown in Figure 3.

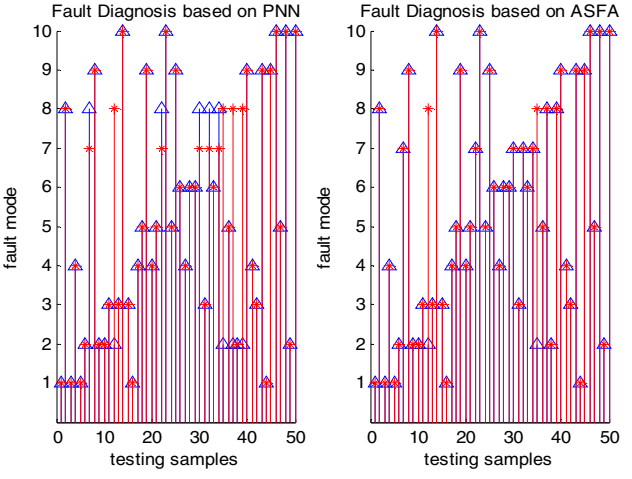

Fig. 3. "△" means the type of fault which has been trained through network diagnostics, "*" means the type of actual failure result. If the "△" and the "*" are in the same place, it means that the diagnostic result is right; otherwise, it is wrong. This figure shows the fault diagnosis based on PNN and ASFA.

It can be seen from the simulation result that the accuracy rate of fault diagnosis in steam which training by the fish-swarm optimized probabilistic neural network is 96%, while that is 86% which training by PNN. Thus, the former has a higher recognition rate in pattern and has obvious advantages than the latter [10-11].Compared with other networks, fish-swarm optimized probabilistic neural network has the advantages of network training simple and faster.

5 Conclusions

To overcome the shortage of the accuracy of PNN network, the fish-swarm algorithm has been introduced to the optimization of probabilistic neural network in this paper. The appropriate training methods have been given and already applied to the steam turbine fault diagnosis by constructing the training model of fish-swarm optimized probabilistic neural network. For 100 groups of fault data, the training accuracy rate of fault diagnosis in steam which training by probabilistic neural network is 87%, while which training by fish-swarm optimized algorithm is 95%, the latter training accuracy rate is higher than the former. For 50 groups of testing data, the testing accuracy rate of fault diagnosis in steam which training by probabilistic neural network is

86%, while that which training by fish-swarm optimized algorithm is 96%, the latter testing accuracy rate is higher than the former. By comparison, we can conclude that in steam turbine fault diagnosis fish-swarm optimized network has a good effect of pattern recognition, and the accuracy rate of fault diagnosis is also quite high.

References

1. Ding, Y.F., Sheng, B.Y.: Study on steam turbine fault diagnosis and maintenance service grid system. J. Proc. Inst. Mech. Eng. Part B J Eng. Manufpp. 224, 517–530 (2010)
2. Kohonen, T.: The Self-Organizing Maps. Proc. IEEE 98, 1464–1480 (2009)
3. Specht, D.F., Romsdahl, H.: Probabilistic neural network and general regression neural network. Proc. IEEE 88, 1203–1208 (2004)
4. Reynolds, C.W.: Flocks herds, schools: a distributed behavioral model. In: Proceeding of SIGGRAPH 1987 Computer GarPhics, Ailaheim, Califomia, vol. 21, pp. 25–34 (1987)
5. Guang-Qiu, H.: Optimization method of multistage stations locating in oil transportation based on fish-swarm algorithm. J. System Engineering Theory and Practice 3, 94–102 (2008)
6. Lee, J.J.: An improved application technique of the adaptive probabilistic neural network for predicting concrete strength. J. Computational Materials Science 3, 988–998 (2009)
7. Xiao-Lei, L.: Optimizing method based on autonomous animats: Fish-swarm Algorithm. J. System Engineering Theory and Practice 11, 415–426 (2002)
8. Ma, X., Liu, Q.: An artificial fish swarm algorithm for Steiner tree problem. In: IEEE International Conference on Fuzzy Systems, pp. 59–63 (2009)
9. Jian-Jun, X., Shi-Yan, Y.: Fault diagnosis of wavelet packet neural network on pump valves of reciprocating pumps based on pressure signal. J. Journal of Dalian Maritime University, 22–25 (2007)
10. Ganchev: Todor1 Enhanced training for the locally recurrent probabilistic neural networks. International Journal on Artificial Intelligence Tools 6, 853–881 (2009)
11. Jian-Jun, X., Chao, L.: Research of small pipeline leak detection applied SPRT algorithm. J. Electric Machines and Control, 448–451 (2009)

Robust Zero-Watermark Algorithms in Hybrid Transform Domains Based on the Parity of Norm's Highest Digit

Tianyu Ye

College of Information & Electronic Engineering,
Zhejiang Gongshang University,
Hangzhou 310018, P.R. China
flystu008@yahoo.com.cn

Abstract. Two robust zero-watermark algorithms in hybrid transform domains are proposed. The first one is realized in hybrid transform domains of discreet cosine transform (DCT) and singular value decomposition (SVD), and the other one is realized in hybrid transform domains of discreet wavelet transform (DWT), DCT and SVD. The first algorithm divides an image into non-overlapping blocks, transforms every block with DCT, and conducts SVD on the upper left corner of every block's DCT matrix. Finally, it produces the zero-watermark sequence by judging the parity of norm's highest digit. The second algorithm transforms an image with DWT, divides its LL band into non-overlapping blocks, and transforms every block with DCT, then conducts SVD on the upper left corner of every block's DCT matrix. Finally, it produces the zero-watermark sequence by judging the parity of norm's highest digit. It is easy to find out that both of them have perfect visual effect. Experimental results show that as to images with different textures, both of them have good robustness against various attacks.

Keywords: Zero-watermark, parity, norm, discreet cosine transform (DCT), singular value decomposition (SVD), discreet wavelet transform (DWT).

1 Introduction

According to different criterions, the watermark algorithms can be classified into different types. According to the function of watermark, they can be classified into robust watermark algorithms, fragile watermark algorithms and semi-fragile watermark algorithms, among which the robust watermark algorithms always play the role of copyright protection. According to the hidden domain of watermark, they can be classified into spatial domain watermark algorithms and transform domain watermark algorithms. For example, transform domains such as discreet wavelet transform (DWT), discreet cosine transform (DCT) and singular value decomposition (SVD) are frequently used to hide watermarks.

When embedding an external watermark into an original image, the visual effect of original image tends to deteriorate. Wen Quan etc [1] firstly suggests the

D. Zeng (Ed.): Future Intelligent Information Systems, LNEE 86, pp. 73–81.
springerlink.com © Springer-Verlag Berlin Heidelberg 2011

zero-watermark technology to solve the conflict between visual deterioration and robustness, which exploits image's characteristic to construct a watermark to protect image.

In this paper, it tries to make full use of different transform domains' features to design robust zero-watermark algorithms. The first algorithm is realized in hybrid transform domains of DCT and SVD, and the other one is realized in hybrid transform domains of DWT, DCT and SVD. Both of them have perfect visual effect. Experimental results show that as to images with different textures, both of them have good robustness against various attacks.

2 Two Robust Zero-Watermark Algorithms

In this section, two robust zero-watermark algorithms are illustrated, which derive their zero-watermark sequences by judging the parity of norm's highest digit. The first algorithm is realized in hybrid domains of DCT and SVD, and the other one is realized in hybrid domains of DWT, DCT and SVD. The original image used in two algorithms is denoted as I , and its size is $M \times M$.

2.1 The First Algorithm

The first algorithm produces its original zero-watermark sequence W from the original image I in the following way.

a1: The original image I is divided into non-overlapping blocks of $n \times n$ size. Every block is denoted by I_k , $k = 1, 2, \cdots, \Omega$, where Ω is the total number of blocks.

a2: Every block is transformed with DCT, i.e., $I_k^{DCT} = dct(I_k)$, where $dct(\cdot)$ denotes DCT computation, I_k^{DCT} is the DCT matrix of I_k .

a3: The $m \times m$ ($m < n$)upper left corner of I_k^{DCT} , denoted as $I_k^{DCT_{m \times m}}$, is picked up to conduct with SVD, i.e., $svd(I_k^{DCT_{m \times m}}) = U_k S_k V_k^T$, where $svd(\cdot)$ denotes SVD computation.

a4: Compute norm for $I_k^{DCT_{m \times m}}$, i.e., $norm_k = \sqrt{\sum_{i=1}^{m} (s_k^i)^2}$, where s_k^i denotes the ith singular value of $I_k^{DCT_{m \times m}}$.

a5: The original zero-watermark sequence W from I is derived by judging the parity of norm's highest digit. If the highest digit of $norm_k$ is odd, let $w_k = 1$; otherwise let $w_k = 0$, where w_k is the kth bit of W . For example, if $norm_k = 985$, then $w_k = 1$, because the highest digit of $norm_k$, i.e., 9, is odd.

Make sure that $I_k^{DCT_{m \times m}}$ is merely made up of DC coefficient and low frequency DCT coefficients. The reason lies in that DC coefficient and low frequency DCT

coefficients gather most energy of I_k, and that conducting SVD on them is beneficial to enhance the robustness against attacks.

The first algorithm extracts its zero-watermark sequence W' from the attacked image I' in the following way.

a1: The attacked image I' is divided into non-overlapping blocks of $n \times n$ size. Every block is denoted by I_k', $k = 1, 2, \cdots, \Omega$.

a2: Every block is transformed with DCT, i.e., $I_k'^{DCT} = dct(I_k')$, where $I_k'^{DCT}$ is the DCT matrix of I_k'.

a3: The $m \times m$ ($m < n$)upper left corner of $I_k'^{DCT}$, denoted as $I_k'^{DCT_{m \times m}}$, is picked up to conduct with SVD, i.e., $svd(I_k'^{DCT_{m \times m}}) = U_k' S_k' V_k'^T$.

a4: Compute norm for $I_k'^{DCT_{m \times m}}$, i.e., $norm_k' = \sqrt{\sum_{i=1}^{m} (s_k'^i)^2}$, where $s_k'^i$ denotes the ith singular value of $I_k'^{DCT_{m \times m}}$.

a5: The zero-watermark sequence W' from I' is derived by judging the parity of norm's highest digit. If the highest digit of $norm_k'$ is odd, let $w_k' = 1$; otherwise let $w_k' = 0$, where w_k' is the kth bit of W'.

a6: Define similarity to evaluate the robustness against various attacks. The similarity between W and W' is defined as $\gamma = 1 - (\sum_{k=1}^{\Omega} w_k \oplus w_k') / \Omega$, where $\oplus$ denotes XOR operation.

2.2 The Second Algorithm

The second algorithm produces its original zero-watermark sequence W from the original image I in the following way.

a1: The original image I is transformed with DWT at level c, and its LL band of level c is denoted as LL.

a2: The LL band of level c is divided into non-overlapping blocks of $n \times n$ size. Every block is denoted by LL_k, $k = 1, 2, \cdots, \Psi$, where Ψ is the total number of blocks.

a3: Every block is transformed with DCT, i.e., $LL_k^{DCT} = dct(LL_k)$, where LL_k^{DCT} is the DCT matrix of LL_k.

a4: The $m \times m$ ($m < n$)upper left corner of LL_k^{DCT}, denoted as $LL_k^{DCT_{m \times m}}$, is picked up to conduct with SVD, i.e., $svd(LL_k^{DCT_{m \times m}}) = U_k S_k V_k^T$.

a5: Compute norm for $LL_k^{DCT_{m \times m}}$, i.e., $norm_k = \sqrt{\sum_{i=1}^{m} (s_k^i)^2}$, where s_k^i denotes the ith singular value of $LL_k^{DCT_{m \times m}}$.

a6: The original zero-watermark sequence W from I is derived by judging the parity of norm's highest digit. If the highest digit of $norm_k$ is odd, let $w_k = 1$; otherwise let $w_k = 0$.

The LL band gathers most energy of the original image I after DWT, and transforming DCT on it is beneficial to enhance the robustness against attacks. Moreover, make sure that $LL_k^{DCT_{m\times m}}$ is merely made up of DC coefficient and low frequency DCT coefficients. The reason lies in that DC coefficient and low frequency DCT coefficients gather most energy of LL_k, and that conducting SVD on them is beneficial to enhance the robustness against attacks.

The second algorithm extracts its zero-watermark sequence W' from the attacked image I' in the following way.

a1: The attacked image I' is transformed with DWT at level c, and its LL band of level c is denoted as LL'.

a2: The LL band of level c is divided into non-overlapping blocks of $n\times n$ size. Every block is denoted by LL_k', $k = 1, 2, \cdots, \Psi$.

a3: Every block is transformed with DCT, i.e., $LL_k'^{DCT} = dct(LL_k')$, where $LL_k'^{DCT}$ is the DCT matrix of LL_k'.

a4: The $m\times m$ upper left corner of $LL_k'^{DCT}$, denoted as $LL_k'^{DCT_{m\times m}}$, is picked up to conduct with SVD, i.e., $svd(LL_k'^{DCT_{m\times m}}) = U_k' S_k' V_k'^T$.

a5: Compute norm for $LL_k'^{DCT_{m\times m}}$, i.e., $norm_k' = \sqrt{\sum_{i=1}^{m} (s_k'^i)^2}$, where $s_k'^i$ denotes the ith singular value of $LL_k'^{DCT_{m\times m}}$.

a6: The zero-watermark sequence W' from I' is derived by judging the parity of norm's highest digit. If the highest digit of $norm_k'$ is odd, let $w_k' = 1$; otherwise let $w_k' = 0$.

a7: Define similarity to evaluate the robustness against various attacks. The similarity between W and W' is defined as $\gamma = 1 - (\sum_{k=1}^{\Psi} w_k \oplus w_k') / \Psi$.

3 Experimental Results

Elain, Boat and Baboon, shown in figure 1, are used as test images in both algorithms. They are grayscale images, and have the same size of 512×512. In the first algorithm, every image is divided into non-overlapping 8×8 blocks, and the 3×3 upper left corner of the DCT matrix of every block is picked up to conduct with SVD.

Therefore, the length of zero-watermark sequence from the first algorithm is 4096 bit. In the second algorithm, Harr wavelet is used to perform DWT at level one. Then the LL band is divided into non-overlapping 8×8 blocks, and the 3×3 upper left corner of the DCT matrix of every block is picked up to conduct with SVD. Therefore, the length of zero-watermark sequence from the second algorithm is 1024 bit.

Elain Boat Baboon

Fig. 1. Three test images

The results of robustness tests against various attacks for Elain, Boat and Baboon are listed in Table 1, 2 and 3, respectively. Not only the results of the first algorithm and the second algorithm are listed, but also the results of reference [2] are listed for comparison. As to reference [2], Harr wavelet is used to perform DWT at level one. Then the LL band is divided into non-overlapping 8×8 blocks to conduct with SVD. Therefore, the length of zero-watermark sequence from reference [2] is 1024 bit. PSNR, located below "/" in every table, is used to evaluate the visibility discrepancy between I and $I^{'}$. Similarity, located above "/" in every table, is used to evaluate the robustness against various attacks. The window size of gaussian low-pass filter in all tests is [3,3]. Downward shifting refers to downward shifting the whole image several rows, filling the top blank rows with black and dropping the below rows. Random row removal refers to shifting upward line-by-line from the first row underneath the deleted row, and filling the below blank rows with black.

According to Table 1, 2 and 3, it can be concluded that: (1) For three images with different textures, i.e., Elain, Boat and Baboon, all three algorithms have good robustness towards various attacks. (2) For Elain, Boat and Baboon, the second algorithm is close to reference [2] in the robustness towards various attacks. In most cases, their performances are slightly better than the first algorithm.

Table 1. Robustness tests for Elain

Attack	Gaussian noise		Salt&Pepper noise		Gaussian low-pass filter	
Parameter	Variance		Intensity		Standard deviation	
Algorithm	0.01	0.03	0.03	0.06	0.3	0.5
The first algorithm	0.9373/ 20.1040	0.8816/ 15.6226	0.9402/ 20.6334	0.9043/ 17.5882	0.9861/ 50.6173	0.9851/ 37.9009
The second algorithm	0.9834/ 20.1174	0.9688/ 15.6192	0.9707/ 20.5483	0.9639/ 17.5301	0.9922/ 50.6173	0.9863/ 37.9009
Reference [2]	0.9795/ 20.1355	0.9727/ 15.6084	0.9697/ 20.5705	0.9658/ 17.5906	0.9893/ 50.6173	0.9834/ 37.9009
Attack	Median filter		JPEG compression			
Parameter	Window size		Quality factor			
Algorithm	[3,3]	[5,5]	40	30	20	10
The first algorithm	0.9866/ 32.4891	0.9810/ 31.3020	0.9878/ 32.3094	0.9788/ 31.8758	0.9712/ 31.1849	0.9419/ 29.5205
The second algorithm	0.9961/ 32.4891	0.9932/ 31.3020	0.9902/ 32.3094	0.9951/ 31.8758	0.9961/ 31.1849	0.9766/ 29.5205
Reference [2]	0.9951/ 32.4891	0.9912/ 31.3020	0.9932/ 32.3094	0.9941/ 31.8758	0.9961/ 31.1849	0.9766/ 29.5205
Attack	Cropping		Anticlockwise rotation		Downward shifting	
Parameter	Size		Angle		Row number	
Algorithm	1/32 upper left corner	1/16 upper left corner	1	2	2	4
The first algorithm	0.9688/ 23.5394	0.9375/ 19.8880	0.8906/ 21.0234	0.8496/ 17.7116	0.9170/ 23.3952	0.8618/ 20.0095
The second algorithm	0.9980/ 23.5394	0.9971/ 19.8880	0.9004/ 21.0234	0.8311/ 17.7116	0.9541/ 23.3952	0.9111/ 20.0095
Reference [2]	0.9980/ 23.5394	0.9971/ 19.8880	0.9004/ 21.0234	0.8291/ 17.7116	0.9580/ 23.3952	0.9150/ 20.0095
Attack	Random row removal		Scaling			
Parameter	Row number		Proportion			
Algorithm	1	2	First lessen to 80%, then magnify to 125%		First lessen to 50%, then magnify to 200%	
The first algorithm	0.9678/ 27.2462	0.9482/ 24.8460	0.9421/ 25.6332		0.9517/ 28.2653	
The second algorithm	0.9785/ 27.2462	0.9648/ 24.8460	0.9697/ 25.6332		0.9863/ 28.2653	
Reference [2]	0.9766/ 27.2462	0.9678/ 24.8460	0.9678/ 25.6332		0.9854/ 28.2653	

Table 2. Robustness tests for Boat

Attack	Gaussian noise		Salt&Pepper noise		Gaussian low-pass filter	
Parameter / Algorithm	Variance		Intensity		Standard deviation	
	0.01	0.03	0.03	0.06	0.3	0.5
The first algorithm	0.9482/ 20.1214	0.8970/ 15.7354	0.9385/ 20.4693	0.9043/ 17.4375	0.9944/ 50.4958	0.9915/ 38.0670
The second algorithm	0.9600/ 20.1246	0.9209/ 15.7563	0.9365/ 20.4704	0.9131/ 17.4084	0.9883/ 50.4958	0.9873/ 38.0670
Reference [2]	0.9658/ 20.1545	0.9229/ 15.7287	0.9375/ 20.3570	0.9131/ 17.4275	0.9893/ 50.4958	0.9863/ 38.0670
Attack	Median filter		JPEG compression			
Parameter / Algorithm	Window size		Quality factor			
	[3,3]	[5,5]	40	30	20	10
The first algorithm	0.9856/ 31.5943	0.9678/ 27.4552	0.9910/ 33.2981	0.9873/ 32.2762	0.9775/ 30.8501	0.9514/ 28.2985
The second algorithm	0.9932/ 31.5943	0.9814/ 27.4552	0.9941/ 33.2981	0.9941/ 32.2762	0.9902/ 30.8501	0.9619/ 28.2985
Reference [2]	0.9863/ 31.5943	0.9746/ 27.4552	0.9951/ 33.2981	0.9922/ 32.2762	0.9883/ 30.8501	0.9639/ 28.2985
Attack	Cropping		Anticlockwise rotation		Downward shifting	
Parameter / Algorithm	Size		Angle		Row number	
	1/32 upper left corner	1/16 upper left corner	1	2	2	4
The first algorithm	0.9688/ 24.0198	0.9375/ 20.9471	0.9023/ 19.0361	0.8816/ 16.3330	0.9204/ 21.1523	0.8950/ 17.8263
The second algorithm	1.0000/ 24.0198	0.9990/ 20.9471	0.9248/ 19.0361	0.8789/ 16.3330	0.9453/ 21.1523	0.9043/ 17.8263
Reference [2]	1.0000/ 24.0198	0.9990/ 20.9471	0.9229/ 19.0361	0.8789/ 16.3330	0.9502/ 21.1523	0.9092/ 17.8263
Attack	Random row removal		Scaling			
Parameter / Algorithm	Row number		Proportion			
	1	2	First lessen to 80%, then magnify to 125%		First lessen to 50%, then magnify to 200%	
The first algorithm	0.9451/ 25.9921	0.9236/ 21.7300	0.9360/ 23.8443		0.9507/ 25.6498	
The second algorithm	0.9736/ 25.9921	0.9453/ 21.7300	0.9590/ 23.8443		0.9736/ 25.6498	
Reference [2]	0.9707/ 25.9921	0.9424/ 21.7300	0.9551/ 23.8443		0.9746/ 25.6498	

Table 3. Robustness tests for Baboon

Attack	Gaussian noise		Salt&Pepper noise		Gaussian low-pass filter	
Parameter	Variance		Intensity		Standard deviation	
Algorithm	0.01	0.03	0.03	0.06	0.3	0.5
The first algorithm	0.9448/ 20.0692	0.8970/ 15.5703	0.9441/ 20.6341	0.9121/ 17.6883	0.9883/ 50.2079	0.9768/ 30.7797
The second algorithm	0.9678/ 20.0675	0.9561/ 15.5743	0.9707/ 20.7026	0.9463/ 17.6937	0.9912/ 50.2079	0.9893/ 30.7797
Reference [2]	0.9775/ 20.0625	0.9541/ 15.6025	0.9658/ 20.6472	0.9541/ 17.6359	0.9893/ 50.2079	0.9873/ 30.7797
Attack	Median filter		JPEG compression			
Parameter	Window size		Quality factor			
Algorithm	[3,3]	[5,5]	40	30	20	10
The first algorithm	0.9373/ 22.8452	0.8911/ 20.4224	0.9871/ 26.4833	0.9824/ 25.5517	0.9702/ 24.3669	0.9321/ 22.5293
The second algorithm	0.9893/ 22.8452	0.9707/ 20.4224	0.9951/ 26.4833	0.9941/ 25.5517	0.9932/ 24.3669	0.9824/ 22.5293
Reference [2]	0.9863/ 22.8452	0.9678/ 20.4224	0.9922/ 26.4833	0.9912/ 25.5517	0.9902/ 24.3669	0.9814/ 22.5293
Attack	Cropping		Anticlockwise rotation		Downward shifting	
Parameter	Size		Angle		Row number	
Algorithm	1/32 upper left corner	1/16 upper left corner	1	2	2	4
The first algorithm	0.9731/ 19.6534	0.9465/ 16.4457	0.8462/ 16.1203	0.8132/ 15.3637	0.8696/ 15.9186	0.8306/ 15.3179
The second algorithm	0.9883/ 19.6534	0.9736/ 16.4457	0.9414/ 16.1203	0.9023/ 15.3637	0.9609/ 15.9186	0.9355/ 15.3179
Reference [2]	0.9883/ 19.6534	0.9746/ 16.4457	0.9414/ 16.1203	0.9004/ 15.3637	0.9639/ 15.9186	0.9297/ 15.3179
Attack	Random row removal		Scaling			
Parameter	Row number		Proportion			
Algorithm	1	2	First lessen to 80%, then magnify to 125%		First lessen to 50%, then magnify to 200%	
The first algorithm	0.9619/ 21.9399	0.9377/ 19.6000	0.8997/ 19.8552		0.9065/ 19.4893	
The second algorithm	0.9893/ 21.9399	0.9814/ 19.6000	0.9629/ 19.8552		0.9688/ 19.4893	
Reference [2]	0.9951/ 21.9399	0.9814/ 19.6000	0.9688/ 19.8552		0.9746/ 19.4893	

4 Conclusions

In the paper, two robust zero-watermark algorithms in hybrid transform domains are proposed. The first algorithm divides an image into non-overlapping blocks, transforms every block with DCT, and conducts SVD on the upper left corner of every block's DCT matrix. Finally, it produces the zero-watermark sequence by judging the parity of norm's highest digit. The second algorithm transforms an image with DWT, divides its LL band into non-overlapping blocks, and transforms every block with DCT, then conducts SVD on the upper left corner of every block's DCT matrix. Finally, it produces the zero-watermark sequence by judging the parity of norm's highest digit. It is easy to find out that both of them have perfect visual effect.Experimental results show that as to images with different textures, both of them have good robustness against various attacks.

References

1. Wen, Q., Sun, Y.-f., Wang, S.-x.: Concept and Application of Zero-watermark. Acta Electronica Sinica 31(2), 214–216 (2003)
2. Ye, T.-y., Ma, Z.-f., Niu, X.-x., Yang, Y.-x.: A Zero-watermark Technology with Strong Robustness. Journal of Beijing University of Posts and Telecommunications 33(3), 126–129 (2010)
3. Huang, D.-r., Liu, J.-f.: An Embedding Strategy and Algorithm for Image Watermarking in DWT Domain. Journal of Software 13(7), 1290–1297 (2002)
4. Liu, R.-z., Tan, T.-n.: SVD Based Digital Watermarking Method. Acta Electronica Sinica 29(2), 168–171 (2001)
5. Lahouari, G., Ahmed, B., Mohammad, K.I., Said, B.: Digital Image Watermarking Using Balanced Multiwavelets. IEEE Trans. on Signal Processing 54(4), 1519–1536
6. Sharkas, M., ElShafie, D., Hamdy, N.: A Dual Digital-image Watermarking Technique. In: Proc. of 3rd World Enformatika Conference (WEC 2005), Istanbul, Turkey, pp. 136–139 (2005)
7. Xu, L.-l., Wang, Y.-m.: Robust Digital Watermarking Scheme Resistant to Gaussian Noise, Geometric Distortion and JPEG Compression Attacks. Journal of Electronics & Information Technology 30(4), 933–936 (2008)
8. Niu, S.-z., Niu, X.-x., Yang, Y.-x., Hu, W.-q.: Data Hiding Algorithm for Halftone Images. Acta Electronica Sinica 32(7), 1180–1183 (2004)
9. Yuan, D.-y., Xiao, J., Wang, Y.: Study on the Robustness of Digital Image Watermarking Algorithms to Geometric Attacks. Journal of Electronics & Information Technology 30(5), 1251–1256 (2008)

Optimal Test Time and Power for System-On-Chip Designs Using Game Theory

Jingbo Shao[1], Lijun Lun[1], Mingyu Liu[1], Yingmei Li[1], and Ruixue Zhang[2]

[1] College of Computer Science and Information Engineering,
Harbin Normal University, 150025 Harbin, China
ttsmonica@yahoo.com.cn
[2] Computer department, Harbin Financial College,
150030 Harbin, China
zrxhdz@yahoo.com.cn

Abstract. This paper proposes a nonzero two-person no-cooperative game theory model for core based SoC test scheduling to minimize test application time and test power. The existence of Nash equilibration has been proved. Nash equilibration gives the Pareto solution of the problem. Experimental results prove that the proposed method achieves better results than the existing methods.

Keywords: test scheduling; game theory; Nash equilibration.

1 Introduction

The development of manufacturing abilities propels IC into VDSM phase. In conformity to Moore's law, the ever-increasing complexity of IC, more and more shrinking feature size of semiconductor device results in lower and lower cost and more complicated System-on-Chip (SoC). Therefore SoC design is confronted with the following challenges:

Urgent time-to-market and the high design complexity make it necessary for design reuse;

Problems that have been ignored at the early stage of IC design becomes significant;

Test scheduling for high complexity SoC needs to minimize test application time under multiple constraints.

Many researchers have explored core based SoC test scheduling extensively. Zhao explored SoC test scheduling, subject to n cores and m test resources SoC [1], test resources were utilized uniformly without causing test conflict, single source single sink network graph were established for such problem. Therefore the problem is converted into –shortest path model. It requires that only one test resource is available for one core at one interval, while different cores can use different test resources simultaneously. Monte studies test scheduling problem based on multi-processor for one task at some moment. Such problem can be modeled as linear program problem. Both the two methods forbid alter or preempt the launched test. Some author proposes preemptive test scheduling, the lower bound of each test session is determined by the test

D. Zeng (Ed.): Future Intelligent Information Systems, LNEE 86, pp. 83–86.
springerlink.com © Springer-Verlag Berlin Heidelberg 2011

time of each test, it makes full use of test access mechanism (TAM), however test controller design becomes difficult [2], some author proposes integer linear program and hybrid integer linear program for SoC test scheduling, the readers are referred to detailed algorithm in [3]. Author takes SoC test scheduling as network transportation [4], and Koranne models the problem as Minimum cost maximum network flow [5]. Harmanani investigates test scheduling under constraints of test priority, test power and idle test time slot minimization [6] (ST-1). Larsson proposes a comprehensive framework for parallel SoC core test scheduling to minimize test application and test power without causing test conflict(ST-2).

SoC test scheduling aims at test application time minimization and avoid test conflict. Parallel test might increase test time, and might destroy the whole system under test in severe situation. Therefore it is necessary to take into account of test power, the limited test resources. The existing solutions do not offer an optimal solution for simultaneous multiple objectives, usually they optimize one major objectives, and take others as constraints. Game theory offers perfect solution for interactive multi-objective problems. This paper explores SoC test scheduling from perspective of game theory.

1.1 Game Theory

Game theory was originally proposed by von Neumann and Nash respectively [7]. It is mainly about optimal solutions for confrontation and conflict problems. Standard game theory model consists of three parts: participants, behavior and payoff. Every rational decision maker in the game theory is called a participant, if other participant has decision, all the participants take some policies to minimize their own benefits; payoff refers to the gain or loss of the participants after making decision, it is the function of behavior of the participants. Two interactive objectives-test application time and test power are models as two confronted parts in game theory in order that a solution that achieves equilibration can be found.

2 SoC Test Scheduling Model Based on Game Theory (ST-GT)

Two-person non-cooperative and static game theory can be formulated for SoC test scheduling scheme. It contains three parts: participant No.1-test application time; participant No.2-test power. $A_1 = \{A_1^1, A_2^1, \ldots, A_m^1\}$ denotes policy set for participant No.1; $A_2 = \{A_1^2, A_2^2 \ldots, A_n^2\}$ denotes policy set for participant No.2; P_1 and P_2 refers to payoff function for participant No.1 and participant No.2.

3 Existence of Nash Equilibration

Theorem: Nash Equilibration exists for non-cooperative game theory.

Proof: let p_{max} denotes the maximum test power. $P(k) = 1/2 \cdot f \cdot V_{DD}{}^2 \cdot \sum C_i \cdot S_i(k)$

For policy space of participant No.1 and No.2, policy space A_1 and A_2 are non-empty, bounded and closed convex set in Euclidean space, the derivative function exists.

4 Experimental Results

All of our tests were conducted in a Solaris environment on Sun Blade 2500 workstation (with an Intel Pentium IV 3 GHz CPU and 1GB of RAM). We used ISCAS 89 SoC benchmarks (p93791, p34392, p22810), circuit p93791 has 32 embedded cores, and p22810 has 30 embedded cores and p34932 has 21 embedded cores. Experimental results are shown as figure.

Test power comparison between the proposed method ST-GT, ST-1 and ST-2.

It can be concluded from Fig.1 that the proposed method consumes least power ($10^6 mw$) for circuit p93791.

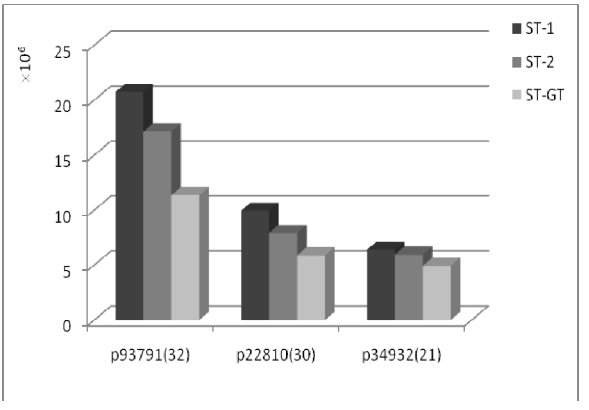

Fig. 1. Test power comparison

Test application time ($10^4 \mu s$) comparison on the three types of circuits is shown as Fig.2.

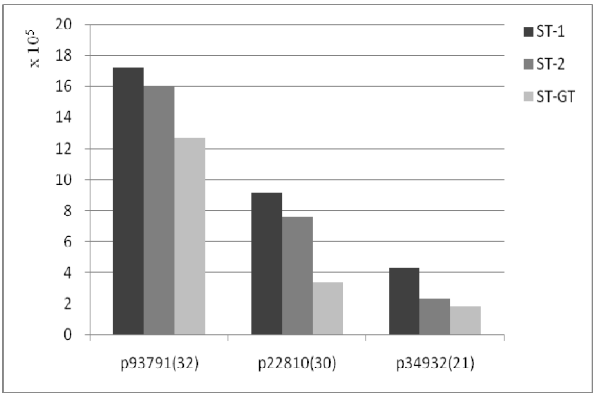

Fig. 2. Test application time comparison

From the two figures, it can be seen that with the increasing number of embedded cores on SoC, test application time increases, for circuit p93791, method ST-1 consumes the most test time, and proposed method ST-GT consumes the least test time. For circuit p22810, test application time for the three methods decreases, the proposed method ST-GT still consumes the least test power. And for circuit p34932, method ST-1 consumes the most test power, and the proposed method ST-GT consumes almost the equal test power as method ST-2. While ST-GT consumes slightly less test power than ST-2. On the whole the proposed method ST-GT succeeds in power consumption minimization.

5 Conclusion

This paper proposes a novel approach to SoC test scheduling using game theory, nonzero two-person no-cooperative game theory model was established for test time minimization and test power optimization, experimental results demonstrate the advantages of the proposed methods over the previous methods.

Acknowledgment

The author Jingbo Shao would like to thank her colleagues for discussions and useful help at early stages of this work. This work was supported in part by the Harbin Normal University Foundation under grant No. KGB200902, Natural Science Foundation of Heilongjiang Province under Grant No. F200932, Science and Technology Research Project for Department of Education of Heilongjiang Province under Grant No. 11531245.

References

1. Zhao, D., Upadhyaya, S.J.: A generic resource distribution and test scheduling scheme for embedded core-based SoCs. IEEE Transactions on Instrumentation and Measurement 53(2), 318–329 (2004)
2. Larsson, E., Arvidsson, K., Fujiwara, H., et al.: Integrated test scheduling, test parallelization and TAM design. In: Proceedings of 11th Asian Test Symposium (ATS 2002), pp. 397–404 (2002)
3. Chakrabarty, K.: Design of System-on-a-Chip test access architectures using integer linear programming. In: VLSI Test Symposium, pp. 127–134 (2000)
4. Koranne, S.: A novel reconfigurable wrapper for testing of embedded core-based SOCs and its associated scheduling algorithm. Journal of Electronic Testing: Theory and Applications 18(4-5), 415–434 (2002)
5. Koranne, S.: Design of reconfigurable access wrappers for embedded core based SoC test. IEEE Transactions on Very Large Scale Integration Systems 11(5), 955–960 (2003)
6. Harmanani, H.M., Salamy, H.A.: Power-constrained system-on-a-chip test scheduling using a genetic algorithm. Journal of Circuits, Systems, and Computer 15(3), 1–19 (2006)
7. Gibbons, R.: Game Theory of Applied Economists. Princeton University Press, Princeton (1992)

An Electrochemical Approach Coupled with Sb Microelectrode to Determine the Activities of Carbonic Anhydrase in the Plant Leaves

Yanyou Wu [1,2,*], Qianqian Shi [1], Kun Wang[1], Pingping Li[1], Deke Xing[2], Yongli Zhu[1], and Yangjiao Song[1]

[1] Key Laboratory of Modern Agricultural Equipment and Technology, Ministry of Education & Jiangsu Province, Institute of Agricultural Engineering, Jiangsu University, Zhenjiang, Jiangsu 210213, P.R. China
yanyouwu@ujs.edu.cn
[2] State Key Laboratory of Environmental Geochemistry, Institute of Geochemistry, Chinese Academy of Sciences, Guiyang 550002, P.R. China

Abstract. The electrochemical approach coupled with Sb microelectrode was developed to determine the carbonic anhydrase activity in a wide range. The sensing response of the microelectrode had a good linear relationship between potential and pH value in barbital buffer. The temperature would not affect the linear relationship. During the determination, the open-circuit potential method was taken to monitor the whole course of the reversible conversion catalyzed by carbonic anhydrase, and then the initial part of uniform velocity from the reaction curve was chosen to calculate the reaction velocity (the time to change one unit of pH). This technique, in comparison with the conventional method was used to determine the activities of bovine red blood cells carbonic anhydrase, foliar carbonic anhydrase and extracellular carbonic anhydrase in some plants. The result showed that the electrochemical approach coupled with Sb microelectrode would obtain more credible, accurate data than the conventional method.

Keywords: pH change; Carbonic anhydrase; Sb microelectrodes; Open-circuit potential (OCP).

1 Introduction

Carbonic anhydrase（CA; carbonate hydrolyase, EC 4.2.1.1）is a zinc-containing metalloenzyme that catalyses the reversible hydration of carbon dioxide. It has an important role in photosynthesis that reduces the diffusion resistance in the mesophyll cell for CO_2 by its catalysis, and provides reaction substrate for the carboxylation. Meanwhile, it has an exceptionally high CO_2 hydration turnover rate about 10^6 s^{-1} [1]. Extracellular CA, which is distributed on cytoplasm membrane, can facilitate the availability of CO_2 for photosynthesis [2].

* Corresponding author.

D. Zeng (Ed.): Future Intelligent Information Systems, LNEE 86, pp. 87–94.
springerlink.com © Springer-Verlag Berlin Heidelberg 2011

The conventional method to assay CA, described by Wilbur and Anderson [3], has been used by most works so far. This electrometric determination has some disadvantages. Firstly, the electrodes, which were used to determine the pH change in the reversible conversion of CO_2 to bicarbonate by the catalysis of CA, were commercial glass electrodes. The size of glass electrode is too large to be miniaturized because of its brittleness of the glass membrane, and its sluggish response will restrict its determination range of CA. When the CA activity of the sample is too low, it will be hard to measure owing to great measurement error. While the CA activity of the sample is too high, it will also affect the result of determination because the meter changes too fast to be caught by human eyes. Secondly, the data recorded by different operators would be diverse. Finally, only the data from two points were recorded by stopwatch at the interval of the pH drop in one unit, and the calculation of the CA activity was based only on the data. The measurement error was very great because the reaction process between the two points was incompletely uniform. Because of the above disadvantages, the CA activity, which is too low or too high, cannot be measured with the method. In addition, no documents have recorded the accurate data of extracellular CA activity in the leaves. Therefore, a new method aimed at determining the CA activity in a wide range should be developed.

In recent years, many metal oxide microelectrodes have been studied for pH measurement. Metal oxides such as PtO_2, IrO_2, RuO_2, TiO_2, Sb_2O_3, WO_3, Co_3O_4, PbO and Bi_2O_3 were used as pH sensitive film [4-6]. By far, of the various metal oxides that have been applied for pH measurement, antimony oxide is the most widely used. Compared with other metals of the platinum family such as iridium, platinum, and palladium, which are also frequently used as pH sensing materials, antimony oxide is much cheaper and easier [7-8].

In this research, several species of plants were chosen to assay their CA and extracellular CA with an electrochemical approach (open-circuit potential, OCP) coupled with Sb microelectrode. The whole course of the reaction of CO_2 to bicarbonate catalyzed by CA was monitored, and the pH value at any time can be recorded. This technique improves the determination accuracy, especially that of the activity of CA which is either too high or too low.

2 Materials and Methods

2.1 Fabrication of Sb Microelectrode

In this method, copper wires with a diameter of 0.6 mm and a length of about 5 cm were used as the substrate, and Sb_2O_3 solution as the electroplating solution. When polished by metallographic sandpaper, a copper wire was electroplated as the anode (platinum wire as the cathode) by i-t (Amperometric i-t Curve, CHI660C, Shanghai Chenhua Instrument Company). A bright and smooth grayer Sb metal was grown on the surface of the copper wire. The fabricated Sb microelectrodes were placed in oven at 120℃ overnight.

The Sb microelectrode was characterized in barbital buffer with the composition of 20 mmol L^{-1} sulfuric acid and 20 mmol L^{-1} barbital sodium.

2.2 Carbonic Anhydrase Activities Assay

1.5 mg pure carbonic anhydrase (SIGMA Company, 4860 WA units mg^{-1}) was solved in 100 ml deionized water. The enzyme solution was used for producing the curve of the relative CA activity *vs.* volume.

All the leaves were picked at 9:00 a.m. in one same day. The activities of CA were measured in 0.3-0.5 g samples of leaves. The leaves were quickly frozen in liquid N_2, ground into powder with a mill, and then homogenized with 3 ml of extraction buffer (10 mmol L^{-1} barbital buffer with 50 mmol L^{-1} 2-mercaptoethanol, pH 8.2). The homogenate was centrifuged at 10 000 g for 5 min. The supernatant was cold stored for determination.

Acetazolamide (acetazolamide, AZ), which did not go through the cell membrane, can inhibit CA activity [9]. Therefore, the extracellular CA was determined by adding AZ. The leaves were rinsed in AZ solution for two hours at 25℃, with light intensity of 200 μmol m^{-2} s^{-1}, the control experiment was deionied water instead of AZ. After that, the leaves were cleaned; the next steps were the same as above.

The conventional method of determination on CA activities is the electrometric one with glass electrode [3]. The samples were assayed at 0℃ by adding certain volume of the enzyme solution to 3 ml of 20 mmol L^{-1} barbital buffer, pH 8.2. The reaction was initiated by the addition of 2 ml ice-cold CO_2-saturated water. Units of activity were calculated with the equation t_0/t_1-1. The time (t_1) required for the drop in one unit pH from 8.2 to 7.2 was measured with glass electrode, while t_0 (the control) was the time required for the pH change (8.2-7.2) when buffer was substituted for the enzyme solution. Values are the means of three replicates.

Sb microelectrode, instead of the glass electrode, with a reference electrode was used to monitor the pH change during the whole course of the reaction by OCP (open-circuit potential, CHI660C, Shanghai Chenhua Instrument Company). The reaction system was the same as described above. The potential-t curves were saved. The data, where the potential changed uniform with time, were chosen to produce the linear equation. The slope of the linear equation can be obtained and recorded as k_1 referring to the reaction system with CA, so the value of t_1 was $41.7/k_1$ (41.7 is the sensitivity of microelectrode responding to the change of one pH unit, which is described in Characterization of the Sb microelectrode). Correspondingly, k_2 was the slope of the linear equation referring to the reaction system without CA, so the value of t_0 was $41.7/k_2$. Units of CA activity were also calculated with the equation t_0/t_1-1.

3 Results and Discussion

3.1 Characterization of the Sb Microelectrode

The microelectrode yielded a fast and stable response toward pH change of the test solution, with an average response time less than 1 s, and the measured pH range of 3-9. A good linear relationship was found in the calibration curves of the

potential response to the pH value of the solution (R^2=0.996, n=5, p<0.001). The average slope of the linear equation was 41.7 mV/pH, which showed that the present fabrication method for Sb microelectrodes had high sensitivity to pH change and good reproducibility.

The determination of CA activity was conducted under the reaction system of 0℃. Therefore, the effect of temperature on the reactivity was studied. The calibration curve of the microelectrodes' potential response to the pH value in the test solution under room temperature and 0℃ were shown in Fig.1. The temperature did not change the slopes of linear equations.

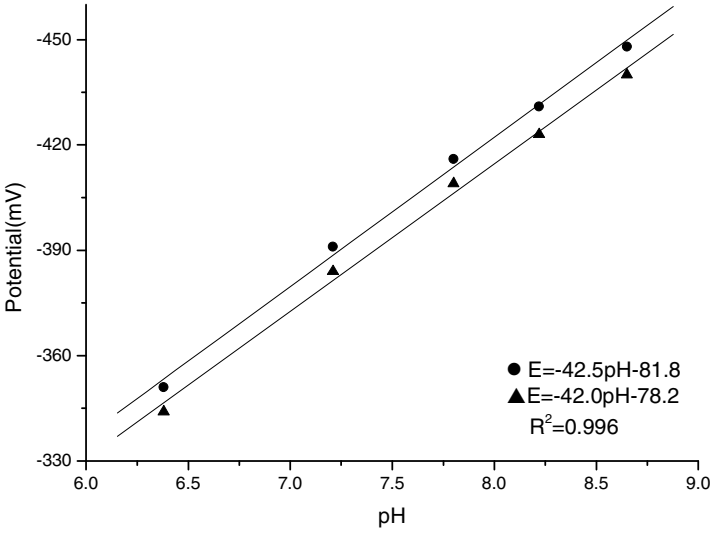

Fig. 1. Calibration curves of the potential *vs*. pH in barbital buffers responded by the Sb microelectrode at the room temperature and 0℃ (● 20℃, ▲ 0℃).

3.2 CA Activity of Standard Enzyme Solution *versus* Volume Curve

The CA activity of standard enzyme solution *versus* volume curve, measured with the glass electrode, was plotted as Fig.2. When CA activity was too low or too high, its value deviated from the curve. The pause duration of our human eyes, which saw a goal to get the visual impression, on the average took 172 ms [10]. Our vision may not catch the data on the pH meter owing to the timing by stopwatch when the CA activity was too high. In addition, when the CA activity was too low, the pH meter may not make an accurate record because of its sluggish response. However, the OCP method with microelectrode can overcome the above defects because of its continuous timing and fast transfer rate. The CA activity of standard enzyme solution *versus* volume curve, measured with Sb microelectrode, was plotted as Fig.3. A good linearity measured by the microelectrode can be seen from Fig.3.

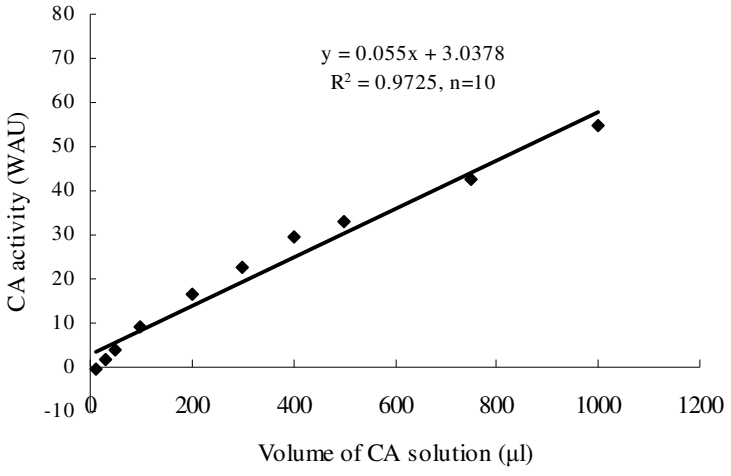

Fig. 2. The CA activity of standard enzyme solution *versus* volume curve measured with glass electrode in pure enzyme solution

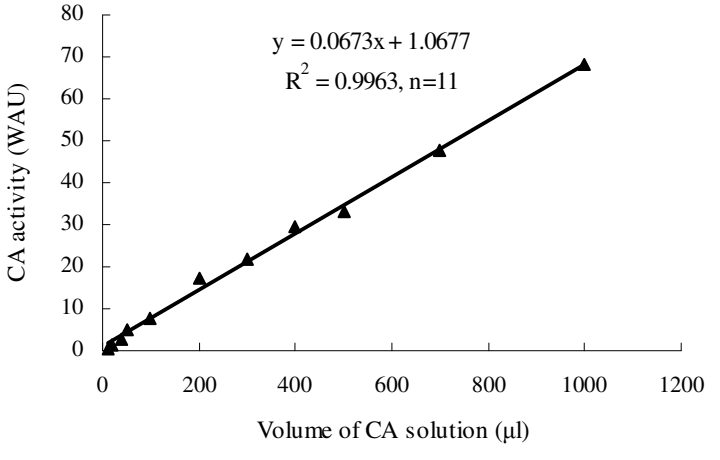

Fig. 3. The CA activity of standard enzyme solution *versus* volume curve measured with Sb microelectrode

3.3 Determination of Carbonic Anhydrase in the Leaves

Several different species of plants were chosen to determine their foliar CA activities. Table 1 gave the CA activities of *Morus alba*, *Ailanthus altissima*, *Brassica juncea* and *Parthenocissu tricuspidatas*, which were measured with the Sb microelectrode and the glass electrode, respectively. In addition, a series of volumes of 10 µl to 400 µl leaf extracts from *Morus alba* were also measured with the Sb microelectrode and the glass electrode, respectively. The CA activity in the leaves from *Parthenocissu tricuspidatas* or 10µl leaf extracts from *Morus alba* was too low to be measured with

the conventional method (glass electrode). The results of the two methods had no significant difference for the determination of the CA activities in the medium range. Therefore, the new method, the OCP approach coupled with Sb microelectrode, which measured the CA activity, had demonstrated the advantage for the determination of low CA activity.

Table 1. Comparison between the microelectrode and the conventional glass electrode in determining the CA relative activity (Unit: WAU) and the CA activity (Unit: WAU g^{-1}FW) in several plant leaves

Plant materials	Volume of leaves extracts (μl)	Sb microelectrode		Glass electrode	
		CA relative activity	CA activity	CA relative activity	CA activity
Morus alba	10	0.19	190	ND*	ND*
	30	0.36	120	0.32	107
	50	0.86	172	0.50	100
	100	1.06	106	1.87	187
	200	1.86	93	2.52	126
	300	3.37	112	3.06	102
	400	4.26	106	3.56	89
	Average ± standard error		127±15		119±15
Ailanthus altissima	Average ± SE		679±38		610±19
Brassica juncea	Average ±SE		490±9		547±22
Parthenocissus tricuspidata	Average ± SE		34.2±5		ND*

**ND stands for the CA activity not be determined*

At present, little information about the extracellular CA activity has been documented owing to the low accuracy of the conventional pH glass electrode. The results of the determination and calculation of extracellular CA by means of the new approach is highly credible. The activities of the extracellular CA in *Broussonetia papyrifera* and *Morus alba* leaves were determined by OCP approach coupled with Sb microelectrode and the conventional glass electrode, respectively; and the results were shown in Table 2. The variability of the extracellular CA activities, determined with the new method, was much smaller than that with the conventional method. A negative value was even observed in the results measured with the glass electrode. As a result, the OCP approach coupled with Sb microelectrode can be more successfully used for the determination of extracellular CA activities than the conventional method with glass electrode.

Table 2. Comparison between the microelectrode and the conventional glass electrode in determining the CA activity (Unit: WAU g^{-1}FW) and the extracellular CA activity (Unit: WAU g^{-1}FW) in *Broussonetia papyrifera* and *Morus alba* leaves

Determination	Plant materials	CA activity (without AZ)	CA activity (with AZ)	Extracellular CA activities and its proportion
Sb microelectrode	*Broussonetia papyrifera*	1478	919	559 (38%)
		1485	1163	322 (22%)
		1738	1140	598 (34%)
	Morus alba	150	111	49 (26%)
		212	138	74 (35%)
		159	108	51 (32%)
Conventional glass electrode	*Broussonetia papyrifera*	1041	854	187 (18%)
		1196	909	287 (24%)
		1586	983	603 (38%)
	Morus alba	187	136	51 (27%)
		143	152	-9 (-6%)
		132	108	24 (18%)

4 Conclusions

In summary, the electrochemical approach (open-circuit potential, OCP) coupled with a new calculation (the new method) has solved the long-standing deficiencies in the determination of CA activity by means of the electrometric method with the glass electrode (conventional method). Firstly, the new method obtains the time that is equivalent to one pH unit of potential changes in the reaction system through the statistics of multi-point data, so it is more credible compared with the conventional method to calculate two-point data responding to the change of a pH unit. Secondly, the new method is based on potential changes in the uniform part of the curve to calculate the CA activities; therefore, it is more precise compared with the conventional method. Thirdly, the reaction system of the new method took only little volume as the needle-like morphology of Sb microelectrode; therefore, it is possible to measure the foliar CA activity in a small range.

Acknowledgments. The authors gratefully acknowledge the financial support from projects of National Natural Science Foundation of China (No. 40973060) and National Basic Research Program of China (973 Program) (No. 2006CB403206).

References

1. Lindskog, S.: Structure and mechanism of carbonic anhydrase. Pharmacol. Ther. 74, 1–20 (1997)
2. Nimer, N.A., Brownlee, C., Merrett, M.J.: Extracellular carbonic anhydrase facilitates carbon dioxide availability for photosynthesis in the marine Dinoflagellate Prorocentrummicans. Plant Physiol. 120, 105–112 (1999)

3. Wilbur, K.M., Anderson, N.G.: Electrometric and colorimetric determination of carbonic anhydrase. J. Biol. Chem. 176, 147–154 (1948)
4. Yao, S., Wang, M., Madou, M.: A pH electrode based on melt-oxides iridum oxide. J. Electrochem. Soc. 36, H29–H36 (2001)
5. Li, Q.W., Luo, G.A., Shu, Y.Q.: Response of nanosized cobalt oxide electrodes as pH sensors. Anal. Chim. Acta 409, 137–142 (2000)
6. Chen, D.C., Lai, Y.T., Li, W.F.: Study of the H^+ response behavior of WO_3 based pH electrochemical sensor. Micronanoelectronic. Tech. 7, 397–399 (2007)
7. Wang, M., Yao, S.: Carbonate-melt oxide iridium wire for pH sensing. Electroanal. 15, 1606–1615 (2003)
8. Imokawa, T., Williams, K.J., Denuault, G.: Fabrication and characterization of nanostructured Pd hydride pH microelectrodes. Anal. Chem. 78, 265–271 (2006)
9. Moroney, J.V., Husic, H.D., Tolbert, N.E.: Effect of carbonic anhydrase inhibitors on inorganic carbon accumulation by *Chlamydomonas reinhardtii.*. Plant Physio. 79, 177–183 (1985)
10. Arnold, D.C., Tinker, M.A.: The fixational pause of the eyes. J. Exp. Psycho. 25, 271–280 (1939)

Calculating on Permanent Magnet with Distributing Leakage Flux

Liu Lingshun, Shi Xianjun, and WangDong

Naval Aeronautical and Astronautical University,
264001 Yantai,
China
lingshunliu@sohu.com

Abstract. Leakage magnetic flux is not ignoring in the course of calculating magnetic circuit. The permanent magnet with distributing leakage flux is decomposed into a series of magnetic circuit with lumped parameters in this paper. The universal calculating formulae for magnetic circuit with distributing leakage flux are derived. This method is favorable for magnetic circuit programming with nonlinear magnetic circuit, especially for variable section permanent magnet or leakage magnetic conductor per length changes.

Keywords: Distributing leakage flux; Permanent magnet; Calculating; Magnetic circuit.

1 Introduction

Calculating of permanent magnet circuit is very important with wide apply in various electrical machines and instrument with high performance permanent magnet. Considering leakage magnetic flux exist in magnetic circuit and it is not ignoring in many situations. Leakage magnetic flux must be disposed properly to improve the precision of calculating. This paper is devoted to study the calculating of permanent magnet with distributing leakage flux, the decomposing method is used to make the permanent magnet with distributing leakage flux decompose into a series of magnetic circuit with lumped parameters, the universal flow chart of computer is given, which is simple and easy to relized.

2 Analysizing and Calculating on Permanent Magnet Circuit

The decomposing of permanent magnet circuit with distributing leakage flux is shown as fig. 1(a). The magnetic flux, Magnetic potential and leakage flux for the ith segment is shown as fig. 1(b). The fundamental status of other segments are similar with this segment.

D. Zeng (Ed.): Future Intelligent Information Systems, LNEE 86, pp. 95–101.
springerlink.com © Springer-Verlag Berlin Heidelberg 2011

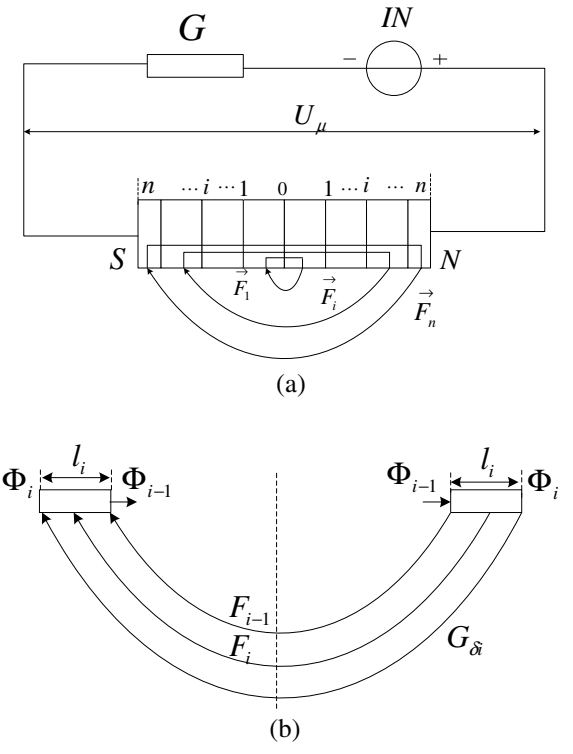

Fig. 1. Decomposing of permanent magnet circuit with distributing leakage flux

Where, IN is ampere-turn of coils. G is magnetic conductance. The permanent magnet. is subsected properly along the midst section. Supposing magnetic induction intensity H_i of each segment is constant. The magnetic flux of the midst section is Φ_0. Magnetic flux of terminal part is $\Phi_n = \Phi_\mu$. Length and section area of permanent magnet is l_μ and S respectively. Magnetic potential of permanent magnet is U_μ. Leakage magnetic conductance of each segment is $G_{\delta 1}, G_{\delta 2} \cdots G_{\delta i}$.

The initializing magnetic flux is supposed as $\Phi_0^{(0)}$, the magnetic potential and magnetic flux $(F_1, \Phi_1) \cdots (F_n, \Phi_n)$ of each segment can be calculated by guess method. And making the terminal magnetic circuit equilibrium, $\Phi_n = \Phi_\mu$, $F_n = U_\mu$, $(IN) + \dfrac{\Phi_\mu}{G} = U_\mu$.

(1) Supposing convex coefficient $r = 0.25$, B-H curve is shown as fig. 2.

Where B_r is magnetic retentive induction intensity, H_c is coercive force, C is working point.

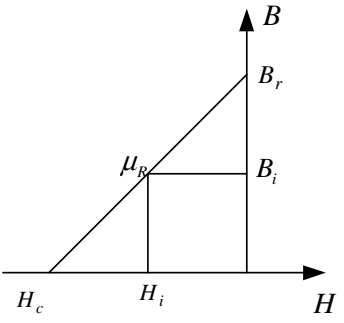

Fig. 2. Magnetization curve of $r = 0.25$

The flow chart of main program is shown as fig. 3(a). Evaluating flow chart for initializing magnetic flux is shown as fig. 2(b). The zeroth flow chart is shown as fig. 2(c). The 1th flow chart is shown as fig. 2(d).

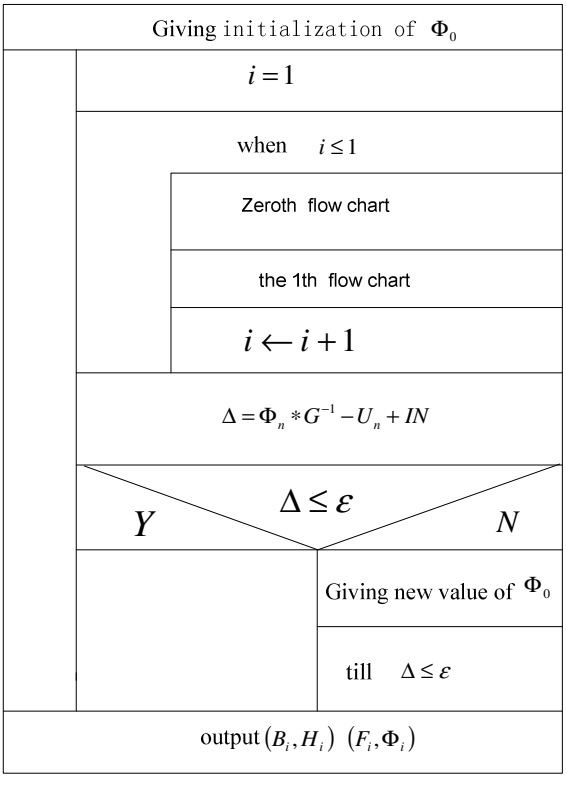

(a) Main chart flow

Fig. 3. Flow chart

$\mu_R = B_r/(-H_c)$
$\mu_G = Gl_\mu/S_\mu$
$f = IN/l_\mu$
$\Phi_0 = k_q(-H_c - f)(\mu_G^{-1} + \mu_R^{-1})$

(b) Evaluating flow chart for initializing magnetic flux

$B_i = \Phi_{i-1}/S$
$H_i = H_c + B_i/\mu_R$
$\Phi_i = \Phi_{i-1} - (F_{i-1} - H_i l_i)G_{\sigma i}$

(c) The zeroth flow chart

$B_i = (\Phi_{i-1} + \Phi_i)/(2S)$
$H_i = H_c + B_i/\mu_R$
$F_i = F_{i-1} - H_i l_i$
$\Phi_i = \Phi_{i-1} - (F_{i-1} - H_i l_i)G_{\sigma i}$

(d) The 1th flow chart

Fig. 3. (*continued*)

From fig. 1, evaluating flow chart for initializing magnetic flux Φ_0

$$-IN = \Phi_\mu * G^{-1} - U_n \tag{1}$$

Divided by length of permanent magnet l_μ, then

$$-H_\mu - f = \frac{1}{\mu_G} B_\mu \tag{2}$$

Where $f = IN/l_\mu$.

Replace $H_\mu = H_c + B_\mu/\mu_R$ into (2), then

$$-H_c - \frac{1}{\mu_R} B_\mu - f = \frac{1}{\mu_G} B_\mu \tag{3}$$

Then

$$\Phi_\mu = B_\mu S_\mu = \frac{1}{\frac{1}{\mu_G} + \frac{1}{\mu_R}}(-H_c - f)S_\mu \tag{4}$$

Adding coefficient k (k<1), then

$$\Phi_0 = \frac{\Phi_\mu}{k} \tag{5}$$

Some disposal for evaluating Φ_0 again is

$$\Delta = \Phi_n * G^{-1} - U_n + IN \tag{6}$$

$\Delta > 0$ denotes Φ_0 larger. Several status are presented for the 2th and the post evaluating.

(a) Δ_{k-1} and Δ_k are both positive as fig. 4

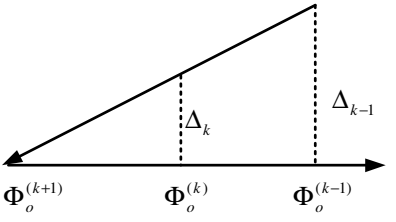

Fig. 4. Δ_{k-1} and Δ_k are both positive

From fig. 4,

$$k_\Delta = \frac{\Delta_k}{\Delta_{k-1}} = \frac{\Phi_o^{(k)} - \Phi_o^{(k+1)}}{\Phi_o^{(k-1)} - \Phi_o^{(k+1)}} > 0 \tag{7}$$

then

$$\Phi_0^{(k+1)} = \frac{\Phi_0^{(k)} - k_\Delta \Phi_0^{(k-1)}}{1 - k_\Delta} \tag{8}$$

(b) Δ_{k-1} is positive and Δ_k is negative, as fig. 5

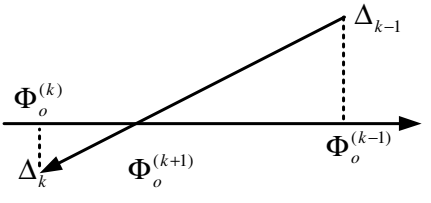

Fig. 5. Δ_{k-1} is positive and Δ_k is negative

$$k_\Delta = \frac{\Delta_k}{\Delta_{k-1}} = \frac{\Phi_o^{(k)} - \Phi_o^{(k+1)}}{\Phi_o^{(k-1)} - \Phi_o^{(k+1)}} < 0 \tag{9}$$

(c) Δ_{k-1} and Δ_k are both negative as fig. (6)

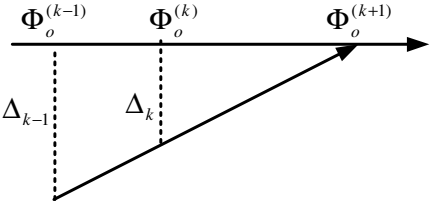

Fig. 6. Δ_{k-1} and Δ_k are both negative

$$k_\Delta = \frac{\Delta_k}{\Delta_{k-1}} = \frac{\Phi_o^{(k)} - \Phi_o^{(k+1)}}{\Phi_o^{(k-1)} - \Phi_o^{(k+1)}} > 0 \tag{10}$$

(d) Δ_{k-1} is negative and Δ_k is positive as fig. 7

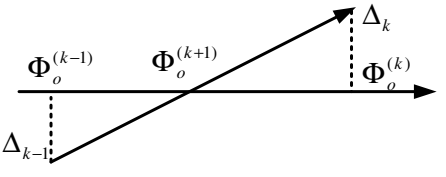

Fig. 7. Δ_{k-1} is negative and Δ_k is positive

$$k_\Delta = \frac{\Delta_k}{\Delta_{k-1}} = \frac{\Phi_o^{(k)} - \Phi_o^{(k+1)}}{\Phi_o^{(k-1)} - \Phi_o^{(k+1)}} < 0 \tag{11}$$

2. Supposing convex coefficient $0.25 < r < 1$, magnetization curve of permanent magnet is shown as fig. 8.

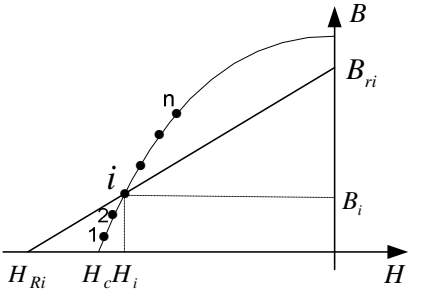

Fig. 8. Magnetization curve of $0.25 < r < 1$

The start point of reverting line is dicided by demagnetization field of permanent magnet. The decision of start points 1,2$\cdots$ n is at the maximal demagnetization state. $G = G_{\min}$, $(IN) = (IN)_{\max}$, $\Phi_{\mu} = (\Phi_{\mu})_{\min}$. The flow chart of $0.25 < r < 1$ is similar with that of $r = 0.25$.
The differences include as follows

(a) H_i is examining the demagnetization curve by B_i.

(b) Output each parameter (H_{Ri}, B_{Ri}) of reverting ling.

For different point of demagnetization curve, reverting magnetic conductivity is different, it can be got by calculating or examining demagnetization curve. If magnetic conductivity is tiny, it can be considered as constant. Thus, if the start point is decided, each reverting line is drew. Magnetic field density is calculated by $H_i = H_{Ri} + B_i / \mu_{Ri}$.

3 Conclusions

The analysis is presented by decomposing permanent magnet with distributing leakage flux into a series of magnetic circuit in this paper. The correlative calculating expressions for magnetic circuit of two kinds of convex coefficient are derived. This method is very convenient to calculate the magnetic circuit with nonlinear magnetic reluctance, Especially for the variable section magnet or leakage magnetic conductivity per length is different.

References

1. Huimin, L., Guofu, Z., Fubiao, L.: Fictitious design of reversal line's initialization working point in polarized system based on finite element method. Proceedings of the CSEE 25(9), 147–152 (2005)
2. Guansheng, Z.: Theory of electrical appliances. China Machine Press, Beijing (1990)
3. Lingshun, L., Huimin, L., Maokai, L.: Calculating and analysis of polarized system. Relay 29(10), 19–21 (2001)
4. Lingshun, L., Zhongshan, J., Huimin, L.: The compute arithmetic of permanent magnet circuit considering distributing magnetic leakage. Electrician Technology 11, 49–50 (2000)

Calculating on Mechanical Character of Contact Spring System for Electromagnetic Relay

Liu Lingshun, Shi Xianjun, and WangDong

Naval Aeronautical and Astronautical University, 264001 Yantai, China
lingshunliu@sohu.com

Abstract. Spring is the part of providing mechanical force for electromagnetic relay..In this paper, calculating about the softness of contact spring in the electromagnetic relay by deformation energy method is derived. Calculating about the deflection of the contact spring by electric network method is derived. The results are rebound to the design and calculation of the spring system for the electromagnetic relay.

Keywords: Electromagnetic relay; Contact spring system; Deformation energy; Electric network method; Softness; Deflection.

1 Introduction

Spring is the part of providing mechanical force for electromagnetic relay.The mechanical character of relay is the relation between equivalent counterforce of spring at the gap and armature distance. The mechanical force is various because of spring structures are various. In this paper, calculating about the softness of contact spring in the electromagnetic relay by deformation energy method is derived. Calculating about the deflection of the contact spring by electric network method is derived. The unitive calculating formulae are derived. The mechanical character of 2JR-2 relay is presented.

2 Calculating of Spring Softness

The twi-integral method for differential equation of spring bending is always adopted for calculating of spring softness in the past. It is much complex for spring of complicated configuration and no suitable for CAD. The deformation energy method is used to calculate the softness of spring.

Spring of relay is bend deforming at working state, shown as Fig.1.

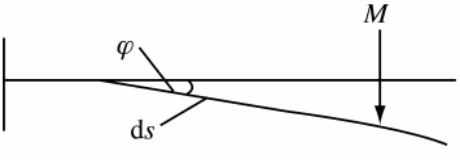

Fig. 1. Bend deform of spring

D. Zeng (Ed.): Future Intelligent Information Systems, LNEE 86, pp. 103–109.
springerlink.com © Springer-Verlag Berlin Heidelberg 2011

Deforming energy of spring differential element ds is

$$du = 0.5M \cdot d\varphi \tag{1}$$

Where, du is deforming energy of spring differential element. M is torque of differential element section. $d\varphi$ is angle increment at perpendicularity section caused by torque.

Differential equation of spring bend is

$$d\varphi / ds = 1/\gamma = M/(EJ) \tag{2}$$

Where, γ is curvature radius. E, J is spring module and section inertial torque.
The deforming energy of the whole spring is

$$u = \int \frac{M^2}{2EJ} ds \tag{3}$$

The bend status of spring at the acting of double torques is shown as fig.2. The deforming energy is

$$u = \int \frac{M_1^2}{2EJ} ds + \int \frac{M_2^2}{2EJ} ds + \int \frac{M_1 M_2}{EJ} ds \tag{4}$$

Where, M_1, M_2 is bend torque forced by P_1 and P_2 respectively, $M = M_1 + M_2$ is bend torque forced by y P_1 and P_2 commonly.

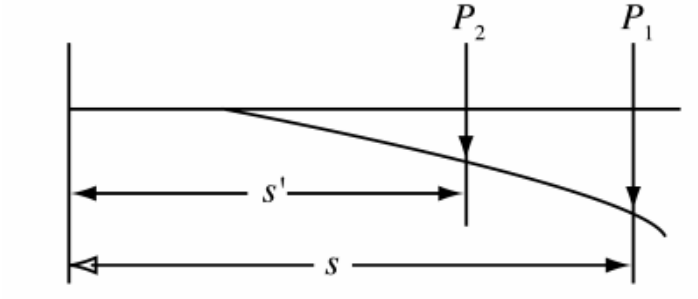

Fig. 2. Bend status of spring at the acting of double torques

The spring works within spring limit ,so it is a linear system. The superposition principle and conversion principle are obedient for the system, the deforming energy is nothing with order of force. The deflection of point 1 and 2 is Y_1 and Y_2 respectively forced by P_1 and P_2 commonly. From fig.3, by superposition principle the expressions are

$$\begin{cases} Y_1 = Y_{11} + Y_{12} = C_{11}P_1 + C_{12}P_2 \\ Y_2 = Y_{21} + Y_{22} = C_{21}P_1 + C_{22}P_2 \end{cases} \tag{5}$$

Where , C_{11}, C_{12} is self-softness of point 1 and mutual softness of point 1 and 2 respectively. Y_{11} and Y_{12} is deflection forced by P_1 at point 1 and 2. C_{22}, C_{21} is self-softness of point 2 and mutual softness of point 2 and 1 respectively. Y_{22} and Y_{21} is deflection forced by P_2 at point 1 and 2.

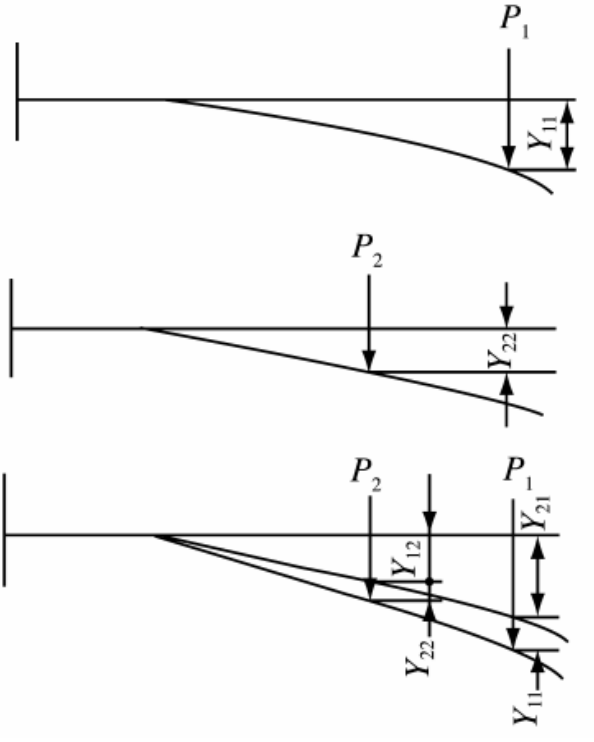

Fig. 3. Relation between deflection and force of spring by double force

Making $C_{21} = C_{12} = C_M$. P_1 acts solely, the outside force power is

$$W_{11} = \frac{1}{2}P_1Y_{11} = \frac{1}{2}C_{11}P_1^2 \tag{6}$$

Then P_2 acts solely, the outside force power is

$$W = W_{22} + W_M = \frac{1}{2}P_2Y_{22} + \frac{1}{2}P_1Y_{12} = \frac{1}{2}C_{22}P_2^2 + C_{12}P_1\ P_2 \tag{7}$$

Spring is a conservative system. The outside power equal spring energy. Then

$$\frac{1}{2}C_{11}P_1^2+\frac{1}{2}C_{22}P_2^2+C_{12}P_1\ P_2=\int\frac{M_1^2}{2EJ}ds+\int\frac{M_2^2}{2EJ}ds+\int\frac{M_1M_2}{EJ}ds \quad (8)$$

Abvously, the outside force power of P_1 or P_2 equals its deforming energy correspondingly

$$C_{11}=\frac{1}{P_1^2}\int\frac{M_1^2}{EJ}ds \quad (9)$$

$$C_{22}=\frac{1}{P_2^2}\int\frac{M_2^2}{EJ}ds \quad (10)$$

The outside force power increment equal spring energy increment,then

$$C_{12}=C_{21}=\frac{1}{P_1P_2}\int\frac{M_1M_2}{EJ}ds \quad (11)$$

(9)-(11) are the universal formulae for calculating softness of spring. The factual calculation must combine the shape of spring because of the variable shapes of spring.

3 Deflection Calculating

The direction of amarture pushing force is vertical to spring plane for any shape moving spring. The spring can be considered as girder which one terminal is fixed and the other terminal lay on the bracket, as fig.4.

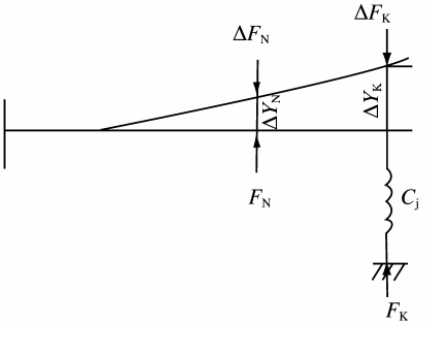

Fig. 4. Spring deflecting of double forces

Where, F_N is pushing force of amarture. F_K is moving spring force of spring bracket. C_j is softness of spring bracket. $\Delta F_N, \Delta F_K$ is variational quantity of moving course forced by double forces. $\Delta Y_N, \Delta Y_K$ is deflection variational quantity, then

$$\begin{cases} \Delta Y_N = C_{NN}\Delta F_N + C_{NK}\Delta F_K \\ \Delta Y_K = C_{NK}\Delta F_N + C_{KK}\Delta F_K \end{cases} \tag{12}$$

From (12), then

$$\begin{cases} \Delta F_N = -\dfrac{C_{KK}}{C_{NK}}\Delta F_K + \dfrac{1}{C_{NK}}\Delta Y_K \\ \Delta Y_K = -C_{NK}\left(\dfrac{C_{KK}C_{NK}}{C_{NK}^2} - 1\right)\Delta F_K + \dfrac{C_{NN}}{C_{NK}}\Delta Y_K \end{cases} \tag{13}$$

Where, $\Delta Y_K = C_j \Delta F_K$.

Making $A = -\dfrac{C_{KK}}{C_{NK}}$, $B = \dfrac{1}{C_{NK}}$, $C = -C_{NK}\left(\dfrac{C_{KK}C_{NK}}{C_{NK}^2} - 1\right)$, $D = \dfrac{C_{NN}}{C_{NK}}$

Then, (13) is changed into

$$\begin{cases} \Delta F_N = A \cdot \Delta F_K + B \cdot \Delta Y_K \\ \Delta Y_K = C \cdot \Delta F_K + D \cdot \Delta Y_K \end{cases} \tag{14}$$

The (14) is replaced by a two ports network of electric circuit theory

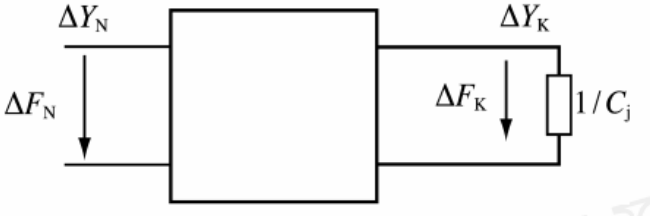

Fig. 5. Two ports network

From fig.5, then

$$\begin{cases} \Delta F_K = D \cdot \Delta F_N - B \cdot \Delta Y_N \\ \Delta Y_K = -C \cdot \Delta F_N + A \cdot \Delta Y_N \end{cases} \tag{15}$$

The mechanical character of relay spring can be calculated conveniently by (14) and (15).

4 Example for Mechanical Character of Spring

2JR-2 relay spring system is shown as fig.6 .

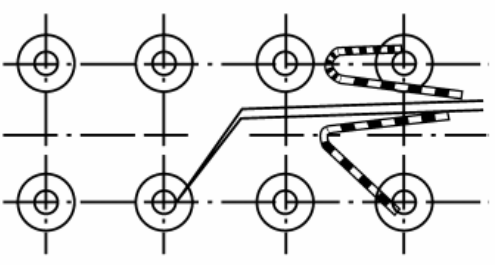

Fig. 6. 2JR-2 relay spring system

The mechanical character of 2JR-2 relay spring system is calculated and shonw as fig.7

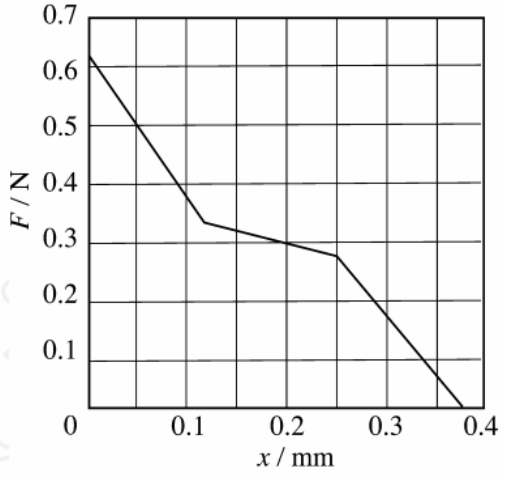

Fig. 7. The mechanical character of 2JR-2 relay spring

5 Conclusions

The calculating methods and formulae of mechanical character for electromagnetic relay are promoting to design criterion. The factual calculation must combine the shape of spring because of the variable shapes of spring.

References

1. Weiming, T., Guofu, Z.: Low voltage electrical equipment relay and control system. Harbin Industry Institute Press, Harbin (2000)
2. Guansheng, Z.: Electrical equipment theory base. Machine Industry Press, Beijing (1990)
3. Jiujiang, Z.: Material mechanics. Harbin Industry Institute Press, Harbin (2000)

The P System Model for Solving Deadlock

Kang Wang, Hong Peng, Chenliang Zhu, Yuhong Fan, and Hao Wang

School of Mathmatic and Computer Engineer,
University of Xihua, Chengdu, Sichuan, 610039, China
plmmwk@163.com
ph@mail.xhu.edu.cn

Abstract. The P systems are a class of novel computing models which are abstracted from the mechanism of the living cells, and the structure and function of the cells and tissues, organs consisting of the cells. They have distributed, maximum parallel features. This paper presents a P system model to remove deadlock. The P system model of degree *m* is used to simulate the procedure of removing deadlock processes, and we can make the best choice to determine which deadlock process should be killed. The proposed model can solve the problem in a linear time complexity, and is superior to the traditional methods.

Keywords: Membrane computing; P system; deadlock problem; removing of deadlock.

1 Introduction

Biology and Information Science are two quick-developed and the most influential subjects, so far, and molecular computing is a new interdisciplinary subject based on the two research fields. Judging from the current research, molecular computing can be summarized as two major research directions: one is DNA computing [1]; the other is membrane computing [2].

Membrane computing (known as P systems) is a computing model, abstracted from the structure and function of the living cells and tissues, organs or other structures comprised of cells [2, 3]. Living organisms have a large number of cells, the various computing units which are abstracted from cell can independently accomplish specific calculations, and so the model can calculate in a maximum parallelism, its computing ability will exceed current computers further. P systems are generally divided into three types as follows: cell-like P systems, tissue-like P systems, and neural-like P systems. They are computing models which are abstracted from cell, tissue, and neural system respectively [2].

P system is a distributed, great parallel, non-deterministic, and new computing model. Many studies have shown [4-7], a lot of simple computing models have the same computing power as Turing machine in theory, what's more, it probably exceed the limitations of Turing machines. The motivation of membrane computing is abstracting computational model from the structure and function of the cells and analyzing its computing power. The computing efficiency of P systems is mainly to analyze whether the membrane system can solve computationally hard problem, such

D. Zeng (Ed.): Future Intelligent Information Systems, LNEE 86, pp. 111–118.
springerlink.com © Springer-Verlag Berlin Heidelberg 2011

as NP hard problem, PSPACE problem and so on. In the P systems, according use operational rules such as membrane division, dissolution, creating, merging and string copy, it can solve a variety computationally hard problem, such as the satisfiability problem, vertex coloring problem.

Deadlock is a classic problem in operating systems. It involves several aspects, such as deadlock detection, prevention, removing and so on [8, 9]. Here, we only focus on removing of deadlock. For removing deadlock, we need to solve the problem: Which process should be killed? Typically, killing deadlock processes should satisfy three goals: (1) the number of the process to be killed is as less as possible; (2) the cost of the system is as less as possible; (3) meet the deadline request.

Because P systems have distributed, parallel computing features, we will introduce P systems to deadlock problem and present a cell-like P system model. For a deadlock problem consisting of m deadlock processes, we can construct a P system model of degree m, which includes m nested membranes. In the model, each membrane includes $m\times(m\text{-}1)$ evolution rules except for the innermost layer with m evolution rules, all of the evolution rules are dissolution rules and the priority relationships of the rules are determined by the cost of killing process. With the help of a distributed, parallel computing features of P systems, we can determine which deadlock process should be killed in a linear time. In addition, it has more advantages than the traditional methods.

2 Cell-Like P Systems

Cell-like P systems have a hierarchical structure similar to the cell structure, the outer membrane known as the skin includes a lot of sub-membranes, and the sub-membrane can also be nested in the other sub-membrane. There are some strings and corresponding evolution rules in each membrane, and system computes in a maximum parallelism. For each step, the configuration of the system will change into a new configuration based on the evolution of the rule until there are no available rules, and then system halts. At this time, the output string is the computation result.

Formally, a P system of degree m, $m\geq 1$, is a construct:

$$\Pi = (V, \mu, w_1, \ldots, w_m, (R_1, \rho_1), \ldots, (R_m, \rho_m)) \tag{1}$$

where

(i) V is the alphabet, its elements are called objects;

(ii) μ is a membrane structure of degree m, with the membranes and regions labeled in a one-to-one manner with element in a given set H, $H=\{1,2, ..., m\}$, and the m is the degree of Π;

(iii) $w_i \in V^*$ $(1\leq i\leq m)$ are strings from V^* representing multiset over V associated with the region i of μ;

(iv) An evolution rule is a pair (u,v), which we will usually write in the form $u\rightarrow v$, where u is a string over V and $v=v'$ or $v=v'\delta$, v' is a string over $\{a_{here}, a_{out}, a_{in_j} \mid a\in V, 1\leq j\leq m\}$, and δ is a special symbol not in V. When a rule with δ can be used in one

membrane, it is dissolved and its objects are introduced into the upper membrane. The length of u is called the radius of the rule $u \rightarrow v$. R_i ($1 \leq i \leq m$) are finite sets of evolution rules associated with the region i of μ, ρ_i is a partial order relation over R_i, specifying a priority relation among rules of R_i.

In summary, P systems are consisted of three parts usually: the hierarchical structure of membranes, the multiset of the objects and evolution rules.

3 Two Traditional Methods of Removing Deadlock

Deadlock is a traditional problem in computer operating system. It occurs when a group of processes each have been granted exclusive access to some resources, and one wants yet another resource that belongs to another process in the group. All of them are blocked and none will ever run again [8]. In term of operating system, this is an extremely wasteful phenomenon, which cause the losses of the system are more than system failure sometimes. This state will never end if we don't provide effective external forces. In addition to prevention and discovering of a deadlock, removing deadlock is also an important technique in dealing with deadlock problem. We only focus on the removing of deadlock in this paper.

In general, a deadlock should be removed immediately once happened. Killing process is a way often used to removing deadlock. The key problem that should be considered is that which process should be killed when there are m processes in a deadlock? Generally speaking, the process to be killed should meet certain requests, such as the minimum cost of elimination. Therefore, we should have an effective way to determine which process should be killed. Typically, two methods are used to remove the deadlock process. Here we briefly review the two methods.

Formally, we assume that at deadlock state S, there are m deadlock processes $P_1,P_2,\ldots,P_m$, and we denote their set by $D_P=\{ P_1,P_2,\ldots,P_m \}$. The set $\{U_1,U_2,\ldots,U_m\}$ represents m states at removing deadlock. Under the deadlock state S, if we kill process P_i, then the states becomes U_i, where $t(S \rightarrow U_i)$ represents the spending time, (i=1,2,…,m). If the current state is U_i and the process P_j is killed, then the state becomes U_j, and $t(U_i \rightarrow U_j)$ represents the spending time, (i=1,2,…,k, j=1,2,…,m).

3.1 The First Method of Killing Deadlock Process

The method is essentially an exhaustive method. First of all, we kill a process in process set $\{P_1,P_2,\ldots,P_m\}$ from the state S respectively, and system's states become $U_1,U_2,\ldots,U_m$ respectively. Then, we kill a process P_r from above remaining processes, system's state becomes U_r from U_i, (r=1,2,…,m, $r \neq i$). This continues until the deadlock state is removed.

Without loss of generality, we assume that the time spending on killing each deadlock process is always the same. So, in the worst case, the cost needed in total is:

$$T_1=m\times(m-1)\times(m-2)\times\ldots\times(1/2)\times t \tag{2}$$

Clearly, the method has high time cost, so this is an unrealistic approach.

3.2 The Second Method of Killing Deadlock Process

The main principle of this method can be described as follows [10]. First, deadlock process P_1 is killed from S, system's state becomes U_1, P_1 is putted into a killed process set $d(T)$, and add the corresponding cost t_1 into a spending time set $rc(T)$. Repeating the procedure for the deadlock processes $P_2,P_3,\ldots, P_m$, the $U_2,U_3,\ldots,U_m$ are obtained respectively. Then, the new states evolving from state S are putted into the queue L on the basis of the size of the spending costs on the killing processes. Obviously, the first state which is evolved from state S in queue L is the minimum cost of killing processes. Without loss of generality, we assume the first state in L is U_1. If the current system is still in deadlock, starting from the U_1, we kill the process one by one according to above principle. The procedure goes on until the deadlock is removed.

Without loss of generality, we assume that the spending time on killing each deadlock process is always the same. So, in the worst case, the cost needed in total is:

$$T_2=mt+(m\text{-}1)t+\ldots+t=(m+1)\times(m/2)\times t \tag{3}$$

The time complexity of the algorithm is $O(m^2)$. There is a great improvement in time complexity compared with first method.

4 The P System Model of Removing Deadlock

To further improve the efficiency of removing deadlock, the paper presents a P system model. Suppose there are m processes in a deadlock, we design a P system of degree m to deal with the deadlock.

The P system model can be defined formally as follows:

$$\Pi = (V, \mu, w_1, \ldots, w_m, (R_1, \rho_1), \ldots, (R_m, \rho_m)) \tag{4}$$

where

(i) $V=\{S,U_1,U_2,\ldots,U_m\}$;

(ii) The meanings of μ, $w_i(1\le i\le m)$ and δ are similar to Eq. (1);

(iii) Membrane 1 contains an object S and the following evolution rules:

$$R_1 = \left\{ S \xrightarrow{P_1} U_1\delta, S \xrightarrow{P_2} U_2\delta, \ldots, S \xrightarrow{P_m} U_m\delta \right\} \tag{5}$$

(iv) There is no object in membrane 2 to membrane m, and each membrane has the $m\times(m\text{-}1)$ same rules, the rules of R_2 to R_{m} are defined as:

$$R_2 = R_3 = \cdots = R_m = \left\{ \begin{array}{l} U_1 \xrightarrow{P_2} U_2\delta, U_1 \xrightarrow{P_3} U_3\delta, \ldots, U_1 \xrightarrow{P_m} U_m\delta \\ U_2 \xrightarrow{P_1} U_1\delta, U_2 \xrightarrow{P_3} U_3\delta, \ldots, U_2 \xrightarrow{P_m} U_m\delta \\ \ldots\ldots \quad \ldots\ldots \quad \ldots\ldots \\ U_m \xrightarrow{P_1} U_1\delta, U_m \xrightarrow{P_2} U_2\delta, \ldots, U_m \xrightarrow{P_{m-1}} U_{m-1}\delta \end{array} \right\} \tag{6}$$

The priority relationship of evolution rules above is $\rho_2=\rho_3=\ldots=\rho_m=\{f_1,f_2,\ldots,f_m\}$, where each rule in ith column of the matrix has the same priority f_i.

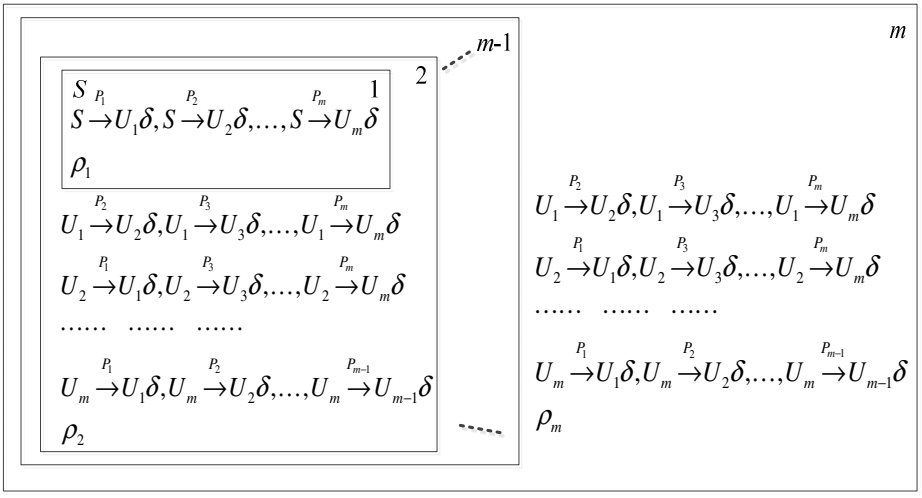

Fig. 1. The P system model of removing deadlock

The P system model can be shown in Fig.1. Additionally, note that all of the evolution rules are dissolution rules. That is to say, when one certain evolution rule can be executed in a membrane, the membrane will be dissolved once the execution is finished and the generated object will enter its upper membrane.

In the P system model, we specify the cost function for each killed process. In general, the elimination needs to meet certain needs, such as the minimum cost, so we can assign a cost function according to the request. Suppose the cost functions of killing processes $P_1,P_2,\ldots,P_m$ are $f_1, f_2, \ldots, f_m$. The greater the value f_i, the larger the spending cost on killing processes, the contrary is true. We can define a priority for each rule according to the cost function. So, f_1 corresponds to the priority of killing process P_1 of the rules in each membrane, f_2 corresponds to the priority of killing process P_2 of the rules in each membrane, and so on. The smaller the value f_i, the less the spending cost on killing corresponding process, the higher its priority and the rule will be first executed.

Next, we will describe the operation of the P system model. First of all, the most inner membrane (membrane 1) contains only one object S, so the m evolution rules of membrane 1 may be selected. However, due to the priority mechanism, the rule with the highest priority (corresponding to the minimum cost of killing process) will be selected. For simplicity, we assume that this rule corresponds to the process P_i to be killed (state becomes U_i), the process is added to a killed process queue T. Since the rule is a dissolution rule, membrane 1 is dissolved and the generated object U_i will enter the upper membrane (membrane 2). Note that, if there are two or more rules with the same priority in this step, one of the generated objects will be chosen as result non-deterministically, such as U_i, Now, membrane 2 has the object U_i, because

membrane 1 has been dissolved. Then, the (m-1) evolution rules which has the highest priority corresponding object U_i is stimulated. After executing this evolution rule, the membrane 2 has been dissolved by the rule with the minimum cost of the system, the generated object U_j will enter the upper membrane 3, and the corresponding process P_j will be added to queue T. Similarly, if several rules have the same priority, then one of the generated objects is chosen as result non-deterministically. Because the membrane 2 to membrane m have exactly the same evolution rules, their executions are similar to membrane 2. When the evolution rule corresponding the highest priority is executed of membrane m, the generated object U_s will be sent to the environment with the dissolution of membrane m and the corresponding process P_s will be added to queue T. At this point, the system halts. As a result, the queue T contains m processes $\{P_i,P_j, \ldots,P_s\}$.

We need a judgment mechanism in the application of the P system model to simulate the process of removing the deadlock. When a process is killed, we call the judgment mechanism to judge whether the system is still in a deadlock. If the deadlock has been removed, the system halts and the processes in queue T are killed processes which satisfy the minimum killing cost. Otherwise, the P system model continues to run.

Without loss of generality, we assume that the time spending in killing each deadlock process is always the same. So, in the worse case, the time cost needed in total is:

$$T_3 = m \times t \tag{7}$$

The time complexity of the algorithm is $O(m)$. The proposed P system model can remove deadlock in a linear time, which has obvious advantages over above two traditional methods. What's more, the P system model select the rule with the highest priority each time, the killing cost has been minimized. Therefore, proposed P system model can solve the problem in the minimum number of killing processes, cost and time of the system.

5 An Illustration Example

Here we give an example about how the P system solves a deadlock problem. Assume that the system has three types of resources R_1, R_2 and R_3, in the deadlock state S, there are several deadlock processes P_1, P_2, P_3, P_4, P_5 and P_6, shown in Fig. 2(a), In Fig. 2(a), a circle represents a process, while a square represents a resource of some certain category. The request side is from a circle (process) to a square (resource); the allocation side is from a square (resource) to a circle (process). The resources allocation graph can be seen, P_1, P_2 compete for R_2 while occupy R_1; P_3, P_4 compete for R_3 while occupy R_2; P_5, P_6 compete for R_1 while occupy R_3. The process of the group can't move forward and trap into an endless waiting. In order to remove the deadlock, if such four processes are killed, a process in P_1, P_2, together with a process in P_3, P_4, a process in P_5, P_6, and the fourth process is a process in the remaining three processes. Then the loop of resource allocation graph has been killed, and the graph becomes Fig. 2(b), deadlock has been removed already. For simplicity, we only consider the spending time of killing process, let the time of killing process P_i be t_i. Suppose the time of killing each deadlock process satisfies the following partial ordering relation: $t_1<t_3<t_5<t_2<t_4<t_6$.

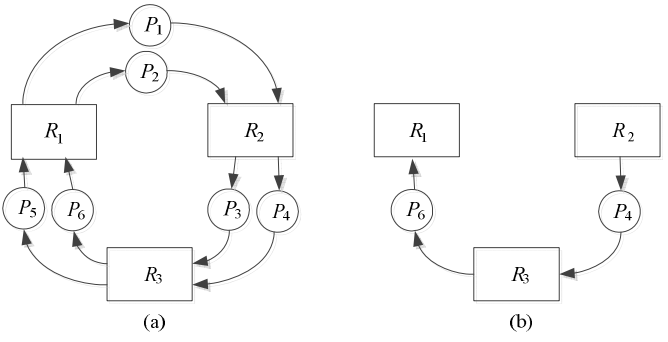

Fig. 2. (a) Resource allocation graph; (b) Resources allocation graph after removing the deadlock

For the sake of solving the deadlock problem using P system model, we can construct a P system of degree 6, its formal definition is:

$$\Pi = (V, \mu, w_1, \ldots, w_6, (R_1, \rho_1), \ldots, (R_6, \rho_6)) \cdot \tag{8}$$

where

(i) $V=\{S,U_1,U_2,\ldots,U_m\}$;

(ii) The meanings of μ, $w_i(1\le i\le m)$ and δ are similar to Eq. (1);

(iii) Membrane 1 contains an object S and 6 evolution rules as Eq. (5). Here, for simplicity, we only associate the priority with the spending time on killing process, so the priority relationship is $\rho_1=\{t_1<t_3<t_5<t_2<t_4<t_6\}$.

(iv) Membrane 2 to membrane 6 have no object, each membrane contains 30(=5×6) rules as Eq. (6), and the priority relationship is $\rho_2=\rho_3=\rho_4=\rho_5=\rho_6=\{t_1<t_3<t_5<t_2<t_4<t_6\}$.

For above P system model, due to membrane 1 contains an object S, the rule which have the highest priority in its 6 rules is selected, that is, the rule ($S \xrightarrow{P_1} U_1\delta$). Thus, the process P_1 is added to a killed process queue T, and the generated object U_1 will enter the upper membrane (membrane 2). Because the deadlock state of the system has not been removed, the system continues to run. At this time, the membrane 2 has the object U_1, then the evolution rule which has the highest priority is stimulated, that is ($U_1 \xrightarrow{P_3} U_3\delta$), The process P_3 is added to queue T. Similarly, the rule ($U_3 \xrightarrow{P_5} U_5\delta$) of membrane 3 and the rule ($U_5 \xrightarrow{P_2} U_2\delta$) of membrane 4 will be executed one after another. At this point, the deadlock state of the system has been removed, so the system halts. As a result, the queue T contains 4 processes $\{P_1,P_3,P_5,P_2\}$. Therefore, in order to remove deadlock, we should kill four deadlock processes P_1, P_3, P_5 and P_2 in turn.

From the analysis above, we can see the spending time on removing deadlock state by P system model is $T=t_1+t_3+t_5+t_2$, therefore the time is shortest. As the P system model with distributed, maximum parallelism and non-deterministic features, it can determine which deadlock process should be killed optimally in a linear time, so it has an obvious advantage for removing deadlock.

6 Conclusions

In this paper, we propose a cell-like P system computing model to remove the deadlock. We give an example about *m* deadlock processes and demonstrate how the P system works. The removal of the deadlock is simulated by constructing a P system containing *m* nested membranes. The key is to determine which deadlock process should be killed and ensure the minimum cost of system. Since the P system model has its own characters: distributed, parallel computing and non-deterministic, so the P system model can solve the problem in a linear time complexity. We can see that the proposed P system model has a greater advantage over the two traditional methods.

References

1. Păun, G., Rozenberg, G., Salomaa, A.: DNA Computing: New Computing Paradigms. Springer, Heidelberg (2002)
2. Păun, G., Rozenberg, G., Salomaa, A.: The Oxford Handbook of Membrane Computing. Oxford University Press, New York (2010)
3. Păun, G.: Computing with Membranes. Journal of Computer and System Sciences 61, 112–114 (2000)
4. Păun, G., Suzuki, Y., Tanaka, H., Yokomori, T.: On the Power of Membrane Division in P Systems. Theoretical Computer Science 324(1), 61–85 (2004)
5. Bernardini, F., Gheorghe, M.: Cell Communication in Tissue P Systems: Universality results. Soft Computing 9(9), 640–649 (2005)
6. Păun, A., Păun, G.: Small Universal Spiking Neural P systems. Biosystems 90(1), 48–60 (2007)
7. Păun, G.: Introduction to Membrane Computing. In: Proceedings of Brainstorming Workshop on Uncertainty in Membrane Computing. Palma de Mallorca, España, pp. 1–42 (2004)
8. Tanenbaum, A.S.: Modern Operating Systems, 2nd edn., pp. 163–174 (2002)
9. Nutt, G.J.: Operating Systems, 3rd edn., pp. 376–392 (2005)
10. Tang, Z.Y., Zhe, F.P., Tang, X.D.: Computer Operating Systems, pp. 100–101 (2001)

Application of Data Integration on Microwave Detection

Chuan Yin, Yi Luo, Yi Yao, and Xiao-hui Zhu

Department of Machinery & Electronics,
Si Chuan University of Science and Technology, China
286317609@qq.com, luoyi@suse.edu.cn,
Yy6166@126.com, zhxh@126.com

Abstract. The purpose of this paper is mainly to detect the sample of polluted river by means of microwave, and may determine what pollutants the surface water contains and the concentrations of pollutants by using various pollutants to estimate the different absorption and attenuation of electromagnetic wave and by the data tables and related conclusions obtained by the timely monitoring system of electromagnetic wave and a large number of experiments. Then considering the combination of Matrix VB &VB as a experimental platform and by fitting experimental data based on the method of date fitting, the concentration of pollutants－concentration curves and mathematical model can be obtained.

Keywords: microwave; date fitting; water Pollution; VB.

1 Introduction

It is known that China's environmental protection departments and its corresponding research institutions have presented a variety of monitoring techniques and monitoring methods for a long time in terms of timely monitoring of water quality. these techniques and methods can be roughly classified into three categories as A, B and C. Category A is the standard method for the country and the industry. Category B is the mature unified method conformed by experiments, Category C is the new method provided for scientific research personnel. Category C has the great value of research and trial even though it is not mature [1].The traditional method is the sample analysis, that is to say, firstly sampling from a certain selected section of river, then analyzing the concentration and density of the tested material in the river by means of chemical analysis. This method is more precise but not simultaneous and it can not meet the demand of timely detection. Besides, in terms of present timely detecting method, sensors method is normally used at home and abroad, which is to change the concentration signals of the tested material into electrical signals with a series of chemical or biological sensors. Although it can detect timely and has a fairly high speed, it can only detect a few Index of rivers and even the detecting accuracy is susceptible to environmental factors on account of the limitations of the sensors categories. In addition, the sensors can easily be blocked by sediments or moss can easily grow on them affected by the environment of sensors locations, which on the one hand can affect the

D. Zeng (Ed.): Future Intelligent Information Systems, LNEE 86, pp. 119–125.
springerlink.com © Springer-Verlag Berlin Heidelberg 2011

precision and the reliability of test results, on the other hand can shorten the life of the sensors. Generally speaking, the life of the chemical or biological sensors used in water are about two years, which will greatly increase the cost. As the above problems have not been resolved, so this paper will present a kind of technology which can timely detect on surface water pollution by microwave.

2 The Theory of Microwave Detection

When the electromagnetic wave whose frequency is between 300 ~ 3000MHz is transmitting in the river, it can produce polarization and magnetization to polluted materials in the water, whose result is to produce the attenuation of polarization and magnetization to the the electromagnetic wave. In addition, as the conductivity of pollutants in the river is generally not equal to zero, it can absorb the energy of electromagnetic wave and the electromagnetic wave of some frequency can stimulate the transmission of electron to the molecular of pollutants [2]. Therefore, when the electromagnetic wave is transmitting in the river, its amplitude will decrease with the transmission distance according to the exponential and part of the electromagnetic energy will be absorbed. Besides, the sensing ratio of absorption of different pollutants is quite different to the electromagnetic wave, and the sensing ratio of absorption of the different density of pollutants is quite different to the electromagnetic wave.

3 The Construction of Microwave Detecting System and Experimental Methods and Ideas

The system mainly consists of sweep frequency signal, power amplifiers, antenna, receiving antenna, small signal amplifiers, detectors. The concrete block diagram of the system is shown in figure 1 :

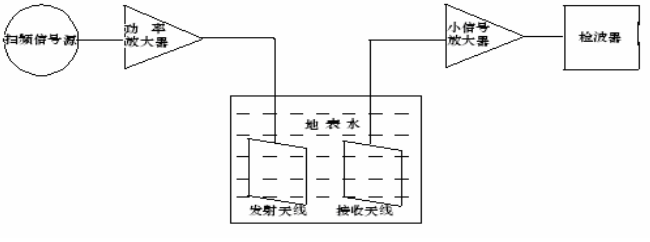

Fig. 1. Concrete block diagram of the system

From the above diagram we can draw the conclusion that the system can be divided into several parts such as the design of antenna, the design of power amplifier and the design of small signal amplifier. While the sources of the signals and the receiving of the signals can be accomplished by network analyzer. As for the antenna, according to the feature that the band of this system should be extraordinary wide, we can choose

the Archimedes spiral antenna, then simulate with the software CST of antenna design. Power amplifiers and small signal amplifiers are simulated and designed by using the simulation software ADS (Advanced Design System) of microwave frequency. Finally the source device and chips are needed to be purchased to complete welding in the laboratory.

Now, we can take the experiment after the completion of the above steps. At the first stage of the experiment, we should focus on the measurement of the near-field antenna, then fix the antenna and receiving antenna to the plastic pipe bracket, and adjust the distance to 22 cm, finally connect antenna, power amplifier and network analyzer. After that, we can measure the curve of attenuation and absorption of various pollutants in the samples respectively [3]. And we can find the sensitive frequency of respective absorption the relationship between the rate and density of the absorption. The experimental method of comparison can be adopted. And we can compare the curve in the clean water and that of attenuation in which the different compounds are added in the clean water. In order to get more clear result, we should connect transmitting antenna and power amplifiers to the receiving antenna, then put them into clean water to measure with other instruments [4]. After the measurement, we should put the antenna into the solution to be measured, so it is easy to see the variation of the curve in each solution. The idea of the experiment is to measure from near to far distance, from the large-scale sweep frequency to the small-scale precision measurement.

4 The Analysis of Experimental Results

According to the basic project standard value of the environmental quality standard of surface water, the surface water pollution can be divided into the categories of I, II, III, IV and V. Pollution includes the heavy metals such as mercury and lead, the various chemical compounds such as acid and alkali, poisonous chemical compounds such as cyanide and sulfide and micro-organisms and suspended solids etc [5]. According to the national standard of the People's Republic of China, the quality standard of surface water environment and the main pollutants in rivers and lakes, the three chemical compounds of five water copper sulfate, seven water zinc sulfate and lead nitrate are chosen at the early stage of the experiment [6]. According to the basic principle that these compounds will generate bivalent ionization ion channels of copper, zinc, lead ions when they are dissolved in water, it is easy to find the changes of conductivity will give the reasons to the changes of the dielectric constants, and it can also lead to the changes of the electromagnetic energy through the solution. As the absorption of heavy metals is more obvious in the system, this experiment mainly measures heavy metal ions. Heavy metal contamination of water pollution are mainly copper, zinc, selenium, arsenic, mercury, cadmium, cr (superscript 6), etc [7]. Considering the characteristic that the compounds can be dissolved in water, thereby, the three ions of copper, zinc and lead are chosen to be discussed and analyzed. At first, we use the network analyzer to measure five water copper sulfate, seven water zinc sulfate, nitrate lead and so on in the way of frequency sweep and the sweep frequency ranges from 200MHz to 2000MHz. After doing this work, we find that the absorption

peaks of the band is between 200MHz~ 600MHz, then we adjust the sweep frequency between 200MHz to 600MHz to observe and do the experiment.

Pour 50 liters clean water into the barrel and connect the instruments, and finally use the network analyzer to respectively measure five water copper sulfate, seven water zinc sulfate and the liquid of nitrate lead. The output power of the network analyzer can be setted as 15dBm, 10 times experiments have been made on the three compounds respectively, and finally we can find that the results have a good repeatability.

We can read the attenuation extent of various ions in the sensitive frequency from the network analyzer directly. 5 different marker points can be settled on the network analyzer and we can read the number of attenuation of various ions in the sensitive frequency precisely by the five different marker points on the screen of the network analyzer [8]. Relatively stable dates can be chosen through many measurements. The sensitive frequency of different concentrations of metal ions is shown in table1, and the attenuation extent of different concentrations of metal ions is shown in table 2.

Table 1. Sensitive frequencies of different concentrations of metal ions

Number	Density of Copper ion (mg/l)	Sensitive frequency of copper ion (MHZ)	Zinc ion (mg/l)	Sensitive frequency (MHZ)	Milligram of Lead ion (mg/l)	Sensitive frequency (MHZ)
1	2.0	276.20	3.0	305.89	1.5	346.45
2	2.25	276.88	3.25	306.74	2.0	347.24
3	2.5	276.50	3.5	306.45	2.5	347.26
4	2.75	277.63	3.75	306.78	2.5	347.01
5	3.0	278.08	4.0	307.45	3.0	346.72
6	3.25	277.35	4.25	308.01	3.5	346.10
7	3.5	277.56	4.5	306.45	4.0	346.31
8	3.75	278.70	4.75	306.45	4.5	346.23
9	4.0	276.45	5.0	307.28	5.0	347.02
10	4.25	278.93	6.25	308.09	5.5	346.03
11	4.5	276.73	7.5	306.25	6.0	346.35
12	4.75	278.56	8.75	307.58	6.5	347.42
13	5.0	276.35	9.0	306.87	7.0	346.23
14	5.25	276.13	9.25	307.01	7.5	346.84
15	5.5	276.45	9.5	308.43	8.0	345.98
16	6.0	278.54	10.0	307.12	8.5	346.21
17	6.25	278.64	10.25	307.52	9.0	348.01
18	6.5	277.06	10.5	307.79	9.5	346.46
19	6.75	276.54	10.75	308.01	10.0	346.07
20	7.0	278.86	11.0	307.95	11	347.08

Table 2. Attenuation extent of different concentrations of metal ions

Number	Copper ion (mg/l)	Extent of absorption (DB)	Zinc ion (mg/l)	Extent of absorption (DB)	Lead ion (mg/l)	Extent of absorp-tion (DB)
1	2.0	-31.73	3.0	-30.45	1.5	-40.33
2	2.25	-32.45	3.25	-31.33	2.0	-41.34
3	2.5	-33.45	3.5	-32.07	2.5	-42.16
4	2.75	-34.07	3.75	-32.85	3.0	-43.08
5	3.0	-35.02	4.0	-32.92	3.5	-43.42
6	3.25	-35.88	4.25	-33.02	4.0	-43.78
7	3.5	-36.54	4.5	-33.57	4.5	-43.05
8	3.75	-36.74	4.75	-34.02	5.0	-44.08
9	4.0	-36.80	5.0	-34.48	5.5	-45.38
10	4.25	-37.41	5.5	-34.79	6.0	-46.05

From the two tables above we can find that the sensitive frequencies change a little as the concentration increases, but always in a small range. And the attenuation extent has the tendency of gradual increase with the increase of concentration. We can also observe the resonance frequency of the five water copper sulfate is between 276～280MHz, Seven water zinc sulfate is between 305～307MHz and lead nitrated is between 346～347MHz respectively [9].

In the choice of software of processing data, Visual Basic (VB) is chosen as the development tool due to the particularity of the industrial field and considering the data has the characteristic of multiple tasks, multiple interferences and powerful time adaptation. However, the calculating function of VB is rather weak, and it is a very big task to complete the complicated calculating, in addition, graphics rendering function of VB is also weak, and it is also a very big task to draw a delicate graphics program.

So we combine the VB with MATLAB, and use the technology of ActiveX automation and dynamic data exchange (DDE). Besides, we also use the program of Matrix VB offered by MATLAB and the tool of Mat com to change the MATLAB function to the Dynamic Link Library (DLL) and change the MATLAB function to the Executable File (EXE). Finally the application program may release from the MATLAB environment and can be operated independently.

Owing to the space of the paper, we only carry on date fitting on experimental dates from the principle. The dates we have got in the measurement are the discrete random dates, and the date fitting is to get the relationship formula of approximate function and the empirical formula between dependent variables and independent variables from these discrete random dates. and these issues in graphics are to get a curve from the measured point. The curve fitting is an experimental method which deals with the empirical dates or experimental dates in engineering.

In this paper, we will present the data fitting process of copper ions and simulation diagram, and it is a simple and effective method to change the curve fitting function into linear function or polynomial function. The polynomial fitting function whose dates are offered by MATLAB is Poiyfit and it is the polynomial coefficients with given dates by fitting in the sense of least squares [10]. And it is much more convenient and simpler than other calculation methods and it also has the sufficient accuracy. Based on the measured dates, we can get the fitting curve with this function conveniently.

The following dates can be got as follows from the attenuation extent of Copper ions.

Table 3. The attenuation extent of Copper ions

X	-31.73	-32.45	-33.45	-34.07	-35.02	-35.88	-36.54	-36.74	-36.80 -37.41
Y	2.0	2.25	2.5	2.75	3.0	3.25	3.5	3.75	4.0 4.25

After the VB program is to be inputed and simulated with the above principle, we can obtain the simulation diagram after sixth times later, it is shown in figure 2.

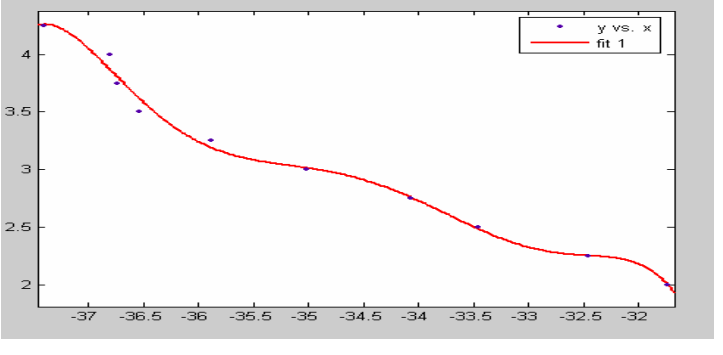

Fig. 2. Sixth fitting curve of copper ions

Likewise, we can also get the polynomial equations of fitting curves of six times as follows:

$$y = (-1.437e+006) - (1.044e+005)x - 4038x^2 - 87.85x^3 - 1.018x^4 - 0.004916x^5$$

As is shown above, all the experimental points are on the curve or near to it after six times data fitting of copper ion, that is to say, the fitting equation of the experimental curve has the great reliability. Thereafter, we can calculate the concentration of copper ions and the degree of pollution by using this equation as the date model later. Certainly we can use the same method to fit on zinc ions and lead ions so as to get the the polynomial equation of respective curves.

5 Conclusion

Aiming at the problems existing in water detecting technology, this paper has proposed a new method which can timely detect water pollution, and also verified the correctness and feasibility of this method through a large number of experiments. This method has the particular advantages such as fast speed, accuracy, and being easy to implement. So it is one of the most important means for timely detecting water pollution and has a very important practical value and a broad application prospect on water quality detection.

References

1. Wang, Y., Wang, J., Ma, Y., et al.: Biophoton Emission Free Radical and Toxicity of Benzene to Aquatic Biosystem. Journal of Environmental Science, 18–20 (1996)
2. Guan, L.-j.: The Current Situation of Water Pollution in Our Country and Its Countermeasures. Information Development and Economy of Science and Technology, 23–25 (2004)
3. Xu, X., Jin, C.-l., Shi, Y.-b.: Water Environment Situation and Problems in China. China Water Conservation Project, 35–37 (1997)
4. Zhu, X.-h.: Research in Water Pollution of Timely Monitoring System by Microwave (2007)
5. Chen, K.-s., Lei, C.-q.: Reservior Trophic State Evalution Using Landsat TM Data. Journal of the American Water Resource Association 37(5) (2001)
6. Yao, Y., Jia, J.-l., Yao, Y.-c.: Data Collection and Signal Treatment of Timely Monitoring to the Surface Water. Journal of Sichuan Institute of Light and Chemical Industry, 37–40 (2003)
7. Yao, Y.: A Study of Timely Detecting Technology on the Surface Water Pollution. Journal of Apparatuses and Instruments (2003)
8. Ze-song Quan, C.: The Theory of Electromagnetic Field. Pressing House of University of Electronic Science and Technology, Chengdu (1995)
9. Yun, L.-J.: Megahertz Acoustic Attenuation in Fluidized Mud. Technical Acoustics (2004)
10. Li, D.-s., Li, H.-j.: Application of Microwave Technology on the Analysis and Measurement and the Pollution Treatment (2003)

Differential Evolution Algorithm Based One Dimension Real Valued Searching for Feature Selection*

Jun Wang and Yan Zhao

Department of Electronics Engineering, Shantou University,
Daxue Road 243#, Shantou Guangdong Province, China
{wangjun,Yanzhao3}@stu.edu.cn

Abstract. Forming an efficient feature space for classification problems is a grand challenge in pattern recognition. Many optimization algorithms are adopted to do feature selection, but these algorithms do searching in multi-dimensions space and always cannot get the optimal feature subset. In this paper, a feature selection method with differential evolution algorithm doing searching in only one dimension real valued space is proposed to improve the classification performance. Experimental results show that the proposed method can do feature selection more effectively than the compared method and get much higher classification accuracy.

Keywords: Differential evolution algorithm, Feature selection, One-dimension real valued searching.

1 Introduction

Feature selection constitutes a key development phase of pattern recognition and to a significant extent predetermines the effectiveness of overall classification schemes [1]. A typical real-world dataset consists of as many features as are deemed necessary. It is clear that not all the features that are stored in the resulting data set are necessary or sufficient to learn the concept of interest. Assuming that all the necessary features are present in these data, feature selection is the problem of choosing a small subset of features that ideally are necessary and sufficient to describe the target concept. Basically, the object of the feature selection problem is to find a subset of variables that can be used to carry out the classification task in an optimum way. One usually starts with a given set of features and then attempts to derive an optimal subset of features leading to high classification performance [2].

The term feature selection refers to algorithms that output a subset of the input feature set. In supervised learning we have a set of examples characterized by the same attributes as the instances and another attribute corresponding to the class they belong to. Using this set of examples we can create and generalize a rule or set of rules that allows us to classify the instance set with the greatest possible precision. The research

* This work was supported by the Natural Science Foundation of Guangdong Province of China (No.9451503101003263), Educational Commission of Guangdong Province of China and the Youth Foundation of Shantou University.

D. Zeng (Ed.): Future Intelligent Information Systems, LNEE 86, pp. 127–134.
springerlink.com © Springer-Verlag Berlin Heidelberg 2011

on feature selection dates back to the early 1960s [3]. Extensive research into feature selection has been carried out over the past four decades. The spectrum of feature selection techniques is typically split into two main categories: wrappers and filters. Each category has well-defined advantages and possible drawbacks. Filters offer a more general view of the feature space however they cannot guarantee effectiveness as far as a specific classification scheme is concerned. Wrappers, on the other hand, are focused on feature space optimization that takes into account a specific classification scheme. It could well be that the optimality of the feature space could vary quite substantially and rely upon the assumed classification scheme. No matter which category is adopted, the feature selection (choosing minimum "m" discriminatory features out of "n" total features) is inherently a combinatorial optimization problem that is a NP-hard problem [4]. There are many searching algorithms used to determine the promising feature subset candidates, such as exhaustive search, branch and bound search (BB), sequential forward selection (SFS), Tabu search (TB), Simulated annealing algorithm (SA), Genetic Algorithm (GA), Binary Particle Swarm Optimization (BPSO) and etc. Exhaustive search algorithm can get the optimal feature subset but its computing complexity increases exponentially with the number of original features increasing [4]. BB can work well only when the objective function is monotonic which cannot be always satisfied in practice [5]. SFS suffers from the so-called "nesting effect" and cannot obtain the optimal feature subset. Computing complexity of TB or SA is too high to be qualified for feature selection of high dimension dataset [6]. In recent years, stochastic searching algorithms for its good global search ability and relative lower computing complexity have been adopted to do feature selection, such as GA, Hybrid GA, Binary or Discrete PSO etc. GA has been proposed to do feature selection by many researchers, but this method always can not obtain the optimal feature subset for it's often falling into local optimum especially when the searching space is too high or too complicate [7]. PSO has much better global optimization ability and relatively lower computing complexity than GA or Hybrid GA, and has been widely used to do feature selection [8]. Recently, an optimization algorithm named Differential Evolution algorithm (DE) was proposed to do global optimal searching. And many evidences have been shown that the DE algorithm did better optimal optimization than other random searching algorithm such as PSO algorithm [9].

Unfortunately, all of the existing random searching or optimizing algorithms for feature selection did searching in the discrete search space and always fell into local optimum and could not get optimal feature subset, especially when the number of original features to which the dimension of the searching space is equal is too great. In this paper, we proposed a novel feature selection method by differential evolution algorithm doing searching in the only one dimension real valued space and adopted the SVM as the classifier for testing the performance of classification with the selected feature subset. The experimental results showed that this method was much easier to get optimal feature subset and obtained the higher classification accuracy rate.

2 Technical Backgrounds

2.1 The Principle of Differential Evolution Algorithm

Differential evolution is a novel approach in evolutionary algorithms. It was proposed by Storn and Price in 1997 [10]. It is a stochastic, population-based optimization method. Differential evolution algorithm consists mainly of four steps: initialization, mutation, recombination and selection. DE differs from other population-based techniques in that it employs differential mutation.

In DE, it starts with the random initialization of a population of individuals in the search space and works on the cooperative behaviors of the individuals in the population. Therefore, it finds the global best solution by utilizing the distance and direction information according to the differentiations among population. However, the searching behavior of each individual in the search space is adjusted by dynamically altering the differentiation's direction and step length in which this differentiation performs.

The *i*th individual in the *d*-dimensional search space at generation *t* can be represented as $X_i(t)= [x_{i,1}, x_{i,2},\ldots, x_{i,d}]$, ($i$ = 1, 2, …, NP, where NP denotes the size of the population). At each generation *t*, the mutation and crossover operators are applied on the individuals, and a new population arises. Then, selection takes place, and the corresponding individuals from both populations compete to comprise the next generation.

For each target individual $X_i(t)$, according to the mutation operator, a mutant vector $V_i(t+1)=[v_{i,1}(t + 1), \ldots, v_{i,d}(t + 1)]$ is generated by adding the weighted difference between a defined number of individuals randomly selected from the previous population to another individual, which is described by the following equation:

$$V_i(t+1) = X_{best}(t) + F(X_{r1}(t) - X_{r2}(t)) \tag{1}$$

where r_1, $r_2 \in \{1, 2, \ldots, N\}$ are randomly chosen and mutually different and also different from the current index *i*. $F \in [0, 2]$ is constant called scaling factor which controls amplification of the differential variation $X_{r1}(t) - X_{r2}(t)$, and NP is at least 4 so that the mutation can be applied. $X_{best}(t)$, the base vector to be perturbed, is the best member of the current population so that the best information could be shared among the population.

After the mutation phase, the crossover operator is applied to increase the diversity of the population. Thus, for each target individual $X_i(t)$, a trial vector $U_i(t + 1) = [u_{i,1}(t + 1), \ldots, u_{i,d}(t + 1)]$ is generated by the following equation:

$$u_{i,j}(t+1) = \begin{cases} v_{i,j}(t+1), \ if \ (rand(j) \le CR) \\ \qquad\qquad or \ j = randn(i), \ j = 1,2,...,d \\ x_{i,j}(t), \quad otherwise \end{cases} \tag{2}$$

where *rand*(*j*) is the *j*th independent random number uniformly distributed in the range of [0, 1]. *Randn*(*i*) is a randomly chosen index from the set {1, 2, . . ., d}. $CR \in [0, 1]$ is constant called crossover parameter that controls the diversity of the population.

Following the crossover operation, the selection arises to decide whether the trial vector $U_i(t+1)$ would be a member of the population of the next generation *t*+1. For a minimum optimization problem, $U_i(t+1)$ is compared to the initial target individual $X_i(t)$ by the following one-to-one based greedy selection criterion:

$$X_i(t+1) = \begin{cases} U_i(t+1), & if \quad F(U_i(t+1)) < F(X_i(t)) \\ X_i(t), & otherwise \end{cases} \tag{3}$$

where F is the objective function under consideration, $X_i(t+1)$ is the individual of the new population. The procedure described above is considered as the standard version of DE, and it is denoted as DE/best/1/bin. Several variants of DE have been proposed, depending on the selection of the base vector to be perturbed, the number and selection of the differentiation vectors and the type of crossover operators.

The key parameters in DE are NP (size of population), F(scaling factor) and CR (crossover parameter). Proper configuration of the above parameters would achieve good tradeoff between the global exploration and the local exploitation so as to increase the convergence velocity and robustness of the search process. Some basic principles have been given for selecting appropriate parameters for DE [10]. In general, the population size NP is choosing from $5 \bullet d$ to $10 \bullet d$ (number of dimension). F and CR lies in the range of [0.4, 1.0] and [0.1, 1.0], respectively.

2.2 Support Vector Machine

In the process of feature selection, a performance index or a fitness function that assesses the quality of the selected features in terms of classification error should be adopted to guide the forming of a reduced feature space. So a classifier will be used. Here we adopt the support vector machine (SVM) as the classifier [8]. SVM which is an emerging data classification technique proposed by Vapnik in1995, and has been widely adopted in various fields of classification problems in recent years. SVM technique is briefly described as follows. Let (x_i, y_i), $1 \le i \le N$, denote a set of training data, where N represents the number of training data. Each datum must conform to the criteria $x_i \in R^d$ and $y_i \in \{-1, 1\}$, where d denotes the number of dimensions of input data.

SVM attempts to identify a hyper-plane, which functions as a separating plane for classification of data, in a multidimensional space. The parameters w and b are given by

$$\left(\langle w \square x_i \rangle + b \right) = 0, i = 1, 2, ..., N \tag{4}$$

If a hyper-plane exists that satisfies Eq. (4), linear separation is obtained. In this case, w and b can be rewritten as follows. Eq. (4) becomes

$$\min_{1 \le i \le N} y_i \left(\langle w \cdot x_i \rangle \right) \ge 1, i = 1, ..., N \tag{5}$$

Let the distance from the data point to the hyper-plane be $1/\|w\|$. Among separating hyper-planes, there exists one optimal separating hyper-plane (OSH), and the distance between two support vector points on two sides of this hyper-plane is maximal. Because the distance between two support vector points is $1/\|w\|^2$, the minimal distance to OSH, $\|w\|^2$, may be derived from Eq. (5).

The margin of a separating hyper-plane, calculated as $2/\|w\|$, determines the hyper-plane's generalization ability. The OSH has the largest margin among separating hyper-planes. $\|w\|^2$ is minimized with Eq. (5) and Lagrange's polynomial. Let a

denote ($a_1,\ldots,a_N$). Combining Lagrange's polynomial (in the order of N) with Eq. (5) produces the following equations for maximization.

$$W(a)=\sum_{i=1}^{N}a_i-\frac{1}{2}\sum_{i,j=1}^{N}a_ia_jy_iy_jx_ix_j \tag{6}$$

where $a_i\geq 0$ and under constraint $\sum_{i=1}^{N}y_ia_i=0$.

Quadratic programming method can be adopted to solve the above maximization problem. If a vector $a^0=\left(a_1^0,...,a_N^0\right)$ satisfies the Eq.(6) in maximization, then the OSH expressed in terms of (w_0,b_0) may be expressed as follows:

$$w_0=\sum_{i=1}^{N}a_i^0y_ix_i \tag{7}$$

where the support vector points must comply with $a_i^0\geq 0$ and Eq. (5). When considering expansion in constraint Eq. (7), the determinant function of hyper-plane is expressed as follows:

$$f(x)=sign\left(\sum_{i=1}^{N}a_i^0y_ix_ix+b_0\right)=0 \tag{8}$$

In most cases, the data are not linearly separable, and are consequently mapped to a higher-dimensional feature space. Therefore, if the data cannot be classified clearly in the current dimensional space, then the SVM will map them to a higher dimensional space for classification.

Input data are mapped to a higher dimensional feature space by plotting a nonlinear curve. The OSH is constructed in the feature space. By constructing the feature space $\phi(x)$ can be adopted in constrained Eq. (6) as shown below:

$$W(a)=\sum_{i=1}^{N}a_i-\frac{1}{2}\sum_{i,j=1}^{N}a_ia_jy_iy_j\phi(x_i)\phi(x_j) \tag{9}$$

Given a symmetric and positive kernel function $K(x,y)$, the existence of Mercer's theorem can be deduced. Therefore, $K(x,y)=\phi(x)\phi(y)$. Provided that the kernel function K satisfies Mercer's theorem, the derived training algorithm is guaranteed for minimization

$$W(a)=\sum_{i=1}^{N}a_i-\frac{1}{2}\sum_{i,j=1}^{N}a_ia_jy_iy_jK(x_i,x_j) \tag{10}$$

The decision function is expressed as follows:

$$f(x)=sign\left(\sum_{i=1}^{N}a_iy_iK(x_i,x_j)+b\right) \tag{11}$$

3 Differential Evolution Algorithm Based One Dimension Real Valued Searching for Feature Selection in the Pattern Recognition

In the existing works that adopted the random searching algorithms to do feature selection, a binary string is used for representing the feature set in which the presence of a feature is coded as "1" and the absence of a feature as "0". So these algorithms such as BPSO [11] does searching in high dimension real-valued space in which every original feature is viewed as a dimension and converts the searched real-valued result into a binary string to test the performance of the searched feature subsets in each iterations. And the computing time will increase substantially as the number of original features increasing. Furthermore, the more dimension, the more complicate searching space. The searching space will have much more extreme points, and the feature selection algorithms will have more chances to trap into the local optimum and cannot get the optimal feature subset. Some reason may be founded from the following example. Let the corresponding objective function or fitness function value to "*xx*…..*xx*10" is the global optimum, and the objective function is monotone from "*xx*….*xx*01" to "*xx*…*xx*10", where "*x*" can be "1" or "0". But, there will be two extreme points corresponding to the "*xx*…*xx*01" and "*xx*…*xx*10" that are not adjacent in multi-dimension search space. This example shows that the complexity of multi-dimension searching space is much higher than that of one dimension searching space. The existing random searching algorithms may be trapped into the local optimum in "*xx*…*xx*01" and always cannot get the optimal feature subset. In this paper, differential evolution based one-dimension real-valued searching algorithm for feature selection is proposed, in which the search space will less complicate than that of traditional discrete random searching algorithms such as BPSO and has less chances to trap into local optimum i.e. more chances to get optimal feature subset. This approach consists of the following steps.

Step1: A population of individuals $\{X_i(t) \mid X_i(t) \in R^1, i = 1,...,NP\}$ is initialized, where iteration t=0.

Step2: For every individual $X_i(t)$ is coded into a binary string $BinaryString(X_i(t))$ in which every bit indicates a feature present or not, and its fitness is evaluated. Here, the fitness valued is determined by an SVM classifier, which is defined as following form:

$$fitness(X_i(t)) = classification \quad accuracy + \alpha \times \frac{The\ number\ of\ "0"\ in\ BinaryString(X_i(t))}{total\ number\ of\ original\ features} \tag{12}$$

where α is a balance factor.

Step3: For all individuals, the best solution $X_{best}(t)$ at iteration t can be obtained as the Equation (13).

$$\left\{ X_{best}(t) = \max_{i \in \{1,2,...,NP\}} fitness(BinaryString(X_i(t))) \right\} \tag{13}$$

Step4: For every individual $X_i(t)$, a mutant vector is generated by the equation (14).

$$V_i(t+1) = X_{best}(t) + F(X_{r1}(t) - X_{r2}(t)) \tag{14}$$

where r_1, $r_2 \in \{1, 2, \ldots, N\}$ are randomly chosen and mutually different and also different from the current index *i*.

Step5: For every individual $X_i(t)$, crossover operation is applied to increase the diversity of the population and a trial vector $U_i(t)$ is generated by the equation (15).

$$U_i(t+1) = \begin{cases} V_i(t+1), & if \ \ (rand(1) \le CR) \\ X_i(t), & otherwise \end{cases} \tag{15}$$

where *rand*( ) is the function to generate the random number uniformly distributed in the range of [0, 1] and $CR \in [0, 1]$ is the crossover parameter.

Step6: Next generation of the individuals are generated by the equation (16).

$$X_i(t+1) = \begin{cases} U_i(t+1), & if \ \ fitness(U_i(t+1)) < fitness(X_i(t)) \\ X_i(t), & otherwise \end{cases} \tag{16}$$

Step7: Stop the algorithm and output $BinaryString(X_{best}(t))$ if termination criterion is satisfied; return to *Step2* otherwise.

4 Experimental Results

Four datasets from the UCI Machine Learning Repository are used to compare the performance of the BPSO based feature selection algorithm with SVM classifier (Algorithm a) and the Differential evolution based One-dimension real valued searching algorithm for feature selection with SVM classifier (Algorithm b), as shown in Table 1. Four datasets are Breast Cancer (DataA), Segmentation dataset (DataB), Dermatology dataset (DataC), and Optdigits dataset (DataD). From Table 1, we can find that the proposed method gets higher classification accuracy and obtains smaller feature subset. These results indicate that the proposed method can get the solution that is much closer to the optimal solution, i.e. better feature subset. So the proposed algorithm is better qualified for applications with high dimension database than the Algorithm a.

Table 1. Feature selection performance and classification performance comparison of two algroithms

Dataset	Number of original features	Average number of reduced features with 20 runs		Average classification rate with 20 runs(%)	
		Algorithm a	Algorithm b	Algorithm a	Algorithm b
DataA	9	6.9±0.34	**2.9±0.17**	95.4±1.24	**99.38±0.08**
DataB	19	6.2±0.34	**2.8±0.11**	92.8±2.05	**96.67±0.15**
DataC	34	12.6±0.61	**7.6±0.26**	80.89±0.19	**98.70±0.23**
DataD	64	25.0±0.36	**15.7±0.19**	97.5±0.37	**99.50±0.00**

5 Conclusions

Differential evolution based one dimension real valued searching for feature selection method is proposed in this paper. For the random searching algorithm does searching in the only one dimension space, the complexity of searching may be less than that of searching in the multi-dimension discrete space. Experimental results demonstrate that the proposed method can get much better feature subsets and much higher classification accuracy than the compared method. The experimental results verified our assumption that the complexity of searching in one dimension real valued space is less than that of searching in the multi-dimension discrete valued space. So the proposed method is more effective for feature selection and more qualified for applications with high dimensions.

References

1. Pedrycz, W., Park, B.J., Pizzi, N.J.: Identifying core sets of discriminatory features using particle swarm optimization. Expert. Syst. Appl. 36, 4610–4616 (2009)
2. Yusta, S.C.: Different metaheuristic strategies to solve the feature selection problem. Pattern Recognition Letter 30, 525–534 (2009)
3. Siedlecki, W., Sklansky, J.: On automatic feature selection. International Journal of Pattern Recognition and Artificial Intelligence 2, 197–220 (1988)
4. Cover, T.M., Van Campenhout, J.M.: On the possible orderings in the measurement selection problem. IEEE Trans. Syst. Man. Cy. 9, 657–661 (1997)
5. Narendra, P.M., Fukunaga, K.: A branch and bound algorithm for feature subset selection. IEEE T. Comput. 26, 917–922 (1977)
6. Zhang, H., Sun, G.: Feature selection using tabu search method. Pattern Recognition 35, 701–711 (2002)
7. Chen, L., Hsiao, H.: Feature selection to diagnose a business crisis by using a real GA-based support vector machine: An empirical study. Expert Systems with Application 35, 1145–1155 (2008)
8. Lin, S., Ying, K., Chen, S., Lee, Z.: Particle swarm optimization for parameter determination and feature selection of support vector machines. Expert Systems with Applications 35, 1817–1824 (2008)
9. Munich Personal RePEc Archive, `http://mpra.ub.uni-muenchen.de/1005/`
10. Peng, B., Liu, B., Zhang, F.Y., Wang, L.: Differential evolution algorithm-based parameter estimation for chaotic systems. Chaos, Solution and Fractals 39, 2110–2118 (2009)
11. Chuang, L., et al.: Improved binary PSO for feature selection using gene expression data. Computational Biology and Chemistry 32, 29–38 (2008)

Research on Modeling and Experiment of Vehicle License Plate Recognition System

Changbao Wen, Yongfeng Ju, Dong Yan, Yan Shao, and Chen Zhao

Institute of Micro-nanoelectronics, School of Electronics and Control Engineering, Chang'an University, Xi'an 710064, China
Changbao Wen, wchbdn@163.com

Abstract. A novel model of vehicle license plate (VLP) recognition system was proposed in this paper. The model of VLP recognition system consists of preprocessing, location, character segmentation and the VLP character recognition. The image graying and binary technology were applied to VLP preprocessing. The Sobel edge detection operator was incorporated into the VLP location. The vertical projection method was used to character segmentation of VLP. The VLP character recognition adopted the BP (Back Propagation) neural network technology. Experiments results conform that the VLP recognition system can achieve a good recognition result, and the correct rate of VLP recognition is about 94%. Furthermore, in order to overcome some unsatisfactory conditions for the VLP, a train module of BP neural network was integrated in the VLP recognition system.

Keywords: Vehicle license plate (VLP); Recognition; Modeling.

1 Introduction

With the economic development, the production and holding rates of vehicles are rapidly increasing in worldwide. It will generate a great deal of pressure and challenge to the transport and vehicle management, and bring an urgent need to intelligent traffic system for various countries and governments [1, 2].

Vehicle license plate is an important identity of vehicle, and also the specific identity to distinguish vehicle in international ranges. Thus, the recognition of vehicle license plate not only can reduce the error probability caused by labor booked, but also realize the automatically troubleshoot and track down of vehicle [3]. Therefore, as the one of the core technology in intelligent transportation system (ITS), the vehicle license plate (VLP) recognition technology have received considerable attention and application in transportation sectors and public safety management department, such as the traffic enforcement, charges, traffic surveys, tracking and surveillance of vehicle.

However, the current many researches are more focused on specify technology, such as the VLP location, the character recognition, character segmentation, but few have a complete system of VLP recognition system. In this paper, a VLP recognition system has been realized by modular modeling, and an experimental result was presented.

D. Zeng (Ed.): Future Intelligent Information Systems, LNEE 86, pp. 135–141.
springerlink.com © Springer-Verlag Berlin Heidelberg 2011

2 Modeling of VLP Recognition System

The model of VLP recognition system consists of preprocessing, location, character segmentation and the VLP character recognition technology.

2.1 Preprocessing

The main purpose of VLP preprocessing is to strengthen some information needed by VLP recognition, and is to weaken other unwanted detail information. In this preprocessing model, there have three technology and algorithm including image graying and image enhancement, binary VLP.

The weighted average method is used to make 24-bit true color bitmap convert to 256 gray scale images. The transformation relationship between three components (R, G, B) of VLP image and gray level (G) as follows.

$$G = 0.3R + 0.59G + 0.11B \tag{1}$$

Image enhancement can make the overall image more clearly, and can improve correct rate of VLP recognition system.

Binary VLP is also called bi-level. It means that each pixel of VLP is stored as a single bit 0 or 1. The binary formula can be defined as

$$B(x, y) = \begin{cases} 0, g(x, y) \le \theta \\ 1, g(x, y) > \theta \end{cases} \tag{2}$$

2.2 Location

The VLP location means to find the location of VLP from the pretreatment image, and to select the area of VLP. The VLP location is the basis of VLP recognition and plays an important role in the overall processing.

Although there are some usual methods in VLP location, such as morphology method, color image edge extraction and principal component analysis, all these methods are proved not quite satisfactory in various conditions, or are influenced by some factors.

In this model of VLP location system, the Sobel edge detection operator is incorporated into the model of VLP recognition system. The Sobel operator is a discrete differentiation operator, computing an approximation of the gradient of the image intensity function [4]. At each point in the VLP image, the result of Sobel operator is either the corresponding gradient vector or the norm of this vector. The Sobel operator is based on convolving the VLP image with a small, separable, and integer valued filter in horizontal and vertical direction and is therefore relatively inexpensive in terms of computations. In actual engineering, the Sobel operator is defined as

$$S(x, y) = \sqrt{(S_x^2 + S_y^2)} \tag{3}$$

where S_x and S_y are two images which at each point contain the horizontal and vertical derivative approximations. If A is the source image, their computations are as follows.

$$S_x = \begin{bmatrix} -1 & -2 & 1 \\ 0 & 0 & 0 \\ 1 & 2 & 1 \end{bmatrix} * A \tag{4}$$

and

$$S_y = \begin{bmatrix} -1 & 0 & 1 \\ -2 & 0 & 2 \\ -1 & 0 & 1 \end{bmatrix} * A \tag{5}$$

The edge of the image is the beginning of a region is another area of the end, and is the most basic features of the image. Thus the image edge detection plays an important role in the VLP recognition system.

2.3 Character Segmentation

In china, the current plates are of the 1992 standard, which consist of the one character provincial abbreviation, a letter of the alphabet and five number or letters of the alphabet.

After VLP location, the sub-area image including VLP is extracted. It is quite difficult to recognize a character in an image contained more than one character, while the single character recognition is relatively simple. Therefore, the image of VLP should be segmented before character recognition, and form seven single characters.

The vertical projection method is used to character segmentation in the model of VLP recognition system. It can serve for detection of white space between successive letters, and can indicate locations of vertical strokes of character [5]. A peak-to-valley function was designed to improve on this method. A minimum of the projection is located and the projection value noted. The sum of the differences between this minimum value and the peaks on each side is calculated. The ratio of the sum to the minimum value itself is the discriminator used to select segmentation boundaries. This ratio exhibits a preference for low valley with high peaks on both sides.

2.4 VLP Character Recognition

The character recognition is one of important components and can affect directly the ability of VLP recognition system. Currently, several approaches have been applied to

the specific task, such as neural networks, principal component analysis and template matching. In this works, the BP (Back Propagation) neural network is adopted. It is a supervised learning method, and is an implementation of the Delta rule [6]. The BP learning algorithm can be divided into two phases: error propagation and weight update.

The first step is to propagate the input forward through the network:

$$a^0 = p \tag{6}$$

$$a = f^{m+1}(W^{m+1}a^m + b^{m+1}) \quad m = 0,1,...,M-1 \tag{7}$$

where p is a input vector; W is a weight matrix; b is a bias of neuron, and M is the number of layers in the network.

The next step is to propagate the sensitivities backward through the network

$$s^M = -2F^M(n^M)(t-a) \tag{8}$$

where t is the corresponding target output.

$$s^m = F^m(n^m)(W^{m+1})^T s^{m+1} \quad m = M-1,...,2,1 \tag{9}$$

Finally, the weights and biases are updated using the approximate steepest descent rule as follows.

$$W^m(k+1) = W^m(k) - \alpha s^m (a^{m-1})^T \tag{10}$$

$$b^m(k+1) = b^m(k) - \alpha s^m \tag{11}$$

where α is the learning rate.

3 Experiments

The VLP recognition system consists of the VLP preprocessing function module, VLP location function module, the VLP character segmentation function module and the VLP character recognition function module. The VLP recognition system uses lighting and a camera to take the image of the front or rear of the vehicle which is then analyzed by the VLP recognition system without installing any additional tracking apparatus. The system can extract the image and the plate information, and this data is then used for enforcement or record collection and maintenance.

In order to verify the VLP recognition system, we here realize the preprocessing, location, character segmentation and the character recognition by an actual VLP recognition process. The VLP recognition system is running on Inter Xeon CPU Quad-Core E5540. The recognition result of VLP can be achieved about 10 ms.

The interface of VLP recognition system is shown in Fig. 1.

Fig. 1. Interface of VLP recognition system

Fig. 2 shows the preprocessing result of VLP. Fig. 2 (a) is the graying and enhancing VLP, Fig. 2 (b) is the binary VLP.

(a) (b)

Fig. 2. Graying and enhancing VLP and binary VLP

The result of VLP location is shown in Fig. 3 using the VLP recognition system.

Fig. 3. Result of VLP location

Fig. 4 shows the result of character segmentation for the VLP.

Fig. 4. Result of VLP character segmentation

The final recognition result of VLP is shown in Fig. 5.

Fig. 5. Result of VLP recognition

In actual conditions, the images of VLP are rarely perfect, if the VLP is unclear or skewed, or they are over segmented or under segmented, the VLP will not be correctly recognized. In this case, we can expand the sample training database, and can train the BP neural network by the VLP recognition system.

Using a similar approach, a sample set containing 100 VLP is processed by the VLP recognition system. The correct rate of VLP recognition is about 94%. In addition, the VLP recognition system can save and output the recognition result for future references.

4 Inclusions

In this paper, we have presented a VLP recognition system. The VLP recognition system consists of four key technology modules including the VLP preprocessing

module, VLP location module, the VLP character segmentation module and the VLP character recognition module. Experiments results demonstrate that the VLP recognition system can achieve a good recognized result. The VLP recognition system will be an attractive subject of intelligent transport system.

Acknowledgments. This project is supported by the National Natural Science Foundation of China (Grants Nos.60806043 and 60876038), the China Postdoctoral Science Foundation Funded Project, the Special Fund for Basic Scientific Research of Central Colleges, Chang'an University (Grants No. CHD2009JC025 and CHD2010JC077), the Key Laboratory Foundation of Shaanxi Engineering and Technique Research Center for Road and Traffic Detection.

References

[1] Chang, S.L., Chen, L.S.: Automatic License Plate Recognition. IEEE Trans. on Intelligent Transportation Systems 5, 42–53 (2004)

[2] Liu, Y.: Design of License Plate Recognition System Based on the Adaptive Algorithm. In: Proceedings of the IEEE International Conference on Automation and Logistics, pp. 2818–2821. IEEE Press, Piscataway (2008)

[3] Deb, K.S., Jo, K.H.: A Vehicle License Plate Detection Method for Intelligent Transportation System Applications. Cybernetics and Systems 40, 689–705 (2009)

[4] Zheng, D., Zhao, Y., Wang, J.: An Efficient Method of License Plate Location. Pattern Recognition Letters 26, 2431–2438 (2005)

[5] Pan, M., Yan, J., Xiao, Z.: Vehicle License Plate Character Segmentation. International Journal of Automation and Computing 5, 425–432 (2008)

[6] Li, Y., Li, M., Lu, Y., Yang, M., Zhou, C.: A New Text Detection Approach Based on BP Neural Network for Vehicle License Plate Detection in Complex Background. In: Liu, D., Fei, S., Hou, Z., Zhang, H., Sun, C. (eds.) ISNN 2007. LNCS, vol. 4492, pp. 842–850. Springer, Heidelberg (2007)

Study on Architecture and Performances of Dual Track SAW Device

Changbao Wen, Yongfeng Ju, Dong Yan, Yi Kang, Li Liu, and WanLin Li

Institute of Micro-nanoelectronics, School of Electronics and Control Engineering, Chang'an University, Xi'an 710064, China
Changbao Wen, wchbdn@163.com

Abstract. To improve the performances of surface acoustic wave (SAW) device, the architecture of dual track SAW device was proposed in this paper. The dual track architecture and the multistripe couplers (MSCs) were skillfully applied to the dual track SAW device. The bulk acoustic wave (BAW) excited by input IDT was separated and eliminated by the full transfer MSC. The bidirectional SAW launched by input interdigital transducer (IDT) can be totally received by two output IDTs connected in parallel. The triple transit echo signals were suppressed by dual track in input IDT. Furthermore, the dummy electrodes were used as eliminate the phase front distortion of waves propagating through apodized IDTs, and split electrodes were used as minimize acoustic reflections within transducers. By means of a dual track SAW device with center frequency at 203.559 MHz, the results of test and analysis are presented. Experiments results confirm that the dual track SAW device has good response characteristics in frequency domain and time domain, and the passband ripples and the side lobes are acceptable and better than ones of traditional SAW device.

Keywords: Surface acoustic wave (SAW) device; Dual track; Bulk acoustic wave (BAW); triple transit echo signals.

1 Introduction

Surface acoustic wave devices have been widely applied to various electronic systems, particularly radar, ECM, domestic TV, spread spectrum and mobile communications. These applications benefit from the excellent properties of surface acoustic wave (SAW) devices: passive, small size, real-time, high reproducibility and high reliability [1-3]. Moreover, as the SAW device frequency increases, its physical size scales down, resulting in smaller device permitting a greater variety of applications.

Usually, there are some main issues in the design of SAW devices. Firstly, owing to inverse piezoelectric effects of piezoelectric crystals, the input IDT in SAW device excites not only SAW propagating along crystals surface, but also bulk acoustic wave (BAW) that has higher frequency than that of SAW signals. The BAW affects the performance of SAW device, such as producing some ripples and spurious components in response curve [4, 5]. Secondly, the interdigital transducer (IDT) generates SAW propagating equally in two opposite directions, and the unidirection

D. Zeng (Ed.): Future Intelligent Information Systems, LNEE 86, pp. 143–149.
springerlink.com © Springer-Verlag Berlin Heidelberg 2011

receiving will result in 6 dB insertion losses. Therefore, reducing the insertion loss is very important to the SAW device [4]. Thirdly, when output IDT converts the SAW signal into the electrical signal by means of piezoelectric effects; partial acoustic signal can be reflected to input IDT. The triple transit echo signals arising from the reflection of the signal at the output IDT followed by a second reflection at the input IDT. The triple transit echo signals also can affect the performance of SAW device, and can produce excessively some ripples and side lobes in response curve due to the presence of spurious signals [1, 4]. Furthermore, the effects of electrode reflections and impedance discontinuities should be solved in the design process of SAW device.

To solve the above problem, we here propose model of dual track SAW device. By means of an actual dual track SAW device, the comparison between the simulation of model and the actual test results is presented.

2 Architecture and Performances Analysis of Dual Track SAW Device

The schematic architecture of dual track SAW device is shown in Fig. 1. Where I is input IDT that can be an uniform IDT or a apodization IDT; M_1 and M_2 are two full transfer multistripe couplers (MSCs) with identical design parameters; O_1 and O_2 are two output IDTs that can be uniform IDTs or apodization IDTs with identical design parameters.

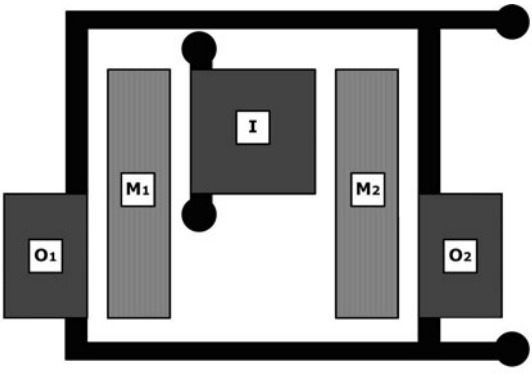

Fig. 1. Schematic architecture of dual track SAW device

When input signal is fed into input IDT I in SAW device, the input IDT can excite SAW propagating along crystals surface, and the SAWs equals in two opposite directions. Two full transfer MSCs M_1 and M_2 are symmetrically deposited on the two acoustic propagation tracks of input IDT respectively. The SAW can be transferred into down acoustic track. The output IDTs O_1 and O_2 with the same design parameters are symmetrically deposited on the two output acoustic tracks of MSCs M_1 and M_2, respectively. The SAW separated by full transfer MSC M_1 and M_2 can be received by the output IDT O_1 and O_2. Hence, two acoustic tracks $I \rightarrow M_1 \rightarrow O_1$ and $I \rightarrow M_2 \rightarrow O_2$ are symmetrically formed on both sides of input IDT I.

Because the dual track and the MSC are incorporated into the architecture model, the performances of dual track SAW device are much better than traditional SAW device.

2.1 Separation and Elimination of BAW

The two acoustic tracks $I \rightarrow M_1 \rightarrow O_1$ and $I \rightarrow M_2 \rightarrow O_2$ are symmetrically in the dual track SAW device, thus we can only analyze one track. Owing to the inverse piezoelectric effects of the substrate, the input IDT I excites not only SAW propagating along crystals surface, but also BAW. The BAW has higher frequency than SAW, and can produce some ripples and spurious components in response curve [4-6]. In Fig. 2, the SAW and BAW excited by input IDT I will be bidirectional transmission, and the MSC M_1 and M_2 can fully transfer SAW without affecting BAW to continue to propagate in the primitive acoustic track. In this case, the SAW and the BAW launched by input IDT can be separated into different tracks. Therefore, one can spread some sound absorption materials at the transmitting terminal of BAW, and ultimately eliminate the BAW that interferes in the performance of SAW device.

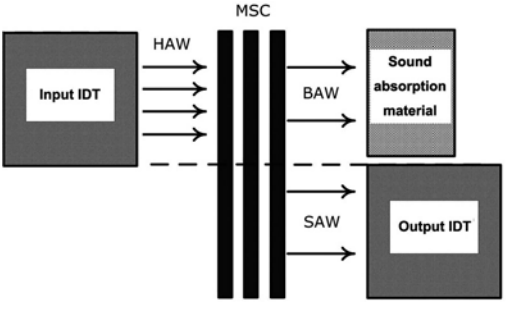

Fig. 2. Separation and elimination of BAW

2.2 Degrading Insertion Loss

Since the output electrodes of O_1 and O_2 are in parallel connection in Fig. 1, the bidirectional SAW launched by input IDT I would be totally received. The insertion loss will reduce 3dB to a single output IDT without considering the location effect and the phase difference between two output tracks.

The architecture of dual track was used in this scheme, thus, the receiving energy will be twice as much as that of single output IDT.

2.3 Suppression Triple Transit Echo Signal

When signal has been applied to input IDT I, the full transfer MSC M_1 and M_2 will transfer the SAW into output IDTs O_1 and O_2, respectively. The acoustic wave signal L_1 and L_2 will simultaneously be reflected by two output IDTs O_1 and O_2, as shown in Fig.3, and can be coupled to the input IDT via MSC again. Because the bidirectional acoustic signal were launched by input IDT at the same time, and the MSC and output IDT have identical structure and parameters, the two reflection acoustic waves equal

in energy and opposite in direction, i.e., R_1=R_2. Hence, the triple transit echo signal generated by output IDTs O_1 and O_2 must be offset in input IDT I, and the input IDT I is now a perfect absorber of the acoustic signals reflected from the output IDTs O_1 and O_2.

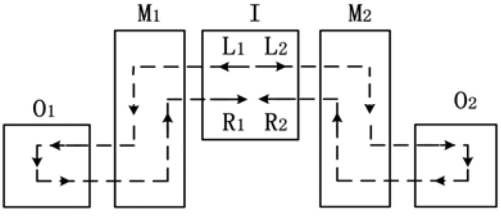

Fig. 3. Suppression triple transit echo signal

2.4 Eliminating Electrode Reflections and Impedance Discontinuities

In the IDT geometry of single electrode, the excitations from consecutive gaps are spaced by one-half an array period, and that they have opposite electrical polarity. At the synchronous frequency, the propagation phase shift between consecutive gaps is π radians and there is an equal shift in phase of the electrical drive. Unfortunately, the electrode reflections from adjacent electrodes also add in phase at the synchronous frequency. Hence, the IDT geometry of single electrode maximizes the deleterious effects of electrode reflections.

Fig. 4. Split electrodes and dummy IDT

Fig. 4 shows that the split electrodes can substantially reduces the problem of electrode reflections by essentially doubling the periodicity of the metal electrodes without altering the periodicity of the excitation gaps. The split electrodes geometry is strongly recommended for all SAW IDT [4].

The impedance discontinuities problem referred to above is caused by the decrease in surface wave velocity resulting from the presence of metal electrodes. When the IDT electrodes are apodized, SAW propagation along the middle of apodization IDT crosses more electrodes, and is slowed more substantially than a wave propagating closer to the contact pads. Curvature of the wave front is equivalent to defocusing of the beam, and it produces severe distortion in the transducer response.

A simple remedy for this problem is to include dummy electrodes in IDT. This change does not affect the electrical properties of the transducer, but it does make the physical conditions within the IDT. With dummy electrodes, the surface wave velocity remains uniform over the width of the transducer aperture and defocusing is prevented. For this reason dummy electrodes should always be employed in the geometry of apodized IDT [4].

3 Experimental Results and Discussion

In order to confirm the architecture of dual track SAW device, we here present a dual track SAW device with centre frequency at 203.559MHz.

There are a number of piezoelectric materials available to SAW device. The choice depends on the operation frequency and the type of the device to be prepared. In this works, in order to decrease the insertion loss and the size of device, we designed and fabricated the dual track SAW device on 128°Y-X $LiNbO_3$ crystal's substrate. The velocity of the SAW propagating on the 128° Y-X $LiNbO_3$ substrate is 3870 m/s, and the electromechanical coupling constant K^2 is 5.5%.

In our previous works [7, 8], we found that the smaller side lobe can be obtained if the IDT of SAW device is apodized by the envelope of Morlet wavelet function. In this dual track SAW device, the input IDT and two output IDT apodized by the envelope of Morlet wavelet function without using uniform IDT. Aluminum IDTs, with uniform spacing and metallization ration of 50%, are directly deposited by the conventional contact ultraviolet photolithography on the top of the 128° Y-X $LiNbO_3$ substrate.

Fig. 5 shows the internal architecture of dual track SAW device. Furthermore, we have coated some sound absorption material at the substrate edges in order to suppress unwanted acoustic wave.

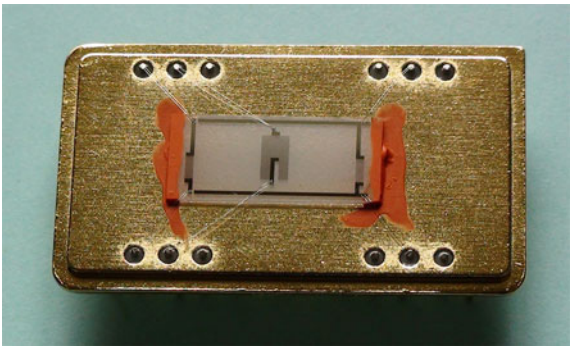

Fig. 5. Internal architecture of dual track SAW device

Fig. 6 shows the frequency response characteristics of dual track SAW device measured by the network analyzer (Agilent E5062A ENA-L). The BAW generated by the input IDT can be separated and eliminated by the MSC, and the triple transit echo

signal also can be suppressed by the architecture of dual track. Hence, the passband ripples in frequency response curve are acceptable for signal processing, and the side lobes are smaller than ones of traditional SAW device [4].

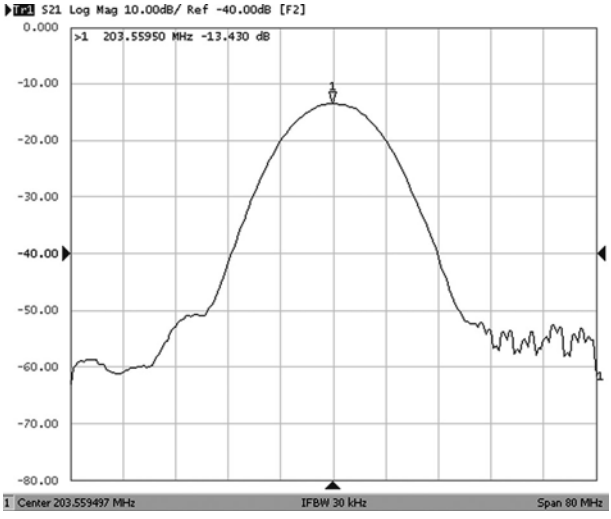

Fig. 6. Frequency response characteristics of device

Fig. 7 shows the impulse response characteristics of dual track SAW device measured by the network analyzer (Agilent E5062A ENA-L). Because the design scheme of split electrodes and the dummy IDT is employed to the dual track SAW device, the problems of electrode reflections and impedance discontinuities are eliminated. Hence, we can find that the impulse response curve of dual track SAW device is uniform without spurious components and wave front distortion.

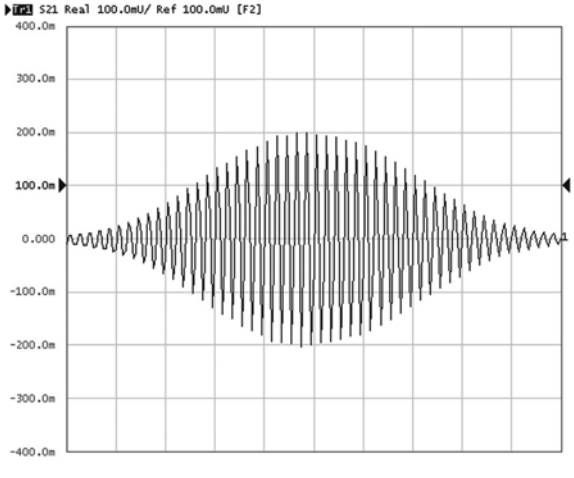

Fig. 7. Impulse response characteristics of device

4 Conclusions

In this paper, we have presented a novel architecture of dual track SAW device. The design scheme can separate and eliminate BAW by the MSCs, and suppress the triple transit echo signals, and improve the side lobe rejection. The electrode reflections and impedance discontinuities are overcome by the split electrodes and the dummy IDT. Experiments results demonstrate that the dual track SAW device has good response characteristics. Furthermore, the design scheme can be applied to other SAW device and physical device.

Acknowledgements

This project is supported by the National Natural Science Foundation of China (Grants Nos.60806043 and 60876038), the China Postdoctoral Science Foundation Funded Project, the Special Fund for Basic Scientific Research of Central Colleges, Chang'an University (Grants No. CHD2009JC025 and CHD2010JC127), the Key Laboratory Foundation of Shaanxi Engineering and Technique Research Center for Road and Traffic Detection.

References

[1] Morgan, D.P.: Netherlands: Surface-Wave Devices For Signal Processing. Elsevier Science Publisher, Amsterdam (1985)
[2] Weigel, R., Morgan, D.P., Owens, J.M., Ballato, A., Lakin, K.M., Hashimoto, K.Y., Ruppel, C.C.W.: Microwave Acoustic Materials, Devices, And Applications. IEEE Transactions on Microwave Theory and Techniques 50, 738–749 (2002)
[3] Caliendo, C., Verardi, P., Verona, E., D'Amico, A., Di Natale, C., Saggio, G., Sarafini, M., Paolesse, R., Huq, S.E.: Advances In SAW-Based Gas Sensors. Smart Materials and Structures 6, 689–699 (1997)
[4] Oliner, A.A.: Acoustic Surface Waves. Springer, New York (1978)
[5] Marshall, F.G., Newton, C.O., Paige, E.G.S.: Theory And Design Of The Surface Acoustic Wave Multistrip Coupler. IEEE Transactions on Sonics and Ultrasonics 20, 124–133 (1973)
[6] Marshall, F.G., Paige, E.G.S.: Novel Acoustic Surface Wave Directional Coupler With Diverse Applications. Electronics Letter 7, 460–462 (1971)
[7] Wen, C.B., Zhu, C.C., Ju, Y.F., Xu, H.K., Qiu, Y.Z.: A Novel Dual Track SAW Gas Sensor Using Three-IDT And Two-MSC. IEEE Sensors Journal 9, 2010–2015 (2009)
[8] Wen, C.B., Zhu, C.C.: Time Synchronous Dyadic Wavelet Processor Array Using Surface Acoustic Wave Devices. Smart Materials and Structures 15, 939–945 (2006)

Adaptive Function Projective Synchronization of the New Chaotic Systems with Uncertain Parameters

Shaowei Shen[1] and Junbiao Guan[2]

[1] NO.18, Xuezheng Str., Zhejiang Gongshang University, Xiasha University Town, Hangzhou, 310018, China
shao-wei-shen@163.com
[2] Hangzhou Dianzi University, Xiasha University Town, Hangzhou, 310018, China
jbguan@hdu.edu.cn

Abstract. This Letter investigates the function projective synchronization of the new chaotic systems with uncertain parameters. Based on Lyapunov stability theory, the nonlinear adaptive control law and the parameter update law are derived to make the state of two chaotic systems function projective synchronized. Numerical simulations are presented to demonstrate the effectiveness of the proposed adaptive scheme.

Keywords: function projective synchronization; Lyapunov stability theory; chaos; adaptive control.

Synchronization of chaotic systems has attracted considerable attention from scientists and engineers and has been investigated intensively both theoretically and experimentally over the last decade. A variety of methods have been introduced for the synchronization of chaotic systems which include complete synchronization, generalized synchronization, phase synchronization, lag synchronization, adaptive synchronization, time scale synchronization, intermittent lag synchronization, projective synchronization and function projective synchronization, see [1-10] and references therein. Amongst all these synchronization schemes, it is worthwhile to mention that function projective synchronization has attracted much attention recently due to its potential application in secure communications. Function projective synchronization is the more general definition of projective synchronization. As compared with projective synchronization, function projective synchronization means that the master and slave systems could be synchronized up to a scaling function, but not a constant. This feature could be used to get more secure communication in application to secure communications, because it is obvious that the unpredictability of the scaling function in function projective synchronization can additionally enhance the security of communication. To the best of our knowledge, at present, there are few theoretical results about function projective synchronization [4,6,9]. Motivated by the aforementioned reasons, this Letter investigates function projective synchronization of recently developed chaotic systems with uncertain parameters using nonlinear adaptive controller.

D. Zeng (Ed.): Future Intelligent Information Systems, LNEE 86, pp. 151–155.
springerlink.com © Springer-Verlag Berlin Heidelberg 2011

The chaotic system introduced by Liu [11] recently is described by

$$\begin{cases} x_1' = a(x_2 - x_1 + x_2 x_3) \\ x_2' = b x_2 - c x_1 x_3 \\ x_3' = g x_2 - h x_3 \end{cases} \tag{1}$$

Where a, b, c, g, h are the system parameters, when $a = 1, b = 2.5, c = 1, g = 1, h = 4$, the system is chaotic.

We take the system (1) as the master system, and the slave system with an adaptive control scheme is given by

$$\begin{cases} y_1' = a_1(y_2 - y_1 + y_2 y_3) + u_1 \\ y_2' = b_1 y_2 - c_1 y_1 y_3 + u_2 \\ y_3' = g_1 y_2 - h_1 y_3 + u_3 \end{cases} \tag{2}$$

where a_1, b_1, c_1, g_1, h_1 are parameters of the slave system which needs to be estimated, and u_1, u_2, u_3 are the nonlinear controllers such that the two chaotic systems are function projective synchronized in the sense that

$$\lim_{x \to \infty} \| y_i - \alpha(t) x_i \| = 0, i = 1, 2, 3. \tag{3}$$

Where $\alpha(t)$ is the scaling function.

From system (1) and system (2), we get the error dynamical system which can be written as

$$\begin{cases} e_1' = a_1(y_2 - y_1 + y_2 y_3) + u_1 - a\alpha(t)(x_2 - x_1 + x_2 x_3) - \alpha'(t) x_1 \\ e_2' = b_1 y_2 - c_1 y_1 y_3 + u_2 - b\alpha(t) x_2 + c\alpha(t) x_1 x_3 - \alpha'(t) x_2 \\ e_3' = g_1 y_2 - h_1 y_3 + u_3 - g\alpha(t) x_2 + h\alpha(t) x_3 - \alpha'(t) x_3 \end{cases} \tag{4}$$

Where $e_i(t) = y_i(t) - \alpha(t) x_i(t), i = 1, 2, 3.$

In order to stabilize the error variables of system (3) at the origin, we propose the adaptive control law and the parameter update law for system (3) as follows:

$$\begin{cases} u_1' = -a_1(y_2 - y_1 + y_2 y_3) + \alpha'(t) x_1 + a\alpha(t)(x_2 - x_1 + x_2 x_3) - k_1 e_1 \\ u_2' = -b_1(y_2 - \alpha(t) x_2) + c_1(y_1 y_3 - x_1 x_3 \alpha(t)) + \alpha'(t) x_2 - k_2 e_2 \\ u_3' = -g_1(y_2 - \alpha(t) x_2) + h_1(y_3 - x_3 \alpha(t)) + \alpha'(t) x_3 - k_3 e_3 \end{cases} \tag{5}$$

and the update rule for the five uncertain parameters a_1, b_1, c_1, g_1 and h_1 are

$$\begin{cases} a_1' = (x_1 - x_2 - x_2x_3)\alpha(t)e_1 - k_4e_a \\ b_1' = -x_2\alpha(t)e_2 - k_5e_b \\ c_1' = -x_1x_3\alpha(t)e_2 - k_6e_c \\ g_1' = -x_2\alpha(t)e_3 - k_7e_g \\ h_1' = x_3\alpha(t)e_3 - k_8e_h \end{cases} \tag{6}$$

where $k_i > 0 (i = 1, 2, ..., 8)$ and $e_a = a_1 - a, e_b = b_1 - b, e_c = c_1 - c, e_g = g_1 - g$, $e_h = h_1 - h$.

Theorem 1. For the given scaling function $\alpha(t)$, the function projective synchronization between the master system (1) and the slave system (2) can be achieved if the nonlinear controller (5) and the update law (6) are adopted.

Proof. Construct the following Lyapunov function

$$V = \frac{1}{2}\sum_{i=1}^{3} e_i^T e_i + \frac{1}{2}(e_a^2 + e_b^2 + e_c^2 + e_g^2 + e_h^2) \tag{7}$$

Calculating the time derivative of V along the trajectory of error system (4), we have

$$\begin{aligned} V' = {} & e_1(t)[a_1(y_2 - y_1 + y_2y_3) + u_1 - a\alpha(t)(x_2 - x_1 + x_2x_3) - \alpha'(t)x_1] \\ & + e_2(t)[b_1y_2 - c_1y_1y_3 + u_2 - b\alpha(t)x_2 + c\alpha(t)x_1x_3 - \alpha'(t)x_2] \\ & + e_3(t)[g_1y_2 - h_1y_3 + u_3 - g\alpha(t)x_2 + h\alpha(t)x_3 - \alpha'(t)x_3] \\ & + e_a(t)[(x_1 - x_2 - x_2x_3)\alpha(t)e_1 - k_4e_a] + e_b(t)[-x_2\alpha(t)e_2 - k_5e_b] \\ & + e_c(t)[-x_1x_3\alpha(t)e_2 - k_6e_c] + e_g(t)[-x_2\alpha(t)e_3 - k_7e_g] \\ & + e_h(t)[x_3\alpha(t)e_3 - k_8e_h] \\ = {} & -e^T Ke \end{aligned} \tag{8}$$

where $e = [e_1, e_2, e_3, e_a, e_b, e_c, e_g, e_h]^T$ and $K = \text{diag}\{k_1, k_2, k_3, k_4, k_5, k_6, k_7, k_8\}$.

It is clear that V' is negative definite and $V' = 0$ if and only if $e(t) = 0$. According to the Lyapunov stability theorem, the function projective synchronization is achieved. This completes the proof.

In what follows we shall perform some numerical simulations to verify the effectiveness of the proposed adaptive synchronization controllers. The fourth-order Runge-Kutta method is used to solve the master system (1) and the slave system

(2) with time step size 0.001. The initial conditions of the master system are $x_1(0)=0.2, x_2(0)=-1.2, x_3(0)=0.6,$ and those of the slave system are $y_1(0)=0.4, y_2(0)=0.2, y_3(0)=-1.8.$ Moreover, the true values of the uncertain parameters are $a=1, b=2.5, c=1, g=1, h=4,$ and the initial values of the estimated parameters are chosen as $a_1(0)=2, b_1(0)=3, c_1(0)=3, g_1(0)=5,\ h_1(0)=5,$ the scaling function is chosen as $\alpha(t)=0.3+0.2\sin(t).$ Furthermore, the control gains are chosen as $(k_1,k_2,k_3,k_4,k_5,k_6,k_7,k_8)$ =(0.2, 0.2, 0.2, 0.2, 0.2, 0.2, 0.2, 0.2). The error variables e_1, e_2, e_3 which tend to zero with $t\to\infty$ is illustrated in Fig.1 and Fig.2 shows that the estimated values of the uncertain parameters converge to $a=1, b=2.5, c=1, g=1, h=4$ as $t\to\infty.$

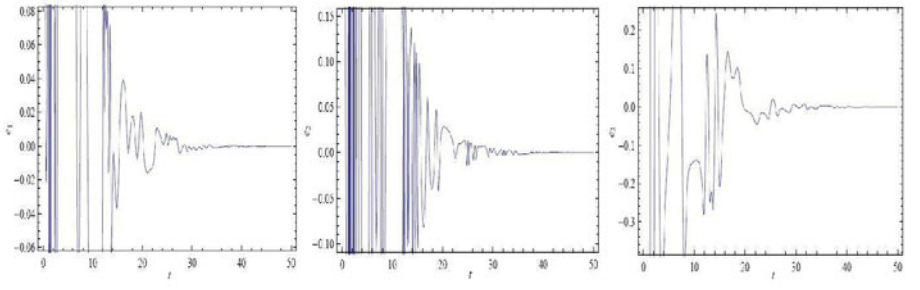

Fig. 1. Error dynamics between the master system (1) and the slave system (2)

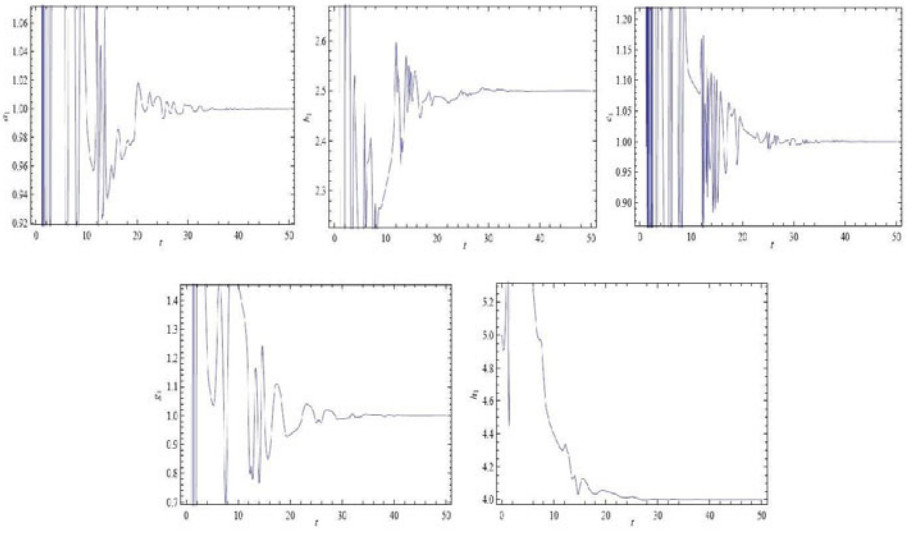

Fig. 2. The time evolution of the estimated parameters

In summary, this work has investigated the function projective synchronization of the new chaotic systems with uncertain parameters. Based on the Lyapunov stability theory, we have designed the adaptive synchronization controllers with corresponding parameter update laws to stabilize the error dynamics between the master and the slave systems. All the theoretical results are verified by numerical simulations to illustrate the effectiveness of the proposed adaptive function Projective synchronization scheme.

References

1. Pecora, L., Carroll, T.: Synchronization in chaotic systems. Phys. Rev. Lett. 64, 821–824 (1990)
2. Rosenblum, M., Pikovsky, A., Kurths, J.: Phase Synchronization of Chaotic Oscillators. Phys. Rev. Lett. 76, 1804–1807 (1996)
3. Hramov, A., Koronovskii, A.A.: An approach to chaotic synchronization. Chaos 14, 603–610 (2004)
4. Sudheer, K., Sabir, M.: Adaptive modified function projective synchronization between hyperchaotic Lorenz system and hyperchaotic Lu system with uncertain parameters. Phys. Lett. A. 373, 3743–3748 (2009)
5. Mainieri, R., Rehacek, J.: Projective synchronization in three-dimensional chaotic systems. Phys. Rev. Lett. 82, 3042–3045 (1999)
6. Ahn, C.: Newblock approach to anti-synchronization for chaotic systems. Phys. Lett. A. 373, 1729–1733 (2009)
7. Ge, Z., Yang, C.: Pragmatical generalized synchronization of chaotic systems with uncertain parameters by adaptive control. Physica D 231, 87–94 (2007)
8. Guan, J.: Synchronization Control of Two Different Chaotic Systems with Known and Unknown Parameters. Chin. Phys. Lett. 27, 020502 (2010)
9. Wu, Z., Fu, X.: Adaptive Function Projective Synchronization of Discrete Chaotic Systems with Unknown Parameters. Chin. Phys. Lett. 27, 050502 (2010)
10. Runzi, L.: Adaptive function project synchronization of Rssler hyperchaotic system with uncertain parameters. Phys. Lett. A. 372, 3667–3671 (2008)
11. Liu, C.: A novel chaotic attractor. Chaos Solions Fractals 39, 1037–1045 (2009)

Study on the Amplitude Characteristics of Pitch and Heave Motions for a Ship Based on Frequency Scattering

Chen Junfeng and Zhu Jun

College of Ship and Power Engineering, Naval University of Engineering,
Wuhan 430033, China
Chenjf3210@126.com, Zhjun101@sina.com

Abstract. Based on the coupled equations of ship oscillatory motions including pitch and heave, and where wave forces and moments were calculated by using Ordinary Strip Method(OSM), the amplitude of oscillatory motions of a ship in regular waves was numerically simulated in this paper. The simulation of oscillatory motions was also carried out in the case of changing the scattering intensity and frequency. By comparing oscillatory amplitudes with and without encounter frequency scattering, the following conclusions can be obtained: the encounter frequency scattering can change the oscillatory amplitudes of a ship in regular waves, and the changing values were relative to the scattering intensity and frequency. It can also be obtained from the numerically simulation that the oscillatory amplitudes can be reduced by adopting reasonable scattering mechanism.

Keywords: ship; maneuvering; regular waves; frequency scattering.

1 Introduction

Since 1948, when a pioneering study of ship steering in a following sea was carried out by K. S. M. Davidson [1], the problem of ship maneuvering in waves has been a subject of keen interest. Rydill [2] got the linear results of controllable and uncontrollable of ships in waves on the basis of Froude-Krylov force. With the linear theory, Eda [3] obtained the results of course stability by adding harmonic wave force into the linearized equations of maneuvering motion, and studied the coursekeeping stability using the PD rudder action in waves [4]. Studies on ship maneuverability in waves were based on the theory that adding high frequency wave force into low frequency equations of maneuvering motion, and it has been proved by Nonaka [5] by using two-time-scale expanding method in trend stream theory. Using the strip method, Zhu [6] calculated the maneuvering motions by adding incident wave forces into maneuvering equations, and simulated the coupled motion of rolling and maneuvering with the concise model.

Earlier studies were mostly concentrated on the wave influence on ship maneuvering motion, however they haven't took into account the maneuvering infection on the oscillatory motion in waves. Chen and Zhu [7] found the phenomena of irregular oscillatory motion when studied the ship maneuvering in regular waves, and considered

D. Zeng (Ed.): Future Intelligent Information Systems, LNEE 86, pp. 157–164.
springerlink.com © Springer-Verlag Berlin Heidelberg 2011

the mechanism of irregular response on the change of the frequency of encounter. Based on the concept of frequency scattering, the changing of the amplitude of pitch angle and heave displacement were numerically simulated and proved by model test, using the coupled equations of pitch and heave and Ordinary Strip Method. The conclusion that the oscillatory amplitude can be reduced by the mechanism of encounter frequency scattering was gained.

2 The Scattering Mechanism of Encounter Frequency in Regular Waves

2.1 The Concept of Frequency Scattering

The frequency of wave encounter is given by

$$\omega_e(t) = \omega_0(1 + \frac{\omega_0}{g} U \cos\beta), \tag{1}$$

where ω_0 represents the natural frequency of waves, while U and β are ship speed and wave angle, and we assume here that 0°is head wave, and 180°is following wave. In the seakeeping theory, $\omega_e(t)$ is constant since U and β don't change in time domain. However, U and β are variable in the real navigation, which induces that $\omega_e(t)$ is variable too. Now, we assume that $\omega_e(t)$ has the following harmonic form:

$$\omega_e(t) = \omega_{e0} + \delta_\omega \cos(\omega_\delta t), \tag{2}$$

where ω_{e0} represents the scattering constant, while $|\delta_\omega|$ and ω_δ are scattering intensity and frequency respectively.

2.2 The Mechanism of Frequency Scattering

According to the formula (1), ship speed U and wave angle β are main influencing factors of the encounter frequency. So the mechanism of frequency scattering has two types, speed and course scattering, accordingly.

Ship speed scattering

If ship speed has the following harmonic form in regular waves:

$$U = U_0 + \Delta U(t) = U_0 + \delta_U \cos(\omega_U t), \tag{3}$$

where δ_U is speed scattering intensity, and ω_U is speed scattering frequency. We assume that ship course doesn't change, namely wave angle β is constant β_0, and substitute formula (3) into formula (1), $\omega_e(t)$ can also be expressed in the following form

$$\begin{aligned}\omega_e(t) &= \omega_0[1+\frac{\omega_0}{g}(U_0+\Delta U)\cos\beta_0] \\ &= \omega_0(1+\frac{\omega_0}{g}U_0\cos\beta_0)+\frac{\omega_0^2}{g}\delta_U\cos\beta_0\cos(\omega_U t).\end{aligned} \tag{4}$$

Comparing formula (2) and (4), we can obtain

$$\omega_{e0}=\omega_0(1+\frac{\omega_0}{g}U_0\cos\beta_0)\,,\quad \delta_\omega=\frac{\omega_0^2}{g}\delta_U\cos\beta_0\,,\quad \omega_\delta=\omega_U\,. \tag{5}$$

Ship course scattering

If ship course has the following harmonic form in regular waves:

$$\beta=\beta_0+\Delta\beta(t)=\beta_0+\delta_\beta\cos(\omega_\beta t), \tag{6}$$

where δ_β is ship course scattering intensity, and ω_β is ship course scattering frequency. We assume that ship speed is constant, namely $U=U_0$, then substitute formula (6) into formula (1), $\omega_e(t)$ can also be expressed in the following form

$$\omega_e(t)=\omega_0\{1+\frac{\omega_0}{g}U_0\cos[\beta_0+\delta_\beta\cos(\omega_\beta t)]\}. \tag{7}$$

Keeping the linear part of cosine term in formula (7), which is

$$\cos[\beta_0+\delta_\beta\cos(\omega_\beta t)]\approx\cos\beta_0-\delta_\beta\sin\beta_0\cos(\omega_\beta t), \tag{8}$$

we can obtain

$$\omega_e(t)=\omega_0(1+\frac{\omega_0}{g}U_0\cos\beta_0)-\frac{\omega_0^2}{g}U_0\delta_\beta\sin\beta_0\cos(\omega_\beta t). \tag{9}$$

Comparing formula (5) and (10), the following relation can be obtained

$$\omega_{e0} = \omega_0(1 + \frac{\omega_0}{g} U_0 \cos\beta_0), \quad \delta_\omega = -\frac{\omega_0^2}{g} U_0 \delta_\beta \sin\beta_0, \quad \omega_\delta = \omega_\beta. \tag{10}$$

Formula (5) and (9) are the scattering relation of encounter frequency because of the changing of ship speed and course. Comparing with formula (2), we can gain the following rules:

① The scattering constant is equal to the encounter frequency of a ship which keeps steady speed and course.

② For the speed scattering, the scattering intensity depends on the amplitude of ship speed and wave angle, and it doesn't induce scattering in beam sea. For the course scattering, the scattering intensity has direct proportion with $\sin\beta_0$, and the scattering intensity has the largest value in beam sea, while it doesn't exist in head and following sea.

③ The scattering frequency is equal to the frequency of ship speed and wave angle respectively.

3 Numerical Simulation of Pitch and Heave

3.1 Coupling Equations

According to the theory of ship seakeeping, the coupling equations of pitch and heave of a ship can be written in the form

$$\left.\begin{aligned} &(M + A_{zz})\ddot{z} + B_{zz}\dot{z} + C_{zz}z + A_{z\theta}\ddot{\theta} + B_{z\theta}\dot{\theta} + C_{z\theta}\theta = F_{zc}\cos\omega_e t + F_{zs}\sin\omega_e t \\ &(I_{\theta\theta} + A_{\theta\theta})\ddot{\theta} + B_{\theta\theta}\dot{\theta} + C_{\theta\theta}\theta + A_{\theta_z}\ddot{z} + B_{\theta_z}\dot{z} + C_{\theta_z}z = M_{\theta c}\cos\omega_e t + M_{\theta s}\sin\omega_e t \end{aligned}\right\}, \tag{11}$$

where z, θ, M, ω_e, $I_{\theta\theta}$ represent ship heave displacement, pitch angle, mass, encounter frequency, moment of inertia referred to y-axis respectively, and F_{zs}, F_{zc}, $M_{\theta s}$, $M_{\theta c}$ are partial values of wave force and moment. A_{ij}, B_{ij}, C_{ij} $(i, j = z, \theta)$ are hydrodynamic coefficient, which can be obtained by Ordinary Strip Method, according to the ship linetype.

3.2 Simulated Model

Using the simulink toolbox of Matlab, formula (10) can be modeled in the following form (Fig.1)

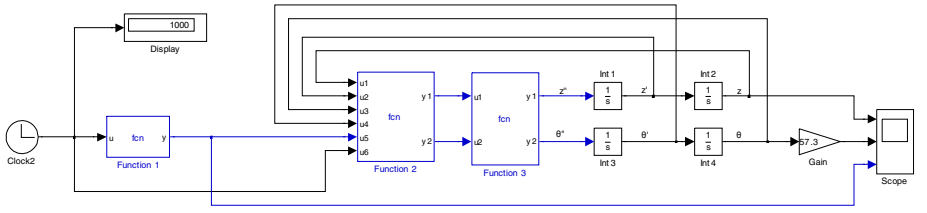

Fig. 1. Frame of Simulation

In above model, three Matlab functions are adopted, where function 1 is used to realize the scattering of encounter frequency, and function 2 has the following input/output relation

$$\begin{cases} y_1 = -B_{zz}u_2 - C_{zz}u_1 - B_{z\theta}u_4 - C_{z\theta}u_3 + F_{zc}\cos(u_5u_6) + F_{zs}\sin(u_5u_6), \\ y_2 = -B_{\theta\theta}u_4 - C_{\theta\theta}u_3 - B_{\theta z}u_2 - C_{\theta z}u_1 + M_{\theta c}\cos(u_5u_6) + M_{\theta s}\sin(u_5u_6). \end{cases} \tag{12}$$

and function 3 has the following input/output relation

$$\begin{cases} y_1 = [A_{z\theta}u_2 - (J_{\theta\theta} + A_{\theta\theta})u_1]/[A_{z\theta}A_{\theta z} - (M + A_{zz})(J_{\theta\theta} + A_{\theta\theta})], \\ y_2 = [A_{\theta z}u_1 - (M + A_{zz})u_2]/[A_{z\theta}A_{\theta z} - (M + A_{zz})(J_{\theta\theta} + A_{\theta\theta})]. \end{cases} \tag{13}$$

3.3 Simulation and Analysis

According to the linetype and main parameters of a ship, which natural frequency of pitch and heave are $n_\theta = 0.773\ \mathrm{s}^{-1}$、 $n_z = 0.745\ \mathrm{s}^{-1}$ respectively. The hydrodynamic coefficients and wave force(moment) are calculated by strip method. The encounter frequency ω_e has formula (2), where the scattering intensity δ_ω = 0.02、0.04、0.06、0.08、0.10 s^{-1}, and scattering frequency ω_δ = 0.10、0.20、0.30、0.40、0.50 s^{-1}. The time history of pitch and heave motions in regular waves can be obtained by calculating formula (10) using Runge-Kutta method.

For example, Figure 2 displays the time history of pitch angle and heave displacement under the initialized condition—the ratio of wave length to ship length is 1.0, the scattering constant ω_{e0} is $0.621\mathrm{s}^{-1}$, the scattering intensity δ_ω is $0.04\mathrm{s}^{-1}$, the scattering frequency ω_δ is $0.2\mathrm{s}^{-1}$. While t = 0~200s is the numerical result without frequency scattering, and t =200~1000s is the numerical result with frequency scattering, and the initialized value of pitch angle θ, heave displacement ς are zero when t = 0s. We can find that pitch and heave motion have stable oscillatory amplitude which are

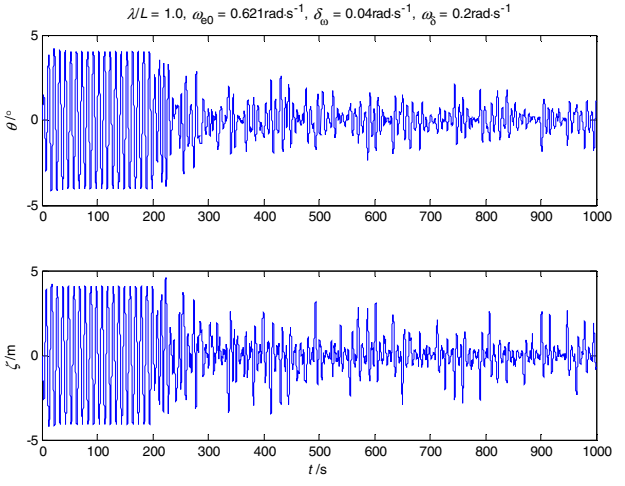

Fig. 2. Time history of the coupled oscillatory motions with frequency scattering

θ_{a0} = 4.099°, ζ_{a0} = 4.065m before frequency scattering, while they occur irregular response after frequency scattering, and the oscillatory amplitude are decreasing.

Due to the irregular oscillatory response after encounter frequency scattering, we can calculate the oscillatory amplitude from the results of simulation under different scattering intensity and frequency, and obtain the relation between the oscillatory amplitude and frequency scattering. Figure 3 shows the relation between relative reducing amplitude of pitch and heave motions and frequency scattering, while the y-axis is defined as

$$\frac{\Delta\theta_a}{\theta_{a0}} = \frac{\theta_a - \theta_{a0}}{\theta_{a0}}, \qquad \frac{\Delta\zeta_a}{\zeta_{a0}} = \frac{\zeta_a - \zeta_{a0}}{\zeta_{a0}}. \tag{14}$$

where θ_{a0}, ζ_{a0} represent average amplitude of pitch and heave without frequency scattering, and θ_a, ζ_a are effective amplitude of pitch and heave with frequency scattering.

Figure 3 shows that the oscillatory amplitude will change after frequency scattering. In the above case, the pitch angle and heave displacement are reduced, which reason is that the scattering constant is close to the resonant frequency of pitch and heave, and the encounter frequency keeps away from the resonant frequency after scattering. The reducing value of oscillatory amplitude exceeds 60 percent mostly, and has obvious relation with encounter frequency scattering—the bigger of the scattering intensity and frequency, the bigger of the reducing amplitude.

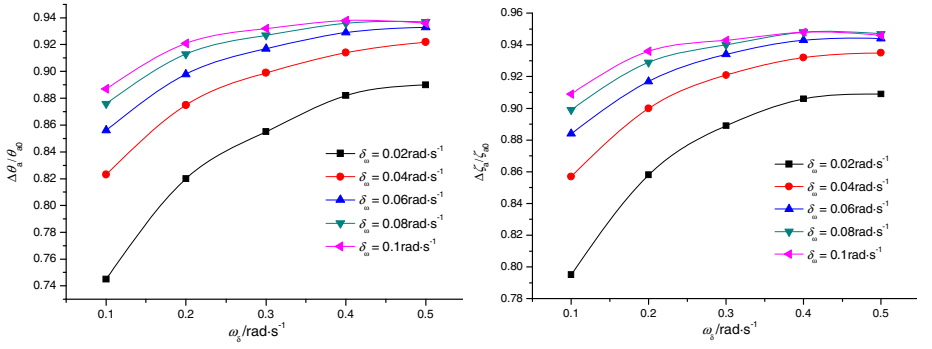

Fig. 3. Relation between relative reducing amplitude of pitch and heave motions and frequency dispersion

4 Mode Test

To check up the rationality of the scattering mechanism, a model test was carried out in towed basin in huazhong science and technology university. The ship speed scattering was thought about alone. Figure 4 and 5 show the time history of ship speed V, pitch angle θ and heave displacement ζ under the condition that wave length λ was equal to 3m, and wave height was equal to 62mm, and the form of speed impulse was 1.3→1→1.3m/s。 We can find that the pitch angle and heave displacement reduced with the change of ship speed which leaded the change of encounter frequency, which has similar changing trend with the numerical simulation.

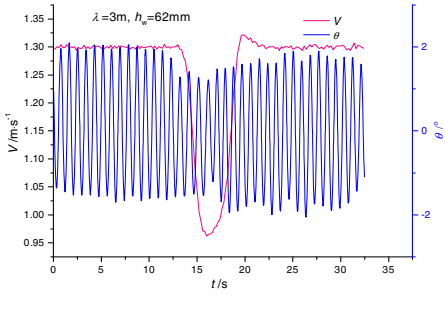

Fig. 4. Time history of ship speed and pitch angle

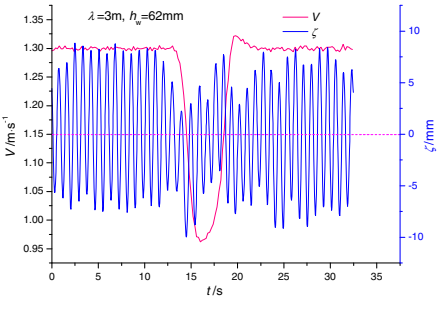

Fig. 5. Time history of ship speed and heave displacement

5 Conclusion

The concept and mechanism of encounter frequency was introduced in this paper. The influence of scattering intensity and frequency on the coupled oscillatory amplitude of pitch and heave motions was studied, by adopting the ordinary strip method to calculate the wave force and moment and hydrodynamic coefficient. Some conclusions can be obtained as follows:

① The scattering of encounter frequency has strong influence on the oscillatory amplitude which changing value is relative to the scattering constant. When the constant lies in the range of ship resonant frequency, the oscillatory amplitude will reduce after scattering.

② The reducing value of pitch and heave motions can reach 60 percent comparing with non-scattering.

③ The reducing value of oscillatory amplitude has obvious relations with encounter frequency scattering, which is that the bigger of the scattering intensity and frequency, the bigger of the reducing amplitude.

References

1. Davidson, K.S.M.: The steering of ships in following seas. In: Proceeding of the 6th International Congress for Applied Mechanics, pp. 554–568. IEEE Press, Tokyo (1948)
2. Rydill, L.J.: A linear theory for the steered motion of ship in waves. Quarterly Transactions of the Institution of Naval Architects 101, 81–112 (1959)
3. Eda, H.: Steering characteristics of ships in Calm water and Waves. SNAME 173, 135–177 (1965)
4. Eda, H.: Direction stability and control of ships in Waves. Journal of Ship Research 16, 205–218 (1972)
5. Nonaka, K.: On the maneuvering motion of a ship in waves. Transaction of the West-Japan Society of Naval Architects 80, 73–86 (1991)
6. Zhu, J., Pang, Y.-j., Xu, Y.-r.: Maneuvering prediction of a ship in regular waves. Journal of Harbin Engineering University 25, 1–5 (2004)
7. Chen, J.-f., Zhu, J., Ge, Y.-j.: Simulation and characteristics analysis of the coupling motion of maneuvering and rolling for a ship in regular waves. Journal of Ship Science and Technology 31, 46–50 (2009)

Interior Point Algorithms and Applications

Longquan Yong

Department of Mathematics, Shaanxi University of Technology,
Hanzhong 723001, Shaanxi, P.R. China
yonglongquan@sohu.com

Abstract. Modern interior point methods originated from an algorithm introduced by Karmarkar in 1984 for linear programming. In the years since then, algorithms and software for linear programming have become quite popular, while extensions to more general classes of problems, such as convex quadratic programming, linear complementarity problem, semi-definite programming, second order cone programming and nonconvex and nonlinear problems, have reached varying levels of maturity. In this paper we review the interior point algorithms and applications in some optimization problems, such as linear programming, linear complementarity problem, semi-definite programming and some convex programming. Combining with the current studies, we conclude that " applications of interior point algorithms and kernel function-based interior point algorithms" will be the research focuses in the future.

Keywords: interior point algorithm, linear programming, linear complementarity problem, semi-definite programming, second order cone programming, kernel function interior point algorithm.

1 Introduction

The purpose of this article is twofold: to provide a synopsis of the major developments in interior point methods for mathematical programming in the last 25 years for the researcher who is unfamiliar with interior points, and to discuss current and future research directions in interior point methods for researchers who have some familiarity with interior point methods. Throughout the article, we provide brief selective guides to the most lucid relevant research literature as a means for the uninitiated to become acquainted (but not overwhelmed) with the major developments in interior point methods.

Interior point methods in mathematical programming have been the largest and most dramatic area of research in optimization since the development of the simplex method for linear programming. The name interior point methods lie in the interior of the feasible region. This is contrast with the famous and well-established simplex method where the iterations move along the boundary of feasible region from one extreme point to another. Over the last 25 years, interior point methods have attracted some of the very best researchers in operations research, applied mathematics, and computer science. Approximately 5, 000 papers have been written on the subject following the seminal work of Karmarkar [1].

D. Zeng (Ed.): Future Intelligent Information Systems, LNEE 86, pp. 165–172.
springerlink.com © Springer-Verlag Berlin Heidelberg 2011

Interior point methods have permanently changed the landscape of mathematical programming theory, practice, and computation. Linear programming is no longer synonymous with the celebrated simplex method, and many researchers now tend to view linear programming more as a special case of nonlinear programming due to these developments.

Although various interior point methods had been considered one way or another from the 1950s, and investigated quite extensively during the 1960s [2], it was the publication of the seminal paper of Karmarkar that placed interior point methods at the top of the agenda for many researchers. A new era was inaugurated with Megiddo's paper [3], originally presented in 1987, which described a framework for primal-dual framework algorithms. The primal-dual viewpoint proved to be extremely productive. It yielded new algorithms with interesting theoretical properties, formed the basis of the best practical algorithms, and allowed for transparent extensions to convex programming and linear complementarity.

On the theoretical side, subsequent research led to improved computational complexity bounds for linear programming (LP), quadratic programming (QP), linear complementarity problems (LCP), semi-definite programming (SDP) and some classes of convex programming problems. In 1989, Mehrotra described a practical algorithm for linear programming that remains the basis of most current software; his work appeared in 1992 [4]. Meanwhile, Nesterov and Nemirovskii [5] were developing the theory of self-concordant functions, which allowed algorithms based on the primal log-barrier function for linear programming to be extended to wider classes of convex problems, particularly semi-definite programming and second-order cone programming (SOCP). Nesterov and Todd [6,7] extended the primal-dual approach along similar lines to a more restricted class of convex problems that still included SDP and SOCP. Other work on interior-point algorithms for SDPs, which have a wide variety of applications in such areas as control and structural optimization, was already well advanced by this point. Work on these algorithms gained additional impetus when it was recognized that approximate solutions of NP-hard problems could thereby be obtained in polynomial time.

On the computational side, high-quality software was eventually produced, much of it freely available. The general performance of computational tools for linear programming improved greatly, as the sudden appearance of credible competition spurred significant improvements in implementations of the simplex method.

We now outline the remainder of the paper. Section 2 discusses linear programming and its interior point methods, outlining the pedigree of the most important algorithms and various computational issues. In Section 3, we discuss linear complementarity problems and its interior point methods. Semi-definite programming is the topic of Section 4. Section 5 contains second-order cone programming and convex programming. Finally, we present some current and future research directions in interior point methods in Section 6.

We now describe our notation. All vectors will be column vectors unless transposed to a row vector. The scalar (inner) product of two vectors x and y in the n-dimensional real space $\mathbb{R}^n$ will be denoted by $x^T y$. For $x \in \mathbb{R}^n$ the 2-norm will be denoted by $\|x\|$, while $|x|$ will denote the vector with absolute values of each component of x. The notation $A \in \mathbb{R}^{m \times n}$ will signify a real $m \times n$ matrix. For such a

matrix A^T will denote the transpose of A. A vector of zeros in a real space of arbitrary dimension will be denoted by **0**.

2 Linear Programming

Considering the standard form linear programming problem

$$\min \quad c^T x \quad s.t. \quad Ax = b, \quad x \geq 0.$$

Where $c, x \in R^n$ and $b \in R^m$, A is an $m \times n$ matrix. Linear programming problem (LP) is a fundamental problem in mathematical programming. A number of direct as well as iterative methods have been proposed for their solution. The simplex method developed by Dantzig between 1947 and 1951 has been the method of choice for linear programming. While performing very well in practice, its worst-case computational complexity is exponential, as shown by the example of Klee and Minty from 1972. The problem of existence of a polynomial algorithm for solving linear programs with integer data was solved by Khachiyan in 1979. He proved that the ellipsoid method solves such programs in $O(n^2L)$ iterations, requiring a total of $O(n^4L)$ bit operations, where L is the length of a binary coding of the input data.

Interior point methods (IPMs) are an important method for LP. Modern interior point methods originated from an algorithm introduced by Karmarkar in 1984 for linear programming. The merit of the Karmarkar's algorithms consisted not so much in lowering the bound on the computational complexity of LP to O(nL) iterations, requiring a total of $O(n^{3.5}L)$ bit operations in theory. Quite recently, Anstreicher [5] proposed an interior-point method, combining partial updating with a preconditioned gradient method, that has an overall complexity of $O(n^3/\log n)$ bit operations.

IPMs are classified as affine scaling algorithms, projective algorithms and path-following algorithms, etc. In all interior point algorithms, the most successful interior point method is the primal-dual method. The primal-dual IPMs for linear optimization problem was first introduced in [8] and [9], Kojima et al. [9] first proved the polynomial computational complexity of the algorithm for linear optimization problem, and since then many other algorithms have been developed based on the primal-dual strategy.

In the primal-dual algorithms we assumed that a starting point satisfying exactly the linear constraints and lying in the interior of the region defined by the inequality constraints is given. In practice, however, it may be difficult to obtain such a starting point, so many efficient implementations of interior-point methods use starting points that lie in the interior of the region defined by the inequality constraints but do not necessarily satisfy the equality constraints. Such methods are called infeasible-interior-point methods, and they are more difficult to analyze. The first global convergence result for such methods was obtained by Kojima, Megiddo and Mizuno, while the first polynomial complexity result was given by Zhang. The computational complexity of the infeasible-interior-point algorithms typically is worse than in the feasible case. An advantage is that these algorithms can solve problems for which no strictly feasible points exist. They also can be used to detect the infeasibility of certain linear programming problems.

The theoretical computational complexity of interior-point methods for LP was eventually lowered to $O(n^{0.5}L)$ iterations, requiring a total of $O(n^3L)$ bit operations by a number of authors.

3 Linear Complementarity Problem

The linear complementarity problem (LCP) is to determine a vector pair (x, y) satisfying

$$y = Mx + q, \;\; x^T y = 0, \;\; x \geq 0, \;\; y \geq 0.$$

Where $x, y, q \in R^n$ and $M \in R^{n \times n}$. Linear complementarity problem is a fundamental problem in mathematical programming. It is known that any differentiable linear and quadratic programming can be formulated into an LCP. LCP also has wide range of applications in economics and engineering. The interested readers are referred to the survey paper [16].

A number of direct as well as iterative methods have been proposed for their solution. The book by Cottle et al. [17] is a good reference for pivoting methods developed to solve LCP. Another important class of methods used to tackle LCP is interior point methods. Interior point methods (IPMs) are an important method for LCP. Most IPMs for LCP can be viewed as natural extensions of the interior point methods for linear programming. LCP is called monotone LCP if M is positive semi-definite.

We call the set $S_{cen} = \{(x, y) \in S_{++} : Xy = \mu, \mu > 0\}$ path of centers of the LCP. And we call $N(a) = \{(x, y) \in S_{++} : \left\| Xy - n^{-1} x^T y \right\| \leq a n^{-1} x^T y\}$ neighborhood of path of center S_{cen} for a small $a \in (0,1)$. Here $S_{++} = S_{af} \bigcap R_{++}^{2n}$, $S_{af} = \{(x, y) \in R^{2n} : y = Mx + q\}$.

Suppose that the LCP is monotone and a feasible interior point $(x^0, y^0) \in N(a)$ of LCP is known. The order $O\left(\sqrt{n} \log \varepsilon^{-1} (x^0)^T y^0\right)$ is known as the best iteration upper bound for feasible interior point algorithms for solving the monotone LCP to date [18].

4 Semi-definite Programming

As mentioned in the introduction, semi-definite programming (SDP) has been one of the most active areas of optimization research in the 1990s. SDP consists in minimizing a linear functional of a matrix subject to linear equality and inequality constraints, where the inequalities include membership of the cone of positive-semi-definite matrices. SDP is a broad paradigm; it includes as special cases linear programming, (linearly constrained) QP, quadratically constrained QP and other optimization problems (see [19,23]). Semi-definite programming has numerous applications in such diverse areas as optimal control, combinatorial optimization, structural optimization, pattern recognition, trace factor analysis in statistics, matrix

completions, etc. See the excellent survey paper [21] for some instances. It was only after the advent of interior-point methods, however, that efficient solution methods for SDP problems were available. During the past few years an impressive number of interior-point methods for SDP have been proposed. Some of them have been successfully implemented and used to solve important application problems. However the theory and practice of interior-point methods for SDP has not yet reached the level of maturity of interior-point methods for LP, QP, and LCP. One reason that the study of interior-point methods for SDP is extremely important is that while LP, QP, and LCP can also be solved by other methods (e.g. the simplex method or Lemke's method), interior-point methods appear to be the only efficient methods for solving general SDP problems presently known.

The paper of Todd [22] is witness to the intensity of research in SDP interior-point methods: It describes 20 techniques for obtaining search directions for SDP, among the most notable being the following:

(1) the AHO search direction proposed by Alizadeh, Haeberly and Overton;

(2) the KSH=HRVW=M search direction independently proposed by Kojima, Shindoh and Hara; Helmberg, Rendl, Vanderbei and Wolkowicz; and later rediscovered by Monteiro;

(3) the NT direction introduced by Nesterov and Todd.

Monteiro and Zhang proved that algorithms acting in large neighborhoods of the central path have O(nL) iteration complexity if based on the NT direction and $O(n^{1.5}L)$ if based on the KSH/HRVW/M search direction. The analysis of infeasible interior-point algorithms for SDP is considerably more difficult than that of their feasible counterparts. The first complexity result in this respect was obtained by Kojima, Shindoh, and Hara, who showed that an infeasible-interior-point potential reduction method for SDP has $O(n^{2.5}L)$ iteration complexity. Subsequently, Zhang analyzed an infeasible-interior-point method, based on the KSH/HRVW/M search direction, that has $O(n^2L)$ iteration complexity when acting in the semi-large neighborhood and $O(n^{2.5}L)$ iteration complexity in the large neighborhood of the central path. If the starting point is large enough according to some specific criteria, then the algorithm terminates in at most O(nL) steps either by finding a strictly complementary solution or by determining that the primal-dual problem has no solution of norm less than a specified size.

Superlinear convergence is especially important for SDP since no finite termination schemes exist for such problems. The local convergence analysis for interior-point algorithms for SDP is much more challenging than for linear programming. Kojima, Shida and Shindoh [23] established superlinear convergence of the Mizuno-Todd-Ye predictor-corrector algorithm based on the KSH/HRVW/M search direction under three assumptions.

Over the past several years we have witnessed an intense research effort on the use of SDP for finding approximate solution of (NP-hard) combinatorial optimization problems, such as the MAX CUT problem [23].

5 Second Order Cone Programming

Over the past few years, primal-dual interior point methods have been developed for all kinds of nonlinear optimization problems. Second-order cone programming (SOCP) is one of these. SOCP addresses the problem of minimizing a linear objective function over the intersection of an affine set and the direct product of quadratic cones. Numerous applications have been discussed in [24,27]. Recently, many researchers have shown that the primal-dual IPM has high theoretical efficiency for SOCP. In particular, Tsuchiya [27] and Monteiro and Tsuchiya [25] have proved the complexity of variants of IPMs based on different scaling directions. Specifically, Tsuchiya [26] shows that the long-step path-following algorithm using the Nesterov and Todd (NT) direction has log iteration complexity which is also the best result for the scaling methods they considered.

6 Current Trends

One of the most surprising results in interior-point methods is the fact that interior-point algorithms from LP can be extended to general convex programming problems, at least in a theoretical sense. A number of researchers have used interior-point methods in algorithms for combinatorial and integer programming problems. A great deal of literature is available to the reader interested in learning more about interior-point methods. A number of recent books [28-32] give overviews of the area, from first principles to new results and practical considerations.

Recently, kernel function interior point algorithm and infeasible-interior-point methods have been made great progress. The applications of interior point algorithms in industry and engineering, such as power systems [33-34], and kernel function interior point algorithm [35] will be another research focuses in the future.

Acknowledgments

The author is very grateful to the referees for their valuable comments and suggestions. This work is supported by Shaanxi Provincial Department of Education Foundation under Grant No.09JK381.

References

1. Karmarkar, N.: A new polynomial-time Algorithm for linear programming. Combinatorica 4, 373–395 (1984)
2. Fiacco, A.V., McCormick, G.P.: Nonlinear Programming: Sequential Unconstrained Minimization Techniques. Wiley, New York (1968)
3. Megiddo, N.: Pathways to the optimal set in linear programming. In: Megiddo, N. (ed.) Progress in Mathematical Programming: Interior-Point and Related Methods, pp. 131–158. Springer, New York (1989)
4. Mehrotra, S.: On the implementation of a primal-dual interior point method. SIAM J. Optim. 2, 575–601 (1992)

5. Nesterov, Y.E., Nemirovskii, A.S.: Interior Point Polynomial Methods in Convex Programming: Theory and Applications. SIAM, Philadelphia (1994)
6. Nesterov, Y.E., Todd, M.J.: Self-scaled barriers and interior-point methods for convex programming. Math. Oper. Res. 22, 1–42 (1997)
7. Nesterov, Y.E., Todd, M.J.: Primal-dual interior-point methods for self-scaled cones. SIAM J. Optim. 8, 324–362 (1998)
8. Anstreicher, K.M.: Linear programming in O([n3/lnn]L) operations, CORE Discussion Paper 9746, Universite Catholique de Louvain, Louvain-la-Neuve, Belgium (1999)
9. Kojima, M., Megiddo, N., Noma, T., Yoshise, A.: A Primal-dual Interior Point Algorithm for Linear Programming. In: Megiddo, N. (ed.) Progress in Mathematical Programming; Interior Point Related Methods, pp. 29–47. Springer, New York (1989)
10. Megiddo, N.: Pathways to the optimal set in linear programming. In: Megiddo, N. (ed.) Progress in Mathematical Programming; Interior Point and Related Methods, pp. 158–313. Springer, New York (1989)
11. Frisch, K.R.: The Logarithmic Potential Method of Convex Programming. University Institute of Economics, Oslo (1955)
12. Fiacco, A., McCormick, G.: Nonlinear Programming: Sequential Unconstrained Minimization Techniques. John Wiley and Sons, Chichester (1968)
13. Monteiro, R.D.C., Adler, I.: Interior Path Following Primal-dual Algorithms, Part I: linear programming. Math. Prog. 44(1), 27–41 (1989)
14. Freund, R.M., Mizuno, S.: Interior point methods: current status and future directions. Optima 51, 1–9 (1996)
15. Terlaky, T.: Interior Point Method of Mathematical Programming. Kluwer Academic Publishers, Dordrecht (1996)
16. Billups, S.C., Murty, K.G.: Complementarity Problems. Journal of Computational and Applied Mathematics 124, 303–318 (2000)
17. Cottle, R.W., Pang, J.S., Stone, R.E.: The Linear Complementarity Problems. Academic Press, London (1992)
18. Kojima, M., Mizuno, S., Yoshise, A.: A Polynomial-time Algorithm for a Class of Linear Complementarity Problems. Math. Prog. 44, 1–26 (1989)
19. Monteiro, R.D.C., Zhang, Y.: A unified analysis for a class of long-step primal-dual path-following interior-point algorithms for semidefinite programming. Math. Programming Ser. A 81(3), 281–299 (1998)
20. Potra, F.A., Sheng, R.: Superlinear convergence of interior-point algorithms for semidefinite programming. J. Optim. Theory Appl. 99(1), 103–119 (1998)
21. Renegar, J.: A polynomial-time algorithm, based on Newton's method, for linear programming. Math. Programming 40, 59–93 (1988)
22. Todd, M.J.: A study of search directions in primal-dual interior-point methods for semidefinite programming,Technical Report, School of Operations Research and Industrial Engineering, Cornell University, Ithaca, NY (February 1999)
23. Vandenberghe, L., Boyd, S.: Semidefinite programming. SIAM Rev. 38(1), 49–95 (1996)
24. Lobo, M.S., Vandenberghe, L., Boyd, S.: Application of second-order cone programming. Linear Algebra Application 284, 193–228 (1998)
25. Vanderbei, R.J., Yurttan, H.: Using LOQO to solve second-order cone programming problems, Report SOR 98-09, Princeton University (1998)
26. Monteiro, R.D.C., Tsuchiya, T.: Polynomial convergence of primal-dual algorithms for the second-order cone program based on the MZ-family of directions. Mathematical Programming 72, 61–83 (2000)

27. Tsuchiya, T.: A convergence Analysis of the Scaling-invariant Primal-dual Path-following Algorithms for Second-order Cone Programming. Optimization Methods and Software 11(12), 141–182 (1999)
28. Wright, M.H.: Interior methods for constrained optimization. In: Acta Numer, pp. 341–407. Cambridge University Press, Cambridge (1992)
29. Wright, S.J.: Primal-Dual Interior-Point Methods. SIAM, Philadelphia (1997)
30. Wright, S.J.: Recent developments in interior-point methods, preprint ANL/MCS-P783-0999, Mathematics and Computer Science Division. Argonne National Laboratory, Argonne (1999)
31. Ye, Y.: Interior Point Algorithms: Theory and Analysis. Wiley-Interscience Series in Discrete Mathematics and Optimization. Wiley, New York (1997)
32. Zhang, Y.: On the convergence of a class of infeasible-interior-point methods for the horizontal linear complementarity problem. SIAM J. Optim. 4, 208–227 (1994)
33. Quan, R., Jian, J.B., Zheng, H.Y.: Globally convergent interior-point algorithm and its application to optimal power flow. Information, Management and Algorithms II, 184–187 (2007)
34. Wei, H., Sasaki, H., Yokoyama, R.: An application of interior point quadratic programming algorithm to power system optimization problems. IEEE Transactions On Power Systems 11(1), 260–266 (1996)
35. Bai, Y.: Kernel Function-based Interior-point Algorithms for Conic Optimization. Science Press, Beijing (2010)

Synchronization Design in Multi-channel DRFM Module

Yun-Jie Li, Mei-Guo Gao, and Hong-Fei Shi

School of Information and Electronics, Beijing Institute of Technology, Beijing, 100081

Abstract. In many applications involving multiple DRFM processing channels like radar jamming source design, corresponding digital processing arithmetic may require the different channels can operating in a synchronous mode exactly, including both the ADC sampling and the DAC converting. This paper puts focus on this problem during one DRFM module's design and implementation. Taking the designed DRFM module as example, the paper attempts corresponding methods for synchronization realization. For two ADCs channels, a serial of resetting and timing controlling operations are employed. For two DACs channels, resetting the DAC's clock source and an additional XOR operation are used. Performance evaluating results show the effective of the methods proposed.

Keywords: synchronization; DRFM; clock distribution; MLP.

1 Preface

DRFM(Digital Radio Frequency Memory) technology can implementing signal storage and retransmitting. When used in radar jamming, DRFM can sample the input signal, storing it and making some jamming modulation, in which way the deceptive jamming signal correlative with the jammed radar can be obtained [1]. The generated jamming signal can acquire the same signal processing gain as the real target's echo signal in radar processing channel, so jamming source based on DRFM technology is one of the most important component for modern radar EW system. At the same time, DRFM has also been used widely in the fields of signal fingerprint analysis, RF signal simulating and IF signal processing, etc. Some companies have developed many kinds of commercial DRFM products both in domestic and abroad [2]. From the hardware aspect, signal sources based on DRFM technology are mainly consisted of ADC/DAC with high converting rate and DSP/FPGA chips with powerful digital processing capabilities. Then here comes the analog and digital mixed circuits design challenges for designers. In the occasions of multiple DRFM processing channels needed, the subsequent digital processing arithmetic, such as sampling the input signals in I&Q format, usually require the different channels can operating synchronously. Synchronization design seems to be a more challenging task in certain DRFM module's R&D.

This paper puts focus on synchronization design problem of multiple DRFM channels during one DRFM module's design and implementation. Firstly, Module's architecture and the clock network are introduced in Section II. Then synchronization

D. Zeng (Ed.): Future Intelligent Information Systems, LNEE 86, pp. 173–181.
springerlink.com © Springer-Verlag Berlin Heidelberg 2011

problem between two ADCs channels is described in section III and that problem between two DACs channels in section IV. These two sections both have two parts as the problem description and the corresponding solution to the problem. The synchronous performance evaluation results are presented in section V, and final section is some conclusions.

2 Module Overview

To fulfill the requirements of many DRFM applications, the expected processing module should feature some common characters, including general-purpose, reconfiguration flexibly, multiple processing channels based on standard platform structures, etc. DSPEED_DRFM-D1200 (abbreviated as D1200 in this paper) is such a kind of DRFM module. It has a 6U board size accord with Compact PCI standard while the processing ability relies on the two parallel processing channels on it [3].

D1200 have powerful signal processing chips and signal converting chips selected from word-wide leading manufacturers as its main units. The module's structure (Fig.1) can be diagrammatic represented with ADCs, DAC, DSPs and FPGAs. In default, D1200 works with one left channel and one right channel in parallel. Every channel includes one ADC chip from ATMEL called AT84AD001B, one Xilinx DSP platform FPGA Virtex4 SX55 chip (abbreviated as V4-R and V4-L in this paper) and one 14bits 1200MSPS DAC chip called AD9736 (abbreviated as DAC-R and DAC-L in this paper). One TMS320C6455 DSP chip from TI is connected with two Virtex4 FPGAs for host communicating and co-processing. Additional, one Virtex5 LX30 FPGA chip (abbreviated as V5 in this paper) is connected to both V4-R and V4-L FPGA as the data bridge between two Virtex4 FPGA chip and two DAC chips.

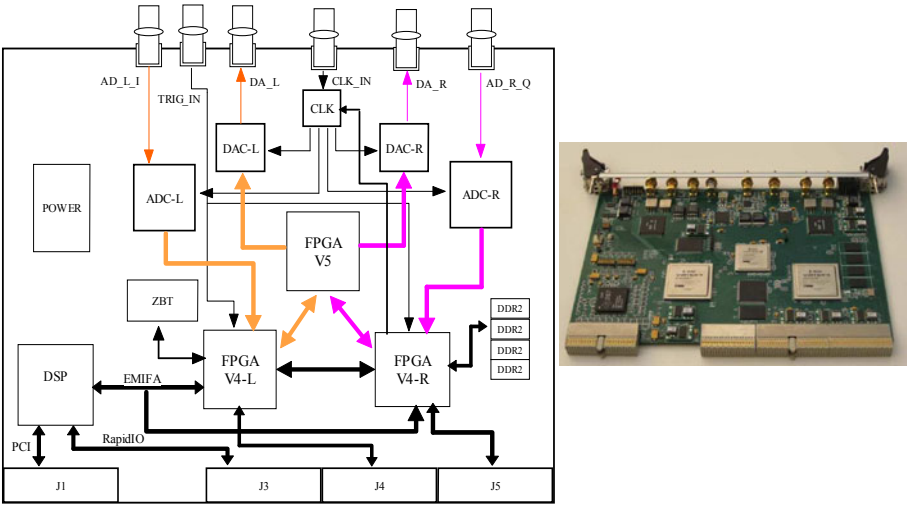

Fig. 1. Diagram and photo of the D1200 Module

For interconnection between different boards in system, the two V4 FPGAs can realize data transfer with other system board through high speed data link defined in J4/J5 connector. And the DSP can communicate with other DSPs through Serial Rapid IO data link defined in J3 connector.

It is the last but not the least that the clock network is be dealt with carefully. It takes the responsibility of clock signals generation base on the internal or external reference clock and distributing them to different processing units. The D1200 needs clock signal with frequency high up to 1200MHz, and one kind of chip called AD9518 comes from ANALOG is selected as the main unit in the clock generation and distribution network design. It can be programmed to perform a multi-output clock generation and distribution functions with outstanding jitter performance. The diagram of the clock network (Fig.2) describes the connection of AD9518 1200MHz clock signals with other processing units: two clock signals (#2 & #3) are connected to two ADC chips, two clock signals (#4 & #5) are connected to DAC-L and DAC-R chips, one clock signal (#0) connected to V4R FPGA and the last one clock signal (#1) routed to V5 FPGA.

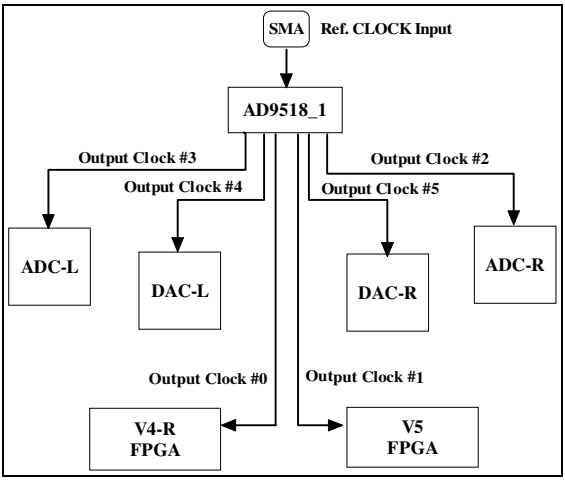

Fig. 2. Diagram of Clock Generating and Distribution Network

3 Synchronization between Two ADCs

3.1 Synchronization Problem Description

Synchronization between multiple ADC channels means the different channels sampling data at exactly the same clock edge and latching the sampled data synchronously. This is one of the key problems in high-speed data acquisition system.

There are two 1200MSPS ADCs in D1200 and every ADC is followed with a V4 FPGA. The high rate output signal can't be latched by FPGA directly. So every ADC has four DEMUX output paths for its digital signal output. All the four paths have one lower rate clock signal CLKO. The lower clock signal comes along with the digital data from ADC to corresponding V4 FPGA, and it can be used to simplify the data synchronous receiving at FPGA boundary [4]. In fact, every path arranges the data in DDR format of 150MHz clock rate, so data rate in every path is 300MSPS.

Virtex4 platform FPGA nowadays can hardly run the logical processing clock high up to 300MHz, so additional DMUX operation should be done by FPGA at the data receiving stage. ISERDES in FPGA can be used to performing data rearrange from serial to parallel with ratio of 1:4, then the four input DDR data streams are converted into 16 lower rate SDR streams with 75MHz clock. Finally, sixteen FIFO memories are employed for data buffering for every data stream.

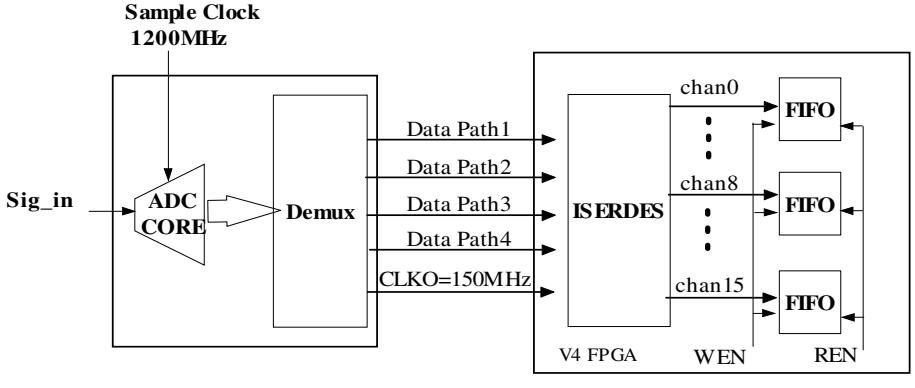

Fig. 3. Data Receiving Procedure in ADC Channel

The data receiving procedure above (Fig.3) is mainly consisted of four stages: ADC sampling, DMUX in ADC, ISERDES DEMUX in FPGA and FIFOs buffering after ISERDES. Every stage should be dealt with carefully for synchronous sampling between two ADC channels.

3.2 Solution of Synchronization between Two ADCs

Some measures have been taken for synchronization of two ADC channels in D1200.

(1) Using Synchronized 1200MHz Sampling Clock Signals

This is the most basic requirement for synchronization implementation and can be done by the high performance clock generation unit and carefully designed clock signal distribution network.

(2) Using ADC's DDRB Reset Signal

In order to ensure the synchronization between the digital data output clock signal CLKO and the four lower rate (300MHz) data streams, ADC chip provides the synchronous data ready reset signal called DDRB. Its timing diagram (Fig.4) shows that two ADC chip's output data paths can be synchronized when they are using synchronized DDRB signal. This can be ensured by routing the DDRB signal from one common chip, such as the V5 FPGA or V4-R FPGA, to the two ADC chip with strictly ruled length.

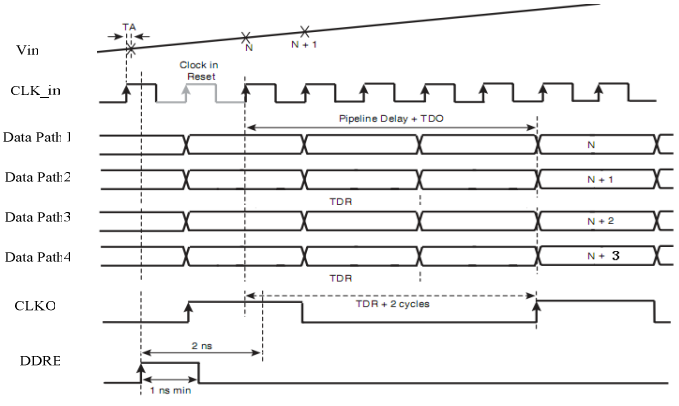

Fig. 4. Timing Diagram of DDRB Signal

(3) Synchronous Resetting the ISERDES

Using ISERDES in FPGA can lower the input data rate from high speed ADC output data paths, but it may lead to mismatch in the multiple channels sampling applications. Because the ISERDES operating and subsequently data latching are all working with a more lower rate clock, which need frequency division operation on the input clock signal CLKO. The division operations of two ADC channel are completed in two different V4 FPGAs, then asynchronous problems may arise in the divided clock signals the two ISERDES components used. So resetting ISERDES should be done for ISERDES synchronization. The reset act is carried out during the CLKO signals are absent (when the ADC in reset status).

(4) Synchronizing FIFOs Operations

The relative operations about FIFOs are resetting and write enable signal generating.

After the resetting operations on ADC and ISERDES, the new coming data in input data path are well matched according the corresponding time maker. So the FIFOs should be reset for the first input data storing. On the same time, the write enable signals for FIFOs need to be synchronized. The WEN signal used inV4-L and V4-R FPGA should be routed from one common component, such as DSP or V5 FPGA, and completed under strictly ruled length (Fig.5). V4-L and V4-R FPGA will latch the WEN signal for one clock and then sending it into the time circuit routing step.

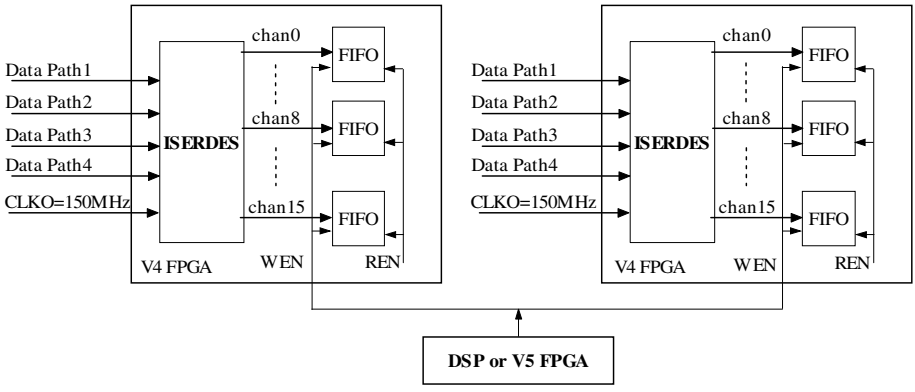

Fig. 5. FIFO's WEN Signal Implementation

4 Synchronization between Two DACs

4.1 Synchronization Problem Description

The D1200 have two high speed DACs both connected to V5 FPGA, and every DAC has converting clock signal DAC_CLK high up to 1200MHz. For simplify the digital input data receiving, DAC can output one DATA_CLK_OUT signal of half of the DAC_CLK frequency to V5 FPGA. Then V5 FPGA can generate the data output clock signal DATACLK_IN from the DATACLK_OUT signal, which will come out from the FPGA along with the output digital data to both DAC chips. The DATACLK_IN signal can be used by DAC for data latching and then driving the DAC core for data converting at 1200MSPS clock rate.

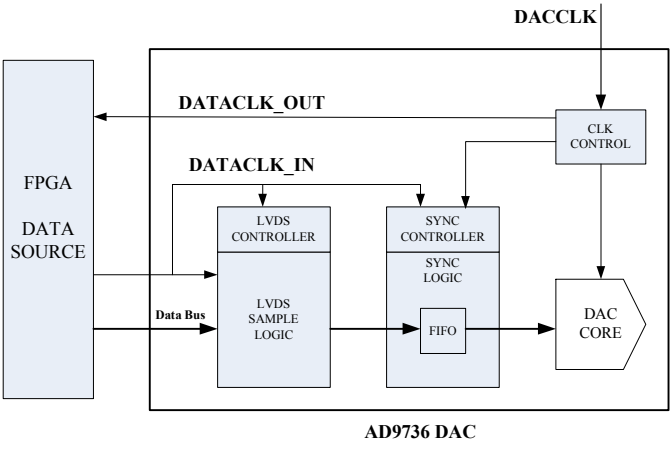

Fig. 6. Interface between FPGA and DAC

The interface between FPGA and DAC (Fig.6) shows that the DACCLK signal and DATACLK_OUT signal are correlative. The later on is the 1:2 division of the former one. DAC chip can't guarantee the initial phase of the DATACLK_OUT signal relative to DACCLK. In fact, the phase of the output DATACLK_OUT may be either zero or PI. Because there is no approach to control these initial phase. So in multiple channel applications, different DAC's DATACLK_OUT signals may have different initial phases even they have a synchronous relationship in DAC_CLK signal. This will inevitably lead to asynchronous problem in DAC output, usually results in one sample data mistake.

4.2 Solution of Synchronization between Two DACs

The asynchronous problem in DAC arises from the uncertain initial phase of DATACLK_OUT signal. Because there is no way to control these phase by DAC itself, the only method can influence those phases is switching off the DAC's clock from extern logic to force the chip to perform frequency division again. On the other hand, extern logic needed to make a judge whether the two DATACLK_OUT signals have the same initial phase already [5].

The DAC's clock switching off can be done through resetting the clock generation module if needed and synchronization judge can be realized through XOR operating on the two DATACLK_OUT signals until the results signal almost have a constant low logic level (Fig.7). The XOR operation can be implemented in V5 FPGA and the two DAC's DATACLK_OUT signals are routed into the FPGA with strictly ruled length. Because the intermediate status of the two input DATACLK_OUT signals, the XOR output signal may have some jitters during the edge changing period of the input clock signals. So the final judge conclusion should be drawn from level verification for a period of time.

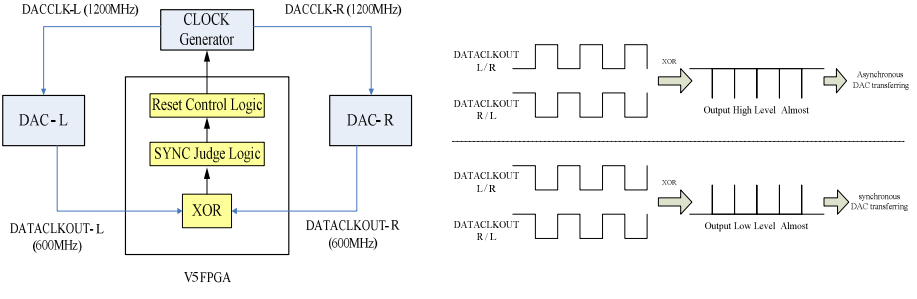

Fig. 7. Solution of Synchronization between Two DACs

5 Synchronous Performance Evaluation

5.1 ADC Synchronization Evaluation

For ADC synchronous performance evaluation, the sampled data in V4-L and V4-R FPGA can be saved in DATA file format. And the data files will feed into certain analysis program in MATLAB software. The MATLAB functions employ MLP arithmetic [6] for the signal's initial phase calculation. Combination of the signal frequency and the two calculated initial phase results, the different time between the two sampled signals will be obtained (Table 1).

Table 1. Synchronous Performance between Two ADC Channels

Input Signal Freq. (MHz)	Initial Phase Error (Deg. : L-R)	Time Delay between Two Channels (ps: L-R)	Average Performance (ps: L-R)
50	0.34	18.74	18.69
	0.35	19.68	
	0.32	17.66	
150	1.00	18.58	18.22
	0.97	18.01	
	0.98	18.08	
300	2.61	24.2	24.79
	2.71	25.05	
	2.71	25.13	
450	2.66	16.43	16.65
	2.68	16.52	
	2.76	17.01	

The test data show that the different time brought out during the sampling procedure can be confined in the scope of 30ps and the two 1200MSPS ADC channels are synchronized well.

5.2 DAC Synchronization Evaluation

DAC synchronization evaluation flow is similar to that of the ADC test. The two DAC's output analog signal are connected into digital oscilloscope using cables of exact the same length. The oscilloscope saves the two input signal in DATA file format, and the data file will be processed in MATLAB program. The MATLAB functions employ MLP arithmetic for the signal's initial phase calculation. Combination of the signal frequency and the two calculated initial phase results, the different time between the two converted output signals will be obtained (Table 2).

Table 2. Synchronous Performance between Two ADC Channels

Trans. Signal Freq. (MHz)	Initial Phase Error （Deg.: R-L）	Time Delay between Two Channels (ps: R-L)	Average Performance （ps: R-L）
50	0.30	16.59	23.03
	0.41	22.64	
	0.54	29.88	
150	2.05	37.90	39.57
	2.12	39.28	
	2.24	41.54	
300	4.31	39.91	40.52
	4.41	40.83	
	4.41	40.82	
450	3.81	23.54	23.01
	3.75	23.12	
	3.63	22.39	

The test data show that the different time brought out during the converting procedure can be confined in the scope of 50ps and the two 1200MSPS DAC channels are synchronized well.

6 Conclusions

This paper puts focus on the multiple channels synchronization problem during DRFM module design and implementation. Taking the designed D1200 as example, the reasons leading to the asynchronous problems both in ADCs channels and in DACs channels are examined and corresponding solutions are analyzed and verified. For nowadays high speed applications combined ADC chips and DAC chips with powerful FPGA or DSP, the problem discussed here has something in common and the synchronization methods brought out in this paper can be referenced.

References

1. Schleher, D.C.: Electronic War Fare in the Information Age. Artech House, MA (1999)
2. Wang, Z.-b.: Research on Jamming Techniques for Broadband and Wide Pulse Signals. Beijing Institute of Technology, Beijing (2009)
3. Li, Y-j.: Hardware Design of DRFM-D1200. Beijing Institute of Technology, Radar Research Lab (2008)
4. Implement the AT84AD001B, Application Note, E2V Semiconductors SAS (2007)
5. Timing Synchronization for Multiple AD9786 TxDACs, Application Note, Analog Devices Corp (2004)
6. Hui, D., Jiang, Q.-x., Bi, D.-p.: The Technology of Measuring nstant Frequency in Digital Reconnaissance Receiver. Electronic Warefare Technology 20, 7–10 (2005)

Design and Implimentation on Registry of Geographic Information Sharing Platform Based on SOA

Yanjun Wang* and Lei Huang

State Key Laboratory of Information Engineering in Surveying,
Mapping and Remote Sensing, Wuhan University,
129 Luoyu Road, Wuhan 430079, China
wongyanjun@163.com

Abstract. This paper, based on SOA architecture, described the definition, principle and technique of SOA. For the multi-source and multi-scale geographical data sharing through Internet and display on distributed web, this paper proposed the registration center model of geographic information-sharing platform solution, detailed the realization, principle, functional design and technical approach of this registry. The registry could achieve the data release, access request and service binding interoperability. The ultimate examination validated the feasibility of this method.

Keywords: geographic information sharing, registry, spatial information service, SOA, WMS, WFS.

1 Introduction

SOA (Service-Oriented Architecture) provides an important means to achieve the current "the new era for geo-information" [1] Web GIS and geographic information sharing and is a new reasearch subject in the new geographic information era. In order to managing multi-source, multi-temporal and many types of geographic information and GIS interoperability, many mainstream companies, research institutions, commercial software applications have proposed technology of establishing SOA solutions and has made lots of research and application effort.

The core of SOA Web Services technology, including many of the IT industry standards, such as: XML, SOAP (Simple Object Access Protocol), UDDI (Universal Description, Discovery, and Integration), WSDL (Web Services Description Language), etc.[2]. SOA-based geographical information sharing platform registry, primarily provides a basis for the geographic information sharing management information, data services and function services, registration of external data services and access interface [3]. This paper mainly introduced the SOA technology and discussed the principle of geographic information registry, function and implementation, proposed a construction solution of the registry for geographical information sharing platform based on SOA.

* Corresponding author.

D. Zeng (Ed.): Future Intelligent Information Systems, LNEE 86, pp. 183–188.
springerlink.com © Springer-Verlag Berlin Heidelberg 2011

2 Geographical Information Sharing Based on SOA

SOA is a service-oriented software architecture model which can be distributed deployment, composition and access based on the demand of the loosely coupled coarse-grained application components. Several important characteristics of SOA is the coarse-grained and loosely coupled service architecture, the simple and precise definition of interfaces for communication between service, does not involve low-level programming interface and communications model.

Generally speaking, SOA will be the application of different functional units or services through well-defined interfaces between services and contracts linked to the interface, which is defined in a neutral way and independent of services implementation hardware platform, operating system, programming language. In different SOA systems, services can be built in a uniform and common way to interact. The structure of the SOA, including three roles: service providers, service agents and service users, three acts: service release, service discovery and service binding [4], as shown below:

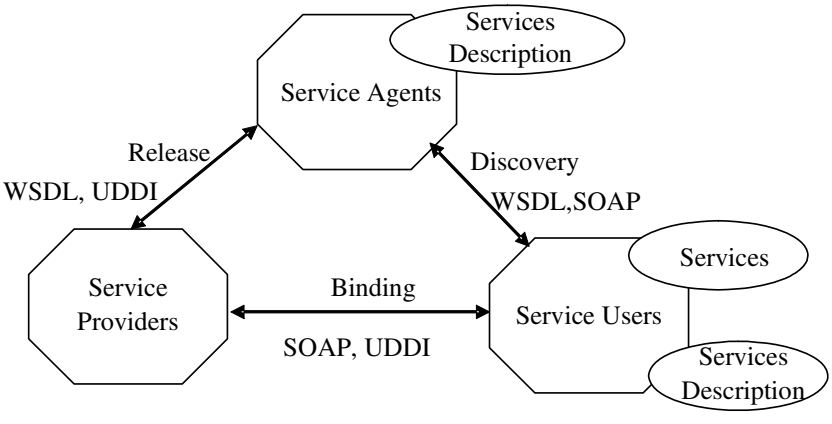

Fig. 1. Structure of SOA (Service-Oriented Architecture)

Geographic information sharing platform registry should include all the features and characteristics of SOA and achieve the purpose of SOA.

Service providers, usually generated by units of geographic data or spatial analysis function module primal developers to provide a variety of loosely coupled, fine-grained service entity, is the primary role of geographical information sharing, directly reflects the quality of the information sharing and efficiency.

Service agents, as generally sharing platform, mainly register and publish service providers' data services and functional services, respond the request for service users, find and bind the request of geographic information services.

Service users, a shared platform users or spatial information service requesters, mainly through the registry using the UDDI request for various types of geographic information services[5], to complete own data need and business operation.

Based on SOA, geographic information can be shared and achieve full interoperability, in particular OGC (Open Geospatial Consortium) organizations developped WMS(Web Map Service), WFS(Web Feature Service), WCS(Web Coverage Service) and other standard[6] to provide the uniform standards and rules of the sharing of geographic information, may be accessed and called by the broad platforms by standard Web service interface.

3 Registry Based on SOA

3.1 Sharing Mechainsm in Registry

Geographic information sharing platform registry, publishing and binding of spatial information services, provides services organization and management of spatial information service, the registration of a variety of services and users to discover and binding function.

Registration center provides space for the release of information services and registration capabilities, service providers can convert many types of spatial data to meet the OGC spatial information services standards, including WMS, WFS, WCS, etc.[7-9]. The spatial information services provide the basis and guarantee for the geographic information sharing platform.

A shared platform may include types data sources and a large number of different spatial information services. It is necessary to provide search and find information service functions, there help users quickly and accurately locate the required services. Registry can provide spatial information service metadata information, including the description of spatial information services, properties, performance, input and output and so on, thus can provide the necessary services interface to the user and can be accessed.

3.2 Specific Design

1) the publication and registration of spatial information services

Spatial data service is the core of geographic information sharing platform, the publication and registration is the first step in the geographic information sharing. The registration of spatial information services is to establish services metadata to facilitate search and access. The key information includes data service URL, title, keyword, geography coordinate system, geographic scope.

2) the discover and binding of spatial information services

The discover and binding of spatial information services based on the HTTP protocol, which support the URL request. GIS server according to the description of documents of services, WSDL, can retrieve related information of services such as WMS, WFS. The main parameters are as follows:

<ows:ServiceIdentification>: description of the GIS server's key information, including the GIS server title, abstract, keywords, service type and version information.

<ows:OperationsMetadata>: GIS server supports the operation of metadata, mainly explain various types of GIS operations interface specification, such as the

GetCapabilities operation with the request URL, version supported and data format interface.

<FeatureTypeList>: description of the GIS server, including the service information of all types of Service, including service name, title, abstract, keywords, the default spatial reference, etc.

<ogc:Filter_Capabilities>: the filter interface description of spatial analysis operations GIS server supported, including geometry and geo-spatial operation, logical comparison and arithmetic manipulation.

3) the analysis and operation of spatial information services

Based on the analysis and operation of spatial information services, can provide users with a variety of professional applications and solutions. Specific processing can according to OGC information services filter specification[10].

In the WFS request, the main parameters include:

<wfs:GetFeature service="WFS" version="1.0.0" …>: mainly describe the GIS operation such as WFS request, version, output format, the server URL and other information. GIS operation GetFeature correspond with <ows: OperationsMetadata> in 2).

<wfs:Query typeName>: description of the WFS request type and service name;

<ogc:PropertyIsLike/>: is the OGC filter encoding specification interface which developed to describe the value of the element property field comparison operation, the specific content of the definition under the <ogc:PropertyName/> and <ogc:Literal/>.

The results are the GML encoding geographic data, available on the client resolving the requested graphic elements and attribute information, for further conversion, rendering, and visualization can meet user operational requirements, without having to understand the distributed storage database or data source.

4 Experimental Analysis

The registration center design and development can be based on the above principle specification and design of geographic information sharing platform registry.The realization entironment of the registration center are: (1) windows XP professional SP3 operating system; (2)development language: a server-side C # and client JavaScript; (3) development environment: Microsoft Visual Studio.Net 2008.

4.1 Functional Design and Implementation

SOA-based geographical information sharing platform registry, all users and function design are:

Administrator, is the highest authority in the registry, primarily responsible for the management and maintenance of registry, edit and improve the realization of the function of various functional modules, data services, organizations and management services catalog, normal user specific authorization and cancellation of such permission.

Service providers, mainly distribute in the GIS server, such as ArcGIS Server, GeoServer servers, etc., store descriptions of WMS, WFS and other spatial information and function service through WSDL language in distributed servers. In this way, it can add data service and function service to the registry.

Ordinary users, discover and bind various types of services through the UDDI to establish a spatial information catalog service, while spatial analysis services can build spatial filtering and geo-processing services by sending XML format specific request to the GIS servers, parsing the returned XML/GML data.

4.2 Experimental Summary

According to the above SOA-based geographical information sharing platform registry design, the experiment reached the following conclusions:

(1) the various types of spatial information services (including the common WMS, WFS and WCS, etc.) in the release and registration system can be remote data center or database.

(2) implements the search and binding function for spatial information services, allow authorized users to discover needed spatial information services.

(3) establish realization mechanism for services and analysis function, making functional operation separated from the underlying data, access to data while no longer need the physical copy.

5 Conclusion

This paper studied the building theoretical principles and implementation for SOA-based geographic information sharing platform registry, designed solution of establishing the registry and had the experimental validation. The results showed it idea to establish an effective registry. As the development of spatial information services research depth, the semantics support of spatial information services, service chain, intelligent service-oriented semantic search need further study.

References

1. Li, D.R., Shao, Z.F.: The new era for geo-information. Science in China Series F: Information Sciences 52(7), 1233–1242 (2009)
2. Chen, Y.D., Cui, T.J., Lu, Z.W.: The model of spatial information service architecture based on SOA. Geomatics World 12(6), 49–52 (2008)
3. Gong, J.Y., Li, D.R.: Review of the development of geospatial information service technology. Bulletin of Surveying and Mapping 5, 5–10 (2008)
4. Deng, S.J., Lv, X.H., Wang, L.M., et al.: Reasearch on geographical information service architecture based on SOA. Journal of Geomatics Science and Technology 26(4), 261–264 (2009)
5. Zhao, S., Guo, J.Z., Chen, Y., et al.: A geospatial information grid registry based on UDDI extension. Journal of Geomatics 33(2), 36–38 (2008)

6. Di, L.P., Chen, A.J., Yang, W.L., et al.: The development of a geospatial data Grid by integrating OGC Web services with Globus-based Grid technology. Concurrency and Computation: Practice and Experience 20, 1617–1635 (2008)
7. Open GIS Consortium(OGC). OpenGIS Web Map Service (WMS) Implementation Specification (1.3.0) (March 15, 2006), http://www.opengeospatial.org/standards/wms
8. Open GIS Consortium (OGC). OpenGIS Web Feature Service (WFS) Implementation Specification (1.1.0) (May 3, 2005), http://www.opengeospatial.org/standards/wfs
9. Open GIS Consortium (OGC). Web Coverage Service (WCS) Implementation Standard (1.1.2) (March 19, 2008), http://www.opengeospatial.org/standards/wcs
10. Open GIS Consortium (OGC). OpenGIS Filter Encoding Implementation Specification(1.1) (May 3, 2005), http://www.opengeospatial.org/standards/filter

Design of Wideband Vivaldi Antenna Array

Chang Liu[1,2], Chenjiang Guo[1], and Haobin Zhang[2]

[1] School of electronic and information of Northwestern Polytechnical University, 710072, Xi'an, China
liuchang535583@yahoo.com.cn
[2] The science and info control national lab., 610036, chengdu, China

Abstract. Designing a finite wideband Vivaldi antenna array is investigated in this article. Firstly, the optimal finite array element is designed by periodic boundary for the sake of reducing the computation resource. The optimized antenna exhibits good active reflection coefficient and gain performance over the operating frequency range over 6 to 18GHz. Then small arrays with optimal element parameters construct. Simulation analysis and experimental measurements are conduct to investigate mutual coupling effects on the performance.

Keywords: Wideband, Vivaldi antenna, finite array, active reflection coefficient.

1 Introduction

The tapered slot antenna (TSA) was initially introduced as an array element by Lewis et al. [1] in 1974. Because of its potential for wide-band and wide scan arrays, Vivaldi antenna array has become prime candidate for high-performance phased-array systems[2] [3],[4]. Many valuable insights were obtained and Vivaldi antenna gained growing attention [5-8]. Parametric studies on infinite Vivaldi antennas were implemented to gain an insight into the cause-effect relationship of different design parameters and antenna array performance [7-8]. However, very little work focuses on the finite array, and the relationships between antenna parameters and array performance are not well understood, because mutual coupling between the antenna elements is significant in determining the ultimate performance.

In this study, our objective is to design an 8×8 Vivaldi antenna array operating in the active mode. Due to the large scale of the array and limited computational resources, it is impossible to simulate the array directly. Instead, we simulate one element cell with periodic boundary, which can provide reasonably accurate and reliable results in an acceptable amount of time. The optimized antenna exhibits good active reflection coefficient and gain performance over the operating frequency range over 6 to 18GHz. Having achieved the optimized design of an infinite Vivaldi array, we construct some small arrays with optimal element parameters. Simulation analysis and experimental measurements are conduct to investigate mutual coupling effects on the performance and isolation between two polarizations which demonstrate the reasonableness of our design.

D. Zeng (Ed.): Future Intelligent Information Systems, LNEE 86, pp. 189–194.
springerlink.com © Springer-Verlag Berlin Heidelberg 2011

2 Optimal Design of the Array

A typical Vivaldi element structure was proposed in [1] and [4]. Elements separated by metallic posts are placed on a metallic ground plane. The bilateral slotline is terminated at one end with a circular slot cavity and at the other end it opens into an exponentially tapered slotline with an opening rate of R, which is defined below. The stripline feed is terminated in a radial line stub. In this design, the array element space 10mm is prescribed and the substrate used is RO-4230 of thickness 1.524mm. The exponential taper profile is defined by the opening rate R and two points P1(z1,y1)and P2(z2,y2)

$$y = c_1 e^{R \cdot z} + c_2 \tag{1}$$

where

$$c_1 = \frac{y_2 - y_1}{e^{Rz_2} - e^{Rz_1}}$$

$$c_2 = \frac{y_1 e^{Rz_2} - y_2 e^{Rz_1}}{e^{Rz_2} - e^{Rz_1}}$$

In particular, it is found that the upper operating frequency is limited by the diameter of slot cavity D_{SL} and radius of stripline stub R because of the presence of the anomaly. Therefore, an appropriate design of D_{SL} and R are achieved to ensure the upper frequency f_U around 18GHz as a starting point.

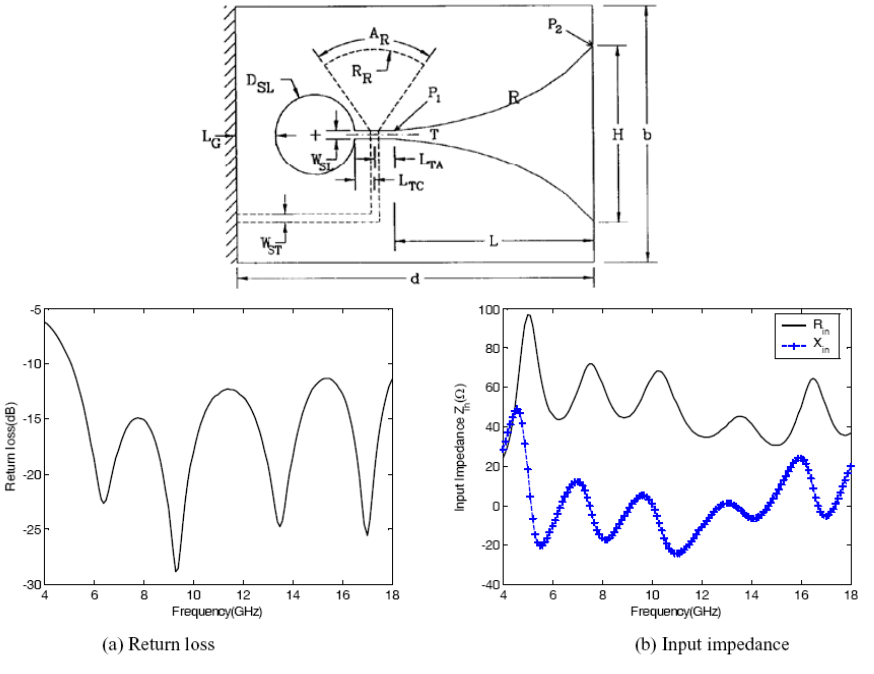

(a) Return loss (b) Input impedance

Fig. 1. Vival element structure and the optimized array results

After a limited amount of numerical "cut and try", optimal parameters are chosen as follow: $D_{SL=}$ R-2.6mm, L_{TC}=L_{TA}=1mm,W_{ST}=W_{SL} =0.6mm H = 8mm, R =1mm^{-1} and d = 30mm. The corresponding return loss and input impedance results are plotted in Fig. 1.

It is shown that the desired return loss performance has been achieved over the overall frequency range of 6 to 18GHz, with respect to the characteristic impedance Z = 50Ω. radiation patterns of an 8×8 single-polarized array at different frequencies (6, 9, 12, 15, 18GHz) are measured. Table 1 shows the corresponding gain and beamwidth results. The designed antenna exhibits good active reflection coefficient, isolation, and gain performance over the operating frequency range of 6 to 18GHz.

Table 1. Gain and Beamwidth results of the 8×8 array

Frequencies(GHz)	Gain(dB)	Beamwidth(°))
6	15.4	31.6
9	19.0	20.3
12	21.3	15.8
15	23.2	13.1
18	24.7	11.2

3 Mutual Coupling of Finite Array

Above simulations are carried out using the periodic boundary conditions by modeling a unit cell instead of modeling the entire array. The entire array can be considered as an infinite single-polarized array, which exhibits some differences with the proposed finite array, as expected. Therefore, we simulate some small arrays to investigate the mutual coupling between the same depolarized elements and their effects on return loss, which provides an insight into the performance of the proposed array.

Firstly, a single element antenna is considered as the reference. Taking the unit cell as an independent antenna, the input impedance and return loss are calculated and shown in Fig. 2, which differs greatly with those of infinite array. It is shown that the return loss of an independent Vivaldi antenna has completely deteriorated, due to the increasing swing amplitude of the input impedance.

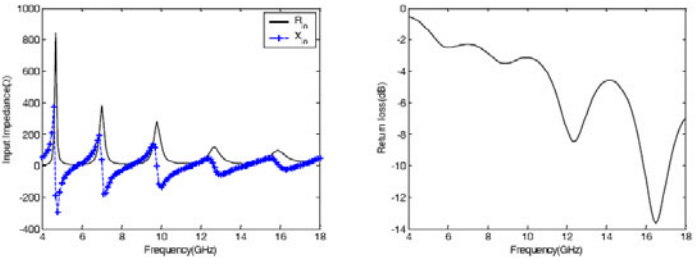

(a) Input impedance (b) Return loss

Fig. 2. Simulation results for the performance of an independent element

A 2×2 single-polarized array is considered to study the mutual coupling coefficients and they effects on return loss results. Considering the active case, in which all elements are excited simultaneously, the active reflection coefficient for port #1 is

$$\Gamma_{11} = \frac{b_1}{a_1} = S_{11} + S_{12}\frac{a_2}{a_1} + S_{13}\frac{a_3}{a_1} + S_{14}\frac{a_4}{a_1} \tag{2}$$

Therefore, the driving impedance and active reflection coefficient can be calculated at port #1.

Simulated input impedance and S parameters results are shown in Fig. 3 (a) and (b),while the active driving impedance and active reflection coefficient are shown in Fig. 3 (c) and (d). It has been found that, though the S_{11} of the 2 by 2 array has the similar aggravation as that of the single element antenna (shown in Fig. 2(a)), the active reflection coefficient exhibits greatly improved wide-band performance, which is very similar to the return loss of the element in an infinite array (shown in Fig. 1(a)). It attributes to the improvement of the active driving impedance by the mutual coupling from other adjacent elements. Therefore, the designed finite single-polarized array can be expected to have a desired bandwidth the mutual coupling from other adjacent elements. Fig. 4 shows the comparison of simulated and measured S-parameters results, which are in good agreement.

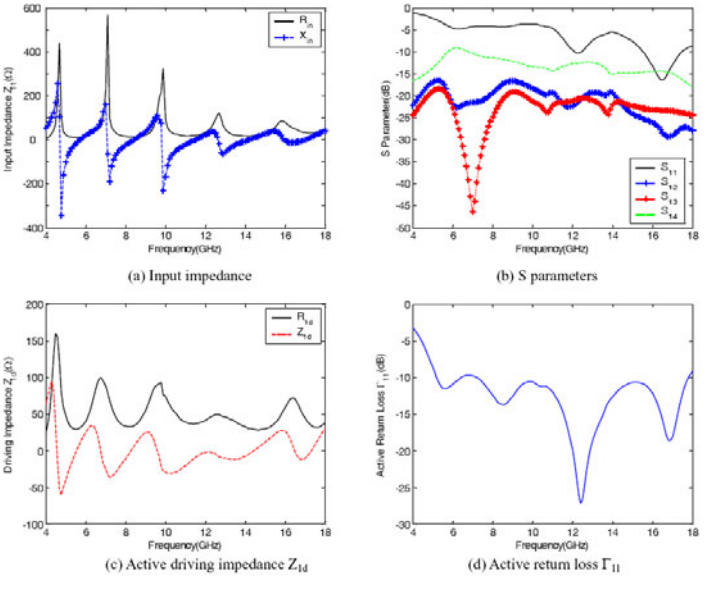

Fig. 3. Simulation results for the performance of 2×2 Elements array

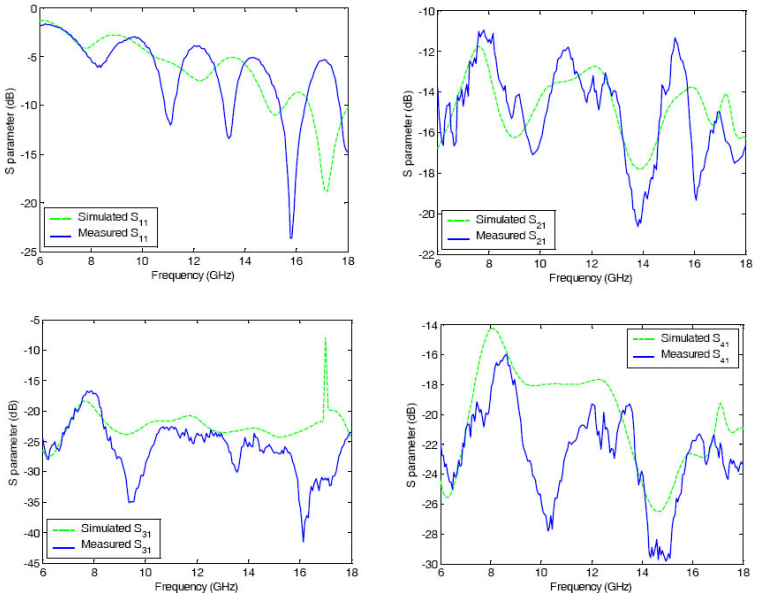

Fig. 4. contrast of measured S-parameters and the simulated results

4 Conclusion

Design of Vivaldi array has been presented by calculating one cell with periodical boundary. Key parameters which affect the bandwidth of Vivaldi array are found. Simulation return loss result of the unit cell with periodical boundary is lower than -10dB over the wide frequency range over 6 to 18GHz. Theoretical simulation results of small arrays demonstrate that the designed Vivaldi antenna can be expected to have good active reflection coefficient, isolation, and gain performance. Measured return loss results exhibit good agreement with simulated results. However, theoretical studies or simulations on larger arrays should be conducted to further demonstrate that a finite Vivaldi array, e.g. 8×8 array, can achieve desirable performance with the optimum element parameters which are obtained for an infinite array.

References

[1] Lewis, L.R., Fasset, M., Hunt, J.: A broadband stripline array element. In: IEEE Antennas Propagation Symposium, Atlanta, GA, pp. 335–337 (June 1974)

[2] Gibson, P.J.: The Vivaldi aerial. In: Proceedings of the 9th European Microwave Conference, Brighton, U.K, pp. 120–124 (1979)

[3] Janaswamy, R., Schaubert, D.H.: Analysis of tapered slot antenna. IEEE Transaction on Antennas and Propagation 35(9), 1058–1065 (1987)

[4] Schaubert, D.H.: Endfire tapered slot antenna characteristics. In: Sixth International Conference on Antennas and Propagation, vol. 1, pp. 432–436 (1989)

[5] Thiele, E., Taflove, A.: FD-TD analysis of Vivaldi flared horn antennas and arrays. IEEE Transaction on Antennas and Propagation 42(5), 633–641 (1994)
[6] Oraizi, H., Jam, S.: Optimum design of tapered slot antenna profile. IEEE Transaction on Antennas and Propagation 51(8), 1987–1995 (2003)
[7] Shin, J., Schaubert, D.H.: A parameter study of stripline-fed Vivaldi notch-antenna arrays. IEEE Transaction on Antennas and Propagation 47(5), 879–886 (1999)
[8] Chio, T.-H., Schaubert, D.H.: Parameter study and design of wide-band widescan dual-polarized tapered slot antenna arrays. IEEE Trans. Antennas and Propagation 48(6), 879–886 (2000)

Quality Factors of Business Value and Service Level Measurement for SOA*

Youngkon Lee[1] and Ukhyun Lee[2]

[1] e-Business Department, Korea Polytechnic University,
2121 Jeongwangdong, Siheung city, Korea
yklee777@kpu.ac.kr
[2] Dept. of Computer & Information Science, Hanbuk University,
233-1 Sangpae dong, Dongducheon city, Korea
uhlee@hanbuk.ac.kr

Abstract. This paper presents the quality factors of web services with definition, classification, and sub-factors for business and service level measurement. Web services, main enabler for SOA, usually have characteristics distinguished from general stand-alone software. They are provided in different ownership domain by network. They can also adopt various binding mechanism and be loosely-coupled, platform independent, and use standard protocols. As a result, a web service system requires its own quality factors unlike installation-based software. For instance, as the quality of web services can be altered in real-time according to the change of the service provider, considering real-time property of web services is very meaningful in describing the web services quality. This paper focuses especially to the two quality factors: business value and service level measurement, affecting real world business activities and a service performance.

1 Introduction

The importance of web services has been increased as an enabler of Service Oriented Architecture (SOA) [1]. Most software communities who are related in the plan, development and management of SOA have significantly interested in web service quality.

Web services have distinguished characteristics different from installation-based software because of their service-oriented nature (see Fig. 1). The provider and consumer of services could belong to different ownership domains so that there are many cases that a service cannot meet the consumer's service requirements in respect of service quality and content. Web services are usually invoked through networks, so the network performance critically affects the overall web service quality. As a web service client binds to a web service server with loosely-coupled manner and various binding mechanisms, both client and server could be bound easily and flexibly [2]. On the contrary, the client and the server cannot guarantee proper operating performance. They may be operated platform-independently, so preserving interoperability requires

* This research has been sponsored by NIA (National Information Society Agency) in Korea.

D. Zeng (Ed.): Future Intelligent Information Systems, LNEE 86, pp. 195–204.
springerlink.com © Springer-Verlag Berlin Heidelberg 2011

more efforts in regard to service contents and protocols. Even though web services are based on standard protocols of communication, misconception of the protocols can produce critical results in non-interoperable services.

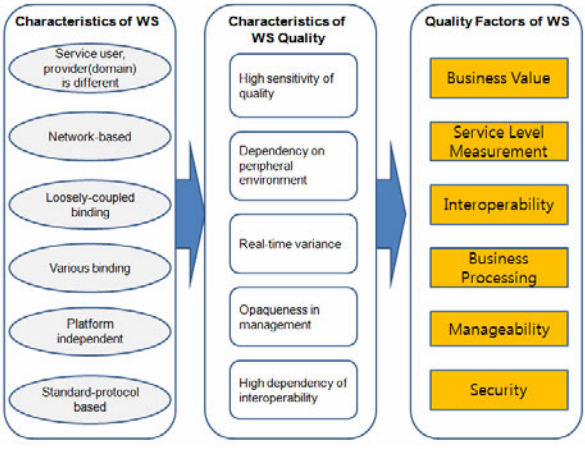

Fig. 1. Extracting Quality Factors of WS

Due to the characteristics described above, web services show distinct quality characteristics from those of general software. Firstly, the usage of web services is highly sensitive to their quality, especially in regard to performance and business. A web service consumer is willing to change a service while using it if it cannot satisfy his requirements on performance or business. Most of web service consumers have an interest in the quality of web services and thus would correspond to the quality problem immediately. Secondly, as web services are operated in the close relation with the other systems, the web service quality depends on the peripheral technical environment: network, security system, and software resource system, UDDI [3] and business effectiveness. For example, the quality of transport media influences deeply on the web service quality. Consequently, even though a web service shows very rapid response time on the server side, we cannot expect rapid response time if the bandwidth of transport network is narrow. In the same way, although a web service has been implemented efficiently, it is difficult to expect good performance of the web service when a service provider has low processing capability.

Thirdly, a web service client and a server are bound loosely and variously. The web service client can change the web service server dynamically, so the client can experience considerable variation of web service quality. The client can change web services in real-time when the quality is not satisfied. Fourthly, a web service consumer is usually not able or restricted to manage and control a web service, because in many cases a consumer's domain is different from a service provider's. Accordingly, the web service consumer requires guaranteeing the higher level of web service quality. Finally, more effort to assure interoperability of web services is required, because a web service client and a server system could be deployed on heterogeneous platforms and web service developers could misunderstand related standards.

To summarize above, the characteristics of web services lead to the distinguished characteristics of web service qualities unlike those of installation-based software. Therefore, it is required to induce quality items in alignment with consideration of these characteristics of web service quality during overall web service lifecycle. The value of these service qualities can be described in a script formalized according to *WSQDL* (Web Service Quality Description Language) [4].

In this paper, we provide the web service quality factors for representing business value and measuring service level metric. The business value quality has the meaning that it can provide a criterion for evaluating the value of web services in regard to the business. The quality factor of service level measurement is used to measure service performance in metric values. We also analyze the sub-factors of both quality factors, which could be measuring targets in real world.

In section 2, we summarize the related works about web service quality. Section 3 presents the overall classification for web service quality factors and section 4 describes the business value and service level quality factors, and we conclude in section 5.

2 Related Works

The study in [5] revisited the state of the art in managing *QoS* in distributed systems and to raise the new issues in SOA. They discussed further open issues related to *QoS* management of Web services in general. Subsequently, they investigate how existing approach from the area of distributed systems and performance management help address some of the *QoS* management issues.

The paper [6] presented a *QoS*-based web service framework, called *WebQ*, which enables to select appropriate Web services, dynamically bind the services with the underlying workflow, and perform the refinement of existing services. Since evaluation and refinement of services tend to be subjective, the generation of them needs a formal matrix, which can measure the requirements and quality of services. In the *WebQ* framework, criterion is quantitatively set to evaluate whether a particular service is appropriate for specific service flow and to define service quality. This generic framework can be applicable to the various domains, such as e-commerce, medicine, and bioinformatics.

The study [7] presented a conceptual framework for evaluating the applicability and viability of web services to create enterprise information architectures that will support the business requirements of manufacturing enterprises. It examines economic, technical, and organizational contexts that will influence the ability of manufacturing enterprises to deploy web services to support virtual enterprise operations.

In the work [8], they focused on the composition of services with *QoS* properties, which is similar to integration process in workflow management systems. The goal of a composition is to have a collection of network resident services, whose functionality can be automatically discovered and integrated into applications. The common point of service composition and workflow management is that both presume the existence of a central peer, which is mediating the execution.

In *WSDM* (Web Service Distributed Management) specification [9], they provide a framework to manage the quality level of web services by introducing the concept of

management capability in the type of MOWS (management of web service) and MUWS (management using web service).

3 Classification for Quality Factors

A web service quality factor refers to a group of items which represent web service's functional and non-functional properties (or values) to share the concept of web services quality among web service stakeholders. Based on the characteristics of web service quality described previously, the web service quality factors are composed of business value quality, service level measurement quality, interoperability quality, business processing quality, manageability quality and security quality.

Based on whether quality factors are related with business perspective or system perspective, they can be categorized into two groups: the business quality group and the system quality group (Fig. 2). Business quality group includes only the business value quality factor. System quality group is comprised of the variant quality part and the invariant quality part. The variant quality part includes quality factors whose values can be dynamically varied in run-time while a service is being used. On the while, the invariant quality part refers to quality factors whose values are determined as soon as the service development is completed. The invariant quality part includes interoperability quality, business processing quality, manageability quality and security quality.

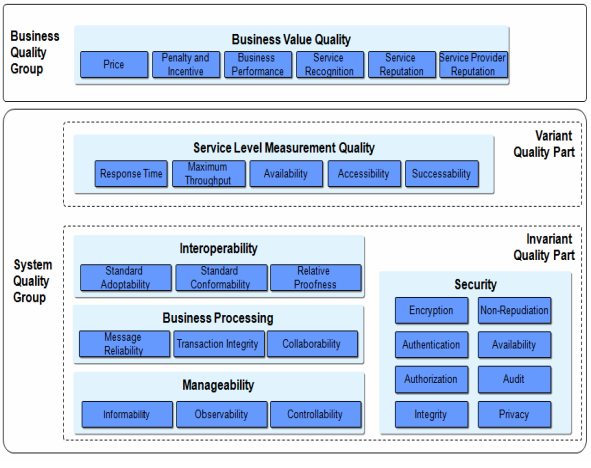

Fig. 2. Classification of web service quality factors

Business value quality refers to a business perspective to help to make the right selection of a service by evaluating the business value of web services. For evaluating business value, it includes the sub-factors: price, penalty and incentive, business performance, service recognition, service reputation and service provider reputation. Service level measurement quality measures the performance of web services in

numeric value: response time, maximum throughput, availability, accessibility and successability.

Interoperability quality is a quality factor to evaluate whether a web service system conforms to standard adoptability, standard conformability and relative proofness. Web services may be used in mission-critical work between business partners, and in that case reliability and stability of web services are very important quality items. The business processing quality factor evaluates these items, including messaging reliability, transaction integrity and collaborability. Manageability quality is about to whether web services are manageable or managed items, including informability, observability and controllability, web services are also vulnerable to security attack and fraud of their frequent exposure to open networks. Security quality guarantees the safety of web services for use. That is, it is a collection of quality items to evaluate the functionality and the metric performance of a security system. It includes the sub-factors: encryption, authentication, authorization, integrity, non-repudiation, availability, audit and privacy.

4 Quality Factors

A. Business Value Quality

When a service party decides to use a web service for business, it should consider surely the value of the service on the business. In some cases, the web service may give positive value such as profit, convenience, collaboration to the service party. But in the other cases, it may impose more burdens on the party than the value it delivers. For example, it may require an extra cost for keeping the service in stable condition or cause economic loss due to service provider's failure to meet promised quality. As a result, web service consumers tend to be very sensitive generally to the value of web services on a business.

The business value of web services means the economic worth delivered by applying web services on a business. The business value depends on the price of a service, a penalty/compensation policy, service recognition, service reputation and service provider reputation. In addition to those sub-factors, business benefit, profit, and ROI (return on investment) caused by web services could be added in the business value quality. But, it's very difficult to evaluate these values by the effect caused by web services alone because the values depend heavily on each individual business context. Thus, we exclude the business benefit, profit, and ROI from the business value quality.

The price and the penalty/compensation sub-factors represent the monetary value, which could be determined by a service provider or the contract between a service provider and a consumer. The service recognition, the service reputation and the service provider reputation are related with the trust of web services, so they could be evaluated as a part of business value.

Business value quality provides a business perspective to help to make a right selection of service by evaluating the business value of web services. Consumers refer to the value of this factor to reach a decision to select the most appropriate web service for a given business.

■ Price

The price sub-factor is a monetary value of service that a consumer pays for services to a provider while or after using web services. The price of a web service can be determined by a service provider. A service consumer considers the price of a web service in respect of the functions, contents, and the quality of the web service in order to make the decision whether he uses the web service. For general software, users pay overall price for a software package. On the contrary, a consumer has to pay the fee of a web service continuously based on the amount of time usage or use data, so he has continuously interest in the service price. Therefore, the price of a web service affects in the usage of the web service. A service provider should decide the appropriate price by considering the service quality and value. In relation to the price factor, a billing method is also important quality factor for measuring business value of a web service. For example, a reasonable and systematic billing system can improve the trust of a web service. A convenient billing system, a discount policy, and mileage points enhance consumer's loyalty.

■ Penalty and Incentive

Penalty or compensation is the financial compensation for business losses due to non-fulfillment of a contract or failure to meet promised quality. Penalty can be charged to a service provider or a service consumer based on a contract. When a service provider fails to keep service quality levels specified in the contract, the service provider needs to compensate for the loss of a service consumer. The compensation rules need to be specified in the contract. Penalty can be calculated based on service downtime, maximum or average response times, or security requirements of a service, and so on. The performance monitoring of the web service is necessary to determine whether compensation is required or not, and how much compensation is required. Penalty can be charged to a service consumer when the consumer breaches the contract unilaterally, which brings financial loss to a service provider.

On the contrary, incentives as positive rewards can be specified in a contract. For example, an incentive can be paid when a service provider has provided higher quality than the quality level specified in the contract. In addition, an incentive can be paid to a service consumer when the servicer consumer uses a service more than a certain usage level during a given time period.

■ Business Performance

In the case that a service provider provides commodities and services in the real world as well as information by web services, the performance of business activity provided for them affects the business value of the web services directly. For example, consider a delivery service with which web services are provided for an order and a payment process. In this case, all the processes including the order, confirmation, delivery, notification and payment, which are all connected within the information flow and business activity flow. Overall service quality is related with the capability of the business body as well as the quality of web services.

Business performance is defined as the capability of a business party performing business activities for services. The business performance can be measured by the time it takes to complete a business service or the throughput. The time to complete is

composed of the duration for performing business activities and a latency for ready or a condition. The throughput is the amount of outcomes for a service per a unit time.

■ Service Recognition

Service recognition quality is defined by how many potential consumers perceive the existence of a service. That is, it is related to the popularity of the service. A highly recognized service means that it has more potential for many people to use the web service. Service recognition can be measured by various methods. For example, it can be estimated by the number of clicks on a service description in a service registry or the number of page views on a service web page.

Service recognition is not derived from the service consumer's experience of service usage. Also, the service recognition level can be improved through promotion or advertising of a web service. However, it does not guarantee the superiority of the other quality factors of the web service such as response time, availability, and reliability.

■ Service Reputation

Service reputation is a social evaluation of service consumers toward a web service. It refers to consumers' opinions on the quality of web services. Service reputation can be evaluated by performing a survey or vote on service quality and consumer satisfaction. In addition, service reputation can be estimated from the replies, comments or reviews of service consumers. Service reputation is very influential for potential service consumers to select web services.

While service recognition reflects expectation of the service value before use, service reputation mainly refers to the experienced service quality after use.

■ Service Provider Reputation

Service provider reputation is the opinion of the group of service parties toward a service provider on certain criteria. Service provider reputation is an asset that gives the service provider a competitive advantage because a service provider with a good reputation will be regarded as a reliable, credible, trustworthy and responsible one for service consumers. It can be sustained through consistent quality management activities on services as a whole. Service provider reputation can be influenced by customer's previous experience on other services of the provider as well as advertisement or public relations.

Service consumers pay attention to service provider reputation as well as a service itself. Service provider reputation can be estimated by brand value, financial soundness, the quality of customer service, technical support and sustainability of a service provider.

B. Service Level Measurement Quality

As a service could be provided by third parties and invoked dynamically via network, service performance might be varied by the network speed or the number of connected users at a given time. Service Level Measurement quality is a set of quantitative attributes which describe the runtime service responsiveness in a view of

consumers. This quality factor represents how quickly and soundly web services can respond which can be measured numerically on system.

Service Level Measurement Quality consists of five sub-quality factors; response time, maximum throughput, availability, accessibility, and successability.

■ Response Time

Response time refers to duration from the time of sending a request to the time of receiving a response. The response time can be varied by the point of measurement and affected by three types of latency: client latency, network latency and server latency as depicted in Fig. 3.

Client latency refers to the delay time caused by a client system in the whole processing time for a service request. It is a sum of the time taken between 'a client application requests a service' function and 'the request is sent by a client' function (t1-t2), and the time taken between the 'response arrives to the client' function and 'the application system receives the response' function (t7-t8).

Network latency refers to the time taken on a network for transmitting request message and response message. It is a sum of the time taken between 'a client sends a request' function and 'the web services server receives the request' function (t2-t3), and the time taken between 'the server sends a response' function and 'the client receives the response' function (t6-t7).

Server latency is a delay time caused by a server system in the whole processing time for a service request. It is a sum of the time taken between 'the server sends the request' function and 'web services receives the request' function (t3-t4), 'the time taken for processing the service' function (t4-t5), and the time taken between 'the response is sent by the web services' function and 'the server receives the response' function (t5-t6).

Three types of latency and response time can be calculated by the following formulas.

$$ClientLatency = CL1 + CL2$$
$$NetworkLatency = NL1 + NL2$$
$$ServerLatency = SL1 + SL2 + SL3$$
$$ResponseTime = ClientLatency + NetworkLatency + ServerLatency$$

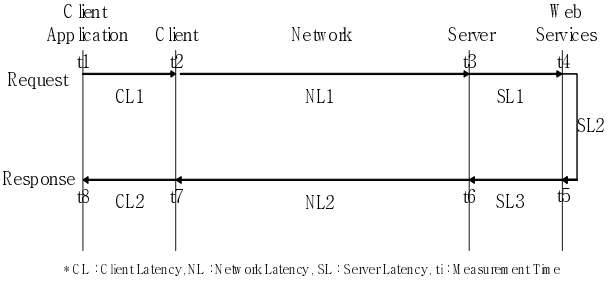

Fig. 3. Response Time and Latency

■ Maximum Throughput

Maximum throughput refers to the maximum amount of services that the service provider can process in a given time period. It is the maximum number of responses which can be processed in a unit time. The following formula expresses the maximum throughput.

$$Maximum\ Throughput = \max\left(\frac{Number\ of\ \mathrm{Re}quests\ \mathrm{Pr}ocessedbyService\ \mathrm{Pr}oviderIn\ Measured\ Time}{Measured\ Time}\right)$$

■ Availability

Availability is a measurement which represents the degree of which web services are available in operational status. This refers to a ratio of time in which the web services server is up and running. As the *DownTime* represents the time when a web services server is not available to use and *UpTime* represents the time when the server is available, Availability refers to ratio of *UpTime* to measured time. In order to calculate Availability, it is conveniently rather using *DownTime* than *UpTime* and it can be expressed as the following formula.

$$Availability = 1 - \frac{DownTime}{Measured\ Time}$$

■ Accessibility

Accessibility represents the probability of which web services platform is accessible while the system is available. This is a ratio of receiving Ack message from the platform when requesting services. That is, it is expressed as the ratio of the number of returned Ack message to the number of request messages in a given time. To increase accessibility, a system needs to be built in expansible architecture.

$$Accessibility = \frac{Numberof\ AckMessage}{Numberof\ \mathrm{Re}questedMessage}$$

■ Successability

Successability is a probability of returning responses after web services are successfully processed. In other words, it refers to a ratio of the number of response messages to the number of request messages after successfully processing services in a given time. 'Being successful' means the case that a response message defined in WSDL is returned. In this time, it is assumed that a request message is an error free message.

$$Successability = \frac{Numberof\ \mathrm{Re}sponseMessage}{Numberof\ \mathrm{Re}questedMessage}$$

5 Conclusion

In this paper, we presented the quality factors of business value and service level measurement of web services. It's difficult to evaluate objectively the business value of web services, because the value of recognition and reputation could be determined

subjectively in private user's opinion. The quality factor of service level can be measured systematically and objectively. Both quality factors have an importance in regard to business aspect and technology aspect and they compose of the major quality factors of web services. We did not provide the detail of measuring both quality factors. Further study is required to reveal how to measure and evaluate both qualities in detail.

References

[1] Mackenzie, C.M., et al.: Reference Model for Service Oriented Architecture 1.0. OASIS Committee draft (August 2006)

[2] Min, D., Kim, E.: A Study for Web service quality Model and Test guideline. NCA IV-RER-04052 (December 2004)

[3] UDDI TC Universal Description, Discovery and Integration v3.0.2 (UDDI) (February 2005), http://www.oasis-open.org/committees/uddi-spec/doc/spec/v3/uddi-v3.0.2-20041019.htm, OASIS Standard

[4] Lee, Y., Kim, E.: A Study for Web Service Quality Description Language. WSQDL NCA IV-RER-04052 (November 2006)

[5] Ludwig, H.: Web Services QoS: External SLAs and Internal Policies Or: How do we deliver what we promise? RC23092 (W0401-142) Computer Science (January 29, 2004)

[6] Patel, C., Supekar, K., Lee, Y.: A QoS Oriented Framework for Adaptive Management of Web Service based Workflows. School of Interdisciplinary Computing and Engineering University of Missouri-Kansas City (August 2005)

[7] Estrem, W.A.: An evaluation framework for deploying Web Services in the next generation manufacturing enterprise. Robotics and Computer Integrated Manufacturing 19, 509–519 (2003)

[8] Jaeger, M.C., Rojec-Goldmann, G., Muehl, G.: QoS Aggregation for Web Service Composition using Workflow Patterns. Technische Universit at Berlin (January 2007)

[9] Sedukhin, I.: Web Services Distributed Management: Management of Web Services (WSDM-MOWS) 1.0 (May 2005), http://docs.oasis-open.org/wsdm/2004/12/wsdm-mows-1.0.pdf, OASIS Standard

Service Chain Optimization (SCO) Scheme Based on Business Performance

Youngkon Lee[1] and Ukhyun Lee[2]

[1] e-Business Department, Korea Polytechnic University,
2121 Jeongwangdong, Siheung city, Korea
yklee777@kpu.ac.kr
[2] Dept. of Computer & Information Science, Hanbuk University,
233-1 Sangpae dong, Dongducheon city, Korea,
uhlee@hanbuk.ac.kr

Abstract. This paper presents a methodology for composing a SOA service chain by evaluating and selecting a service for the purpose of business result optimization. The methodology requires the business performance model for applied services to measure the value produced by services in a specific business context. Understanding the business characteristics where services are applied is a prerequisite for evaluating the business value of a business process that uses these services. The quality characteristics of SOA services could lead to the varieties of business optimization result, or to select simply optimal path of service chain. In this paper, we analyze the business performance and quality characteristics of SOA services and present a service composition scheme for optimizing business result.

1 Introduction

As Service-Oriented Architecture (SOA) has matured as a development, deployment, and governance paradigm, the performance of SOA deployments has received increasing attention. According to OASIS Reference Model for Service Oriented Architecture [1], SOA is a paradigm for organizing and utilizing distributed capabilities that may be under the control of different ownership domains. The service within SOA is a mechanism to enable access to one or more capabilities, where the access is provided using a prescribed interface and is exercised consistent with constraints and policies as specified by the service description.

Modeling the business characteristics of a service is a prerequisite for estimating the business value of the process that uses those services; likewise, the reliability of the service provided needs to be understood. Finally, establishing agreements about the business service is essential to long-term value chain improvement.

The discovery, selection, assembly, and management of services supporting business processes have to be performed in the pattern of optimizing for business results. Monitoring and evolution over time of both the set of services selected and of the performance of the business process itself affect the optimization.

Business value is maximized by enabling optimized real-life e-Business process and resource planning. Optimization can take place at both design time and run time.

D. Zeng (Ed.): Future Intelligent Information Systems, LNEE 86, pp. 205–213.
springerlink.com © Springer-Verlag Berlin Heidelberg 2011

Enabling technology includes definition of the framework for representing business service characteristics (how to represent cost, time, quality, and intended result), a means to describe the reputation of the service providers to solicit and report information, and a means to describe what we call business service-level agreement.

Services are performed by people, machines, and hardware/software applications, and represented by SOA services. The qualities of a business service are expressed by means of the Business Quality of Service (*bQoS*) [2], which is the business characteristic of a service for estimating the business value of one or a set of services in a business process. The nature of *bQoS* varies across industries and services. Businesses improve their business processes in order to reduce cost, improve efficiency, and otherwise improve business results. Parties related with the processes would include enterprises that deploy and manage solutions that use SOA techniques and which want to develop effective business processes and improve the performance and agility of those solutions.

In contrast to the *QoS* in the software/IT world, where the message is network/system oriented measurement that deals with network performance and system availability, the contents of *bQoS* is a business oriented measurement that deals with business characteristics of a service, such as price, performance, and quality.

Business Rating defines credibility, reliability and reputation of the service need to be understood for estimating the overall business quality of the process that uses those services. It has two major kinds of rating: Rating and Credentials. Rating are provided by the rating provider to show the ranking and reputation of a given service provider, in comparison of other providers. In contrast, Credentials are provided by the service provider itself to show the credibility of providing a given service.

Business Service Level Agreement (*BSLA*) is the agreement between the service requestor and the service provider, and primary address the *bQoS* content, Rating and Credentials. These contents are all business related. In contrast to the SLA in the software/IT world, where SLA is the contract between the service provider and the network/system provider, and the SLA is network/system oriented agreement that deals with network performance and system availability. The Business SLA is business oriented agreement that deals with price, time to deliver, and the quality/rating of the service.

In this paper, we present a new scheme, service chain optimization (SCO), to facilitate service composition and improve business results based on the value of business performance, business rating, and *BSLA*. Different deployments of services onto a business process have varying business value. SCO models the business process and the range of potential services, and then guides the selection and deployment of services based on the overall end-to-end business value. SCO evaluates services and their composition in the respect of optimizing end-to-end business results by measuring business performance, business rating, and BSLA.

In section 2, we summarize the related works about web service selection based on the *QoS* metrics. Section 3 presents the SCO process model including message flows and section 4 describes the business quality of services in the respect of SLA, and we conclude in section 5.

2 Related Works

In the paper [3], they discuss open research issues related to the *QoS* management of Web services. While the representation of Web services *QoS* properties has been addressed in current work, the implementation of *QoS* relies mainly on existing work related to allocating dedicated resources and managing the workload of shared resources. However, due to the virtualization of services and the trend to compose services to complex aggregates and to re-offer them, new approaches are needed to be able to implement the *QoS* of those complex services on a level required by business customers.

In a study [4], they applied the composition of services in the workflow domain for automated integration. In order to enable the selection of services and to leverage the advantages of the dynamic binding, the composition process must also take the *QoS* into account. They proposed a mechanism to determine the *QoS* in a composition by using a generic workflow model as a basis for the algorithmic aggregation of local *QoS* dimensions.

The paper [5] presented a *QoS*-based web service framework, called *WebQ*, which enables to select appropriate Web services, dynamically bind the services with the underlying workflow, and perform the refinement of existing services. Since evaluation and refinement of services tend to be subjective, the generation of them needs a formal matrix, which can measure the requirements and quality of services. In the *WebQ* framework, criterion is quantitatively set to evaluate whether a particular service is appropriate for specific service flow and to define service quality. This generic framework can be applicable to the various domains, such as e-commerce, medicine, and bioinformatics.

The study [6] presented a conceptual framework for evaluating the applicability and viability of web services to create enterprise information architectures that will support the business requirements of manufacturing enterprises. It examines economic, technical, and organizational contexts that will influence the ability of manufacturing enterprises to deploy web services to support virtual enterprise operations.

In *WSDM* (Web Service Distributed Management) specification [7], they provide a framework to manage the quality level of web services by introducing the concept of management capability in the type of MOWS (management of web service) and MUWS (management using web service).

3 SCO Process Model

This section describes the SCO model conceptually. Fig. 1 shows the conceptual model, and of messages flows with brief descriptions to demonstrate fitness of the overall SCO architecture. We also include timeline and sequence diagrams Fig. 2 and Fig. 3 to show how an implementation would use SCO model and build a continuous business process improvement loop. In Fig. 1, the business quality of Service is abbreviated as *bQoS*, business rating is abbreviated as *Rating*, and business service level agreement is abbreviated as *BSLA*. The service requester is the client system who asks the SCO system to find an optimal solution. Service providers provide business

services. Each service provider may offer the same service but with different *bQoS* and *Ratings*. Services may be running on different platforms with different implementations, but they all support message exchanges of *bQoS*, *Rating*, and *BSLA* information in the XML formats.

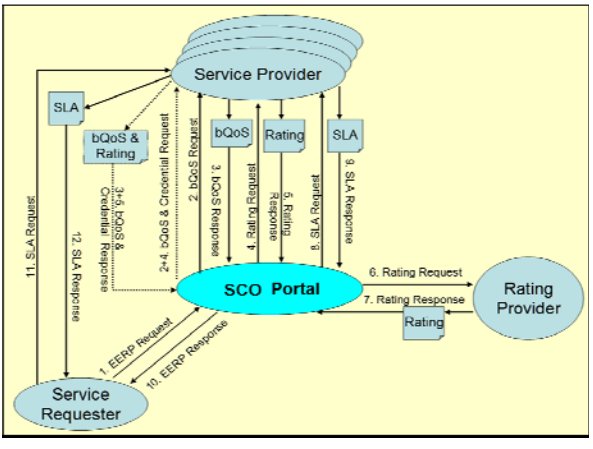

Fig. 1. Process Model for SCO

The SCO Portal accepts the request from the Service requester, performs *bQoS* and rating queries, calculates optimal solution(s), and then returns the result to the service requester.

The Rating Provider is a party unaffiliated with either the requester or the target of the rating request, such as a third party rating organization, given a reference to a particular business service and provider, issues either a number or a classification description.

There can be another way to implement the SCO without the SCO Portal. For example, there can be a case for some services providers and service consumers using SOA Registry-Repository to find each other, to exchange business quality of services information among them, and to begin negotiations for establishing Service Level Agreements (SLAs). The results of messages 2 through 9 in Fig. 1 are used to calculate the optimal deployment for a given set of services requests. A list of alternatives might be returned in message 10. Each step in the process would have a service provider determined for each service and for each alternative. Messages 11 and 12 are exchanged between the service requester and the selected service providers to define the *BSLA*. Fig. 2 is a message sequence diagram without the optional messages.

The service requester wants to search for the optimal end-to-end solution for a given set of services. Optionally, a protocol might send a single message combining messages 2 and 4 with the response combining messages 3 and 5. These are shown in Fig. 2 as messages 2+4 and 3+5. The Fig. 3 shows a message sequence diagram with the optional messages.

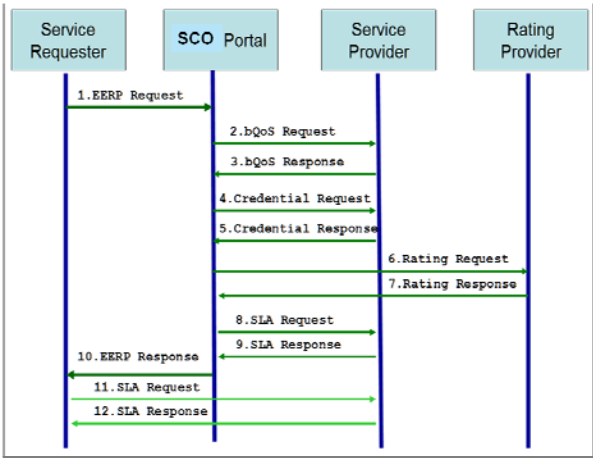

Fig. 2. SCO Message Sequence without optional messages

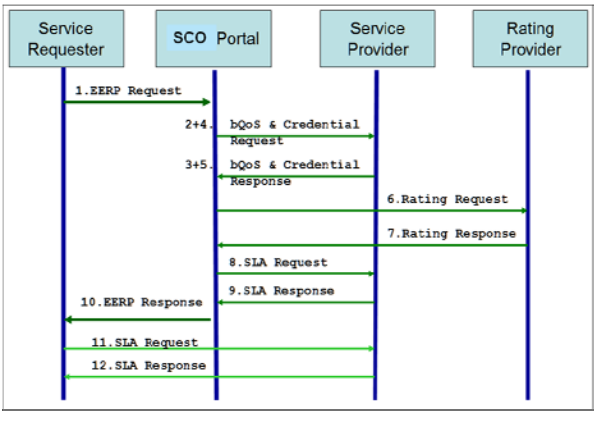

Fig. 3. SCO Message Sequence with optional messages

4 Business Quality of Services

SCO applies service discovery, composition, simulation, and optimization techniques in a novel way to improve business results. It takes as input a model of a business process and the range of potential services, and then guides the selection and deployment of services based on the end-to-end business value.

Business Quality of Service (*bQoS*) is an XML vocabulary by which a business application may communicate selected business characteristics of the service it provides. Modeling the business characteristics of a service is a prerequisite for estimating the business value of the process that uses those services.

Business Rating of Services is an XML vocabulary for information exchange on business credibility, reliability and reputation of the service providers. The creditability, reliability and reputation of the service need to be understood for estimating the overall business quality of the process that uses those services.

The business characteristics of the service defined in the *bQoS* and the Business Rating characteristics of the service defined in the Business Rating together will enable SCO to determine the varieties of optimization to be supported, and to select an optimal end-to-end solution.

Business Service Level Agreement for (*BSLA*) is an XML vocabulary for information exchange by which a business application can manage and evaluate services with agreed business quality of service, obligations and terms.

Modeling the business service-level agreements to manage and evaluate services and establishing agreements about the business service is essential to long-term value chain improvement. The details of the business service level agreement defined in the *BSLA* will enable SCO to determine the varieties of optimization to be supported, and to effectively manage the end-to-end business process.

For example, when a service requester sends an SCO request message to the SCO Portal, the SCO Portal can query the business characteristics and the business rating characteristics of each service within the business process for all qualified service providers in the network, and calculate the possible optimized alternatives for the requester. To achieve end-to-end business value for the business process, additional message exchanges can be done to establish the business service-level agreements, and to manage and evaluate services.

The b*QoS* is defined in XML Schema format that defines many quality measurement indicators as Fig. 4. It has the following major elements:

- *BQoSPrice* indicates price or cost for the service
- *BQoSPerformance* indicates time to complete the service, or in the alternative, throughput and latency
- *BQoSQualities* indicates additional properties and attributes
- Additional elements for quality of service

The Business Rating is for business reliability and reputation of the service and its services provider. It can have one or more of the following elements: *ListOfRating* element is for the rating provider to rating of service. Each Rating element in the *ListOfRating* is issued by a rating organization that has either an aggregated numeric rating or an aggregated classification description to represent the rating of the given business service.

Credentials element is for credentials for the service that the service provider owns or holds. Credentials are issued by organizations regulating the service, such as licenses, permissions, certifications, associations, or affiliations. This is not the credential for authentication in the security term. Instead, they are credentials that the service provider wishes to shown its credibility for providing the service. Each individual element in Credentials contains a single credential for the given business service.

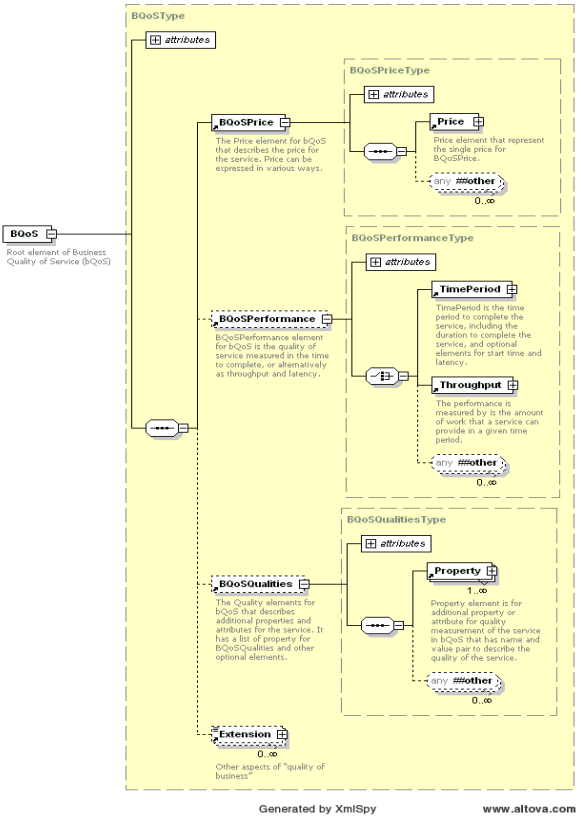

Fig. 4. XML Schema for Business Quality of Service

Additional elements for rating the service could be one or more elements of Performance Quality Assertion Evaluation that provides a mechanism for Service Rating Entities to render their evaluation for how well the Service Provider fulfills the Service Provider's own Quality Assertion(s) of its service.

BSLA defines business Service Level Agreement (SLA) between the service requestor and service provider for a given service. *BSLA* is a formal contract between a service provider and a client guaranteeing quantifiable business quality of service (*bQoS*) at defined levels.

It can have one or more of the following elements: *SLAParties* describes the parties involved in the SLA for the service *SLAParameters* describes the parameters for the service, which are defined ways of monitoring of *QoS* metrics. *SLAObligations* describes the agreed SLA obligations for the service. *SLATerms* describes the agreed SLA Terms for the service.

Fig. 5 is a XML Schema for *BQoSPerformance*, which is the quality of service measured in the time to complete, or alternatively as throughput and latency. There may be zero or one *BQoSPerformance* element present in the business quality of service.

```
<bQoS:BQoSPerformance xmlns:bQoS="..."
...>
  <bQoS:TimePeriod ... >bQoS:TimePeriod
Type
    <bQoS:Duration unitCode="clm66411:U
nitCodeContentType">cbc:DurationMeasure
Type</bQoS:Duration>
    <bQoS:Latency unitCode=="clm66411:U
nitCodeContentType">cbc:DurationMeasure
Type</bQoS:Latency> ?
    <bQoS:StartTime>udt:DateTimeType</b
QoS:StartTime> ?
    </bQoS:TimePeriod> |
  <bQoS:Throughput ...>
    <bQoS:Quantity unitCode="clm66411:U
nitCodeContentType"> ... </bQoS:Quantit
y>
    <bQoS:Duration unitCode="clm66411:U
nitCodeContentType"> cbc:DurationMeasur
eType</bQoS:Duration>
    <bQoS:Latency unitCode="clm66411:Un
itCodeContentType"> cbc:DurationMeasure
Type</bQoS:Latency> ?
  </bQoS:Throughput> |
  ...
</bQoS:BQoSPerformance>
```

Fig. 5. XML Schema for *BQoSPerformance*

5 Conclusion

In this paper, we presented a service chain optimization scheme for SOA. We proposed a new concept of *bQoS*, which includes overall metrics for evaluating a service chain for the direction of maximizing the business result. We presumed a SCO portal which provides the best service composition by evaluating the value of *bQoS* of each service chain. In this paper, we also assumed that service quality factors could be simply determined by service users case by case. However, in most cases, it would give them confusion in the process of selecting a quality factor. What is worse, there could be a case that a service consumer cannot know which kind of quality factors exist. Further study is required to define and classify the quality factor group for business case by case. It has to be studied what is the additional factors for *BQoSPerformance* in various business cases.

References

[1] Mackenzie, C.M., et al.: Reference Model for Service Oriented Architecture 1.0. OASIS Committee draft (August 2006)
[2] Min, D., Kim, E.: A Study for Web service quality Model and Test guideline. NCA IV-RER-04052 (December 2004)
[3] Ludwig, H.: Web Services QoS: External SLAs and Internal Policies. IBM T. J. Watson Research Center (October 11, 2004)

[4] Jaeger, M.C., Rojec-Goldmann, G., Muehl, G.: QoS Aggregation for Web Service Composition using Workflow Patterns. Technische Universit at Berlin (January 2007)
[5] Patel, C., Supekar, K., Lee, Y.: A QoS Oriented Framework for Adaptive Management of Web Service based Workflows. School of Interdisciplinary Computing and Engineering University of Missouri-Kansas City (August 2005)
[6] Estrem, W.A.: An evaluation framework for deploying Web Services in the next generation manufacturing enterprise. Robotics and Computer Integrated Manufacturing 19, 509–519 (2003)
[7] Sedukhin, I.: Web Services Distributed Management: Management of Web Services (WSDM-MOWS) 1.0 (March 2005), http://docs.oasis-open.org/wsdm/2004/12/wsdm-mows-1.0.pdf, OASIS Standard

QAM: QoS-Assured Management for Interoperability and Manageability for SOA*

Youngkon Lee[1] and Ukhyun Lee[2]

[1] e-Business Department, Korea Polytechnic University,
2121 Jeongwangdong, Siheung city, Korea
yklee777@kpu.ac.kr
[2] Dept. of Computer & Information Science, Hanbuk University,
233-1 Sangpae dong, Dongducheon city, Korea
uhlee@hanbuk.ac.kr

Abstract. This paper presents the quality factors of web services with definition, classification, and sub-factors for interoperability and manageability. In SOA systems, service consumers and service providers are usually placed in different ownership domains. They are also developed independently on various platforms and loosely-coupled by network. Services are consumed generally without direct management by service consumers. As a result, interoperability and manageability for SOA systems are core issues for enabling SOA services. This paper addresses the new concept of sub-quality factors for interoperability and manageability in the view point of management. This is a result of SOA project designed for implementing and evaluating Korea e-government system.

1 Introduction

In computing area, a service-oriented architecture (SOA) is becoming a core paradigm used during the phases of computing systems development and integration. A deployed SOA-based architecture will provide a loosely-integrated suite of services that can be used within multiple business domains. SOA also generally provides a way for consumers of services, such as web-based applications, to be aware of available SOA-based services. For example, several disparate departments within a company may develop and deploy SOA services in different implementation languages; their respective clients will benefit from a well understood, well defined interface to access them.

Service-orientation requires loose coupling of services with operating systems, and other technologies that underlie applications. SOA separates functions into distinct units, or services [1], which developers make accessible over a network in order to allow users to combine and reuse them in the production of applications. These services and their corresponding consumers communicate with each other by passing data in a well-defined, shared format, or by coordinating an activity between two or more services [2].

* This research has been sponsored by NIA (National Information Society Agency) in Korea.

D. Zeng (Ed.): Future Intelligent Information Systems, LNEE 86, pp. 215–222.
springerlink.com © Springer-Verlag Berlin Heidelberg 2011

Due to the service-orientation nature of SOA, a service client and a server are bound loosely and variously. The web service client can change the service provider dynamically, so the client can experience considerable variation of web service quality. The client can also replace a web service with others in real-time when the quality is not satisfied. In addition, a web service consumer is usually not able or restricted to manage and control a web service, because in many cases a consumer's domain is different from a service provider's.

The web service consumer requires a mechanism to ensure a level of web service quality. More effort to assure interoperability of web services is required, because a web service client and a server system could be deployed on heterogeneous platforms and web service developers could misunderstand related standards. A SOA management system would require an access point which could provide the capability of acquiring the web service status information and controlling a few operations.

This paper addresses the definition and classification of sub-quality factors for guaranteeing interoperability and manageability for managing SOA systems. This paper also introduces a new concept of *QoS-assured management* (*QAM*) which is based on refining sub-factors of interoperability and manageability.

In this paper, we provide the web service quality factors for representing interoperability and manageability. The interoperability has the meaning that it can provide a criterion for evaluating the value of web services in regard to the business. The quality factor of service level measurement is used to measure service performance in metric values. We also analyze the sub-factors of both quality factors, which could be measuring targets in real world.

In section 2, we summarize the related works about web service quality. Section 3 presents the overall classification for web service quality factors and section 4 describes the business value and service level quality factors, and we conclude in section 5.

2 Related Works

The specification in [3] presented the interoperability framework for ebXML. They discussed about test requirements for validating interoperability. They also addressed architecture for test harness composed of test driver and test service adapter, whose operation are described in test case scripts. In the test harness, the conformance test of ebXML system can be performed.

The paper [4] presented a *QoS*-based web service framework, called *WebQ*, which enables to select appropriate Web services, dynamically bind the services with the underlying workflow, and perform the refinement of existing services. Since evaluation and refinement of services tend to be subjective, the generation of them needs a formal matrix, which can measure the requirements and quality of services. In the *WebQ* framework, criterion is quantitatively set to evaluate whether a particular service is appropriate for specific service flow and to define service quality. This generic framework can be applicable to the various domains, such as e-commerce, medicine, and bioinformatics.

The study [5] presented a conceptual framework for evaluating the applicability and viability of web services to create enterprise information architectures that will

support the business requirements of manufacturing enterprises. It examines economic, technical, and organizational contexts that will influence the ability of manufacturing enterprises to deploy web services to support virtual enterprise operations.

In the work [6], they focused on the composition of services with *QoS* properties, which is similar to integration process in workflow management systems. The goal of a composition is to have a collection of network resident services, whose functionality can be automatically discovered and integrated into applications. The common point of service composition and workflow management is that both presume the existence of a central peer, which is mediating the execution.

In *WSDM* (Web Service Distributed Management) specification [7], they provide a framework to manage the quality level of web services by introducing the concept of management capability in the type of MOWS (management of web service) and MUWS (management using web service).

3 Interoperability Quality Factors

For executing web services, there should be no semantic and technical problems in processing a message transmitted between a service provider and a service consumer. No semantic problem refers to the process when a receiver understands a message in the exact meaning as the sender intended. A prerequisite condition for the mutual understanding of semantics in a message, the name of service, the name and type of parameters, the type of return vales are consistent between a service provider and a service consumer. This prerequisite condition may be satisfied if the service consumer implemented its system exactly according to the information of a service description (i.e. WSDL). But, this requires an agreement between all service parties for using service contents such as the name of items in e-documents and codes without any semantic problems. No technical problem refers to the conditions when all components for messaging including transport, security, reliability, encoding, and message structure coincide during implementation. Two systems of communication parties are said to be interoperable when they exchange and use information as if both could operate appropriately on the same platform. Implementing the messaging technology adapts related standards for assuring interoperability. If there is no standard available, one of service associates could adjust its technical implementation to the other's or both can agree to match their implementation specifications bilaterally. However, if a standard exists, the service associates can achieve interoperability by adjusting their implementation to the standard specification. Even though a service associate follows a standard, interoperability problems could arise in the case that an implementer misunderstands the standard or implements a module with a different intention. In some cases, the implementer may add new functions not described in the standard arbitrary. However this difference of a platform or network device could damage the interoperability between the two parties.

Considering the above cases, we can categorize the problems of interoperability into 3 groups: ① a system which has been implemented by not adapting a standard, ② a system which has been implemented according to a standard, with some functions implemented without regard to the standard, ③ a system which has been

implemented according to standards properly, but which has a problem of interoperability due to difference of platform of network. All of these issues must be considered in evaluating interoperability of a service system.

Interoperability quality includes standard adoptability, standard conformability and relative proofness as shown in Fig. 1. Standard Adoptability of web services evaluates how many functions of a web service are implemented by adopting related standards. The function of a web service means necessary requirements such as user authentication, data encryption, service delivery, transaction processing, etc. They could also include the original features of the business such as codes, document formats, business terms etc. Standard conformability of a web service evaluates whether the standards adopted to implement the functions of the web service conforms completely and correctively to the specification of the standards. Relative proofness evaluates whether a client and a service can communicate successfully on specific platforms.

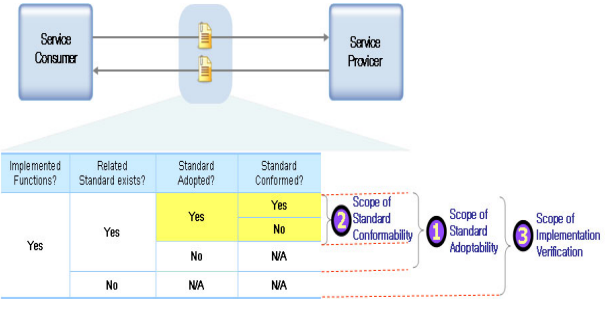

Fig. 1. Interoperability of web services

Standard Adoptability

In order to guarantee interoperability of web services, functions of a web service should be implemented by adopting related standards. Standard Adoptability is measured by the ratio of functions which are implemented by adopting related standards. Standard adoption function f is defined on the set of functions X={x_1, …., x_n} of a web service S and returns one of binary values, 0 and 1. f is formulated as follows:

$$f(x_i) = \begin{cases} 1 & \text{if function } x_i \text{ is implemented by adopting of related standards} \\ 0 & \text{otherwise} \end{cases}$$

Based on the standard adoption function f, standard adoptability of web service S is defined as follows:

$$StandardAdoptability(S) = \frac{\sum_{i=1}^{n} f(x_i)}{n}$$

Standard Conformability

Assuming that a web service S has n functions, and only m functions of them are implemented by adopting related standards. Standard conformability function g is

defined by the set of standard adopted functions Xa = { x_1, …., x_m} of web service S and returns one of binary values, 0 and 1. g is defined as follows:

$$g(x_i) = \begin{cases} 1 & \text{if function } x_i \text{ comforms all adopted standards} \\ 0 & \text{otherwise} \end{cases}$$

Based on the standard conformability function, standard comformability of web service S is defined as follows:

$$StandardConformability(S) = \frac{\sum_{i=1}^{m} g(x_i)}{m}$$

Relative Proofness

Relative proofness indicates that web services are successful in exchanging and using the information between two special system platforms. In real environments, services based on a technology platform cannot be fully interoperable with other services on a different technology platform even if it passes a standard conformability test. Whether the functions of web services are implemented by standards, vendor specification or non-standards, relative proofness of service interoperability is tested and verified in a real service platform that satisfies specific environments. VPI(Verified Platform Information) represents the basic information of an opponent's platform and additional descriptions of the verification when web services are tested and verified in real service environments of the opponent's platform.

$$Relative\ Proofness = \{VPI_1, VPI_2, \ldots, VPI_n\}\ if\ n\ is\ an\ integer$$

VPI(Verified Platform Information) can be any platform information as the followings, for example:

- Technology relative proofness of service interoperability verifies whether web services are able to maintain a basic communication capability between different system platforms such as J2EE, MS .Net.
- ESB(Enterprise Services Bus) relative proofness of services interoperability verifies whether the web services have a basic communication capability on middleware services, ESB.

4 Manageability Quality Factors

The more web services gain weight in business, the more the web service management scheme is needed for maintaining web service quality. Web service can be managed not only locally by a web service manager or provider, but also remotely by a consumer and a third party system. Web service management may be a prerequisite for the foundation of trust between a service consumer and a provider.

Manageability is defined as an ability which keeps a web service and its resources being manageable. At this point, the web service resource includes the software and

hardware components used by the web service and a platform on which the web service operates. Manageability can be achieved by implementing manageability capabilities, which are exposed as an access point, for each web service. A manageability implementation means an implementation of a manageability endpoint and all of its manageability capabilities.

The manageability capability helps targeting a web service, provides a function to monitor operational status, and controls operations along with web service protocol. As the manageability capability enables a service consumer to use web services with reliability and stability, it may be an important criterion for one to select a web service. The manageability is classified into 3 sub-factors: informability, observability and controllability.

Informability

The management of a web service requires the primitive information to be settled in the implementation phase in order to cope with troubles and to support a web service operation. Informability is a sub-quality factor to measure whether the primitive information can provide enough to manage a web service. The primitive information for managing a web service is divided into the manageability access information, assessment of web service management capability and the web service primitive information.

The manageability capabilities are exposed as a web service access endpoint thus a manageability consumer should get the access point for managing a web service and manageability access information. There are two ways to achieve this. One is to implement an additional web service whose functionality is to return a manageability endpoint for managing a web service. The other is to implement each web service equipped with an operation which returns its own manageability endpoint. The former has a disadvantage that a consumer has to know previously the reference of a web service which informs the access point of manageability capabilities. In the latter, a web service developer is burdened to implement an additional operation to inform the manageability endpoint. By utilizing both, a manageability consumer SHOULD get the manageability endpoint precisely through simple web service interface.

The manageability capability can provide primitive information of a web service to be managed. The primitive information includes web service properties (e.g. protocol version number, encryption algorithm, messaging pattern, etc), description of web services and their resources, characteristics of a manageability implementation, relation information between web services and resource. The manageability endpoint should also have an identity capability to discriminate whether two web services are the same by referring to their identity information.

Observability

Observability measures how effectively a manageability implementation can provide status information of a web service. The status of a web service system can be revealed by gathering the values of performance metrics. Therefore, observability can be evaluated by how effectively the metrics are taken when gathering information. The effectiveness of gathering metrics is represented in three aspects:

- How much are metrics provided?
- How exactly metrics are provided?
- Are the metrics provided in real-time?

A manageability consumer can get the status information by two methods: monitoring and notification. In the former, he can request the information anytime to a manageability endpoint actively, then a corresponding manageability capability returns a metric value based on monitoring results. In the latter, a manageability consumer subscribes previously significant events or issues to be notified. Then, when a subscribed event or trouble occurs, he will be notified. The target information to be observed includes all the operational status information such as performance metrics, a utilization ratio of memory, and a history of messages.

Controllability

There may be a case that a web service and its resources have to be regulated for keeping a stable status or coping with performance degradation. For example, a manageability consumer may increase the size of a web service message queue when there are too many messages received at the same time. If there is an error found in the messaging process, a web service platform should be stopped to cope with the problem. Thus, Controllability measures whether a manageability implementation can provide enough control functions to keep a web service in controllable status. The control functions are classified into operation control functions and configuration control functions.

- **Operation control functions**
  These are to change an operational status of a web service by executing commands such as start, stop, fork, and exit to the web service or related resources.
- **Configuration control functions**
  These are to modify the value of configuration parameters. For example, according to the change of a circumstance, a manageability consumer wants to adjust the value of a web service configuration such as a queue size, an encoding method and an encryption algorithm.

For measuring controllability, the scope, stability, voluntary, and easiness of control functions in a manageability implementation must be evaluated.

5 Conclusion

In this paper, we presented the quality factors of interoperability and manageability for SOA. We proposed a new concept of standard adoptability, a sub-factor of interoperability, which is a prerequisite for assuring conformability and relative proofness of SOA system. Theses sub-factors clarify how to measure the level of interoperability and refine efforts to assure interoperability. We defined the sub-factors, informability, observability, and controllability, which facilitate SOA management. The sub-factors for manageability can be evaluated whether the manageability capability for them is provided. Further study is required to define the granularity of functions for evaluating interoperability and manageability.

References

[1] Mackenzie, C.M., et al.: Reference Model for Service Oriented Architecture 1.0. OASIS Committee draft (August 2006)
[2] Min, D., Kim, E.: A Study for Web service quality Model and Test guideline. NCA IV-RER-04052 (December 2004)
[3] Durand, J.: ebXML Test Framework. Committee Specification Version 1.1 DRAFT, OASIS (October 11, 2004)
[4] Patel, C., Supekar, K., Lee, Y.: A QoS Oriented Framework for Adaptive Management of Web Service based Workflows. School of Interdisciplinary Computing and Engineering University of Missouri-Kansas City (August 2005)
[5] Estrem, W.A.: An evaluation framework for deploying Web Services in the next generation manufacturing enterprise. Robotics and Computer Integrated Manufacturing 19, 509–519 (2003)
[6] Jaeger, M.C., Rojec-Goldmann, G., Muehl, G.: QoS Aggregation for Web Service Composition using Workflow Patterns. Technische Universit at Berlin (January 2007)
[7] Sedukhin, I.: Web Services Distributed Management: Management of Web Services (WSDM-MOWS) 1.0 (March 2005), http://docs.oasis-open.org/wsdm/2004/12/wsdm-mows-1.0.pdf OASIS Standard

Application of Fuzzy Control in TIG Welding Seam Tracking

Jian-ping Jia, Wei Jin, Hong-li Li, and Shun-ping Yao

Key Lab of Robot & Welding Automation of Jiangxi
School of Mechanical and Electrical Engineering, Nanchang University
330031 Nanchang, China

Abstract. The TIG(Tungsten Inert Gas) automation welding procedure is highly nonlinear and time-various. Based on these characteristics, the fuzzy control approach is applied to the TIG welding seam tracking. The system structure of seam tracking and the specific design procedure of fuzzy controller are introduced. The fuzzy control rule and fuzzy control table are given. The V groove seam tracking experiment results show that this controller has Well-behaved control property and effect and the fuzzy control can be employed into the TIG welding seam tracking successfully.

Keywords: TIG welding; Seam tracking; Fuzzy control.

1 Introduction

The automatic seam tracking system first obtains deviation signals between welding torch and seam center by sensors and processes the deviation signals, then employs different algorithms to obtain displacements and drive welding torch to aim at seam in the process of welding. The accurate seam tracking technology is very important to assure weld quality, but welding process is complicated, the welding system is a multivariable system influenced by multiparameters. In automatic welding system, many factors can cause the deviation of welding torch position, such as the walk deviation of welding dolly, the shape of seam groove and the welding temperature distortion, etc, these factors are highly nonlinear, time-various and uncertain so that there are many difficulties in course modeling [1]. It is impracticable that the classical control theory and method are employed into welding seam tracking. Recently, the finite element and finite difference method are adopted to build the more accurate model, but model calculating of which is too labor-intensive to control in real time in the process of welding. With the development of automatic control technology, the fuzzy control of the intelligent control theory has been developed rapidly due to its simpler control form, ease of comprehension and implement, imitating one's mind and so on. The most important advantages of the fuzzy control are that it has a strong robustness on regulating changes of object parameter and the fuzzy control category can be established which based on experience without accurate mathematical model of the controlled object. The fuzzy control has became more and more popular on the application of

D. Zeng (Ed.): Future Intelligent Information Systems, LNEE 86, pp. 223–229.
springerlink.com © Springer-Verlag Berlin Heidelberg 2011

welding seam tracking [2-3]. The method is applied to the TIG welding seam tracking system in this paper which achieves the tracking control of V groove seam.

2 System Structure of Welding Seam Tracking

The TIG welding seam tracking system mainly consists of voltage transducer, PC, crosshead shoe and so on. The welding torch is controlled to aim at the seam in real time and kept a certain height relative to the seam in the process of welding. The crosshead shoe which fixed torch is driven by two electrical motors to correct the position of the torch. In the process of welding, the signals of electric arc first filtered by hardware and output from the voltage transducer then converted into digital signals by data collecting card, the deviations of the torch relative to the seam in the left-right and high-low direction are got after the digital signals are processed by PC. The rectifying deviation signals are output from the fuzzy controller by comparing the deviations with the given value, which drives crosshead shoe to rectify deviation in two directions through the interface circuit, accordingly welding seam tracking is achieved [4-5]. The system structure is shown in Fig. 1.

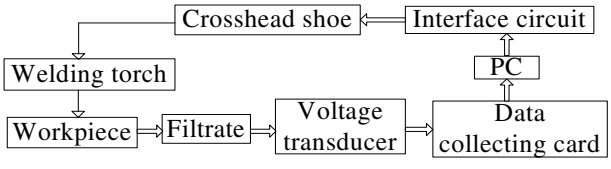

Fig. 1. Structure of welding seam system

3 Design of Fuzzy Controller

The design of fuzzy controller is to design the controller which be required to suit the controlled process in order to achieve a scheduled control objective based on practical problem [6]. For the TIG welding seam tracking system, the task of fuzzy controller is controlling the movement of welding torch to ensure that the torch points at the center of seam in the process of welding. The torch is mainly controlled in the left-right and high-low directions. The processing and rectifying deviation are little simple in the high-low direction. The welding voltage is relative to height at the given welding current and wire feed rate. The variation of the welding torch height can be got according to the variation of the voltage, thus the control of the welding torch is achieved in the high-low direction. The lateral deviation control of seam is been mainly introduced in this paper by the fuzzy control approach. The fuzzy controller structure of lateral rectifying deviation for welding torch is depicted in Fig. 2.

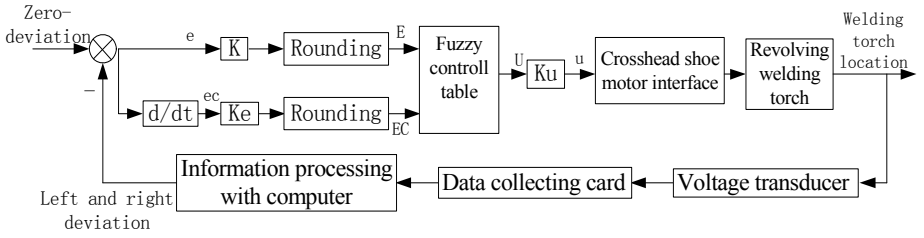

Fig. 2. Fuzzy control structure of lateral rectifying deviation for welding torch

3.1 Input and Output of Fuzzy Controller

The input quantities of fuzzy controller for lateral rectifying deviation are e and ec, which represent the left or right deviation and the change of deviation between the torch and the seam center. The output quantity is u which represents the movement time of crosshead shoe. The design process is shown in Fig. 3.

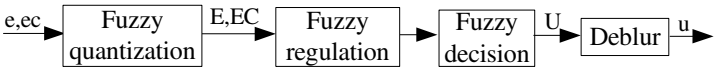

Fig. 3. Process of fuzzy control

The regions of E, EC and U are defined as [-6, 6]. Such three linguistic variables can be expressed by seven linguistic terms, respectively: {NB, NM, NS, Z(zero), PS, PM, PB}, in which negative(N) represents left and positive(P) represents right.

The membership function is often represented with triangular waveform, Gaussian waveform and trapezoidal waveform. According to the requirement of practical control and the amount of calculation, the triangular waveform is adopted here. The adjacent linguistic value, namely the overlapping value of membership function is often chosen between 0.4 and 0.8. If the overlapping value is small, the controller is qualified with inferior robustness. If it is big, the fuzzy subset is not easy to identify which can lead to a poor resolution capability of controller. So the adjacent overlapping value of membership function is 0.5 based on experience here. The curve of membership function is shown in Fig. 4 [7-8].

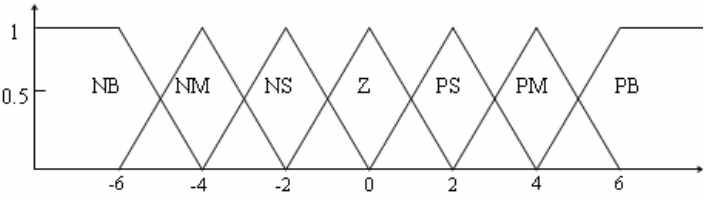

Fig. 4. Curve of membership function

3.2 Fuzzy Control Rule

The fuzzy control rule is human's generalization and summary of thought and experiences, and it is the key to design fuzzy controller. Whether the rule is correct or not directly influences the performance of controller. In short, the selected controlled quantity should try to reduce the deviation as quickly as possible when the deviation is bigger, the selected controlled quantity should prevent the overshoot and keep the stability of system when it is smaller. According to this principle, the fuzzy controller for lateral rectifying deviation has 49 fuzzy conditional statements [9-10] as follows,

(1) if E=NB and EC=NB then U=PB,
(2) if E=NB and EC=NM then U=PB,

⋮

(49) if E=PB and EC=PB then U= NB, thus the table of fuzzy control rule is achieved which is shown in Table 1.

Table 1. Table of fuzzy control rule

U / E \ EC	NB	NM	NS	Z	PS	PM	PB
NB	PB	PB	PB	PB	PM	PM	PS
NM	PB	PB	PB	PB	PM	PM	PS
NS	PM	PM	PM	PS	Z	NS	NS
Z	PM	PM	PS	Z	NS	NM	NM
PS	PS	PS	Z	NS	NM	NM	NM
PM	NS	NM	NM	NB	NB	NB	NB
PB	NS	NM	NM	NB	NB	NB	NB

3.3 Fuzzy Reasoning and Defuzzification

The defuzzification is a process according to the membership relation between the fuzzy linguistic value output and the fuzzy variable output, the controlled quantity is calculated accurately in the light of input quantity and related algorithm. The MIN-MAX deduction and the weighting barycenter algorithm are adopted in the TIG welding seam tracking.

The format of fuzzy control rule is

$$if\ E = A_i\ and\ EC = B_j\ then\ U = C_{ij}\ (i = 1 \cdots m,\ j = 1 \cdots n). \tag{1}$$

The fuzzy relation is

$$R = \bigcup_{ij} A_i \times B_j \times C_{ij}. \tag{2}$$

The membership function of fuzzy relation is

$$\mu_R(a,b,c) = \bigvee_{i=1,j=1}^{i=m,j=n} \mu_{Ai}(a) \wedge \mu_{Bj}(b) \wedge \mu_{Cij}(c) \quad , \tag{3}$$

in which "∨"represents "max" while "∧"represents "min".

For the specific input such as a* and b*, the fuzzy output is

$$U=(a^* \times b^*) \circ R \ . \tag{4}$$

The membership function output is

$$\mu_U(c) = \bigvee_{a\in A, b\in B} \mu_A(a^*) \wedge \mu_B(b^*) \wedge \mu_R(a,b,c) \quad . \tag{5}$$

The weighting barycenter algorithm is adopted in defuzzification which can be expressed as

$$U^* = \frac{\sum \mu(U_i) \cdot U_i}{\sum \mu(U_i)} \ . \tag{6}$$

According to the above method of defuzzification, the output correspondence table is acquired, and the fuzzy control table which is modified eventually is shown in Table 2.

Table 2. Chart of fuzzy control

U EC / E	-6	-5	-4	-3	-2	-1	0	1	2	3	4	5	6
-6	5.3	5.3	5.2	5.2	5.2	5.1	5.1	4.3	4	2.1	0	0	0
-5	5.3	5.2	5.2	5.2	5.2	5.2	5.2	4.3	4	2.1	0	0	0
-4	5.2	5.2	5.3	5.2	5.2	5.2	5.3	4.25	2	2.05	0	0	0
-3	4.3	4.3	4.3	4.3	4.3	3.8	3.1	2.7	2.1	0.8	-0.9	-0.9	-0.9
-2	4	4	4	4	4	3	2	1	0	-0.9	-2	-2	-2
-1	4	4	4	3.1	3.1	3.1	1.1	0	-0.85	-2	-3	-3	-3
0	4	4	4	3	2	1	0	-1	-2	-3	-4	-4	-4
1	3.1	3	3.1	2.1	1	0	-1	-2	-3	-3	-4	-4	-4
2	2.1	2.1	2.1	1.1	0	-0.9	-2	-3	-4	-4	-4	-4	-4
3	1	1.1	1.1	-0.8	-2	-2.3	-3.1	-3.3	-4.3	-4.3	-4.3	-4.3	-4.3
4	0	0	0	-2	-4	-4.3	-5.3	-5.2	-5.3	-5.2	-5.3	-5.2	-5.3
5	0	0	0	-2	-4	-4.3	-10.5	-5.2	-5.2	-5.2	-5.2	-5.2	-5.2
6	0	0	0	-2	-4	-4.3	-5.3	-5.2	-5.3	-5.2	-5.2	-5.2	-5.3

4 Result of Welding Experiment

The welding conditions are as follows, the welding current, I=150A, and travel speed, v=30cm/min. Pure argon arc is used as protection gas. The gas flow-rate is 8L/min, the diameter of tungsten needle is 2.4mm, the scanning frequency is 15Hz and the scanning radius is 2mm. The 90° V groove seam which consists of two stainless steel plates of 5mm thickness is horizontally placed as a workpiece material. The across distance is 3mm between the arcing point A and the seam center. The arc blowout is at point B.

The parameters of control system are as follows, the rectifying deviation velocity is 5mm/s, the control cycle is 700ms and the welding velocity is 27cm/min. The experimental result is shown in Fig. 5.

Fig. 5. Experiment result of welding seam tracking

5 Conclusions

Many influencing factors such as time-variant, non-linearity make it difficult to build accurate mathematical models in the control of the TIG welding seam tracking. Based on these characteristics, in this paper the fuzzy control approach is adopted which does not need model and is achieved easily. So, the fuzzy controller is designed for the control of TIG welding seam tracking. The experiment results of V groove seam tracking show that the designed controller is reliable and the experiment effect is excellent in the TIG welding seam tracking.

Acknowledgments. The authors wish to thank the financial support for this research from the Hi-tech Research and Development Program of China, No. 2007AA04Z242, and Tackle Key Problem Item of Jiangxi Province, China, No. 2007BG09200.

References

1. Mao, P.-j., Huang, S.-s., Xue, J.-x., Wang, X.-y.: The Researching Status and Development Trend of Arc Welding Robotic Seam Tracking System. Electric Welding Machine 31(10), 9–12 (2001)
2. Li, S.-y.: Fuzzy Control Neurocontrol and Intelligent Cybernetics, pp. 45–49. Harbin Institute of Technology Press, Harbin (1998)

3. Hu, S.-s., Li, S.-h., Sun, D.: Development of the Fuzzy Controller for the Seam Tracking. Electric Welding Machine 30(9), 32–34 (2000)
4. Chen, Q., Wang, Q.-r., Xie, C.-y.: Application of Fuzzy Controller for the Seam Tracking. Journal of Guangdong University of Technology 22(2), 41–44 (2005)
5. Li, H.-l.: Structure Design on Rotating Arc Sensor for TIG and Research of Welding System. Thesis of Master Degree, pp. 48–59. Nanchang University (2010)
6. Zhang, J.-l.: Control Principle and Engineering Application of Fuzzy Neural Network, pp. 61–73. Harbin Institute of Technology Press, Harbin (2004)
7. Chen, K.-q., Cheng, P.-f., Peng, M.: Application of Fuzzy Control Technology in High-Pressure Water Descaling System. Mining Research and Development 30(1), 70–72 (2010)
8. Jia, D.-y., Zeng, Z.-g.: Computer Simulation in DC Motor Speed-Controlling System Based on Fuzzy Control. Technology of Electric Motor and Appliance (5), 3–5 (2002)
9. Xiong, Z.-y., Wan, W.: A Fuzzy Control System of Weld Seam Tracking Based on Arc Sensor in Welding Robot. New Technology & New Process (8), 6–8 (2003)
10. Chen, Q.: Fuzzy Control of Arc Welding. Welding & Joining (8), 2–6 (1994)

Design of CMOS Wilkinson Power Divider Incorporating Semi-passive Inductors

Sen Wang

Graduate Institute of Computer and Communication Engineering,
National Taipei Univerisyt of Technology, Taipei, Taiwan
1, Sec.3, Chung-Hsiao E.Rd., Taipei 10608, Taiwan, R.O.C.
wangsen@ntut.edu.tw

Abstract. In this paper, a Wilkinson power divider incorporating semi-passive inductors is designed in a standard 0.18-μm CMOS process. The lumped power divider is based on series-C and shunt-L networks, and the shunt inductors utilize a center-tapped inductor feedback technique to achieve high-Q factors. Compared with conventional transformer feedback architectures, this proposed technique not only compensates resistive losses with low-power consumption but also achieves high-Q factors. The lumped power divider is designed at a center frequency of 5.0 GHz for equal power dividing with all ports matched to 50 Ω. The circuit consumes a total power of 2.5 mW from a 0.8-V supply voltage, and the isolation between the output ports is about 28 dB. Moreover, the insertion, input, and output return losses of the circuits at 5 GHz are 0.02 dB, 30 dB, and 35 dB, respectively.

Keywords: Wilkinson power divider, monolithic microwave integrated circuit (MMIC), center-tapped inductor, transformer.

1 Introduction

The Wilkinson power dividers are widely used for power combining and spitting in many microwave and millimeter-wave system applications. The distributed 3-port power dividers and other 4-port couplers are often realized in planar transmission lines which can be easily incorporated in monolithic microwave integrated circuits (MMICs) at high frequencies [1-3]. However, the transmission-line based power dividers and couplers consume too much chip area to be integrated, which limits their applications at low frequencies. In order to reduce the size of these components effectively, the lumped elements to replace transmission-line based components were successfully implemented [4-7]. Low-Q inductors suffer silicon substrate losses in standard CMOS process, therefore, the Q-enhanced inductors such as active, semi-passive, and micromachined inductors were proposed [7-9]. Typically, the active inductors are power-consuming designs, and the micromachined inductors require a non-standard CMOS process. The semi-passive inductors incorporating passive components and active devices reported in [8] seems to be a low-power design, however, it consumes large area because of the transformer-feedback architecture.

D. Zeng (Ed.): Future Intelligent Information Systems, LNEE 86, pp. 231–238.
springerlink.com © Springer-Verlag Berlin Heidelberg 2011

In this paper, a CMOS Wilkinson power divider incorporating semi-passive inductors is presented, and the inductors using tapped-inductor feedback technique are also analyzed and designed. The design procedure is detailed in the following sections. Section 2 describes the circuit design of the proposed Wilkinson power divider and semi-passive inductor. Moreover, simulated results and circuit verifications of the design in a 0.18-μm CMOS process are also reported in Section 3. Finally, Section 4 concludes this work.

2 Design of Wilkinson Power Divider and Semi-passive Inductor

2.1 Lumped Wilkinson Power Divider

Fig. 1(a) depicts a conventional transmission-line based a Wilkinson power divider. Typically, the power divider consists two $\lambda/4$ or $3\lambda/4$ transmission lines with characteristic impedance $\sqrt{2}\,Z_0$, and a $2Z_0$ resistor for high isolation between the output ports. However, the distributed power divider consumes larger chip area which is impractical at low frequencies. A distributed transmission line with a characteristic impedance Z_0 and an electrical length βl can be replaced by its lumped equivalent T-networks [4]. Fig. 1(b) and 1(c) represent the lumped T-networks which are equivalent to the $\lambda/4$ and $3\lambda/4$ Wilkinson power dividers in Fig. 1(a), respectively. The four series inductors in Fig. 1(b) consume large chip area, and low-Q factors of the inductors degrade the performance of the lumped power divider such as insertion and return losses drastically. Moreover, the series capacitors and shunt inductors networks in Fig. 1(c) reduce the number of inductors, the performance of power divider is still limited by the low-Q inductors. Typically, an acceptable performance of a power divider requires inductors with Q-factor 30 at least.

The lumped LC components shown in Fig. 1(c) can be derived from the ABCD matrices of a $3\lambda/4$ transmission line and the lumped T-network. Therefore, the corresponding C_s and L_p can be obtained by equating the matrices in (1).

$$\begin{bmatrix} \cos\beta l & jZ_0\sin\beta l \\ jY_0\sin\beta l & \cos\beta l \end{bmatrix} = \begin{bmatrix} 0 & -jZ_0 \\ -jY_0 & 0 \end{bmatrix} = \begin{bmatrix} 1-\dfrac{1}{\omega^2 L_p C_s} & \dfrac{2}{j\omega C_s}-\dfrac{1}{j\omega^3 C_s^2 L_p} \\ \dfrac{1}{j\omega L_p} & 1-\dfrac{1}{\omega^2 L_p C_s} \end{bmatrix} \tag{1}$$

$$C_s = \frac{1}{\sqrt{2}Z_0\omega} \tag{2}$$

$$L_p = \frac{\sqrt{2}Z_0}{\omega} \tag{3}$$

ω is the operating frequency, and Z_0 is 50 Ω in these equations. From (2) and (3), a 5-GHz lumped power divider can be obtained with C_s of 0.45 pF and L_p of 2.25 nH in Fig. 1(c). Fig. 2 demonstrates the simulated S-parameters of the power divider in Fig. 1(c). The results are obtained by assuming ideal series capacitors and non-ideal shunt

inductors with Q-factor of 10. The insertion loss, input return loss, and output return loss is 4.5 dB, 15 dB, and 22 dB, respectively. Moreover, the isolation between the output ports is about 21 dB. The low Q-factor of on-chip inductors in standard CMOS process suffers from the lossy Si-substrate, degrading the performance of the lumped power divider.

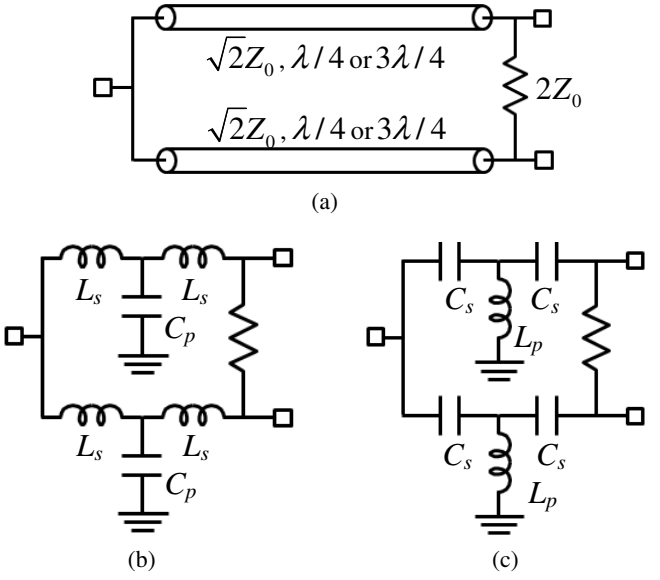

Fig. 1. (a) A Wilkinson power divider realized by two transmission lines. (b) A lumped Wilkinson power divider realized by series-L and shunt-C networks. (c) A lumped Wilkinson power divider realized by series-C and shunt-L networks.

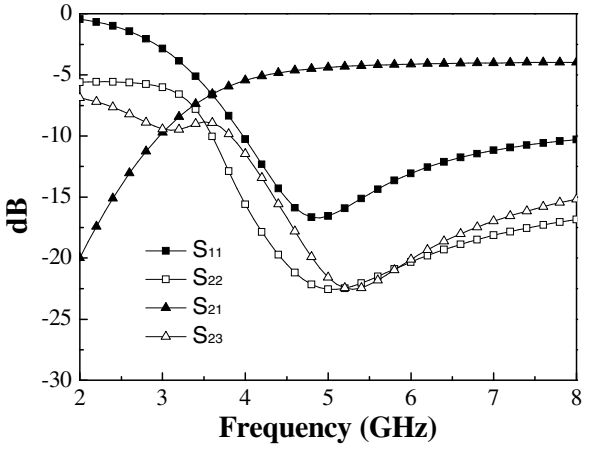

Fig. 2. Simulated S-parameters of the Wilkinson power divider in Fig. 1(c). (Assume the quality factor (Q) of the shunt inductors is 10.

2.2 High *Q* Semi-passive Inductor

Fig. 3(a) shows the schematic of the proposed semi-inductor using tapped-inductor feedback. The semi-passive inductor consists of a NMOS transistor, a capacitor, and a center-tapped inductor. L_1 and L_2 form the center-tapped inductor, and M is the mutual inductance between L_1 and L_2. C is applied to generate voltage drop of V_{gs}. The input impedance Z_{in} and the Q-factor of the proposed semi-passive inductor can be derived from the small-signal analysis.

$$\begin{aligned} Z_{in} &= j\omega L_1 + R_1 + j\omega M\left(\frac{i_2+i_1}{i_1}\right) + \left(\frac{i_2+i_1}{i_1}\right)\left[j\omega L_2 + R_2 + j\omega M\left(\frac{i_1}{i_2+i_1}\right)\right] \\ &= \left(R_1 + R_2 - \frac{Mg_m}{C} - \frac{L_2 g_m}{C}\right) + j\omega\left(L_1 + L_2 + 2M + \frac{g_m R_2}{\omega C}\right), \end{aligned} \tag{4}$$

$$Q = \omega\left(L_1 + L_2 + 2M + \frac{g_m R_2}{\omega C}\right) \Big/ \left(R_1 + R_2 - \frac{Mg_m}{C} - \frac{L_2 g_m}{C}\right). \tag{5}$$

The g_m, R_1, and R_2 are transconductance of the transistor, resistance of L_1, and resistance of L_2, respectively. As shown in (4) and (5), the g_m, C, M, and L_2 forms negative resistances which compensates the resistive losses of L_1 and L_2. Therefore, a high-Q inductor in standard CMOS process can be obtained by tuning g_m, or the gate bias of the transistor. Fig. 3(b) shows a physical layout of 3-turn center-tapped inductor. The black and the gray metal lines represent the L_1 and L_2 of the symmetrical inductor, respectively. For reducing metal losses of the inductors in a standard 0.18-μm CMOS process, L_1 and L_2 are mainly implemented on thick metal layer, or top metal layer (M6). Moreover, M5 are used at the crossovers L_1 and L_2. The blue metal line realized on M4 is a tapped line of the inductor. The ports of black, gray, and blue metal lines are connected to Z_{in}, ground, and source of the transistor, respectively, as shown in Fig. 3(a).

In order to make a quick assessment and validation of the proposed semi-passive inductor, simulations are performed by ADS and HFSS simulators. Moreover, the physical layout of 3-turn tapped-inductor with a chip area of 160μm × 200μm is used for the verification, and the width, spacing, and inner radius of the layout in Fig. 3(b) is 9 μm, 2 μm, and 50 μm, respectively. Assuming C, drain bias of the transistor V_D, and aspect ratio of the transistor in Fig. 3(a) are 2 pF, 0.8 V, and (32μm/0.18μm), respectively. The semi-passive inductor is grounded at one end, therefore one port S-parameters simulation is performed at the other end. Fig. 4 shows the simulated inductance and S_{11} of the proposed semi-passive inductor under different biasing conductions. V_G represents the gate bias of the transistor, and controls the bias current and g_m to adjust desired negative resistances. When V_G is 0 V, the equivalent inductance and self-resonant frequency is about 2.0 nH and 10.4 GHz, respectively, as shown in Fig. 4(a). In this condition, the Q-factor is about 6 at 5 GHz because g_m is 0, or no negative resistance is achieved. Moreover, when the V_G is 0.65 V, the semi-passive inductor draws 1.0 mA from a 0.8-V supply voltage, and the equivalent inductance and self-resonant frequency is about 2.1 nH and 10.1 GHz, respectively.

Fig. 4(b) shows the Smith Chart of the S_{11} from 2 to 12 GHz. It is obvious that Q-factors at V_G of 0.65 V are higher than those at V_G of 0 V. The results are all confines to the unit circle of the Smith Chart to maintain the overall stability of the circuit, or the equivalent resistance is positive and close to zero. The equivalent Q-factor of the semi-passive inductor under V_G of 0.65 V is 31 around 5 GHz. The characteristics of the flat inductance and high-Q factor around 5 GHz are applicable to other applications. As discussed above, it concludes that the proposed semi-passive inductor provides high-Q factor with low-power consumption, and the inductance varies slightly under different bias conditions. In other words, the bias voltage merely affects the negative resistance of the circuits.

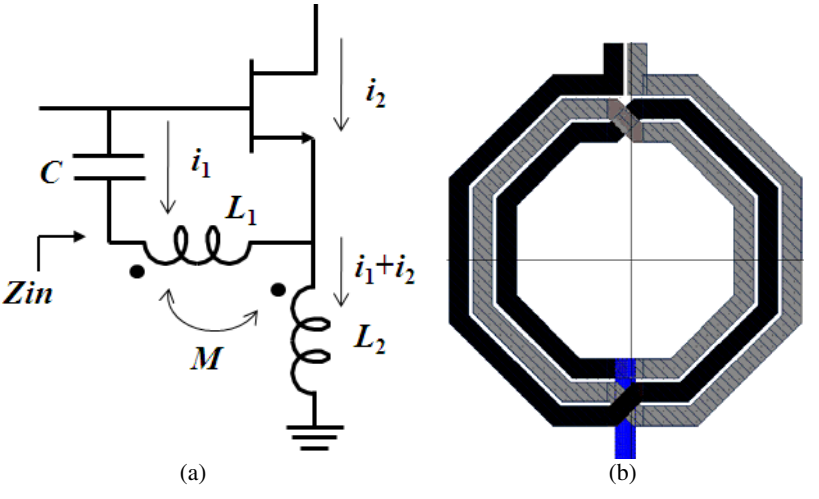

Fig. 3. (a) Schematic of the proposed semi-inductor using tapped-inductor feedback. (b) Physical layout of a 3-turn center-tapped inductor.

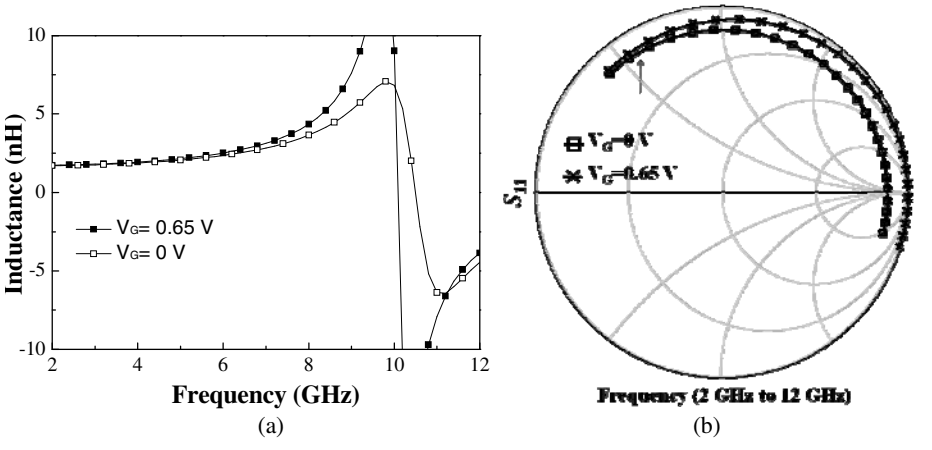

Fig. 4. (a) Simulated inductance and (b) simulated S_{11} of the proposed semi-passive inductor under different biasing conductions

3 Simulation Results of the Lumped Power Divider

The proposed semi-passive inductor is designed in a standard mixed-signal/RF bulk 0.18-μm CMOS process, which provides a single poly layer and six metal (1P6M) layers (from M1 to M6 layers) for interconnection. Capacitors in this design are realized by metal-oxide-metal (MOM) capacitors implemented from M1 to M5 layers for high capacitance density. The tapped inductor is implemented on the thick AlCu metallization layer, or M6 layer for reducing resistive losses. Fig. 5 shows the schematic of proposed series-C and shunt-L circuit, which is equivalent to a $3\lambda/4$ transmission line. R is a high-resistive resistor providing RF signal blocking, and eliminating the need for an RF choke. And C_1 and C_2 are bypass capacitors. The R, C_3, C_a, V_D, and aspect ratio of M_1 in Fig. 5 are 10 KΩ, 2 pF, 0.45 pF, 0.8 V, and (32μm/0.18μm), respectively, and physical layout of the center-tapped is same as mentioned in Section 2.2.

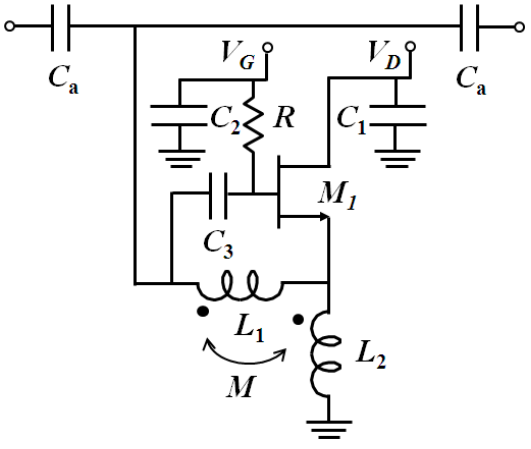

Fig. 5. Schematic of the proposed series-C and shunt-L circuit, which is equivalent to a $3\lambda/4$ transmission line

Fig. 6 demonstrates the characteristic impedance Z_c and S-parameters of the proposed circuit in Fig. 5 with V_G of 0.72 V. The real part of the Z_c is 71.3 Ω at 5 GHz close to the desired $\sqrt{2}\,Z_0$. Moreover, the imaginary part is close to 0 at 5 GHz, representing that it is equivalent to a lossless transmission line. As results of it, the insertion loss of 0.01 dB and return loss of 26 dB at 5 GHz is further presented in Fig. 6(b). A lumped power divider can be obtained by two circuits as shown in Fig. 5 and a 100-Ω resistor for high isolation between the output ports. The lumped power divider is designed at a center frequency of 5.0 GHz for equal power dividing with all ports matched to 50 Ω. Fig. 7 shows the simulated S-parameters of the proposed Wilkinson power divider using semi-passive inductors. The circuit consumes a total power of 2.5 mW from a 0.8-V supply voltage, and the isolation between the output ports is about 28 dB. Moreover, the insertion losses, input, and output return losses of the circuits at 5 GHz are 0.02 dB, 30 dB, and 35 dB, respectively. Table 1 summarizes the comparisons of previously reported CMOS Wilkinson power dividers. It reveals that

the proposed power divider using semi-passive inductor demonstrates better electrical characteristics than using active and micromachined inductors.

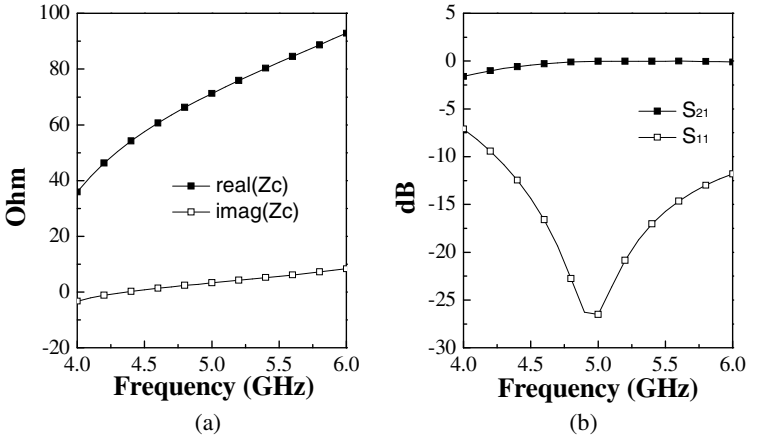

Fig. 6. (a) Simulated characteristic impedance and (b) S-parameters of the circuit in Fig. 5

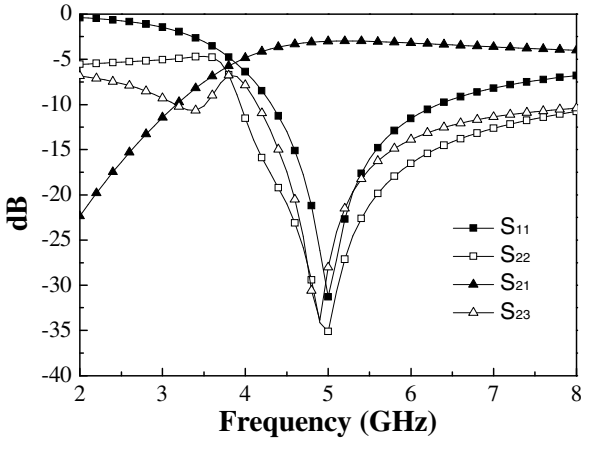

Fig. 7. Simulated S-parameters of the proposed Wilkinson power divider using semi-passive inductors

Table 1. Comparisons of Previously Reported CMOS Wilkinson Power Dividers

Reference	Technology	Technique	Frequency (GHz)	S_{21} (dB)	S_{11} (dB)	S_{22} (dB)	S_{23} (dB)	P_{DC} (mW)
This Work	0.18-μm CMOS	Semi-passive inductors	5.0	-3.02	-30	-35	-28	2.5
Ref. 5	0.25-μm CMOS	Micromachined inductors	8.5	-3.57	-24.5	-28.1	-14.1	0
Ref. 7	0.18-μm CMOS	Active inductors	5.0	-3.7	-22.6	-22.6	-23	19.4

4 Conclusion

In this paper, the design of CMOS Wilkinson power divider incorporating semi-passive inductors is designed. The semi-passive inductor using center-tapped inductor feedback technique not only compensates resistive losses but also provides high-Q factor with low-power consumption. The lumped power divider is based on series-C and shunt-L network, and validates the feasibility of the concept in a standard 0.18-μm CMOS process. Comparing with other published works, the proposed design shows advantages in terms of low insertion losses, good return losses, and low-power consumption. In addition, it is the first design using semi-passive inductors feedback to realize a lumped power divider. Finally, it is also believed that the hig-Q inductor is suitable for further practical applications.

Acknowledgments. The author would like to thank the National Science Council (NSC) and Chip Implementation Chip (CIC) of Taiwan for financial and technical supports. This work was supported by the NSC under Contract NSC-99-2218-E-027-004.

References

1. Chiajg, M.-J., Wu, H.-S., Tzuang, C.-K.C.: A Ka-band CMOS Wilkinson Power Divider Using Synthetic Quasi-TEM transmission lines. IEEE Microwave Wireless Component Letters, 837–839 (2007)
2. Bamba, S., Ogawa, H.: Multilayer MMIC directional Coupler Using Thin Dielectric Layer. IEEE Trans. Microwave Theory and Techniques, 1270–1275 (1995)
3. Gokdemir, T., Robertson, I.D., Wang, Q.H., Rezazadeh, A.A.: K/Ka-band Coplanar Waveguide Directional Coupler Using A Three-Metal-Level MMIC Process. IEEE Microwave Guided Wave Letters, 76–78 (1996)
4. Chiang, Y.-C., Chen, C.-Y.: Design of Lumped Element Quadrature Hybrid. IEE Electronics Letters, 465–467 (1998)
5. Lu, L.-H., Bhattacharya, P., Katehi, L.P.B., Ponchak, G.E.: X-band and K-band Lumped Wilkinson Power Dividers with A Micromachined Technology. IEEE MTT-S, 287–290 (2000)
6. Ng, C.Y., Chongcheawchamnan, M., Robertson, I.D.: Lumped-Distributed Hybrids in 3D-MMIC Technology. In: IEE Proc. Microwave Antennas and Propagation, pp. 370–374 (2004)
7. Lu, L.-H., Liao, Y.-T., Wu, C.-R.: A Miniaturized Wilkinson Power Divider with CMOS Active Inductors. IEEE Microwave Wireless Component Letters, 775–777 (2005)
8. Soorapanth, T., Wong, S.S.: A 0-dB IL 2140 ± 30 MHz Bandpass Filter Utilizing Q-Enhanced Spiral Inductors in Standard CMOS. IEEE J. Solid-State Circuits, 579–586 (2002)
9. Yoon, J.-B., Choi, Y.-S., Eo, Y., Yoon, E.: CMOS-Compatible Surface-Micromachined Suspended-Spiral Inductors for Multi-GHz Silicon RF ICs. IEEE Electron Device Letters, 591–593 (2002)

A Novel Scalable MPSoC Architecture Based on FPGA

Yijia Zhang and Jian Wang

School of Electronics and Information Engineering,
Dalian University of Technology,
Dalian 116023, China
zhyj@dlut.edu.cn

Abstract. The scalability problem is an important topic in computer architecture. In this paper, we first extend the multicore architecture theory of Hill and Marty to the condition considering the additional parallel cost. We then propose a novel scalable multiprocessor system-on-chip (MPSoC) architecture based on FPGA focusing on the characteristics of embedded applications and analyze the maximum of speedup. Finally, we implement our MPSoC system on FPGA platform and test on MIBench. The results show that our MPSoC architecture outperforms other architectures under different workloads.

Keywords: scalability, MPSoC, architecture, FPGA.

1 Introduction

In recent years, since the performance of unicore architectures already approaches its limit, more attention has been given to the study of multicore architectures. Multicore architectures integrate multiple processing units into one chip to overcome the physical constraints of unicore architectures, and their exponentially growing power consumption [1]. According to Pollack's Rule [2], multicore architectures offer a cost-effective alternative, delivering more computing capability via parallel processing, while consuming less power and board space.

In the multicore era, the scalability problem is an interesting long-term goal which is indicated by Jim Gray [3] in the first place of the dozen long-term information technology research goals. Hill and Marty [4] augment Amdahl's law to multicore architectures by constructing a cost model for the number and performance of cores that the chip can support. They indicate that obtaining optimal performance will require the multicore architectures to be tailor-made according to the different workloads. On one hand, with the rapid development of embedded system, the high embedded applications, such as high-speed video decoder and high-quality image processing, have put forward higher requirement for embedded processors. On the other hand, the large capacity FPGA chip and the MPSoC solutions of FPGA vendors, such as Xilinx and Altera, provide an opportunity to design optimal multiprocessor architectures according to the different embedded applications and ultimately realize it based on the "tailor to the needs" principle of the embedded system.

D. Zeng (Ed.): Future Intelligent Information Systems, LNEE 86, pp. 239–245.
springerlink.com © Springer-Verlag Berlin Heidelberg 2011

In this paper, based on the hardware cost model proposed by Hill and Marty, we obtain the formulas for the maximum speedups using architecture of symmetric and asymmetric under the condition of considering the additional parallel cost. Furthermore, we propose a novel scalable MPSoC architecture based on FPGA focusing on the characteristics of embedded applications. To demonstrate the feasibility of our MPSoC architecture, we implement the MPSoC system on FPGA and test our system on MIBench.

1.1 Amdahl's Law

The original idea presented by Amdahl [5] was a general observation about the performance improvement limitation of any enhancement, and was later summarized as Amdahl's law. Let speedup be the original execution time divided by an enhanced execution time. The modern version of Amdahl's Law states that if one enhances a fraction f of a computation by a speedup of m, then the overall speedup is:

$$Speedup(f,m) = \frac{1}{(1-f) + \frac{f}{m}} \tag{1}$$

Amdahl's Law implies that when m increases to infinity, the speedup upper bound is $\lim_{m\to\infty} Speedup(f,m) = \frac{1}{1-f}$.

1.2 Hill and Marty's Cost Model for Multicore Chips

In [4], Hill and Marty propose a simple hardware model for multicore chips. First, they assume that a multicore chip of given size and technology generation can contain at most n base core equivalents (BCE) (where a single BCE implements the base line core). Then, they assume that architects can use the resources of multiple BCEs to create a core with greater sequential performance. Let the performance of a single-BCE core be 1, they assume that architects can expend the resources of r BCEs to create a powerful core with sequential performance $perf(r)$. The value of $perf(r)$ can be an arbitrary function, but in this paper we assume $1 < perf(r) < r$ according to the actual hardware technique and implementation.

Based on the hardware model, Hill and Marty conclude that the speedups of symmetric multicore architecture and asymmetric multicore architecture respectively are:

$$Speedup_{symmetric}(f,n,r) = \frac{1}{\frac{1-f}{perf(r)} + \frac{fr}{perf(r)n}} \tag{2}$$

$$Speedup_{asymmetric}(f,n,r) = \frac{1}{\frac{1-f}{perf(r)} + \frac{f}{perf(r)+n-r}} \tag{3}$$

2 A Scalable MPSoC Architecture

2.1 Speedup Model under Additional Parallel Cost

We follow the Hill and Marty cost model and analyze the scalability of multicore architectures under the condition by considering the additional parallel cost. Let w_0 denote the additional parallel cost and w denote the total workload. The speedups of symmetric multicore architecture and asymmetric multicore architecture under the condition of considering the additional parallel cost respectively are:

$$Speedup_{symmetric}(f,n,r) = \frac{1}{\frac{1-f}{perf(r)} + \frac{fr}{perf(r)n} + \frac{w_0}{w}} \tag{4}$$

$$Speedup_{asymmetric}(f,n,r) = \frac{1}{\frac{1-f}{perf(r)} + \frac{f}{perf(r)+n-r} + \frac{w_0}{w}} \tag{5}$$

w_0 is mainly related to w, the number of processing cores and the architectures of multicore. When we consider the additional parallel cost, if the parallel portion of workload, f, is very small, the multicore architecture won't outperform unicore architecture. Let e denote the critical value of paralleled portion to determine whether workload is fit for multicore architecture or not. For symmetric multicore architecture, when $Speedup = perf(r)$ ($perf(r)$ is the speedup achieved by a uniprocessor which performance is $perf(r)$), $f = e$. According to Eq. (4), we obtain the following equation:

$$e_{symmetric} = \frac{nw0\,perf(r)}{w(n-r)} \tag{6}$$

For asymmetric multicore architecture, we use the same method to obtain the following equation:

$$e_{asymmetric} = \frac{w_0 perf(r)[perf(r) + n - r]}{w(n-r)} \tag{7}$$

Result 1. For a multicore chip, n, r and $perf(r)$ are fixed, when $f < e$, workload isn't fit for multicore architecture and when $f > e$, workload is fit for multicore architecture. For symmetric multicore architecture and asymmetric multicore architecture, the expressions of e are Eq. (6) and Eq. (7), respectively.

2.2 A Scalable MPSoC Architecture

Based on the above analysis, we propose a novel scaleable MPSoC architecture focusing on the characteristics of embedded applications. We divide the total workload into two categories. One category of the parallel portion is so low that it is more fit for unicore architecture, in which $f < e$ and the other one is enough to fit for multicore architecture, in which $f > e$. Moreover, Hill and Marty [4] have proved asymmetric multicore architecture can always offer greater potential speedups than symmetric multicore architecture.

Focusing on the different workloads, we propose a scaleable MPSoC architecture (see Fig. 1).

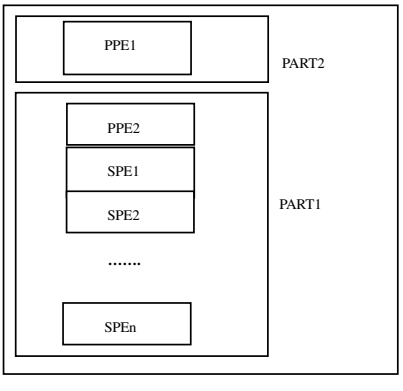

Fig. 1. The scalable MPSoC architecture

The whole MPSoC architecture consists of two processing parts. The PART1 is asymmetric architecture and mainly in charge of handling the workload fitting for multicore architecture, which consists of a powerful master processor denoted by PPE2 and some coprocessors denoted by SPE1 to SPEn. The PART2 is a powerful uniprocessor and mainly in charge of handling the workload fitting for unicore architecture.

Let g denote the portion of total workloads which is fit for multicore architecture and let $1-g$ denote the portion of total workloads which is fit for unicore architecture. According to Hill and Marty's cost model, we assume the total resource of MPSoC is n BCEs, the performance of PPE1 is $perf(s)$ which expends s BCEs, the performance of PPE2 is $perf(r)$ which expends s BCEs and the performance of $n-s-r$ coprocessors is 1. Following the above assumption, the speedup of our MPSoC architecture is:

$$Speedup(f,n,r,s,g,w,w_0) = \min\{\frac{perf(s)}{1-g}, \frac{1}{\frac{g(1-f)}{perf(r)} + \frac{gf}{perf(r)+n-r-s} + \frac{w_0}{w}}\} \tag{8}$$

Let $K(s) = \frac{1-g}{perf(s)}$ and $L(r,s) = \frac{1}{\frac{g(1-f)}{perf(r)} + \frac{gf}{perf(r)+n-r-s} + \frac{w_0}{w}}$.

According to current hardware technique and implementation, $perf(x)$ is an increasing function and the function value ranges from 1 to x, for example we can support $perf(x) = x^c$, $0 < c < 1$. When $s \in (1, n-r)$, $K(s)$ is a decreasing function of s and $L(r,s)$ is an increasing function of s. Hence, when $K(s) = L(r,s)$, the maximum speedup in Eq. (8) occurs at some unique $r_0 \in (1, n-s)$.

Result 2. For achieving the best speedup, the system architects must design for the characteristic of different workloads and balance the processing capacity of system relaxing the processing bottlenecks of different kinds of workloads.

3 Experiments

To demonstrate the validity of our MPSoC architecture, we implement our MPSoC architecture on FPGA platform and test on MIBench [6]. The following subsections describe the experiments and discuss the results.

3.1 MPSoC Based on FPGA

We implement MPSoC system using a development board (Virtex-II pro) that has a Xilinx FPGA (XC2VP30) and a DDR SDRAM DIMM interface. The XC2VP30 has 30816 Logic Cells, 136 18-bit multipliers, 2448Kb of block RAM, and two PowerPC Processors. In addition, Xilinx provides the solution of MicroBlaze soft core for embedded applications.

Fig. 2 shows the whole MPSoC architecture and the MPSoC system consists of Part 1, Part 2 and Part 3. Part 1 is an asymmetric processing part including a PowerPC processor and 4 MircoBlaze soft processors, which is mainly in charge of processing

the workload fitting for multicore architecture. Part 2 is a PowerPC processor which is mainly in charge of processing the workload fitting for unicore architecture. Part 3 is the peripherals of MPSoC system.

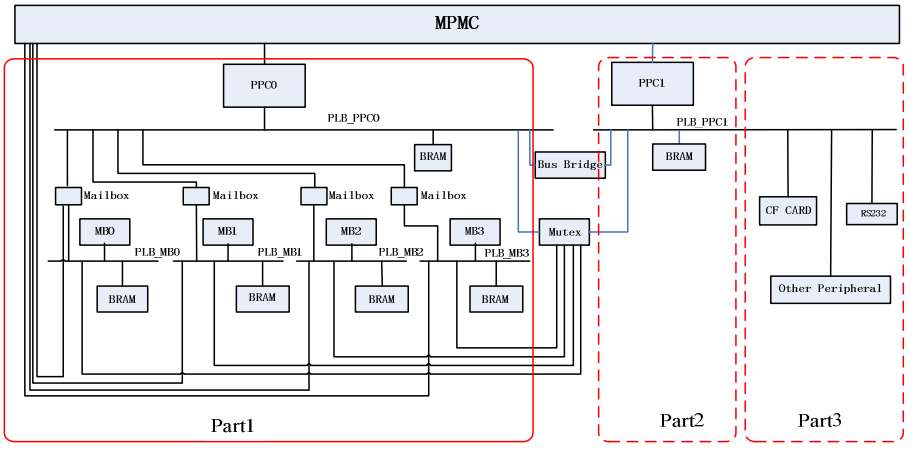

Fig. 2. The architecture of MPSoC system

3.2 Experimental Results and Discussions

MIBench [6] is a free, commercially representative embedded benchmark suite. Compared to SPECCPU2000 and EEMBC, MIBench is developed for the embedded applications, therefore MIBench is more suitable for testing embedded system.

We choose susan as workload fitting for multicore architecture and dijkstra as workload fitting for unicore architecture. Table 1 shows the results evaluated on MIBench. We fix the frequency of FPGA platform at 100MHZ and use the time function provided by Xilinx EDK within one millisecond.

Table 1. Experimental results of 4 architectures

	MB	4MB	PPC+4MB	2PPC+4MB
Dijkstra（20）Susan（8k）	10926(ms)	5231(ms)	2765(ms)	1735(ms)
Dijkstra（50）Susan（8k）	14084(ms)	8763(ms)	4352(ms)	2612(ms)
Dijkstra（80）Susan（8k）	18231(ms)	12273(ms)	6133(ms)	4373(ms)
Dijkstra（100）Susan（8k）	19722(ms)	14176(ms)	7209(ms)	5448(ms)

In Table 1, MB denotes the unicore architecture consisting of a MicroBlaze soft processor, 4MB denotes the symmetric architecture consisting of 4 MicroBlaze soft processors,PPC+4MB denotes the asymmetric architecture consisting of 1 PowerPC processor and 4 MicorBlaze soft processors and 2PPC+4MB denotes our MPSoC architecture in Fig. 2. Dijkstra (20) denotes that we use dijkstra algorithm to compute the shortest paths of 20 nodes in the directed graph consisting of 100 nodes, and so on. Susan (8k) denotes we use susan algorithm to deal with 8KByte image.

Form Table 1, we can get speedup of different architectures in Table 2. As seen in Table 2, our MPSoC architecture outperforms other architectures under different workloads. In addition, with the increase of workload fitting for unicore architecture, the performance of all architectures decreases significantly. This implies that the key to get better performance is to relieve the bottleneck of workloads effectively.

Table 2. Speedup of 4 architectures

	MB	4MB	PPC+4MB	2PPC+4MB
Dijkstra（20）Susan（8k）	1．00	2．09	3．95	6．30
Dijkstra（50）Susan（8k）	1．00	1．61	3．24	5．39
Dijkstra（80）Susan（8k）	1．00	1．49	2．97	4．17
Dijkstra（100）Susan（8k）	1．00	1．39	2．74	3．62

4 Conclusions

In this paper, based on the hardware cost model proposed by Hill and Marty, we obtain the formulas of symmetric multicore architectures and asymmetric multicore architectures under the condition of considering the additional parallel cost. Furthermore, we propose a novel scalable MPSoC architecture based on FPGA focusing on the characteristics of embedded applications and analyze the maximum speedup. To demonstrate the feasibility of our MPSoC architecture, we implement the MPSoC system on FPGA platform and test our MPSoC system on MIBench. The results show that the scalable MPSoC architecture outperforms other architectures under different workloads.

Currently, we implement the prototype of MPSoC architecture on FPGA platform, which only consists of 2 PowerPC processors and 4 MicroBlaze soft processors, due to the limited capacity of the FPGA. Future work will include implementing more complex MPSoC architecture on the latest FPAG platforms and testing the MPSoC system on actual embedded applications.

References

1. Xian-He, S., Yong, C.: Reevaluating Amdahl's law in the multicore era. J. Parallel Distrib. Comput. 70, 183–188 (2010)
2. Pollack, F.: New Microarchitecture Challenges in the Coming Generations of CMOS Processing Technologies. In: Keynote Speech in the 32nd International Symposium on Microarchitecture (1999)
3. Jim, G.: What next?: A dozen information-technology research goals. Journal of the ACM 50(1), 41–57 (2003)
4. Hill, M., Marty, M.R.: Amdahl's law in the multicore era. IEEE Computer 41(7), 33–38 (2008)
5. Amdahl, G.M.: Validity of the single-processor approach to achieving large scale computing capabilities. In: AFIPS Conference (1967)
6. Guthaus, M.R., Ringenberg, J.S., Ernst, D., et al.: MiBench: A free, commercially representative embedded benchmark suite. In: The IEEE International Workshop on Workload Characterization, pp. 266–277. IEEE Computer Society Press, Los Alamitos (2000)

Analysis of Electrical Characteristics for Conductive Particle in Anisotropic Conductive Adhesive Film (ACF) Assembly

Jun Zhang[1], Yamei Geng[2], and Liugang Huang[1]

[1] School of Chemical Engineering and Energy, Zhengzhou University, Zhengzhou, 450001, P.R. China
zhang_jun@zzu.edu.cn, hanglg@zzu.edu.cn
[2] School of Chemical Engineering & Technology, Tianjin University, Tianjin, 300072, P.R. China
gengym@tju.edu.cn

Abstract. Anisotropic conductive adhesive film (ACF) as one kind of green and environmental protective interconnected material is widely used in electronic industry. Fully understanding of electrical characteristics of ACF particles can help to optimize the assembly process and improve the efficiency of ACF interconnection. The effects of the bonding parameters such as particle cracks, the deformation degree and the number of particles were considered to calculate the particle resistance. A mathematical model was used to predict the particle resistance of the nickel-coated polymer particle with the different deformation. The variability of the particle resistance under temperature load and the number of particles was also conducted. The particle resistance for different conditions was then obtained to compare with experiment, and the predicting results of the model were fit well with the experiments.

Keyword: Anisotropic conductive adhesive films(ACF); particle resistance; deformation.

1 Introduction

Anisotropic conductive adhesive film(ACF) is widely used as an electrical interconnection for fine-pitch flip chip applications, such as chip-on-glass (COG), chip-on-flex (COF) and tape carrier package (TCP), because of its compactness, reliability, process simplicity and environmental friendliness [1]. The polymer particle coated with a thin metal layer is usually adopted in liquid crystal display (LCD) assembly as the interconnection between the bumps of integrated circuit (IC) and corresponding conductive tracks on the glass substrate. Recently, much work has been performed to understand the ACF bonding mechanism and to predict the contact resistance of the interconnection using mathematical analysis, experimental technique and finite element (FE) modeling methods. Mathematical models were constructed to reveal the electrical conductive characteristics of the nickel-coated polymer particle and study the relationship of the particle deformation and the contact resistance [2], [3]. Paik *et al.* and

D. Zeng (Ed.): Future Intelligent Information Systems, LNEE 86, pp. 247–253.
springerlink.com © Springer-Verlag Berlin Heidelberg 2011

Kwon *et al.* studied the effects of ACF bonding process on the electrical characteristics of the metal-coated polymer particles experimentally [4]. However, further studies are still necessary to investigate the variability of the particle resistance under temperature load and different deformation of particles.

In this paper, the effects of the bonding parameters such as particle cracks, the deformation degree and the number of particles were considered to calculation the particle resistance. A mathematical model was used to predict the particle resistance of the nickel-coated polymer particle with the deformation degree. The variability of the particle resistance under temperature load and the number of particles was also conducted. The particle resistance for different conditions was then obtained to compare with experiment.

2 Analysis of Conductive Particles Resistance

Anisotropic conductive adhesive bonding steps are shown in Fig. 1. First, place the corresponding size of the conductive adhesive or conductive adhesive film (ACF) on the substrate. Secondly, pre-bond the conductive adhesive with the substrate. And then swap the divide film on the top of conductive adhesive. Finally, Pressure the circuit or chip on the conductive adhesive, in a certain temperature and pressure the specimen become solid.

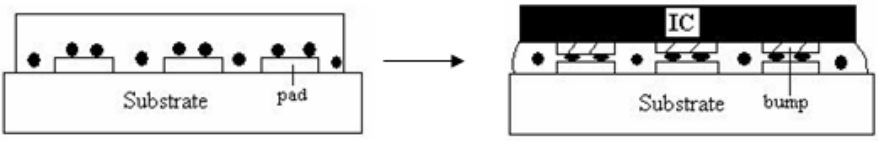

Fig. 1. Schematic figure of ACF bonding processing

The particle resistance $R_{particle}$ is the major contribution to the total contact resistance. The $R_{particle}$ can be predicted by the mathematical model and the approach is applicable for all the ACA assembly no matter which kind of metal-coated polymer particle used [2]. Therefore, the investigation of the electrical resistance mainly focused on the $R_{particle}$ in this study. Nickel was used as the conductive material. The nickel-coated polymer particle was generally in drum-shape after the ACA bonding but with two circular planes at the top and bottom respectively contacted with the Au bump and the glass.

The particle resistance after the ACF bonding described as

$$R_{particle} = R_{crack} + 2R_{circle} \tag{1}$$

After the ACA bonding, two cracks occurred in the most metal coated polymer particles used in the LCD assembly. The cracks were parallel to the direction of bonding

pressure and vertical to the planes of Au bump and glass. The resistance of the drum-shaped nickel coating with two cracks was denoted as the crack resistance R_{crack} .The circular planar nickel coating contributed to the circle resistance R_{circle} shown in Fig. 2.

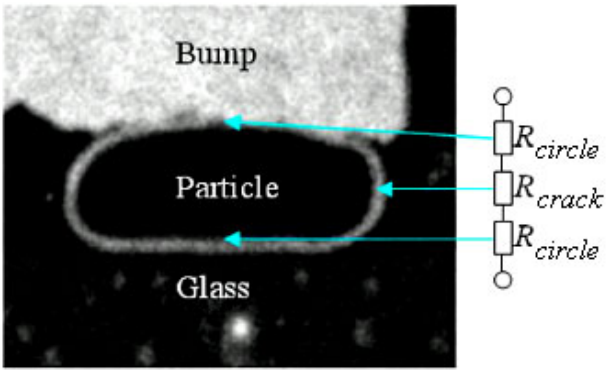

Fig. 2. Components of particle resistance in a single conductive particle

The R_{circle} can be calculated by

$$R_{circle} = \frac{1}{\sigma_N \pi} \int_{\frac{h}{2}}^{\frac{h}{2}+t} \frac{dy}{\left[\sqrt{\left(\frac{h}{2}+t\right)^2 - y^2} + r\right]^2} \cdot \tag{2}$$

Where, h is the height of deformed polymer core, t is the thickness of the nickel coating, r is the radius of circle resistance R_{circle} as shown in Fig. 3. The height and radius are various with the bonding pressures, and measured from the modeling results, while the thickness is assumed to be constant as 0.15μm, σ_N is the nickel conductivity.

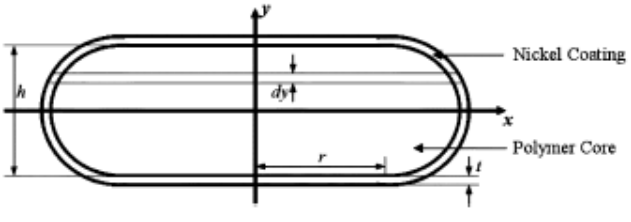

Fig. 3. Profile of a nickel-coated polymer particle

The crack resistance R_{crack} can be derived by

$$\frac{1}{R_{crack}} + \frac{2}{R_{virtual}} = \frac{1}{R_{ring}} \quad . \tag{3}$$

The R_{ring} and $R_{virtual}$ can be calculated by

$$R_{virtual} = \frac{2}{\sigma_N \pi} \int_0^{\frac{h}{2}} \frac{dy}{\frac{\theta_{crack}}{360}\left\{\left[\left(\frac{h}{2}+t\right)^2 - y^2\right] - \left[\left(\frac{h}{2}\right)^2 - y^2\right]\right\}} \quad . \tag{4}$$

$$R_{ring} = \frac{2}{\sigma_N \pi} \int_0^{\frac{h}{2}} \frac{dy}{\left[\sqrt{\left(\frac{h}{2}+t\right)^2 - y^2} + r\right]^2 - \left[\sqrt{\left(\frac{h}{2}\right)^2 - y^2} + r\right]^2} \quad . \tag{5}$$

The form of $R_{virtual}$ is similar with R_{ring} except it is a slice determined by the crack angle θ_{crack} from a sphere rather than from a drum. The θ_{crack} is defined by the angle of the plane which is perpendicular to the axis of the crack slice and cuts the crack slice. The θ_{crack} is various with the bonding pressures and relates to the deformation h of the particle.

3 Effect of Deformation Degree on the Particle Resistance $R_{particle}$

In accordance to the above analysis, when $r = \pi(d-h)/4$ and σ_N is the nickel conductivity as $2.5\times10^6\ \Omega^{-1}\cdot m^{-1}$, the relationships of the particle deformation h with the particle resistance $R_{particle}$ can be expressed as

$$\begin{aligned} R_{particle} = {} & \frac{2}{2.5\pi} \int_0^{\frac{h}{2}} \frac{dy}{\left[\sqrt{\left(\frac{h}{2}+0.15\right)^2 - y^2} + \frac{\pi(3.7-h)}{4}\right]^2 - \left[\sqrt{\left(\frac{h}{2}\right)^2 - y^2} + \frac{\pi(3.7-h)}{4}\right]^2} \\ & + \frac{2}{2.5\pi} \int_{\frac{h}{2}}^{\frac{h}{2}+0.15} \frac{dy}{\left[\sqrt{\left(\frac{h}{2}+0.15\right)^2 - y^2} + \frac{\pi(3.7-h)}{4}\right]^2} \end{aligned} \tag{6}$$

Where h variable ranges is from d to 2/3 d , because of the practice fracture limit, d is the diameter of polymer core, d =3.7μm. The calculation results of the relationships of the particle deformation h with the particle resistance $R_{particle}$ as shown in Fig. 4.

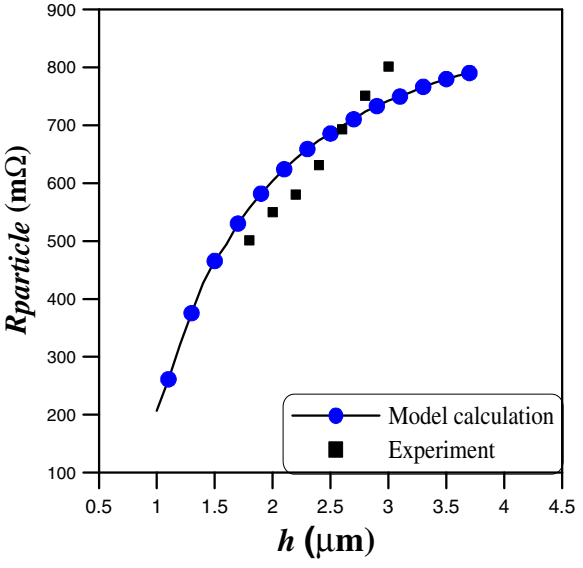

Fig. 4. Relationship of h and $R_{particle}$

The results indicated that the particle resistance strongly depended on the particle deformation h . Under the bonding pressure, the $R_{particle}$ decreased with h increasing, as shown in Fig. 4. However, if bonding pressure is too high, the conductive particle will be crushed which will lead to short-circuit. The particle resistance will be high when the particle is not cracked. Therefore, the model calculation results were not fit with the experiment in this tow conditions.

4 Effect of Rebound on Particle Resistance

In order to study the effects of thermal load, the bonding pressure was applied on the top particle and resulted in the deformation as shown in Fig. 5(a). A 2-D FEA model was constructed for the particle deformation under temperature 120℃. The simulation was performed with ABAQUS code of version 6.7-1. 2-D four-node elements were used to construct the solid particle. The simulation result of particle is shown as Fig. 5(b).

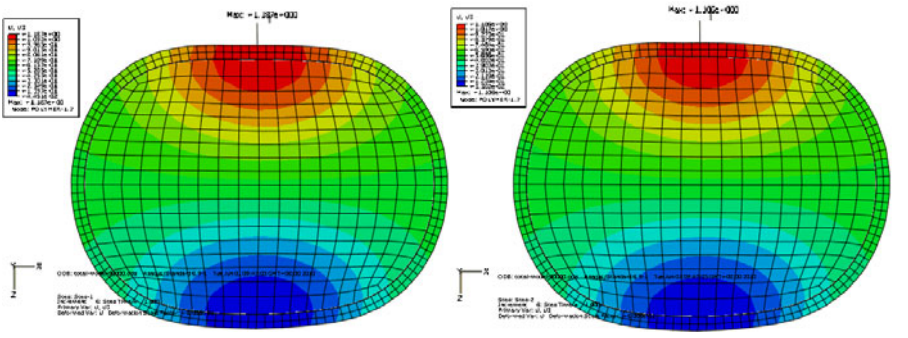

(a) (b)

Fig. 5. Simulation of the particle (a) before temperature (b) after temperature

The simulation results show that the particle spring back is 0.08μm under the thermal load. The particle resistance increases about 13mΩ calculated by Eq. (6), the increasing rate is 2.6%. The result is fit well with the experiment.

5 Effect of Particle Number on the Total Resistance

With the assumption that each particle resistance is equal, and the parallel relationship between the particle resistances $R_{particle}$, the total particle resistance of a conductive track can be expressed as

$$R_{toparticle} = R_{particle} / n \ . \tag{7}$$

Where n is the number of particle, therefore, with increasing of the number of particles, the total particles resistance decreases. The number of particles is not less than five on one conductive track in practice ACF assembly.

6 Conclusions

In the optimized bonding pressure range, the electrical resistance of the nickel-coated polymer particle with the cracks was strongly depended on the deformation degree of the particle. The calculation results are fit well with the experiment except the two conditions. The variability of the particle resistance under temperature load was obtained, which is useful to the analysis the effect of temperature to the ACF assembly. The effect the number of particles to the total particle resistance of a conductive track was also conducted. Those results can be concerned in the reliability of ACF assembly and further improve the design for manufacturability of the LCD panel.

Acknowledgement

This work was supported by National Natural Science Foundation of China (No.10972200).

References

1. Yamaguchi, M., Asai, F., Eriguchi, F.: Development of novel anisotropic conductive film (ACF). IEEE Trans. Compon. Packag. Technol. 35, 360–364 (1999)
2. Xie, B., Shi, X.Q., Ding, H.: Investigation of mechanical and electrical characteristics for cracked conductive particle in anisotropic conductive adhesive (ACA) assembly. IEEE Trans. Compon. Packag. Technol. 30(3), 361–369 (2008)
3. Xie, B., Shi, X.Q., Ding, H.: Understanding of Delamination Mechanism of Anisotropic Conductive Film (ACF) Bonding in Thin Liquid Crystal Display (LCD) Module. IEEE Trans. Compon. Packag. Technol. 30(3), 509–516 (2007)
4. Paik, K.W., Kwon, W.S.: Experimental analysis of mechanical and electrical characteristics of metal-coated conductive spheres for anisotropic conductive adhesives (ACAs) interconnection. IEEE Trans. Compon. Packag. Technol. 29(3), 528–534 (2006)

Study and Design of Transcutaneous Coupling Power Supply Device Energy Transmission

Junli Liu, Yanbo Xue, Yimei Chen, and Hui Xiong

School of Electrical Engineering and Automation Tianjin Polytechnic University
junliliu15@163.com, xue-yanbo@163.com,
chenplum@sohu.com, fine_xh@163.com

Abstract. With low energy transmission efficiency and low frequency of the transcutaneous coupling power supply device, factors affecting inefficiency are analyzed, formula under resonance is derived, relevant parameters of the primary and secondary coils are designed, and actually circuit is built in this paper. The circuit based on the coupling model of spatial isolated coils consists of the transmitting coil, the receiving coil and the load circuit. The distance between two transcutaneous coupling coils would be approximately equal to the thickness of the human's skin, nominally between 5–15 cm. Through theoretical analysis and practical tests, the experimental result indicates that the maximum transmission efficiency is achieved 54.24% through a distance of 10 cm and at the resonance frequency of 300KHz, and the maximum transmission efficiency is achieved 19.536% under non-resonance, and optimal frequency region of high frequency carrier is 200KHz-400KHz. So transmission efficiency and frequency presented the design achieve requirements.

Keywords: transcutaneous coupling; resonance; efficiency; frequency.

1 Introduction

The advantage of transcutaneous coupling power supply device is that in vivo devices are not limited by battery capacity through using wireless power supply or charged way, which largely reduces the cost. Moreover, the device avoids frequent operations changing battery when in vivo battery capacity is run out, and largely relieves surgery pain and economic burden of patients [1].

The transcutaneous coupling power supply device utilizes the law of electromagnetic induction. In vitro windings build alternating magnetic field in order to make in vivo windings generate induced electromotive force which makes two coupling coils achieve energy transmission. In vitro transmitting coil nexts to the skin, and the distance between the two coils would be approximately equal to the thickness of the human's skin, nominally between 5–15mm, and coupling coefficient of two coils is lower, so how to improve transmission efficiency becomes a difficulty point of transcutaneous coupling applications.

The optimal frequency tested is 60 KHz through a distance of 5cm based on circuit of reference [2], subsequently efficiency quickly lowers, but the frequency is too

D. Zeng (Ed.): Future Intelligent Information Systems, LNEE 86, pp. 255–261.
springerlink.com © Springer-Verlag Berlin Heidelberg 2011

low for the transcutaneous coupling power supply device. Improving efficiency of transcutaneous energy transmission system mainly depends on increasing frequency of energy transmission. Increasing operating frequency not only can improve coupling coefficient of transcutaneous transformer, but also can reduce the volume of system components, and especially reduce the volume of transcutaneous transformer, which can better meet requirements of transcutaneous coupling power supply device. However, core loss, copper loss and temperature raising all increase as the operating frequency increases, instead transmission efficiency of system is lowered. Therefore, transmission frequency of transcutaneous energy transmission system is nominally from dozens KHz to several MHz in terms of specific designs.

An isolated pulse generator with adjustable polarity and amplitude is designed in reference [5], and the design is provided power supply by in vitro high frequency signals. In order to improve signal transmission efficiency, the relation among efficiency, distance, frequency and coils is researched in terms of coupling coils equivalent circuit model, and the relation between transmission efficiency and wireless transmission system is derived at resonance and non-resonance, and vast experimental data are verified and therefore higher operating frequency is obtained, which provide basis for further design of wireless transmission system of the transcutaneous coupling power supply device.

2 The Scheme of Signal Transmission Module

The scheme of signal transmission module is shown in Fig. 1. It consists of the transmission circuit, the receiving circuit and the load. The transmission circuit consists of power supply, high frequency contravariant module and primary coil. The high frequency contravariant module can generate high frequency sine wave, and then acts on the primary coil. In order to improve transmission efficiency, the transmitting terminal adopts series resonant circuit. The transmitting terminal generates high frequency alternating magnetic field in order to makes secondary coil of the receiving terminal generate alternating induced electromotive force via waveform turning module to generate needed waveform of internal stimulation module.

Transcutaneous transformer consists of a couple of coupling coils respectively placed internal and external to the body. So the leakage inductances of the transcutaneous transformer are very large.

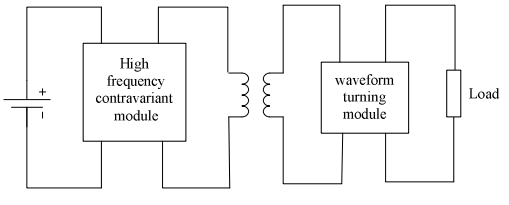

Fig. 1. Schmetic of Transcutaneous Transformer System

3 Efficiency Analysis and Optimal Design of Signal Transmission

In order to simplify analysis, the coupling primary coil L1 and the coupling secondary coil L2 are just equivalent analyzed in this paper. In Fig. 3, self-inductance L1, capacitor C1 and resistance R10 of the primary, and self-inductance L2, capacitor C2, resistance R20 and load ZL of the secondary are added in circuit.

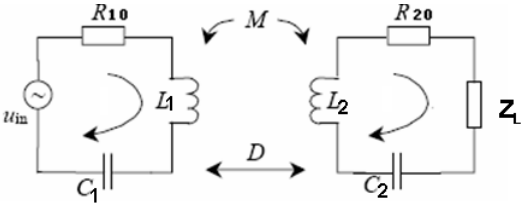

Fig. 2. Circuit model of coupling windings

In Fig. 2, the loop impedance is

$$\begin{cases} Z_1 = R_{10} + jwL_1 + \dfrac{1}{jwC_1} \\ Z_2 = R_{20} + jwL_2 + \dfrac{1}{jwC_2} + Z_L \end{cases} . \tag{1}$$

where ω is an operating frequency.

From Fig. 2, the loop equation is

$$\begin{cases} \dot{I}_1 Z_1 + jwM\dot{I}_2 = \dot{U}_{IN} \\ \dot{I}_2 Z_2 + jwM\dot{I}_1 = 0 \end{cases} . \tag{2}$$

The equivalent impedance of the input circuit is

$$Z_{IN} = Z_1 + \frac{(wM)^2}{Z_2} . \tag{3}$$

Analysis of input terminal power factor is

$$\lambda_{IN} = \cos\Psi_{IN} = \frac{\mathrm{Re}[Z_{IN}]}{|Z_{IN}|} . \tag{4}$$

Analysis of output terminal power factor is

$$\lambda_L = \cos\Psi_L = \frac{\mathrm{Re}[Z_L]}{|Z_L|} \tag{5}$$

Output power of load is

$$P_L = |U_L I_L| \cos\Psi_L = \left|\frac{U_L{}^2}{Z_L}\right| \cos\Psi_L \tag{6}$$

Input power is

$$P_{IN} = |U_{IN} I_{IN}| \cos\Psi_{IN} = \left|\frac{U_{IN}{}^2}{Z_{IN}}\right| \cos\Psi_{IN} \tag{7}$$

Transmission efficiency of two coils is

$$\eta = \frac{P_L}{P_{IN}} \times 100\% \tag{8}$$

From (1) to (8), the resulting equation of the η is as follows:

$$\eta = \frac{(wM)^2 \,\mathrm{Re}[Z_L]}{|Z_2|^2 [R_{10} + (wM)^2 E]} \times 100\% \tag{9}$$

where

$$E = \frac{R_{20} + \mathrm{Re}[Z_L]}{(R_{20} + \mathrm{Re}[Z_L])^2 + (wL_2 - \dfrac{1}{wC_2} - \mathrm{Im}[Z_L])^2} \tag{10}$$

For the transcutaneous coupling system, by improving external circuit, choosing appropriate frequency, adding compensation circuit and by choosing compensation

technique of the primary and secondary, the primary coil can operate at zero phase angle and the secondary coil can operate at resonance, which only make system larger transmission efficiency, but also makes system stably run.

The imaginary part of captance of the secondary compensating capacitor and the imaginary part of impedance of the secondary are equivalent at resonance and the value is zero, and the transmission efficiency is maximum. So equation as follows can be obtained.

$$\left|Z_2\right|^2 = (R_{20} + \mathrm{Re}[Z_L])^2 + (\mathrm{Im}[Z_L])^2 \tag{11}$$

4 Design of Relevant Parameter of System

Design of transcutaneous transformer contains core material and specification, turns per coil and line width and so on, which is a difficult point. Transmission efficiency of transcutaneous coupling windings is mainly studied in this paper. A transcutaneous coupling transformer with a large air gap between the primary and the secondary has large leakage inductances, which limits transmissive real power.

Based on the variation rate of magnetic flux is proportional to the value of induction electromotive force, larger induction electromotive force is obtained by higher frequency. But the absorption ratio of transcutaneous transformer nearby organizations and current density obviously increase as frequencies increase, which results in temperature rising. Therefore transmission frequency cannot infinitely be added, and the frequency usually is under 10MHz.

In order to reduce leakage inductances, pair of magnetic tank coupling coils is adopted in this paper. The type of the magnetic tank is ferrite, and its specification is G18*11. In order to reduce core loss, iron core generally uses MnZn ferrite material. Through analysis and calculation, turns of primary coil are 100, and turns of secondary coil are tested 150 by experimental methods. The primary and the secondary adopt enamel wire of line width 0.21mm by calculation and considering magnetic core window and reducing coils resistance.

5 Experimental Result and Analysis

According to designs above, the relation between every parameter of secondary coil and frequencies is tested by experiments at resonance and non-resonance.

When the distance between two coils is 10mm and amplitude of input signal is 5V, experimental results as follows are obtained by changing input frequency.

5.1 Relation between Output Power and Frequencies

Fig. 3 shows that the maximum output power tested at 300 KHz is 28.7mW, and efficiency at non-resonance is much lower than that at resonance.

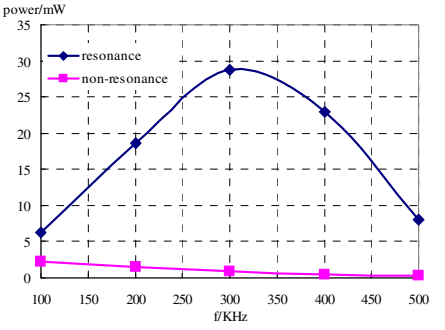

Fig. 3. Output power curves of resonance and non-resonance with frequency at D=10mm

5.2 Relation between Efficiencies and Frequencies

Fig. 4 shows that the maximum efficiency tested at 300 KHz is 54.24%, and frequency variation at non-resonance is almost stable but the value is lower, and the maximum efficiency at non-resonance is 19.536%.

According to experiments above, the optimal operating frequency ranges approximately from 200 KHz to 400 KHz when the distance between the two coils is 10mm and is in the state of resonance. When coil sizes and distance are constant, there is a maximum efficiency as input frequencies are changed. The optimal frequency of transcutaneous transformer is 300 KHz when the load is constant in this experiment.

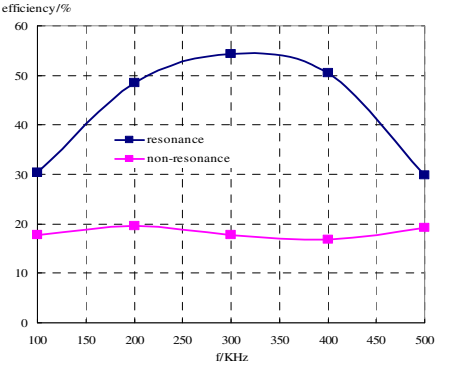

Fig. 4. Efficiency curves of resonance and non-resonance with frequency at D=10mm

6 Conclusion

Every parameter of transcutaneous coupling power supply device is correlative and interactional. With low energy transmission efficiency and low frequency of the transcutaneous coupling power supply device, transmission efficiency at resonance

oscillation and non-resonance is derived basing on model of transcutaneous coupling windings, and model of windings is theoretically designed, and experimental result shows that the optimal operating frequency ranges approximately from 200KHz to 400KHz and the maximum transmission efficiency is achieved 54.24% when the distance between the transformer windings is 10 mm, which achieves requirements of transcutaneous coupling power supply device. This design realizes maximization of energy transmission in terms of circuit designs.

References

1. Pernia, A.M., Orille, I.C., Martinez, J.A., et al.: Transcutaneous microvalve activation system using a coreless transformer. Sensors and Actuators A-Physical 136(1), 313–320 (2007)
2. Niu, C., Hao, H., Li, L., et al.: The transcutaneous Charger for Implanted Nerver Simulation Device. In: Proceeding of the 28th IEEE EMBS Annual International Conference, pp. 4941–4944 (2006)
3. Wu, Y., Yan, L.G., Xu, S.: Modeling and performance analysis of the New Contactless Power Supply System. In: Proceedings of the Eighth International Conference on Electrical Machines and Systems, pp. 1983–(1987)
4. Ben Hmida, G., Dhieb, M., Ghariani, H., et al.: Transcutaneous power and high data rate transmission for biomedical implants. In: International Conference on Design & Test of Integrated Systems in Nanoscale Technology, pp. 374–378 (2006)
5. Li, G., Bai, B., Lin, L., et al.: Design of a isolated pulse generating circuit with adjustable polarity for implantable stimulators (accepted)
6. Shiba, K., Nukaya, M., Tsuji, T., et al.: Analysis of Current Density and Specific Absorption Rate in Biological Tissue Surrounding Transcutaneous Transformer for an Artificial Heart. IEEE Transactions on Biomedical Engineering 55(1), 205–213 (2008)
7. Blad, B., Bertenstam, L., Rehncrona, S., et al.: Measurement of contact impedance of electrodes used for deep brain stimulation. ITBM-RBM 26, 344–346 (2005)
8. Sato, F., Nomoto, T., Kano, G., et al.: A new contactless power-signal transmission device for implanted functional electrical stimulation (FES). IEEE Transactions on Magnetics 40(4), 2964–2966 (2004)
9. Arai, S., Miura, H., Sato, F., et al.: Examination of Circuit Parameters for Stable High Efficiency TETS for Artificial Hearts. IEEE Transactions On Magnetics, 4170–4171 (2005)
10. Chen, Q., Wong, S.C., Tse, C.K., et al.: Analysis, Design, and Control of a Transcutaneous Power Regulator for Artificial Hearts. IEEE Transaction On Biomedical Circuits And Systems, 23–31 (2009)
11. Lee, S.-Y., Lee, S.-C.: An Implantable Wireless Bidirectional Communication Microstimulator for Neuromuscular Stimulation. IEEE Transactons on Circuits and Systems 5(12), 2526–2538 (2005)
12. Ghovanloo, M., Atluri, S.: A wide-band power-efficient inductive wireless link for implantable microelectronic devices using multiple-carriers. IEEE Transactions on Circuits and Systems I-Regular Papers 54(10), 2211–2221 (2007)

Invariant Zeros of Linear Singular Systems via the Generalized Eigenvalue Problem

Jerzy Tokarzewski

Warsaw University of Technology,
Faculty of Electrical Engineering,
Pl. Politechniki 1, 00-661 Warsaw, Poland
jtokarzewski@zkue.ime.pw.edu.pl

Abstract. The notion of invariant zeros of continuous time MIMO LTI singular control systems is derived from the generalized eigenvalue problem. This notion is intimately related to the concepts of state-zero and input-zero directions, and consequently to the problem of zeroing the system output, and essentially extends the classical concept of Smith zeros. As invariant zeros we take only those generalized eigenvalues which generate nontrivial solutions of the state equation and yield the identically zero system response. Some important algebraic and geometric consequences of the adopted definition of invariant zeros for standard and singular systems are presented. Finally, it is indicated how the concept of invariant zeros can be extended to linear fractional-order systems and to systems with time delay in state.

Keywords: invariant zeros, singular systems, generalized eigenvalue problem.

1 Introduction

The knowledge of zeros of linear multivariable systems is needed for many control problems, including zeroing the output, tracking the reference output, disturbance decoupling, non-interacting control (see [4], [9] and the references therein).

Consider a generalized linear time-invariant control system of the form

$$\begin{aligned} E\dot{x}(t) &= Ax(t) + Bu(t) \\ y(t) &= Cx(t) + Du(t) \end{aligned} \tag{1}$$

where $x \in R^n$ is the state vector, $u \in R^m$ is the control vector and $y \in R^r$ is the output vector; E is a real $n x n$ matrix and A, B, C, D are real matrices of dimensions $n x n$, $n x m$, $r x n$ and $r x m$ respectively. It is assumed that $\det(sE - A) \neq 0$ and matrices B and C are nonzero, i.e., $B \neq 0$ and $C \neq 0$. The standard case is obtained for $E = I$ where I is the identity matrix.

The following two matrices are strictly related to the system (1):

- the system (Rosenbrock) matrix (the $(n + r) x (n + m)$ polynomial matrix of the complex variable s)

D. Zeng (Ed.): Future Intelligent Information Systems, LNEE 86, pp. 263–270.
springerlink.com © Springer-Verlag Berlin Heidelberg 2011

$$P(s) = \begin{bmatrix} sE - A & -B \\ C & D \end{bmatrix} \tag{2}$$

-the transfer-function matrix (the rxm matrix of the complex variable s)

$$G(s) = C(sE - A)^{-1}B + D\,. \tag{3}$$

The system matrix (2) can be also written in the form ([2], [5], [8])

$$P(s) = s\begin{bmatrix} E & 0 \\ 0 & 0 \end{bmatrix} - \begin{bmatrix} A & B \\ -C & -D \end{bmatrix}. \tag{4}$$

The most commonly used notion of zeros of (1) are the Smith zeros ([3, 4], [7], [12, 13], [15]). These zeros are defined on the basis of the Smith canonical form of $P(s)$ (2). With the aid of elementary row and column operations (2) is transformed to the Smith diagonal form ([4], [10]). The product of diagonal polynomials is called the zero polynomial of (1) and its roots are the Smith zeros of (1). The Smith zeros can be equivalently defined as those points of the complex plane for which the pencil (2) loses its normal (determinantal) rank. The set of Smith zeros is at most finite. For $r = 0$ (or $m = 0$) the Smith zeros are the input (or output) decoupling zeros [14].

In [2], [8] it is indicated that the Smith zeros can be treated as generalized eigenvalues of the matrix (4). In this paper we derive from the generalized eigenvalue problem for the matrix (4) a more general concept of zeros of (1) than the Smith zeros. Then, we mention how to extend this new concept to linear systems of frac-tional order and systems with time delay in state.

2 The Generalized Eigenvalue Problem

Consider real matrices N and M of dimensions pxq and the polynomial matrix pencil $sN - M$. In the *generalized eigenvalue problem* [5] we are looking for all complex numbers $\lambda \in C$ such that

$$\lambda N w = M w \tag{5}$$

for some vector $0 \neq w \in C^q$. Each number $\lambda \in C$ with the above property is called the *generalized eigenvalue* of the pair (N, M) and the corresponding to it vector w is called the *generalized eigenvector*. It is clear that λ is a generalized eigenvalue of (N, M) if and only if rank of $\lambda N - M$ is smaller than q. The set of all generalized eigenvalues of (N, M) we denote as

$$\sigma(N, M) := \{\lambda \in C : rank(\lambda N - M) < q\}\,. \tag{6}$$

It is important to note that generalized eigenvalues are not only those complex numbers λ for which rank of $\lambda N - M$ is smaller than normal rank of $sN - M$.

In general case, $\sigma(N,M)$ can be empty, finite or equal to the whole complex plane. The last case takes place if for example $p < q$ or, more generally, if normal rank of $sN - M$ is smaller than $\min\{p,q\}$.

3 Invariant Zeros and Generalized Eigenvalues

The system matrix of (1) can be written in the form

$$P(s) = sN - M, \text{ where } N = \begin{bmatrix} E & 0 \\ 0 & 0 \end{bmatrix}, \; M = \begin{bmatrix} A & B \\ -C & -D \end{bmatrix}. \tag{7}$$

Immediately from the definition of Smith zeros it follows that each Smith zero of (1) is a generalized eigenvalue of the pair (N,M) determined in (7). In fact, if λ is a Smith zero of (1), we have the following relations

$$rank(\lambda N - M) < normal\ rank(sN - M) \le \min\{n+m, n+r\} \le n+m$$

and, consequently, λ is an element of $\sigma(N,M)$.

Taking into account the definition of generalized eigenvalues presented in Section 2, we can formulate the following definition that corresponds to the case (7).

Definition 1. A number $\lambda \in C$ is a generalized eigenvalue of $P(s)$ (7) if and only if there exists a nonzero vector $\begin{bmatrix} x^o \\ g \end{bmatrix} \in C^{n+m}$ such that $P(\lambda)\begin{bmatrix} x^o \\ g \end{bmatrix} = \begin{bmatrix} 0 \\ 0 \end{bmatrix}$, i.e.,

$$\lambda E x^o - A x^o = Bg, \quad Cx^o + Dg = 0. \tag{8}$$

◊

In this section we try to answer the question whether beside the Smith zeros some other generalized eigenvalues of (7) can serve as zeros of (1). To this end, we need to establish first which elements of $\sigma(N,M)$ may be treated as good candidates for zeros of (1). As a zero of (1) we will take any generalized eigenvalue λ (see Definition 1) which satisfies the following two conditions:

a) λ generates a nontrivial solution of the state equation of (1) (i.e., a solution that is not the identically zero solution);
b) this solution yields the identically zero system response (i.e., $y(t) = 0$ for all $t \ge 0$).

Remark 1. It is easy to note that if λ is a generalized eigenvalue as in Definition 1, then $x^o e^{\lambda t}$ is a solution of the state equation of (1) which corresponds to the initial condition x^o and to the input $ge^{\lambda t}$. To this end it is enough to multiply both sides of

the first equality in (8) by $e^{\lambda t}$ and then to interpret the result in the context of the state equation in (1). Multiplying the second equality in (8) by $e^{\lambda t}$ and taking into account the above and the output equation in (1), we get $y(t) = Cx^o e^{\lambda t} + Dge^{\lambda t} = 0$ for all $t \geq 0$. The term $x^o e^{\lambda t}$ is called the solution of the state equation of (1) generated by λ (see the condition a) above). Thus, the condition b) for good can-didates for zeros of (1) is fulfilled for all generalized eigenvalues of $P(s)$ (7).

Of course, λ, x^o and g in Definition 1 can in general case be complex. On the other hand, from the practical point of view, we are interested only in real initial conditions, inputs and solutions. The latter we obtain by taking $\operatorname{Re} x^o$ as the initial condition, $\operatorname{Re}(ge^{\lambda t})$ and $\operatorname{Re}(x^o e^{\lambda t})$ as the corresponding input and solution or $\operatorname{Im} x^o$ as the initial condition, $\operatorname{Im}(ge^{\lambda t})$ and $\operatorname{Im}(x^o e^{\lambda t})$ as the corresponding input and solution. ◊

However, as the following simple example shows, Definition 1 is too general for our purposes.

Example 1. Consider a system (1) with the matrices

$$E = \begin{bmatrix} 1 & 0 \\ 0 & 0 \end{bmatrix},\ A = \begin{bmatrix} -1 & 0 \\ 0 & -1 \end{bmatrix},\ B = \begin{bmatrix} -2 & 1 & 0 & 1 \\ 0 & 0 & 1 & 0 \end{bmatrix},\ C = \begin{bmatrix} 1 & 0 \\ 0 & 1 \end{bmatrix},\ D = 0.$$

According to Definition 1 each $\lambda \in C$ is a generalized eigenvalue. Since the mat-rix C is invertible, the equations (8) are fulfilled if and only if $x^o = 0$ and $0 \neq g \in \ker B$. But none of the considered generalized eigenvalues satisfies the condition a). ◊

In order to narrow down Definition 1 we consider the set of only those generalized eigenvalues of (7) which satisfy simultaneously the conditions a) and b). As we know from Remark 1, the condition b) is satisfied for any generalized eigenvalue of (7). For the analysis of the condition a) we consider the following two disjoint cases:

- the subspace $\ker \begin{bmatrix} -B \\ D \end{bmatrix}$ is trivial (i.e., it contains merely the zero vector);
- the subspace $\ker \begin{bmatrix} -B \\ D \end{bmatrix}$ is nontrivial.

In the first case we shall show that if $\lambda \in C$ satisfies Definition 1, then $x^o \neq 0$. For this aim, suppose that λ satisfies Definition 1 and $x^o = 0$. Then, however, since

$\begin{bmatrix} -B \\ D \end{bmatrix}$ has full column rank, we must have $g = 0$ which contradicts the assumption that $\begin{bmatrix} x^o \\ g \end{bmatrix}$ is a nonzero vector (see Definition 1).

In the second case, let λ satisfy Definition 1 and let $x^o = 0$. Then, however, g must satisfy the relation $0 \neq g \in \ker \begin{bmatrix} -B \\ D \end{bmatrix}$. Such generalized eigenvalue is not interesting for our purposes since it does not satisfy the condition a).

Summarizing the above discussion, we restrict the set of all generalized eigenvalues of (7) to the subset which consists of all those generalized eigenvalues for which there exists a generalized eigenvector $\begin{bmatrix} x^o \\ g \end{bmatrix}$ with the property $x^o \neq 0$. The elements of this subset we call, in order to distinguish from the Smith zeros, the *invariant zeros* of (1). In this way we obtain the following definition of invariant zeros.

Definition 2. ([16, 17]) A number $\lambda \in C$ is an invariant zero of (1) if and only if there exist vectors $0 \neq x^o \in C^n$ and $g \in C^m$ such that the triple λ, x^o, g satisfies the equalities (8). ◊

4 Consequences of Definition 2 for Standard and Singular Systems

For standard systems (1) (i.e., when $E = I$) some of their algebraic and geometric properties following from Definition 2 were analyzed in [16, 17]. The most important of these properties are listed below.

1) The set of invariant zeros is an extension of the set of Smith zeros (i.e., each Smith zero is also an invariant zero).
2) The set of invariant zeros may be empty, finite or infinite (i.e., equal to the whole complex plane).
3) If the set of invariant zeros is empty or finite, it is equal to the set of Smith zeros. Moreover, if the set of invariant zeros is finite, the invariant and Smith zeros are the same objects (i.e., they are the roots of the same polynomial).
4) Definition 2 induces the decomposition of the class of all standard systems (1) into two disjoint subclasses:
   - the subclass of non-degenerate systems (when the set of invariant zeros is a at most finite);
   - the subclass of degenerate systems (when the set of invariant zeros is infinite).

5) If (1) is degenerate, the set of its Smith zeros may be empty or nonempty (i.e., in the class of degenerate systems we have two disjoint subclasses).
6) To each invariant zero (in particular, by virtue of the property 1), to each Smith zero) there corresponds a real initial condition and a real valued input which generate a nontrivial solution of the state equation and the identically zero system response (see Remark 1). Note that such dynamical interpretation of zeros is essentially simpler than that given in [6].
7) If (1) is asymptotically stable and a triple λ, $x^o \neq 0$, g satisfies Definition 2, then the input $\mathrm{Re}(ge^{\lambda t})$ (or $\mathrm{Im}(ge^{\lambda t})$) when applied to the system at an arbitrary initial condition yields the asymptotically vanishing system response.
8) The set of invariant zeros is invariant under the following set of transformations: change of basis in the state space, nonsingular transformations of the inputs or outputs, constant state or output feedback to the inputs.
9) Each output decoupling zero of (1) is its invariant zero (however, an output decoupling zero does not need to be a Smith zero of (1)).
10) The transmission zeros of (1) are defined as invariant zeros of the observable and controllable subsystem of (1) (in the four-fold Kalman decomposition [11]). The transmission zeros of (1) are its invariant zeros.
11) If (1) has the identically zero transfer-function matrix, then the system is degenerate and its Smith zeros are input-output decoupling zeros of (1).
12) If a transfer-function matrix G(s) is given and (1) is its minimal state-space realization, then zeros of G(s) are defined as invariant zeros of the system (1). By virtue of the property 8), such definition is well posed, i.e., it does not depend upon the choice of minimal realization. G(s) is called degenerate if the number of its transmission zeros is infinite.
13) The set of invariant zeros of (1) is empty if and only if the maximal output-nulling subspace ([17], p.197) of the system is trivial. This equivalence does not hold if instead of invariant zeros we consider the set of Smith zeros (i.e., there exist systems (1) for which the set of Smith zeros is empty while the subspace under consideration is nontrivial).
14) If (1) is non-degenerate, then the dimension of the maximal output-nulling subspace is equal to the degree of the zero polynomial.
15) If (1) is degenerate, then the dimension of the maximal output-nulling subspace is strictly greater than the degree of the zero polynomial and the zero dynamics [9] of (1) depend upon the control vector.
16) If G(s) has a common zero and pole, then they can be distinguished merely by their dynamical state-space interpretations (see [17], p.35).
17) The individual kinds of decoupling (input or output decoupling, input-output decoupling) zeros of (1) can be determined (including multiplicities) as the roots of appropriate polynomials obtained from characteristic polynomials of the diagonal submatrices of the A-matrix in the four-fold Kalman decomposition of (1) (see [17], p.16).

Of course, only a few of the above statements can be derived directly from Definition 2. The greater part of them, however, requires some additional information on the system. Such information can be extracted from the first non-zero Markov parameter of (1) by using its Moore-Penrose pseudo-inverse or singular value decomposition [1] as the tools (comp. [16, 17]).

For singular systems (1) the statements 1)-6) and 8)-9) as above remain valid ([17], chap.8). Recall that (1) is degenerate if and only if

$$normal\ rank\, \mathrm{P}(s) < n + rank \begin{bmatrix} -\mathrm{B} \\ \mathrm{D} \end{bmatrix}$$

and (1) is non-degenerate if and only if in the above inequality the sign '<' can be replaced by '='. Further consequences of Definition 2 for singular systems require a more detailed research.

5 Conclusion

The following two questions concerning an extension of the notion of invariant zeros to linear systems with time delay in state and fractional order systems can also be an-alyzed.

Consider the system $\dot{x}(t) = Ax(t) + A_1 x(t-h) + Bu(t)$, $y(t) = Cx(t)$, $t \geq 0$; where $h > 0$ is a known delay, $x(\theta) = \varphi(\theta)$ for $\theta \in [-h, 0]$ is a given initial condition and $x \in R^n$, $u \in R^m$, $y \in R^r$, A, A_1, B, C are real matrices. It is assumed, for simplicity, that admissible inputs and initial conditions are continuous. The associated system matrix is $\mathrm{P}(s) = \begin{bmatrix} sI - A - A_1 e^{-sh} & -B \\ C & 0 \end{bmatrix}$. The task to be solved is to derive from the generalized eigenvalue problem for the quasi-polynomial matrix pencil $\mathrm{P}(s) = sN - Qe^{-sh} - M$ the following definition (comp.[19]): a number $\lambda \in C$ is an invariant zero of the system if and only if there exist $0 \neq x^o \in C^n$ and $g \in C^m$ such that $\mathrm{P}(\lambda) \begin{bmatrix} x^o \\ g \end{bmatrix} = \begin{bmatrix} 0 \\ 0 \end{bmatrix}$.

Consider the fractional order system (comp. [20]) ${}^{C}\mathrm{D}_{0+}^{\alpha} x(t) = Ax(t) + Bu(t)$, $y(t) = Cx(t)$, where $0 < \alpha < 1$ and ${}^{C}\mathrm{D}_{0+}^{\alpha}$ stands for the Caputo derivative. The associated system matrix is $\mathrm{P}(s) = \begin{bmatrix} s^{\alpha} I - A & -B \\ C & 0 \end{bmatrix}$. The task to be solved is to derive from the generalized eigenvalue problem for the pencil $\mathrm{P}(s) = s^{\alpha} N - M$ the following definition (comp. [18]): a number $\lambda \in C$ is an invariant zero of the system if

and only if there exist $0 \neq x^o \in C^n$, $g \in C^m$ and a $\mu \in C$ such that $\mu = \lambda^\alpha$ and $P(\mu)\begin{bmatrix} x^o \\ g \end{bmatrix} = \begin{bmatrix} 0 \\ 0 \end{bmatrix}$, where $P(\mu) = \begin{bmatrix} \mu I - A & -B \\ C & 0 \end{bmatrix}$.

References

1. Ben-Israel, A., Greville, T.N.E.: Generalized Inverses: Theory and Applications. Springer, NY (2003)
2. Berg, J.M., Kwatny, H.G.: Unfolding the Zero Structure of a Linear Control System. Linear Algebra and Its Applications 258, 19–39 (1997)
3. Bourles, H., Fliess, M.: Finite Poles and Zeros of Linear Systems: an Intrinsic Approach. Int. Journal of Control 68, 897–922 (1997)
4. Callier, F.M., Desoer, C.A.: Multivariable Feedback Systems. Springer, NY (1982)
5. Cohen, S., Tomasi, C.: Systems of Bilinear Equations. Technical Report STAN-CS-TR-97-1588, Dept. of Computer Science, Stanford Univ. (1997)
6. Desoer, A.D., Schulman, J.D.: Zeros and Poles of Matrix Functions and their Dynamical Interpretation. IEEE Trans. on Circuits and Systems 21, 3–8 (1974)
7. Gantmacher, F.R.: The Theory of Matrices. Nauka, Moscow (1988) (in Russian)
8. Hoagg, J.B., Bernstein, D.S.: Nonminimum-phase Zeros. IEEE Control Systems Magazine 27, 45–57 (2007)
9. Isidori, A.: Nonlinear Control Systems. Springer, NY (1995)
10. Kaczorek, T.: Polynomial and Rational Matrices: Applications in Dynamical Systems Theory. Springer, London (2007)
11. Kalman, R.E.: Mathematical Description of Linear Dynamical Systems. SIAM Journal of Control 1, 152–192 (1963)
12. MacFarlane, A.G.J., Karcanias, N.: Poles and Zeros of Linear Multivariable Systems: a Survey of the Algebraic, Geometric and Complex Variable Theory. Int. Journal of Control 24, 33–74 (1976)
13. Misra, P., Van Dooren, P., Varga, A.: Computation of Structural Invariants of Generalized State-Space Systems. Automatica 30, 1921–1930 (1994)
14. Rosenbrock, H.H.: State-Space and Multivariable Theory. Nelson-Wiley, NY (1970)
15. Schrader, C.B., Sain, M.K.: Research on System Zeros: a Survey. Int. Journal of Control 50, 1407–1433 (1989)
16. Tokarzewski, J.: Zeros in Linear Systems: a Geometric Approach. Warsaw University of Technology Press, Warsaw (2002)
17. Tokarzewski, J.: Finite Zeros in Discrete Time Control Systems. Springer, Heidelberg (2006)
18. Tokarzewski, J.: Zeros and the Output-Zeroing Problem in Linear Fractional Order Systems. Archives of Control Sciences 18, 437–451 (2008)
19. Tokarzewski, J.: Zeros in Linear Systems with Time Delay in State. Int. J. of Applied Mathematics and Computer Science 19, 609–617 (2009)
20. Vinagre, B.M., Monje, C.A., Calderon, A.J.: Fractional Order Systems and Fractional Order Control Actions. Lecture 3, TW#2: Fractional Calculus Applications in Automatic Control and Robotics. In: Proc. 41st IEEE Conf. on Decision and Control, Las Vegas, USA (2002)

A Node Importance Assessment Method of Complex Networks Based on Reliability Measure

Fu-yun Li, Yue-zu Cao, and Guang Li

Department of Basic Science, Beijing Institute of Graphic Communication
102600 Beijing, China
liguang68000@163.com

Abstract. Based on researches of node assessment methods in complex networks environment, a kind of node importance assessment method of complex networks based on reliability measure was presented. Introducing the concept of reliability, the network connectivity measure was defined to analyze the change of network reliability index in the node attack strategy, so as to determine the validity of node assessment method. On this basis, network vulnerability parameter was given to measure network damage and to find key nodes. The method solves the problem of difference in node assessment caused by different index selection and network topology of traditional node assessment methods. The final example analysis also verifies the effectiveness and feasibility of this method.

Keywords: complex network; key nodes; reliability; network connectivity; measure.

1 Introduction

Non-homogeneous topology nature of complex network determines the importance of each node in the network is different. It is a problem worthy deepen research that whether there is some connection and which one is the most important of existing various indexes of node importance in the network, such as node degree [1], mediate number and etc. Based on the different network structure environment where nodes locate and specific requirements of reality, there is difference on the definition of key points. The existing node assessment method may not be suitable to different complex network. Different topology of the same network, such as directed graph, undirected graph, weighted network, non-weight network, has different impact on key points [2-4]. Therefore, it is the basic problem to be solved of the paper that how to effectively assess node and find key nodes that meet to actual situation. The paper focused on difference of complex network node assessment using idea of node delete method and introduction the concept of reliability. Two factors of average path length and connectivity branch that affect network performance were considered and a kind of node importance assessment method based on reliability index was presented. The specific arrangement of the paper is as follows: Section 2 introduces general methods of node importance measurement of complex network; Section 3 presents the node

D. Zeng (Ed.): Future Intelligent Information Systems, LNEE 86, pp. 271–278.
springerlink.com © Springer-Verlag Berlin Heidelberg 2011

importance assessment method based on reliability measure; Section 4 verifies the effectiveness and reliability of the proposed method with experiment; Section 5 concludes our work.

2 Node Importance Measurement Method of Complex Network

2.1 Association between Complex Network Characteristics and Node Importance

Complex network has not precise definition till now, which can be seen as topology abstract of large amount of actual complex systems. If we abstract elements inside complex system as nodes and relations among elements as connections, it constitutes a network with complex connection relationships. Researches of many physicists and mathematicians have shown that network topology determines their properties. The complex network abstracted from various kinds of real networks has three basic statistical characteristics. One is small world characteristic, that is average distance between node pairs in the network is short, where the definition of distance is the number of edges that passed by the shortest path connect two nodes. Large number of experimental studies have shown that almost all real networks have small world effect. The second is scale free characteristic, namely the degree of network node obeys power-law distribution. The third is clustering characteristic, which is measured by the clustering coefficient of nodes. The importance difference of nodes in complex network has closely relation with abstracted basic characteristics of complex networks. Researches show that the invulnerability of network topology under different damage strategies is also different. Under random damage, the scale-free network has more tolerance than random network. But under the index selection damage based on node degree, the scale-free network was extremely fragile. Damage on 5% core nodes will basically paralyze the whole network. Then we can find importance core node through node importance assessment, so as to improve the network reliability through protecting these key nodes.

2.2 Node Importance Assessment Methods

There were many methods to assess node importance in the network, the essence of which are derived from graph theory and data mining based on graph. The methods to study on node importance mainly include social network analysis and node deletion.

(1) Social network analysis

Node importance is equivalent to significantly in the social network analysis. It considered about node importance according to location characteristic of node in the whole network not destroy the integrity of network. The basic idea of social network analysis tries to find useful attribute information from the network to highlight difference of nodes in the network. The presented node importance measurement methods

were divided into two types of centrality and prestige. The measurement indexes include degree, closeness, betweenness, information, eigenvector and cumulated nomination. Among them, degree uses number of edges of adjacent nodes, which only consider about direct connections, so it can only reflect local characteristics of network. The definition of closeness is the reciprocal of summation of distance from this node to all other nodes, which reflect the center level of this node in network. Betweenness is defined as percentage of path number that includes node i account for the number of all shortest paths, which reflect the control role of this node on other nodes. The information considers about the information flow that transmitted in all paths. The eigenvector index considers from the status or prestige of network member and sees the prestige of single member as the linear combination of all other members, so as to obtain a linear equation. The eigenvector vector corresponding to maximum eigenvector of this equation is the importance index of each node.

(2) Node deletion method

The node importance is equivalent to destructive in node deletion method, which reflect the importance of network node or node set through measurement of destructive role on network connection in case of deleting node. It is mainly based on core and core degree, spanning tree and graph entropy. Among them, the idea of node importance measurement method based on core and core degree is to measure destructive extent of network connection. The minimum spanning tree index is that the node importance determines change of number of trees after nodes deleted. After node and related edges were deleted, less is the number of spanning tree, more important is the node. The idea of node importance measurement method based on graph entropy is that the deletion of node and its related edge will affect information transmission of the graph, and then change the entropy of graph.

3 Node Importance Assessment Method Based on Reliability Measurement

3.1 Concept of Reliability

Reliability is the characteristics of system to complete specific functions in regulated time under regulated conditions. As to a complex network system, the reliability is an important overall index. It not only related to equipment and link, but also has close relation with network topology. From the existing network reliability definition we can see that the involved elements mainly include reliability research object, regulated conditions, regulated time, regulated functions and probability. In the reliability research, invulnerability and survivability are two main aspects [5]. Invulnerability refers to the ability of network to complete regulated functions after network topology changes or reorganization in case of human destruction or node failure. Survivability mainly describes reliability of network under random failure. Based on topology of

complex networks, the paper mainly research on connectivity reliability based on invulnerability of complex network.

3.2 Measurement of Connection Reliability

The invulnerability of network generally describes the reliability of network topology from the perspective of connection. The past connectivity determination basis is that there exist paths between any two nodes in the network. But such kind of connectivity constraint is not suitable for complex network with large number of nodes. Because as to complex networks, interconnectivity among nodes in the network does not means good connectivity of the network, which is also related to network diameter. Therefore, we should comprehensively consider two indexes of average path length and network connectivity that can reflect network performance to give a new connectivity measure of complex networks:

$$C = 1 \Big/ W \sum_{i=1}^{W} \frac{N_i}{N} L_i \tag{1}$$

Where, C is the connectivity coefficient; W is the number of network connectivity branches; N is the total number of network nodes; N_i is the number of node in the i-th connectivity branch; L_i is the average shortest path of the i-th connectivity branch, namely the average value of shortest connect distance among any two nodes in the connectivity branch. From the definition we can know that the essence of connectivity coefficient is the reciprocal of the product that weighted average of average shortest distance and number of connectivity branches. Less is the number of connectivity branches, smaller is the average shortest path of each branch. And the better the network connectivity, connectivity coefficient C will be. Therefore, through the comparison analysis of change of network connectivity coefficient under random and intentional attacks, we can verify the validity and feasibility of traditional node assessment methods.

3.3 Network Vulnerability Coefficient

Although connectivity coefficient index is useful to analysis of network reliability, but it is impossible to measure the destructive extent of network when surfed from attacks. Use the concept of toughness in graph theory as parameter to measure network vulnerability, so as to judge the damage extent when the network surfed from node attack. The definition is as follows:

$$T(G) = \min\left\{ \frac{|S| + m(G-S)}{w(G-S)}, S \subseteq V \right\} \tag{2}$$

Where, V is the node set; S is the removed node set; $|S|$ is the number of removed nodes; $m(G\text{-}S)$ is the node number of maximum branch after $|S|$ nodes were removed; $w(G\text{-}S)$ is the maximum branch number of network after $|S|$ nodes were removed. From (2) we can see that, $T(G)$ arrives at the minimum value when the following conditions are met:

(1) The removed node number $|S|$ is the minimum.

(2) After removing of $|S|$ nodes, $m(G\text{-}S)$ is the minimum, which indicates that the network is divided into many braches after destruction.

(3) The $w(G\text{-}S)$ is maximum, namely the network collapse into many branches, which has the most obvious damage.

In summary, when the tightness of network reaches minimum and causes maximum damage to network connectivity, the removed $|S|$ nodes are key nodes to be found.

4 Experiment Analysis

Defined 20 × 20 network as Fig. 1 shows, where there is 20 nodes and 28 edges.

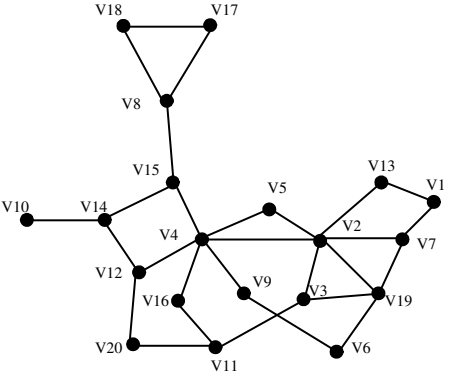

Fig. 1. Network of 20×20

(1) Use degree, closeness, contract method and deletion method to conduct importance assessment on nodes respectively. The computation result of each index and the rank based on node index value are listed in Table 1. As the idea of node deletion can avoid problem of accuracy of assessment caused by difference of methods, for the problem of data consistent of node importance, we can use spanning tree to determine its importance. The node assessment example is shown in Table 1.

Table 1. Node assessment examples

Number	Degree		Closeness		Contract method		Deletion method	
1	V4	6	V4	0.027778	V4	0.430245	V8	1
2	V2	6	V2	0.024390	V15	0.317455	V14	1
3	V19	4	V15	0.022727	V2	0.274234	V15	1
4	V8	3	V12	0.021277	V12	0.214752	V4	0.9987
5	V15	3	V5	0.020833	V14	0.204054	V2	0.9947
6	V11	3	V16	0.020000	V11	0.184797	V19	0.9608
7	V12	3	V19	0.019608	V8	0.182406	V20	0.9608
8	V7	3	V9	0.019608	V1	0.138103	V11	0.9352
9	V3	3	V3	0.019231	V13	0.138103	V12	0.9337
10	V14	2	V11	0.018519	V7	0.134075	V7	0.8915
11	V20	2	V14	0.018182	V20	0.132061	V3	0.8788
12	V6	2	V7	0.018182	V16	0.132061	V6	0.7443
13	V9	2	V13	0.017544	V3	0.126020	V9	0.7443
14	V1	2	V8	0.017241	V6	0.117965	V10	0.7349
15	V13	2	V6	0.017241	V9	0.117965	V1	0.7229
16	V16	2	V20	0.016949	V19	0.109910	V13	0.7229
17	V17	2	V1	0.014085	V17	0.087087	V16	0.6862
18	V18	2	V10	0.013699	V18	0.087087	V17	0.6667
19	V5	2	V17	0.013333	V10	0.083283	V18	0.6667
20	V10	1	V18	0.013333	V5	0.035736	V5	0.619

(2) Based on the values of node assessment, use degree, closeness, contract method and deletion method to conduct random and intentional attack on nodes [6]. After deletion of 5%, 10%, 25% and 50% nodes, formula (1) is introduced to compute network connectivity coefficient, so as to analyze network reliability change and determine the effectiveness of node assessment methods, which is shown in Fig. 2.

Restricted by network scale of experiment, after deletion of 5% nodes according to four standards, there is large change on network connectivity coefficient, and the node attack effect almost same under different indexes. With the increase of node removal proportion, the network connectivity coefficient continuously decreases, and the effect of node attack is significantly different. Data shows that in the node attack process, when the removal proportion up to 10%, the effect of degree index attack is the most obvious, the network connectivity coefficient is 0.1134. Afterwards, the node intentional attack effect of degree index gradually reflect, which minimize the network coefficient firstly. When the node removal proportion is 50%, all nodes in the network are not connected. So we can arrive at the conclusion that selecting node intentional attack based on degree index is the most effective in case of network destruction.

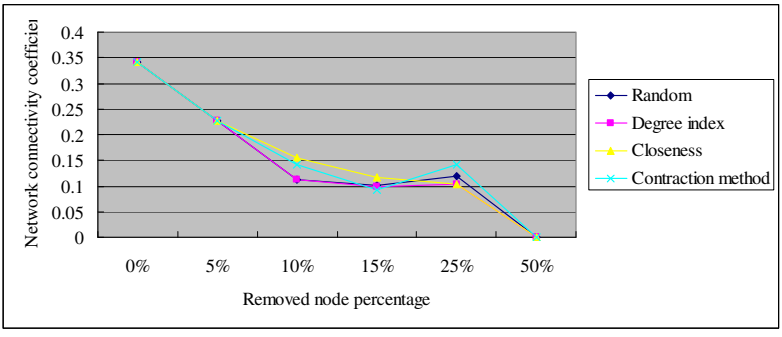

Fig. 2. Network reliability coefficient statistical comparison under node attack strategies

(3) To conduct node intentional attack on experimental network based on degree index and measure network destructive extent with tightness, so as to find the minimum and key points, which is shown in Fig. 3.

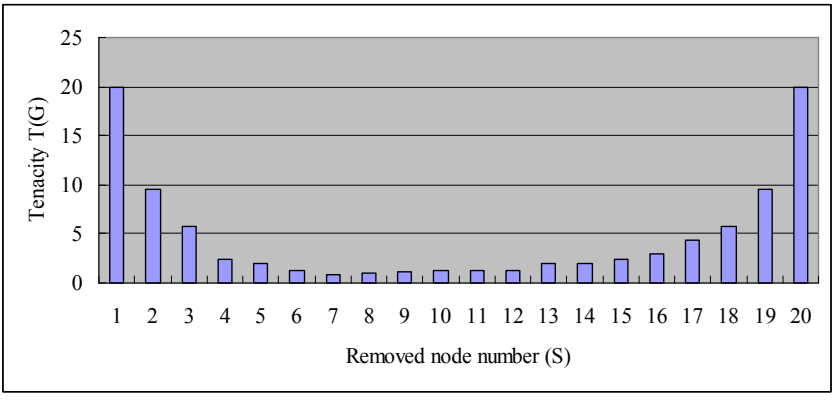

Fig. 3. Tightness statistics under node intentional attack based on degree index

The data shows that the tightness of network decreased to the minimum as 0.9 when 7 nodes were removed. The minimum network branches number $m(G\text{-}S)$ is 2 and the maximum number $w(G\text{-}S)$ is 10, which indicates that the damage on network is the maximum. Therefore, the former 7 nodes are key nodes, namely V2, V4, V8, V14, V19 and V1. It is consistent with expectation of maximum network damage effect.

5 Conclusion

The paper utilized reliability index to assess on node importance, which overcome shortcoming s that is different of traditional node assessment method. It quantitatively assess on node importance in complex networks comprehensively and objectively, so

that it can be measured in the uniform standard. It is a new attempt on network node importance assessment. Because there are many measurement indexes and analysis methods of network reliability, it will have great impact on key points that how to determine more reasonable measurement indexes and analysis method, which is also the future research focus.

References

1. Xu, J., Fei, Q., Wang, Y.L.: Core and Coritivity methods for optional designs of information intercourse network systems. Journal of Systems Engineering 16, 275–281 (2001)
2. Washio, T., Motoda, H.: State of the Art of Graph-based Data Mining. SIGKDD Explore News 5, 59–68 (2003)
3. Zhao, Y.H., Wang, Z.L., Zheng, J., Guo, X.J.: Finding most vital node by node importance contribution matrix in communication networks. Journal of Beijing University of Aeronautics and Astronautics 35, 1076–1079 (2009)
4. Shetty, J.: Discovering Important Nodes through Graph Entropy the Case of Enron E-mail Database. In: Proc of KDD, pp. 74–81 (2005)
5. Wu, J., Tan, Y.J.: In: Study on measure of complex network invulnerability, vol. 20, pp. 128–131 (2005)
6. Tan, Y.J., Wu, J., Deng, H.Z.: Evaluation method for node importance based on node contraction in complex networks. System Engineering Theory and Practice 11, 79–83 (2006)

Experimental Research on the Degradation of MOV Used in Multiplate Paralleling

Xing Xiong[1], Yong Sun[2], Zhi-hang Du[3], and Hai-juan Fan [4]

[1] School of Control and Computer Engineering of NCEPU,
Beijing 102206, China
[2] Bei Jing Testing Center of Surge Protective Devices, Beijing 100176, China
[3] College of Electrical Engineering, Xi'an Jiaotong University,
Xi'an 710049, China
[4] College of Information and Control Engineering of NUIST,
Nanjing 210049, China

Abstract. The structure of multiplate paralleling of MOV (metal oxygen varistor) are widely used in practical, which can not only decrease the residual voltage, but distribute current and prolong MOV's lifetime. But the characteristic of the group of MOV would be largely effected without preparation by screening strictly. We forced our research on three pieces of MOV used in paralleling whose U1mA were different to each others. By analysising the variation of U_{1mA}, $I_{leakage}$ and nonlinearity coefficient (α), the conclusions are obtained as following. Firstly, the piece with the minimum U_{1mA} initial would be the most likely to be degradation, the group of paralleling pieces would be more easier to be degradation because of the piece with initial minimum U_{1mA}, degradation ratio was 1% varied in each stock, about 2.7 times than other pieces, and the other pieces in paralleling would be also degradation comparatively. Secondly, analysising the variation trend of nonlinearity coefficient (α), the degradation finally leaded MOV to be short circuit.

Keywords: metal oxide varistors; U_{1mA}, $I_{leakage}$, nonlinearity coefficient (α); paralleling; degradation.

1 Introduction

MOV was widely used in over-voltage protection for its excellent nonlinear characteristics. Generally, the U_{1mA} was defined as the voltage under one milliampere in direct current. $I_{leakage}$ is the current got from the voltage of 75% U_{1mA}. nonlinearity coefficient (α) is a parameter calculated as: $\alpha=1/\log(U_{1mA}/U_{0.1mA})$ to measure the nonlinearity current varies along with the voltage changes in the middle electric field region. The paper would research the characteristics of three pieces of MOV used in paralleling by analysising the U_{1mA}, $I_{leakage}$, nonlinearity coefficient (α).

D. Zeng (Ed.): Future Intelligent Information Systems, LNEE 86, pp. 279–285.
springerlink.com © Springer-Verlag Berlin Heidelberg 2011

SPD (Surge Protective Device) of 40～100kA discharge capacity are always consist of three pieces of MOV, so as to increase the discharge capacity and decrease its residual voltage. Literature [1] researched MOV's characteristic under 8/20μs impulse current, Literature [2] putted forward the "resistance chain theory" to analysis the degradation of MOV. We experimental researched three pieces of MOV paralleling, statistical analysised their U_{1mA}, $I_{leakage}$ and nonlinearity coefficient (α), to get the disciplines between the interoperation groups and the single ones.

2 The Arrangement of Experiments

(1) Carefully screened MOV manufactured by one factory, ensuring the U_{1mA} differences of three pieces of MOV is 1Volts in group A, 6Volts in group B, 10Volts in group C. The initial parameters are given as table 1 showed.

Table 1. The initial data of MOV

Number	U_{1mA} (V)			
	1	2	3	Paralleled
Group A	619	619	620	589
Group B	615	621	620	588
Group C	610	619	620	592
Number	Leakage current (μA)			
	1	2	3	Paralleled
Group A	10.1	9.66	11.1	31.8
Group B	16.4	8.94	9.10	37.4
Group C	12.3	9.46	8.05	33.0

(2) Testing the groups with 8/20μs waveform [3] and nominal through-flow 40kA. five times cycling, and measuring the U_{1mA}, $I_{leakage}$, nonlinearity coefficient (α) of the pieces during the spacing interval.

(3) Sorting and analysising the datas.

3 Experimental Results and Analysising

3.1 Testing Results of U_{1mA}

According to the principle, Now we get the ultimate test data in table 2.

Table 2. The U_{1mA} data after 25 groups impulse

Number	U_{1mA} (V)			
	1	2	3	Paralleled
Group A	610	612	615	600
Group B	584	616	612	591
Group C	562	607	606	574

3.1.1 The Analysis of U_{1mA} Data in Group C

We set the group C which has the most obvious change trend as analysising object, and draw trend curves by C1, C2, C3 single data. Showed in figure 1.

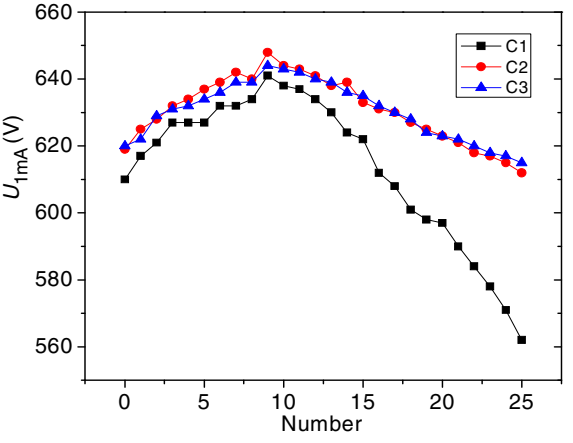

Fig. 1. The trend curves of U_{1mA} in Group C

From figure 1,we can get that：

(1) Due to the nuances of shunt amplitude, According to the theory [4], Every piece shunt:

$$I_n=I_a+(U-U_{an})/R_{zn} \quad (1)$$

Where R_{zn} is dynamic resistance, I_a is amplitude of impulse current, U is overall residual value, U_{an} is residual value of each piece.

So the effects of aging in every piece is different, The initial U_{1mA} voltage have 10V difference, after 3 groups impulse, only 5V at last.

(2) According to standard GB18802.1 [3], change range of U_{1mA} allows for ±20%, the piece of C1 reaches the limit degradation firstly, it's almost on the

degradation rate 1% per impulse group beyond the limits; The degradation degree is 2.7 times higher than other pieces on the data of U_{1mA}.

The conclusion is that, when MOV pieces are used paralleling, the one with minimum U_{1mA} initial will be degradation firstly, and the speed and degree of degradation is the highest compared with others.

3.1.2 The Analysis of U_{1mA} Data Among Group A, B, C

Figure 2 shows that the U_{1mA} trend curve of group A, B, C paralleling.

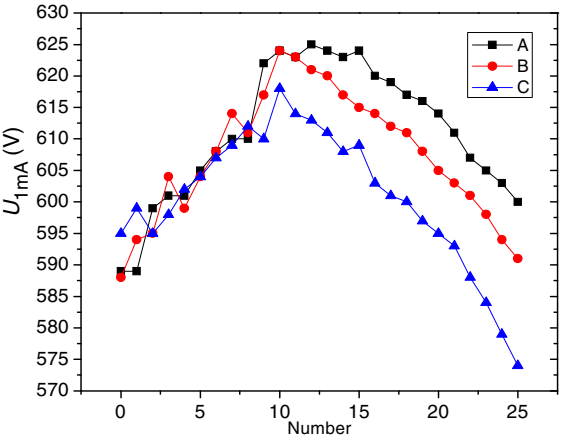

Fig. 2. The trend curves of U_{1mA} among Group A, B, C

Obviously, we can get:

(1) The paralleled data of U_{1mA} is lower than each piece about 30V.

(2) The U_{1mA} voltage of each paralleled group is have just 4V differ, although there is a lower piece. And there is minimal difference during the 8 times before.

That shows the performance of one piece MOV, will not affect overall during the prior period of protection。

(3) At last, group C is degradation first, because that there is a lower U_{1mA} voltage piece paralleled. The degradation speed of group B is centered. The degradation degree of group C is almost 1.7 times higher than group A.

Therefore, the performance of life span will be reduces which lower U_{1mA} voltage piece paralleled.

3.1.3 Other Experimental Phenomenons

From the datas, the initial U_{1mA} voltages which the pieces named A3, B3, and C3 are 620V. They also appear different change; we can draw the trend curve of degradation part and showed in figure 3.

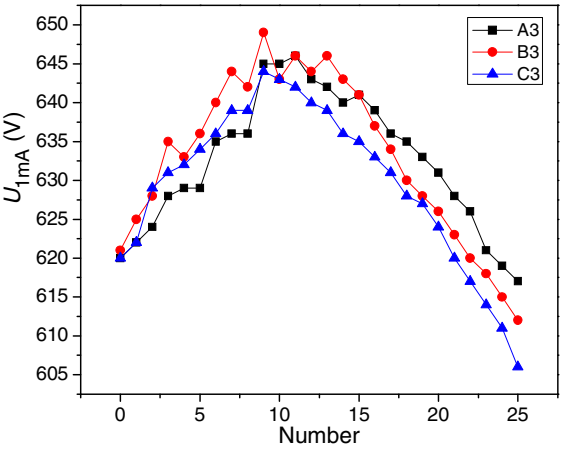

Fig. 3. The trend curves of U_{1mA} of A3, B3, C3

Pieces A3, B3 and C3 also appear degradation after 25 groups impulse. The degradation speed and degree of C3 is the highest, because that there is a lower U_{1mA} voltage piece 'C1' paralleled. B3 is centered.

So get inference: the performance of other piece will be influenced by lower U_{1mA} voltage piece paralleled.

3.2 The Analysis of Leak Current Data

According to the principle of experiment, we get the ultimate test data in table 3.

Table 3. The leakage current datas after 25 groups impulse

Number	leak current /μA			
	1	2	3	Paralleled
Group A	11.7	10.4	10.8	33.4
Group B	20.4	9.74	9.35	39.8
Group C	25.3	12.1	13.7	51.2

Obviously, the paralleled data of leak current is a little higher than each piece, and compared with U_{1mA} the direction of curve is opposite, but they have the same trend.

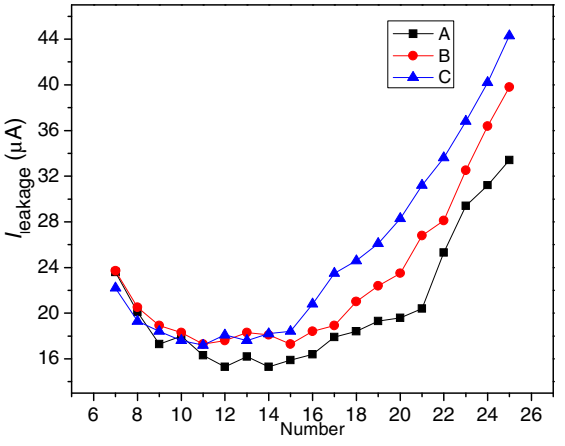

Fig. 4. The trend curves of I_{leak} among Group A, B, C

3.3 The Analysis of Nonlinearity Coefficient

The nonlinearity coefficient (a) is characteristic parameters. For example, there is a normal MOV piece which α=48, when the voltage has 5% change, the current should be change 10 times.

α is defined as：

$$\alpha=1/\log(U_{1mA}/U_{0.1mA}); \tag{2}$$

Where $U_{0.1mA}$ is a voltage which tested under 0.1mA direct current.

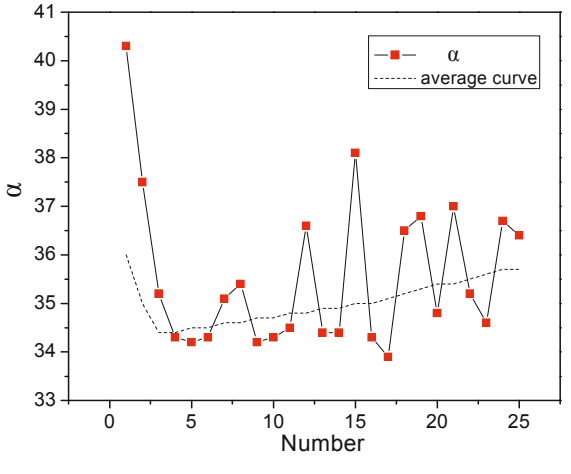

Fig. 5. The trend and fitting curve of 'α' of Group C

It can be seen from Figure 5 the curve of coefficient 'α' is volatility. After a number of measured by logarithmic calculation, the results show certain discrete.

Overall trends such as fitting curve, after a rapidly falling it increases stability. Analyzing the phenomenon, we find that the same trend of $U_{0.1mA}$ and U_{1mA}, but the changes amplitude of $U_{0.1mA}$ is lower almost 50%.

In group C, for example, The initial data of $U_{0.1mA}$=569V, at last is 556V, the changes amplitude is 13V, similarly U_{1mA}=21V。 According to the formula (2), we can see that the rule of trend is numerical value embodiment of $U_{0.1mA}$ and U_{1mA}.

When the U_{1mA} voltage continues to fall and nearly coincidence with $U_{0.1mA}$ value, the 'α' will be rose to infinity. Of course in this situation, MOV was seriously degradation even short-circuit breakdown.

4 Conclusions

The experiments showed that MOV with different U_{1mA} would not be degradation in initial testing, but the stability of paralleling group would change, and lifetime shortened. The conclusions are as follows:

(1) The piece of MOV with minimum U_{1mA} inital degradated most quickly, and the group with the maximum difference of U_{1mA} would also be the most quickly degradation one.
(2) The other MOVs paralleled in the group degradated slower than the one with minimum U_{1mA} initial.
(3) The variation behavior of nonlinearity coefficient (α) showed that the degradation leaded MOV to be short circuit finally.

References

[1] Shu, J., Duan, Q., Zhang, N.-f.: Discussion about Physical Concepts of MOV. Low Voltage Apparetus (6), 37–41 (2008)
[2] Zhang, S.-g., Ji, Y.-z.: Degradation Mechanism of Zno Waristors. Journal of Functional Materials 24(6), 529–532 (1993)
[3] International Electrotechnical Commission. IEC 61643-1: 2005 Low-voltage surge protective device-Part 1: surge protective devices connected to low-voltage power distribution systems- Requirements and tests. IEC publiced (2005)
[4] Wang, M.-h., Hu, K.-a., Zhang, N.-f.: The Method and Theoretical Analysis of Parallel Connection of Varistors in Surge Protective Device. Insulators and Surge Arresters (6), 26–33 (2004)

A Kind of Integrated Resource Scheduling Framework for PMP WMAN

Liang Luo[1] and Yuan Gao[2]

[1] School of Computer Science and Engineering,
Beijing University of Aeronautics and Astronautics, 100191 Beijing, China
[2] School of Computer Science and Technology,
Beijing Institute of Technology, 100081 Beijing, China
{luolianng,alexandagy}@gmail.com

Abstract. Scheduling strategy is directly related to performances of throughput, delay and others in IEEE 802.16 system. The paper presented a kind of IEEE 802.16 Integrated Resource Scheduling Framework (IRSF) of broadband wireless access system specializing in Point to Many Point (PMP) network structure of WSN (Wireless Sensor Network), including two parts of access control and bandwidth allocation. In the aspect of access control, the access of RTPS traffic can steal partly reservation bandwidth of NRTPS traffic to improve channel utilization. In the bandwidth allocation system, the proposed D-DRR algorithm can avoid status of low priority traffic in starvation for source occupied and can also guarantee QoS of high priority traffic. The Urgent-threshold Proportion Delay Fair (UDPF) scheduling of RTPS traffic was also presented to meet requirements of delay and capacity characteristics of real-time traffic. The framework can provide different scheduling schema for traffics with different QoS level, so as to meet QoS requirements of different traffics.

Keywords: IEEE 802.16; PMP; QoS; integrated resource scheduling; access control.

1 Introduction

With the continuous advance of Internet, requirements of users on broadband network access and broadband multimedia applications are also increasing. IEEE 802.16 working group proposed IEEE Wireless MAN interface standard. It is a air interface specification for band 2-66 GHz, the wireless access system coverage scope regulated by which is up to 50km. Total rate provided by each base station is up to 280Mbps, which is mainly used in MAN. IEEE 802.16 defines two kinds of network topology, namely PMP and MESH modes. PMP mode is a kind of point-to-point network topology, which at least includes a Base Station (BS) and a number of Subscriber Stations (SS). As central station, the BS manages communication of all SS in its serve range and connects to backbone. Each SS locates in various locations of the service area. The paper laid emphasis on the PMP mode and researched on its resource scheduling algorithm. The MAC in IEEE 802.16 system uses connection-oriented

D. Zeng (Ed.): Future Intelligent Information Systems, LNEE 86, pp. 287–293.
springerlink.com © Springer-Verlag Berlin Heidelberg 2011

mechanism to provide appropriate QoS for services as voice, data, multimedia and others. However, the standard has not regulated more about details of resource scheduling and bandwidth allocation. Scheduling strategy is directly related to performances of throughput, delay, blocking rate and others. The paper researched on resource scheduling strategy of 802.16 systems and put forward effective resource scheduling framework. The framework was made up of two parts, namely access control program and bandwidth allocation program. The two-layer scheduling mechanism provided different scheduling program for different traffic type, so as to ensure users' QoS requirements. The specific arrangement of the paper is as follows: Section 2 introduces IEEE 802.16 and its MAC protocol; Section 3 gives integrated resource scheduling framework and designs detail access and bandwidth allocation program; Section 4 concludes our work.

2 MAC Protocol of IEEE 802.16

In the PMP mode, communication between BS and SS can be divided into downlink from BS to SS and uplink from SS to BS. Under Time Division Duplex (TDD) mode, downlink is broadcast channel and Time Division Multiplexing (TDM) manner is used. The uplink is sharing channel, which is divided several mini time slots and use TDM manner. In the downlink, only BS sends data. When SS receives broadcast information from BS, it will select packets sent to it. While in the uplink, each SS will firstly send bandwidth request to BS. According to request, BS will allocate occupied slot in each uplink data frame for each SS and include result in UL-WAP message, then broadcast to SS through downlink channel. SS will transmit data based on the specified slot in UL-WAP.

The MAC layer of IEEE 802.16 is connection-oriented. After SS connected to Bs, the BS will assign Connection Identifier (CID) for one or more applications in it. Different connection corresponds to different QoS level. In the bandwidth allocation, MAC of 802.16 uses request-grant mechanism, which can consider about stability of non-competitive access and effectiveness of competitive access, so that it can maintain usage efficiency when there are a large number of statistical multiplexing users.

To differentiate QoS level of service, 802.16defines four kinds of traffic:

(1) Unsolicited Grant Service (UGS) is used to transmit fixed-rate real-time data service as T1/E1 and VOW. BS will periodically grant fixed bandwidth based on maximum sustainable rate of service flow. The main parameters include maximum sustain transmission rate, maximum tolerable transmission delay and allowed delay jitter.

(2) Real-time Polling Service (RTPS) support variable rate real-time service as MPEG. BS will provide periodic unicast request opportunities, the main parameters of which include minimum reserved transmission rate, maximum sustain transmission rate, maximum tolerable transmission delay and traffic service priority.

(3) Non Real-time Polling Service (NRTPS) supports services that have periodical variable packets with minimum bandwidth request, sucha as FTP. BS will provide unicast request opportunities with a longer period than RTPS of non-period, which

can use competitive request. The main parameters include minimum reserved transmission rate, maximum sustain transmission rate and traffic service priority.

(4) Best Effort (BS) supports non-real-time packet data services without any request on rate and delay jitter, such as E-mail. The main QoS parameters include maximum sustain transmission rate and traffic service priority.

3 Design of Integrated Resource Scheduling Algorithm

The overall framework of scheduling strategy was made up of two parts. One is access control strategy used to restrict amount of service access to network so as to avoid overload or starvation. The other is bandwidth allocation strategy to determine packet sequence and number of services in specific queue, which is the core of scheduling strategy. These two parts interact with each other to promise QoS of system.

3.1 Access Control Program Design

The role of access control program is to restrict traffic amount access to network so as to avoid overload, so that to prevent service being served can not obtain assured QoS for congestion. When the traffic was launched, SS sent message DSA to BS to request for connection. At the same time, it will notice traffic priority level and QoS type to BS. BS then determines that according to access control strategy. If it is allowed, the access is permitted and return management message of access permission, so that the new connection is built. Otherwise, the access will be rejected. The specific access control policy is as follows [2]: Suppose that total amount allocated to uplink transmission is C. When new traffic arrived, total amount assigned to current UGS connection is $C_{ugs,used}$ and that assigned to current RTPS connection is $C_{rtps,used}$. If all NRTPS connections reserve minimum bandwidth, the minimum total amount of all NRTPS connection is $C_{nrtps,used,min}$. The total amount has been assigned is $C_{used}=C_{ugs,used}+C_{rtps,used}+C_{nrtps,used}$. So the obtained minimum total amount is $C_{used,min}=C_{ugs,used}+C_{rtps,used}+C_{nrtps,used,min}$.

(1) If the new access traffic is UGS, the needed maximum bandwidth is equal to minimum bandwidth, namely $C_{ugs,min}=C_{ugs,max}$. If $C_{ugs,max}\leq C-C_{used}$, the UGS traffic is permitted to access and assigned maximum reserved bandwidth, then update $C_{used}=C_{used}+C_{ugs,max}$. Otherwise it is rejected.

(2) If the new access traffic is RTPS, the needed minimum bandwidth is $C_{rtps,min}$ and maximum bandwidth is $C_{rtps,max}$. If $C_{rtps,max}\leq C-C_{used}$, the RTPS traffic is permitted to access and assigned maximum reserved bandwidth, then update $C_{used}=C_{used}+C_{ugs,max}$. Else if $C-C_{used}\leq C_{rtps,max}\leq C-C_{used,min}$, the RTPS traffic is permitted to access and assigned maximum reserved bandwidth, then update $C_{used}=C$, which means RTPS traffic steal partly reserve bandwidth of NRTPS traffic [3]. Otherwise it is rejected.

(3) If the new access traffic is NRTPS, suppose that the needed minimum bandwidth of NRTPS is $C_{nrtps,min}$, maximum bandwidth as $C_{nrtps,max}$, and actual reserved bandwidth as C_{nrtps} ($C_{nrtps,min}\leq C_{nrtps}\leq C_{nrtps,max}$). If $C_{nrtps,min}\leq C-C_{used}$, the NRTPS traffic is permitted to access and assigned corresponding bandwidth. If $C_{used}+C_{nrtps}\leq C$, the

reserved bandwidth is C_{nrtps}, otherwise it is $C_{nrtps,min}$. Then C_{used} is updated. When $C_{used}+C_{nrtps} \leq C$, $C_{used}=C_{used}+C_{nrtps}$. If $C_{used}+C_{nrtps} \geq C$, $C_{used}=C$. Otherwise, it is rejected.

(4) If the new access traffic is BE, it is permitted but does not assign bandwidth, which means that the minimum reserved bandwidth is 0 by default.

The proposed access control strategy above is determined by priority level of traffic. The UGS traffic has highest priority, so the system should reserve bandwidth for UGS. RTPS is real-time traffic, which should be permitted as possible and steal partly reserved bandwidth for NRTPS traffic in the condition of ensuring minimum reserved bandwidth for NRTPS, so as to improve channel utilization. While NRTPS is non-real-time traffic, it can reserve needed bandwidth if resource is adequate, or it will reserve minimum bandwidth. BE is best-effort traffic without QoS requirements, which can be permitted for access. If there is residual bandwidth, it is allocated, or it will be rejected retaining connection.

3.2 Bandwidth Allocation Program

To meet QoS requirement of various traffic in IEEE 802.16, the paper presented integrated scheduling framework as Fig. 1 showed and brought out different scheduling strategies for different traffic type.

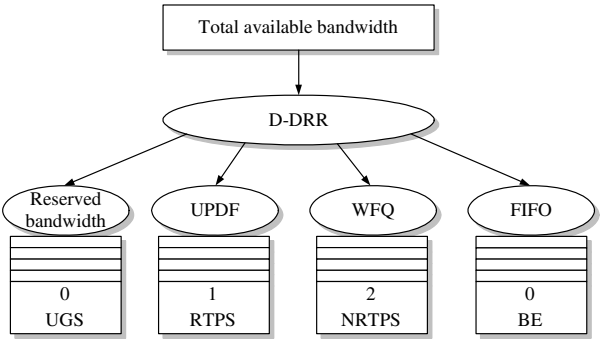

Fig. 1. Scheduling framework

For the four kinds of traffic UGS, RTPS, NRTPS and BE in IEEE 802.16, the Dynamic Deficit Round Robin (D-DRR) algorithm can be used for scheduling [4, 5]. It mains a quantum and deficit counter for each service queue and tries to send packet whose length is quantum in a round. Then it will adjust quantum through tracking length of specific queue in real-time, so as to change reserved bandwidth. The quantum is average number of bytes be served in a round and deficit counter is initialized to quantum, so as to serve non-empty queues. The number of bytes in each scheduling round is equal to quantum in principle. As long as deficit count is greater than zero, the service queue has access to service. After packet is served, deficit counter will reduce byte number of this packet. When the deficit counter is not greater than

zero, the queue will not obtain service. Whenever a new round begins, all deficit counters of non-empty queues will increase its quantum. In this way, different reserved bandwidth is supported through setting different quantum for different queue. It can also meet QoS requirements of some specific low- delay traffic through tracking length of specific queues to adjust quantum, so as to avoid local queue starvation. Set *quantum*[*i*] and *deficit*[*i*](*i*=0,1,2,3) as quantum and value of deficit counter of UGS, RTPS, NRTPS and BE. The algorithm flow of D-DRR is shown in Fig. 2.

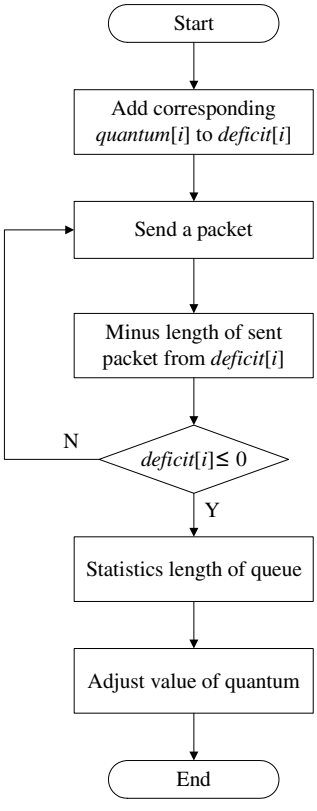

Fig. 2. D-DRR algorithm flow

In the figure, *quantum*[*i*]=queue length $L_i \times W_i$(*i*=0,1,2,3), where W_i is the weight of queue. The weight of UGS is the highest, followed by that of RTPS, NRTPS and BE. The corresponding weight of UGS and RTPS can be set to higher, so that they can obtain more bandwidth to meet the QoS requirements.

D-DRR algorithm adjusts quantum through tracking corresponding service queue in real-time to change reserved bandwidth, so that it can not only meet QoS requirements of some specific real-time traffic, but also avoid unfair phenomenon that low

priority traffic can not obtain service caused by strict priority scheduling. Each traffic type has its own packet scheduling strategy to secondly allocate obtained bandwidth.

(1) UGS traffic

For UGS traffic, BS provides bandwidth authority for it periodically with a manner of preemptive. The size of authorized bandwidth has got consultation when SS built connection with BS. So SS needs to explicitly send bandwidth request packet to BS, which eliminate overhead and delay of bandwidth request packet, so as to meet requirement of delay and jitter.

(2) RTPS traffic

To ensure fair and real-time requirements, the Urgent-threshold Proportion Delayed Fair (UPDF) algorithm is utilized for RTPS traffic [6]. The scheduling strategy is as follows: Set time t, the request rate of RTPS as $R_i(t)$, the queuing delay of first packet in its corresponding traffic queue i as D_i, maximum delay of traffic flow as T_i, then the threshold delay related to T_i of queue i is D_i/T_i. The UPDF algorithm is:

$$K = \arg\max\{P_i \times C + (D_i / T_i) \times R_i(t)\} \tag{1}$$

Where, P_i is priority parameter; C is priority differentiation constant and $C > (D_i / T_i) \times R_i(t)$.

$$P_i = \begin{cases} 1 & D_i \geq T_i \\ 0 & D_i \leq T_i \end{cases} \tag{2}$$

UPDF scheduling algorithm divides queue into two priorities, namely pre-overtime and normal. Each level is scheduled with the maximum queue of $(D_i / T_i) \times R_i(t)$. If pre-overtime state is compared with normal state, the queue in pre-overtime state will obtain priority. The algorithm not only takes into account delay requirement of real-time traffic, but consider about capacity characteristics.

(3) NRTPS traffic

For NRTPS traffic, Weighted Fair Queue (WFQ) [7] scheduling mechanism can be used for bandwidth allocation. The NRTPS is scheduled according to weight of connection, which is the ratio of average data rate of NRTPS to total average number of data.

(4) BE traffic

For BE, the first-in-first-out (FIFO) can be used. At the same time, different priority can also be specified according to users' priority. For it needs not QoS guarantee, simple polling or average allocation mechanisms can also be utilized.

4 Conclusion

The paper presented a set of resource scheduling and allocation program for IEEE 802.16, including access control and bandwidth allocation. First of all, it promise QoS requirement of UGS and RTPS as well as access as possible. It can also ensure RTPS access steals partly reserved bandwidth of NRTPS, so as to significantly increased channel utilization.

References

1. IEEE 802.16-2004, Standard-local and metropolitan area networks part 16 (2004)
2. Wongtha Varawat, K., Ganz, A.: Packet Scheduling for QoS Support in IEEE 802.16 Broadband Wireless Access Network. International Journal of Communication Systems 16, 81–96 (2003)
3. Wang, H.-t., Wei, L., Agrawal, D.P.: Dynamic Admission Control and QoS for 802.16 Wireless MAN. In: Proceedings of IEEE 2005 Wireless Telecommunications Symposium, pp. 60–66 (2005)
4. Yamakosh, K., Nakai, K.: Dynamic Deficit Round-robin Scheduling Scheme for Variable Length Packets. Electronics Letters 28, 148–149 (2002)
5. Sun, L.-j., Bin, W., Zhang, D.-y.: D-DRR: Dynamic Deficit Round Robin Scheduling Algorithm. Jiangsu Communication Technology 20, 5–8 (2004)
6. Liu, P.-z., Yang, L.-j., Wei, K.: Research on Scheduling Algorithms of Real-time Services in Wireless Networks. Journal of Wuhan University of Technology 29, 136–139 (2007)
7. Chu, G.-s., Deng, W., Mei, S.-l.: A QoS Architecture for the MAC Protocol of IEEE 802.16 BWA System. In: Proceedings of IEEE International Conference on Communications Circuits and System and West Sino Expositions, pp. 435–439 (2002)

Security Association Management between Mobile Nodes Based on IKEv2

Xing Hong-zhi, Luo Chang-yuan, and Huo Shi-wei

Information Engineering University, Electronic Technology Institute,
Zhengzhou 450004, China
xinghongzhi@gmail.com, Luocyzz@126.com,
xiangya_85211@sina.com

Abstract. Through analyzing security association management methods between mobile nodes in IETF standards, this paper points out disconnection problems in IKEv2's security association update when nodes changed IP address during disconnection and low efficiency in MOBIKE's security association update. In order to resolve those problems, this paper presents an improved management design based on IKEv2 via creating relativity between security association and mobile node's home address. It is showed in the analyze result that the design ensures the security association update practibility when mobile nodes changing addresses during disconnection and behaves better in efficiency and security than MOBIKE.

Keywords: MIPv6; Security Association; IKEv2; MOBIKE.

1 Introduction

Mobile IPv6 (MIPv6) [1] protocol allows nodes remain connective when moving from one place to another. When a mobile node (MN) moves to a new area, it will get a care of address (CoA) without changing its home address (HoA), and then it will bind update the CoA to its home agent (HA) and correspondent nodes. After binding update, the CoA is the current communication address for routing. One MN may get many CoAs but the HA keeps unchanged. The mobility brings convenience to mobile nodes and problems in security management.

The IP security (IPsec) architecture that has been revised in RFC 4301[2] describes how to provide security services at the IP layer. The IPsec defines how the security protocols, security associations (SAs), key management and cryptographic algorithms work together. It is also the main security solution for MIPv6 and should be modified for implement due to the specificity of MIPv6 networks.

SA is fundamental to IPsec. The IKEv2 [3] protocol is an important component of IPsec for performing mutual authentication and establishing and maintaining SAs. SA establishing is a time-wasted procedure that could cause congestion if executed frequently. Reference [4] designs how to maintain SAs between mobile node and home agent using IKEv2 in MIPv6 network, but does not define explicitly when IKEv2 works between mobile nodes (the correspondent node is also a mobile one). If both the communication sides are mobile nodes, the SA update is more difficult, and sometimes

D. Zeng (Ed.): Future Intelligent Information Systems, LNEE 86, pp. 295–302.
springerlink.com © Springer-Verlag Berlin Heidelberg 2011

causes disconnection problems. Therefore it is still needed to put out new ways to solve the problems.

2 SA Management

A revised IP security architecture is putted forward in RFC 4301 by IETF. A new database, the Peer Authorization Database (PAD), is set in the architecture to store the peers' authentication data for IKE SAs and authorization data for establishing IPsec SAs.

SAs are stored in SA Database (SAD), used by IPsec protocols (e.g. AH or ESP), created by protocols like IKEv2 manually or automatically. There are three results for all dataflow passed SPD, discard, bypass and protect. Only the protected dataflow can be protected by IPsec. (If there is no SA for the dataflow, system should ask key exchange protocol for SA establishing).

In mobile environment, IP addresses change when nodes moving from one area to another, which does cause troubles when querying SAs by nodes' IP addresses. The SA searching procedure in IETF is:

(1) Search the utmost matching, including the Security Parameter Index (SPI), source address and the destination address in the SAD. When finding the exact SA, the searching procedure is completed. If no SA matches, go to (2).

(2) Search the matching SPI and destination address. When finding the exact SA, the searching procedure is completed. If no SA matches, go to (3).

(3) Only search the SPI. If no SA matches, the searching procedure is over.

The IP addresses are needed to querying SA, however, one IP address could be used to create many SAs. When the mobile node moves to a new area, the created SAs may not be available any more. Because the SA renegotiation consumes too much system resource, the SA management needs to maintain the corresponding relationship between IP addresses and SAs dynamically instead of renegotiation.

3 Problems When Using IKEv2 in Mobile Environment

IKEv2 protocol is used to manage SAs in MIPv6 network, however, it does not work efficiently in mobile environment. Accordingly, the IETF has made rules to restrict SA management between home agent (HA) and mobile node in RFC 4877[4]. Mobile nodes need not to renegotiate SAs with HAs (HA is not movable) when moving to a new area. Problems still exist when both communication sides are mobile nodes.

3.1 Standard IKEv2 in Mobile Environment

IKEv2 protocol uses mobile nodes' current IP addresses to create SAs. During the communication, mobile nodes use binding update message to update SAs if IP address has changed when handover happens. Supposing both side nodes are not at home link, they communicate with each other using care of addresses (CoA) and the SAs creating and updating procedure is showed in Fig. 1.

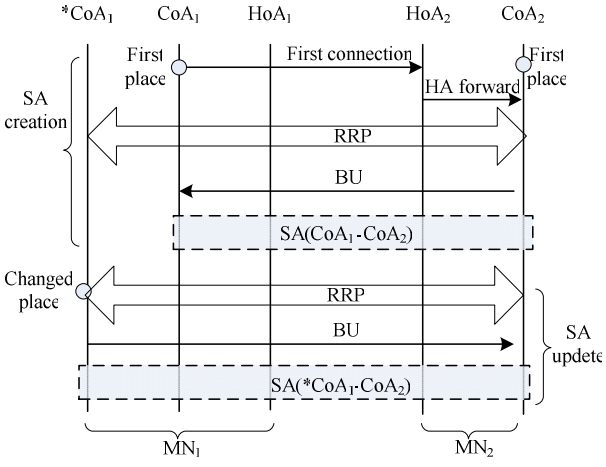

Fig. 1. SA management during connection

In Figure 1, both nodes are at foreign link using CoA1 and CoA2 to communicate, but they do not know the other's place. The mobile node 1(MN1) starts the communication and only knows the MN2's home address(HoA2), therefore the first connection is from CoA1 to HoA2. Then the MN2's HA forward the connection request to CoA2. After the Return Routability Procedure(RRP) and bind update(BU), the SA is created between two sides (SA{CoA1－CoA2}).

When area changed during connection and the current IP address changed to *CoA1, MN1 will starts RRP to tell MN2 its new address. After binding update(the "K" bit is set to tell MN2 that the SA need to update), MN2 will get the *CoA1 and change the SA's IP address correspondingly. The SA is updated to SA{*CoA1－CoA2}.

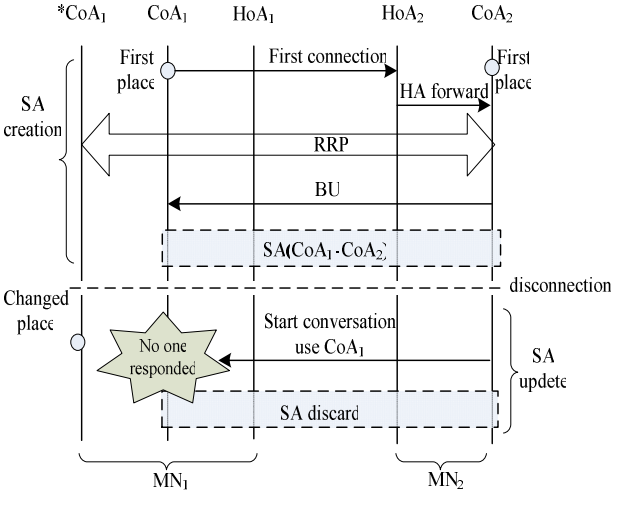

Fig. 2. SA updates failure after moving during disconnection

During the whole communication, MN2 does not know MN1's home address if MN1 did not tell. As a result, if MN2 wants to communicate with MN1 and MN1 changed its IP address during disconnection, MN2 can not contact MN1 and the SA is overdue. This connection failure is showed in Fig. 2.

That MN2 does not know *CoA1 caused the failure. If MN2 knows HoA1, the SA needs to recreate because MN2 does not understand CoA1 and HoA1 are MN1's addresses. Therefore it is necessary to take some measures to solve the problem.

3.2 Mobile IKEv2 (MOBIKE)

In order to solve the problem above, the IETF put MOBIKE protocol forward in RFC 4555[5]. Based on IKEv2, the changes are:

The protocol added MOBIKE_SUPPORTED option for MOBIKE support;

(1) Add UPDATE_SA_ADDRESS option to notify the other side to update SA;

(2) Add ADDITIONAL_IP_ADDRESSES option to notify the other side to keep the addresses that may change if handover happens.

(3) When a mobile node may move to another area, after movement detection, it sends the addresses that may change in ADDITIONAL_IP_ADDRESSES. [6] Then if the handover happens during connection, the mobile node will send UPDATE_SA_ADDRESSES message to update SA. If handover happens during disconnection, the MOBIKE works as in Fig. 3 to solve the problem.

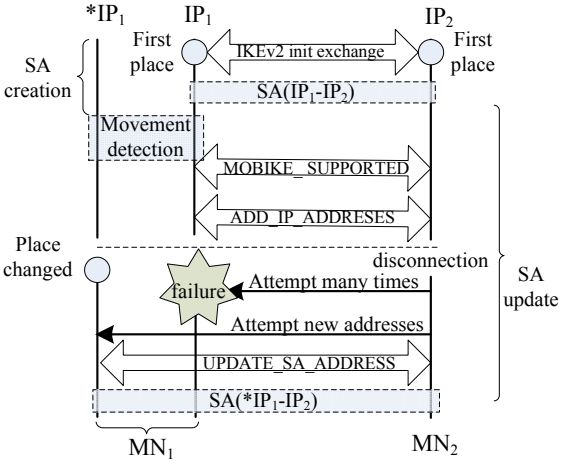

Fig. 3. MOBIKE works during disconnection

Before disconnection, the mobile node which may move to a new area tells the maybe addresses. If the old address can not be contacted, the other side will try the addresses one by one until it find a useable address. If all addresses are failed, the communication failed. MOBIKE provides a new way to avoid SA renegotiation when nodes moving, however, it still has many problems:

(1) It is too complex. The many procedures added make IKEv2 inefficient for handover.

(2) It is unsafe to possess many addresses that a node may not use. Vicious nodes can use those addresses.

(3) If a mobile node moved more than one time during disconnection and changed a new address that is not in ADDITIONAL_ADDRESSES, the corresponding node may not contact it again. It means that MOBIKE still has the disconnection problem.

Although reference [7] puts out an interface method to solve the IKEv2's problem, it is unsafe to make IKEv2 consult IP address using mobile IPv6's registers. So we put out an improved design to make little modification on IKEv2.

4 Improved IKEv2 Design

4.1 SA Creation

Because IKEv2 uses CoA to create SAs, it can not update SAs if the CoA is changed during disconnection. Although MOBIKE introduce a complex method to avoid SA renegotiation, it does not solve the disconnection problem absolutely and it is inefficient. If using mobile node's unchanged ID to create SA, it will be easy to manage SA according to the changeable ID. The home address is unique to a mobile node and is not often changed after registration in home link. So our method is to use home address to create SAs. The details are as fallows:

(1) At the beginning of SA negotiation, it is necessary to make each node know the other's home address. If one wants that the message stands to arriving at the other, it can use the other's home address as its destination. (The corresponding node is maybe at foreign link; its home agent will forward the message.) Then the MIPv6 header looks as follows:

IPv6 header (source = care-of address,
destination = correspondent node home address)
Destination Options header
Home Address option (home address)

(2) In SA negotiation process, it is needed to set the Traffic Selector (TS). TS is used to decide which IP packet need protection according to the source address and the destination address. The TS is also negotiated in the SA setting-up process. The TS negotiation result will write in SPD (Figure 1). So we need that in the TS negotiation home address is in the protected list as is show in Fig. 4.

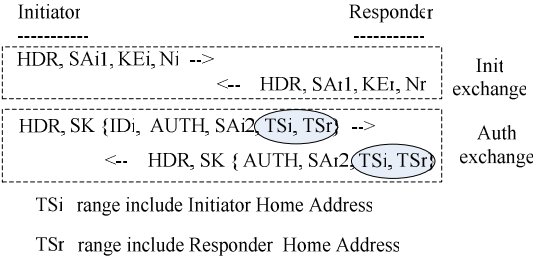

Fig. 4. Traffic Selector negotiation

TS negotiation is a part of IKE_SA negotiation. After IKE_SA created, the Child_SA (used by AH or ESP) will be created and is used to protect usual packets. We require the home address must be included in the TS's list so that the packets with home address could be recognized and protected by the right SA.

(3) In order to make SA and home address match, it is necessary to modify the SA structure. We need add a new option in the SA's structure as is showed in Fig. 5.

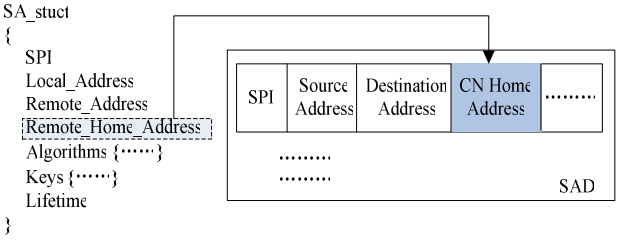

Fig. 5. The revised SA structure

A new option, Remote_Home_Address, is added in SA struct and matches the corresponding node's home address in SAD. No matter where the node moves, the CN home address does not change. If needed update, just update the source address and the destination address. If mobile nodes have stored the HoA-SA matching relationship, they do not renegotiate SA when moving.

4.2 SA Update

Mobile nodes set the "K" bit 1 to notify the home agents that the SAs' addresses need update in the BU message. Since both sides are mobile, the ways to update SAs are a bit more complex. The update process is of two conditions.

(1) During connection

In this condition, when one node moves, it will tell the corresponding node that the address will change. After RRP process, they update their communication address by sending BU message. In the BU message, the mobile one should set the "K" bit 1 and they both update the SAs' addresses.

(2) During disconnection

When the node moves during disconnection, it will not tell another the new address. If the node creates SA in the section 4.1's way, it knows the home address and just updates the destination address. The flow process is as follows:

Step1: The initiator sets the "K" bit 1, and sends the message using MIPv6 header like 4.1(1);

Step2: If the responder is not at home link, the message will be forward to it by its home agent. Then the responder checks the home address option and the "K" bit. If the responder finds the right SA to this home address, it updates the SA.

Step3: If the responder is not at home link, it need start the RRP process to update both CoAs. Then the responder sends the BU message with the "K" bit set directly to the initiator's CoA.

Step4: the initiator receives the message and updates the SA.

In this way, the disconnection problem can be solved absolutely and it is more efficient than MOBIKE method. The messages sent in the process are protected by the old SAs.

5 Analysis of the Improved Design

The improved design performs the same as IKEv2 during connection when updating SA. In this section, we compare the improved design with IKEv2 and MOBIKE during disconnection SA update. We divide the conditions by the initial communication place, who starts the first session and who starts the next session. Supposing there are two mobile nodes, MN1 and MN2, and MN1 starts the first session, and after the first session MN1 moves to another area (it is symmetric for MN2), there exist 8 cases(showed in Table 1):

Table 1. 8 cases

	MN_1 place	MN_2 place	Who starts the next session
Case1	home	home	MN_1
Case2	home	home	MN_2
Case3	home	foreign	MN_1
Case4	home	foreign	MN_2
Case5	foreign	home	MN_1
Case6	foreign	home	MN_2
Case7	foreign	foreign	MN_1
Case8	foreign	foreign	MN_2

The 8 cases include conditions about one time movement. Another three conditions should be included:

Case9: MN1 starts the first session and moves more than one time, then MN1 starts the second session.

Case10: MN1 starts the first session and moves more than one time, then MN1 starts the second session.

Case11: after first session, both nodes move to another area.

The 11 cases could compose many other conditions, however, they are the bases.

According to the 11 cases, we define 5 kinds of processes:

Process1: Disconnection problem. Nodes con not update SA in IKEv2 and maybe in MOBIKE. It is the worst condition that one node con not contact the other.

Process2: Create new SA. If one node can not find the old SA has matching relationship with the new address, the nodes has to renegotiate SA again. Because SA negotiation needs complex algorithmic operation, this process will consume much time.

Process3: After many address attempts, update SA. This process happens in MOBIKE. One node will try many times to connect to a new address, and then update the SA.

Process4: After RRP, update SA. This happens in our improved design. Because the design needs home address to be the destination address when updating SA, the nodes may be not at home link and the RRP runs.

Process5: Update SA. Just use a BU message, and then both sides update the SA.

The time consumption is Process5<Process4<Process3<Process2<Process1 [8]. IKEv2, MOBIKE and the improved design's performance in the 11 cases is displayed in Table 2.

Table 2. Comparison

	IKEv2	MOBIKE	Our design
Case1	Process2	Process5	Process5
Case2	Process1	Process3	Process4
Case3	Process2	Process5	Process4
Case4	Process1	Process3	Process4
Case5	Process2	Process5	Process5
Case6	Process1	Process3	Process4
Case7	Process2	Process5	Process4
Case8	Process1	Process3	Process4
Case9	Process2	Process2	Process5
Case10	Process1	Process1	Process4
Case11	Process1	Process3	Process4

As is showed in the table, it is only in Case3 and Case7 that our design is less efficient than MOBIKE. In other cases, our design is better and do not have disconnection problem.

6 Conclusion

In this paper, IKEv2 and MOBIKE is analyzed and the deficiencies are pointed out when the protocols working in mobile environment. Then an improved design of IKEv2 is put forward. The design changes IKEv2 less than MOBIKE and works more efficient than MOBIKE.

References

[1] Johnson, D., Perkins, C., Arkko, J.: Mobility Support in IPv6 IETF RFC 3775 (June 2004)
[2] Kent, S., Seo, K.: Security Architecture for the Internet Protocol. IETF RFC 4301 (December 2005)
[3] Kaufman, C.: Internet Key Exchange (IKEv2) Protocol. IETF RFC 4306 (December 2005)
[4] Devarapalli, V., Dupont, F.: Mobile IPv6 Operation with IKEv2 and the Revised IPsec Architecture. IETF RFC 4877 (April 2007)
[5] Eronen, P.: IKEv2 Mobility and Multihoming Protocol (MOBIKE). IETF RFC 4555 (June 2006)
[6] Karbasioun, M.M., Berenjkub, M., Taji, B.: Securing Mobile IP Communications Using MOBIKE Protocol. In: IEEE International Conference on Telecommunications (2008)
[7] Ke, X., Qi, M.-p., Li, H.-t., et al.: A Novel Interfacing Solution to Make IKEv2 Work in MIPv6 Environment. In: IEEE ICC 2008, pp. 450–454 (2008)
[8] Faigl, Z., Lindskog, S., Brunstrom, A.: Performance evaluation of IKEv2 authentication methods in next generation wireless networks. Journal of Security and communication Networks 3(1), 83–98 (2010)

Analysis on the Mathematical Model of the Six-Phase Induction Motor of the Electric Vehicle

Chaoyong Tuo

Hunan Mechanic & Electric Polytechnic, ChangSha, 410151, China
hnjstcy@126.com

Abstract. The electric vehicle is a power-driven vehicle, and with the increasing tense of resources in modern society, it has important significant for the development and application of electric vehicle. This paper introduces the common types of electric vehicles, and studies the control techniques of six-phase Induction Electric Machine. In order to improve the direct torque control system of six-phase induction motor, it made dynamic mathematical model for six-phase induction motor, made system simulation, and provided simulation model under Simulink.

Keywords: Six-phase induction motor; direct torque control; dynamic mathematical modeling; simulation.

1 Introduction

Electric vehicles are the integrated products of "electrification" and "car", the energy crisis and oil shortage in 1970s made electric vehicles vital, however, until to 1970s, with the people's concern of the air quality and greenhouse effect, the study of electric vehicles became a very hot topic [1]. Since 1990s, a lot of large vehicle groups and companies, such as FORD, GM, NISSAN, TOYOTA, HONDA, etc. invested larger funds in electric vehicles, and developed a variety of electric vehicles and electric vehicle concept car [2]. With the developing of the national tenth five-year plan "863", the important science and technology projects of electric vehicles start. There is a research and development boom in the whole country.

The power-driven system of electric vehicle is the tie between energy storage system and the wheels, its role is to change the energy (chemical energy, electrical energy) output by energy storage system to mechanical energy, to promote the vehicles to overcome rolling resistance, air resistance, acceleration resistance and climbing resistance, and to convert kinetic energy to electrical energy feedback to energy storage systems during braking. There are some differences between modern electric vehicles and conventional fuel vehicles, the power drive systems of modern electric vehicles can eliminate the complex and heavy mechanical gear speed change mechanism, providing to meet the torque-speed characteristic of wide vehicle speed scope and large load change, namely the low speed constant torque and high speed constant torque [3]. In the design of electric vehicle power-driven system, especially the power battery characteristics and electric vehicle system structure should be considered. Motor is the drive unit of electric vehicle, and its technical performance

D. Zeng (Ed.): Future Intelligent Information Systems, LNEE 86, pp. 303–310.
springerlink.com © Springer-Verlag Berlin Heidelberg 2011

can directly impact on the power and economy of vehicle, so it needs computer-aided to design, analyze the finite element for motor's electromagnetic field, temperature field and stress field, select and design the electric vehicle which is consistent with the operational requirements of the motor, and it has the features of wide speed adjustable range, large starting torque, high stand-by power, high efficiency, large power density and high reliability.

The selection of the motors of electric vehicles generally includes two main types of multi-phase induction AC motor and permanent magnet DC motor. The DC motor has larger dead weight and poorer maintenance, while induction AC has the features of reliable, simple maintenance, cheap, high efficient, higher specific power and large change of power factor, so it is widely used in the current electric vehicle manufacturing industry.

The second part introduces the control technique of six-phase induction motor; the third part introduces the winding structure of it; the fourth part builds a dynamic mathematical model of it; the fifth part makes a simulation analysis of this model; the last part makes a conclusion.

2 The Research Status of The Control Technology of Multi-phase Induction Motor

The multi-phase induction motor mainly studies the modeling, harmonics, PWM control technology and high performance control strategies of multi-phase induction motor. The multi-phase induction motor is a multi-variable coupled nonlinear system, and according to the unified theory of motor, it shows that the multi-phase induction motor can always be equivalent to two-phase motor [4]. According to the selection of appropriate conversion, the analysis model of multi-phase induction motor can be decomposed into the core components of the two-phase motor model and the dynamic part of related component of non-electromechanical energy conversion.

The analytical approach of symmetric multi-phase induction motor can use instantaneous symmetrical component conversion [5] and generalized two-phase orthogonal conversion [6]. According to the symmetrical components, it can convert symmetrical multi-phase motors into generalized α-β-γ stationary coordinate system. Under the α-β plane of implementing energy conversion, the model of the multi-phase motor and the three-phase motor is the same; the other component does not produce energy conversion, which can obtain the general analysis method which can be used to multi-phase motor.

Three-phase PWM technique can be extended to multi-phase motor control, such as taking symmetrical three-phase windings as a subset, N subsets constitute multi-phase system, which can divide multi-phase winding into three-phase winding structure [7], it can consider multi-phase inverter as three-phase inverter to control separately, which can directly apply the three-phase PWM techniques to multi-phase PWM control.

For the relatively fewer multi-phase motors, the current hysteresis PWM technology can be used, and the method is the same with three-phase motor, each phase can have an independent current hysteresis controller. When this phase current exceeds the hysteresis of the given current value difference, the switch state of this

phase will change one time. For example, in the 5-phase system of non-midpoint connection [8], due to there is only four independent current variables, so it only needs four independent current hysteresis controllers.

The conventional SVPWM method can divide the α-β plane of six-phase induction motor into 12 sectors, and each sector composes reference vector of the largest two non-zero vector and zero vector in dodecagon, it is shown in Figure 1.

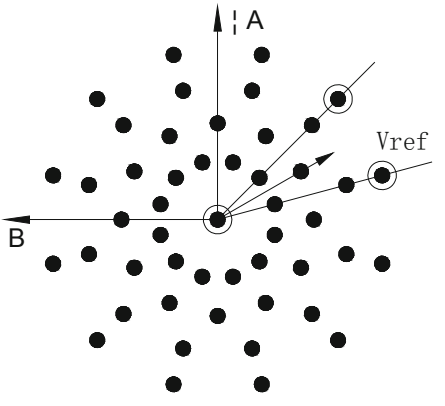

Fig. 1. The conventional SVPWM method

Multi-level SVPWM method composes the reference vector of the largest two non-zero vectors and a voltage vector near reference vector, it is shown in Figure 2.

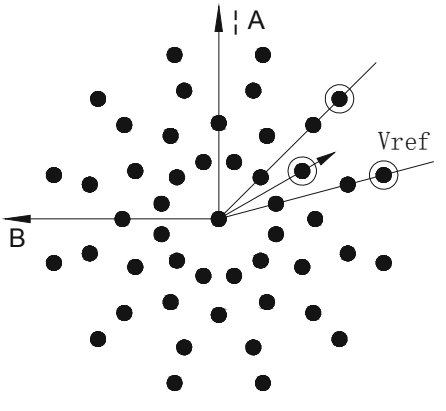

Fig. 2. Multi-level SVPWM methods

As the unified theoretical basis of multi-phase motors and three-phase motor, therefore, the control strategy of three-phase system can be applied to multi-phase motor control, the vector control of multi-phase motor and direct torque control has been reported one by one, and the typical control strategies include vector control and direct torque control. Vector control method is based on current hysteresis vector control,

vector space decoupling vector control, dual d-q synchronous current control, etc. The direct torque control includes traditional DTC, dead beat DTC and fuzzy DTC.

3 The Winding Structure of Six-Phase Induction Motor

It divided each phase belt of "spatial distribution of 60 ° phase belt winding" which is connected by star connection into two phase belts, and it changes one star connection into two star connection by the displacement of 30 ° electrical angle in space, to make a six-phase and double star 30 ° winding. At this time, the internal stator slot along the inner circle is divided into 12 phases for each polar distance, and the width of each phase is 30 ° electrical angle, so it is a "spatial 30 ° phase belt winding."

The connection method and the vector of bipolar binary six-phase 30 ° winding are shown in Figure 3 and Figure 4. The 12 phase belts distributed along the stator circumference is shown in Figure 3, which can be regarded as the actual position of the upper coil along the circumference edge, as the position of the lower coil, which can be depended on the coil pitch, it isn't showed in the figure.

The double-Y connection method of 12-phases composed into six-phase and the two parallel slips each phase has is shown in Figure 4. The vector of the six-phase electric potential is shown in Figure 3, which includes three-phase electric potential whose phase difference is 30 °, which composes a asymmetrical six-phase system (symmetrical six-phase system should be b phase difference 60 ° between phase and phase).

When the current passes any degrees in the current, the fundamental wave of three-phase synthesis magnetic potential wave can turn the same electric angle in the space; and when the current of any phase reach up to maximum, there must be a volatility in the coil axis of this phase in the fundamental wave of three-phase synthesis magnetic potential wave. Now, set the A_1-phase current of the above first star of six-phase windings is the maximum, so the positive amplitude coincides with the $+A_1$ phase belt coil axis of the magnetic potential fundamental wave produced by the Ⅰ star three- phase. As the current of the Ⅱ falls behind the Ⅰ star current 30 °, showing that the A_2-phase current of the n star has not yet reached the maximum. It must wait for time to pass 30 °, the A_2 phase current work can reach the maximum, so the positive amplitude coincides with the $+A_2$ phase belt coil axis of the magnetic potential fundamental wave produced by the Ⅰ star three- phase. As it passes time 30 °, it can be seen that the positive amplitude of magnetic potential fundamental wave produced by the Ⅰ star must turn 30 ° from the coil axis of $+A_2$ phase, the coil axis of $+A_2$ phase belt can be seen in Figure 4. Thus, the magnetic potential fundamental wave produced by two stars has the same phase, and they all can spin clockwise with synchronous speed, so they can obtain the synthesis magnetic potential fundamental wave of the whole six-phase wounding through adding directly. From the motor parameters, it also shows that the armature reaction reactance of the six-phase double-Y moved by 30 ° winding motor is twice of each Y connection of armature reaction reactance.

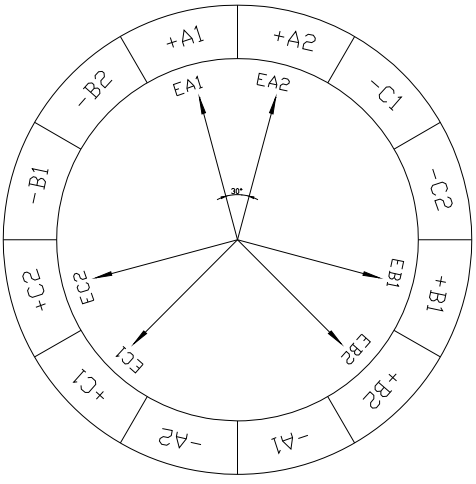

Fig. 3. The winding structure of six-phase induction motor

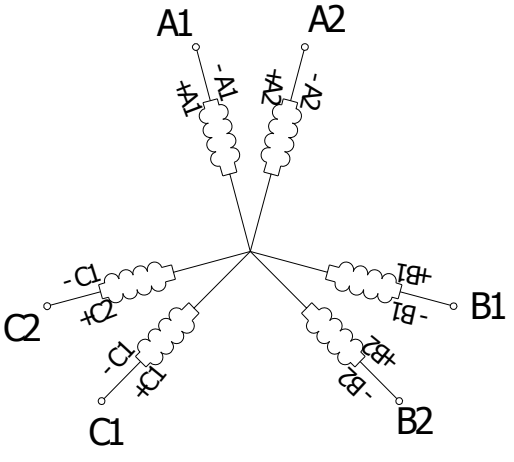

Fig. 4. The wiring diagram of six-phase induction electric motor

4 The Dynamic Mathematical Model of Six-Phase Induction Motor

Whether the rotor is winding or squirrel cage, they will all be equivalent to coil type, and converse to the stator side, the stator after translation and the turns rotor windings are equal, namely, N, = Nr = N.

The mathematical model of six-phase induction motor is composed of four equations: flux equation, voltage equation, torque equation and equation of motion. In

engineering it always used matrix form to express multi-winding system, this is simple and universal, thus, the establishment of the equation often is written in matrix form, and instead operation symbols $\frac{d}{dt}$ of the differential operator P.

The flux of each winding is the total of its own self-inductance flux and its other winding inductance magnetic chains, therefore, the flux of six winding can be expressed as

$$\psi = Li \tag{1}$$

L is the inductance matrix of 12 × l2, including the diagonal elements L^{asas}, L^{bsbs}, ……, L^{fsfs}; L^{arar}, L^{brbr}, ……, L^{frfr} is the self-induction coefficient of each winding, while the other is the mutual inductance between windings. For each phase winding, its self-induction coefficient can be decomposed into leakage self-induction coefficient and main inductance coefficient, and the mutual inductance coefficient between windings can be also decomposed into leakage self-induction coefficient and main inductance coefficient. The complete flux equation can be expressed as:

$$\begin{pmatrix} \psi^s \\ \psi^r \end{pmatrix} = \begin{pmatrix} L^{ss} & L^{sr} \\ L^{rs} & L^{rr} \end{pmatrix} \begin{pmatrix} i^s \\ i^r \end{pmatrix} \tag{2}$$

ψ^s is the complete flux matrix of stator winding, ψ^r is the complete flux matrix of rotor winding, i^s is the current column matrix of stator winding, i^r is the current column matrix of rotor winding, L^{ss} is the inductance coefficient matrix of stator winding for the rotor winding, L^{rr} is the inductance coefficient matrix of rotor winding for the rotor winding, L^{sr} is the inductance coefficient matrix of stator winding for the rotor winding, L^{rs} is the inductance coefficient matrix of rotor winding for the stator winding.

According to Kirchhoff voltage law (KVL) and the Faraday law of electromagnetic induction can be obtained the voltage equation, it can be written in matrix form as follows

$$u = Ri + p\psi \tag{3}$$

The above equation can be written separately in stator voltage equation and the rotor voltage equation:

$$u^s = R^s i^s + p\psi^s \tag{4}$$

$$u^r = R^r i^r + p\psi^r \tag{5}$$

Electromagnetic torque is the partial derivatives of magnetic field's magnetic energy for mechanical angular displacement when the current is constant and only the mechanical angular displacement changes:

$$T_e = \frac{\partial W_m^{'}}{\partial \theta_m}\bigg|i = const. = n_p \frac{\partial W_m^{'}}{\partial \theta_m}\bigg|i = const. \tag{6}$$

Under normal circumstances, the equation of motion of electric drive system is

$$T_e = T_l + \frac{J}{n_p}\frac{d\omega^r}{dt} + \frac{D}{n^p}\omega^r + \frac{K}{n_p}\theta^r \tag{7}$$

For constant torque loads, D = 0, K = 0, then

$$T_e = T_l + \frac{J}{n_p}\frac{d\omega^r}{dt} \tag{8}$$

Formula 2, Formula 3, Formula 6, Formula 8 and Formula 9 together form a dynamic mathematical model of six-phase induction motor under constant torque load.

$$\omega^r(t) = \frac{d\theta^r(t)}{dt} \tag{9}$$

5 Simulation Results

The simulation parameters of motor are: rated power P_N = 5500w, rated phase voltage U_N = 86v, the number of pole pairs n_p = 3, moment of inertia J = $0.116\,kg \cdot m^2$, stator resistance R^s = $0.22\,\Omega$, rotor resistance R^r = $0.47\,\Omega$, stator inductance L^s = 0.0395H, rotor inductance L^r = 0.0395H, rotor mutual inductance L^m = 0.0364H. Simulation results show that: in the process of motor starting, it has high starting torque, fast spinning up; electromagnetic and electrical transient is short. The time that torque required to reach steady-state value is about 0.255, and the rotational speed required to reach steady-state value is about 0.255, too. On sudden load conditions, it has the features of fast torque response, good tracking performance and steady speed, indicating the impact of anti-load ability.

Simulation results show that the six-phase induction motor has the advantages of fast dynamic response, quasi-steady-state response, and higher reliability. Based on the model, it can make further study on the motor variable-frequency adjusting-speed system of six-phase induction motor. Since this model is based on the d-q subspace α-β in stationary coordinate system, therefore, it is particularly helpful to the motor DTC system of six-phase induction.

6 Conclusions

Electric vehicle is still at the stage of research and improvement, there are many problems to solve themselves. This paper studies based on six-phase induction motor, and after analyzing the winding structure of six-phase induction motor, it makes a dynamic mathematical modeling for six-phase induction motor and the dynamic simulation analysis in Simulink. Experimental data show that the six-phase induction motor has the advantages of fast dynamic response, quasi-steady-state response, and high reliability. Based on this model, it can be further studied for the motor variable-frequency adjusting-speed system of six-phase induction motor.

References

1. Cao, B., Zhang, C., Bai, Z.: Technology Progress and Trends of Electric Vehicles. Journal of Xi' An Jiaotong University 38(1), 38–41 (2004)
2. Chan, C.C.: The state of the art of electric and hybrid vehicles. Proceeding of IEEE 90(2), 1–29 (2002)
3. Fengchun, S., Ming, C.: The States and Trendsin Electric Pro Pulsion System of Electric Vehicles. Automative Engineering, 22(4), 221–224 (2000)
4. Jones, C.V.: The unified theory of electrical machines. Butterworths, London (1967)
5. Klingshirn, E.A.: High phase order Induction motors-Part I Description and theoretical considerations. IEEE Trans. Power App. Syst. PAS-102, 47–53 (1983)
6. Abbas, M.A., Christen, R., Jahns, T.M.: Six-phase voltage source inverter driven induction motor. IEEE Trans. Ind. Applicat. IA-20, 1251–1259 (1984)
7. Matsumoto, H., Takami, H.: Optimal pulse patterns of six-phase voltage source PWM inverter for double three-phase wound AC motor. Electrical Engineering in Japan (English translation of Denki Gakkai Ronbunshi) 111(2), 125–134 (1991)
8. Toliyat, H.A.: Analysis and simulation of five phase varible-speed induction motor drives under asymmetrical connections. IEEE Trans. Power Elec. 13(4), 748–756 (1998)

A Modified Visual Perception-Based Image Segmentation Method

Chunjiang Zhao

Department of Electronic Information and Electrical Engineering,
Hefei University, Hefei, 230601, China
zhaocj@hfuu.edu.cn

Abstract. The visual perception method based on the adaptability of the eye and its minimal perceptible can segment the image, which call visual perception-based image segmentation (VPS) method. However, VPS method oversegments and undersegments the image. Modified VPS method was proposed. By changing the brightness stimulus of the object background in VPS method, the modified VPS method shows the better properties. Without regard to the position of the objects, the proposed method segments the image accurately and can neither enlarge nor diminish the objects.

Keywords: image segmentation; visual perception; object; background.

1 Introduction

Image segmentation has received extensive attentions in computer vision and image processing research communities.

The goal of image segmentation is to split the image into regions. A region is a set of connected pixels which have roughly the same value for some property, such as the gray level usually (or some other scalar property), surrounded by a closed contour representing its boundary. Image segmentation is an essential task for many applications including object recognition, tracking, and recently coding and compression with the introduction of the MPEG-4 standard for video. With such an extensive and rapidly increasing variety of applications using a wide range of imagery, it is of fundamental interest to the signal processing community to develop image segmentation algorithm.

In general, there are three basic approaches to image segmentation [1-3]: the region-based extraction, the block-based merging, and edge-based detection. The region-based extraction method is the most used one to segment the image. In the region-based image segmentation method, the threshold plays a key role in estimating what sets of pixels belong to. The ideal situation for threshold is an object of uniform brightness on a background of uniform brightness, where the intensities of the two regions are different. But this method suffers the problems such as oversegmentation, determination of threshold, and large computational complexity [2]. Recently, many new region-based image segmentation methods have been proposed, such as fuzzy logic [2][4-6], Genetic Algorithm (GA) [7][8], and neural network (NN) [9][10].

D. Zeng (Ed.): Future Intelligent Information Systems, LNEE 86, pp. 311–316.
springerlink.com © Springer-Verlag Berlin Heidelberg 2011

In [11], authors proposed a new visual perception-based segmentation (VPS) algorithm, which is derived from psycho visual experiments on adaptability of the eye and its minimal perceptible contrast. VPS method is a method of region-based image segmentation. This approach solves the problem of binary segmentation in low quality images, and breaks through the traditional framework by using psycho visual phenomena. However, this method has some drawbacks and there is still considerable room for improvement to this approach. Thus, we propose a modified VPS as the rest sections described to overcome the drawbacks and improve the quality.

2 The Modified VPS Method

The VPS algorithm [11] simulates the mechanism of the human retina. When human beings observe the object, the eyes are stimulated by the different brightness of regions: object, object background, and surround background [12], as shown in Fig.1. Though the object of different brightness is on the nonuniform background or on the different backgrounds, human beings can also recognize the object exactly. The reason is the human's ability to adapt to different illuminants in a wide range. The VPS makes use of this adaptation to segment the image.

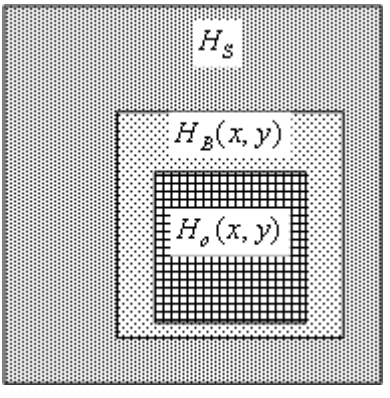

Fig. 1. The different brightness of the regions. H_O (x,y), H_B (x,y) and H_S represent the brightness of object, object background and surround background, respectively.

We firstly describe the traditional visual perception-based segmentation method [11] briefly. The brightness stimulus of the object H_o can be simplified for the model:

$$H_o(x,y) = \frac{1}{N_o} \sum_{m=-\frac{p_o}{2}}^{\frac{p_o}{2}} \sum_{n=-\frac{p_o}{2}}^{\frac{p_o}{2}} I(x-m, y-n) \tag{1}$$

where $N_o=p_o^2$ is the number of pixels in the simulated fovea centrality, and a change of N_o represents the accommodation ability. Thus, during the image segmentation process, we can adjust the N_o according to the size of the different objects.

The brightness stimulus of the object background H_B can be simplified as follows:

$$H_B(x,y)=\frac{1}{N_B}\sum_{m=-\frac{p_B}{2}}^{\frac{p_B}{2}}\sum_{n=-\frac{p_B}{2}}^{\frac{p_B}{2}}\frac{I(x-m,y-n)}{\sqrt{(x-m)^2+(y-n)^2}} \tag{2}$$

where $N_B= {p_B}^2$ and $p_B=2\times p_o$.

The brightness stimulus of the surround background H_S can be simplified as follows:

$$H_S=\frac{1}{N}\sum_x\sum_y I(x,y) \tag{3}$$

where N is the all numbers of pixels in the image, so it can be considered as the average gray level of the whole image.

When there is perceived difference in luminance between object and background, the object can be observed, which is called the contrast. The contrast C between H_o and H_B can be defined as follows:

$$C(x,y)=\frac{\left|H_o(x,y)-H_B(x,y)\right|}{H_B(x,y)} \tag{4}$$

The adaptation illuminance H_A is the core of the VPS. By the psycho visual experiments and simplification, it can be defined as follows:

$$H_A(x,y)=0.923\times H_B(x,y)+0.077\times H_S(x,y) \tag{5}$$

The minimal perceptible contrast is a function of the adaptation illuminance, which is defined as follows:

$$C_{A\min}(x,y)=\begin{cases}\dfrac{C_w}{H_B(x,y)}\left[0.808+\sqrt{H_A(x,y)}\right]^2, & H_A\ge H_B\\ \dfrac{C_w}{H_B(x,y)}\left[0.808+\sqrt{\dfrac{H_B(x,y)^2}{H_A(x,y)}}\right], & H_B\ge H_A\end{cases} \tag{6}$$

where C_w is coefficient.

An image pixel is considered to belong to the object, if its contrast C is greater or equal to $C_{A\min}$. The following decision rule is performed:

$$I'(x,y)=\begin{cases}object, & C(x,y)\ge C_{A\min}(x,y)\\ background, & otherwise\end{cases} \tag{7}$$

Due to the adaptability of the VPS method, it can be used for several types of low quality images. However, the VPS method has some drawbacks. For example, the segmented image is oversegmented and undersegmented. The result is not even or accurate.

Hence, we propose a modified VPS method, which can overcome these drawbacks. We change the brightness stimulus of the object background H_B of Eq. (2), and define the H_B again as follows:

$$H_B(x,y) = \frac{1}{N_B - 1} \sum_{\substack{m=-\frac{p_B}{2} \\ m\neq 0}}^{\frac{p_B}{2}} \sum_{\substack{n=-\frac{p_B}{2} \\ n\neq 0}}^{\frac{p_B}{2}} \frac{I(x-m, y-n)}{\sqrt{m^2+n^2}} \tag{8}$$

where also $N_B = {p_B}^2$, but $p_B = 3 \times p_o$, and the denominator is different.

Though the change is not much, the effect is changed markedly, and the result is excellent. The next section gives the analyses in detail.

3 Experiments and Discussion

We experiment this proposed modified method by MATLAB, and compare the VPS method with the proposed modified VPS method.

Fig. 2 is the results. In the all experiments, we choose the p_o=3. From the Fig. 2, we can see that the result by the proposed modified VPS method is much better than the one by VPS method. The segmented image by the proposed method is very accurate, and there is few oversegmetation and undersegmentation. However, VPS method not only oversegments, but also undersegments the image. From Fig. 2(b), in the central part of the segmented image, the size of the objects is bigger than the original objects, but around the segmented image, the objects are smaller, or even disappear.

The reason is that the brightness stimulus of the object background H_B is expressed as the weighted intensity of the region [11]. The denominator in Eq. (2) of VPS method consists of the coordinate value x and y of the considered pixel (x,y), which means that the weighted intensity varies along with both the intensity of the gray level and the value of x and y in the pixel (x,y). The image segmentation task is to produce a segmented image to approximate the true scene as closely as possible. Whereas, the segmented objects by VPS method are not even. Some objects are oversegmented, and others are undersegmented. However, the proposed modified VPS method is not like that. In Eq. (8) of the proposed method, the denominator does not consist of x and y. Hence, Eq. (8) is really expressed as the weighted intensity, which calculates only the gray level. Moreover, there is another change that $p_B = 3 \times p_o$, which makes the size of the object background much larger than VPS method, so the brightness of the real object background contributes the $H_B(x,y)$ much more. In result, all these measures make the segmentation image even and accurate.

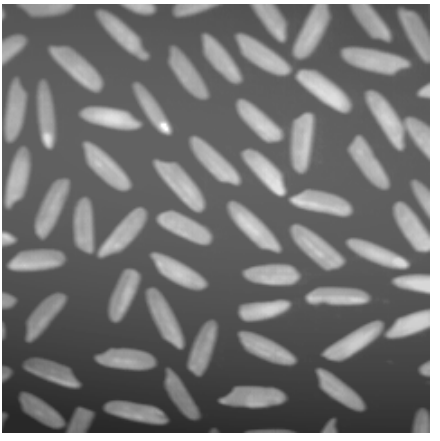

(a) Original image

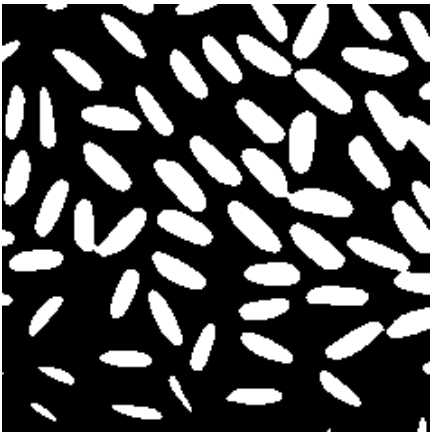

(b) Result by VPS

(c) Result by modified VPS

Fig. 2. Experiment results

4 Conclusion

A common task in computer vision is to partition an image into regions that are homogeneous in some sense. This task, called segmentation, can also be defined as the process that subdivides a sensed scene into its constituent parts or objects. Segmentation of an image is a complex, but extremely important task in computer vision, and usually is prerequisite to high-level vision algorithms, such as object description, recognition, or scene analysis.

The visual perception-based segmentation method is to adapt to the laws governing the human visual perception. The essence of the VPS method is the threshold, but it simulates the human visual perception. Thus, the adaptation is more powerful, so it can segment poor quality images with low contrast and low SNR. Moreover, it provides another artificial intelligence method for the digital image processing. However,

this method has still some drawbacks. In this paper, the modified VPS method is proposed. This method outperforms VPS method, which oversegments and undersegments the image. Compared with VPS method, this proposed modified VPS method improves the quality of the segmented image, and the result is even and accurate.

Acknowledgments. This paper is supported by Natural Science Foundation of Anhui Province in University (KJ2010B179), and Excellent Youth Talents Foundation of Anhui Province in University (2010SQRL154).

References

1. Jaehyun, P., Ludwik, K.: Unsupervised segmentation of textured images. Information Sciences 92(7), 255–276 (1996)
2. Huang, Y.-P., Chang, T.-W.: A fuzzy inference model for image segmentation. Fuzzy Systems 2(5), 972–977 (2003)
3. Baranwal, R., Singh, R., Bora, P.K.: An Information Theoretic Approach to Image Segmentation, vol. 1(10), pp. 218–222 (2003)
4. Wong, F., Nagarajan, R., Yaacob, S., et al.: An image segmentation method using fuzzy-based threshold. Signal Processing and its Applications 1(8), 144–147 (2001)
5. Karmakar, G.C., Dooley, L.S.: A generic fuzzy rule based image segmentation algorithm. Pattern Recognition Letters 23(10), 1215–1227 (2002)
6. Karmakar, G.C., Dooley, L.S.: Extended fuzzy rules for image segmentation. Image Processing 7(8), 1099–1102 (2001)
7. Lo Bosco, G.: A genetic algorithm for image segmentation. In: Proceedings of 11th International Conference on Image Analysis and Processing 2001, September 26-28, pp. 262–266 (2001)
8. Hangchuan, P., Fuhui, L., Zheru, C., et al.: Hierarchical genetic image segmentation algorithm based on histogram dichotomy. Electronics Letters 36(10), 872–874 (2000)
9. Zümray, D., Tamer, Ö.: Segmentation of ultrasound images by using a hybrid neural network. Pattern Recognition Letters 23(14), 1825–1836 (2002)
10. Fatih, K., Bülent, S., Harmanc, E.A.: A Image segmentation by relaxation using constraint satisfaction neural network. Image and Vision Computing 20(7), 483–497 (2002)
11. Heucke, L., Knaak, M., Orglmeister, R.: A new image segmentation method based on human brightness perception and foveal adaptation. IEEE Signal Processing Letters 7(6), 129–131 (2000)
12. Belkacem-Boussaid, K., Beghdadi, A., Depoisot, H.: Edge detection using Holladay's principle. Image Processing 1(9), 833–836 (1996)

A Home Nursing Robot System

Tingjun Wang, Huanhuan Zhang, Xipei Ma, Yan Zhu,
Zhiyong Zhou, and Bingfeng Qian

School of Mechanical Engineering, Shanghai Dianji University,
200245 Shanghai, China
wtingjun@163.com

Abstract. A kind of new home nursing robot system (HNR) with the function of health diagnosing expert system and human physiological parameters monitor is designed for satisfying older, weak or sick persons at home. This paper discusses HNR's mechanical structure, control system and communication. Its main subsystems are presented in detail, including product appearance design, mobile mechanism, arm mechanism, human physiological parameters monitor system, expert database in human health diagnosis for six basic life parameters, human-machine interface, entertainment system, LED lighting system and changing colors control, sensing and detection system, control system, robot's positioning and vision correct motion deviation system, communication system, long-distance alarm system based on GSM short message. The result indicates that HNR has a humanized cartoon appearance by means of ergonomics and industrial design. A patient or an elder can expediently operate it by its wireless voice control system or touch-screen. A global localization with monocular vision suspended from the ceiling in unknown indoor environment ensures HNR's motion precision and repeatability accuracy. Health diagnosing expert system gives states or an alarm on the condition of an over-standard physiological parameter value.

Keywords: Appearance design, structure design, control system, health diagnosing, vision, repeatability accuracy.

1 Introduction

Various home service robots are coming into homes [1]. Economical price and convenient use is important for a household robot [2]. Home nursing robot is one robot of an intelligent home multi-robot system. It provides services for the old, weak or sick persons who have the demand of bed rest at home. A kind of new home nursing robot system tries to be developed. The HNR can independently move indoor condition. It administers accompanying and nursing sick or old persons. It has some main functions, such as moving, turning, avoiding obstacle, safety, carrying some foods and a bottle of water, carrying medicine, timing voice reminder, giving the correct time and calling. It also has health expert system, and human physiological multi-parameters monitor system. These provide some high-level functions of health consultation,

D. Zeng (Ed.): Future Intelligent Information Systems, LNEE 86, pp. 317–324.
springerlink.com © Springer-Verlag Berlin Heidelberg 2011

monitoring human physiological multi-parameters and etc. It can automatically give an alarm note by GSM/GPRS when a physiological parameter is no normal data. It achieves long-distance interaction with long-distance kinfolks and doctors by LAN.

2 Appearance Design

Appearance design of household robot generally is divided into three kinds of imitational animal sculpt, imitational plant sculpt and imitational person (or humanoid robots). Household robot has closer relationship with people. Therefore the user friendly design is important for a household robot [3].

Fig. 1. A product appearance design for HNR

HNR works indoor environment. According to the robot's task and main servicing object, HNR's product appearance design has user friendly design. So HNR designed as a humanized cartoon sculpt by the method of ergonomics and industrial design. Figure 1 shows a kind of product appearance design for HNR. Whole crust is made of engineering plastic material which has definite flexibility and rigidity. And fixing hole of sensors is opening on the crust. Transparent body of LED lighting adopts translucent yakeli material, and it is semipermeable through abrade. It can present its status through colors of its LED lights. In color, silvery white and night black are adopted. They have strongly contrasted and form seeing concussion. The robot looks high-tech feeling and household appetency. There is a rectangle hole for fixing touch LCD of human and robot interaction.

3 HNR'S Framework

Robot system is commonly divided into two main parts, namely, mechanical structure and control system [4]. Figure 2 shows the framework of the home nursing robot system.

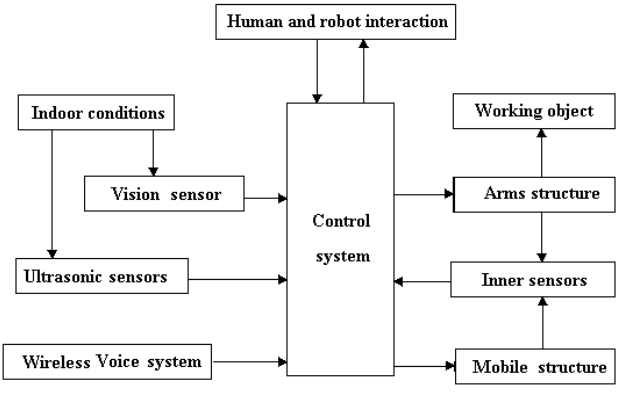

Fig. 2. Framework of the HNR system

4 Mechanical Structure and Transmission Mechanism

Mechanical structure is the foundation of that a robot implements prearranged functions. HNR is 1.1 meters in height. Its mechanical structure consists of a mobile mechanism, double robot arms, and a trunk frame. Structural parts use aluminum alloy materials. Transmission mechanism parts use steel materials.

4.1 Motion Mode

In comparison with foot and track motion, wheeled motion mode has simple mechanical structure, more motion agility, high stability and good operation [5]. And indoor terrain is taken into account, HNR adopts wheeled motion mode. Through encoders, its motion parameters can easily measure and feed back.

The robot's double arms adopt joint structure. They commonly move synchronously. Their joints corporately motion realize multi-axes unite movement.

4.2 Mobile Mechanism[6]

Mobile mechanism adopts three wheeled structure and two wheel independent driving model. The three wheeled structure includes two driving wheels and a pilot wheel. Figure 3 shows sketch of the mobile mechanism. Two driving wheels are driven by two DC servo motors independently. Therefore the motion direction of the robot is determined by different velocity value.

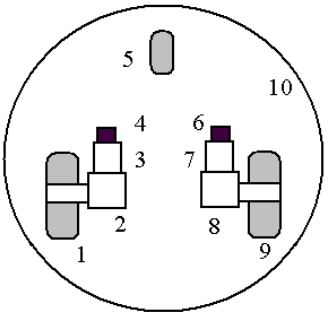

1. left driving wheel; 2. left reducer; 3. left DC servo motor; 4. left encoder; 5. pilot wheel; 6. right encoder;7. right DC servo motor; 8. right reducer; 9. right driving wheel; 10. bodywork

Fig. 3. Sketch of the mobile mechanism

This structure form has agile movement and is simple. It satisfies indoor environment. The mobile mechanism sets seven pairs of ultrasonic sensors and PSD position sensors to detect the position of an obstacle and come true autonomous obstacle avoidance.

Main design parameters of HNR's mechanical structure are as follows: maximum travel velocity is no less than 1m/s; maximum travel slope angle on a slope is no less than 10°; the vertical height of an obstacle it can surmount is no less than 50mm; the width of a raceway it can span is no less than 50mm.

4.3 Arms Design

Two arms and hands have the same mechanism structure and driving mode. They adopt personate joint structure. Each arm has three degrees of freedom. And a hand can free open and close its paw. Figure 3 shows scheme of analyzing about HNR's degrees of freedom. These degrees of freedom ensure HNR can hold appropriate pose in order to catch hold of objects. At meantime, arms' movements are agility.

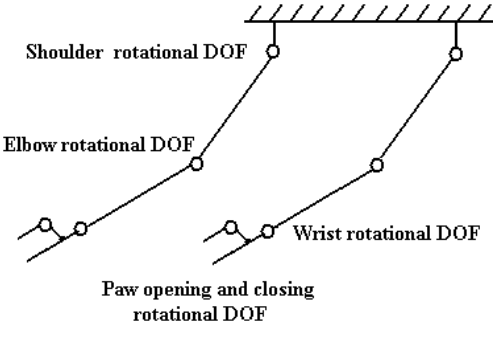

Fig. 4. Scheme of analyzing about HNR's degrees of freedom

Each arm is a planar linkage mechanism. Its joints are rotating on a vertical plane. Three joints (including shoulder joint, elbow joint and wrist joint) rotate either associatedly or independently. These ensure to achieve planning path of the palm of the hand. Paw opening and closing joint of an arm is rotating independently, it has no motion relation with other joints at same time. But two paw opening and closing joint are rotating synchronously.

The arms are set on a trunk frame. The trunk frame is used for setting some control system hardware.

5 Control System

HNR's control system consists of an industrial personal computer, two motion control cards, motor drivers, motors, sensors and control software. And it has voice control system and visual orientation system. Its motion control hardware system is shown as in Figure 5.

HNR's control system of adopts host computer and client computer model. The industrial personal computer is HNR's host computer. It accomplishes robot's programming and depositing, program running, parameter setting, logic calculating, human-robot interface (touch LCD and wireless voice recognition) and etc. Motion control cards uses as client computer.

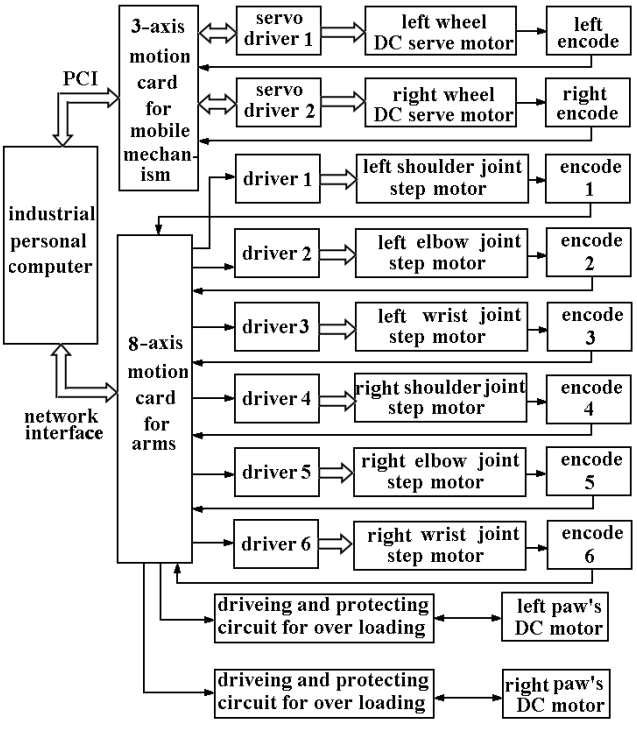

Fig. 5. HNR's motion control hardware system

A 3-axis motion control card is used for motion controlling of mobile mechanism. And it communicates with host computer by PCI. An 8-axis motion control card is used for motion controlling of two arms and paws. And it communicates with host computer by ethernet network interface. The two cards receive control commands from the industrial personal computer, calculate and send control signals to drivers.

Two paw's DC motors have protecting circuit. And they can self-protect when over loading. This avoids using limit switches for paw's opening and closing position.

By some sensors, HNR achieves autonomous obstacle avoiding, fetching something work's veracity, and adapting it to indoor surroundings. Encodes are used for detecting motors' rotating angular displacement. Three ultrasonic sensors and seven PSDs are used for detecting the distance of an obstacle. A monochrome CCD sensor is suspended and fastened on ceiling. It provides a positioning system to correct motion deviation when it is at some key places.

6 Health Diagnosing Expert System

Health diagnosing expert system is a characteristic part of HNR. It consists two parts of a human physiological parameters monitor and a health expert system. The human physiological parameters monitor is for detecting and processing six life parameters. It has some life parameters sensors, for instance, blood pressure sleeve strap, electrocardiograph cable, body temperature sensor, blood oxygen explorer and etc. Therefore, the six life parameters which it detects and processes are electrocardiograph, saturation, blood pressure, pulse, respiration and body temperature. It sends these parameters to HNR's IPC by wireless network in order to accomplish real-time monitoring and long-distance transmission. And it can send a long-distance alarm based on GSM short message.

The health expert system adopts building knowledge database with classification by means of six life parameters. It does certainty reasoning according to receiving physiological parameters from the physiological parameters monitor, and then presents health status and some suggesting for health or reminds to see a doctor when a parameter oversteps natural region.

7 Vision Correct Motion Deviation System

The vision correct motion deviation system consists of a monochrome CCD sensor, an image acquisition and an industrial personal computer. It provides position coordinate and motion directional angle when HNR moves a correct place and region.

According to indoor environment, two black circles are used as robot's identifier. The diameters of two circles are twice times discrepancy. They arrange along robot's advance and back direction. And the big circle is rearwards. The centre of big circle is robot's position coordinate value. The centre of big circle and the centre of little circle line show robot's motion positive direction. Figure 6 shows the HNR's position identifier on the top of its head. OA is HNR's moving direction currently, and OB denotes its goal direction. Therefore $\triangle\theta$ denotes motion deviation in direction. Point O

denotes the robot's position coordinate point. The robot's anticipate position coordinate value and motion direction angle are deposited to the IPC through system's demarcation previously.

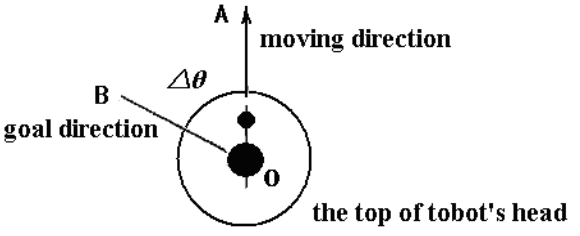

Fig. 6. HNR's position and direction identifier on the top of its head

Vision system's date is used to correct motion deviation before HNR go the next step motion. So the vision system can ensure robot's final position precision when HNR arrive a goal position. And it also ensures robot's repeatability accuracy when HNR works continuously.

8 Conclusions

(1) HNR designed as a humanized cartoon sculpt by the method of ergonomics and industrial design. It can present its status through colors of its LED lights. Touch LCD is used for human and robot interaction.

(2) The mobile mechanism adopts three wheeled structure and two independent driving wheel model. It is driven by two DC servo motors. The two driving wheels are controlled independently and driven cooperatively. This structure form has agile movement and is simple. It satisfies indoor environment. The mobile mechanism sets seven pairs of ultrasonic sensors and PSD position sensors to detect the position of an obstacle and come true autonomous obstacle avoidance.

(3) Two arms and hands have the same mechanism structure and driving mode. They adopt personate joint structure. Each arm has three degrees of freedom. And a hand can free open and close its paw.

(4) HNR's control system of adopts host computer and client computer model. IPC used for host computer. And a 3-axis motion control card is used for motion controlling of mobile mechanism. An 8-axis motion control card is used for motion controlling of two arms and paws. The IPC communicates with the two cards by PCI and ethernet network. The robot sets voice control mode, touch LCD human-robot interaction mode, and autonomous movement mode.

(5) Health diagnosing expert system consists two parts of a human physiological parameters monitor and a health expert system. The human physiological parameters monitor can detecting and processing six life parameters. It sends these parameters to IPC by wireless network. It sends a long-distance alarm based on GSM short message.

(6) The vision correct motion deviation system satisfies for correcting position coordinate and motion directional angle by a monochrome CCD. Two black circles on the top of HNR's head are used for position and motion direction identifier.

Acknowledgments

The work has been Supported by Leading Academic Discipline Project of Shanghai Municipal Education Commission, Project Number: J51902, and in part by the National High Technology Research and Development Program of China (863 Program, Grant No. 2007AA041600).

References

1. Xiao, X.G., Cai, Z.X.: Development of Service Robots. J. Automation Panorama (6), 10–13 (2004)
2. Wu, A.Y., Cui, X.W.: Research Achievements of Domestic Robots. Journal of Tangshan College 22(3), 69–71 (2009)
3. Peng, Q.: The Discussion of Household Robot Design under the Instruction of User Friendly Design. J. Art and Design (2), 151–153 (2008)
4. Ding, X.G.: Research on Robot Control. Zhejiang University Press, Hangzhou (2006)
5. Xu, D., Zhou, W.: The Apperceiving, Positioning, and Control of Motion-type Indoor Service Robot. Science Press, Beijing (2008)
6. Wang, T.J.: A Mobile Mechanism for Home Nursing Robot with Human Physiological Parameters Monitor. In: Proceeding of 3rd International Conference on Information and Computing, vol. 2, pp. 348–351. IEEE Computer Society Press, Los Alamitors (2010)
7. Duan, X.X., Wang, Y.L.: Control System of Ankle Rehabilitation Robot Based on Galil Control Card. J. Control Engineering of China 16(S1), 199–201 (2009)
8. Li, Y.X., Huang, Y.Q.: Design of system for simple home service robot. J. Transducer and Microsystem Technologies 27(5), 102–104 (2008)
9. Liu, C., Xiao, N.F.: Design and implementation of home service robot and home intelligent security control. J. Micro Computer Communication 22(2), 212–215 (2006)
10. Lu, X.H., Zhang, G.L.: Summarization on indoor service robot navigation. J. Robot 25(1), 81–86 (2003)
11. Jia, S.M., Hada, S., Takase, K.K.: Telecare robotic system for support of elderly and disable people. In: Proceeding of the 2003 IEEE/ASME International Conference on Advanced Intelligent Mechatronics, vol. 2, pp. 1123–1128. IEEE Press, New York (2003)
12. Rothtabak, Y., Weymouth, T.E.: Environment model for mobile robots indoor navigation. In: The International Society for Optical Engineering. SPIE, vol. 1388, pp. 453–463 (1991)
13. Liu, H.Y., Song, W.G.: Foundation of Robotic Technology. Metallurgical Industry Press, Beijing (2002)
14. Huang, Q.C., Li, M.H., Cai, Z.S.: Environment cognition method of home robot based on extension theory. Journal Huazhong University of Science and Technology (Natural Science Edition) 36(suppl. 1), 213–216 (2005)
15. Yang, J.J., Lin, J.B., Yuan, Q.Y.: Research and implementation of surveillance-alarm system based on GSM short message. Journal of South China Normal University (Natural Science Edition) (3), 33–35 (2009)

Analytical Model for Dynamic Spectrum Decision in Cognitive Radio Ad Hoc Networks: A Stochastic Framework*

Jiang Li and Long Zhang

Department of Communication Engineering, School of Information Engineering
University of Science and Technology Beijing
Beijing, 100083, P. R. China
kanghua88@sohu.com

Abstract. The newly emerging cognitive radio paradigm can address the fundamental issue of spectrum scarcity and inefficiency in spectrum usage for widely developing wireless communications. In this paper, we study the dynamic spectrum decision problem in cognitive radio ad hoc networks (CRAHNs). We define two functions for secondary users (SUs) in a self-organizing CRAHN, i.e., the revenue function of the exploited spectrum usage and the cost function of the spectrum consumption, to construct the payoff functions of SUs. Then we propose an analytical model via stochastic differential game for dynamic spectrum decision, which is controlled by a single entity, i.e., the spectrum broker, within the given CRAHN, and obtain the non-cooperative Nash equilibrium solution to the analytical model. The proposed analytical model essentially reflects the stochastic dynamics of SUs. Furthermore, we introduce a spectrum access threshold and present a procedure for stochastic dynamic spectrum decision, in which the concrete application requirements are indirectly guaranteed.

Keywords: Cognitive radio; Ad hoc networks; Dynamic spectrum decision; Stochastic differential game; Analytical model, Stochastic dynamics.

1 Introduction

The measurements sponsored by the Spectrum Policy Task Force of the Federal Communications Commission (FCC) indicated that the typical occupancy of the allocated spectrum through static assignment policies was less than 15%, while the peak usage was close to 85% [1]. Cognitive radio (CR) [2] has newly emerged as a promising solution to the problem of spectrum scarcity and under-utilization for widely developing wireless communications. It is an enabling technology [3] that enables unlicensed users, i.e., secondary users (SUs) or CR users to periodically

* This work is funded in part by the National Natural Science Foundation of China under Grant No. 60903004, the National Research Foundation for the Doctoral Program of Higher Education of China under Grant No. 20090006110014, and the Beijing Municipal Natural Science Foundation under Grant No. 4102042.

D. Zeng (Ed.): Future Intelligent Information Systems, LNEE 86, pp. 325–332.
springerlink.com © Springer-Verlag Berlin Heidelberg 2011

sense, intelligently identify and opportunistically access the unused but licensed spectrum, known as the spectrum holes or spectrum opportunities (SOPs) [4], while preventing interference to primary networks.

In a cognitive radio ad hoc network (CRAHN) [5], the users are composed of the licensed primary users (PUs) and SUs. The SUs constitute a self-organizing CR network without infrastructure backbone over the total exploited available authorized spectrum in a multi-hop ad hoc manner to share the corresponding SOPs. Due to the hybrid coexistence with primary networks, the spectrum management functions required for CR networks impose some unique critical design challenges [6], e.g., interference avoidance, quality of service (QoS) awareness, seamless connection, and so on. Once all the available authorized spectrum bands are detected via spectrum sensing, SUs need to perform the selection of the proper SOPs for communications through the process of spectrum decision. The spectrum decision is an important but yet unexplored topic in CR networks [7]. In [8], Kaplan, et. al. proposed a spectrum decision algorithm for spectrum brokers [9] through considering user type and spectrum channel properties. The decision algorithm brings the advantage of proper spectrum management which matches the user requirements and spectrum characteristics at most. In [7], Lee, et. al. proposed a spectrum decision framework to confirm a set of available spectrum bands by considering the application requirements as well as the dynamic nature of spectrum bands. In the proposed framework, a minimum variance-based spectrum decision (MVSD) for real-time applications, and a maximum capacity based spectrum decision (MCSD) for best effort applications are presented, respectively. In [10], Martin, et al. proposed three spectrum decision schemes, i.e., load-based spectrum decision scheme, interference-based spectrum decision scheme, and joint load and interference based spectrum decision scheme, which take into account the load of the spectrum band and/or the measured interference temperature as decision-making inputs.

As an alternative framework for modeling, game theory has gained more attention as an effective tool to study the problem of spectrum management in CR networks. In [11], Xie, et al. indicated that the competitive equilibrium (CE) of the competitive market model for dynamic spectrum management is the solution of a linear complementary problem, and proposed a decentralized method to solve the CE. In [12], Niyato, et al. modeled the problem of dynamic spectrum sharing under competition as an oligopoly market, and the Bertrand game model for price competition was applied to analyze and obtain the equilibrium pricing scheme.

Despite some game-theoretic formulations for dynamic spectrum management found in the literature, one interesting feature of these methods is that they just use static games or discrete dynamic games (e.g., repeated games) to model the problem of dynamic spectrum management, which is not suitable for the stochastic and dynamic properties within CR networks. As a result, these existing methods cannot meet the requirements that the CR networks in practice are stochastic and dynamic systems. This observation highlights the need for study novel dynamic spectrum management approaches in CR networks that can resolve stochastic spectrum management overtime. In this paper, we study the problem of dynamic spectrum decision in CRAHNs. We define two functions for secondary users (SUs), including the revenue function of the exploited spectrum usage and the cost function of the spectrum consumption, to further build up the payoff functions of SUs. Then we propose an analytical model based on stochastic differential game theory for dynamic spectrum decision and obtain the Nash equilibrium solution to the analytical model in a non-cooperative fashion. The

proposed analytical model reflects the stochastic dynamics of SUs in essence. Moreover, we introduce a spectrum access threshold and present a procedure for stochastic dynamic spectrum decision, in which the concrete application requirements are indirectly guaranteed.

The rest of the paper is organized as follows. Section 2 describes the system model and problem formulation. In Section 3, the stochastic differential game theory is introduced. The analytical model for dynamic spectrum decision is proposed in Section 4. Section 5 concludes this paper and discusses the future work.

2 System Model and Problem Formulation

We consider a primary wireless system with a finite number of PUs operating on the authorized spectrum bands $\mathcal{X}$ and a finite number of SU-pairs randomly distributed in a single area over the time interval $[t_0,T]$ in a fixed or slowly moving manner. The SU-pairs which can reuse some detected SOPs within the primary wireless system constitute a spread spectrum self-organizing CRAHN over the total available authorized spectrum bands $\mathcal{X}' \subseteq \mathcal{X}$ in an ad hoc mode to share the corresponding SOPs. Let n denote the number of the transmitting-receiving SU-pairs and $\mathcal{N} = \{1,2,\cdots,n\}$ denote the set of SU-pairs. The terms "SU" and "pairs" are used interchangeably in the following and SU i, for $i \in \mathcal{N}$, means transmitting SU i and receiving SU i. Due to the property of self-organizing, the CRAHN does not contain any infrastructure backbone within it. For the simplicity of spectrum decision, assume that the dynamic spectrum decision of CRAHN is controlled by a single entity in a single area, known as spectrum broker [9]. The spectrum broker may collect SOP information sensed by SU-pairs within its area to decide which SOPs can be allocated through dynamic spectrum decision. The SU-pairs can communicate with spectrum broker via special control channels.

Assume that at time instant $s \in [t_0,T]$, the amount of total available authorized spectrum bands exploited by SU-pairs is given by $x(s)$, for $x(s) \subseteq \mathcal{X}$, and the demand for the spectrum bands within SU i is denoted by $u_i(s)$, for $u_i(s) \subseteq x(s)$.

Definition 1. The revenue function of the exploited spectrum usage for SU i, at time instant $s \in [t_0,T]$, is denoted by $R^i[x,u_i]$, which can be defined as

$$R^i[x,u_i] = k \cdot u_i^2(s) / x(s) \tag{1}$$

where k is a revenue factor, for $k > 0$.

Definition 2. The cost function of the spectrum consumption for SU i, at time instant $s \in [t_0,T]$, is denoted by $C^i[x,u_i]$, which can be defined as

$$C^i[x,u_i] = \varphi \cdot (x(s) - u_i(s)) \tag{2}$$

where φ is a cost factor, for $\varphi > 0$.

3 Stochastic Differential Game

A general static game can be modeled as a 3-tuple $\Gamma=\{\mathcal{N},\{\mathcal{S}_i\}_{i\in\mathcal{N}},\{\mathcal{U}_i\}_{i\in\mathcal{N}}\}$, where $\mathcal{N}$ denotes the set of players, $\mathcal{S}_i$ denotes the strategy set of player i, and $\mathcal{U}_i$ denotes the set of utility (payoff) function of player i. Stochastic differential game [13] which investigates interactive decision making with stochastic dynamics and uncertain environments over time differs from static game, and is a continuous-time stochastic dynamic game model. The evolution of the states of players in stochastic differential game is described by stochastic differential equations and the players act throughout a time interval.

In particular, in a n-player stochastic differential game, the payoff of player i, for $i\in\mathcal{N}=\{1,2,\cdots,n\}$, is expressed as [13]

$$E_{t_0}\left\{\int_{t_0}^{T} g^i\left[s,x(s),u_i(s)\right]\exp\left[-\int_{t_0}^{s} r(y)\mathrm{d}y\right]\mathrm{d}s + \exp\left[-\int_{t_0}^{T} r(y)\mathrm{d}y\right]q^i\left(x(T)\right)\right\} \tag{3}$$

where $x(s)\in X\subset \boldsymbol{R}$ is the state variables of game (X is the state space), $u_i(s)\in U^i$ is the control of player i (U^i is the control space of player i), $s\in[t_0,T]$ is the time point of game (t_0 and T are starting time and finishing time of game, respectively), $g^i[s,x,u_1,\cdots,u_n]$ is the instantaneous payoff of player i, $r(s)$ is a time-varying instant discount rate, $q^i(x(T))$ is a terminal payment, E_{t_0} is the expectation operator performed at time t_0.

The state variable $x(s)$ in equation (3) depends on the state dynamics and satisfies the vector-valued stochastic differential equations [13]

$$\begin{cases}\mathrm{d}x(s)=f\left[s,x(s),u_1(s),\cdots,u_n(s)\right]\mathrm{d}s+\sigma\left[s,x(s)\right]\mathrm{d}z(s)\\ x(t_0)=x_0\end{cases} \tag{4}$$

where $\sigma\left[s,x(s)\right]$ is a $m\times\Theta$ matrix, $z(x)$ is a Θ-dimensional Wiener process, and x_0 is the initial state. Let $\Omega\left[s,x(s)\right]=\sigma\left[s,x(s)\right]\cdot\sigma\left[s,x(s)\right]^{\mathrm{T}}$ denote the covariance matrix with its element in row h and column ς denoted by $\Omega^{h\varsigma}\left[s,x(s)\right]$ [13]. Note that functions $g^i[s,x,u_1,\cdots,u_n]$ and $f[s,x,u_1,\cdots,u_n]$ are differentiable functions, respectively.

Theorem 1. A n-tuple set of feedback strategies $\left[\phi_1^{(t_0)}(t,x),\cdots,\phi_n^{(t_0)}(t,x)\right]$, for $i\in\mathcal{N}$, provides a Nash equilibrium solution to the stochastic differential game structure in equations (3) and (4), if there exist continuously differentiable functions $V^{(t_0)i}(t,x)$: $[t_0,T]\times\boldsymbol{R}^n\to\boldsymbol{R}$, satisfying the following Fleming-Bellman-Isaacs partial differential equations [13]

$$
\begin{aligned}
&-V_t^{(t_0)i}(t,x)-\frac{1}{2}\sum_{h,\varsigma=1}^{m}\Omega^{h\varsigma}(t,x)V_{x^h x^\varsigma}^{(t_0)i}(t,x)= \\
&\max_{u_i}\Big\{g^i\Big[t,x,\phi_1^{(t_0)*}(t,x),\cdots,\phi_{i-1}^{(t_0)*}(t,x),u_i,\phi_{i+1}^{(t_0)*}(t,x),\cdots, \\
&\qquad \phi_n^{(t_0)*}(t,x)\Big]\cdot\exp\Big[-\int_{t_0}^{t}r(y)\mathrm{d}y\Big] \\
&\qquad +V_x^{(t_0)i}(t,x)f\Big[t,x,\phi_1^{(t_0)*}(t,x),\cdots, \\
&\qquad \phi_{i-1}^{(t_0)*}(t,x),u_i,\phi_{i+1}^{(t_0)*}(t,x),\cdots,\phi_n^{(t_0)*}(t,x)\Big]\Big\} \\
&=g^i\Big[t,x,\phi_1^{(t_0)*}(t,x),\cdots,\phi_n^{(t_0)*}(t,x)\Big]\cdot\exp\Big[-\int_{t_0}^{t}r(y)\mathrm{d}y\Big] \\
&\qquad +V_x^{(t_0)i}(t,x)f\Big[t,x,\phi_1^{(t_0)*}(t,x),\cdots,\phi_n^{(t_0)*}(t,x)\Big]
\end{aligned}
\tag{5}
$$

and

$$
V^{(t_0)i}(T,x)=\exp\Big[-\int_{t_0}^{T}r(y)\mathrm{d}y\Big]\cdot q^i(x) \tag{6}
$$

4 Proposed Analytical Model for Dynamic Spectrum Decision in a Given CRAHN

4.1 Analytical Model via Stochastic Differential Game

Here, we just consider the problem of the stochastic dynamic spectrum decision within a given CRAHN consisting of n transmitting-receiving SU-pairs. Considering the stochastic differential game theory [13], $x(s)$ in the revenue function and the cost function (see equations (1) and (2)) can be regarded as the state variable in stochastic differential game. Accordingly, $u_i(s)$ in the revenue function and the cost function (see equations (1) and (2)) can be considered as the control variable in stochastic differential game. At time instant $s\in[t_0,T]$, the instant payoff function of SU i can be expressed as the difference between the revenue function and the cost function, i.e.,

$$
\begin{aligned}
g^i &= R^i[x,u_i]-C^i[x,u_i] \\
&= k\cdot\frac{u_i^{\,2}(s)}{x(s)}-\varphi\cdot\big(x(s)-u_i(s)\big)
\end{aligned}
\tag{7}
$$

For the convenience of derivation, we set the starting time $t_0=0$. Therefore, at time instant $s\in[t_0,T]$, the payoff function of SU i can be written as

$$
E_0\left\{\int_0^T\left[k\cdot\frac{u_i^{\,2}(s)}{x(s)}-\varphi\cdot\big(x(s)-u_i(s)\big)\right]\cdot e^{-rs}ds+e^{-rT}\cdot qx(T)\right\} \tag{8}
$$

According to (8), $x(s)$ is assumed to satisfy the following stochastic differential equation, i.e.,

$$\begin{cases} \mathrm{d}x(s) = \left[x(s) - \sum_{i \in \mathcal{N}} u_i(s) \right] \mathrm{d}s + \sigma x(s) \mathrm{d}z(s) \\ x(0) = x_0 \end{cases} \tag{9}$$

Note that the spectrum broker is in charge of performing decision-making based on the analytical model in equations (8) and (9).

4.2 Nash Equilibrium Solution to Analytical Model

For non-cooperative stochastic dynamic spectrum decision, assume that SU-pairs within the given CRAHN in stochastic differential game abandon the cooperation due to their selfishness and own interests. Let $\{\phi_1^*(t,x), \cdots, \phi_n^*(t,x)\}$ be the Nash equilibrium solution of SUs to analytical model under the condition of non-cooperation and assume that there exists continuously differentiable function $V^i(t,x)$, for $i \in \mathcal{N}$, which should satisfy the following Fleming-Bellman-Isaacs partial differential equations in equation (5), i.e.,

$$\begin{aligned} & -V_t^i(t,x) - \frac{1}{2}\sigma^2 x^2 V_{xx}^i(t,x) \\ & = \max_{u_i} \left\{ \left[k \cdot \frac{u_i^2(t)}{x(t)} - \varphi \cdot \left(x(t) - u_i(t) \right) \right] \cdot e^{-rt} \right. \\ & \quad \left. + V_x^i(t,x) \left[x(t) - u_i(t) - \sum_{j \in \mathcal{N} \setminus i} \phi_j^*(t,x) \right] \right\} \end{aligned} \tag{10}$$

$$V^i(T,x) = e^{-rT} q x(T) \tag{11}$$

Performing the indicated maximization in equations (10) and (11) yields

$$\phi_i^*(t,x) = \frac{x\left[e^{rt} V_x^i(t,x) - \varphi \right]}{2k} \tag{12}$$

Substituting $\phi_i^*(t,x)$, for $i \in \mathcal{N}$, in equation (12) into equations (10) and (11), upon solving equations (10) and (11), we obtain the value function of SU i, i.e.,

$$V^i(t,x) = e^{-rt} \left[A_i(t) x(t) + B_i(t) \right] \tag{13}$$

where $A_i(t)$ and $B_i(t)$ satisfy the following equations

$$\begin{aligned}&-e^{-rt}(-r)\left[A_i x+B_i\right]-e^{-rt}\left[\dot{A}_i x+\dot{B}_i\right]\\&=\left[k\cdot\frac{1}{x}\cdot\frac{x^2(A_i-\varphi)^2}{4k^2}-\varphi x+\varphi\cdot\frac{x(A_i-\varphi)}{2k}\right]\cdot e^{-rt}\\&\quad+e^{-rt}A_i\left[x-\sum_{i\in\mathcal{N}}\frac{x(A_i-\varphi)}{2k}\right]\end{aligned}\tag{14}$$

According to equation (14), we obtain

$$\dot{A}_i=-\frac{1}{4k}A_i^2+\left(r-1-\frac{n\cdot\varphi}{2k}\right)A_i+\frac{A_i}{2k}\sum_{i\in\mathcal{N}}A_i+\frac{\varphi^2}{4k}+\varphi\tag{15}$$

$$\dot{B}_i=rB_i\tag{16}$$

$$A_i(T)=q\tag{17}$$

$$B_i(T)=0\tag{18}$$

Substituting $A_i(t)$ in equation (15) and $B_i(t)$ in equation (16) into equations (13) and (12), we obtain the game Nash equilibrium solution to the analytical model, i.e.,

$$\phi_i^*(t,x)=\frac{x(A_i-\varphi)}{2k}\tag{19}$$

The optimal trajectory of the state variable of the analytical model can be expressed as

$$\begin{cases}\mathrm{d}x(s)=\left[x(s)-\sum_{i\in\mathcal{N}}\frac{x(s)\cdot(A_i-\varphi)}{2k}\right]\mathrm{d}s+\sigma x(s)\mathrm{d}z(s)\\x(0)=x_0\end{cases}\tag{20}$$

4.3 Procedure for Stochastic Dynamic Spectrum Decision

According to the analytical model, the spectrum broker performs the stochastic dynamic spectrum decision in a given time interval $[t_0,T]$. Assume that at time instant $s\in[t_0,T]$, the spectrum access threshold in the CRAHN is denoted by $\Theta(s)$. The spectrum broker makes decisions for dynamic spectrum access based on the following **Procedure 1**.

Procedure 1. In the CRAHN, at time instant $s\in[t_0,T]$, SU i, for $i\in\mathcal{N}$, can access the exploited spectrum bands if and only if $\phi_i^*(s,x)\geq\Theta(s)$. Otherwise, the CRAHN will reject the spectrum access request of SU i.

5 Conclusions and Future Work

In this paper, we investigate the problem of dynamic spectrum decision in the CRAHNs. We first introduce two functions for SUs, i.e., the revenue function of the exploited spectrum usage and the cost function of spectrum consumption. Then we propose a stochastic differential game-based analytical model for dynamic spectrum decision. The proposed analytical model combines the stochastic property with dynamics within a given CRAHN. Furthermore, we introduce a spectrum access threshold and present a procedure for stochastic dynamic spectrum decision.

In the future, we will incorporate the interference to the primary networks into the analytical model, and further give some theoretical analysis or mathematical proofs. Moreover, we will perform the experimental study and present the numerical simulation results to validate the effectiveness of the proposed analytical model.

References

1. FCC. Spectrum Policy Task Force. Technical Report, ET Docket No. 02-135 (2002)
2. Mitola, III, J.: Cognitive radio: an integrated agent architecture for software defined radio. Ph.D. dissertation, KTH Royal Institute of Technology, Stockholm, Sweden (2000)
3. Haykin, S.: Cognitive radio: brain-empowered wireless communications. IEEE Journal on Selected Areas in Communications 23(2), 201–220 (2005)
4. Xin, C., Xie, B., Shen, C.C.: A novel layered graph model for topology formation and routing in dynamic spectrum access networks. In: IEEE DySPAN 2005, pp. 308–317 (2005)
5. Akyildiz, I.F., Lee, W.Y., Chowdhury, K.R.: CRAHNs: cognitive radio ad hoc networks. Ad Hoc Networks 7(5), 810–836 (2009)
6. Akyildiz, I.F., Lee, W.Y., Vuran, M.C., Mohanty, S.: A survey on spectrum management in cognitive radio networks. IEEE Communications Magazine 46(4), 40–48 (2008)
7. Lee, W.Y., Akyildiz, I.F.: A spectrum decision framework for cognitive radio networks. IEEE Transactions on Mobile Computing (2010) (to be published)
8. Kaplan, M., Buzluca, F.: A dynamic spectrum decision scheme for heterogeneous cognitive radio networks. In: ISCIS 2009, pp. 697–702 (2009)
9. Buddhikot, M.M., Kolodzy, P., Miller, S., Ryan, K., Evans, J.: DIMSUMNet: new directions in wireless networking using coordinated dynamic spectrum access. In: IEEE WoWMoM 2005, pp. 78–85 (2005)
10. Marin, L., Giupponi, L.: Performance evaluation of spectrum decision schemes for a cognitive ad-hoc network. In: IEEE PIMRC 2008, pp. 1–5 (2008)
11. Xie, Y., Armbruster, B., Ye, Y.: Dynamic spectrum management with the competitive market model. IEEE Transactions on Signal Processing 58(4), 2442–2446 (2010)
12. Niyato, D., Hossain, E.: Competitive pricing for spectrum sharing in cognitive radio networks: dynamic game, inefficiency of nash equilibrium, and collusion. IEEE Journal on Selected Areas in Communications 26(1), 192–202 (2008)
13. Yeung, D.W.K., Petrosyan, L.A.: Cooperative Stochastic Differential Games. Springer, Heidelberg (2005)

Application of an Improved SVM Algorithm for Wind Speed Forecasting

Huaqiang Zhang, Xinsheng Wang, and Yinxiao Wu

Wenhua xi road 2, Harbin Institute of Technology at Weihai, Weihai, 264209, China
zhq@hit.edu.cn, wangxswh@126.com, wuyinxiaowh@126.com

Abstract. An improved Support Vector Machine (SVM) algorithm is used to forecast wind in Doubly Fed Induction Generator (DFIG) wind power system without aerodromometer. The mathematical model is built after analyzing the principle of wind forecasting with Maximum Power Point Tracing (MPPT), and its kernel functions of SVM is selected. Compares the rapidity and accuracy of parameter optimization methods, we know that the Particle Swarm Optimization (PSO) method is better than the Cross Validation (CV) method. Finally, 3.6MW DFIG wind power system simulation model with wind speed forecasting is established. Simulation results show that the accuracy rate thought improved SVM forecasting algorithm can reach 98.667%, the DFIG system can operate at the MPPT. The whole performance has well robustness and rapidity.

Keywords: Wind power generation; Forecast; Maximum power point tracing (MPPT); Support vector machine; Particle swarm optimization.

1 Introduction

Modern wind power generation technology is focused on its low cost, high efficiency and reliability. Many scholars are studying on the *Maximum Power Point Tracking (MPPT)* strategy to achieve optimal wind energy utilization coefficient [1]. The coiling rotor *Doubly Fed Induction Generator (DFIG)* is usually used in large wind power generator system to realize variable speed constant frequency control scheme.

Current *DFIG* wind power system of maximum wind tracking method is established in the optimal wind speed and power curve of known. Real time detects wind speed and utilizes the characteristic curve to obtain corresponding optimal blade tip velocity ratio λ, so as to control wind generator speed. This method needs high precision aerodromometer, but it is difficult to measure accurately wind speed because of wind leaf disturbance by large airflow, Different points have different speed on the blade. In order to overcome these shortcomings, Wind speed forecasting technology without sensor of *MPPT* becomes more important. It is paid attention to reduce cost and increase the utilization ratio of the whole system.

Many methods can forecast wind speed, such as wind durative prediction, persistent linear regression model, differential Auto-Regressive Integrated Moving Average (ARIMA), Kalman filter, Neural network and fuzzy expert system etc. Using autoregressive statistic model to forecast speed, computing complexity and forecast delay might influence the MPPT performance [2]. Fuzzy logic control must take long time

D. Zeng (Ed.): Future Intelligent Information Systems, LNEE 86, pp. 333–340.
springerlink.com © Springer-Verlag Berlin Heidelberg 2011

to search maximum power point when speed frequent fluctuations. Neural network for nonlinear mapping has arbitrariness approximation ability. Intelligent identification method based on neural network is widely used in complex system. Neural network forecasting method often used in small wind power system; it can quickly and accurately forecast wind speed from electric power of generator [3]. Therefore, Neural network method is expanded in large wind power system to improve performance has important significance. The *Support Vector Machine (SVM)* neural network algorithm is used in *DFIG* wind power system for forecasting speed to achieve maximum wind tracking purposes.

2 Wind Forecasting Principle of MPPT

The relationship between wind machine output power and wind speed is [4]:

$$P_{mech} = \frac{1}{2}\rho A v^3 C_p \ . \tag{1}$$

Where ρ is air density (kg/m^3), v is speed (m/s), C_p is wind energy utilization coefficient, $A = \pi R^2$ is wind machine blade area (m^2), R is wind wheel radius, C_p is a nonlinear function about blade tip velocity ratio λ and the pitch angle β.

$$\lambda = \frac{2\pi Rn}{v} = \frac{\omega R}{v} \ . \tag{2}$$

Where n is wind wheel speed (r/m), ω is angular speed (rad/s), C_p is [4]:

$$C_p(\lambda,\beta) = c_1(\frac{c_2}{\lambda_i} - c_3\beta - c_4)e^{-\frac{c_5}{\lambda_i}} + c_6\lambda \ . \tag{3}$$

Where $\frac{1}{\lambda_i} = \frac{1}{\lambda + 0.08\beta} - \frac{0.035}{\beta^3 + 1}$. The relationship between C_p and λ at different β is shown in fig.1. When β is in certain situation, the λ can influence the magnitude of C_p. When β is constant, there is exclusive optimal λ_{opt}, C_p can reach maximum $C_{p\max}$. If λ deflect the curve of λ_{opt}, C_p reduce at once. Wind energy utilization and conversion efficiency reduce too.

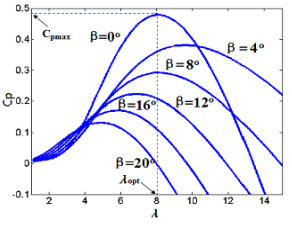

Fig. 1. $C_p(\lambda,\beta)$ Curve

For specifically wind machine, when β is constant and wind machine operates at maximum $C_{p\max}$, it produces optimal $P_{\max}$ and has optimal λ_{opt}. If wind speed is known, we can calculate its corresponding optimal wind machine speed by using the definition λ_{opt}, then the machine operates at the maximum power points. Therefore, if we can obtain real time wind speed, the wind machine can be easily regulated at the optimal output power points. Wind speed forecast algorithm instead of speed sensor to reduce cost and can increase the utilization ratio of the whole wind power system.

From eq.1, $P_{mech} = f(v,\omega,\beta)$ is a nonlinear function about v、ω、β. When forecast wind speed without sensor, the commonly used method is to change the object function into inverse function. That is v is a function about P_{mech}、ω、β, obtaining real time wind speed through look up table method. This method is simple, but requires a lot of memory, and when the data is large, it makes search slowly and delay. System sensitivity and performance is reduced greatly [5].

Neural network is an ideal tool for solving nonlinear input-output mapping functions. It has well nonlinear approximation ability. The improved *SVM* is the same as multilayer perceptron and *Radial Basis Function (RBF)*, which can be used in mode classification and nonlinear regression neural network. Wind speed forecasting SVM algorithm mentioned in this paper is to learn and classification prediction for input samples. For example, taking P_{mech}, ω and β as sample attributes and taking wind speed as sample training label to train, real time data can be accurately classified into corresponding wind speed with the trained *SVM* forecasting functions.

3 Application of SVM Algorithm

3.1 Support Vector Machine

SVM algorithm has training error rate and statistical learning ability. It takes *Vapnik Chervonenkis (VC)* Dimension sum as boundary to divide patterns. *SVM* gives zero to the former item value and makes the 2nd item minimization. The optimal separating hyperplane constructing problem is changed into a quadratic optimization problem. It achieves the global advantages and avoids the local extremum problem. All data will be mapped into high dimensional space to construct linear distinguish function, and achieves nonlinear function judging purpose.

We consider *SVM* as three layers feed forward neural networks. Its structure is shown in fig.2. Input variables are $X = (x^1, x^2, \cdots, x^n)$, output Y is the linear combination between middle nodes, each node corresponds to a support vector, output $Y = \mathrm{sgn}[\sum_{i=1}^{m} \alpha_i y_i K(x_i, x_j) + b]$, network weight value is $\alpha_i y_i$, these number of hidden nodes corresponds to the number of support vector. The kernel function of hidden nodes is $K(x_i, x_j)$.

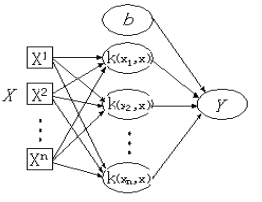

Fig. 2. Network structure of SVM

3.2 SVM Classification Algorithm Compared

We build *SVM* simulation model to forecast speed. Sample training sets and testing sets are selected first. Pretreated data is to train SVM model by training sets. Forecast training sets and model classification accuracy is achieved through SVM model.

Selects $\beta = 0$, regards wind speed 9.0 m/s, 9.2 m/s, 9.4 m/s, 9.6 m/s and 9.8 m/s five kinds speed curve as samples. There are about 2500 samples, 1-500 belongs to the first category and tags for 9.0, 501-1000 belongs to the second category labels and tags for 9.2, 1001-1500 belongs to the third class and tags for 9.4, 1501-2000 belongs to the fourth type and tags for 9.6, 2001-2500 belongs to the fifth category and tags for 9.8. It is not necessary to train every 500 data as samples, only some samples data from each category are extracted and divided into two groups to combine repeat, one parts act as training sets and the other parts act as testing sets.

SVM classifier will train the normalized training sample data. The training function is realized by using svmtrain statement, which comes from *LIBSVM* toolbox, sets Kernel function type *t*. The classification accuracy is adjusted through changing the punish parameter *c* and kernel function parameters *g* given by experience, here are *c*=2.5 and *g*=1, common kernel function are:

- *Linear Kernel Function (LKF)*

$$K(x_i, x_j) = x_i \cdot x_j \ . \tag{4}$$

- *Multinomial Kernel Function (MKF)*

$$K(x_i, x_j) = [(x_i \cdot x_j) + 1]^d \ . \tag{5}$$

- *Radial Basis Function (RBF)*

$$K(x_i, x_j) = \exp(-\frac{\left\| x_i - x_j \right\|^2}{\sigma^2}) \ . \tag{6}$$

In order to select the proper kernel function, the simulation results of the classification with the same sample data in different kernel functions condition is shown in fig.3.

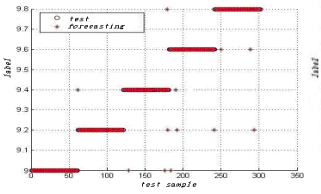

(a) Classification forecasting result at LKF

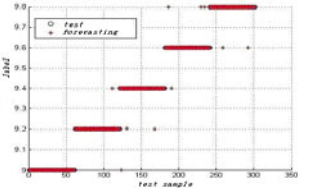

(b) Classification forecasting result at MKF

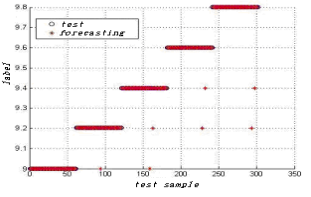

(c) Classification forecasting result at RBF

Fig. 3. Classification forecasting result at different function

From fig.3, when kernel function is *LKF*, there are 12 bias data in 300 test samples; its forecasting classification accuracy rate is 96%. When *MKF* is selected, there are 10 bias data and its forecasting accuracy rate is 96.67%. When *RBF* is selected, only 7 bias data and its accuracy rate is 97.67%. Obviously, the *RBF* has the highest accuracy rate and is selected as the kernel function in this paper.

4 Parameter Optimization of SVM

The *RBF* is selected, punish parameter c and kernel function parameter g should be adjusted when classification forecasting. The *Least Square Support Vector Machine (LSSVM)* learning and generalization ability are determined according to parameter c and g. In order to make classifier correctly predicted the unknown data, the optimal model and parameter combination must be found.

4.1 CV Parameter Optimization Method

Cross Validation (CV) method is a classifier statistical method and used in practical optimization. Using mentioned *RBF* and training the same training samples. Divides

trained data into three groups randomly. The first two groups training classification are used to forecast the third group and achieve the first accuracy rate. The last two groups are used to test the first group and get the second accuracy rate. The first and the third groups are used to test the second group and obtain the third accuracy rate.

Given parameters c and g is $[2^{-10},2^{10}]$, for each parameter combination (c, g) are CV 3 times, calculating the average value as parameter index, the highest parameter index group acts as optimal parameter training classifier, this method can effectively avoid over learning and short of learning case. The CV accuracy rate is 98%, c=1.414 and g =1. Its prediction accuracy rate is higher than experience values c and g. Because of experience values have some blindness and chanciness. Optimal parameters c and g are related to selected validation samples.

4.2 PSO Algorithm Parameter Optimization

Particle Swarm Optimization (PSO) algorithm is based on colony brainpower in intelligence computation field. There is no special requirement for *PSO* algorithm to optimize the model function and to define continuity. The algorithm is more extensive which can't express in traditional optimization method, but can be described as objective function. *PSO* optimization algorithm doesn't adopt evolution operator for individual unit, but regards each individual unit as a particle in n dimension search space without weight and volume, the particle flies in the space by a certain speed. Set $X_i = (x_{i1}, x_{i2}, \cdots, x_{in})$ is the position of particle i, $V_i = (v_{i1}, v_{i2}, \cdots, v_{in})$ is the speed of particle i, $P_i = (p_{i1}, p_{i2}, \cdots, p_{in})$ is the position of particle i.

Solving optimization problem, the proportion relation of local search ability and the global search ability must be determined. The improved *PSO* algorithm with self-adapting inertia right is adopted to enhance the basic *PSO* method astringency. Self-adapting inertia right w in speed evolution equation is:

$$v_{ij}(t+1) = wv_{ij}(t) + c_1 r_{1j}(t)[p_{ij}(t) - x_{ij}(t)] + c_2 r_{2j}(t)[p_{gj}(t) - x_{ij}(t)] \tag{7}$$

Where c_1 and c_2 is accelerate gene, r_1 and r_2 is a random function without relation, $P_g(t)$ is the best position in the global system. When $w=1$, evolution equation is the same as the basic *PSO* algorithm. w Acts as balance operation in maintaining global and local search ability [6]. Reduce w can reduce iteration orders too. When global searching, having higher overall astringency in prophase and higher convergence speed in anaphase are often expected. Sets w reduce from 1.1 to 0.4, $w = 1.1 - 0.7\frac{t}{N}$, here N is the largest iteration order and t is the iteration order. Sets c_1=1.5, c_2=1.7, colony size is 20 and evolution order is 200. Simulation results obtain the best parameters c=12.2567, g=4.3502. The test sets classification prediction accuracy can reach 98.667% through the improved *PSO* algorithm. Its training order is 60 and taking 92.3s. The best fitness and fastest convergence speed are achieved.

5 Simulation Results

DFIG wind power control system simulation platform is built in *Matlab*. *DFIG* rate power is 3.6 MW, rate voltage is 4160V and rated wind speed is 12.5 m/s. The wind generator connected grid through a transformer which capacity is 3.6 MVA 25KV/4160V. The system simulation modules are consists of power module, wind machine module, rotor side converter module, grid side converter module and wind speed forecasting module. 3.6 MW *DFIG* wind power system pitch angle $\beta = 0$, power curve can be got through the system simulation model. Its coordinates units are expressed in P. U. value as shown in fig.4.

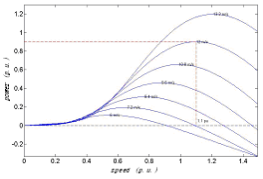

Fig. 4. 3.6MW DFIG power curve

When wind speed is 9.6m/s, the system output active power is about 1.58 MW (3.6MW*0.44=1.584MW). When wind is 12m/s, the output active power is about 3MW (3.6MW*0.86=3.096MW). When rated wind speed is 12.5m/s, the system output power is about 3.6 MW (3.6MW*1=3.6 MW). Fig.5 is simulation results of output active and passive power. The predictor based on *PSO* optimization algorithm predicts results as follow: before 0.3s, wind shaking largely. At 0.3s-0.5s, wind stable in 10m/s. During at 0.5s, wind breaks, after 0.62s, it stable in 12m/s.

After stable, the system output active power is 1.6 MW and 2.9 MW respectively wind speed is 10m/s and 12m/s. Passive power fluctuations decrease gradually, its average is 0. The speed happens step mutation at 0.5s instant, generator kinetic energy increases and active power decreases quickly, it absorbs energy from grid. After 0.62s, it comes into steady state. Simulation results show that the system under different wind speed operating in the maximum power point. The *improved SVM* wind speed forecasting algorithm can capture the maximum wind energy and can operate at maximum power output state.

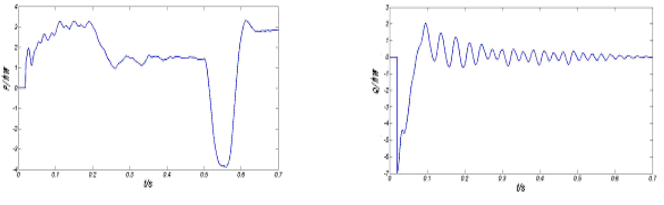

(a) Active power (b) Passive power

Fig. 5. Wind power system output active and passive power

6 Conclusions

The *SVM* neural network forecasting classification model is established in this paper. The improved *SVM PSO* algorithm is adopted to optimize the parameters by power, speed and pitch angle curve. This method has excellent global optimization and local astringency performance. Simulation results show that the test sets classification prediction accuracy can reach 98.667%, the prediction accuracy improved greatly. The improved *SVM PSO* algorithm is applied to predict the wind speed for 3.6MW *DFIG* wind power control system, it can achieve the *Maximum Power Point Tracking* without aerodromometer and it has well robustness and rapidity.

References

1. Liu, Q., He, Y., Zhang, J.: Operation Control and Modeling Simulation of AC excited Variable speed Constant frequency Wind Power Generator. In: Proceedings of the CSEE, Beijing, vol. 26(5), pp. 43–50 (2006)
2. Tan, K., Islam, S.: Optimal control strategies in energy conversion of PMSG wind turbine system without mechanical sensors. IEEE Trans. On Energy Conversion 19(2), 392–399 (2004)
3. Li, H., Shi, K.L., McLaren, P.G.: Neural-network-based sensorless maximum wind energy capture with compensated power coefficient. IEEE Trans. On Industry Application 41(6), 1548–1556 (2005)
4. Sun, T., Chen, Z., Blaabjerg, F.: Flicker study on variable speed wind turbines with doubly fed induction generators. IEEE Trans. Energy Conversion 20(4), 896–905 (2005)
5. Qiao, W., Zhou, W., Aller, J.M., Harley, R.G.: Wind Speed Forecasting Based Sensorless Output Maximization Control for a Wind Turbine Driving a DFIG. IEEE. Trans. On Power Electronics 23(3), 1156–1169 (2008)
6. Zheng, Y.L., Ma, L.H.: On the convergence analysis and parameter selection in particle swarm optimization. In: Proceedings of the IEEE International Conference on Machine Learning and Cybernetics, pp. 1802–1807 (2003)

The Control Method of the New Sensorless BLDCM Control System

Ren Zhi-bin, Long Yu-tao, and Liu Sen

School of Mechanical and Electrical Engineering,
Jiangxi University of Science and Technology, Jiangxi Ganzhou 341000
renzhibin824@yahoo.com.cn

Abstract. This paper presents a novel method to detect the rotor position of the brushless dc (BLDC) motor at a standstill and a startup method to accelerate the rotor up to a certain speed while the conventional position sensorless control methods based on the back electromotive force could not work reasonably. The proposed initial rotor-position estimation method is suitable to avoid the temporary reverse rotation or the starting failure. Based on the saturation effect of the stator iron, six short voltage pulses are applied to determine the initial rotor position and the rotor can be found within 60°. This startup method can be implemented using square voltage, which depend on the value of the current also. Using the proposed method, it is demonstrated experimentally that a stable start-up can be achieved.

Keywords: BLDC Motor; Sensorless control; startup method; initial rotor position.

1 Introduction

Due to the advantages of high power density, robust structure, the brushless DC motor (BLDCM) has played an important role in many applications. It is necessary for high-performance applications, such as servos in machine tools and robotics, to use position sensors for successful starting and operation. The issues on reducing cost, low-performance applications, space-restricted applications, and reliability of the position sensors have motivated research on sensorless control [1-6]. In addition, the fast and continuing improvements of powerful and economical microprocessors and digital signal processors (DSPs) have speeded up the development of sensorless control technology. In fact, enumerates many applications of the BLDCM, for example, air-conditioning compressor, engine cooling fan, fuel/water pump, electric vehicle[7].

The sensorless control technology of the brushless DC motor (BLDCM) based on the back-electromotive force (EMF) detection method has been widely used in the industrial and commercial fields. As we know, the magnitude of the back-EMF is proportional to the motor speed, so the back-EMF detection method cannot be applied properly when the motor is at standstill. In order to solve this problem, many methods

D. Zeng (Ed.): Future Intelligent Information Systems, LNEE 86, pp. 341–347.
springerlink.com © Springer-Verlag Berlin Heidelberg 2011

have been developed. One of them, often referred to as a 3-step startup method, is used to align the rotor first in a predetermined direction, and then accelerate the motor in an open-loop scheme before the back-EMF method is applied. This startup method is easy to implement but tends to be affected by the load and may temporarily cause reverse rotation which is not allowed in some applications.

In this paper, the short pulse sensing method, which is based on the saturation effect of the stator iron and will not cause any reverse rotation or vibration during the startup process. The key hardware implementation is the current sensor detected by Ri and the resistance network used as the voltage divider. The terminal voltage which reflects the back-EMF information is sampled by the A/D converter integrated in the micro-controller.

2 Initial Rotor Position Estimation

The phase inductance of the stator is determined by

$$L = \Phi / I \tag{1}$$

where i is the phase current and Φ is the flux due to magnet rotor and stator coils and core. Fig. 1 shows the inductance of stator windings with nonlinear magnetization characteristics of the stator core, depending upon the position of rotor. As the pole of magnet rotor is close to the stator winding, the ratio of the change of the current in the stator winding flowing in the magnetizing direction is larger than that in the opposite direction because of the magnetic saturation of the stator core. So the value of the current would be different according to the rotor position if a constant voltage vector from inverter is applied to the stator winding of the motor for a constant time period. The estimation of the rotor position is based on strongly magnetized stator field. Three situations of a magnetic pole of permanent magnet of the rotor close to the stator core are considered as shown in Fig. 2. A smaller phase inductance L(sat) is defined when the stator field is in phase with rotor field, shown in Fig. 2(a). Similarly, a larger phase inductance L(linear) is defined when the stator field is out of phase with rotor field, shown in Fig. 2(b). Fig. 2(c) depicts the case of middle value L(mid).

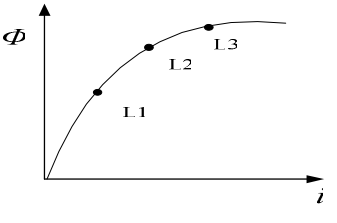

Fig. 1. The inductance of stator windings with nonlinear magnetization characteristics of the stator core

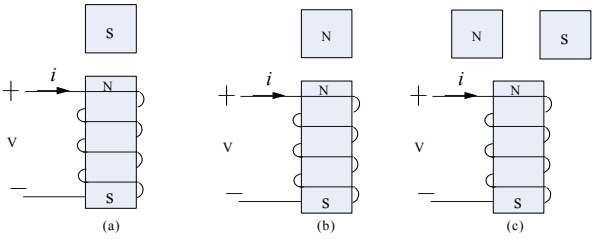

Fig. 2. Magnetic fields. (a) Saturated magnetic field, (b) linear (non-saturated) magnetic field, and (c) middle case.

3 Initial Rotor Position Detection

Based on the operation principle mentioned above, six voltage pulses are injected into the phase windings and the peaks of the response current are compared with each other to determine the rotor position.

As shown in Fig.3(a), the high-side power device VT1 and the low-side power device VT6 are activated first, which can be denoted as A+B-.The resultant magnetic field is represented by arc line. Then the high-side power device VT3 and the low-side powerdeviceVT2 are activated, and are denoted as B+ C-, and arc line Fig.3(b) represents the resultant magnetic field. If the north pole of the rotor is in the same direction as that of the resultant magnetic field arc line and in the opposite direction from that of arc line, the peak of the response current is greater when the north pole of the rotor is in the same direction as that of the resultant magnetic field arc line. Thus the north pole of the rotor can be narrowed down to 60°, as shown in Fig. 3(c).

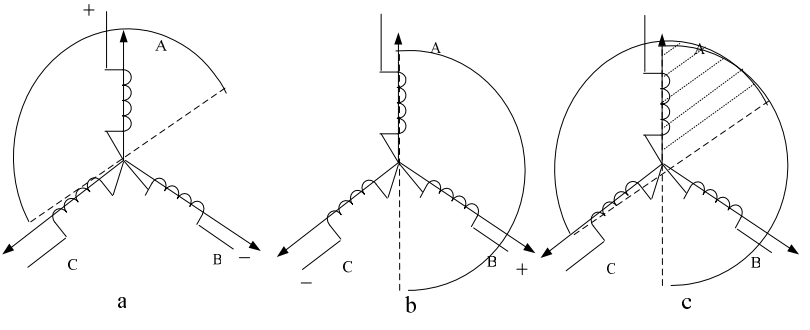

Fig. 3. The schematic diagram of initial rotor position detetion. (a) Energized stator winding and rotorpositionwithin180°; (b) Rotor position within 60°.

When the initial rotor position is identified, the motor is accelerated to a certain speed. Generally, a self-controlled BLDCM with trapezoidal BEMF waveforms is driven by a three-phase inverter with six-step commutation. Each conducting phase is called one step of two phase conducting. The conducting interval for each phase is 120° by electrical angle. Therefore, only two phases conduct current at any time, leaving the third phase floating. In order to produce maximum torque, the inverter should be commutated every 60°, and the commutations occur at 30°delay from the corresponding zero-crossing points (ZCP) of the BEMF waveforms.

4 Motor Start-Up Method

If the initial rotor position has been identified with the proposed method, as shown in fig. 4, the motor should be accelerated from the standstill up to a certain speed where the back EMF is large enough. In the case of the tested motor, the speed that should be reached with the proposed sensorless control method is about 174 r/min, because the back-EMF signal amplitude should be at least about ±40 mV for a reliable back-EMF detection [8].

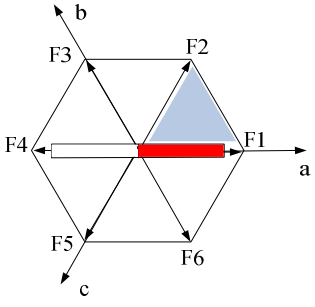

Fig. 4. Initial rotor position

Fig. 5 shows the accelerating procedure of the proposed method. First, as an example, if the initial rotor position is identified and the rotor lies in position 1 shown in Fig. 5(a), a voltage vector V2 should be applied to make the starting torque. In this example, the voltage vector at 60° is applied. If the rotor rotates and the voltage is applied as shown in Fig. 5(b), at that instant, the inductances is not the same. At that time point, the estimated rotor position should be conducted by current sampled to verify the rotor position.

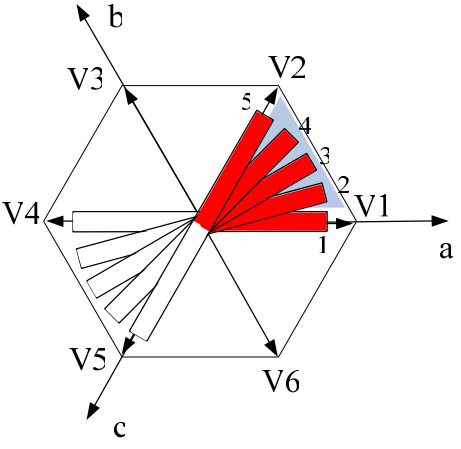

(a)

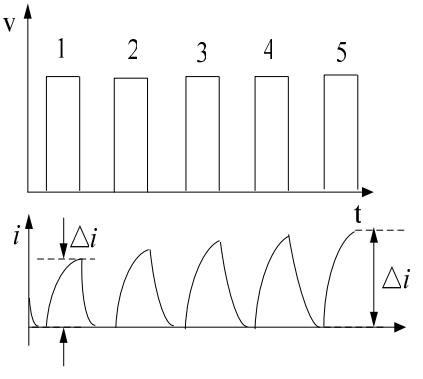

(b)

Fig. 5. The accelerating procedure of rotor position and current

5 Experimental Results

The specifications of the test BLDCM are: 8 poles, 400 W. According to fig. 3 for the initial position detection, Fig.6 display the response of velocity waveform. To verify the proposed method, we conducted some experiments. In experiment, the currents are sampled to verify the rotor position, The key hardware of the current sensor and powerful microprocessors of digital signal processors (DSPs) should be used. Traditional method of 3-step startup is shown in Fig.6(a)(b) and new method is shown in Fig. 6(c). In the experiments, the results show that the use of the methods makes the drive better, with better follow performance.

(a)

(b)

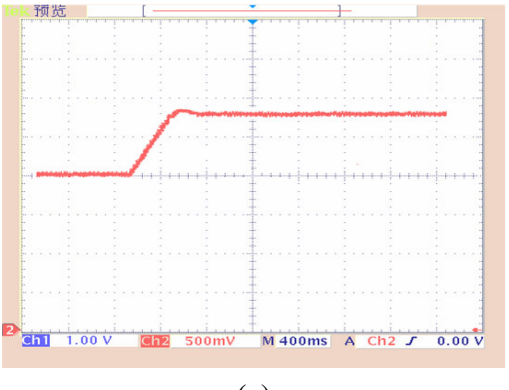

(c)

Fig. 6. Speed response curve

6 Conclusion

In this paper, new startup and smooth switching method of a sensorless brushless DC motor is presented. By using this method, the rotor position at standstill can be estimated with a resolution of 60° and the motor is accelerated to a certain speed at which the back-EMF detection method can be applied. The method will not cause any reverse rotation or vibration during the startup process. The hardware implementation of the driving circuit is simple. It is very suitable to use in the low-cost applications.

References

1. Krishnan, R., Ghosh, R.: Staring algorithm and performance of a PMDC brushless motor drive system with no position sensor. In: 20th Annual IEEE Power Electronics Specialists Conf., IEEE PESC 1989, Milwaukee, WI, USA, June 26-29, pp. 815–821 (1989)
2. Johnson, J.P., Ehsani, M., Guzelgunler, Y.: Review of sensorless methods for brushless dc. In: IEEE-IAS/PCA Cement Industry Technical Conf., IEEE IAS 1999, Roanoke, VA, USA, April 11-15, pp. 143–150 (1999)
3. Kim, T., Ehsani, M.: Sensorless control of the BLDC motors from near zero to high speed. IEEE Trans. Power Electronics 19(6), 1635–1645 (2004)
4. Holtz, J.: State of the art of controlled AC drive without speed sensor. In: IEEE Proc. of the 1995 Int'l. Conf. on Power Electronics and Drive Systems, pp. 1–6 (1995)
5. Kim, T.-H., Lee, H.-W., Ehsani, M.: State of the art and future trends in position sensorless brushless DC motor/generator drives. In: 32nd Annual Conf. of IEEE Industrial Electronics Society, IECON 2005, November 6-10, pp. 1718–1725 (2005)
6. Acarnley, P.P., Watson, J.F.: Review of position-sensorless operation of brushless permanent-magnet machines. IEEE Trans. Ind. Electron. 53(2), 352–362 (2006)
7. Shao, J.: An improved microcontroller-based sensorless brushless DC (BLDC) motor drive for automotive applications. IEEE Trans. on Ind. Appl. 42(5), 1216–1231 (2006)
8. Lee, W.-J., Sul, S.-K.: A New Starting Method of BLDC Motors Without Position Sensor. IEEE Transactions On Industry Applications 42(6), 1532–1538 (2006)

Inspection Robot Suspended on Power Transmission Lines Based on Expert System

Ren Zhi-bin, Liu Sen, and Long Yu-tao

School of Mechanical and Electrical Engineering, Jiangxi University of Science and Technology, Ganzhou, Jiangxi 341000
renzhibin824@yahoo.com.cn

Abstract. The purpose of inspection robot for power transmission lines is to check running state and find damages of extra-high voltage (EHV) power transmission lines equipment. The key of the control design is how to design a robot for obstacles navigation. This paper presents the robot configuration, and describes obstacle-navigation control principle. Inspection robot for power line is in same operation when across same obstacles, control system learns in laboratory and format knowledge base. The expert system use knowledge to produce the behavior sequences which execute the automatic control for the robot to cross obstacles. The paper presents expert system with hybrid architecture and analyzes decision-making of obstacle-navigation in layered planning mode. On-line experiment results show that the control strategy can guide the inspection robot to patrol along the transmission lines and cross obstacles efficiently.

Keywords: Inspection robot; Power transmission lines; Expert system.

1 Introduction

The purpose of inspection tasks for power transmission lines is to know running conditions and find damages of power transmission line equipment. Obviously, inspection tasks are very important for normal operation of power transmission lines. Up to now, power transmission line equipment has been inspected manually by workers with a telescope on the ground. Sometimes, they have to climb the towers. These working modes have many disadvantages, such as long inspection cycle, high working intensity, huge expense and high danger. It is difficult to assure the inspection quality in mountain areas, grasslands and aboriginal forests because of severe environments[1,2].A robot that can inspect the power lines automatically is eagerly expected to appear to replace human from the hard works.

This paper describes an obstacle-navigation control strategy for inspection robot on overhead ground wires of power transmission lines. The control system of the inspection robot is a hybrid architecture system, which can run and navigate obstacles on overhead ground wires automatically. Equipped with camera, the robot can detect the damages of power transmission line equipment. The data and images detected by the robot can be transmitted to the ground base station by the wireless transmission devices. The ground base station can not only receive, store and display the data and

D. Zeng (Ed.): Future Intelligent Information Systems, LNEE 86, pp. 349–357.
springerlink.com © Springer-Verlag Berlin Heidelberg 2011

images but also complete real-time remote control and image processing simultaneously. This paper is organized as follows: Following the introduction, section 2 introduces inspection robot configuration and control system. In section 3, analyzes the process of autonomous obstacles negotiating. Section 4 introduces Expert system. Section 5 is the results of experiments. Finally is the conclusion.

2 Inspection Robot System

The main obstacles on the OGWs(over ground wires) are counterweights, overhang anchor clamps, sees Fig. 1. In power transmission system, the lines arrangement and the structure size of obstacles are approximate style on a power transmission line. Inspection robot for power line is in same operation when across same obstacles, control system learns in laboratory and format knowledge base[3,4]. The expert system use knowledge to produce the behavior sequences which execute the automatic control for the robot to cross obstacles.

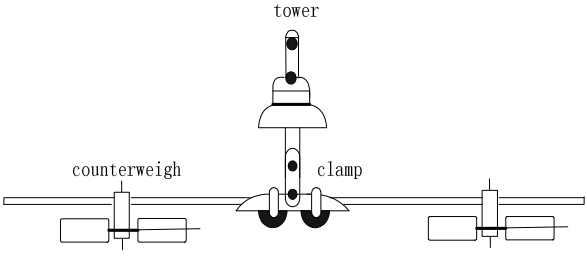

Fig. 1. Obstacles on overhead ground wire

2.1 Mechanical Configurations

After the structure of power transmission lines is carefully studied, a set of the requirements to the robot mechanical configurations has been derived. The mechanical structure of the robot is shown in Figure 2. X1 is shift pair, its function is to cause the robot control box to be allowed to move along orbits for centroid adjustment. The center of mass of inspection robot is concentrated into forearm or rear arm by control box drove in obstacle-navigation process. The control box mainly is used to carry wireless transmitter-receiver set、 motor driver、 computer （PC104）、power supply and camera. X2 and X3 are arm shift pairs, their functions are to go ahead or backwards for forearm and reararm to adjust robot pose. X6 and X7 are arm shift pairs too. Their functions are to go up or down for forearm and reararm. When forearm or reararm is hung on the OGWs in obstacle-navigation process, the reararm or forearm is on or off the OGWs. X4 and X5 are revolving pairs. For example, when forearm is hung on the

OGWs and the reararm has been off the OGWs, the body of inspection robot can rotate by the L3L4 or L1L2 axis under the X5 or X4 driving and implement the driving-wheel-line alignment operation.

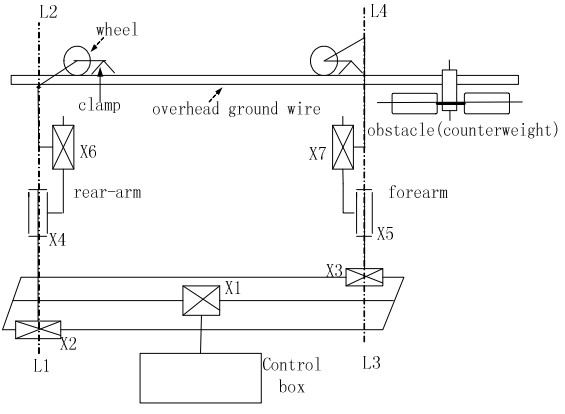

Fig. 2. Configuration of the inspection robot

2.2 Control System of Inspection Robot

A three-layers control system is proposed as shown in Figure 3, which are:1) supervision and management system located at the ground station (upper layer);2) robot control and path planning (middle layer);3) actuations directly controlled by microprocessors(lower layer).The roles of the upper layer are to receive the inspection images in real-time, conduct the fault detection, monitor the operations of the robot and remotely control robot operations. The middle layer plays the role of analyzing, distributing and coordinating the tasks to be completed by the robot. It receives and analyses the commands from the upper layer, then decomposes and distributes the tasks to individual lower level microprocessors and actuator controllers. Under the autonomous operation mode, it makes its own decisions for planning the sequence of operations and actuations without the upper layer's involvement. The sequences of commands from the middle layer are directly sent to the lower layer microprocessors and actuators. The robot is required to work in an uncertain environment under unpredictable weather so the robot system must be very reliable and robust under all disturbances and hazards. The robot is designed for crawling along the suspended transmission lines and crossing many different types of obstacles so the size and weight of the whole system must be small. So the main hardware components must be selected carefully to take all the above factors into consideration. In the project, an embedded computer PC/104 is chosen for the middle layer, and TI DSP(microprocessor TMS320LF2407) is selected for the lower layer as it has the characteristics of low power, high capability, and anti-noise.

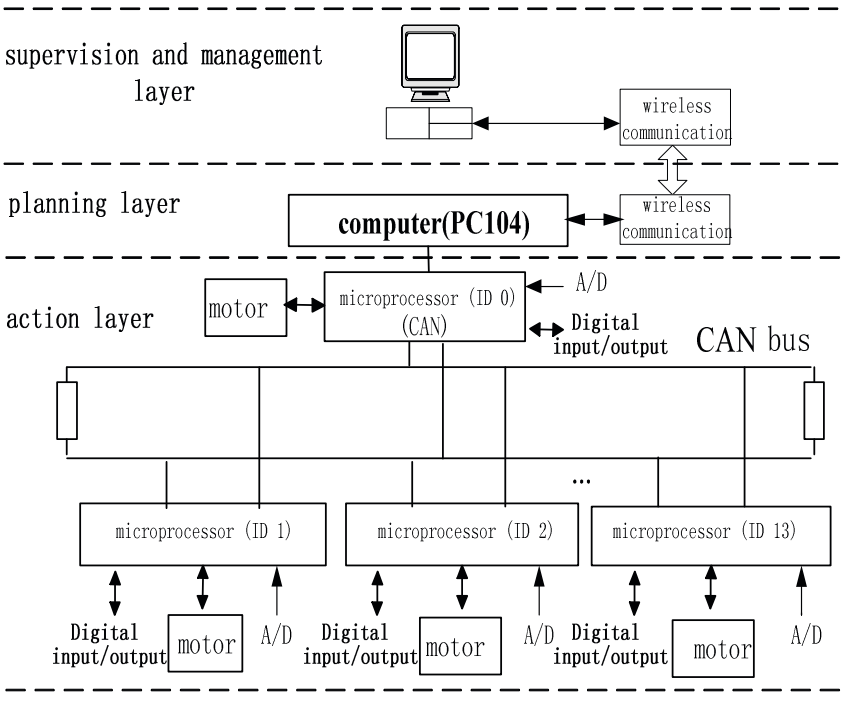

Fig. 3. Distributed control system structure

3 Process of Obstacle Crossing

When inspection robot encounters obstacle (counterweight), it will stop by the proximity transducer, sees Fig. 4.The front clamping jaws will fasten by the gripping servo motor. The rear wheel is in position, see Fig. 4(1), and then rear arm will up-rise by the up and down servo motor, and the rear wheel will be off from OGWs, and the control box move along the orbits for centroid adjustment, sees Fig. 4(2). Then, the rear arm and front arm go ahead and backwards by X2 and X3 arm shift pairs, sees Fig. 4(3). The rear arm will descend by the up and down servo motor, The rear arm and the front arm will rotate by the rotary servo motor through laser sensor navigation of inspection robot for high-voltage transmission line to achieve the driving-wheel-line alignment operation. Finally, the rear wheel negotiates the obstacle—counterweight, and the rear wheel will be on OGWs. In the same way, the front wheel will negotiate the counterweight.

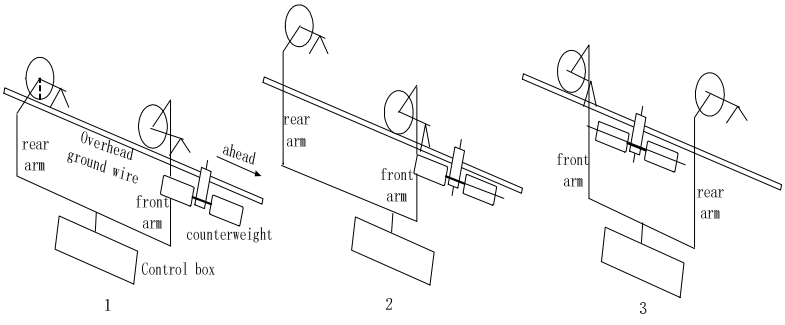

Fig. 4. Process of obstacle negotiating

4 Expert System

4.1 Knowledge Base Establishment

The robot has many controllable joint. When crossing obstacle autonomously, the movement process is complex, the sequence of action plan is one kind of intelligent behavior. If only depends upon robot oneself to carry on the on-line plan, the plan will be extremely complex. Therefore the play is expected to get from off-line movement sequences. When crossing obstacle, robot will carry on according to these sequences of off-line action.

In the ordinary circumstances, when crossing obstacle, the robots first acts according to the line, then definite obstacle type. Combined with the interpretation knowledge database which is produced with off-line planning method tested in lab, the behavior sequence is interpreted to engender motion sequence which is used to execute the automatic control for the robot to cross obstacles. Thus it may be known, experience knowledge might guide the people to solve the question mentality directly to aim at a feasible pattern scope[5,6]. At present, the experience knowledge system uses knowledge to express the method has the frame method of portrayal, like figure 5 shows configuration of knowledge database for robot obstacle navigation.

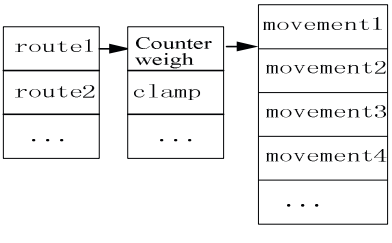

Fig. 5. Configuration of knowledge database for robot obstacle navigation

In order to realize the robot cross obstacle behavior based on knowledge database. For this, the knowledge base is composed by the route database、obstacle database and motor movement database. The route base stores the route number and the corresponding obstacle which robot must cross, its form like table 1.

Table 1. Storage form of route database

Route number	obstacle1	obstacle2	Obstacle n
1	Counter weigh	…	…
2	Overhang clamp	…	…

The obstacle base stores the different obstacle correspondence the movement, like crossing counterweigh movement for counterweight1, counterweight2 and so on, its form like table 2. According to obstacle which the robot inspects, may confirm the robot movement.The motor movement base save correspondence different movement of each motor movement plan, its form like table 3, according to the different movement, may confirm the inspection robot controllable joint motor movement scope. Such as a1、b1 and so on is the scope correspondence with the movement 1、the movement 2.

Table 2. Storage form of balk database

obstacle	movement	movement	movement
Counter-weight	Counter weight1	Counter weight2	…
clamp	clamp1	Clamp2	…

Table 3. Storage form of motor motion database

movement	motor1	motor2	…	motor13
Counter weight1	a1	…	…	…
clamp1	b1	…	…	…
…	…	…	…	…

4.2 Configuration of Expert System

The obstacle-navigation control is a complicated control process, which is realized by a expert system[6]. The robot expert system is made of knowledge base, static database, external information input module and decision-making module, as shown in Fig. 6.

There are external sensor signals, such as laser sensor, proximity sensor, tilt sensor. Via model recognization, these sensor signals are transformed into facts that are put into inference engine as precondition and trigger. Inference can find out the correspondent rules based on the facts.

The static database stores the structure data of power transmission lines and obstacles. All the towers, where the inspection robot runs, are indexed according to the order of the towers in the database. When the inspection robot prepares to navigate obstacles, the structure data of the current obstacles are read into a buffer by the robot expert system. These data includes the number of counterweight, the dimension of tower, clamp, counterweight, the relative position of two overhead ground wires between two adjacent towers etc. The data is wrote into the database offline, and can't be modified when the system runs.

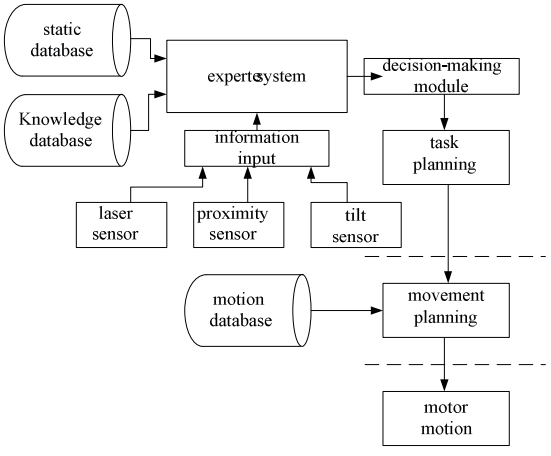

Fig. 6. Hybrid architecture of the robot expert system

Fig. 4 shows a complete obstacle-navigation process. When the mobile robot arrives at the counterweight of the overhead ground wire, optical-fibre sensors touch the counterweight and the robot stops to prepare for obstacles-navigation. The robot expert system reads the data information of current obstacles, for example it is the NO. 1 counterweigh. A task of navigating the NO.1 counterweigh is wrote into the task queue. Based on the data from the static database, the task is decomposed into several steps in subtask planning layer.

In movement planning layer, every subtask is transformed into correspondent motion sequence. For example, moving the forearm needs to lose the gripper and cooperate movement of three motors. These motion sequences are stored in motion sequence base. Only if provides the parameters of movement, the robot controller can move the forearm to appointed position.

The knowledge base of robot expert system can be modified dynamically. The mobile robot can increase its autonomous obstacle-navigation ability and efficiency with online and offline study. When the mobile robot encounters obstacles at the first time, it may navigate the obstacles for a long time. The robot expert system can remember the process and the result that are stored into the knowledge base. If the mobile robot encounters the same obstacles again, it can navigate the obstacles quickly.

Because the environment of power transmission lines is relative unchangeable and the same type of obstacles have the same structure data, the above study method is meaningful. If the mobile can study to navigate a type of obstacle, it can navigate all the obstacles with the same type. In fact, the obstacle types are limited, so the robot can realize autonomous obstacle-navigation after training.

5 Experiment and Tests

The whole robot system has been tested in the laboratory condition and its work status crossing counterweigh is shown in Figure 7. Repeat experiments have been conducted and it shows that the system is realistic for implementation, reliable and robust in the whole system structure.

Fig. 7. Figures of inspection robot to cross overhung counterweigh autonomously

6 Conclusion

In this paper, we have presented a novel method which aims at solving the obstacle-navigation problem in high voltage power transmission line inspection robot. With the analysis of obstacle-navigation control process, the mobile robot can navigate obstacles on overhead ground wire. Through a year laboratory simulation experiment and the scene experiment indicated: The system is normal, the movement is good, and has the practical value.

References

1. Sawada, J., Kusumoto, K.: A mobile robot for inspection of power transmission lines. IEEE Transactions on Power Delivery 6(1), 309–315 (1991)
2. Higuchi, M., Maeda, Y., Tsutani, S., et al.: Development of a mobile inspection robot for power transmission lines. Journal of the Robotics Society of Japan 9(4), 457–463 (1991)

3. Fukuda, T., Hosokai, H., Otsuka, M.: Path planning expert system for pipeline inspection robots. In: Proceeding of the IEEE International Symposium on Intelligent Control, pp. 299–304. IEEE, Albany (1989)
4. Li, Z.J., Lv, Q.S.: Real time robot expert system for avoiding obstacles. Mechanical Science and Technology 19(4), 547–554 (2000)
5. Ye, X.M., Fu, G.Y.: Fault diagnosis expert system implementation using C++ Builder 4 by calling expert system tool – CLIPS. Computer Application and Software 17(10), 50–56 (2000)
6. Giarratano, J., Riley, G., Liu, X.C., Tang, Y.: Principle of Expert System and its Program Design. Mechanical Engineering Press, Beijing (2000)

Influence of Transmission Channel on Propagating Primary User Signals Based on Polarization Adaptation Detector*

Lin Lin, Caili Guo, Chunyan Feng, and Fangfang Liu

Next Generation Communication System Theory and Technology Laboratory
Beijing University of Posts and Telecommunications, BUPT
Beijing, China
linlin376@msn.com

Abstract. Cognitive Radios are proposed for secondary users (SU) recovering spectrum holes unused by primary users (PU) on the multi-dimension. Polarization spectrum sensing technology is a novel spectrum sensing technology which detects spectrum holes of polarization domain exist in the secondary spectrum usage scenario. In this paper, firstly the dual hypothesis models of a polarization spectrum holes sensing scheme—polarization adaptation detector is constructed based on different transmission channels. Secondly, the influence of the transmission channel on the polarization state(α_0, ϕ_0) of the propagating PU signal are evaluated. At last, the detection performance of polarization adaptation detector is analyzed and compared in different transmission channels. The insights gained are potentially useful to those engaged in the development and validation of polarization detection algorithms in polarization spectrum sensing for cognitive radios.

Keywords: cognitive radios; polarization spectrum sensing; virtual polarization adaptation; polarization adaptation detector.

1 Introduction

Cognitive Radios relying on the support of artificial intelligence, allows reusing spectrum on multi-dimension. Currently, CR technology detects the available frequency band by spectrum sensing technology mainly in time and frequency domain [1]. However, it is feasible to reuse spectrum holes of polarization domain [2]. Polarization spectrum sensing technology allows simultaneous operation of PU and SU even in overlapped areas in which SU shares the spectrum at the same frequency and space area simultaneously to take advantage of polarization in spectrum space.

In polarization spectrum sensing technology, polarization detection is necessary. To estimate interference from SU to PU, SU needs to detect the PU polarization. However, SU can't get the information of the PU polarizations directly by communicating with PU in the secondary usage of spectrum scenario, so it's necessary to analyze the

* This paper is funded by Chinese National Science Foundation (No. 60902047 and No.60772110) and National 863 major project (No. 2009AA011802).

D. Zeng (Ed.): Future Intelligent Information Systems, LNEE 86, pp. 359–368.
springerlink.com © Springer-Verlag Berlin Heidelberg 2011

PU signal arrived at SU antenna. A polarization spectrum holes sensing scheme -polarization adaptation detector, which applies virtual polarization adaptation principle (VPA) [3] has been proposed to identify polarization state of PU signals at SU side and the feasibility of polarization adaptation detector have been fully discussed [2]. However, influence of transmission channels on the propagating PU signals and detection performance of polarization adaptation detector in different transmission channels haven't been considered. In general case, the signal at the receiving antenna will have a polarization which differs from that of the transmitted signal. The signal is then said to be depolarized with partial polarization. Depolarization is caused by the different characteristics of transmission channels. The insights of the influence of transmission channels on the propagating signals are significant and potentially useful to the development and validation of polarization detection algorithms.

The focus of this paper is to evaluate the influence of different transmission channels on the propagating PU signals from several aspects based on polarization adaptation detector. What's more, the detection performance of the polarization adaptation detector in different transmission channels is analyzed.

This paper is organized as follows: the system and signal model is introduced in Section II; Section III provides simulation analysis on this work; Section IV gives evaluation of detection performance of polarization adaptation detector in different transmission channels; Section V concludes with simulation results.

2 System and Signal Model

The system and signal model is a dual hypothesis model. It is constructed for polarization adaptation detector in different transmission channels. Considering the characteristics of different transmission channels, two dual hypothesis models are shown as follows.

2.1 Dual Hypothesis Model Based on Traditional AWGN Channel

Consider a PU has the polarization state $\boldsymbol{E}_{\boldsymbol{L}}$ transmitted and $\boldsymbol{E}_{\boldsymbol{nL}}$ received. $\boldsymbol{E}_{\boldsymbol{nL}}$ is also the target polarization state that SU detects.

To learn the impacts of the Gaussian noise on the transmitted polarization states, the relationship between the polarization state of the original PU signal and that of interfered signal is shown as:

$$\boldsymbol{E}_{\boldsymbol{nL}} = \boldsymbol{E}_{\boldsymbol{L}} + \boldsymbol{n} \tag{1}$$

$\boldsymbol{n}$ is the complex Gaussian noise. At the transmitter antenna for PU, the PU signal $\boldsymbol{E}_{\boldsymbol{L}}$ is represented on the orthogonal polarization basis (H, V), denoted as Jones vectors:

$$\boldsymbol{E}_{\boldsymbol{L}} = \begin{bmatrix} E_{LH} \\ E_{LV} \end{bmatrix} = \begin{bmatrix} E^{i}{}_{LH} + jE^{q}{}_{LH} \\ E^{i}{}_{LV} + jE^{q}{}_{LV} \end{bmatrix} \tag{2}$$

$\boldsymbol{E}_{LH}$ and $\boldsymbol{E}_{LV}$ present the horizontal and vertical polarization component on the orthogonal polarization basis. *i* and *q* are the orthogonal components on same phase.

In general case, the receiving antenna will have a polarization which differs from that of the transmitted signal. Hence at the secondary receiving antenna, the PU signal $\boldsymbol{E}_{nL}$ arrived with power E_{out} is:

$$\boldsymbol{E}_{nL} = \begin{bmatrix} E_{nLH} \\ E_{nLV} \end{bmatrix} = \begin{bmatrix} E^{i}_{nLH} + jE^{q}_{nLH} \\ E^{i}_{nLV} + jE^{q}_{nLV} \end{bmatrix} \tag{3}$$

Then the PU signal polarization representation is obtained respectively:

$$\begin{cases} \alpha_{nL} = \arctan\left(\dfrac{|E_{nLV}|}{|E_{nLH}|}\right) \\ \phi_{nL} = \arctan\left(\dfrac{E^{q}_{nLV}}{E^{i}_{nLV}}\right) - \arctan\left(\dfrac{E^{q}_{nLH}}{E^{i}_{nLH}}\right) \end{cases} \tag{4}$$

Before SU communicates with its own transmitter, there are two probabilities at the SU receiving antenna:

$$\begin{cases} Hypothesis \;\; H_0 : \boldsymbol{E}_{nL} = \boldsymbol{n} \\ Hypothesis \;\; H_1 : \boldsymbol{E}_{nL} = \boldsymbol{E}_{L} + \boldsymbol{n} \end{cases} \tag{5}$$

Where H_0 means the absence of PU, and H_1 means that PU is on the use of the spectrum. Decision statistics ξ_n is gained from $\boldsymbol{E}_{nL}$,

$$\xi_n = \left| \boldsymbol{R}^{\dagger} \boldsymbol{E}_{nL} \right|^2 \tag{6}$$

† denotes the complex conjugate transpose and $\boldsymbol{R}$ is the received polarization states of polarization adaptation detector. Compare ξ_n with the predefined threshold λ to make the decision that whether PU is present [4].

$$\xi_n \underset{H_0}{\overset{H_1}{\gtrless}} \lambda \tag{7}$$

Considering Gaussian noise, the interference affects decision statistics ξ_n which results in the increase of false detection and the depolarization of the transmitted polarization.

2.2 Dual Hypothesis Model based on Traditional Rice Channel

We consider a PU has the polarization state SL transmitted and $\boldsymbol{E}_{rL}$ received. $\boldsymbol{E}_{rL}$ is also the target polarization state that SU detects.

The polarization transmission model based on the Rice channel is:

$$\boldsymbol{E}_{rL} = \boldsymbol{H}\boldsymbol{E}_{L} + \boldsymbol{n} \tag{8}$$

$\boldsymbol{n}$ denotes complex Gaussian noise with the covariance matrix $\boldsymbol{R}_{\boldsymbol{n}} = E\{nn^{H}\} = \sigma^{2}\boldsymbol{I}_{2}$ ($\boldsymbol{I}_{2}$ means unit matrix of dimension 2×2). $\boldsymbol{H}$ is the channel matrix. In this case, the channel matrix H is made of a fixed component $\bar{\boldsymbol{H}}$ containing the vectors of the line of sight (LOS) propagation paths and a variable Rayleigh fading component $\tilde{\boldsymbol{H}}$ containing zero-mean complex-valued Gaussian distributed random variables of the None-line-of-sight (NLOS) paths [5]:

$$\boldsymbol{H} = \sqrt{\frac{K}{K+1}}\underbrace{\begin{pmatrix} \bar{h}_{11} & 0 \\ 0 & \bar{h}_{22} \end{pmatrix}}_{\bar{\boldsymbol{H}}} + \sqrt{\frac{1}{K+1}}\underbrace{\begin{pmatrix} \tilde{h}_{11} & \sqrt{\beta}\tilde{h}_{12} \\ \sqrt{\beta}\tilde{h}_{21} & \tilde{h}_{22} \end{pmatrix}}_{\tilde{\boldsymbol{H}}} \tag{9}$$

$\bar{\boldsymbol{H}}$ and $\tilde{\boldsymbol{H}}$ are weighted by the Rician K-factor.

The ratio of specular to defuse energy defines the so-called Rician K-factor, which is given by

$$K(db) = 10\log\frac{\rho^{2}}{2\sigma_{0}^{2}} \tag{10}$$

ρ is the amplitude of the specular component, σ_{0}^{2} is the variance of multipath components. Rician K-factor defines the probability of a fade of certain depth and greatly affects system performance [6].

For the channel coefficients, we obtain:

$$\begin{aligned} &\bar{h}_{11}\bar{h}_{11}^{*} = \bar{h}_{12}\bar{h}_{12}^{*} = \bar{h}_{21}\bar{h}_{21}^{*} = \bar{h}_{22}\bar{h}_{22}^{*} = 1 \\ &E\{\tilde{h}_{11}\tilde{h}_{11}^{*}\} = E\{\tilde{h}_{12}\tilde{h}_{12}^{*}\} = E\{\tilde{h}_{21}\tilde{h}_{21}^{*}\} = E\{\tilde{h}_{22}\tilde{h}_{22}^{*}\} = 1 \end{aligned} \tag{11}$$

where (.)* denotes conjugation and E{.} denotes expectation. $\beta(0<\beta\leq 1)$ describes the attenuated cross coupling for the polarization multiplexing case. If $\beta = 1$, $K \neq 0$ it is the LOS environment.

Similarly, at the transmitter antenna for PU, the PU signal $\boldsymbol{E}_{L}$ is represented on the orthogonal polarization basis (H, V). At the secondary receiving antenna, the PU signal $\boldsymbol{E}_{rL}$ arrived with power E_{out}, then the PU signal polarization representation can be obtained respectively.

Before SU communicates with its own transmitter, there are also two probabilities at the SU receiving antenna:

$$\begin{cases} Hypothesis\ \ H_{0} : \boldsymbol{E}_{rL} = \boldsymbol{n} \\ Hypothesis\ \ H_{1} : \boldsymbol{E}_{rL} = \boldsymbol{H}\boldsymbol{E}_{L} + \boldsymbol{n} \end{cases} \tag{12}$$

Decision statistics ξ is gained from $\boldsymbol{E}_{rL}$, and compare the ξ_r with the predefined threshold λ to make the decision that whether PU is present [4]. The Gaussian noise and channel matrix H affect decision statistics ξ_r.

$$\xi_r = \left| \boldsymbol{R}'^{\dagger} \boldsymbol{E}_{rL} \right|^2 \tag{13}$$

† denotes the complex conjugate transpose and $\boldsymbol{R}'$ is the received polarization states of polarization adapation detector.

Rician K-factor defines the probability of a fade of certain depth and determines the channel matrix $\boldsymbol{H}$. Thus Rician K-factor is an important indicator in analysis of depolarization by Rice channel.

3 Analysis and Results

Based on dual hypothesis models of polarization adaptation detectors (5), (12), the influence of transmission channels on the propagating PU signals are evaluated via simulations from several aspects in this section.

In simulation, the transmit power E_{in} of PU signal is normalized. The transmitted PU signal is described by polarization descriptors (α, ϕ) and set to be (α_0=π/4, ϕ_0=π/4). For each instance of SNR and Rician K-factor considered, we generated almost 1,000 values of received power of PU signals $\{E_{nout}\}$ ($n = 1,2...n$)and received polarization states (α_n, ϕ_n), then calculate mean value of received power $\{\bar{E}_{out}\}$ and received polarization states ($\bar{\alpha}, \bar{\phi}$) to gain the statistics data of propagating PU signals. Finally, we plotted the received polarization states on Poincare sphere and calculate the distances $\{\Delta d_n\}$ from the distributed points $\{p_{\alpha_n \phi_n} \mid SNR = \gamma_i\}$ to the original point $p_{\alpha_0 \phi_0}$ to observe the dispersion of polarization states on the Poincare sphere. The radius of Poincare sphere is unit(r=1).

3.1 Received Power of PU Signals

Fig. 1 shows the average received power $\bar{E}_{out}$ at SU receiving antenna of the PU signal when the signals are transmitted in two different channels. According to VPA, the polarization of SU antenna is traversal $\alpha' \in (0,\pi/2)$, $\phi' \in (0,2\pi)$. Received power E_{nout} is obtained according to VPA [7] and $\bar{E}_{out}$ is the mean value of $\{E_{nout}\}$ at each instance of SNR or Rician K-factor.

From fig. 1(a), it can be observed that when the transmit power is normalized and transmitted in AWGN channel, the interference of noise affects the received power and the maximum received power of PU signal is no longer E_{nout} =1. From SNR=0db, the value difference Δv between the actual average received power $\bar{E}_{out}$ and the expected value 1 is less than 10%.

In Rice channel LOS environment, to study the effects of Rician K-factor for polarization adaption detector, set SNR to be a stable value while K varies. From K=20db, the value difference Δv is constrained to a constant. When SNR increases from 0db to 20 db, the entire curve of received power is much closer to the expected value.

In these two situations, for AWGN channel SNR completely determines the received power of PU signals yet for Rice channel, Rician K-factor and the noise both affect the received power. The interference will cause the false detection in polarization adaptation detector for the decision is made according to energy comparison.

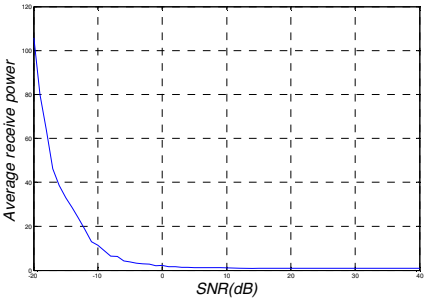

(a) Average received power $\overline{E}_{out}$ in channel

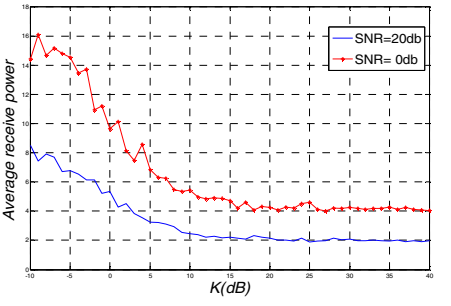

(b) Average received power $\overline{E}_{out}$ in AWGN Rice channel LOS environment

Fig. 1. Average received power $\overline{E}_{out}$ of PU signals

3.2 Variation of Detected Polarization States

In general case, the signal at the receiving antenna will have a polarization which differs from that of the transmitted signal. Then the signal is said to be depolarized with partial polarization.

Fig. 2 indicates the variation of received PU polarization states at SU antenna when the signals are transmitted in different transmission channels. These figures give a straight way to analyze the depolarization by transmission channels.

The transmitted PU signal is in polarization states (α_0 =π/4, ϕ_0 =π/4). For each instance of SNR and Rician K-factor considered, we gain 1,000 received polarization states (α_n, ϕ_n) based on polarization adaptation detector, then calculate average received polarization states ($\overline{\alpha}, \overline{\phi}$). The correlation between average received polarization states ($\overline{\alpha}, \overline{\phi}$) vs. SNR in AWGN channel and that between ($\overline{\alpha}, \overline{\phi}$) vs. Rician K-factor in Rice channel are shown in fig.2.

In fig.2 (a), by observation we can find that SNR affects the received average polarization state ($\overline{\alpha}, \overline{\phi}$). There are less interference, the better polarization obtained. From SNR=10db, the detected polarization states tend to the ideal values (π/4, -π/4). In fig. 2(b), set SNR to be stable, say 20db, while the K increases, we got better identified polarization state. However, with the interference caused by noise, the polarization states won't be the ideal constant even when K is very large.

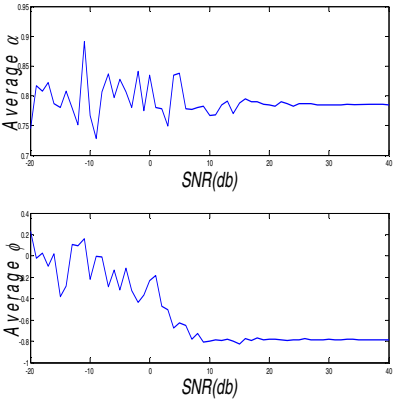

(a) Average polarization states($\bar{\alpha}, \bar{\phi}$) AWGN channel

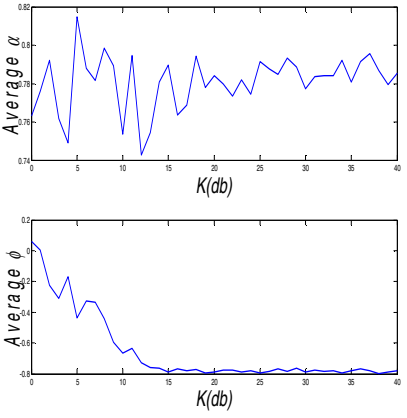

(b) Average polarization states ($\bar{\alpha}, \bar{\phi}$) in in Rice channel LOS environment

Fig. 2. Average polarization states ($\bar{\alpha}, \bar{\phi}$)

3.3 Distribution of Polarization States on Poincare Polarization Sphere

The notion that it may be useful to consider the manner in which the polarization states associated with wireless signals disperse across the Poincare sphere has previously been considered, e.g., [8] and [9]. In this step, the manner in which polarization states are distributed across the Poincare sphere in AWGN channel and Rice channel are analyzed in the point of spherical distances $\{\Delta d_n\}$.

In order to facilitate assessment of the rotational symmetry of the distributions, the spherical distances $\{\Delta d_n\}$ $n=1,2...n$ from the distributed points $\{p_{\alpha_n\phi_n} \mid SNR=\gamma_i\}$ $(n=1,2...n; i=1,2...i)$ and the original point $p_{\alpha_0\phi_0}$ are calculated. The variances $\{\chi_n \mid SNR=\gamma_i\}$ of these distances and average distance $\{\bar{d}_n\}$ $n=1,2...n$ are shown in fig.3.

The variance shows the degree of change for each instance of SNR and Rician K-factor. In fig. 3(a) as SNR increases the variance χ_n and the average distance $\bar{d}_n$ continue to decrease. This illustrates that not only the average distance $\{\bar{d}_n\}$ decrease when SNR is higher but also the stability of the received points is better. From SNR=25db, the average distances remain an expected value ($\bar{d}_{SNR>25db}$<0.2) and the stability is rather fine ($\chi_{SNR>25db}$=0).

The polarization state distributions in fig.3 (b) may be considered as the result of a correlated random walk at each instance of Rician K-factor yet the statistical properties follow the rules. Set SNR=20db. When K is very large, the average distance $\bar{d}_{K\to\infty} \le 0.2$ and $\chi_{K\to\infty}$ approaches zero. The semicircle length of the Poincare sphere is $l_{semi}=\pi$. With the interference of existing noise, the distributed points will never

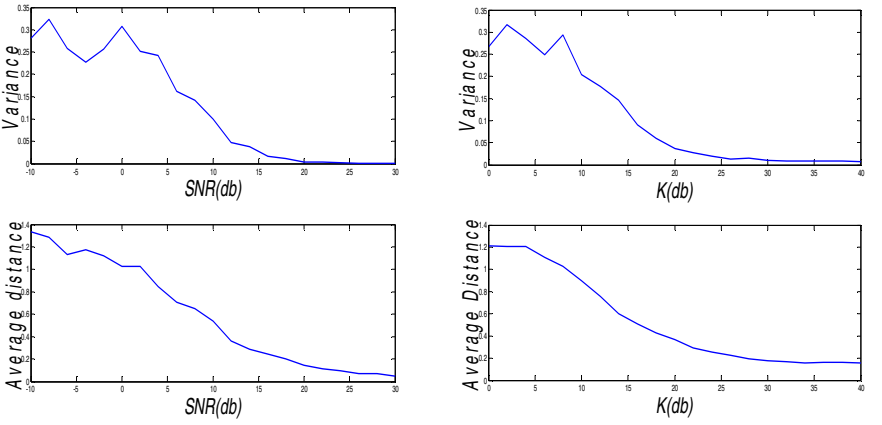

(a) Statistical properties of distances $\{\Delta d_n\}$ AWGN channel

(b) Statistical properties of distances $\{\Delta d_n\}$ in in Rice channel LOS environment

Fig. 3. Statistical properties of distances $\{\Delta d_n\}$

gather at one ideal point but in an area. Thus polarization state distribution is confined to a small portion of the sphere; When K approaches $-\infty$, the polarization state distribution is unconstrained for the average distance $\bar{d}_n \in (0, l_{semi})$ and variance χ_n is large. Thus the received polarization states (α_n, ϕ_n) covers the entire sphere.

4 Detection Performance Analysis

Based on the dual hypothesis model (5), (12), two kinds of detection error happen: false alarm which alarms the existence of the primary users incorrectly and missed detection which misses the existence of the primary users. They are presented by probability of the false alarm Pf and probability of the missed detection Pm:

$$\begin{cases} P_f = \Pr(\xi > \lambda \mid H_0) \\ P_m = \Pr(\xi < \lambda \mid H_1) \end{cases} \tag{14}$$

In fact, P_m and P_f describe the performance of the spectrum sensing technology. In this step, the detection performance is evaluated and expressed by ROC complementary curve which can describe attributes of polarization adaptation scheme.

The Fig. 4 (a) shows the detection performance of polarization adaptation detector when SNR=0db and SNR=5db, the detection threshold and sample number are different at each case. Observing fig.4 (a), the detection performance greatly increases when there is less noise and the probability of missed detection reduces. According to Neyman-Pearson criterion, to improve the spectrum sensing performance, Pf needs constraints as far as reduce Pm. Increase SNR by 5db, at the same Pf, Pm reduces as much as 87.5%. Hence, noise suppression can be effective in improving the detection performance.

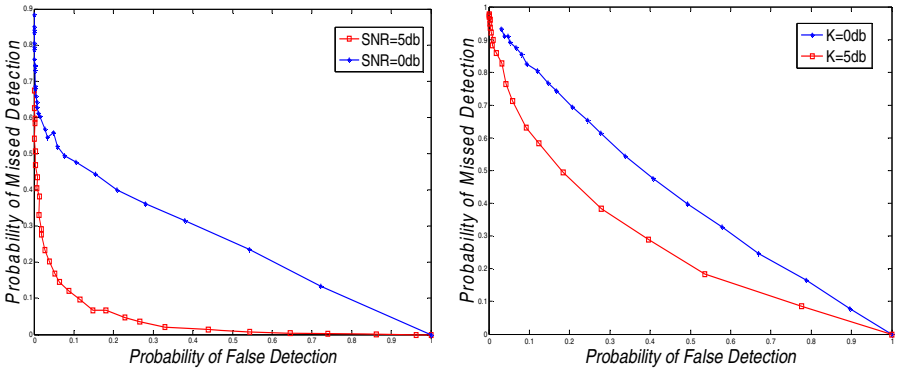

(a) Detection performance of polarization adaptation detector in AWGN channel

(b)Detection performance of polarization adaptation detector in Rice channel

Fig. 4. Detection performance of polarization adaptation comparison

In fig.4 (b) with attenuated cross coupling β =1, for LOS propagation environment when K=0db and K=5db, the detection threshold and sample number are different. Observing fig.4 (b), when K increases by 5db which indicate the enhancement of the LOS path, the detection performance greatly increases and Pm reduces as much as 30%.

5 Conclusions

We have shown the simulation analysis of influence of different transmission channels on propagating PU signals based on polarization adaptation detector and a detection performance comparison of polarization adaptation detector.

When PU signals propagate in AWGN channel, the received power $\{E_{out}\}$ and received polarization states (α_n, ϕ_n) which polarization adaptation detector detects are closely correlated with SNR. The dispersion of received polarization states on Poincare sphere are analyzed by calculating the spherical distances $\{\Delta d_n\}$ between the distributed points and the original point. The statistical properties of the spherical distances $\{\Delta d_n\}$ is also correlated with SNR; When PU signals propagate in Rice channel, the received power $\{E_{out}\}$, received polarization states (α_n, ϕ_n) and the statistical properties of the spherical distances $\{\Delta d_n\}$ are influenced not only by SNR but also Rician K-factor.

Compare the two situations, in same SNR, the polarization adaptation detector has a better detection performance in AWGN channel than that in Rice channel. Enhancement of the LOS path and suppression of the noise will greatly decrease depolarization of propagating primary signals and improve system performance.

References

1. Haykin, S., Thomson, D.J., Reed, J.H.: Spectrum Sensing for Cognitive Radio. Proceedings of the IEEE 97(5), 163 (2009)
2. Liu, F., Feng, C., Guo, C., Wang, Y., Wei, D.: Polarization Spectrum Sensing Scheme for Cognitive Radios. In: 5th International Conference on Wireless Communications, Networking and Mobile Computing WiCom 2009 (2009)
3. Poelman, A.J.: Virtual polarization adaptation - A method of increasing the detection capability of a radar system through polarization-vector processing. In: IEEE Proceedings, Part F -Communications, Radar and Signal Processing, vol. 128(5), pp. 261–270 (1981)
4. Cabric, D., Mishra, S.M., Brodersen, R.W.: Implementation issues in spectrum sensing for cognitive radios. In: Conference Record of the Thirty-Eighth Asilomar Conference on Signals, Systems and Computers (2004)
5. Degen, C., Keusgen, W.: Performance Evaluation of MIMO Systems Using Dual-Polarized Antennas. In: 10th International Conference on Telecommunications, ICT 2003 (2003)
6. Baum, D.S., Gore, D., Nabar, R., Panchanathan, S., Hari, K.V.S., Erceg, V., Paulraj, A.J.: Measurement and characterization of broadband MIMO fixed wireless channels at 2.5 GHz. In: Proc. IEEE ICPWC 2000, pp. 203–206 (2000)
7. Beide, W.: 'The Application and Realization of Virtual Polarization in Radar System. Radar Science and Technology 1(1) (June 2003)
8. McKinnon, M.M.: Three-dimensional statistics of radio polarimetry. Astrophys. J. Suppl. 148(2), 519–526 (2003)
9. Cichon, D.J., Kurner, T., Wiesbeck, W.: Polarimetric aspects in antenna related superposition of multipath signals. In: Proc. ICAP 1993, pp. 80–83 (1993)

Preparation and Characterization of $CuInS_2$ Thin Films by Sulfurization Process*

Jianping Ma, Yang Gao, and Yaming Li

Department of Applied Electronics, Xi'an University of Technology
5 South Jinhua Road, Xi'an Shaanxi, 710048 China
Jianping Ma, majp@xaut.edu.cn

Abstract. I–III–VI_2 groups of ternary chalcopyrite semiconductors have attracted much interest in recent years because of their potential applications in the field of light-emitting diodes, photovoltaic detectors, non-linear optics[1] and solar cells. Ternary compound $CuInS_2$ semiconductor is one of these compounds, due to a superior band-gap of about 1.5eV, matching almost ideally to the solar spectrum, $CuInS_2$ has in principle the highest conversion efficiency among the Cu-chalcopyrite-based solar cells. The Cu-In precursors were grown by magnetron impulse sputtering process. Polycrystalline $CuInS_2$ (CIS) films were prepared by sulfurization of the Cu-In precursors in sulfur atmosphere. The influence of S source temperature and substrate temperature on the film properties was studied respectively. The morphology, microstructure and composition of the films were investigated by scanning electron microscopy (SEM), X-ray diffraction (XRD) and energy dispersive X-ray spectroscopy (EDS). The results explicitly reveal that substrate temperature plays a critical role on the property of the $CuInS_2$ films during the sulfurization process. As the increasing of the temperature, the performance of the films improve gradually, when sulfurization temperature at 550℃ and S source temperature at 350℃, the performance of the film is the best.

Keywords: $CuInS_2$ thin films chalcopyrite Sulfurization Solar Cell.

1 Introduction

Ternary and quaternary compound semiconductors of the type I–III–VI_2 have received much attention in recent years because of their potential application in solar cells. Among ternary chalcopyrite semiconductors, $CuInS_2$ thin films with a direct band-gap of about 1.50 eV and a large absorption coefficient in the range of 10^4-10^5 cm^{-1}[1] are one kind of the most promising optical absorbers for high efficiency and low-cost thin film solar cells. The high absorption coefficient of this material assures a complete absorption of the incident photon flux in an absorber layer as thin as a few microns. Furthermore, since the material does not contain toxic Ga or Se atoms, this may have an advantage in comparison with the frequently studied $CuInSe_2$ and CIGS[2] Composition control for a ternary material is much easier than that for a

* This Project was Supported by Xi'An Applied Materials Fund.

D. Zeng (Ed.): Future Intelligent Information Systems, LNEE 86, pp. 369–376.
springerlink.com © Springer-Verlag Berlin Heidelberg 2011

quaternary material. The best conversion efficiency for polycrystalline $CuInS_2$ solar cells achieved to date is 12.7%[3,4]. Due to a superior band-gap of about 1.5 eV, matching almost ideally to the solar spectrum, $CuInS_2$ has in principle the highest conversion efficiency among the Cu-chalcopyrite-based solar cells[5,6]. Theoretical solar conversion efficiencies of 27-32% have been calculated with $CuInS_2$ as an absorber[7,8]. In addition to solar cells, $CuInS_2$ is also useful as non-linear optical material[9]. Different methods are used to fabricated $CuInS_2$ thin films including iron layer gas reaction (ILGAR)[10], fabricated $CuInS_2$ thin films including iron layer gas reaction (ILGAR)[10], co-evaporation[11], flash evaporation[12], spray pyrolysis[13], rapid thermal process[14], single source evaporation[15], sulfurization of metallic precursors[16], chemical vapor deposition[17], RF reactive sputtering[18], radio frequency sputtering[19], electrodeposition[20]. Among these various methods, sulphurization of metallic precursors is a very promising method for a large-scale industrial production[21]. It is usually described as two-step process that involves first the deposition of CuIn metallic precursor layer, and then sulphurization the precursor in sulphur atmosphere to yield $CuInS_2$ absorber. The sulphurization technique conditions has a great influence on the properties of the final $CuInS_2$ films.

In this study, we choose magnetron impulse sputtering technique for the deposition of CuIn metallic precursor layer, and sulfurization of metallic precursors in sulfur atmosphere, The effect of the S source temperature and Substrate temperature on the film properties were investigated.

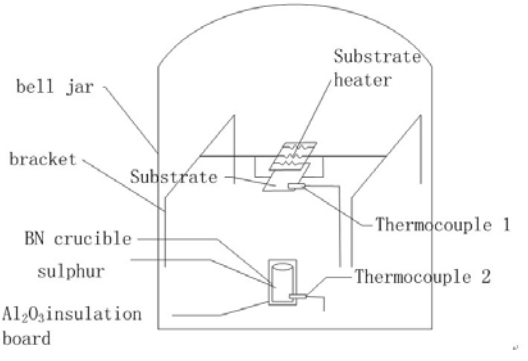

Fig. 1. The schematic of the sulfurization experiment set-up

2 Experiment

2.1 Precursor Deposition

The substrates were chemically cleaned using hot chromic acid, isopropyl alcohol and distilled water in an ultrasonic bath. Metallic precursor layers were deposited onto soda lime glass substrates by pulsed-dc magnetron sputtering process at a base pressure of 1×10^{-3} Pa, the material of the target is CuIn alloy.

Table 1. Various conditions of the films' sulfurization process

Sample No.	Source's temperature(℃)	Sulfurization temperature(℃)	Sulfurization Time (min)
(a)	350	460	40
(b)	350	490	40
(c)	350	520	40
(d)	350	550	40
(e)	260	550	40
(f)	290	550	40
(g)	320	550	40

2.2 Selenization

The schematic of the sulfurization experiment set-up used in this study is shown in Fig. 1. The BN crucible was heated by heater strip, enough S vapor will leak through the hole on the alumina insulation board's lid, metallic precursor layer was heated by substrate heater. During the sulfurization process, metallic precursor layers were sulfurization in the vacuum chamber with a base pressure of 1×10^{-3}Pa. The substrate and S source's temperature were detected by two thermocouples respectively, the substrate's temperature was sulfurization temperature. The temperature was controlled by two digital PID controller. Table1 shows various conditions of the films' sulfurization process.

2.3 Thin Film Characterizations

The phase investigation of the $CuInS_2$ films was performed by X-Ray diffraction/XRD (Rigaku DMAX 2500, Japan) using Cu K α radiation with λ =1.5405Å, The surface morphology was examined by scanning electron microscopy /SEM (Hitachi S-4100, Japan) and the composition of the film is determined using by an Energy Dispersive X-Ray Spectrometer/EDX (EMAX-Horiba, Japan) attached to the Scanning Electron Microscope/SEM.

3 Results and Discussion

3.1 Microstrueture of $CuInS_2$ Thin Films

Fig.2 shows the XRD spectra of the $CuInS_2$ thin films sulphurized at different sulfurization temperature at 460℃, 490℃, 520℃ and 550℃. The peaks at about 27.9°, 32.5°, 46.5°and 55.0°are assigned to (112), (004), (204) and (312) reflections of chalcopyrite $CuInS_2$, respectively. The intensity of the peak (112) is far higher

than (204) in all the samples indicating a relatively preferred structural orientation in the (112) plane. As the increasing of the temperature, the performance of the films improve gradually, When sulfurization temperature at 550℃, the performance of the film is the best. However, the films are not unique to the chalcopyrite peaks corresponding to a minor binary sulfide copper phase are observed in the cases, the peaks at 34.6° and 48.0°associated to Cu_xS can be observed in fig2 and the secondary Cu_xS phase can be observed in all samples, The Cu_xS phase is mainly attributed to the high mobility of Cu and its migration towards the surface layers, which results in a non-uniform composition distribution and incomplete sulfurization reaction. The secondary Cu_xS phase is harm to characterization of $CuInS_2$ thin film solar cells, The KCN etching treatment can remove the secondary Cu_xS phase segregated from $CuInS_2$ surface [21] and we will focus on this investigation in the future.

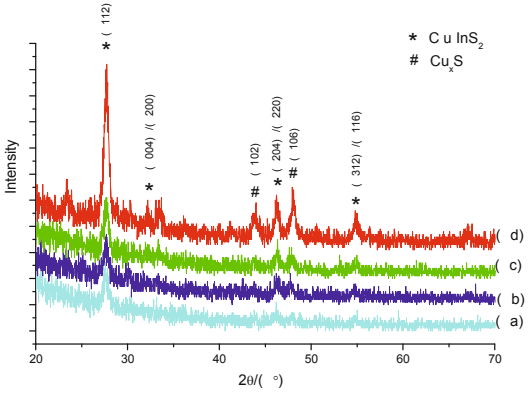

Fig. 2. XRD spectra of the $CuInS_2$ films sulfurized at various sulfurization temperatures

Fig.3 shows the XRD spectra of the $CuInS_2$ thin films S source temperature at different temperature at 260℃, 290℃, 320℃ and 350℃. Similar to fig.2, XRD diagrams of this four samples shows the $CuInS_2$ films with chalcopyrite structure and preferential orientation along the (112) plane, the secondary Cu_xS phase also existence. Compare to fig.2, Fig.3 shows the characterization of this four samples is better in general, compared with other three samples, Fig.3 (d) is relative better, which indicate that the S source temperature has influence on the films, but the substrate temperature has more important effect on $CuInS_2$ films than the S source temperature during the sulfurization process in this experiment.

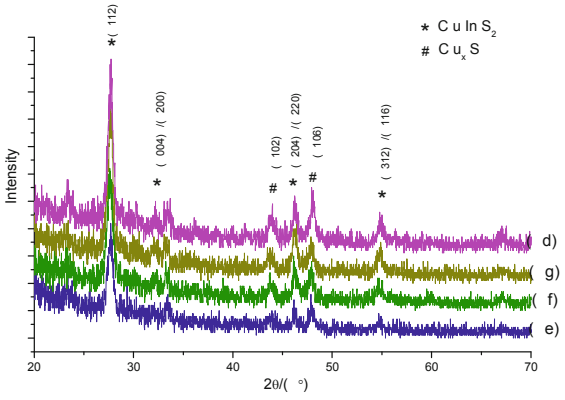

Fig. 3. XRD spectra of the $CuInS_2$ films sulfurized at various S source temperatures

3.2 Surface Morphology of $CuInS_2$ Thin Films

Fig. 4 shows SEM micrographs of the $CuInS_2$ thin films sulphurized at different sulfurization temperature at 460℃, 490℃, 520℃ and 550℃ but S source temperature was fixed to 350℃ (refer to Table 1). The SEM pictures show that sulfurization temperature at 460℃ and 490℃ the films are not uniform and exist small (~500nm) and big (~1μm) two types of grains, this phenomenon is because only part of the CuIn alloy atoms were sulfurization when the sulfurization temperature at 460℃ and 490℃, Fig. 4 (c) show that the grain size of the films is about 4μm when sulfurization temperature at 520℃, it may because more CuIn alloy atoms participated the formation of the secondary Cu_xS phase at 520℃.With the sulphurization temperature increasing to 550°C, the film is uniform and the average grain size of the film is found to be 1μm, which is in accord with the XRD spectra in fig2.

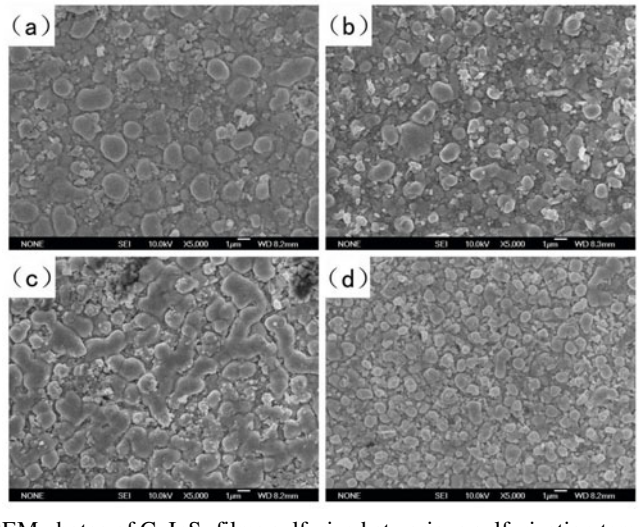

Fig. 4. SEM photos of $CuInS_2$ films sulfurized at various sulfurization temperatures

Fig.5 shows SEM micrographs of the $CuInS_2$ thin films sulphurized at different S source temperature at 260℃, 290℃, 320℃ and 350℃. under sulfurization temperature at 550℃(refer to Table 1). The SEM pictures show that the variation of the films is not obvious and the average grain size of the films is about 1μm, which is in accord with the XRD spectra in fig3.

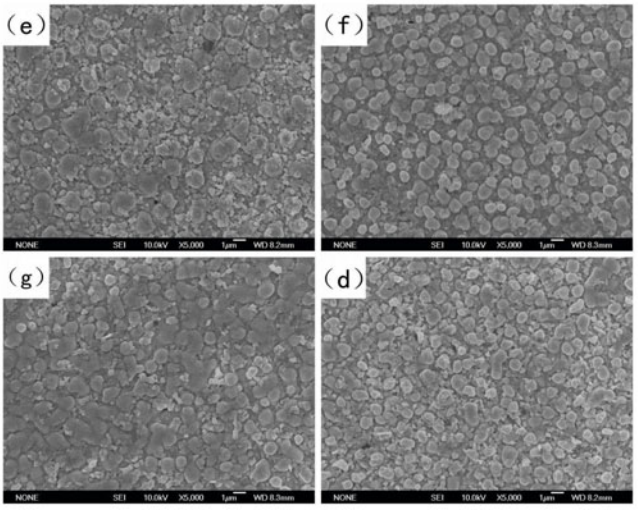

Fig. 5. SEM photos of $CuInS_2$ films sulfurized at various sulfur source temperatures

3.3 The Composition of the Films

Table. 2 shows the composition of the films sulphurized at 460℃, 490℃, 520℃and 550℃. The table show that all the samples are Cu-rich films, this phenomenon is because the existence of the secondary Cu_xS phase, with the sulphurization temperature increasing to 550°C, the content of Cu was highest at 27.2%. We also note that S content is lower than the stoichiometry, when sulphurization temperature at 460°C the S content is closer to the stoichiometry(a). The analysis result is in accord with the XRD spectra.

Table 2. Results of EDS for the films sulfurized at various sulfurization temperatures

No.	*n/at%*			$\frac{n(\text{Cu})}{n(\text{In})}$	$\frac{n(\text{Cu}+\text{In})}{n(\text{S})}$
	Cu	In	S		
(a)	26.2	24.2	49.6	1.08	1.02
(b)	25.7	25.1	49.2	1.02	1.03
(c)	26.8	24.6	48.6	1.09	1.06
(d)	27.2	26.6	46.2	1.02	1.16

Table. 3 shows the composition of the films sulphurized at 260℃, 290℃, 320℃ and 350℃. Compared with table 2, the variation of the ratio （Cu/In） is not obvious. The S content is also lower than the stoichiometry.

Table 3. Results of EDS for the films sulfurized at various sulfur source temperatures

No	*n/at%*			$\frac{n(\text{Cu})}{n(\text{In})}$	$\frac{n(\text{Cu}+\text{In})}{n(\text{S})}$
	Cu	In	S		
(e)	26.8	24.8	48.4	1.08	1.07
(f)	27.2	25.3	47.5	1.08	1.11
(g)	27.4	25.6	47.0	1.07	1.13
(d)	27.3	27.1	45.6	1.00	1.19

4 Conclusion

Polycrystalline $CuInS_2$ (CIS) films and preferential orientation along the (112) direction were prepared by sulfurization of the Cu-In precursors in sulfur atmosphere under high vacuum conditions. The secondary Cu_xS phase is existence in all the samples. Although the composition of the films is Cu-rich, it is also close to the stoichiometry and the impact on the crystal properties is not very serious. The results explicitly reveal that substrate temperature plays a critical role on the property of the $CuInS_2$ films during the sulfurization process. As the increasing of the temperature, the performance of the films improve gradually, when sulfurization temperature at 550℃ and S source temperature at 350℃, the performance of the film is the best.

References

1. Krunksa, M., Bijakinaa, O., Varemaa, T., et al.: Thin solar Films, 338, 25 (1999)
2. Akaki, Y., Nomoto, K., Nakamura, S., Yoshitake, T., Yoshino, K.: Journal of Physics Conference Series 100, 082022 (2008)
3. Klenk, R., Dobson, P., Falz, M., Janke, N., Kaer, J., Luck, I., Perez-Rodiguez, A., Scheer, R., Terzini, E.: In: Proceedings of 16th EPVSEC, Glasgow (2000)
4. Siemer, K., Klaer, J., Luck, I., Bruns, J., Klenk, R., Bräunig, D.: Solar Energy Mater. Solar Cells 67, 159 (2001)
5. Henry, C.H.: J. Appl. Phys. 51, 4494 (1980)
6. Siebentritt, S.: Thin Solid Films 403-404, 1 (2002)
7. Meese, J.M., Manthuruthil, J.C., Locker, D.R.: Bull. Am. Phys. Soc. 20, 696–697 (1975)
8. Braunger, D., Hariskos, D., Walter, T., Schock, H.W.: Sol. Energy Mater. Sol. Cells 40, 97–102 (1996)
9. Abrahams, S.C., Bernstein, J.L.: J. Chem. Phys. 59 (1973) 1695
10. Kajari, D., Panda, S.K., Chaudhuri, S.: Fabrication of nanostructured CuInS2 thin films by ion layer gas reaction method. Appl. Surf. Sci. 253(11), 166 (2007)
11. Bandyopadhyaya, S., Chaudhuri, S., Pal, A.K.: Synthesis of CuInS2 films by sulphurization of Cu/In stack elemental layers. Sol. Energy Mater. Sol. Cells 60, 323 (2000)

12. Hwang, H.L., Tu, C.C., Maa, J.S., et al.: Sol. Energy Mater 2, 433 (1980)
13. Ramaiah, K.S., Raja, V.S.: J. Mater. Science: Mater. Electronics 10, 145 (1999)
14. Siemer, K., Klaer, J., Luck, I., Bruns, J., Klenk, R., Bräunig, D.: Solar Energy Mater. Solar Cells 67, 159 (2001)
15. Kazmerski, L.L., Sanborn, G.A.: J. Appl. Phys. 48, 3178 (1977)
16. Ogawa, Y., Jäger-Waldau, A., Hashimoto, Y., Ito, K.: Jpn. J. Appl. Phys. 33, L1775 (1994)
17. Hwang, H.L., Sun, C.Y., Fang, C.S., Chang, S.D., Cheng, C.H., Yang, H.M., Lin, H.H., Tuwan-mu, T.: J. Cryst. Growth 55, 116 (1981)
18. Liu, X.P., Shao, L.X.: Reactive sputtering preparation of CuInS2 thin films and their optical and electrical characteristics. Surf. Coat. Technol. 201(9-11), 5340 (2007)
19. Hwang, H.L., Cheng, C.L., Liu, L.M., et al.: Thin Solid Films 67, 83 (1980)
20. Hodes, G., Engelhard, T., Cahen, D.: Thin Solid Films 128, 93 (1985)
21. Yan, Y., Liu, Y., Fang, L., Zhao, H., Li, D., Lu, Z., Zhou, S.: Influence of post-grown treatments on CuInS2 thin films prepared by sulphurization of Cu-In films RARE METALS 27(5), 490 (2008)

Preparation and Characterization of the $CuIn_{1-x}Al_x$ Metallic Precursors

Jianping Ma, Yaming Li, and Yang Gao

Department of Applied Electronics, Xi'an University of Technology
5 South Jinhua Road, Xi'an Shaanxi, 710048 China
Jianping Ma, majp@xaut.edu.cn

Abstract. The $CuIn_{1-x}Al_x$ metallic precursors were obtained by DC magnetron impulse sputtering process. Using Al and CuIn alloy targets, by controlling the target power and sputtering time, so as to realize the Al/(Al+In) composition rations of CIA thin film were controlled accurately. The microstructure and crystal structure of the thin films were analysed by X-Ray diffraction ; the composition of the thin films were investigated by EDS. At last obtain the process of realize the CIA thin film with Al/(Al+In) composition rations were regulated continuously; the Cu/(In+Al) composition rations were approximately 1.

Keywords: CuInAl magnetron sputtering chalcopyrite Solar Cell.

1 Introduction

$CuInSe_2$ (CIS) and related chalcopyrite-based solar cells has emerged as promising absorber material for high efficiency and low cost thin film solar cells [1-3]. A major drawback is its band gap is 1.04eV, deviated from the optimum energy gap position of solar cells, affected the conversion efficiency, so when the band gap can be varied from 1.02eV to 1.7eV by substituting Ga to match the solar spectrum, and high efficiencies with a value of 19.9% were achieved in case of CIGS absorbers, and Eg = 1.2 eV [4]. However, wider band gap materials are require for higher voltage and lower current to minimize the electrical and optical losses during the module fabrication and they utilize as top cell material in all tandem $CuInSe_2/CuGaSe_2$ structure [5]. $Cu(In,Al)Se_2$ is considered as an alterative material for CIGS absorber because the less Al alloying is required than Ga to achieve same bandgap [6], and Al is inexpensive and abundant. So the preparation of bandgap CIAS thin film absorbing layer and CIAS thin film solar cells for industrial application is important.

Up to now, the major methods of producing $Cu(In,Al)Se_2$ films have coevaporation from elemental sources [7], selenization of metallic precursors [8].The process of selenization of metallic precursors is deposited Cu(In,Al) (CIA) precursor on the substrate firstly, then selenization of metallic precursors in Se vapor. Preparation of CIA metallic precursors, the sputtering technique holds in principle the advantage of simple and flexible control of the film stoichiometry over a large scale at relatively low cost [9-10].

D. Zeng (Ed.): Future Intelligent Information Systems, LNEE 86, pp. 377–382.
springerlink.com © Springer-Verlag Berlin Heidelberg 2011

In this paper, we use Al and CuIn alloy as sputtering targets, prepare the CIA metallic precursors by the DC magnetron impulse sputtering technology. The power effect on composition、stoichiometry、microstructure and surface morphology of the CuIn、Al、CIA metallic precursors were studied, and the process of preparation metallic precursor were obtained.

2 Experimental Procedure

The CIA thin films were prepared by DC magnetron impulse sputtering technology. The sputtering system is equipped with two sputtering guns, one with purity Al target, and the other with CuIn alloy target, and the atomic ratio of Cu/In is 1:1, the purity of the Al target is 99.999%. The angle between the two targets is 180°, the substrate support can be rotated, Fig.1 displayed the structure of the sputtering system. When preparation of CIA film, the substrate was faced CuIn target to deposit CuIn film, then rotated the substrate support, so that the substrate was faced the Al target, and deposit a layer of Al film, the composition、surface morphology and the crystal phase of the CIA film were effected by controlling the power of Al target.

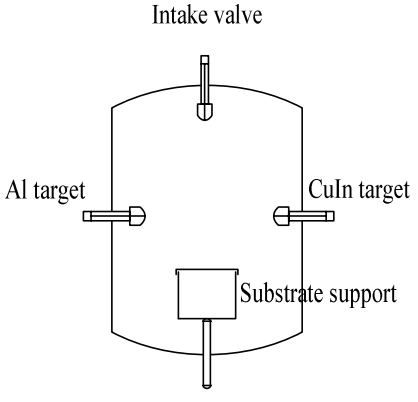

Fig. 1. The struction of the sputtering system

Prior to the deposition the chamber evacuated to the base pressure of $8x10^{-3}$ Pa with turbo molecular pump. High purity Ar was used as working gas, the target and substrate distance was 50 mm. The substrate chemically cleaned using hot chromic acid, isopropyl alcohol and distilled water in an ultrasonic bath.

Preparation of CuIn film, only sputtering the CuIn target, and the target power of CuIn target is 90W、115W、130W, sputtering time is 10 minutes, the data is displayed in the Table 1; preparation of CIA film, first sputtering CuIn target, and the target power is fixed at 115W, sputtering time is 10 minutes; then sputtering Al target, and Al target power is 80W、95W and 110W, sputtering time is 5 minutes, the data is displayed in the Table 2.

Table 1. Sputtering power for the CuIn film deposition

Sample number	*A1*	*A2*	*A3*	
Material	Power			Sputtering time
CuIn	90W	115W	130W	10 min

Table 2. Sputtering power for the CIA film deposition

Sample number	*B1*	*B2*	*B3*	
Material	Power			Sputtering time
CuIn	115W			10 min
Al	80W	95W	110W	5 min

The CIA thin films we obtained were laminated films, so we annealing the films at 300℃ in the vacuum chamber which full of Ar and the pressure was $8.0x10^{-3}$Pa. The composition of the film and the surface morphology was observed with a scanning electron microscope (SEM), the crystal phase was evaluated by X-ray diffraction (XRD) measurements.

3 Results and Discussion

3.1 Film Composition

The SEM analysis of the films prepared at different target power are presented in the Table 3. As can be seen in this table, for A1、A2、A3 sample, the composition of the CuIn films with the increasing of target power are basically closed to CuIn target composition. For the CIA metallic precursors, the ideal atomic ratio of the Cu / (In + Al) is closed to 1 and Al / (In + Al) is adjustable. Table. 3 shows the atomic ratio of Cu / (In + Al) is approximately 1, and Al / (In + Al) atomic was increased from 0.153:1 to 0.330:1 with the target power increased. The results show that preparation

Table 3. Results of EDS analysis for the films (Atomic Ratio)

Sample No.	A1	A2	A3	B1	B2	B3
Cu （%）	47.38	49.08	48.01	45.41	47.24	45.87
In （%）	52.62	50.92	51.99	46.23	40.22	36.22
Al （%）	-	-	-	8.36	12.54	17.91
Cu/In	0.90	0.96	0.92	-	-	-
Cu/(In+Al)	-	-	-	0.831	0.895	0.847
Al/(In+Al)	-	-	-	0.153	0.238	0.330

of the CIA metallic precursors by DC magnetron impulse sputtering technology, the Cu, In, Al ratio of the CIA thin films can be controlled precisely by adjusting the target power. Using this method can be more easily obtained the CIA metallic precursors, which the atomic ratio of Cu / (In + Al) is close to 1, and the Al / (In + Al) ratio can be regulated by controlling the Al target power. It is the basic to prepared $Cu(In_{1-x}Al_x)Se_2$ thin films with the ideal stoichiometric value x.

3.2 The Surface Morphology of Films

Fig.2 and Fig.3 shows the Al、CuIn and CIA film surface morphology images by SEM observation. Fig.2 shows, for B1 picture shows the CuIn film surface morphology is uniform and fine grained gray plane with bright white crystalline particles, by secondary electron image analysis, it can be infer that these particles are of indium-rich phase, while the part of the gray area are of indium-poor phase. Comparison of A1、A2 and A3 of the surface morphology, the film grain size has been increased, but the number decreased, the distribution tends to sparse. Fig.3 shows that the surface morphology changed obviously as the CuIn target power was unchanged and the Al contents was increased. B1 pictures show that the surface morphology of CIA film are gray surface with the smaller particle size, the composition crystal plane are distributed good、white light particles. Comparison of B1、B2 and B3 on the surface morphology, the particle size increased slightly, and B2、B3 films surface are more

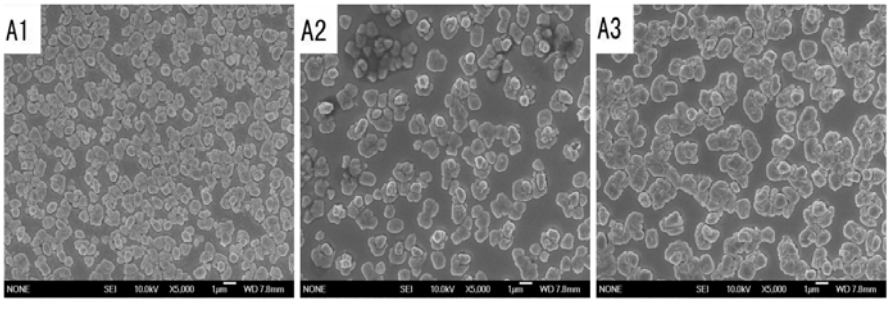

Fig. 2. SEM images of the CuIn film surface

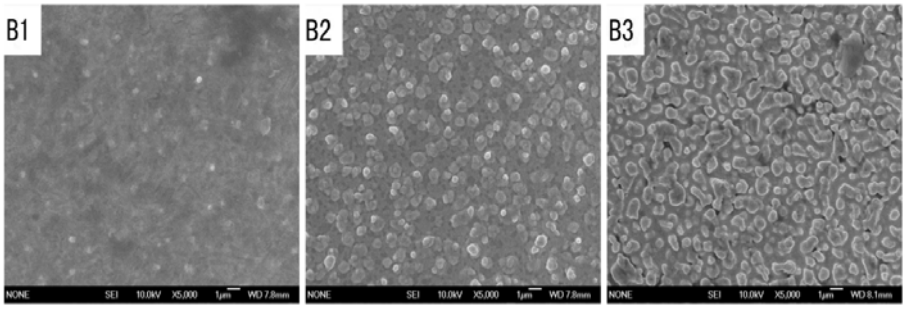

Fig. 3. SEM images of the CIA precursor film surface

uniform than B1, there is no obviously regional boundaries between indium-rich particles and Al-rich particles. These phenomena because with the Al target power increased, atomic kinetic energy、the ability of migration and diffusion distance increases when the Cu、In、Al atoms reach to substrate. To realize high efficiency of CIAS solar cells, it will be necessary to obtain a large crystal grain size or to inactivate grain boundaries [10]. Therefore, the results were basic for the preparation of high efficiency absorption layer.

3.3 The Crystal Structure of Films

Fig.4 shows the XRD spectra of CuIn thin films on the different target power. The peaks at about 29.43° 、32.84° and 41.99° are assigned to $Cu_{11}In_9$ phase, and about 34.50 ° 、38.25° and 43.20° are assigned to CuIn phase. Fig.5 shows the XRD spectra of the CIA thin film with various Al contents. There are three phases in the CIA thin films with $Cu_{11}In_9$、CuIn and In, and CuIn is the basic phase, which is not changed with the Al target power increased. There were not other elements in the films, indicating that Cu 、Al mainly exists in the form of solid solution. Al substitutes In atomic lattice positions and as the form of solid solution will be preserved in the process of

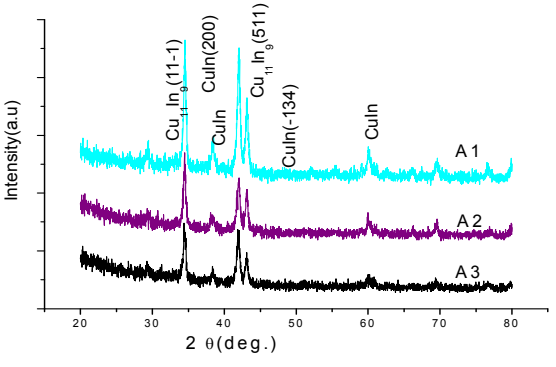

Fig. 4. XRD patterns of CuIn film with various target power

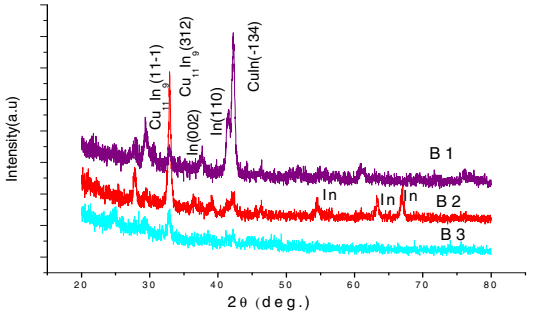

Fig. 5. XRD patterns of CIA film with various of Al contents

selenization, which will help obtain good chalcopyrite phase of CIAS films [11]. The films with $Cu_{11}In_9$ and CuIn mixed-phase has a loose structure that in favor of Se diffusing to the internal of films during the selenization process, which will promote the reaction of selenization.

4 Conclusion

The CIA metallic precursors were prepared by DC magnetron impulse sputtering technology. Using Al target and CuIn alloy targets, by adjusting the target power, can be precisely controlled Cu, In, Al ratio of the thin films, which the atomic ratio of Cu / (In + Al) was closed to 1, and Al / (In + Al) was adjustable. The preparation of CIA metallic precursors surface were uniform and dense with the Al target power increased. The Al atoms mainly substitutes In atomic lattice positions as the form of solid solution in the films, the films with $Cu_{11}In_9$、 In and CuIn mixed-phase has a loose structure that in favor of Se diffusing to the internal of the films during the selenization process, which will promote the reaction of selenization.

References

1. Conteras, M.A., Erasaas, B., Rmanathan, K., Hilner, J., Swartzlander, A., Hasoon, F., Nou, R.: Prog. Photovolt. Res. Appl. 7, 311 (1999)
2. Hagiwara, Y., Nakada, T., Kunioka, A.: Tech. Dig. In: 11th Photovolt. Sci. Eng. Conf., p. 83 (1999)
3. Negami, Y., Hashimoto, S.: Tech. Dig. In: 11th Photovolt. Sci. Eng. Conf., p. 993 (1999)
4. Contreras, M.A., Ramanathan, K., AbuShama, J., Hasoon, F., Young, D.L., Egaas, B., Noufi, R.: Diode characteristics in state-of-the-art ZnO/CdS/Cu(In1−xGax)Se2 solar cell. Prog. Photovolt. Res. Appl. 13, 209–216 (2005)
5. Ramanathan, K., Contreras, M.A., Perkins, C.L., Asher, S., Hasoon, F.S., Keane, J., Young, D., Romero, M., Metzger, W., Nou, R., Ward, J., Duda, A.: Prog. Photovolt. Res. Appl. 11, 225 (2003)
6. Marsillac, S., Paulson, P.D., Haimbodi, M.N., Birkmire, R.W., Shafarman, W.N.: Appl. Phys. Lett. 81, 1350 (2000)
7. Scheer, R., Walter, T., Schock, H.W., Fearheiley, M.L., Lewerenz, H.J.: Appl. Phys. Lett. 63, 3294 (1993)
8. Ogawa, Y., Jger-Waldau, A., Hashimoto, Y., Ito, K.: Jpn. J. Appl. Phys. 33, L1775 (1994)
9. Dhere, N.G., Lynn, K.W.: $CuIn_{1-x}GaxSe_2$ thin film solar cells by two-selenisation processes using Se vapour. Solar Energy Mater. Solar Cells 41/42, 271–279 (1996)
10. Adurodija, F.O., Song, J., Kim, S.D., Kwon, S.H., Kim, S.K., Yoon, K.H., Ahn, B.T.: Growth of $CuInSe_2$ thin films by high vapour Se treatment of co-sputtered Cu-In alloy in a graphite container. Thin Solid Films 338, 13–19 (1999)
11. Yamada, S., Tanaka, K., Minemoto, T., Takakura, H.: Journal of Crystal Growth. 311, 731–743 (2009)

Research on Welding Seam Tracking Based on HSIC

Hai-jun Chen, Hua Zhang, and Yong Xiong

Key Lab of Robot & Welding Automation of Jiangxi
Schoole of Mechanical and Electrical Engineering,
Nanchang University
Nanchang, Chnia

Abstract: In this paper, a Human Simulated Intelligent Control controller that is based on the theory of HSIC is designed. The signal of weld deviation detected by rotating arc sensor and the change of deviation is used to the HSIC controller characteristic primitive, and two-level control structure is combined with motion control level and parameter calibration level, and the corresponding control strategy of HSIC controller is designed, finally HSIC controller is their combination of organic. With the corresponding model, the control simulation with disturbance is also tested. The results show that the HSIC controller has the ability of fast response、accurate tracking and higher robustness. So the HSIC controller is reasonable and effective.

Keywords: seam tracking; Human Simulated Intelligent Control; simulation; rotating arc sensor; robustness.

1 Introduction

The welding seam tracking is one of the key technology for automatic welding. The welding seam tracking mainly include two aspects: identification of deviation and selection of control method. Because welding is a complicated process, accompanied by many phenomenon such as splash, arc, jittering of wire feed, thermal deformation, fluctuating of welding current caused by irregular welding seam, it is difficult to keep an accurate dynamical model. Therefore, it is difficult to measure and calculate system transfer function during actual control [1], and obtaining good effect is hard with the traditional control method based on model. The research of realizing online parameters adjustment and online pattern recognition by assembling various control method has become the new research direction. Such as control method of FUZZY combined with PID [2], neural network combined with PID [3] and self-adjusting scale factor FUZZY-P [4]. In these methods,the traditional control methods (such as lower the PID controller) and high-level controller are linked together simply and loosely.In this paper, a new control method of HSIC was proposed to satisfy the real-time, high speed, high precision control requirements.

D. Zeng (Ed.): Future Intelligent Information Systems, LNEE 86, pp. 383–390.
springerlink.com © Springer-Verlag Berlin Heidelberg 2011

2 Control System Structure

The theory of the arc sensor underwater welding seam tracking is that we can obtain the change of welding torch height from the change of the arc parameters when the arc sensor scans. According to the geometry position relationship between the welding torch and welding seam, we can derived the relative position between the welding torch and welding seam. Therefore, the transitive relation between height of welding torch and arc parameters is the most basic, most critical input-output relation of arc sensor. The structure chart of underwater welding seam tracking control system is shown in figure 1.

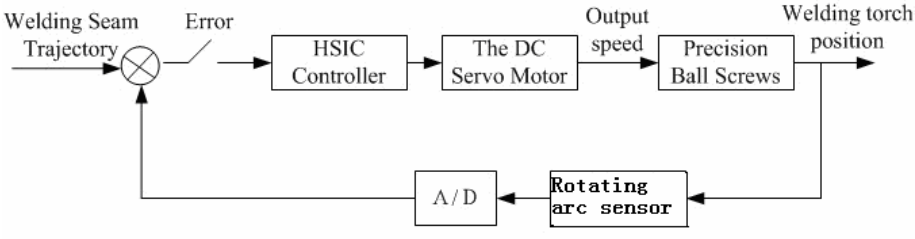

Fig. 1. Seam tracking control system chart

The transfer function of the welding torch height changing with the welding current changes can be expressed as:

$$G_1(s) = k_d \frac{1+T_1 s}{(1+T_2 s)} \tag{1}$$

According to the theory of automatic control theory, when a input of system was be loaded a sine pumping signal, the input-output amplitude ratio and phrase difference will be changed with the change of input sine signal frequency [5]. This rule indicates the dynamic characteristics of the system. According to the characteristic curve, we can get the gain 、 zero and pole of system, then get the transfer function of system. In equation (1), parameter values is selected, such as $k_d = 3.35$, $T_1 = 0.057$, $T_2 = 0.023$. The transfer function of dc servo motor in the figure 1 is as follows:

$$G_2 = \frac{K_m K_a}{T_m s + 1 + K_m K_a} \frac{1}{s} \tag{2}$$

It could be searched from the motor manual, $K_m = 4.844$, T_m =0.006 and in the 4_Q_DC servo amplifier manual K_a =2.4 ; The nominal lead of ball screw is 3mm, reduction ratio of motor reducer is 190:1,it could be derived that K_b =3/190=0.0158. The open-loop transfer function of the system can be get by the welding seam tracking control system structure chart.

$$G(s)=\frac{K_m K_a K_b K_d (1+T_1 s)}{T_m T_2 s^3+(T_m+T_2+T_2 K_m K_a)s^2+(K_m K_a+1)s} \tag{3}$$

$$G(s)=\frac{0.035s+0.615}{0.138\times 10^{-3} s^3+0.296s^2+12.626s}$$

3 HSIC Controller Disign

3.1 HSIC Algorithm

Linear regulation law with PID can not properly resolve stability and accuracy of the system simultaneously. Using integral effect to resolve steady-state error of the system will increase phase lag of system. Using existing nonlinear control, the system of quality can be improve only in a particular conditions,its usage scope is limited. Even if use the complete state feedback control mode, the response speed will be influenced by using integral method. Qi-Jian ZHOU, Jian-Guo BO [6], using "maintain" characteristics to displace integral action can effectively eliminated phase lag and integral saturation caused by the integral action, put forward a new regulator with extreme value sample-and-hold.

With the incteasing of control error, the controller of HSIC restrain sharp increase of error. And when the error begin to decline, control action of HSIC controller will reduce. At the same time, the controller records extreme value of deviation constantly, adjusting control point of controller to adapt the change. The prototype algorithm of HSIC controller is as follow:

$$u=\begin{cases} K_p e+kK_p\sum_{i=1}^{n-1} e_{m,i} & (e\cdot \dot{e}>0 \cup e=0 \cap \dot{e}\neq 0) \\ kK_p\sum_{i=1}^{n} e_{m,i} & (e\cdot \dot{e}<0 \cup \dot{e}=0) \end{cases} \tag{4}$$

Where u is the control output, K_p the scale factor, k the inhibitory coefficient, e the error, $\dot{e}$ the error rate, $e_{m,i}$ the error peak value of i time.

3.2 HSIC Control Strategy

The basic thought of HSIC prototype algorithm is simulating human controller in macroscopical structure and behavior. It adopts the multi-mode control strategy. Which characteristics model is the system through online characteristics memory and identification. And then the corresponding control strategy was taken. The HSIC controller in this paper is divided into two level structure, parameter-adjusting level and operation control level. Specific algorithm is as follows:

(1) Operation control level:

Characteristics model:

$$R_1 = \begin{bmatrix} 0 & 0 & 1 & 0 & -1 \\ 1 & 0 & 0 & 0 & -1 \\ -1 & -1 & -1 & 1 & -1 \\ 0 & 0 & 0 & 0 & 1 \\ -1 & -1 & -1 & -1 & -1 \\ 0 & 1 & -1 & 0 & -1 \end{bmatrix} \tag{5}$$

$$S_1 = [s_{11} \quad s_{12} \quad s_{13} \quad s_{14} \quad s_{15}]^T \tag{6}$$

$$\psi_1 = [\varphi_{11} \quad \varphi_{12} \quad \varphi_{13} \quad \varphi_{14} \quad \varphi_{15}]^T = R_1 \Theta S_1 \tag{7}$$

Where R_1 is the relation matrix, -1,0,1 denotes respectively taking reverse,taking zero,taking positive.

Where S_1 is set of Characteristic primitive, $s_{11} : e_n \bullet \dot{e}_n > 0$, $s_{12} : \dot{e}_n = 0$, $s_{13} : e_n = 0$, $s_{14} : e_n \bullet e_{n-1} > 0$, $s_{15} : |e_n| > M_1$. e_n is the present value of control error e, $e = r - y$ is the system error, r is the given value, y is the regulated variable, n is the serial number of control period, $e_n = e_n - e_{n-1}$ denote the difference of time between two periods, M_1 is the given threshold value of error. Θ denote multiply operation.

Control mode set:

$$\Phi_1 = (\phi_{11} \quad \phi_{12} \quad \phi_{13} \quad \phi_{14}) = \begin{bmatrix} 0 & 0 & 1 & 0 \\ 0 & 1 & 1 & 0 \\ 0 & 0 & 1 & 1 \\ 1 & 0 & 0 & 0 \end{bmatrix} \begin{bmatrix} m_{11} \\ m_{12} \\ m_{13} \\ m_{14} \end{bmatrix} \tag{8}$$

In [8] : $m_{11} : \pm u_{\max}$, $m_{12} : K_p e$, $m_{13} : u_{(n-1)}$, $m_{14} : K_2 K_p e_{m \cdot n}$. $u_{\max}$ is the output of Bang-Bang value. K_p is the proportional gain, K_2 is the restrain coefficient ($0 < K_2 < 1$), $u_{(n-1)}$ is the Maintain value of u , $e_{m \cdot n}$ is the extreme value of e .

Reasoning rules set:

$$if \quad \varphi_{11} \quad then \quad u = \phi_{11} \qquad if \quad \varphi_{12} \quad then \quad u = \phi_{12}$$

$$if \quad \varphi_{13} \quad then \quad u = \quad \phi_{11} \qquad if \quad \varphi_{14} \quad then \quad u = \quad \phi_{14}$$

$$if \quad \varphi_{15} \quad then \quad u = \quad \phi_{13} \qquad if \quad \varphi_{16} \quad then \quad u = \quad \phi_{12}$$

(2) Parameter-adjusting level:

Characteristics model:

$$R_2 = \begin{bmatrix} 1 & 1 \\ 0 & -1 \end{bmatrix} \tag{9}$$

$$S_2 = \begin{bmatrix} s_{21} & s_{22} \end{bmatrix} \tag{10}$$

$$\psi_2 = \begin{bmatrix} \varphi_{21} & \varphi_{22} \end{bmatrix}^T = R_2 \Theta S_2 \tag{11}$$

In (10) : $s_{21} : |e| \leq M_1$, $s_{22} : |e| \geq M_2$, M_2 is the given threshold value of error, $M_2 < M_1$.

Calibration mode set:

$$\Phi_2 = \begin{pmatrix} \phi_{21} & \phi_{22} \end{pmatrix}^T = \begin{bmatrix} 1 & 0 \\ 0 & 1 \end{bmatrix} \begin{bmatrix} m_{21} \\ m_{22} \end{bmatrix} \tag{12}$$

In (12): $m_{21} : K_1 K_p$, $m_{22} : K_p$.

Reasoning rules set:

$$if \quad \varphi_{21} \quad then \quad K_p = \quad \phi_{21} \qquad if \quad \varphi_{22} \quad then \quad K_p = \quad \phi_{22}$$

4 Simulation Analysis

From figure 1, we can get the transfer function $G(s) = \dfrac{0.035s + 0.615}{0.138 \times 10^{-3} s^3 + 0.296 s^2 + 12.626 s}$.

It can be look as a simulation object. HSIC controller、regular PID controller and fuzzy controller will respectively be responded by sine signals、rectangle signals and interfering noise (Input value is rin, Output response is yout). The simulation diagram of HSIC system is shown in figure 2. The different controllers are simulated with matlab 7.0, simulating results are shown in figure 3、figure 4 and figure 5.

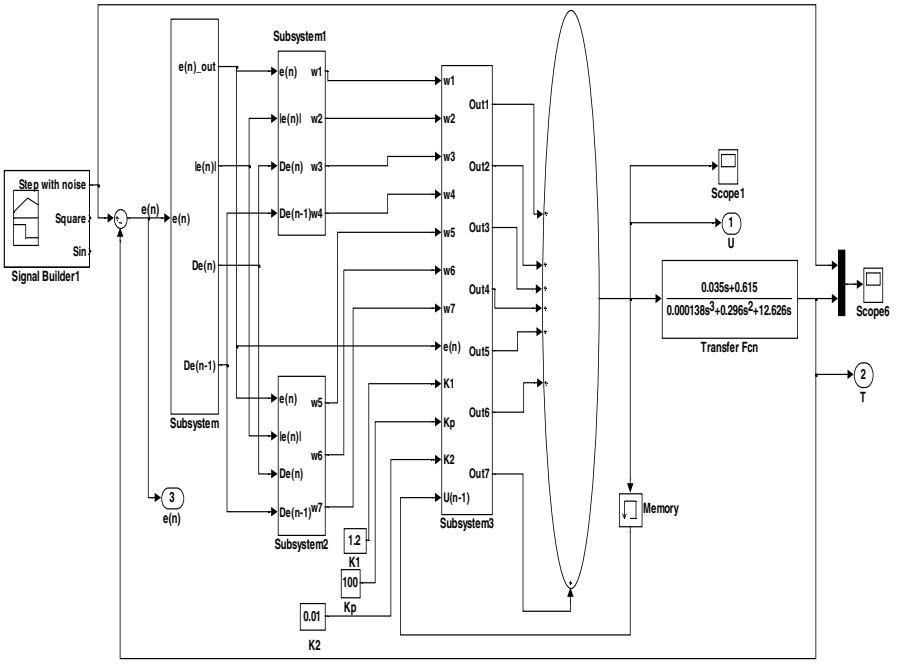

Fig. 2. System Human Simulated Intelligent Control simulation chart

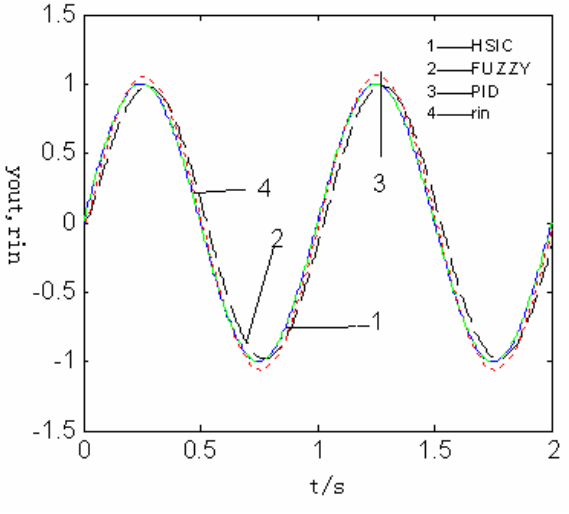

Fig. 3. Sinusoidal response simulation chart

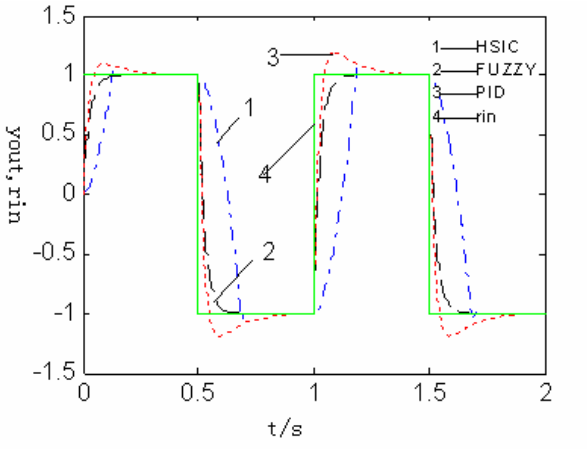

Fig. 4. Rectangular wave response simulation chart

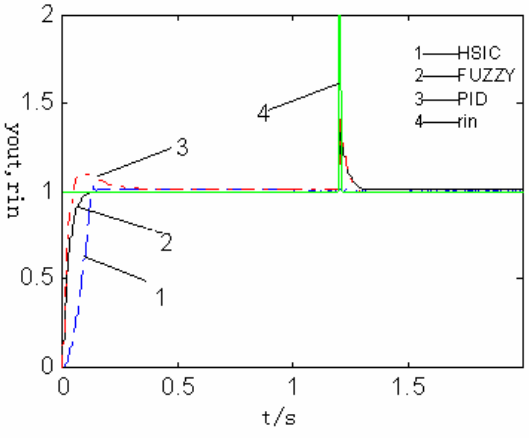

Fig. 5. Step response with noise simulation chart

From figure 3 we know that response effect of HSIC controller to sine singnal is best and tracking effect is best. Figure 4 indicate that the tracking effect of FUZZY controller to rectangular wave is best, but the response speed of HSIC controller is quicker and the overshoot is smaller than PID controller. Figure 5 shows that the anti-interference ability of HSIC is the strongest.

5 Conclusions

(1) In this paper, a new control method is disigned for welding seam tracking, and the method is different with the past control method combinated PID controller with FUZZY controller or nervous network controller simply and loosely.

(2) By means of simulation of corresponding model, the simulation results show that the HSIC controller has the ability of fast response、accurate tracking and higher robustness. So HSIC controller is reasonable and effective.
(3) Meanwhile the result of simulation indicate that the performance of HSIC controller is bad than FUZZY controller in some aspects. The main reason is the control strategy of HSIC controller is too simple.

References

1. Pan, J.-l.: Modern Are Welding Control. Publishing House of Engineering Industry, Beijing (2000)
2. Ye, J.-x., Zhang, H.: FUZZY - PID control of Robot seam tracking. Journal of Welding 26(11), 97–100 (2005)
3. Ren, Z.-w., Gao, J.-s.: PID Controller of Nervous Net. Robotization Technology and Application, 26(5), 16–19 (2005)
4. Hu, S.-s., Hou, W.-k., Qin, B.-z.: The Research of FUZZY-P Controller in the Seam Tracking System. Journal of TianJin University 32(2), 181–185 (1999)
5. Gao, Y.-f., Zhang, H., Xiao, J.-h.: Identification of welding torch attitude based on rotational arc sensor. Journal of Welding 30(3), 81–84 (2010)
6. Li, Z.-s., Tu, Y.-Q.: The Human-simulated Intelligent Control. Publishing House of National Defence Industry, Benjing (2003)

Design and Realization of Turbo-expander Control System

Jintang Yang, Jiaohua Shi, Gongfa Li, Zhaohui Xia,
Shiyang Zhou, and Wen Chen

College of Machinery and Automation, Wuhan University of Science and Technology,
Wuhan, 430081, China
{Jintang.Yang,Jiaohua.Shi,Gongfa.Li,Zhaohui.Xia,
Shiyang.Zhou,Wen.Chen,shijiaohua92}@163.com

Abstract. The inefficient of manual control and isolation of instrument control cannot meet the requirements of production. However, DCS fully reveals its superiority. This paper elaborates the control system based on ECS. A cascade loop was used to control the speed of the expander. This ensured it stably and efficiently in motion. To the problem of destructive surge, a special kind of controller with characteristics of quick opening slow closing was designed. Surge is prevented and security of production process is assured. Their safety was ensured further by the linkage configurations in the end.

Keywords: ECS; Turbo-expander; Control system.

1 Introduction

Turbo-expander is an important equipment in making cold and recycling energy. It achieved its predominance in the areas of air conditioning, cryogenic environment, and energy of exhaust about comprehensive utilization [1]. The principle is to use a certain pressure gas for adiabatic expanding in the turbo-expander. The internal energy of the gas is consumed by doing work outside. Thereby the gas cools rapidly. As the expanded air through the machine quickly, there is no time exchanging energy with the surroundings, so this process is regarded as isentropic expansion and high adiabatic efficiency. The impeller of expander is driven by the expanded air, and the coaxial centrifugal compressor is driven to compress low-pressure gas. That is the work way of the machine this paper studied.

ECS-700 system is a large-scale joint control system. It is made up with the enterprise management network, the process of information networks, the process of control network and I/O bus from top to bottom.

2 Control System of Turbo-expander

The purpose of DCS control is to ensure devices to meet the technological conditions more accurately and ensure the equipment safe.

D. Zeng (Ed.): Future Intelligent Information Systems, LNEE 86, pp. 391–397.
springerlink.com © Springer-Verlag Berlin Heidelberg 2011

Turbo-expander is used to make cold energy. It is very important to ensure that it works effective and steady. The main factors affecting its efficiency are as following: ① the speed of rotor; ② the opening of nozzle; ③ the flow of air; ④ sealing; ⑤ expansion ratio. The air states of import and export of turbo-expander were the main parameters for the control system. Its purpose was to obtain a reasonable expansion ratio. Good cooling effect is guaranteed by a high expansion ratio. Generally speaking, it is feasible to obtain a reasonable expansion ratio by controlling the speed of expander.

Turbo-expander works under high-speed and low-temperature, the safety is particularly important. The surge control, interlocking control and auxiliary control system were considered carefully.

2.1 Loading Control

Turbo-expander is a cooling device, and more cold energy being created is demanded. The cooling capacity Q is calculated by the following formula:

$$Q = q_m h_s \eta_s = q_m h \,. \tag{1}$$

q_m : the inlet flow of expander h_s : the isentropic enthalpy drop

η_s : the isentropic efficiency h : the actual enthalpy drop

Obviously, the cooling capacity is proportional to the inlet flow of expander and the actual enthalpy drop. The inlet flow of expander can be calculated by inlet pressure of expander and valve opening; the actual enthalpy drop is decided by the import and export status of the gas and the expander speed.

Turbo-expander is a cooling device, and more cold energy being created is demanded. However, too much cooling capacity will result in expanded air liquefied. Damage can be caused by the liquid droplets. So the temperature was required between -170~180℃ by the loading control.

There are four ways for loading regulation of turbo-expander as following: controlled by throttling before machine, controlled by changing opening of nozzle block, controlled by adjustable nozzle, and controlled by changing height of nozzle[2]. As the nozzle is made of stainless steel, frequent activity likely to cause wear and tear, so the first ways was chosen. When the outlet pressure of booster is lessening, the loading become bigger, the expansion ratio is increased. To make the pressure return normal condition, the speed of the rotor should be increased. After that, the loading does not change and the expansion ratio become bigger. The outlet pressure of booster is increased and results in smaller expansion ratio. Finally it reaches a dynamic equilibrium. When the outlet pressure of booster is rising, the loading become smaller, the expansion ratio is reduced. To make the pressure back to normal, the speed of the rotor should be reduced. Then the loading has no change and expansion ratio become smaller because of the lower speed. But the outlet pressure of booster is smaller, and results an increase of the expansion ratio. Eventually, it

also reaches a balance. A cascade PID loop was used for its control [3]. The difference between instantaneous value of outlet pressure of booster and the setting was regarded as the input of the outer loop. Then the value between output of the main loop and the setting of the speed was regarded as the input of inner loop. And the output was used to control the speed of the rotor. The principle of the control is shown in figure 1.

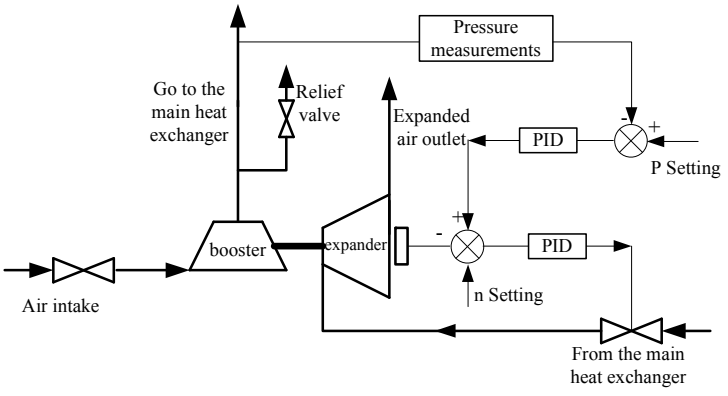

Fig. 1. Cascade PID loop for the turbo-expander

2.2 Surge Control

When the inlet pressure of booster is lower than a certain value, surge will occur. Surge is a non-normal condition, it will cause serious damage to the equipment. According the performance curve provided by the booster manufacturer, a surge curve was gotten by calculating [4], shown in figure 2. Moved the surge curve to right about 8% of the inlet flow, this obtained curve is called the Line of Control.

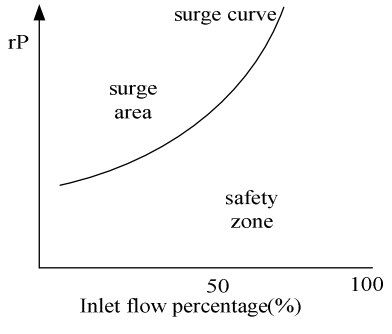

Fig. 2. Surge curve rP stand for pressure ratio of inlet and outlet

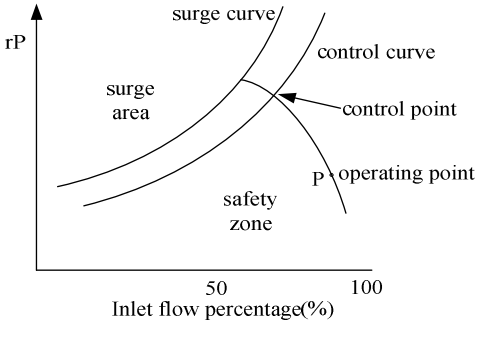

Fig. 3. Control of surge rP stand for pressure ratio of inlet and outlet

In figure 3, P is an operating point [5]. When the operating point reached the control point, the return valve is opened quickly by the controller; while the operating point recoil from the control point, the return valve is closed slowly. An advantage of closing slow is to prevent the inlet flow sudden drop. A surge would be happened again by the sudden drop of the inlet flow. Surge controller was a special controller and it enabled the return valve opened quickly and closed slowly. The controller's inputs were inlet flow of booster, inlet pressure of booster and outlet pressure of booster. The output voltage was decided by the relationship of the three values. The controller outputs high voltage when the return valve is opened and outputs low voltage when the valve is closed. Surge control diagram shown in figure 4.

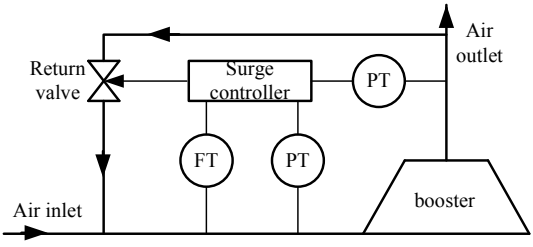

Fig. 4. Surge control diagram

2.3 Interlocking Control

① The interlocking control for driving &parking

This interlocking control is for the turbo-expander driving and parking safely. The interlocking control for driving includes the checking of starting conditions and the control of boot sequence. Only if every parameters and state of every valve meet the starting conditions, the expander can be started. The boot sequence is firstly the seal gas system, then the lubricating oil system and the last is the turbo-expander. Whether to activate the second expander based on the condition. The parking sequence opposites the above order.

② The interlocking control of accident

The set of interlocking control of accident is used to protect the safety of the turbo-expander when an emergency occurs. Emergencies include the out of range of the expander bearing's temperature, low pressure of the sealed gas, abnormal vibration of the booster, over speed of the expander, low pressure of the lubricating oil and so on. Once an incident happened, the turbo-expender is stopped immediately by the interlocking control system.

2.4 Auxiliary Control System

The auxiliary control system includes oil supply control system and the sealing gas control system.

① **Oil supply control system**

Oil supply system was used to protect the bearing by providing a certain temperature, pressure and quantity of clean oil. In order to protect the bearing, pressure vessel should continue to supply one minute's oil for the turbo-expander when sudden stop of the oil pump. In case of oil duct obstructed, the oil pump continues to supply oil at a high pressure, a relief valve was set at the outlet of the pump. Once the pressure of the supplying oil reached the setting value, the power of the relief valve was cut off immediately.

② **Control system of seal gas**

Turbo-expander is working on the condition of low temperature, and using labyrinth seal. The lubricating oil should be protected from cold air. If the oil's temperature is too low, it will freeze and the resistance of bearing will increase. In order to reduce gas leakage, the pressure of the seal was kept below a certain value. Generally the inlet pressure of seal gas was higher than the gas after the nozzle about 0.05MPa.

3 Realization of Control System Based on ECS-700

The realization includes configuration of the control domain and configuration of the operating domain. After the system configuration, hardware configuration, structure configuration and the location number configuration had been completed, the user programming was edited [6]. Thus, the configuration of the control domain was finished. Finally, configuration of the operating domain should been completed, including pictures of overall outlook, pictures of list, pictures of the trend, pictures of flow chart and the journaling for report. Some steps are shown in figures.

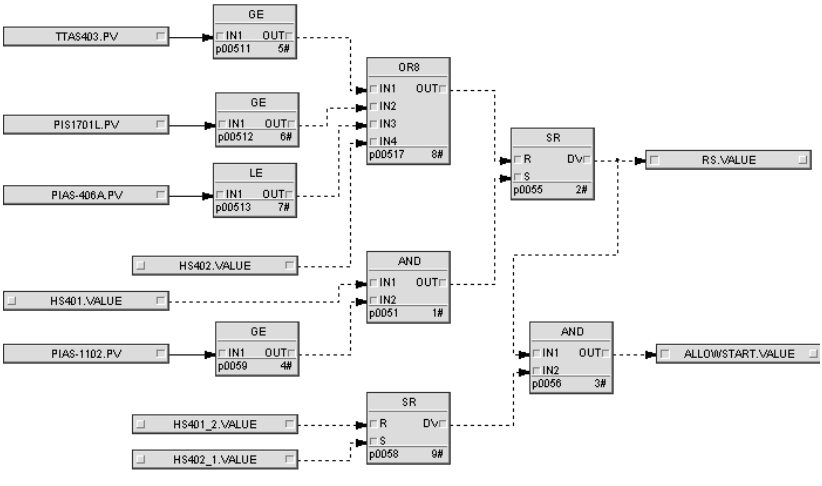

Fig. 5. User programming

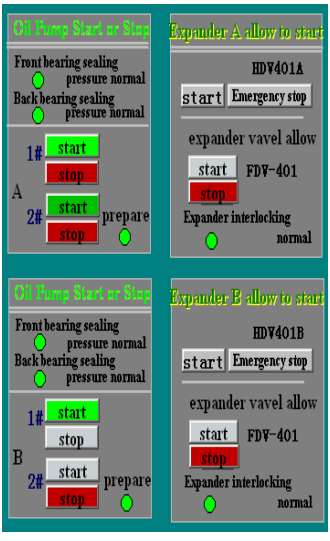

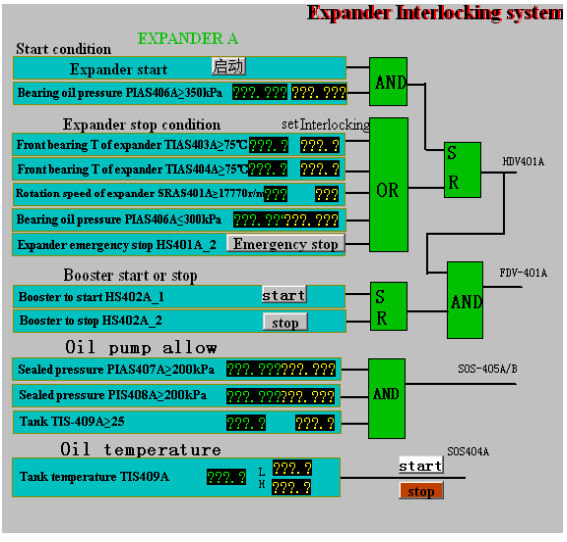

Fig. 6. Configuration of pump control

Fig, 7. Configuration of interlocking control

After all the above steps finished, repeated and serious debug and modify were taken until there was no problem. Then we put the system into industrial production. One of the monitoring pictures is shown in figure 8.

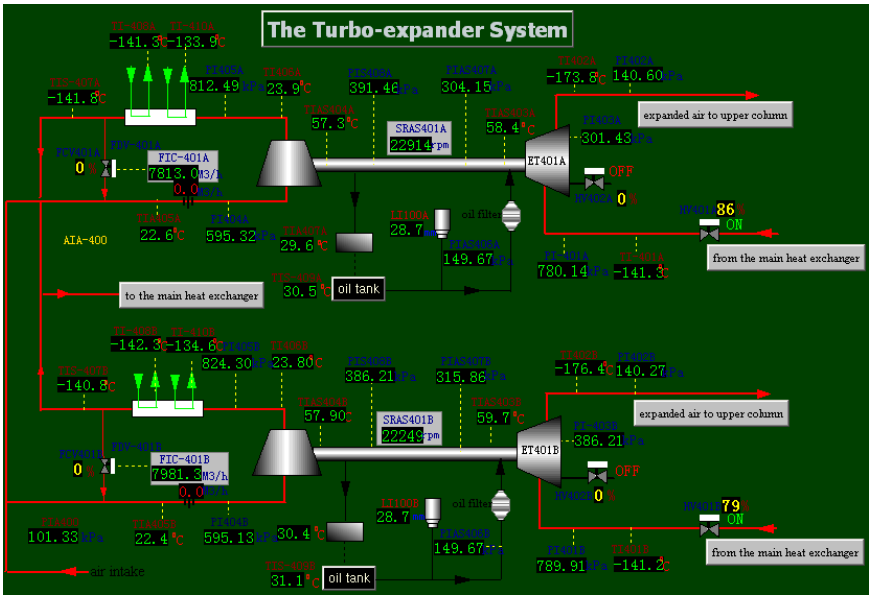

Fig. 8. The main monitoring picture

4 Conclusion

Inefficiency and low accuracy of the manual control was solved. Deficiency of isolation from other machines when using instrument control was overcame. The cascade loop kept the outlet temperature stay normal fluctuation in the range of -172~-178℃, fitting the demands of process. The amount of gas to air was reduced greatly due to the ability of adjusting speed. Efficiency of the whole set was improved and energy-saving effect was remarkable. The controller of surge efficiently prevented the occurrence of surge. There is no serious surge accident as yet. In a word, the project has finished the monitoring perfect and control the Turbo-expander very well. Result shows that this method is feasible and has upper applied value in practice.

Acknowledgments. This research reported in the paper is supported by Key Laboratory of Metallurgical Equipment and Control of Ministry of Education in Wuhan University of Science and Technology (2009A13). This support is greatly acknowledged.

References

1. Ji, G.: Turbo-expander. Mechanical Industry Press, Beijing (1982)
2. Hong, X.: Application of CS3000 in the Control System of the Boost Turbine Expander Unit. J. General Machinery 6, 39–40 (2009)
3. Xiang, X., Wang, Y., Sun, X., et al.: Research on PID Cascade Control System of Expansion-compressor. J. Machine Tool & Hydraulics 36, 115–118 (2008)
4. Zhang, W., Zhang, Q., Zhou, Y.: Transformation of Expander's Control System Based on PLC and Touch-Screen. J. Electrotechnical Application. 25, 38–42 (2005)
5. Tang, L.: Design of air separation plant comprehensive integration control system. Dalian University of Technology, Dalian (2009)
6. Zhang, X.: Control of AIR-COMPRESSOR system based on ECS-700. J. Machinery Design & Manufacture 5 (2010)

TCO Endpoint Control System for Converter Steelmaking

Yanhua Zhao, Jianyi Kong, Jintang Yang, Zhaohui Xia, and Gongfa Li

College of Machinery and Automation, Wuhan University of Science and Technology, 430081 Wuhan, China
ligongfa@yahoo.com.cn

Abstract. In the course of production technology of converter steelmaking, accurate and fast measurement such technical indicators as temperature, content of carbon and content of oxygen of molten steel in the converter, especially the technical indicator of the molten steel of endpoint, it is significant to guarantee the quality of steel products and reducing energy consumption. The structure of equipments, the technological principle of TCO and its application in steelmaking are described and specially the results of TCO application in No. 4 converter in Handan Iron and Steel Co. Ltd are introduced. The converter TCO endpoint control system reaches the equal effect that subsidiary gun measurement controllers, improving two blowing endpoint hit rate, shorting smelt period, and reducing various consumption, improving steel mass effectively. A bright prospect for popularization of this technology in China is pointed out.

Keywords: converter steelmaking, TCO, endpoint control, automatic detection.

1 Introduction

The medium and small-scale converter of our country, has not adopted subsidiary gun to measure automatically because of the limitations of various kinds of factors at present, it is carried on that the majority relies on experience to control blowing endpoint, various kinds of indexes are not very ideal. According to incomplete statistics, among 426 medium and small converters with the capacity of 100t and 58 more than 100t's converters soon, majority still adopt the experience law steelmaking because of technology and fund. No matter producing clean steel or the high-quality steel, or production the stability of steel water quality in continuous casting and continuous rolling, can't meet the follow-up process and demand of the market more and more. Improving the precision of control and hit rate of steelmaking endpoint, have already become urgent technological problem that waits to solve in production at present.

Converter subsidiary gun system has characteristics of high input once, high maintenance cost and huge volume. TCO endpoint control system has solved the difficult problems of most converters haven't or can't install subsidiary gun, and can

D. Zeng (Ed.): Future Intelligent Information Systems, LNEE 86, pp. 399–402.
springerlink.com © Springer-Verlag Berlin Heidelberg 2011

reach equal effect that subsidiary gun measurement controllers, can obtain such information as steel liquid composition and temperature from the converter in case of not stopping blowing or without finial turndown, not only can reduce labor intensity, can also shorten the duration of heating time of each stove, improve two blowing endpoint hit rate, shorten smelt period, reduce various kinds of consumption effectively and improve steel quality.

The equipment has the characteristics of simple structure, compactness, durable use, investment with low costs and little last expenses. Throwing equipment is full-automatically operation, the attendants operate on the man-machine interface, while needing to throw measurement bombing, the attendants click measuring button, throwing equipment will throw it to molten steel from converter unloading mouth or cigarette, measurement time is ten minutes. Data examined are shown on instrument and outdoors screen, the equipment resets automatically right away.

2 TCO Control Technology

The technological principle of the bombing detection technology for steel tapping without final turndown is shown as following. For example, blowing to 85%~90% or to endpoint, under the condition without final turndown and stopping blowing, high temperature measurement bombing is thrown to molten steel in the stove automatically by automatic throwing equipment, then molten steel temperature, content of carbon, content of oxygen measured by the high temperature measurement bombing within ten seconds are shown on the screen to instruct the steelmaking operation, or calculate through the computer, automatically control blowing and tapping.

2.1 TCO Equipment

Bombing detection equipment is shown as Fig.1. Thes TCO system is made up of automatically bombing device and measuring instrument. Bombing device includes bombing mechanism and bombing box, which can store 50~80 high temperature and low temperature bomb. Throwing movement of bombing mechanism and contact of electric signal contact are carried on by two air cylinders, its control system is made up by Siemens S7-400 PLC and picture operation stand, can carry on movements automatically. Measuring instrument is made up of bomb, signal processor and displayer.

The instrument is adopted high integrated design, has few separate packages, and few trouble points, the signal adopts wireless transmission technology, has reduced the trouble incidence of the detection system effectively, the instrument software returns to computing functions, has guaranteed to measure the accuracy of the result, it is extremely convenient to the finding out and download of initial data, the instrument shows and operates the picture machine, operate conveniently.

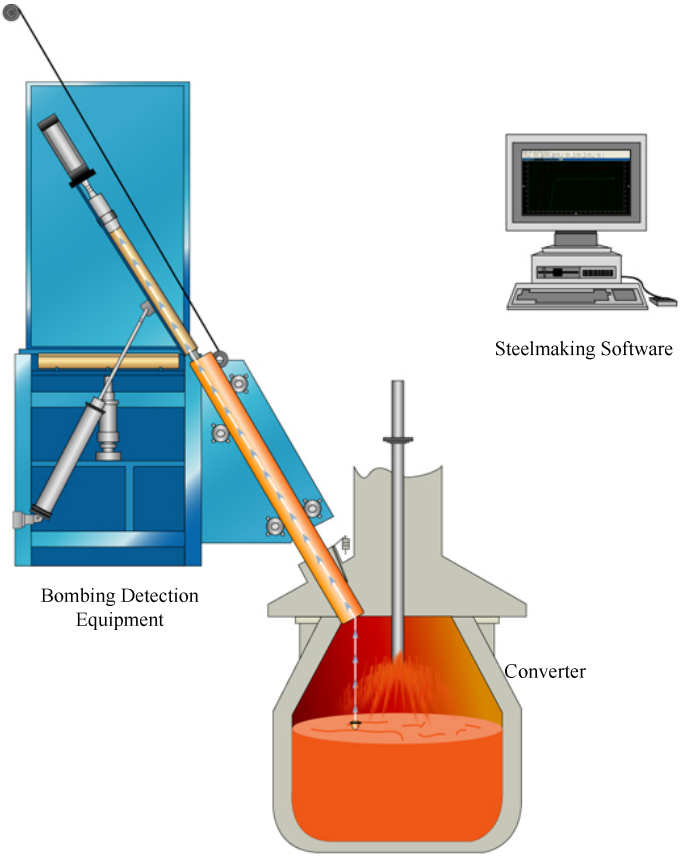

Fig. 1. TCO Equipment Structure

2.2 TCO Steelmaking Operation

In order to improve converter steelmaking endpoint control level, reduce after-blowing, lower consumption, improve production capacity and steel quality, Handan Iron and Steel Co. ltd has developed TCO steelmaking operation technology software, has realized the goal of using bombing detection technique to control steelmaking endpoint.

The main function of TCO steelmaking operation software has calculation of amount of oxygen blown and calculation of the time of dropping a bomb of TCO, through the first TCO examining result, instruct steelmaking endpoint control. Before the converter begins to blow, only the kind of smelt steel planned, amount of main raw materials and relevant packs of raw materials and endpoint goal value are imported into computer artificially, amount of oxygen blown and bombing moment are calculated by computer, the number value points out appearing on the main picture, after dropping a bomb and measuring automatically, measure result is shown on screen, steel worker is instructed to blowing endpoint control operation in order to reduce after-blowing and improve endpoint carbon and temperature hit.

3 Application

Application of TCO technology realizes the goal of steel tapping directly without finial turndown under converter steelmaking endpoint, thus smelt period of converter is shortened. It made the production membership credentials of the steelmaking plant in order, enable producing more orderly. Every stove steel smelts period is shorten by 2.4 minutes calculated according to 60 stoves steel per day under normal working condition, so more steel 6 stove every day can be produced in no. 4 converter of Handan iron and steel Co.ltd, can produce benefit of increasing production. Meanwhile, the hit rate of blowing endpoint is improved and have improved the smelting operation state of the converter to a great extent. On this basis, the supplies consumption and oxygen content of endpoint molten steel are reduced, the artificial experience steelmaking has been avoided, it is automatically control to implement, oxygen consumption is reduced, metal afford charge ratio is improved, the inclusion is reduced, steel quality is improved, has obtained better metallurgical result.

4 Conclusion

The TCO automatic bombing detection technique is an advanced detection technique developed and adopted by Handan Iron and Steel Co. ltd, its function is closed to automatic detection using subsidiary gun in large-scale converter. Fast taking a sample devices designed in converter are all driven pneumatically, is automatically controlled throwing bomb, integrated assemble, reliable compactness, less space, little investment once, low maintenance cost and convenient overhauling, is suitable for the medium and small-scale converter without subsidiary gun. Its technical equipment is simple, it is rational to fix up, fault rate is low, durable in use, suitable for medium and small converter use. Medium and small-scale converters are in large quantity at present in our country, and steelmaking is mostly under the artificial experience operation conditions, the TCO technique has very wide prospects to popularize.

Acknowledgement

This research reported in the paper is supported by Research Center of Green manufacturing and Energy-Saving & Emission Reduction Technology in Wuhan University of Science and Technology (B0911). This support is greatly acknowledged.

References

1. Lihong, Y., Liu, L., Ping, H.: Control of Carbon Content and Temperature at Endpoint for Converter Process Based on 2-Output Neural Network. Chinese Journal of Iron and Steel 37, 13–15 (2002)
2. Yan, H., Song, L., Zhang, W.: Application of boming detection technology in converter steelmaking. Chinese Journal of Steelmaking 24, 9–12 (2008)
3. Shuming, X., Tingyu, S., Tianyou, C.: BOF Intelligent Dynamic Endpoint Control. Chinese Journal of Control Theory and Applications 18, 346–352 (2001)

16 Times Over-Sampling Technique Based on the ADC Module of Stellaris™ Family of Chips

Tu Li[1], Liu Jun'an[2], and Song Juanjuan[3]

[1] Department of Computer Science Hunan City University, Yiyang, Hunan, 413000, China
tulip1907@163.com
[2] Department of Machinery Engineering, Hunan Institute of Engineering, Xiangtan, Hunan, 411101, China
Liu_jun_an@163.com
[3] Department of Chemical and Environmental Engineering, Hunan City University, Hunan, Yiyang, 413000, China
s-jj-18@163.com

Abstract. The ADC module with its 10-bit-resolution is integrated into the partial products of Stellaris series microcontroller. But the actual precision obtained is less than 10. This paper provides a software-based general average over-sampling technology which use an oversampling frequency of the cycle timer which is running, timer in the past triggers a sampling frequency conversion to generate an additional clear ADC interrupt, accumulated 16 times in the conversion, this average value of 16 samples, and it will remove global variables and the total sample count variable. This way improve the results of the effective number of bits (ENOB). However, taking up most of the sampling sequencer resources of the system, this method has a negative impact on the entire system for it requires additional code to perform the average and additional disruption.

Keywords: ENOB, sampling frequency, Oversampling, General average.

1 Introduction

Texas Instruments (TI) Stellaris (stars) product is a high-performance 32-bit microchip which has achieved a revolutionary breakthrough--ARM Cortex-M3 technology. It carried out the system-on-chip and real-time multitasking system with a perfect combination and easy to achieve while the original MCU is not possible to use complex applications. Stellaris family with amazing quick response implemented the first most comprehensive Cortex-M3 and the Thumb-2 instruction set. Thumb-2 technology combines 16-bit and 32-bit instruction to make the best balance of code density and performance to. Thumb-2 uses 26% less memory than the pure 32-bit code, which reduces system cost, while performance increases 25%. Stellaris family, exclusively designed for demanding microprocessors, has the MCU GPIO which is able to generate interrupts, and it supports 5V voltage, as well as programmable drive and slew rate control function; It has the advanced communications capabilities,

D. Zeng (Ed.): Future Intelligent Information Systems, LNEE 86, pp. 403–408.
springerlink.com © Springer-Verlag Berlin Heidelberg 2011

including 10/100 Ethernet MAC / PHY, USB and USB OTG, CAN controller and a rich peripheral interfaces; and its analog comparators and ADC functionality can provide hardware and software performance which can be balance chip option.

2 General Average

N times the input signal sampling, the sampling value and the results divided by the sum of n, it is conventional average. Figure 1 shows the conventional average. While the sampling program uses conventional average, the technology will be used and the average of sampled data is discarded. When each application requires a new conversion results, the treatment will be repeated.

In the application, the conventional program is ideal for the average sampling frequency if ADC sampling rate is relatively small in comparison.

Important: When the average program execution in conventional over-sampling n times, the effective ADC sampling rate will decrease because of the same factor. For example, the input signal is 4 times oversampling, the most effective ADC sampling rate will be reduced to 1 / 4, that the sampling rate of 250K / s the ADC effectively become 62.5K / s for ADC.

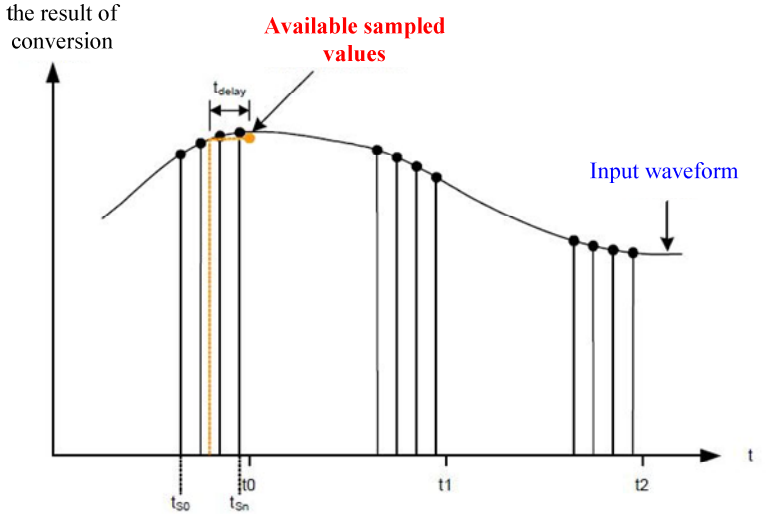

Fig. 1. General average

Figure 1 shows the solution using the conventional average of the input source for 4 times oversampling. In this case, the application requirements at each stage t (t0, t1, t2, etc.) are ready for a new value (the average operation is complete).

The average technology in use, because the conversion results calculated with the above sampling points corresponding to n, therefore is slightly delayed. Delay time using the equation in the formula:

Equation :After an average of sampling delay

$$t_{delay}=(t_{Sn}-t_{S0})/2+t_{process} \quad (1)$$

tS0 the average time for the conduct of the first sampling point of time there, tSn a sampling point for the last time there. Interrupt handler processing time is required for sampling data, and it is calculated by using the average for the supply tproces which is broken down into the equation. In Figure 2, the delay after the transfer structure to highlight that with the orange.

3 The Principle of Over-Sampling

Over-sampling collects additional conversion data from input signals. Analog signal standard specifies: sampling frequency fS is at least as two times as he highest frequency component fH of the input signal. This is called the Nyquist sampling theorem.

Nyquist sampling theorem:

$$fS = 2fH \quad (2)$$

As long as the selected sampling frequency is higher than fS it is regarded as over-sampling. The combination between oversampling and the averaging technique can improve the ENOB. This can be achieved, because in the over-sampling the results will also quantify the average noise of the average, and it raises the signal noise ratio (SNR), whose increase will be in the ENOB to generate a direct impact on improving the ENOB.

With the accuracy improved, the signal over-sampling must be 4 times as it was. That is over-sampling frequency and sampling frequency fS fos relationship:

$$fos=4x*fS \quad (3)$$

x is the number of bits ENOB on the need to improve (for example, need to improve two, then x = 2).

Over-sampling on the accuracy of the results from the improvement shown in Figure 2. In the figure, the input signal is 4 times oversampling (sample group indicated in green and purple) and for average. The figure shows the samples to clarify the original, with the noise signal and the difference between the average. The case of noise in a single sample value on the precision to ± 3 bits. We note that the average (orange dots) than most of the single sample value closer to the ideal value, and much more accurate.

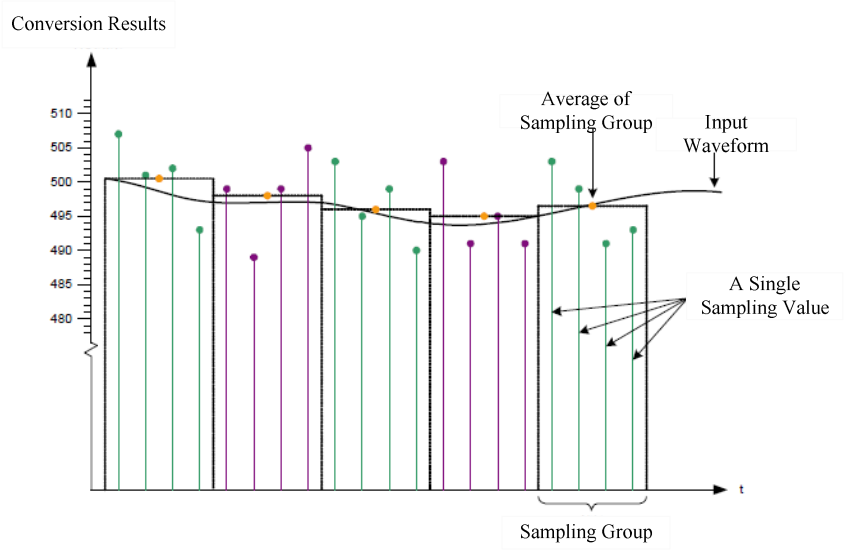

Fig. 2. Over-sampling on the accuracy of the results from over-sampling to improve the accuracy of the results on the improvement of conversion

4 Using Multiple Sequencer or a Timer to Achieve More Than 8 Times Oversampling

Drive the largest library of over-sampling function can only be carried out 8 times over-sampling (sampling sequencer according to the hardware limitations), so the need for greater over-sampling factor of the application must make use of the other implementation. This section describes how to use the following method: sampling frequency in the past to run multiple samples sequencer, and a timer to solve this problem.

Used to run the timer fOS 16x oversampling:

The way to achieve 16x oversampling (ADC sequencer without consuming the majority of resources) is to use an oversampling frequency of the cycle timer which is running. For example, if the conversion process every 10ms to return to the main application and will soon be 16 times oversampling, the timer can be configured to obtain a sample value of each 625μs. Timer in the past triggers a sampling frequency conversion to generate an additional clear ADC interrupt, which must be described in the application.

The ADC and the timer is configured to implement the above operation code, see code a.

Code a. ADC configuration - run the timer in fOS

```
// Initialize ADC, in order to detect when a trigger
channel 1, 3 on the sequencer to get a sample value.
ADCSequenceConfigure(ADC_BASE, 3, ADC_TRIGGER_TIMER, 0);
```

```
ADCSequenceStepConfigure(ADC_BASE, 3, 0, (ADC_CTL_CH1 |
ADC_CTL_IE \
| ADC_CTL_END));
//Initialize timer 0, every 625•s trigger an ADC
conversion
TimerConfigure(TIMER0_BASE, TIMER_CFG_32_BIT_PER);
TimerLoadSet(TIMER0_BASE, TIMER_A, SysCtlClockGet() /
1600);
TimerControlTrigger(TIMER0_BASE, TIMER_A, true);
```

Since the ADC sampling frequency in the past sampling operation, the interrupt handler must know the number of samples have been obtained and the sum of (see Code Section .b). Accumulated 16 times in the conversion, this average value of 16 samples, and it will remove global variables and the total sample count variable.

Code b. ADC interrupt program

```
void
ADCIntHandler(void)
{
ADCIntClear(ADC_BASE, 3);     // Clear interrupt
// Added to the new global sum of sampled values
g_ulSum += HWREG(ADC_BASE + ADC_O_SSFIFO3);
// g_ucOversampleCnt+1
//
g_ucOversampleCnt++;
// If the accumulated value of 16 samples, average, and
they will reset the global variable
if(g_ucOversampleCnt == 16)
{
   g_ulAverage = g_ulSum >> 4;
g_ucOversampleCnt = 0;
g_ulSum = 0;
} // Placeholder for ADC handling code
}
```

Finally, before enabling the timer, the sequencer 3 and the interrupt enables, and clear the counters and the sum of the global variables (see code section c).

Code c . Enable ADC, interrupt and clear the global variable

```
// Enable and interrupt sequencer
ADCSequenceEnable(ADC_BASE, 3);
ADCIntEnable(ADC_BASE, 3);
IntEnable(INT_ADC3);
// The sum of the oversampling counter and clear
```

```
variables
g_ucOversampleCnt = 0;
g_ulSum = 0;
// Enable the timer and start the conversion process
TimerEnable(TIMER0_BASE, TIMER_A);
```

5 Conclusions

This article describes the over-sampling, an additional code to perform on average, an additional interrupt, and / or most of the sampling sequencer resources, so it has a significant impact on the system performance.

Luminary Micro sampling sequencer structure provides many options for the realization of over-sampling technology. When the average technology and software are combined, the structure enables system designers to weigh effectively among the sampling frequency, the system performance and the sampling solution.

References

1. Li, S., Xu, Q.: Harmonic wavelet extraction for weak vibration signal in frequency domain. Hsi2An Chiao Tung Ta Hsueh/ Journal of Xi'an Jiaotong University 38(1), 51–55 (2004)
2. Cheng, D.-f., Lin, J., Yu, S.-b., Duan, Q.-m., Zu, K.-g., Ji, Y.-j.: Study on TEM weak signal detection techniques. Journal of Jilin University (Information Science Edition) 20(2), 1–5 (2002)
3. Wang, X.-s., Qin, W., Ling, X., et al.: A new architecture of cascaded oversampling sigma delta modulators. Acta Electronica Sinica 28(2), 68–71 (2000)
4. Elders-Boll, H., Dettmar, U.: Efficient differentially coherent code/ Doppler acquisition of weak GPS signals. In: Eighth IEEE International Symposium on Spread Spectrum Techniques and Applications, pp. 731–735. IEEE Press, Los Alamitos (2004)
5. Lim, S., Apostolopoulos, J., Gamal, A.E.: Benefits of temporal oversampling in optical flow estimation. In: Proceedings of International Conference on Image Processing, vol. 4 (24 -27), pp. 2567–2570 (2004)
6. Wu, C.W.: Assessing process capability based on Bayesian approach with subsamples. European Journal of Operational Research 184(1), 207–228 (2008)
7. Villiam, M.: Multivariate bayesian control chart. Operations Research 56(2), 487–496 (2008)

Tandem Nonlinear Systems and Structural Controllability: An Extended Transfer Function Method

Qiang Ma

Dept. of Power and Energy Engineering, Wuhan University of Technology,
430063 Wuhan, China
richardkinbvle@yahoo.com.cn

Abstract. In this paper parameter space is introduced to analyze the structural controllability of nonlinear systems. Necessary and sufficient conditions of structural controllability for nonlinear systems are obtained by using transfer function conception. The nonlinear structural controllability condition is extended to nonlinear tandem composite system and the new criterion is derived. Since the non-commutative character of these conditions it is different from that for linear systems in frequency domain. Examples are used to show the application for these conditions and the non-commutative character.

Keywords: nonlinear composite systems, structural controllability, transfer function, non-commutation.

1 Introduction

Controllability was first introduced by Kalman in linear systems analysis. It is a most important conception describing the character of linear systems. We know that controllability is important in linear system theory analysis. Also there are many researches to nonlinear systems controllability.

Sussmann and Jurdjevi [1] gave the controllability analysis of nonlinear systems. They pointed out for nonlinear systems that the geometric structure of attainable set was a sub-manifold in fact and gave an exact answer when the attainable set is of non-empty interior for some state x. Sussmann [2] analyzed the nonlinear system with scalar input using Lie algebra and gave the sufficient condition for controllability. Stefani [3] researched the nonlinear systems with scalar input also and gave the local controllability condition for nonlinear system. The above results are based on the differential geometry.

The conception of transfer function is just considered to belong to linear systems for long time. Until Zheng and Cao [4] introduced the transfer function to nonlinear systems, more researchers accept the fact that nonlinear systems can also have their transfer functions. At the same time we can get the input-output description of nonlinear systems, which is a new way to analyze the composite systems. Zheng etc. [5] explored the controllability of nonlinear systems using transfer function. Halas and Kotta [6] use this method to discrete time nonlinear systems.

D. Zeng (Ed.): Future Intelligent Information Systems, LNEE 86, pp. 409–416.
springerlink.com © Springer-Verlag Berlin Heidelberg 2011

The main work of this presented paper is that parameter space is introduced to nonlinear analysis and structural controllability of SISO nonlinear systems is obtained using transfer function method. The difference with Fradellos etc [7] researched is that in this paper we investigate the effect of parameters on properties for nonlinear systems. However the work Fradellos etc did is that whether nonlinear systems keep controllability under perturbation.

The rest of this paper is organized as follow: in section 2 transfer function of nonlinear systems is introduced; in section 3 structural controllability conditions for nonlinear systems and composite systems are obtained; in section 4 two examples are used to illustrate the applications of these conditions.

2 Transfer Functions of Nonlinear Systems

Consider a SISO nonlinear system described by high order differential equation with the form

$$F(y, \dot{y}, \cdots, y^n, u, \dot{u}, \cdots, u^m) = 0 \ . \tag{1}$$

where F is called meromorphic functions, $u \in R$, $y \in R$.

Let K denote the field of meromorphic functions. Define a derivative operator δ over K, and then making the derivative operation to equation (1) yields

$$\delta F = \sum_{i=0}^{n} \frac{\partial F}{\partial y^i} dy^i + \sum_{j=0}^{m} \frac{\partial F}{\partial u^j} du^j \ . \tag{2}$$

For convenient, we denote as follow by $\delta u = \dot{u}, \delta y = \dot{y}, \delta \dot{u} = \ddot{u}, \delta \dot{y} = \ddot{y}$. Then define a vector space ε, which is spanned by dy^i and du^j, $i = 0,1,\cdots,n-1$, $j \geq 0$. Any vector in ε is called 1-type with the form

$$v = \sum_{i=0}^{n} \alpha_i dy^i + \sum_{j=0}^{r} \beta_j du^j \ . \tag{3}$$

Let K be a field, $\sigma : K \to K$ is a injective endomorphism over the field K. a mapping $\delta : K \to K$ is said to be pseudo-derivation if it satisfy

$$\begin{aligned} &\delta(a+b) = \delta(a) + \delta(b) \\ &\delta(ab) = \sigma(a)\delta(b) + \delta(a)b \end{aligned} \ ,$$

where $a, b \in K$. If $\sigma = 1$, then this derivative is the same as that over general field. Let s be an indeterminate member over differential field K, i.e., field K does not contain s, then the polynomial ring defined by δ and σ in s is denoted by $F[s; \sigma, \delta]$. This polynomial ring satisfy the usual addition rule and the non-commutative multiplication rule with $sa = as + \dot{a}$, for every $a \in K$.

So this polynomial ring is called skew polynomial ring. Finally, we should know what condition two polynomials over skew polynomial ring satisfy when make

division, because the transfer function is expressed by quotient with two skew polynomial. There is no zero divisor over the ring of $F[s;\sigma,\delta]$, and satisfy the so-called Ore condition [5, 6].

Lemma 1 (Ore condition): For all non-zero $a_1, b_1 \in K[s;\sigma,\delta]$, there must exist non-zero $a_2, b_2 \in K[s;\sigma,\delta]$ such that $a_2 b_1 = b_2 a_1$.

We denote the quotient field of skew polynomial by $K\langle s;\sigma,\delta\rangle$.

Now the algebra framework is established. For equation (1) we make derivative and yields

$$\sum_{i=0}^{n} \frac{\partial F}{\partial y^i} dy^i + \sum_{j=0}^{m} \frac{\partial F}{\partial u^j} du^j = 0 \ . \tag{4}$$

Let $\frac{\partial F}{\partial y^i} = a_i$, $\frac{\partial F}{\partial u^j} = b_j$. Clearly, $a_i, b_j \in K$. Since $s^k dy = dy^k$, $s^k du = du^k$, then

$$\sum_{i=0}^{n} a_i s^i dy + \sum_{j=0}^{m} b_j s^j du = 0 \ . \tag{5}$$

Let $A(s) = \sum_{i=0}^{n} a_i s^i$, $B(s) = -\sum_{j=0}^{m} b_j s^j$, equation (5) can be written as

$$A(s)dy = B(s)du \ . \tag{6}$$

Then we change the form of (6) and get

$$F(s) = \frac{dy}{du} = \frac{B(s)}{A(s)} \ . \tag{7}$$

Equation (7) is the transfer function of SISO nonlinear system (1).

3 Structural Controllability of Composite Nonlinear Systems

Reconsider the nonlinear system (1), and introduce the parameter space into system, i.e., there is parameter vector z in system (1). The new system is denoted as

$$F(y, \dot{y}, \cdots, y^n, u, \dot{u}, \cdots, u^m, z) = 0 \ . \tag{8}$$

Definition 2: Let $K(z)$ denote the field of all meromorphic function with parameter vector z. then $K(z)$ can be said to be the meromorphic function field with multi-parameter or simply called the field with multi-parameter.

Definition 3: A polynomial in s with all coefficients over $K(z)$ is called a skew polynomial with multi-parameter. All the skew polynomials with multi-parameter form a polynomial ring, which can be called the skew polynomial ring with

multi-parameter, denoted by $F[s,z]$. We denote by $K\langle s,z\rangle$ the quotient field of skew polynomial ring with multi-parameter.

Definition 4: System (8) is said to be structural controllable if there exist no functions $h: R^{l+1} \to R$ and $w: R^{\tilde{n}+1} \times R^{\tilde{m}+1} \to R$ over $F[s,z]$, such that

$$w = w(y, \dot{y}, \cdots, y^{(\tilde{n})}, u, \dot{u}, \cdots, u^{(\tilde{m})}),\ h(w, \dot{w}, \cdots, w^{(l)}) = 0\ , \tag{9}$$

where $l \geq 1$, $\tilde{n} + l = n$, $\tilde{m} + l = m$.

According to equations (4)-(7), the transfer function of nonlinear system (8) is

$$F^*(s) = \frac{dy}{du} = \frac{B^*(s)}{A^*(s)}\ . \tag{10}$$

where $F^*(s) \in K\langle s,z\rangle$, $A^*(s), B^*(s) \in F[s,z]$.

Theorem 5: Nonlinear system (8) is said to be structural controllable under Definition 4 if and only if $A^*(s)$ and $B^*(s)$ in transfer function (10) has no common left divisor over $F[s,z]$.

Proof: For sufficiency, conversely, assume that system (8) is not structural controllable, then there exists functions h and w over $F[s,z]$ under Definition 4. Then make derivative operation to them and yields

$$dw = \sum_{i=0}^{\tilde{n}} \frac{\partial w}{\partial y^i} dy^i + \sum_{j=0}^{\tilde{m}} \frac{\partial w}{\partial u^j} du^j\ ,\ dh = \sum_{i=0}^{l} \frac{\partial h}{\partial y^i} dw^j = \sum_{i=0}^{l} \frac{\partial h}{\partial y^i} s^i dw = 0\ .$$

Let $A_1(s) = \sum_{i=0}^{\tilde{n}} \frac{\partial w}{\partial y^i} s^i$, $B_1(s) = -\sum_{j=0}^{\tilde{m}} \frac{\partial w}{\partial u^j} s^j$, $R(s) = \sum_{i=0}^{l} \frac{\partial h}{\partial y^i} s^i$, clearly, $A_1(S), B_1(s), R(s) \in F[s,z]$. Then $dh = R(s)(A_1(s)dy - B_1(s)du) = 0$.

Thus we have $\frac{dy}{du} = \frac{R(s)B_1(s)}{R(s)A_1(s)} = \frac{B^*(s)}{A^*(s)}$. This is, there exists common left divisor $R(s)$ between $A^*(s)$ and $B^*(s)$. So if the nonlinear system (8) is structural controllable, then $A^*(s)$ and $B^*(s)$ in transfer function (10) should have no common left divisor over $F[s,z]$.

For necessity, conversely, assume that $A^*(s)$ and $B^*(s)$ have common left divisor $R(s)$ over $F[s,z]$, then the transfer function (10) can be denoted as $\frac{dy}{du} = \frac{R(s)B_1(s)}{R(s)A_1(s)} = \frac{B^*(s)}{A^*(s)}$. Then we have $R(s)(A_1(s)dy - B_1(s)du) = 0$. Thus $\deg R(s) = l \geq 1$, $\deg A_1(s) = \tilde{n} - l$, $\deg B_1(s) = \tilde{m} - l$. Let $R(s) = h_l s^l + h_{l-1} s^{l-1} \cdots + h_0$,

where $h_l \neq 0$, $h_i \in K(z)$, $i = 0, \cdots, l$. Let $\omega = (A_1(s)dy - B_1(s)du) \in D_1$, where $D_1 = \text{span}\{dy^i, du^j \,|\, i = 0, \cdots, n-1; j = 0, \cdots, m-1\}$. Then $R(s)\omega = 0$, i.e.,

$$\sum_{i=0}^{l} h_i \omega^j = 0 \quad . \tag{11}$$

Define a subspace $W_{l+1} = span\{\omega, \omega^1, \cdots, \omega^l\}$, clearly, $W_{l+1} \subseteq D_1$. By (11) it is known that for 1-type $\{\omega^i \,|\, i = 0, \cdots, l\}$, the $l+1$ ones are linear independent over $K(z)$, which implies for $0 \leq k < l$, $\omega^i \in W_k \subset D_1$. Then $\omega \in span\{\omega \,|\, \omega^k \in D_1, \forall k \geq 0\}$, i.e., $\dim span\{\omega \,|\, \omega^k \in D_1, \forall k \geq 0\} \geq 1$. According to Lemma 4.2 in [5] it is known that nonlinear system is not structural controllable. So for nonlinear system (8), only if there exists no common left divisor $R(s)$ between $A^*(s)$ and $B^*(s)$, it is structural controllable. □

For composite nonlinear systems, there are three basic types: tandem, parallel and feedback. In this paper we constrain ourselves to tandem systems only.

Consider two nonlinear systems described by (8):

$\sum_1$, its transfer function is denoted as

$$G_1(s) = \frac{dy_1}{du_1} = \frac{B_1(s)}{A_1(s)} \quad . \tag{12}$$

$\sum_2$, its transfer function is denoted as

$$G_2(s) = \frac{dy_2}{du_2} = \frac{B_2(s)}{A_2(s)} \quad . \tag{13}$$

Then the transfer function of tandem system $\sum_{12}$ (note: the order of subscript denotes the signal flowing from $\sum_1$ to $\sum_2$) can be denoted to (note that $du_2 = dy_1$)

$$G(s) = \frac{dy_2}{du_1} = \frac{B_2(s)}{A_2(s)} \bullet \frac{B_1(s)}{A_1(s)} \quad . \tag{14}$$

Clearly, $G_1(s), G_2(s), G(s) \in K\langle s, z \rangle$, $A_1(s), A_2(s), B_1(s), B_2(s) \in F[s, z]$. Then for equation (14) the non-commutative multiplication is followed as

$$G(s) = \frac{B_2(s)}{A_2(s)} \bullet \frac{B_1(s)}{A_1(s)} = \frac{\alpha(s)B_1(s)}{\beta(s)A_2(s)} \quad . \tag{15}$$

According to Lemma 1, we have

$$\beta(s)B_2(s) = \alpha(s)A_1(s) \quad . \tag{16}$$

Proposition 6: The tandem nonlinear system $\sum_{12}$ is structural controllable if its subsystems $\sum_1$ and $\sum_2$ are structural controllable and polynomials $\alpha(s)B_1(s)$ and $\beta(s)A_2(s)$ in （15） have no common left divisor over $F[s, z]$.

It should be noted that because the different composite style and non-commutation, for the composite system $\sum_{21}$ its transfer function is different from that of $\sum_{12}$. Then the following Corollary is immediate:

Corollary 7: The composite nonlinear system consisting of two subsystems is said to be structural controllable if its subsystems are structural controllable and the numerator and denominator of transfer function of composite system have no common left divisor over $F[s,z]$.

In the view of practice, parameters in each subsystems can be different, then let $z \in R^q$ in subsystems (12) and $z' \in R^{q'}$ in subsystems (13) and $R^q \bigcap R^{q'} = \Phi$, where Φ denotes the empty set. Then for tandem composite system $\sum_{12}$, the following Theorem is true:

Theorem 8: A physical tandem composite nonlinear system is said to be structural controllable if its subsystems are structural controllable and the numerator and denominator of transfer function of tandem composite system have no common left divisor over $F[s;\sigma,\delta]$.

Proof: By the assumption it is known that $A_2(s), B_2(s) \in F[s,z']$, $A_1(s), B_1(s) \in F[s,z]$, then by equation (16) and Lemma 1 it is known that $0 \neq \beta(s) \in F[s,z]$, $0 \neq \alpha(s) \in F[s,z']$. For the non-commutation, it is necessary to consider whether $\alpha(s)$ and $\beta(s)$ have common left divisor or not. Since the polynomial $\alpha(s) \in F[s,z']$, if it can be decomposed then there exist at least one root belonging to the field of $K(z')$ and at the same time not belonging to $K(z)$. Similarly, for polynomial $\beta(s) \in F[s,z]$, if it can be decomposed then there exist at least one root belonging to the field of $K(z)$ and at the same time not belonging to $K(z')$. Because $K \subset K(z)$ and $K \subset K(z')$, then only if $\alpha(s)$ and $\beta(s)$ have the left divisor over $F[s;\sigma,\delta]$ (i.e., the root of left divisor over K) there would be existence elimination. So for two subsystems with different parameters respectively, the tandem composite system is structural controllable if its subsystems are structural controllable and the numerator and denominator of transfer function of tandem composite system have no common left divisor over $F[s;\sigma,\delta]$. □

4 Applications

Example 9: Consider a simple nonlinear passive RLC network shown in [8]. Then by KVL , we have

$$\begin{cases} L\dfrac{\mathrm{d}i}{\mathrm{d}t} + \dfrac{1}{C}\int i\mathrm{d}t + ki^2 = u_i \\ u_o = \dfrac{1}{C}\int i\mathrm{d}t \end{cases}$$

Let $u = u_i$, $y = u_o$, then we can obtain the input-output equation as follow:

$$LC\ddot{y} + kC^2(\dot{y})^2 + y - u = 0 \ . \tag{17}$$

where the parameter $z = (L, C, k) \in R^3$.

Then we take the derivative operation to (17), we can get

$$LCd\ddot{y} + 2kC^2\dot{y}d\dot{y} + dy - du = 0 \ .$$

So the transfer function of this nonlinear system is

$$F(s) = \frac{1}{LCs^2 + 2kC^2\dot{y}s + 1} \ .$$

Obviously, the numerator and denominator of transfer function has no common left divisor, so this nonlinear system is structural controllable, i.e., when parameter z takes values in parameter space R^3, the concrete system is almost controllable.

Example 10: consider two subsystems as follow:

$$\Sigma_1: \quad \dot{y}_1 + ay_1^3 - u_1 = 0 \qquad \Sigma_2: \quad \dot{y}_2 - \dot{u}_2 - au_2^3 = 0$$

By calculation we have $G_1(s) = \dfrac{1}{s + 3ay_1^2}$ and $G_2(s) = \dfrac{s + 3au_2^2}{s}$. We consider the tandem composite system Σ_{12}, then transfer function is

$$G(s) = \frac{dy_2}{du_1} = \frac{B_2(s)}{A_2(s)} \bullet \frac{B_1(s)}{A_1(s)} = \frac{s + 3au_2^2}{s} \bullet \frac{1}{s + 3ay_1^2} \ . \tag{18}$$

Because the signal flows from Σ_1 to Σ_2, then $du_2 = dy_1$. So equation (18) can be written to

$$G(s) = \frac{s + 3ay_1^2}{s} \bullet \frac{1}{s + 3ay_1^2} \ . \tag{19}$$

According to non-commutative multiplication equation (19) changes to

$$G(s) = 1 \Big/ s \ . \tag{20}$$

Then the tandem composite system Σ_{12} is structural controllable.

It is easy to verify that tandem composite system Σ_{21} is structural controllable, but the transfer function is different to that of Σ_{12}.

Now let us consider these two subsystems with different parameters as follow:

$$\Sigma_a: \quad \dot{y}_1 + ay_1^3 - u_1 = 0 \qquad \Sigma_b: \quad \dot{y}_2 - \dot{u}_2 - bu_2^3 = 0$$

Let us consider the tandem system Σ_{ab} only, the transfer function is

$$G_{ab}(s) = \frac{dy_2}{du_1} = \frac{s + 3bu_2^2}{s} \bullet \frac{1}{s + 3ay_1^2} \ . \tag{21}$$

According to non-commutative multiplication, equation (21) changes to

$$G_{ab}(s) = \frac{\alpha(s)}{\beta(s)s}$$

According to Lemma 1 it is known that $\beta(s)(s+3bu_2^2) = \alpha(s)(s+3ay_1^2)$, then $\alpha(s) \in F[s,b]$, $\beta(s) \in F[s,a]$. By calculation we know that $\alpha(s)$ and $\beta(s)$ are one-order polynomials in s, so $\alpha(s)$ and $\beta(s)$ have no common left divisor, no mater the common left divisor over $F[s;\sigma,\delta]$. So the tandem system $\sum_{ab}$ is structural controllable.

5 Conclusions

In this paper structural controllability of SISO nonlinear systems is analyzed with the help of transfer function and parameter space. Controllability of tandem and parallel composite nonlinear systems are also researched. Since the non-commutation of transfer function of nonlinear systems, the controllability conditions of linear systems in frequency domain are not extended to nonlinear case simply. We also give the new definition that the field of meromorphic functions with multi-parameter $K(z)$ and skew polynomial ring with multi-parameter, which establish the whole mathematic framework for explore the properties of nonlinear systems. We can use the structural properties, which can show the effects of parameters on systems, to analyze and design the nonlinear systems.

References

1. Sussmann, H.J., Jurdjevic, V.: Controllability of nonlinear systems. J. Differential Equations 12, 95–116 (1972)
2. Sussmann, H.: Lie brackets and local controllability: a sufficient condition for scalar inputSystems. SIAM Journal on Control and Optimization (21), 686–713 (1983)
3. Stefani, G.: On the local controllability of a scalar input control system. In: Birnes, C., Lindquist, A. (eds.) Theory and Applications of Nonlinear Control Systems, pp. 167–176. North Holland, Amsterdam (1986)
4. Zheng, Y., Cao, L.: Transfer function description for nonlinear systems. Journal of East China Normal University (Natural science) 2, 15–26 (1995)
5. Zheng, Y., Willems, J., Zhang, C.: A polynomial approach to nonlinear system controllability. IEEE Transactions on Automatic Control 46, 1782–1788 (2001)
6. Halas, M., Kotta, Ü.: Extension of the concept of transfer function to discrete-time nonlinear control systems. In: European Control Conference, Kos, Greece (2007)
7. Fradellos, G., Rapanakis, M., Evans, F.J.: Structural controllability in non-linear systems. Inter. J. Systems Science 8, 915–932 (1977)
8. Ma, Q.: Some results on structural controllability of nonlinear systems. In: Proceeding of 2010 International Conference on Intelligent Systems Design and Engineering Appilications, ISDEA 2010 (2010) (to appear)

Surface Energy Analysis for Study on Biomimetic Materials for Historic Stone Sculptures and Buildings

Qiang Liu*, Kunwei Zeng, Yongjun Liu, Hui Zhu, and Feiling Yang

Department of materials science and technology, Yunnan Key laboratory of nanomaterials & nanotechnology, Yunnan University, Kunming 650091, China
yusosliu@yahoo.com.cn

Abstract. The conservation of historic stone sculptures and buildings is receiving growing attention because of increasing bad weathering. In this paper, the surface energy analysis is applied to study the biomimetic conservation of the stone relics. The white stone surfaces were cleaned by some different organic solvents, modified by the organic template solutions with various concentrations and coated by protective films prepared through a biomimetic method. Moreover, their surface energies were tested. The surface treating technologies were optimized according to energy analysis and thus the optimal preprocessing technologies of protective materials' preparation were determined based on the principle of heterogeneous nucleation, which is a help for the further investigation on the conservation of some stone relics.

Keywords: Surface energy, Surface treatment, Stone conservation, Biomimetic.

1 Introduction

Historic stone buildings and sculptures are a sort of important cultural remains, which have been of great value in science, art and history. However, due to the corrosion of the stone materials, the further preservation of historic stones is endangered. Especially, the ageing process of historic sites is accelerating because of air pollution and acid rain during the past few decades, so their conservation is receiving growing attention and becoming a focus of research in many fields [1].

Until now, coating treatments on stones has been regarding as an effective and convenient method to retard corrosion. Coatings in the conservation of historic stones, which are largely provided by epoxies, acrylics, alkoxysilanes, silicones, fluorine-containing polymers, etc. can be used as a water-repellant, acid-repellant and consolidant to preserve damaged historic stones or to protect un-damaged historic stone [2]. Although these materials show excellent effects within first years, but they have some inadequacies and defects: shorter life, poorer compatibility, and change of the face of the treated stones [3]. Therefore, it is an urgent task and research focus now to explore new completely satisfying protective materials and methods which meet the conservation requirements of historic stones — "sympathetic conservation". Among them, the biomimetic protective materials have been represented a new

* Corresponding author.

D. Zeng (Ed.): Future Intelligent Information Systems, LNEE 86, pp. 417–423.
springerlink.com © Springer-Verlag Berlin Heidelberg 2011

prospective in stone conservation because of their unique features— uniform size, novel crystal morphology, specific crystallographic orientation, light weight, mechanically robust and unique functions, well compatibility [4].

However, compared with organic coating treatment on the stones, the biomimetic process is complex and complicated. In this work, in to investigate the regularity and achieve the process conditions, the changes of sample's surface energy in the process of preparing the biomimetic materials for stone conservation were studied, and the surface treating technologies in the various steps were optimized according to energy analysis, which can help the further investigation on the surface of some stone relics.

2 Theories

2.1 Principle of Biomineraliztion and Biomimetics Syntheses

Biomineralization is a natural approach to advanced materials synthesis, by which various forms of laminated nanocomposites (e.g., egg and mollusk shells, crustacean carapaces, diatoms, exoskeleton and spines, sponge spicules, pearls, corals, bones and teeth) are synthesized by living organisms. These structures are formed through template-assisted self-assembly, in which self-assembled organic material form the structural scaffolding for the deposition of inorganic material. They are hierarchically structured composites in which soft organic materials are organized on length scales of 1 to 100 nm and used as frameworks for specifically oriented and shaped inorganic crystals. In some cases, structurally organized organic surfaces catalytically or epitaxially induce growth of specifically oriented inorganic thin films [5].

Nature's way of processing is an invaluable guide to developing new synthetic processes that can produce useful film with similar designs. The first key aspect is the self-assembly of organic materials, which contain anionic functional groups, on the substrate to perform a function as template. Second, the nucleation and growth of inorganic materials is controlled in specific sites by the orienting and shaping action of the assembled organic template, and finally, inorganic minerals of higher order structures are consequently prepared [6].

The key requirement for successful film formation by biomimetic synthesis is to promote the formation of the inorganic phase on the substrate directly (that is, heterogeneous nucleation) and prevent the homogeneous nucleation of particles in the solution. According to the nucleation theory, the free energy change (ΔG) associated with the precipitation of an inorganic cluster from solution onto a surface is given by:

$$\Delta G = -RT\ln S + \sigma_{cl} + (\sigma_{cs} - \sigma_{sl})A_{cs}. \tag{1}$$

Where S represents the degree of supersaturation in the fluid; T is temperature; σ_{cl}, σ_{cs} and σ_{sl} represent the crystal/liquid, crystal/substrate, and substrate/liquid interfacial tension, respectively; and A_{cl} and A_{cs} represent the corresponding interfacial areas. When the interaction between the growing nucleus and substrate surface represents a lower interfacial energy than the crystal/solution interfacial energy [that is, $(\sigma_{cs} - \sigma_{sl}) \leq \sigma_{cl} A_{cl}$], heterogeneous nucleation is favored over homogeneous nucleation,

which can be carried out by surface chemical modification, such as surface functionalization which can provide some anionic functional groups as functional templates. These anionic functional groups include sulfonic group and carboxy group of acidic polysaccharide, carboxy group of protein, etc [7]. Furthermore, another important requirement for the biomimetic processing of thin films is to maintain relatively low levels of supersaturation during the precipitation process in order to minimize the amount of particle formation in bulk solution.

2.2 Solid Surface Energy

The double liquids are recommended for the determination of the solid surface energy. A commonly used approach to the solid surface energies is that of expressing any surface tension (γ) as a sum of components due to dispersive forces (γd) and polar forces (γ^p):

$$\gamma = \gamma^d + \gamma^p . \tag{2}$$

The interfacial tension between two phases α and β is then expressed in terms of the two components for each phase:

$$\gamma_{\alpha\beta} = \gamma_\alpha + \gamma_\beta - 2\left(\gamma_\alpha^d \gamma_\beta^d\right)^{1/2} - 2\left(\gamma_\alpha^p \gamma_\beta^p\right)^{1/2} . \tag{3}$$

For the case of a liquid (L) drop forming a contact angle (θ) on a solid (S) surface, the appropriate forms of Eq. (3) can be combined with Young's equation to give:

$$\gamma_L\left(1+\cos\theta_{LS}\right)/2 = \left(\gamma_L^d \gamma_S^d\right)^{1/2} + \left(\gamma_L^p \gamma_S^P\right)^{1/2} . \tag{4}$$

Since values for ($\gamma^d{}_L$) and ($\gamma^p{}_L$) are to be found in the literature for many liquids, there are two unknowns on the right of Eq. (4), $\gamma^d{}_S$ and $\gamma^p{}_S$, the components of the solid surface 'energy'. The determination of these components for the solid surface therefore requires contact angle data from at least two liquids of different polarity so that simultaneous versions of Eq. (4) can be solved [8]. In this method, to determine the solid surface energy along with the dispersive and polar components of the surface energy, a good selection of liquids must be made. This should include combination of dispersive and polar liquids with a wide range of surface energy as well as variable and different dispersive and polar components. In our experiment, the liquids are distilled water and diiodomethane (CH_2I_2), whose basic data is listed in table 1.

Table 1. Surface energy of the standard testing liquid (unit: mN/m)

Liquid	γ_L^p	γ_L^d	γ_L	γ_L^p / γ_L^d
H_2O	51	21.8	72.8	2.36
CH_2I_2	2.3	48.5	50.8	0.05

3 Experimental Details

3.1 Materials and Reagents

The analytically pure reagents including ethyl alcohol (C_2H_5OH), propyl alcohol (C_3H_7OH), acetone (CH_3COCH_3), butanone ($CH_3COC_2H_5$), calcium chloride ($CaCl_2$) and potassium oxalate ($K_2C_2O_4$) were used for this study. Chondroitin sulfate (chemical formula: — $(C_{14}H_{21}NO_{15}S)_n$—, abbreviated formula: CS, ≥95.0% assay) was commercially available. White marble at the size of 5 cm × 5 cm × 2 cm was selected as sample stone. All water solvents were distilled before use.

3.2 Methods

Surface Cleaning. Sample stones were washed by flowing water and cleaned by distilled water, then soaked in organic solvents for hours. The cleaned stones were taken out and dried. At last, the surface energy of treated stones was tested.

Surface Modification. The CS solutions with various concentrations were made up. The CS solutions were dripped on the cleaned stone and dribbled naturally, and then the surface energy of stones was also tested.

Preparation of Films. The stock solutions of $CaCl_2$ and $K_2C_2O_4$ reactants of light concentration were made up, and then filtered to remove undesirable nucleus of crystallization. After the stones were cleaned and modified, the stock solutions of $CaCl_2$ and $K_2C_2O_4$ reactants was dripped on it in succession and dribbled naturally. The crystallization of calcium oxalate was induced by CS to form film at room temperature. Operating repeatedly, the film became thicker and thicker. Finally, their surface energy was tested.

4 Results and Discussions

4.1 Effects of Organic Solvents

The surface state of substrates is a key influence on the structure and performance of films grown on the substrates, so it is necessary to treat the substrate some treatments, such as cleaning and modification.

During the process of stone conservation, the cleaning operation involves: (1) water washing, by which some dust and soluble substance are removed; (2) organic solvent washing, by which some insoluble organic materials are also removed.

The effects of organic solvents on the treated stone surface energy can be indicated as shown in figure 1. The surface energy of stones washed by organic solvents is increased. The stone treated by ethyl alcohol has a maximum increase in surface energy because the polarity of alcohol is the most strong among the selected organic solvents. Moreover, the alcohol has more hydroxyl groups which will conveniently link the organic templates to stones. In this way, the washing effectiveness of organic solvents can be indicated quantitatively through an index of surface energy.

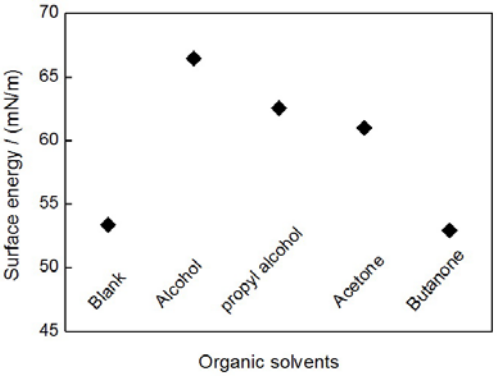

Fig. 1. Effects of organic solvent washing on the stone surface energy

4.2 Effects of Organic Templates

A series of CS solutions with different concentrations was applied to modify the surface of stones. The treating ways involve brushing and soaking. The surface energy of treated stones is shown in figure 2. It is concluded that the surface energy of stones, which are not only brushed but soaked, can be improved. Especially, the soaking way is more efficient than the brushing way because, during the soaking process, the stones are in full contact with the CS solution and the organic templates of CS are deposited on the stone surface uniformly and orderly. When the CS solution concentration is low, the surface energy of stones increases quickly; while the CS solution concentration reached a certain degree, the stone surface energy can be retain an optimum level because all of the stone surface are coated by the organic templates. The similar results are brought about when the CS solution is brushed over the stones. It is also found that when the optimum is achieved, the surface energy will decrease if the coating operation is kept up, because the excessive templates would interfere with the action of the previously-coated templates. Obviously, the optimum surface treatments can be achieved by application of surface energy analysis.

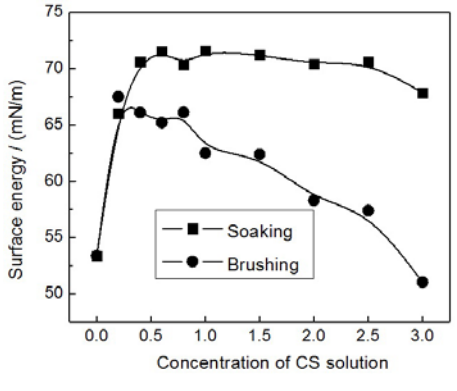

Fig. 2. Effects of the CS solution concentration on the stone surface energy

4.3 Change of Surface Energy in the Preparing Process of Biomimetic Films

Figure 3 shows the change of the stone's surface energy in the preparing process. It is indicated that the stone surface energy increases after being cleaned and modified, which makes for better mineralization. When the film is prepared on the stone, the surface energy maintains a relative low level, which makes for better performances.

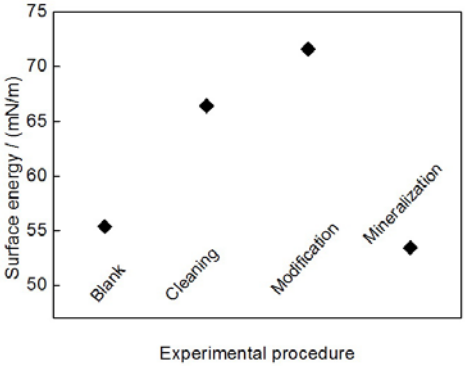

Fig. 3. Change of surface energy during the process of biomimetic synthesis

5 Conclusions

The surface energy analysis is an important method by which the energy relationship in the process of solider surface treatment can be indicated quantitatively. In this work, in order to study the stone conservation through the biomimetic method, the surface energy of stones washed by organic solvents was tested firstly based on the free energy change rule during the crystal growth process. The results show that the stone surface energy washed by ethanol is increased at the most. And then, the washed stones were modified with a series of different concentrations of CS organic template. The surface energy analysis results show that the concentration of 1% is optimum. Under these conditions, according to principles of biomineralization, the protective film of calcium oxalate was synthesised. The protective film's surface energy reaches the minimum for the whole process, which can result in a significant improvement in the main protecting performances including soil-resistance and acid-resistance.

Acknowledgement

This work was supported by grants from the National Natural Science Foundation of China (No. 50963005), the Youth Foundation on Humanities and Social Sciences of Chinese Education Ministry (07JC850006), the Provincial Natural Science Foundation of Yunnan (2007E160M and 08Z0008), and the Scholastic Natural Science Foundation of Yunnan University (2009E26Q).

References

1. Liu, Q., Zhang, B.: Syntheses of a novel nanomaterial for conservation of historic stones inspired by nature. Mater. Lett. 61, 4976–4979 (2007)
2. Price, C.: Stone conservation. Getty Conservation Institute, Los Angeles (1996)
3. Striegel, M.F., Guin, E.B., Hallett, K., et al.: Air pollution, coatings, and cultural resources. Prog. Org. Coat. 48, 281–288 (2003)
4. Liu, Q., Zhang, B., et al.: A crude protective film on historic stones and its artificial preparation through biomimetic synthesis. Appl. Surf. Sci. 253, 2625–2632 (2006)
5. Yao, N., Epstein, A.K., Liu, W.W., et al.: Organic-inorganic interfaces and spiral growth in nacre. J. R. Soc. Interface 6, 367–376 (2009)
6. Aksay, I.A., Trau, M., Manne, S.: Biomimetic Pathways for Assembling Inorganic Thin Films. Science 273, 892–898 (1996)
7. Fendler, J. H.: Biomineralization Inspired Preparation of Nanoparticles and Nanoparticulate Films. Curr. Opin. Solid STM 2, 365–369 (1997)
8. Al-Turaif, H., Bousfield, D.W.: The influence of substrate absorbency on coating surface energy. Prog. Org. Coat. 49, 62–68 (2004)

3D Localization of Moving Object by High-Speed Four-Camera Vision System

Ye Tian, Xiaopeng Chen, Qiang Huang, Peng Lv, Rui Li, and Min Li

Intelligent Robotics Institute of Mechatronical Engineering School,
Beijing Institute of Technology,
5 Nandajie, Zhongguancun, Haidian, Beijing, China
{tianye7248,xpchen,qhuang,hellolp,lirui,min}@bit.edu.cn

Abstract. Take the flying ping-pong ball as an example, this paper focuses on 3D localization of moving object based on a high-speed and high-precision vision system. The vision system is composed of two stereo pairs, and each pair stares at half of the table. The advantage of the system is that: it can redouble the precision while covering the same field of vision. In order to obtain the 3D positions of the whole trajectory, each stereo pair is first off-line calibrated. And then the online process is to detect the 2D position and reconstruct the 3D position of the ping-pong ball in each image frame. The detection process using circularity, color as well as motion features. Multiple visual features fusion method is applied to improve robustness. After 3D reconstruction, the final trajectories are merged from positions obtained by the two stereo pairs. Experiments show the feasibility of the system.

Keywords: 3D localization, high-speed moving object, object detection, four-camera vision system.

1 Introduction

The ping-pong robot amalgamates multi-subjects, such as: camera calibration, high-speed moving object detection, 3D reconstruction, trajectory prediction, hitting strategy, motion control and so on. Many scholars spent a great deal of energy on this area. The ping-pong robot ROXY-1 developed by Homer Liu of Japan quantum vision Cop. adopted the manipulator SCARA with four DOFs and two cameras. It could play ping-pong with people at some specific conditions [1]. The ping-pong robot developed by Fumio Miyazaki of Osaka University adopted binocular vision to capture the flying ping-pong trajectories, and a PC was used to control the manipulator to hit the ping-pong back quickly, flexibly and accurately [2]. Research of ping-pong robots in China began later on. The ping-pong robot developed by Yuanhui Zhang [3] used a single camera to reconstruct the 3D position of the ping-pong ball by the images of the ping-pong and its shadow. Zhengtao Zhang proposed a high-speed vision system and object tracing algorithm of ping-pong robot based on smart cameras [4].

A ping-pong robot is a hand-eye coordinate system. It is composed of a vision system, a robot arm and a control system. The 3D localization of high-speed moving

D. Zeng (Ed.): Future Intelligent Information Systems, LNEE 86, pp. 425–434.
springerlink.com © Springer-Verlag Berlin Heidelberg 2011

object is vital for successful ball hitting task of a ping-pong robot. Usually, only the start part of the trajectory is captured by the vision system, and the remaining of the ping-pong trajectory is predicted by a trajectory prediction algorithm to save enough time for the robot arm to hit the ball. The errors from the vision system will be enlarged due to the prediction algorithm. Thus, the speed and precision of the vision system plays an important role. Paper [5] proposed an algorithm combining frame difference, sieving area and dynamic window to track high-speed moving object. The high-speed flying ping-pong can be detected quickly, but the ping-pong turned to crescent shape in the rising stage. The algorithm is sensitive to the background grayscale change. OTSU and region growing is used in Paper [6] to detect ping-pong ball. The method needs human computer interaction and its speed is not very fast. A pointolite and a monocular camera are used in paper [7] to track the flying ping-pong. The advantage of this method is that the system cost is low and the speed is fast, but the shadow is illegible because there is no ideal pointolite, the demand for environment is critical and the monocular camera's vision scope is small, all of which make the localization precision of the system low.

Unlike previous implementation, the system framework of four color high-speed cameras is used in this paper to redouble the precision while covering the same field of vision and to enable the vision data to be used by robots in both sides. The vision system is composed of two stereo pairs, and each pair stares at opposite side of the table. Each stereo pair is first off-line calibrated to obtain intrinsic and extrinsic parameters. In the on-line process, 2D position and 3D position of the high-speed ping-pong ball in each image frame are calculated. Circularity, color as well as motion features are used in the detection process. Multiple visual features fusion method is applied to improve robustness. After 3D reconstruction, the final trajectories are obtained from both stereo pairs.

The organization of this paper is listed as following: In section II, the system structure is described, and then the detection and localization for moving object based on the system framework of four color cameras is presented. The experiment results and analysis are presented in Section III. Section IV is the conclusion.

2 The Localization System for Moving Object

The high-speed and high-accuracy system for detection and localization of moving object based on four color cameras is shown in fig.1. In fig.1, camera 1, camera 2, camera 3 and camera 4 are four high-speed color cameras used to grab and transmit images to the vision processing computer 1. Camera 5 is a grayscale camera used to locate the manipulator by detecting the MARK on it. Manipulator 9 with 7DOFs is used to hit the ping-pong. There are 3DOFs in the shoulder, 1DOF in the wrist and 3DOFs in the elbow. As shown in fig.1, the origin of the world coordinate system is set in the corner close to the human player, the x-axis is along the short side of the table, the y axis is along the long side of the table, and the z-axis points to upright position. The signal generator 1 and 2 are used to synchronize the camera 1, 2 and 3, 4 respectively. The vision processing computer 1 does the image acquisition, image processing, reconstruction and trajectory prediction work, and then sends the candidate hitting position and time to the control computer by the wireless communicating module 1.

The vision computer 2 analyses and processes the images acquired by camera 5, and then sends the results to the control computer by the wireless communicating module 2. The control computer produces the hitting strategy according to the prediction results, and sends control commands to the manipulator for hitting the ping-pong according to the planned posture and speed.

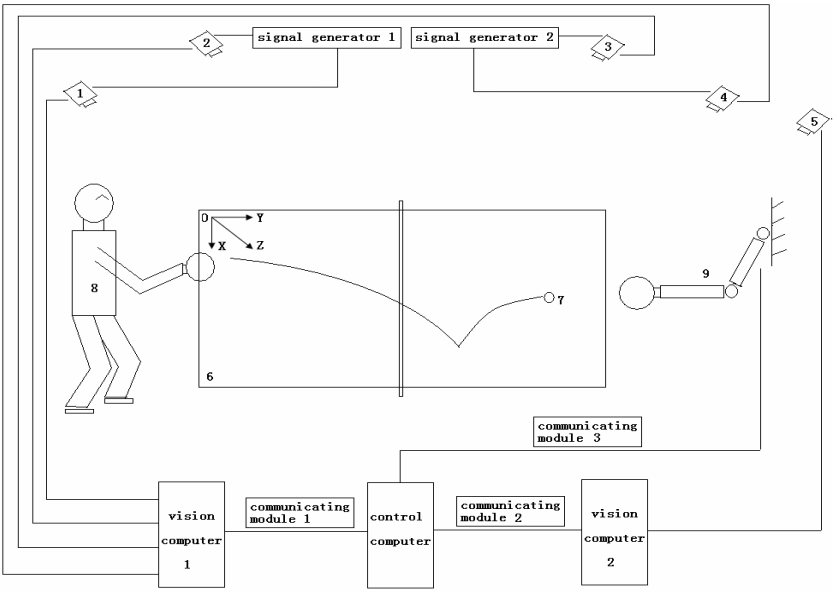

Fig. 1. Sketch of the system framework

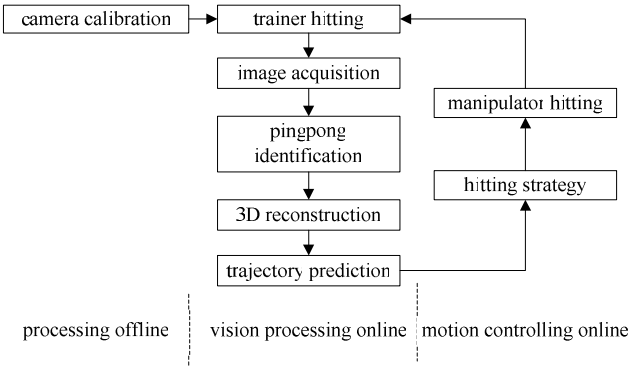

Fig. 2. Processing flowchart of the ping-pong robot

The processing flowchart of the ping-pong robot is shown in fig.2. First, the configuration of two stereo pairs based on vision system is proposed. Second, the offline camera calibration process is illustrated. Third, image acquisition and object

detection using multi features fusion is presented, and finally the ping-pong 3D trajectory extraction from two stereo pairs of camera 1, 2 and 3, 4 is illustrated. Using the prediction model and trajectory as input, the whole ping-pong trajectory can be predicted in several milliseconds. The control computer produces the hitting strategy in virtue of the visual prediction results, and controls the manipulator to hit the ping-pong according to the planned posture and speed.

2.1 The Configuration of Four Cameras' Vision System

For the ping-pong robots, the system frameworks of binocular vision and monocular vision with accessory equipment are very popular. However, there are two disadvantages: the vision scope is small, and usually only one half of the ping-pong table can be observed, the other half is not covered; if vision scope is expanded by changing the focus, the precision of the system will be reduced.

In order to solve the problems, a high-speed vision system framework based on four color cameras is proposed as shown in fig.1. In our vision system, high-speed color cameras are chosen for ping-pong ball trajectory recognition. The sample rate of the cameras can reach up to 200 frames per second, and the processing rate can reach up to 160 frames per second.

In the vision system, Camera 1 and 2 observe one half of the ping-pong table close to the training partner, camera 3 and 4 observe the other half of the ping-pong table close to the manipulator, so the whole ping-pong table can be observed and then the whole ping-pong trajectory can be detected by merging the data of the two stereo pairs. The advantage of the system is that: it can redouble the precision while covering the same field of vision; the symmetric configuration enables the trajectory to be used by robots in both sides; stare at opposite side so that the ball can not be occluded by player or robot.

2.2 Offline Camera Calibration Process

As shown in fig.1, in order to do 3D reconstruction of the moving object from corresponding image position pair in different half of the table respectively, the two pairs of cameras should first be calibrated respectively. Calibration is realized by the classical algorithm of Zhengyou Zhang [8, 9]. The pinhole camera model can be written as $s[u \quad v \quad 1]^T = K[r_1 \quad r_2 \quad r_3 \quad t][X \quad Y \quad 0 \quad 1]^T$, where K is the intrinsic matrix, $[X \quad Y \quad 0 \quad 1]^T$ is the homogeneous coordinate of the point on the calibration board, $[u \quad v \quad 1]^T$ is the homogeneous coordinate of the corresponding point on the image plane projected from the calibration plane, $[r_1 \quad r_2 \quad r_3]$ and t are the rotation matrix and translation vector of the world coordinate system relative to the camera coordinate system, which is the extrinsic parameters of the cameras.

Once the intrinsic and extrinsic matrixes of each camera are obtained, the relative pose of one camera relative to the other camera of the same stereo pair, which is also called stereo parameters, can be derived.

$$[R \quad T] = \left[R_r R_l^{-1} \quad T_r - R_r R_l^{-1} T_l\right] . \tag{1}$$

In our calibration experiment, $[R_l \quad T_l]$ is the extrinsic matrixes of the left camera, and $[R_r \quad T_r]$ is the extrinsic matrixes of the right camera, and $[R \quad T]$ is the relative pose of the left camera relative to the right camera. The calibrated parameters will be used in the 3D reconstruction.

2.3 Object Detection and Four Cameras' Switch

The features of the flying ping-pong: First, motion feature, the ping-pong's speed can reach up to 4-30m/s while people playing. Second, area and shape feature, they are fixed. Third, color feature, it is equable and single.

Process of the detection algorithm is shown in fig.3.

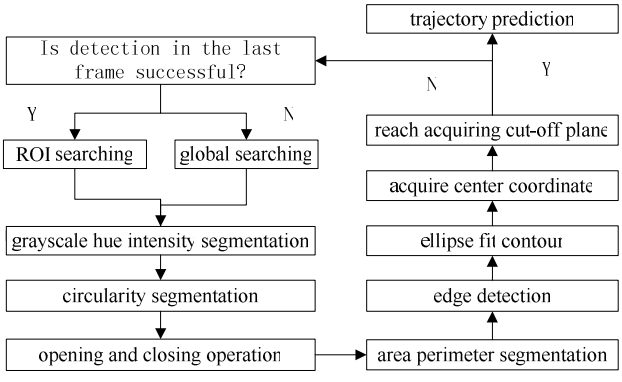

Fig. 3. Detection algorithm

First, a square zone around the ping-pong's last image position is taken as region of interest(ROI) to reduce the searching scope. The size of the square zone can be decided by the product of the ping-pong's highest speed and the average processing time per image.

HSV color model is used to reduce the impact of the intensity. By then, the region of interest is thresholded in each image channel. In our experiments, the threshold of saturation is in the range of [140, 255], the threshold of hue in [0, 70] and the threshold of intensity in [110, 255], and then the interesting area is separated from background. When the ping-pong flies fast, its color features vary a lot because of the disturbance from environment. The complicated background gave great impact on the detection. So color feature itself is not enough for detection.

Since the ping-pong is a sphere, and the focus in x axis and y axis are almost the same, the image of the ping-pong should be a circle. Thus the circularity threshold value in the range of [0.35, 1] can be used to choose the right area.

After that, opening and closing operation is used to corrode and bulge the isolated area of the image. This can help us remove noise and smooth the edge. The image size is 640×480. Measured by experiments, the ping-pong's area threshold value is set in the range of [100, 300], and perimeter in [30, 150]. Using the area and perimeter information, we can detect the ping-pong area finally.

Finally, the ping-pong's edge is abstracted by canny operator. And then the contour of the edge is fit by an ellipse. The center of the ellipse is taken as the ping-pong position in the image frame. The detection method of multiple visual features fusion is simple, fast, accurate and robust. Experiments prove that it has a good effect.

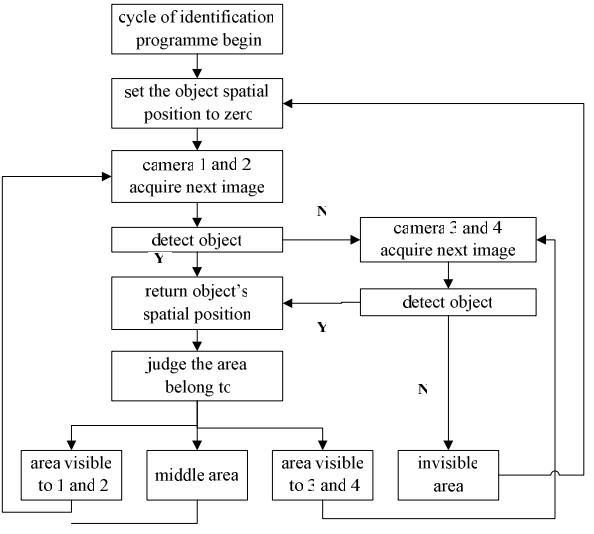

Fig. 4. Camera pair switching algorithm

In order to obtain the whole trajectory, we should merge data from different stereo pair. The ping-pong table is divided into four areas: the area only visible to the camera 1 and 2, the area only visible to the camera 3 and 4, and the middle area which is visible to both pairs and the invisible area. Only one pair of cameras is used to acquire images and detect object at a time. Which pair of cameras can be used to acquire the next image is decided by the area the ping-pong belongs to in current frame. The rule is as following: In each process loop, when the ping-pong belongs to the middle area, all of the two pairs of the cameras can see the object, camera 1 and 2 is preferred; when the ping-pong belongs to the area only covered by camera 1 and 2, camera 1 and 2 is preferred; when the ping-pong belongs to the area only covered by camera 3 and 4, camera 3 and 4 is preferred. This is a way to reduce process time and so speed up the vision process. The cameras 1-4 are triggered by the signal generators 1, 2 to realize the synchronization of acquiring images. Both of the two pairs of cameras use the system time of the vision computer 1 as standard to record the absolute grabing time. See figure 4 for detail.

2.4 3D Trajectory Extraction

With camera parameters, 3D reconstruction of the moving object can be done easily from the ping-pong's image coordinate. This is done by solving the linear equation

$$\begin{cases} x_l = P_l M \\ x_r = P_r M \end{cases} . \tag{2}$$

where x_l, x_r is the 2D coordinate in the left and right camera frames, P_l, P_r is the extrinsic matrixes of the left and right camera, and M is the 3D coordinate in the world frame.

Thus the whole trajectory is obtained from the image frames.

3 Experiments

Sketch of the high-speed and high accuracy system for detection and localization of moving object based on four color cameras is shown in fig.1. In fig.1, the four external cameras 1-4 are high-speed color cameras with speed reaching up to 200 fps and resolution of 640×480. The standard ping-pong table 6 parallels to the horizontal plane, and its size is 2.74×1.525 (unit: m). The standard ping-pong 7's weight is 2.7g, and its radius is 0.02m. The vision computer 1 adopts PC with WINDOWS XP, 3GB RAM, 3 GHZ Intel(R) Core(TM)2 Quad processor and the independent video card of NVIDIA GeForce 210, and its processing rate can reach 160 frm/s. The control computer uses industrial PC with RT-LINUX.

3.1 Four Cameras' Calibration

By virtue of the operators of the HALCON software, the calibration results can be obtained by the Zhengyou Zhang's algorithm [8, 9].

For 3D reconstruction, the transformation matrix from the world coordinate system to the coordinate system of the cameras 1 and 2 is

$$R_{w12} = [294.66 \quad 354.23 \quad 252.95], \; T_{w12} = [-0.35 \quad 0.30 \quad 3.70] \quad . \tag{3}$$

The transformation matrix from the world coordinate system to the coordinate system of the cameras 3 and 4 is

$$R_{w34} = [297.76 \quad 349.34 \quad 76.09], \; T_{w34} = [-0.19 \quad 0.27 \quad 3.39] \quad . \tag{4}$$

The unit of the rotation matrix R is degree, and the translation vector is meter.

3.2 Object Detection

On the experiment platform as shown in fig.1, the external high-speed color cameras 1 and 2 grab the images of half of the ping-pong table close to the human player, and the detection algorithm described in section 2 is used to detect the ping-pong ball.

A group of experiment results of the detection process is shown in fig.5. These pictures demonstrate the process of the detection algorithm and the result after each step. Picture (a) is the origin image the camera 1 acquired; picture (b) is the reduced image by applying region of interest ; picture (c) is the image after color feature thresholding; picture (d) is the image after circularity thresholding; picture (e) is the filtered image after morphological operators, openning and closing. The region which

is within the area and perimeter range is taken as ping-pong; picture (f) is the edge image after canny edge detection; picture (g) is the fitted elliptic outline of ping-pong finally. The ping-pong's center coordinate is obtained. In this experiment, the minor axis of the ellipse had 9 pixels, the major had 10 pixels.

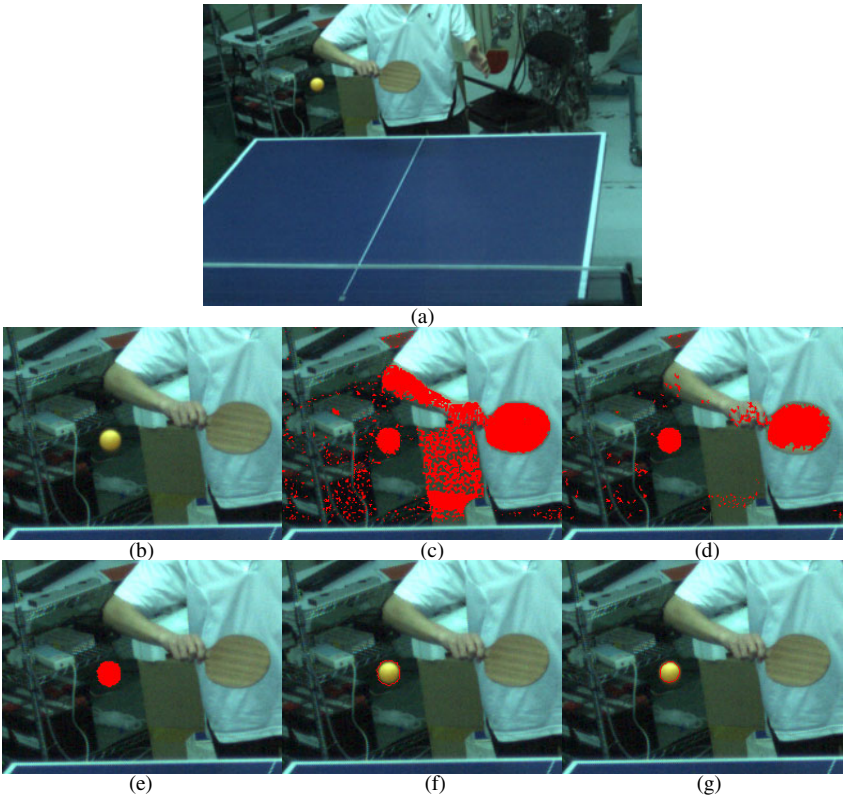

Fig. 5. Image processing

From the experiments, we know that camera 1 and 2 observe half of the ping-pong table close to the human player. Compared with observing the whole table, the cameras' field of vision is smaller, and so the distortion is reduced and the precision is higher in theory. The localization precision of the system measured by a *motion capture* system is 1-3mm. Usually, the processing rate of detection and localization can reach 160 frm/s, and the time used for image grabing, object detection and localization is about 110 us. The performance can meet the system demand to the speed of image processing and save enough time for the following trajectory prediction and manipulator controlling process.

From the analysis of the experiments above, we can infer that the multiple visual features fusion based on detection method satisfies the critical demand for robustness and speed.

3.3 3D Reconstruction Experiments for Comparison

Several trajectories of the flying ping-pong ball are recorded by our vision system. They are compared with trajectories captured by the vision system in paper [5]. One pair of them are shown in fig.6, picture (a) is the trajectory captured by our vision system, while picture (b) is the trajectory captured by paper [5]'s vision system.

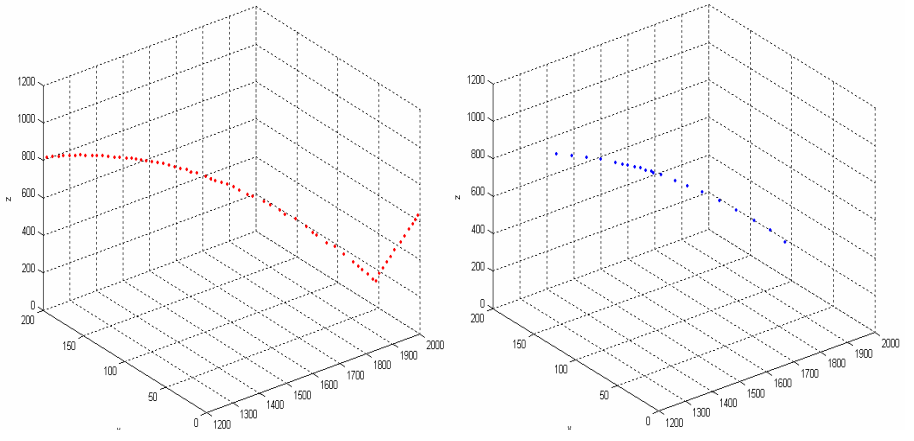

Fig. 6. Comparison experiments

From fig.6, we know that the four cameras based on vision system can expand the vision scope, and observe the whole trajectory of the ping-pong passing over the table, but the binocular vision can only realize the observation for half of the ping-pong table. The flying trajectory captured by our vision system is smooth, the trajectory points are dense and dispose evenly. The algorithm is fast, accurate and robust to noise.

4 Conclusion

Take the ping-pong as an example, this paper presented a high-speed four color cameras' vision system and the detection algorithm to capture moving object's three dimensional trajectory fast and precisely for robot ping-pong players.

First, a vision system framework which is composed of four high-speed color cameras is presented to capture the whole flying trajectory of the ping-pong without losing precision.

Second, ping-pong ball detection algorithm based on multiple visual features fusion is proposed for fast and precise localization for the ping-pong.

Acknowledgments. This work is partially supported by the Hi-tech Research and Development Program of China, grant number is 2007AA04Z241, 2007AA041603 and 2008AA042601, National Natural Science Foundation of China under Grant 60874048, 60925014 and 60705025, and "111 Project" under Grant B08043.

References

1. Wilson, A.: Vision-based robot/human Ping-Pong. Vision Systems Design. 13(2), 21–22 (2008)
2. Miyazaki, F., Matsushima, M., Takeuchi, M.: Learning to Dynamically Manipulate: A Table Tennis Robot Controls a Ball and Rallies with a Human Being. Advances in Robot Control (2006)
3. Zhang, Y., Wei, W., Yu, D., Peng, B.: Shadow Based Single Camera Vision System Calibration. Journal of Image and Graphics 14(9), 1895–1899 (2009)
4. Zhang, Z., Xu, D.: High-Speed Vision System Based on Smart Camera and Its Target Tracking Algorithm. J. Robot. 31(3), 229–234 (2009)
5. Zhang, Z.: Vision Measure and Control for Ping-pong Robot. Institute of Automation, Chinese Academy of Sciences, Beijing (2010)
6. Li, X., Song, C., Liu, H.: Binocular Vision Measurement Applied in Analysis of Speed of Table-tennis. J. Computer Sicience 35(3), 256–257 (2008)
7. Sensen, D.: The Design of Machine Vision for Ping-pong Robot Based on PC. Zhejiang University, Hangzhou (2006)
8. Zhang, Z.: A flexible new technique for camera calibration. IEEE Trans. on Pattern Analysis And Machine Intelligence 22(11), 1330–1334 (2000)
9. Zhang, Z.: Flexible camera calibration by viewing a plane from unknown orientations. In: Proceedings of IEEE International Conference on Computer Vision, vol. 11(1), pp. 666–673 (1999)

A Refractive Index Sensor Based on Microinterferometric Backscatter

Haifeng Wang and Yingchun Ding

Department of Physics, Beijing University of Chemical Technology, Beijing 100029, China
dingyc@mail.buct.edu.cn

Abstract. Refractive index (RI) detection is a common technique used in chemical and biochemical analysis. Rapid monitoring and refractive detection of ultra small volume samples are in great demand. However, it is still a significant challenge for highly precise and miniature detectors to measure ultra small volume samples. This paper will present a flexible method to record the interference fringes which are caused by backscatter with a new linear CCD; furthermore, it will get the information of refractive index by tracking the displacement of fringes with FFT analysis. With this approach, we have been able to obtain detection limits of $2.44\times10^{-7}\triangle$n, corresponding to 1.37×10^{-6} g/mL.

Keywords: Microinterferometric backscatter detector (MIBD), interference fringes, CCD, refractive index (RI).

1 Introduction

Refractive index detection, which is used in chemical and biochemical analysis, is a common technique. Rapid monitoring and refractive detection of ultra small volume samples are in great demand. It can be seen in two major areas of environmental monitoring and care disease detection. This demand covers a huge range of applications, such as drinking water and food quality. So far, several detection techniques have been used to measure change in refractive index of small amounts of analyte, and they are all on the basis of interferometry, waveguiding effect and forward scattering [1]. However, they have their own drawbacks even though some of them produce excellent detection limits. Forward scattering methods are well-suited for working with nanoliter probe volumes, but they use a single pass optical train and are limited in resolution. The waveguiding methods have obvious small probe volumes, but they require long lengths of the waveguide to be interrogated. In large volume flow cells and detection limits, these results are poorer than the methods of interference and scatter [2]. To solve the problems, a late-model common refractive index detector based on backscatter interferometry, which is called the micro-interferometric backscatter detector (MIBD), has been developed in our lab.

Microinterferometric backscatter detector (MIBD) is one of analytical methods, and it relies on the observation that coherent light impinging on a cylindrically shaped object produces a highly modulated interference pattern (Fig. 1). MIBD analyzes

D. Zeng (Ed.): Future Intelligent Information Systems, LNEE 86, pp. 435–441.
springerlink.com © Springer-Verlag Berlin Heidelberg 2011

re-flections from a capillary tube filled with a liquid which is aimed for refractive index measurement. Bornhop is the first person who used and described this technique. In his study, MIBD was capable of measuring changes in refractive index of liquids on the order of 10^{-8} RIU [3] and [4].

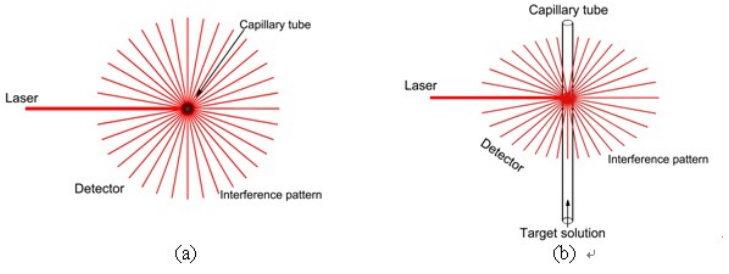

Fig. 1. Schematic view of the experimental setup seen isometric (a) and from the top (b)

2 Principle and Model of Experiment

When a laser beam impinges on a capillary tube, it causes the light to be refracted and reflected at each optical interface due to the different refractive indexes of capillary layers. The solutions of different refractive indexes within the capillary tube cause different interference patterns. As a result of this phenomenon, it produces a fan of scattered light consisting of high contrast light and dark spots. The scattered light is perpendicular to the central axis of the capillary tube. As the refractive index of the solution changes within the capillary tube, the interference fringes are changed because of the difference in optical path length [5]. In other words, we can get the information of refractive index by tracking the displacement of fringes. It is well known that the refractive index of solution is corresponding to its concentration, so we can also get the information of solution concentration.

Because the spatial intensity distribution of backscattered interference fringe pattern is relative to the refractive index of the targeted solution. Some methods are designed based on this phenomenon. These methods include the followings [6]:

(a) A regular PIN photodiode;
(b) A precision air slit;
(c) An area avalanche photodiode;
(d) A CCD camera connected to a laser beam analyzer (LBA);
(e) A CCD array with Fourier analysis.

Each of these fringe position quantification methods has limitations and advantages. For example, by detecting the intensity of interference fringes with a photodetector, the detection limits of refractive index is found to be on the order of 10^{-6} RIU. However, this method has many drawbacks, one of which is particularly sensitive to the stability of the source. Since the displacement of fringes is obtained by measuring changes in light intensity indirectly, any changes from source cause a series of movements of fringes, and it is resulting in appreciable measurement error. This drawback

can be solved by many ways and all solutions are based on detection of the fringes pattern position directly. In this paper, we present a flexible method to directly record the placement of interference fringes which are caused by backscatter with a new linear CCD [7] and [8].

After comprehensive consideration of the experiment, we have designed the experi-mental structure diagram (Fig. 2).

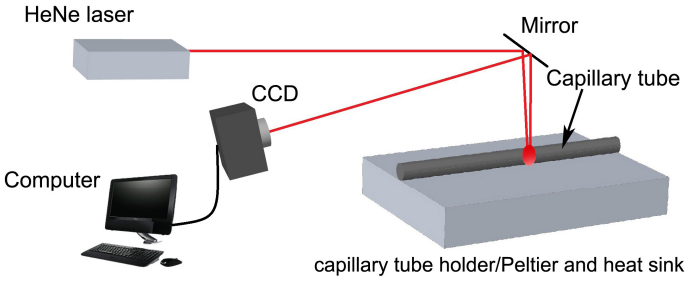

Fig. 2. Block diagram of the experimental setup

3 Experimental Setup

According to the experimental structure diagram, we build the experimental setup shown in Fig. 3. A external cavity He-Ne laser (DHC, DH-HN 1200) operating at 632.8 nm, producing a beam diameter of 1.1 mm, is directed onto a mirror, and then it impinges perpendicularly onto the capillary tube directly which is mounted on a tem-perature control platform. The Capillary tube used in the experiments was purchased from Polymicro Technologies. The dimension of the capillary tube is 531μm inner diameter (ID), 665μm outer diameter (OD) with a 24μm thick polyimid coating (TSP530660). The backscatter interference pattern is directed onto the mirror, and then it is recorded by a new linear CCD (Microvision, MV-VS142FM/FC).

For the He-Ne laser, the requirements are a coherence length of at least twice the diameter of capillary tube and a wavelength at which capillary tube is transparent. In the experimental measurements, the primary source of noise is caused by temperature fluctuations. For most liquids, they all have a relatively high thermal coefficient (dn/dt), such as the thermal coefficient of water is on the order of $8\times10^{-4}℃^{-1}$ and the NaCl is on the order of $1.2\times10^{-4}℃^{-1}$ [9] and [10]. If temperature will be more stable, the experimental data is more accurate. For the temperature controller which is designed by us, the temperature fluctuations can be stabilized within 0.05℃.

In the experiment, we chose NaCl as a target solution. According to the exp-eriment, we have configured seven solutions of different concentrations. Their con-centrations are 0%, 0.496%, 1.997%, 3.986%, 7.999%, 8.991% and 11.637% res-pectively; furthermore, they represent different kinds of refractive indexes.

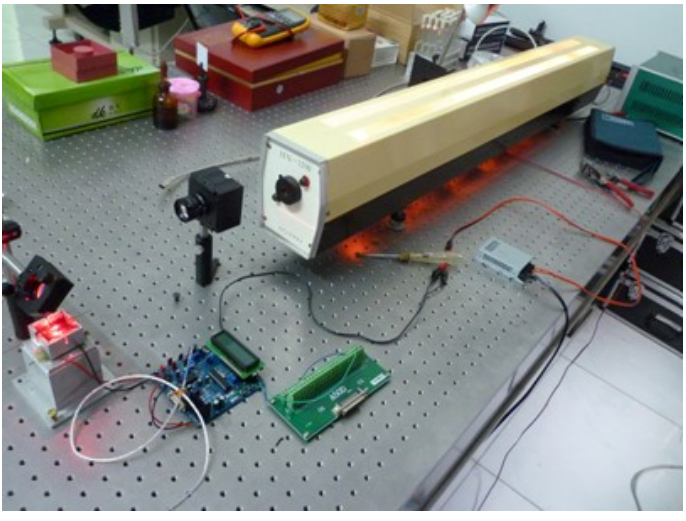

Fig. 3. The laboratory setup of the late-model common refractive index detector

4 Results and Discussion

According to the previous structure of the experimental setup, we set the experimental temperature as 27℃ and adjusted the optical path to a suitable location. We have measured the above-mentioned target solutions and recorded the interference patterns with a new linear CCD. Fig. 4 shows that the interference patterns of deionized water solution and NaCl solution. Their concentrations are 0% and 1.997% respectively.

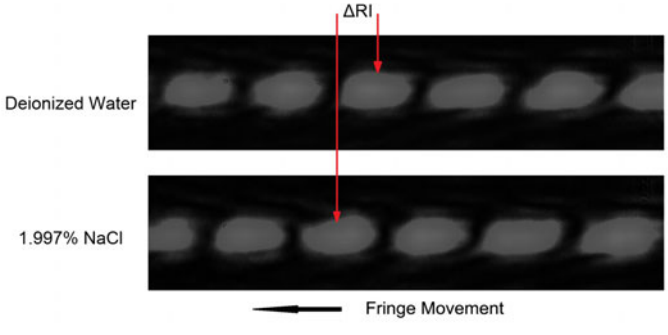

Fig. 4. The interference patterns of deionized water and NaCl

As the temperature is 27℃, their refractive indexes are 1.33373 and 1.33728 res-pectively. It can be seen from Fig.4 that the backscattered interference fringes shift to the left. There have been several experiments were introduced to estimate the behavior of the MIBD system with FFT analysis of interference fringe displacements. Fig. 5 is the Fourier spectra of the fringe patterns corresponding to two different

refractive indexes of the target solutions contained within the capillary. In the Fourier domain, there is only one obvious Fourier peak for the fringe patterns. Since there is no change in shape and spatial frequency of the different fringe patterns which are caused by introducing the solutions of different refractive indexes into capillary tube, and the location of the peak do not change. This is the consistent as we expected. Fig. 5 shows that the Fourier spectrums are basically overlapped as we introduced the NaCl solutions of the refractive indexes of 1.33373 and 1.33728 into capillary tube respectively, and it is also verified that the above conclusions are correct.

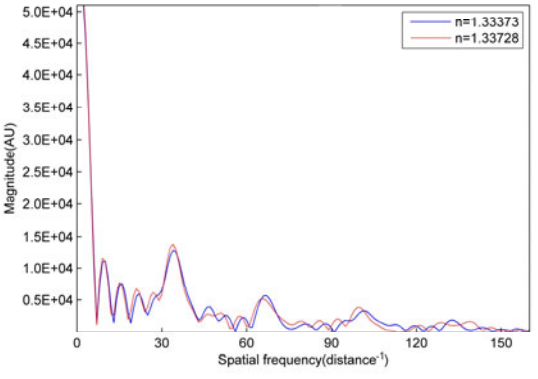

Fig. 5. The Fourier spectrums of interference patterns corresponding to two different refractive indexes of the target solutions

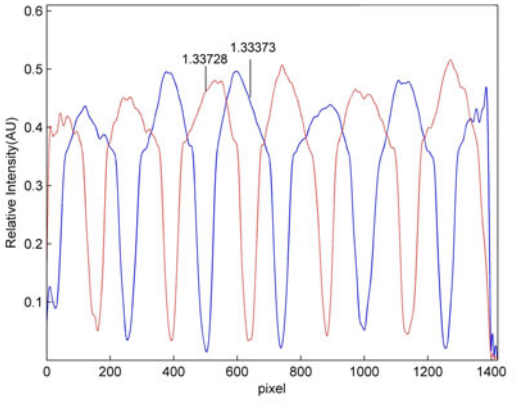

Fig. 6. The relative intensity profiles of two different concentrations of NaCl solutions

Using Matlab mathematical software (Version 7.1) to process images, the relative intensity profiles of two different concentrations of NaCl solutions are obtained with the FFT filtering. In Fig. 6, the horizontal axis represents the pixel number and the vertical axis is normalized to the relative intensity. It is can be seen from Fig. 6, when

the concentration is increased (correspond to refractive index is increased), the profile moves to the left, and all fringes have the similar position sensitivity. The peak of third fringe is at pix number 598 and the refractive index of that solution is 1.33373. The peak of third fringe moved to pix number 572 when its refractive index is changed to 1.33728.

The calibration curves of the fringe response vs. the different refractive indexes are obtained using the representative fringe. The concentrations of the target solutions are 0%, 0.496%, 1.997%, 3.986%, 7.999%, 8.991% and 11.637% respectively, and they represent the refractive indexes of 1.33373, 1.33461, 1.33728, 1.34080, 1.34793, 1.34969 and 1.35438.The results of these measurements are illustrated in Fig.7. The experimental data are conducted to use a linear fit, and r^2 is 0.999. It means that the experimental data is reliable. With our calculation, σ is found to be 0.0081 and it is the average of the standard deviation for refractive indexes. The slope, α, of the best fitted line (r^2= 0.999) is 99510, which with 3σ statistics gives a detection limits found to be $2.44\times10^{-7}\triangle$n, corresponding to 1.37×10^{-6} g/mL.

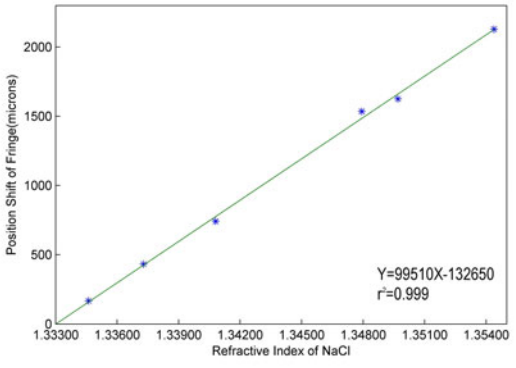

Fig. 7. The calibration curves of the fringe response vs. the different refractive indexes

5 Conclusions

A method for determining change in the MIBD fringe patterns with a new Linear CCD has been demonstrated. In the theoretical modeling of the MIBD, the detection limits is predicted better than $10^{-8}\triangle$n. In experiment, we have been able to obtain detection limits of $2.44\times10^{-7}\triangle$n, corresponding to 1.37×10^{-6} g/mL. If the experimental noise, such as thermal perturbation and environmental effects, is controlled at a minimal range of fluctuations, the theoretically predicted detection limits could be achieved.

Acknowledgment

This work was supported by National Natural Science Foundation of China under the grants 60978006.

References

1. Valcarcel, M., Cardenas, S.: We Need Reliable Ways to Bypass Preliminary Operations in (Bio) Chemical Measurement. Anal. Chem. 21, 211–212 (2002)
2. Markov, D., Begari, D., Bornhop, D.J.: Breaking the 10^{-7} Barrier for RI Measurements in Nanoliter Volumes. Anal. Chem. 74, 5438–5441 (2002)
3. Bornhop, D.J.: Microvolume Index of Refraction Determinations by Interferometric Backscatter. Appl. Opt. 34, 3234–3239 (1995)
4. Markov, D.A., Swinney, K., Bornhop, D.J.: Label-free Molecular Interaction Determinations with Nanoscale Interferometry. Journal of the American Chemical Society 126, 16659–16664 (2004)
5. Bornhop, D.J., Latham, J.C., Kussrow, A., Markov, D.A., Jones, R.D.: Free-solution, Label-free Molecular Interactions Studied by Backscattering Interferometry. Science 317, 1732–1736 (2007)
6. Phayre, A.N., Hartley, N.K., Hayes, M.A.: Microdevices for Biological Analyses Recent Advances and Directions for the Future. Journal of the Association for Laboratory Automation 5, 78–82 (2000)
7. Hendra, J., Tarigan, N.P., Christopher, K., Darryl, J., Bornhop, D.J.: Capillary-Scale Refractive Index Detection by Interferometric Backscatter. Anal. Chem. 68, 1762–1770 (1996)
8. Wang, Z., Darryl, J., Bornhop, D.J.: Dual-Capillary Backscatter Interferometry for High-Sensitivity Nanoliter-Volume Refractive Index Detection with Density Gradient Compensation. Anal. Chem. 77, 7872–7877 (2005)
9. Sorensen, H.S., Pranov, H., Larsen, N.B., Bornhop, D.J., Andersen, P.E.: Absolute Refracttive Index Determination by Microinterferometric Backscatter Detection. Anal. Chem. 75, 1946–1953 (2003)
10. Swinney, K., Markov, D.A., Darryl, J., Bornhop, D.J.: Ultrasmall Volume Refractive Index Detection Using Microinterferometry. American Institute of Physics 71, 2684–2693 (2000)

Study on Channel Parameters of Static Induction Transistor

Jiaxin Ju[1,2], Wanrong Zhang[1], Haolin Du[2], Yanfeng Jiang[2], Tengfei Yang[2], and Yamin Zhang[2]

[1] College of Electronic Information and Control Engineering, Beijing University of Technology, 100124, Beijing, China
[2] College of Information Engineering, North China University of Technology, 100144, Beijing, China
jxju@ncut.edu.cn

Abstract. The electric performance of static induction transistor (SIT) is dependent strongly on the channel parameters of device. The ratio of is an essential combined channel parameter not only for I-V characteristics but also for the high-current performance of device especially for the high frequency SIT (HF SIT), which are researched in this article. The pinch factor is also a key combined channel parameter embodies the general control criterion of fabrication parameters in determining whether it is a mixed, triode-like or pentode-like I-V characteristic which are also studied in detail. A great deal of experimental results is given which are available and convenient for design and fabrication of HF SIT, particularly for mixed I-V non-saturating characteristics.

Keywords: Transistor, SIT, Channel Parameters.

1 Introduction

The static induction transistor (SIT) is a structural sensitive device [1-5] which is composed of vertical multi-channels is markedly dependent on channel parameters. The electrical performance of SIT, especially the I-V characteristics depend strongly on the channel parameters, including the channel length, the channel thickness, channel doping, etc.

The unsaturated triode-like characteristics are both short and narrow channel's properties. With the variation of the channel parameters, the SIT should exhibit a gradual transition from pentode-like to triode-like characteristic or conversely. It is corresponding to the approach of the pinch-off point to the source region and to a regime characterized by barriers control injection carriers from the source region. During the transition of the I-V characteristics, the SIT will exhibit all type of the I-V characteristics: the good saturated pentode-like type, the poor saturated and with a tendency towards triode behavior type, the mixed triode-pentode type, the triode-like type and the triode-like type however with a shifted certain voltage along drain voltage axis. When the SIT applied to low-resistance load direct-drive circuits, the mixed characteristics are desirable. Because of the dead region is reduced and the merits of the triode-like characteristics are maintained. Therefore, we lay emphasis on

D. Zeng (Ed.): Future Intelligent Information Systems, LNEE 86, pp. 443–450.
springerlink.com © Springer-Verlag Berlin Heidelberg 2011

study the control of the mixed I-V characteristics and many useful results are given in this paper. For those channel parameters, the certain optimum matching relationships for the SIT with excellent performances are given in this paper based on experimental studies.

2 Brief Description of Channel Parameters

In general, the depth of the n^+ source region is much smaller compared with the gate region depth x_{jg}. Approximately, the channel length l_c equals gate region depth x_j. By our experience, in a wide range of diffusion temperature from $1100^\circ C$ to $1125^\circ C$, the lateral depth x_{jl} can be approximately equals $0.7x_j$. Therefore, in Fig.1 the designed pitch d between adjacent two gates is approximately by

$$d \doteq d_c + 2x_{jl} \doteq d_c + 1.4x_j \doteq d_c + 1.4l_c \tag{1}$$

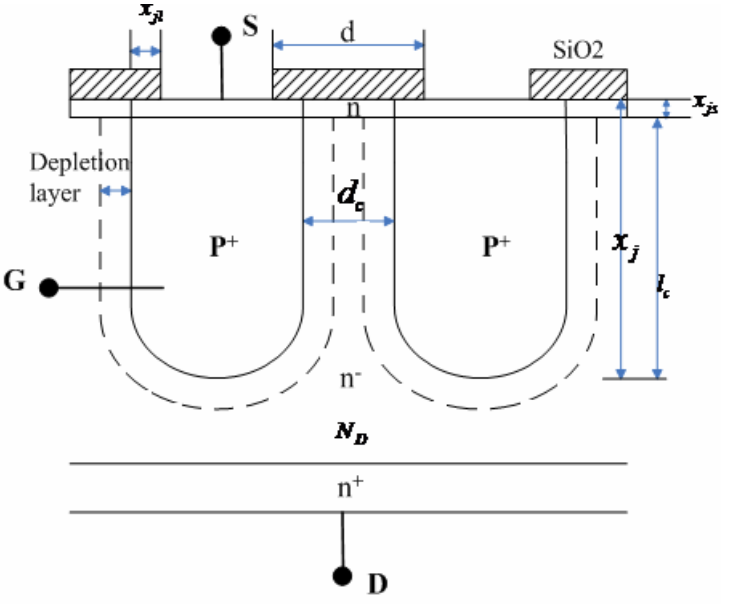

Fig. 1. The geometric structure of the SIT. The designed pitch between adjacent gates is d. During the gate region is formed by means of boron diffusion, the lateral extension x_{jl} of the p^+n^- junction and vertical depth x_j supply adjustment action simultaneously on the channel thickness d_c and channel length l_c respectively.

When gate voltage $V_G = 0$, the depletion layer width a_0 of p^+n^- junction is determined by following equation as a function of substrate impurity concentration N_D, which can express as

$$a_0 \doteq (\frac{2k\varepsilon_0}{qN_D}\psi_B)^{\frac{1}{2}} \doteq 3.14\times10^7\times N_D^{\frac{1}{2}}(\mu m) \tag{2}$$

Where q is the electronic charge, ε_0 is the permittivity of free space, $k=11.8$ is the silicon dielectric constant, $\psi_B = 0.76V$ is the built-in potential of p^+n^- junction in our device structure.

2.1 Ratio of l_c/d_c

In order to improve the high-current performance, we also need both gate voltage V_G and drain voltage V_D control the drain current sensitively. In SIT, those sensitivities are all determined by the combined channel parameter l_c/d_c approximately.

The gate voltage V_G controls drain current by means of controlling the channel potential barrier. Thus, we describe the sensitivity of V_G controlling the channel potential barrier by gate efficiency η which can be expressed as follows, [6]

$$\eta = \frac{\partial\Phi_{\min}(V_G \cdot V_D)}{\partial V_G} \doteq 1 - \frac{2}{\sqrt{\mu_0}} \tag{3}$$

Where $\Phi_{\min}$ is the channel potential barrier, μ_0 is the electrostatic gain which can express as [6].

$$\mu_0 \equiv \exp(\pi\frac{l_c}{d_c}) > 1 \tag{4}$$

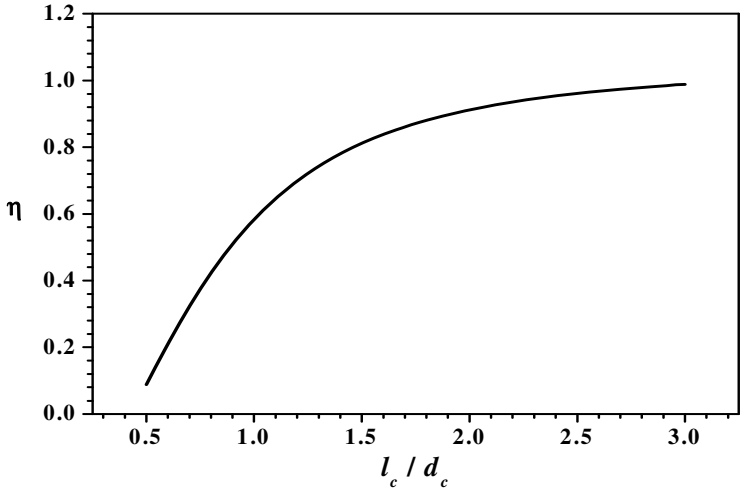

Fig. 2. The relationship between η and l_c/d_c. For a fixed l_c, the d_c should be narrowed suitably in order to obtain large η.

The sensitivity of V_D controlling the channel potential barrier can be described by a sensitivity factor D, which are defined as [6]. Where V_D^* is linear with V_D called as intrinsic drain voltage.

$$D \equiv \frac{\partial \Phi_{\min}}{\partial V_D^*} \doteq \frac{\sqrt{\mu_0}}{\mu_0 + 1} \tag{5}$$

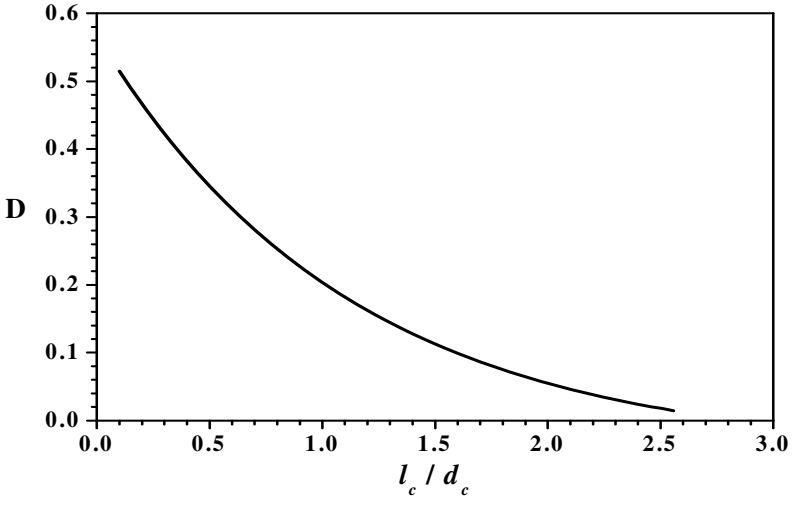

Fig. 3. The relationship between D and l_c/d_c. we can find the l_c/d_c should be small enough to get a large D, even smaller than 1. The channel length should be short and the channel thickness should be large which means the HF SIT should be fabricate by shallow junction. Only the thin gate region can make V_D adjust channel potential barrier easily.

We noticed that it is a inconsistency for η and D, the former need a large l_c/d_c but the latter need a small one. So we must choose an appropriate l_c/d_c considering both of them. From the Fig.2 and Fig.3, the parameter l_c/d_c should be near to 1 which make the channel potential barrier be in critical state that can be adjust sensitively both by V_G and V_D.

2.2 Pinch Factor β

Besides l_c/d_c, we defined a pinch factor β of the channel without gate bias, which play a profound role in determining whether the mixed, triode-like or pentode-like characteristics. β is defined as:

$$\beta \equiv d_c / a_0 \tag{6}$$

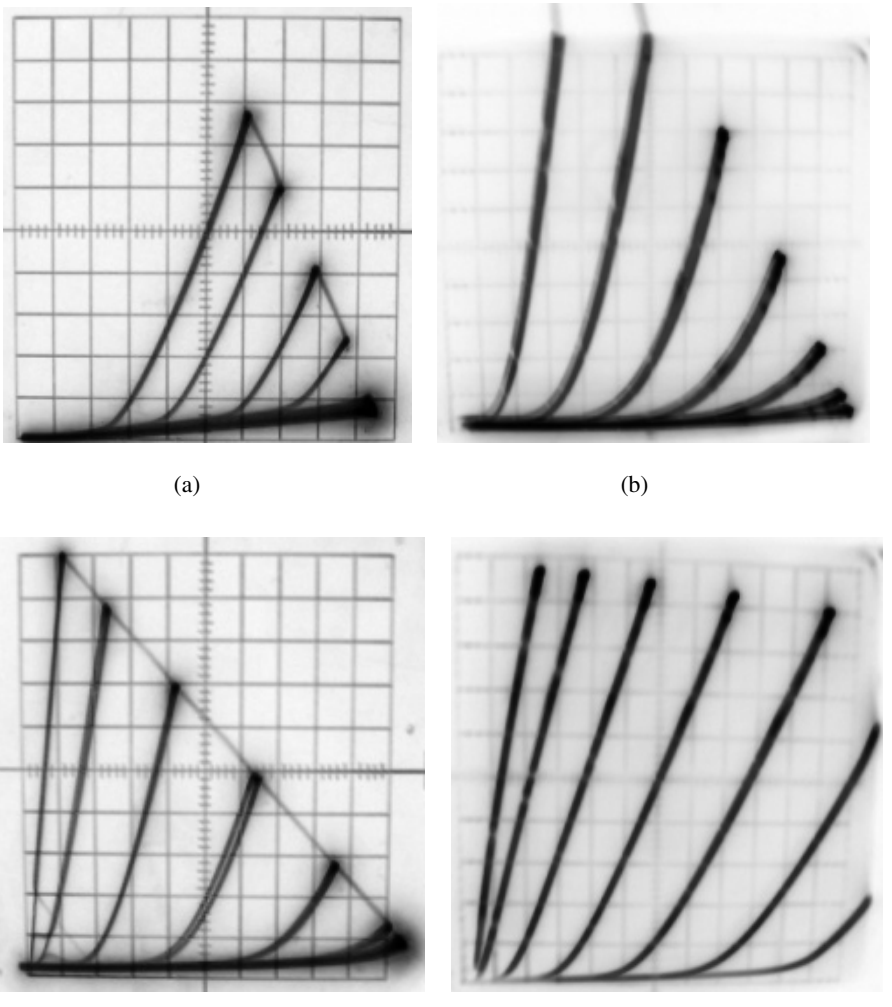

(a) (b)

(c) (d)

Fig. 4. I-V characteristics with different β and l_c/d_c . The influence of β on the I-V characteristic is very obvious, so does l_c/d_c .

(a) $\beta \doteq 1.50, l_c/d_c \doteq 1.21$;(b) $\beta \doteq 2.27, l_c/d_c \doteq 0.40$;(c) $\beta \doteq 2.73, l_c/d_c \doteq 0.47$;

(d) $\beta \doteq 2.50, l_c/d_c \doteq 0.56$;(e) $\beta \doteq 7.50, l_c/d_c \doteq 0.21$

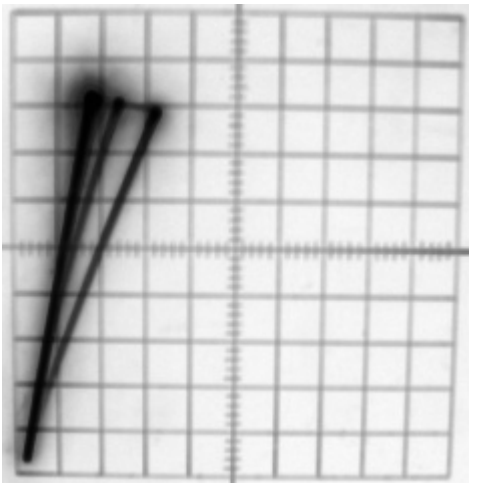

(e)

Fig. 4. (*continued*)

Table 1. The Necessary Channel Parameters for Mixed I-V Characteristics

$N_D(10^{14}cm^{-3})$	$a_0(\mu m)$	$d_c(\mu m)$	$l_c(\mu m)$	l_c/d_c	β	*I-V characteristics* type
2.0	2.2	16.5	3.5	0.21	0.21	Resistance
2.0	2.2	5.0	2.0	0.40	0.40	Triode-like
10.0	1.0	2.5	1.0	0.40	0.40	Triode-like
2.0	2.2	6.0	2.8	0.47	0.47	Mixed
2.0	2.2	6.0	3.0	0.50	0.50	Mixed
10.0	1.0	2.5	1.4	0.56	0.56	Mixed with more pentode
2.0	2.2	4.8	2.7	0.56	0.56	Mixed with more pentode
3.0	1.8	4.2	3.7	0.88	0.88	Lacking saturated pentode

3 Discussion

The channel parameter of l_c/d_c not only determine the electric parameters of η and D but also influence the *I-V* characteristics. The too small l_c/d_c, such as 0.2, make

the behavior of SIT is similar to resistance. When l_c/d_c is great than 0.8, the characteristic exhibits a transition to the lacking saturated pentode type. The experiments also show the SIT exhibits only the JFET's characteristic if l_c/d_c is great than 1.2. We find that typical mixed characteristic occurs at the range of $0.45 \sim 0.55$, the average is:

$$l_c/d_c \doteq 0.5 \tag{7}$$

Then from Eq. (1) and Eq.(7) we can get:

$$d \doteq 1.7 d_c \text{ or } d \doteq 3.4 l_c \doteq 3.4 x_j \tag{8}$$

For the mixed *I-V* characteristic, according to fabrication experience the channel should be pinched off only by low negative biased gate voltage $V_G = -1V$, not by $V_G = 0$, which indicate that the width of depletion layer $a_p(V_G = -1)$ and $a_0(V_G = 0)$ satisfy the relationship of $3a_0 \doteq 2a_p$. Considering the channel thickness d_c is greater than a_0, but no more than $2a_p$. Thus from the definition of β, the pinch factor must be selected in the range of $2 < \beta \le 3$ in order to obtain the mixed *I-V* characteristic. Usually, we selected β in the range of $2.3 \sim 2.7$. From the Eq. (2), Eq. (6) and Eq. (8), we get

$$d \doteq 1.7 a_0 \beta \doteq 5.34 \times 10^7 \sqrt{N_D}\, \beta \tag{9}$$

For HF SIT ($400 \sim 1000MHz$) of dielectric gate with mixed *I-V* characteristic, we select $\beta \doteq 2.7$ and $l_c = 2.5\mu m$. It is can be find that for fixed β, the doping concentration N_D of epitaxial wafer increases with the decreasing of d as Table 2 shows.

Table 2. The relationship between a_0, N_D and d in HF SIT of dielectric gate with mixed I-V characteristic ($\beta \doteq 2.7, l_c = 2.5\mu m$)

$d\ (\mu m)$	10.0	8.3	7.0	6.3	5.8	5.4	5.0	4.8
$N_D(10^{14} cm^{-3})$	2.0	3.0	4.0	5.0	6.0	7.0	8.0	9.0

4 Conclusion

The combined channel parameters l_c/d_c and β are discussed in detail, the general control principle, control criteria and method for fabrication high performance of SIT, especially for mixed I-V characteristic, have been all given. All results are based on our plenty of technical practice. Although these results have some approximations, they are very useful and convenient for design and fabrication of SIT, particularly HF SIT with mixed I-V characteristic. Furthermore, the above discussion are universal and applicable to BSIT, SITH and other static induction device [7].

References

1. Onose, H., et al.: 2001 Design consideration for 2kV SiC-SIT. In: Proc. 2001 Int. Symp. on semiconductor Devices and ICs, Osaka, pp. 179–182 (2001)
2. Nishizawa, J., Motoya, K., Itoh, A.: The 2.45GHz 36W CW Si Recessed Gate Type SIT with High Gain and High voltage operation. IEEE Trans. on Electron Devices 47(2) (February 2000)
3. Strollo, A.G.M.: Trade-off between blocking gain and on-resistance in static induction transistor. Solid-State Electron 38, 309–315 (1995)
4. Wang, Y., Li, S., Yang, J., Hu, D.: A novel buried-gate static induction transistor with diffused source region. Semicond. Sci. Technol. 19, 1–5 (2004)
5. Chen, X., Liu, S., Huang, Q.: A static induction device manufactured by silicon direct bonding. Semicond. Sci. Technol. 19, 819–822 (2004)
6. Li, S.: Theory of the static induction devices. The publishing house of Lanzhou University (2002) (Chinese) ISBN 7-311-00937-5
7. Li, S., Yang, J., Liu, S.: Control of the electrical performance of bipolar mode static induction transistor (BSIT). In: Proc. IPEMC 1994, vol. 1, p. 33 (1994)

Modelling and Characterization of DCO Using Pass Transistors

E. Kanniga[1] and M. Sundararajan[2]

[1] Research Scholar, Department of ECE,
Bharath University, Chennai-73
Kannigatruth@yahoo.com
[2] Principal,
Gojan School of Business & Technology,
Chennai-52

Abstract. In the field of simulation work, it could proceed to an extent that, simulate with arbitrary values of the passive component and the voltage sources. The simulation results recorded various strategic points in the circuit indicate and validate the fact that the circuit is working in the expected lines with regard to the energy transfer in the expected lines with regard to the energy transfer in the tank circuit and sustenance in DC transient Analysis. Also in this proposed experimental work, it is observed that for an arbitrary load, the voltage obtained is agreeing with the theoretically computed DC-Voltage levels. The scope of the work can be extended to the actual calculation of the passives, the initial voltages across the capacitors and inductors. In addition to the exciting DC levels of the sources employed. The small signal analysis can also be done with due regard to the desired behavioural properties of switching devices used.

Keywords: Digital controlled oscillator, steady state transient response, simulation LTSPICE, Varactors.

1 Introduction

In the digital world there is an increased requirement for Digitally Controlled Oscillator (DCO).

The Traditional DCO core with Inductor Capacitor (LC) tank biasing network still makes it complicated with Analog Analysis. Therefore to make it fully digital one can take up a design with pass transistor.

1.1 Varactors

Varactors are a principal component of LC Voltage Controlled Oscillator (VCOs) used for frequency fine tuning. Digitally controlled switched varactors or switched capacitors could also be used for coarse tuning in some designs. [2]

D. Zeng (Ed.): Future Intelligent Information Systems, LNEE 86, pp. 451–457.
springerlink.com © Springer-Verlag Berlin Heidelberg 2011

NMOS (N type metal oxide semiconductor) transistor, with gate as the first terminal and drain, source, and bulk connected together to form the second terminal. MOS varactors operate in four main regions, based on the biasing point (voltage across the varactor terminals) accumulation, depletion, weak inversion, and strong inversion. Accumulation and strong inversion are two regions where most varactors are designed to operate in. Furthermore, a study on accumulation-mode and inversion-mode varactors reveals that LC oscillators based on accumulation-mode varactors demonstrate lower power consumption and lower phase noise at large offset frequencies from the carrier, compared to those based on strong inversion. In most of the applications, designers would like to ensure that the capacitance of the varactor is a monotonic function of the biasing voltage. For instance, in an LC VCO, it would be desirable to have the varactor operating predominantly in accumulation mode. However, using a regular NMOS does not warrant this, as the operation region is voltage dependant. It is also worth noting that the C-V (Current Voltage) curve of a regular nMOS is frequency dependant. It may seem similar to an NMOS transistor; however, the *n*+ regions have been buried in *n*-well, instead of *p*-well. This configuration guarantees that the device does not enter the inversion-mode at all; hence the name accumulation-mode.

Fig1 shows that NMOS transistors configured as a Varactor.

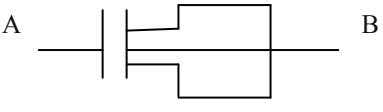

Fig. 1. Symbolic representation Varactor

In most applications, designers would like to ensure that the capacitance of the varactor is a monotonic function of the biasing voltage.

Fig2. Show that the C-V characteristics of an MOS varactor can be predicted using 2D/3D numerical simulators. Unfortunately these simulation tasks require precise knowledge of the underlying doping profiles which usually are not readily available. An alternative is to perform capacitance measurements. However sub Pico Farad capacitance is difficult and requires a fairly expensive S- parameter RF measurement setup. It is therefore very useful to predict the tuning characteristics of LC Oscillators. Using standard foundry supplied models for MOSFETS.

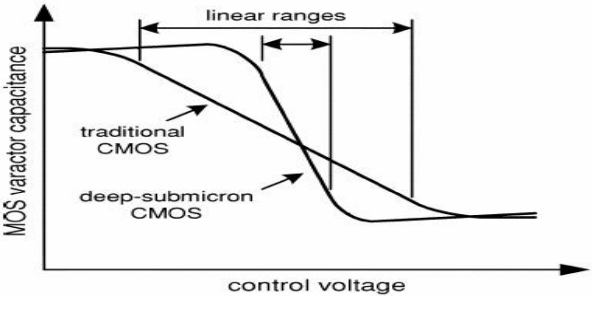

Fig. 2. C-V Characteristics of MOS varactors

Recently, a lot of effort has been expended on modelling the C-V characteristics of MOS varactors.

1.2 Pass Transistor

Fig 2 shows that schematic representation of a pass transistor.

A Pass transistor is a MOSFET in which an input is applied not only to the gate, but also to the drain. The principle is taken up from the multiplier circuitry.

In the multiplier circuit pass transistors are used to reduce the layout complexity. This is done by pass transistors connected to pass a first and second input function to an output node in response to a selected output function on the output node.

The PASS transistor comprises a transistor capable of passing an input function in response to a CONTROL signal applied to the transistor, thereby to generate an output function related to the input function.

The challenge is to replace the capacitor bank (or) the variable capacitor by Transistor. A pass Transistor is a MOSFET in which an input is applied not only to the gate, but also to the drain.

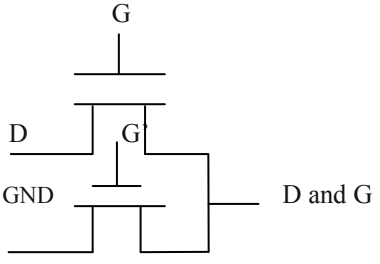

Fig. 3. Schematic representation of a Pass Transistor

2 DCO Design and Tuning Characteristics

Conventional VCO's use the Analog voltage control for frequency tuning. Analog frequency tuning not compatible with deep submicron CMOS processes.

- Varactors highly nonlinear.
- Voltage headroom squeezed.
- Analog voltage resolution unreliable
- Analog interface difficult for integration.

DCOs use digital approach for frequency tuning.

- Easier implementation in advance CMOS processes.
- Allowing fully digital implementation of the PLL loop control circuitry.

The proposed architecture may be successfully implemented for RF application. Differential LC tank Oscillators remain as the standard choice for the oscillator core. Digital control realized by individually switching an array of capacitance devices in

the LC tank. Cross coupled MOS gain stage for negative resistance. Capacitance implementation using MOS Varactors (switched capacitors) array may be used to augment the tuning range high –Z tank to improve effective loaded tank Q. Biasing current digitally tuned for performance optimization.

Digitally controlled switched varactors or switched capacitors used for coarse tuning in some designs.

In DCO design and tuning characteristics, the closed loop system oscillator has to fulfil the following Bharkhausan conditions at all times for continuous oscillation.

$$|H(j\omega)| \geq 1$$

$$\langle H(j\omega) \rangle = 360 \text{ (or)}$$

$$\langle H(j\omega) \rangle = 0 \text{ ---------} \rightarrow 1$$

Where H(jω) is frequency response

The Modelling of the tuning characteristics is a straight forward task, as the oscillation frequency (f_{osc}) is given by the following well known formula,

$$f_{osc} = \frac{1}{2}\Pi\sqrt{LC(v)} \text{--------} \rightarrow 2$$

Where L is the inductance C (v) is the equivalent capacitance for a given biasing point. The equivalent capacitance can be extracted using

$$c(v) = \frac{1}{4}\pi^2 f_{osc}^2 L \text{ ------} \rightarrow 3$$

Having determined c (v) values in eqn (3), an extracted piece wise linear model of the voltage dependent capacitance is reconstructed and fed back to LTSPICE for simulation.

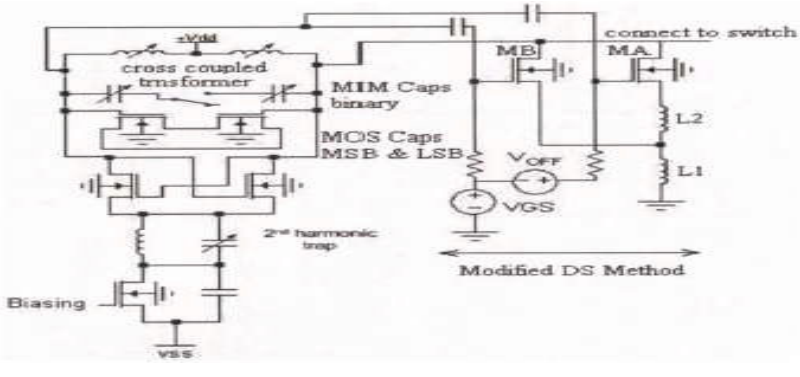

Fig. 4. Detailed Circuit diagram of DCO

In DS method, the magnitude and phase of second order nonlinearity contribution to M3 components is tuned to cancel the third-order nonlinearity contribution to M3 components, thus resulting in an output current with a minimum M3 component. As

shown in fig4, the transistor MA is biased in the strong inversion region, while MB is biased in weak inversion. The two source degeneration inductors L1 and L2 connected to the sources of the two transistors are used to tune the magnitude and phase of the 1M3 components. [Ref.1]

The challenge is to replace the capacitor bank or the variable capacitor.

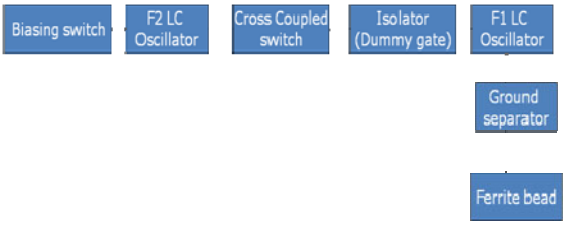

Fig. 5. Block Diagram of proposed DCO

2.1 Basic Theory

The MOS M1 acts as control switch to gain control over the switching of the circuit such that the switching is done by controlling the gate voltage given to it turns on the MOS which grounds the entire circuit voltage from the tank circuit to prepare for full cycle of operation.

The tank circuit F2 enables the selective grounding and control of the oscillations of a particular frequency to pass through the M1 transistor so that the selective tuning is made possible.

The transistors M2 and M3 are the cross – coupled giving rise to a perfect matching of the isolation provided by M4 and M5. MOS transistors offer high input impedance that makes its usage as a much preferred input stage of many devices and circuits to avoid direct grounding of the actual resonance circuits.

The resonance circuits provide the energy sustenance to provide oscillations of the desired frequency, which is passed to the load through a ground noise filtering circuit so as to eliminate ground noise, which is much prevalent in circuit when implemented in the printed circuit boards... The ground traces offer a certain amount of resistance to the signals which need to be protected against the noise to maintain signal quality and strength.

3 Experimental Set and Result Analysis

Arbitrary selection of components and their values need to be done based on the small signal analysis of the circuit and the time domain transient analysis results.

Basically, the two tank circuits that are used in the circuit involve small values of inductors and capacitors which can be tuned or changed depending upon the range of oscillations required. The oscillation frequency can be found from the afore mentioned analysis using small signal model of the circuit.

The ac component part of the equation(1), when let to zero, yields the value of ω, which is a function of the passive components such as L and C (including R, which is a damping component in the oscillations generated).

This ω, is taken as reference radians that would give the value of the exact frequency of oscillations to which the circuit need to be retuned and redesigned for every simulation run done.

The permutation and combination possibility of the number of instances of change in the LC is given as 24. However, since two of the tank circuits are LC for producing sustained oscillations, the values have to be chosen based on the small signal analysis. Thus approximately 10 combinations of L and C can be tried for various settings.

The capacitors C4 and C5 are to be replaced using the values as given by the equation of frequency of oscillations. These capacitors would be replaced by the varactor diodes of the same value available in the market.

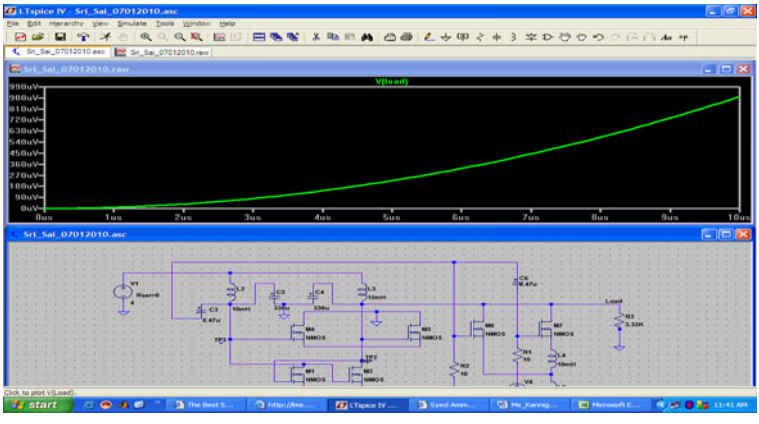

Fig. 6. The probe for one setting of the L and C and the excitation voltage

Table 1. Excitation voltage Vs Time

X axis(Time)	Y Axis(excitation Voltage)
0.91µs	0.083mv
1.33µs	0.041mv
3.05µs	0.0083 mv
4.00µs	0.000 mv

Shown above in fig (6) is the voltage observed through the probe for one setting of the L and C and the excitation voltage. Simulation can be done for various values of L and C by change in the settings and the diode. The different values are tabulated in table1.

Variation in Gating Signal means variation in the output. As we have seen, passing an input function in response to a CONTROL signal applied to the transistor, thereby

to generate an output function related to the input function. In this project the focus is to utilize this quality of the pass transistor in the design of my DCO by having a Gating signal which will help to provide the required output.

The resonance circuits provide the energy sustenance to provide oscillations of the desired frequency, which is passed to load through a ground noise filtering circuit so as to eliminate ground noise, which is prevalent in circuit when implemented in the printed circuit boards. The ground traces offer a certain amount of resistance to the signals which need to be protected against the noise to maintain signal quality and strength.

Advantages

->power supply requirement is reduced
->power dissipation is reduced
->switching time is reduced
->interference between the components is reduced

LTSPICE

Linear Technology Corporation has launched the LTSPICE simulation. This simulation tool is efficiently used for the analysis of range, sampling, frequency, switched mode power supply, high speed CMOS, data compression, timing analysis, instant design files, etc.... than PSPICE.

4 Conclusion

Brief description of the digital – controlled oscillator model is given. The model described in this article is primarily intended to be used for study of the digital controlled oscillator step response in LTSPICE environment. The model is based on idea that step response of a real digital – controlled oscillator can be well modelled as a steady state response.

References

1. Hosseini, A., Gharaee, H.: Optimum Quad Band DCO in DS Method for WCDMA Transmitter in 90nm CMOS. In: Proc. 2008 ICSE, Shariaty University, Tarbiat Modares University, lohor Bahru, Malaysia, pp. 44–47 (2008)
2. Sameni, P., Siu, C., Mirabbasi, S., Djahanshahi, H., Hamour, M., Iniewski, K., Chana, J.: Modeling and Characterization of VCOs with MOS Varactors for RF Transceivers. EURASIP Journal on Wireless Communications and Networking, Article ID 93712, 1–12 (2006)

The Research on Spatial Data Mining Module Based on Geostatistics Analysis Model for Decision Support System

Jiang Qing, Ling Hubin, and Li Jiaoe

Institute of Intelligent Machine, CAS,
Hefei, China
hustjiang@gmail.com

Abstract. In this paper the spatial data mining module based on geostatistics analysis was developed to optimize groundwater level observation networks and improve the quality rather than the quantity of the obtained data, which includes the application of the kriging methodogy and the evaluation of its results in conjuction with the statistical analysis of the available groundwater level data. This procedure that involves different analysis methods of the available data, such as estimation of the interpolation error, data cross-validation and time variation, is applied to evaluation and optimization of Shule river basin in order to demonstrate the potential of improvement of the quality of the observation network.

Keywords: spatial decision making, geostatistics analysis, spatial mining module, kriging.

1 Introduction

Groundwater level measurements have a decisive role in the accuracy of analysis and prediction. Therefore, special attention is required not only during the actual measurements but also in the design of the groundwater level observation network. The extent of the network, its density and the frequency of the measurements affect not only accuracy but also time and money investment. Many related research are characterized by seeking several priori alternatives among a number of existing wells by using search algorithms [1,2,3]. Geostatistics is powerful tool for water resources management and can effectively be used to derive the long term trends of the groundwater [1~6]. Recently, there is a very interesting application in the area of evaluation and optimization of groundwater observation network. Olea and Davis used cross-validation based on kriging to identify errors in water level measurement or erroneous locations of observation wells and thought of relation between the uncertainty in the estimated surface and kriging standard deviation in order to evaluate and optimize the observation network [7,8]. Theodossiou judged groundwater level variability over time by standard deviation of groundwater level variability over time in order to exclude relatively unnecessary observation points considering both time and cost.

D. Zeng (Ed.): Future Intelligent Information Systems, LNEE 86, pp. 459–466.
springerlink.com © Springer-Verlag Berlin Heidelberg 2011

In this paper, we demonstrate how geostatistics analysis can be integrated with GIS to solve monitoring network optimization solutions mining for SDSS. A prototype spatial data mining module is developed for solving the space layout optimization of groundwater.

2 Basic Concepts

2.1 Spatial Decision Support System (SDSS)

In fact, Spatial decision support system is the DSS to solve the spatial and structural problems specific difficult to describe and simulate, which is based on GIS and driven by model library. It provides decision makers with data, information, graphics, images and related data, domain knowledge, even useful knowledge potentially hidden in the back of data to help decision-makers a clear policy objectives, the establishment of decision-making model and space operations and analysis, providing a variety of different alternatives, and programs to be evaluated and optimized for scientific decision-making support and help [9]. The traditional spatial decision support system consists of three components (subsystems): geographic database and management system (DBMS), model base and management system (MBMS), the dialogue generation and management system components (DGMS) , which mainly realize the input of spatial data, spatial analysis and spatial data visualization output function. With the development of knowledge engineering, expert systems and intelligent computing and artificial intelligence and the requirement to resolve more complex spatial decision problems, the spatial decision support system can not only have data management and analysis functions, but also with spatial data mining and knowledge discovery, learning and knowledge accumulation, knowledge representation, knowledge reasoning and other features and functions of expert systems. Therefore spatial knowledge acquisition and knowledge management is particularly important for SDSS. Spatial data mining and knowledge discovery SDMKD (Spatial Data mining and Knowledge discovery) is the main source of spatial knowledge acquisition of knowledge base.

2.2 The Basic Principles of Geostatistics

Many researchers have studied the theoretical basis of geostatistics [10,11,12]. The Variogram is the main tool of geostatistics, which expresses the spatial dependence between neighboring observations. The variogram, $\gamma(h)$, can be defined as one-half the variance of the difference between the attribute values at all points separated by h as follows:

$$\gamma(h) = \frac{1}{2N(h)} \sum_{i=1}^{N(h)} [Z(x_i) - Z(x_i + h)]^2 \tag{1}$$

Where $Z(x)$ indicates the magnitude of variable, and $N(h)$ is the total number of pairs of attributes that are separated by a distance h .

Prior to the geostatistical estimation, a model is required to compute a variogram value for any possible sampling interval. The most common models are spherical, exponential, Gaussian, and pure nugget effect. The adequacy and validity of the developed variogram model was tested satisfactorily by a technique called cross-validation. The idea of cross-validation consists of removing a datum at a time from the data set and re-estimating this value from remaining data using different variogram models. Interpolated and actual values are compared, and the model that yields the most accurate predictions is retained [10,11].

Kriging is a linear optimum unbiased interpolation method with a minimum mean. It presents the possibility of estimation of the interpolation error of the values of the regionalized variable where there are no initial measurements, which offers a measure of the estimation accuracy and reliability of the spatial distribution of the variable. Among the different kriging methods, Ordinary and universal kriging methods are mainly applied for datasets without trend. Detailed discussion of kriging methods and their descriptions can be found in [10]. The general equation of linear kriging estimator is:

$$Z^*(x_p) = \sum_{i=1}^{n} \lambda_i Z(x_i) \tag{2}$$

In order to achieve unbiased estimations in ordinary kriging, the following set of equations should be solved simultaneously.

$$\begin{cases} \sum_{i=1}^{n} \lambda_i \gamma(x_i, x_j) - \mu = \gamma(x_i, x) \\ \sum_{i=1}^{n} \lambda_i = 1 \end{cases} \tag{3}$$

Where $Z^*(x_p)$ is the kriged value at location x_p, $Z^*(x_i)$ is the known value at location x_i, λ_i is the weight associated with the data, μ is the lagrange multiplier, and $\gamma(x_i, x_j)$ is the value of variogram corresponding to a vector with origin in x_i and extremity in x_j.

3 Spatial Data Mining Module

Spatial data mining module acquire knowledge for SDSS to solve monitoring network optimization solutions mining and is an important part of the spatial data acquire and management module. It is made up of four parts: interactive interface, spatial data mining model library, control module and spatial database, see figure 1:

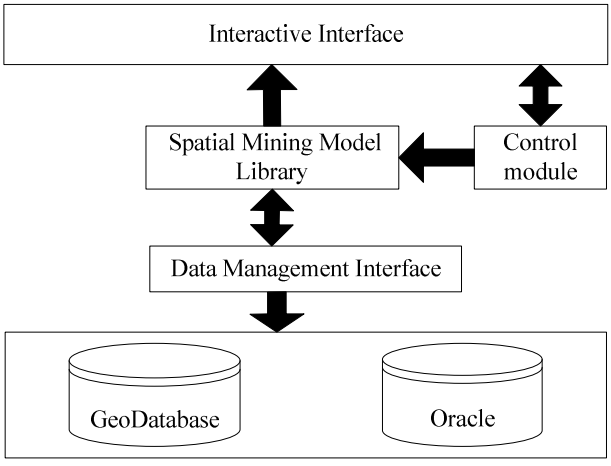

Fig. 1. Spatial data mining module structure

User interface achieves interaction with the user in response to user's operation, transmits the instructions to the master control module and display spatial data mining model output results. Control module calls the corresponding spatial data mining model, while control the complete process of spatial data mining. Spatial mining model library using object-oriented development method, the basic spatial analysis as a base class, geostatistics analysis spatial data mining model as a succession of classes and interfaces, the mapping between spatial analysis and spatial data mining models realizes spatial data mining and visualization. Spatial Data Management Interface completes the calculation of the required model libraries and non-spatial data, spatial data input and output storage. Geodatabase is responsible for spatial data of GIS-based data storage and management model, using elements of sets (Features Dataset) and feature classes (Features) of the hierarchical management style, enhance spatial data read speed and efficiency. Non-spatial database based on Oracle database for storage and management.

3.1 Development Tools

Spatial data mining components of the development, integration and testing is based on windowsXP operating environments, programming environment is based on ArcEngine and netbean6.7 mixed environment, spatial database is based on File Geodatabase format for storage and management and non-spatial database system is based on Oracle10.0 database management software.

3.2 The Application

According to the spatial coordinates of fifty monitoring well in the groundwater monitoring network, described as fig 3, the output results of the monitoring network optimization module is describe as Table1 and Table 2:

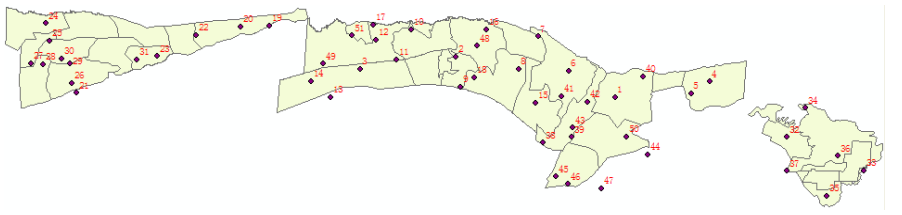

Fig. 2. The grounderwater monitoring network layout

Fig. 3. Distribution of the prediction standard error

Table 1. Properties of the fitted variograms of temporal analysis for groundewater level for each observation well

Well no.	Model	Nugget	Partial Sill	Range	Nugget/Sill	RMS
1	Gaussian	0.067943	0.074395	35.491	0.47733	0.7146
2	Gaussian	0.0033002	0.015762	5.1702	0.17312	0.5362
3	Exponential	0.001038	0.00053006	35.491	0.66196	0.1729
4	Exponential	0.0003740	0.0008915	35.491	0.29556	0.0986
5	Gaussian	0.0003234	0.002371	35.491	0.12005	0.2142
6	Exponential	0.0006831	0.00030963	35.491	0.68812	0.0534
7	Gaussian	0.0019907	0.0028361	32.614	0.41242	0.2278
8	Exponential	0.010107	0.0065993	35.491	0.60498	0.2912
9	Exponential	0.0077133	0.050998	31.655	0.13137	2.251
10	Gaussian	0.0078666	0.051038	5.9041	0.13354	0.0995
11	Exponential	0.0	0.016585	10.479	0.0	0.1578
12	Spherical	0.0007255	0.0072772	35.491	0.09065	0.1831
13	Exponential	0.0	0.00016164	4.2657	0.0	0.0337
14	Spherical	0.0	0.014811	5.6987	0.0	0.1208

Table 1. (*continued*)

15	Gaussian	0.0002302	0.00074693	4.2593	0.23561	0.1068
16	Exponential	0.0	0.013698	9.3823	0.0	0.2771
17	Exponential	0.0000386	0.0062954	44.125	0.00609	0.1114
18	Spherical	0.0000119	0.0022173	7.7812	0.00537	0.2225
19	Spherical	0.0000055	0.001187	33.574	0.00465	0.2807
20	Exponential	0.0	0.020667	8.9236	0	0.4944
21	Exponential	0.096006	0.50443	44.125	0.19032	0.3331
22	Spherical	0.14355	0.31485	44.125	0.45593	0.4904
23	Exponential	0.15996	0.076316	44.125		-0.0099
24	Gaussian	0.0049822	0.00090878	10.631		0.0681
25	Spherical	0.17282	0.09679	45.085		0.8932
26	Spherical	0.014004	0.064171	44.125		0.8365
27	Spherical	0.016176	0.25458	4.0137		0.8851
28	Exponential	0.010744	0.59104	33.574		0.2791
29	Spherical	0.0096985	0.13868	36.451		0.111
30	Exponential	0.13499	0.16973	16.081		0.4349
31	Exponential	0.14728	0.40707	41.247		0.3406
32	Spherical	0.35809	0.20783	31.655		0.7355
33	Spherical	0.019479	0.0079954	24.941		0.1527
34	Gaussian	0.0022889	0.025179	19.753		0.0469
35	Exponential	0.017265	0.019447	49.88		0.1532
36	Exponential	0.037913	0.031421	44.125		0.1794
37	Exponential	0.03035	0.24668	44.125		0.1917
38	Spherical	0.0	0.12078	8.6878		0.1218
39	Gaussian	0.064082	0.069421	19.105		0.2756
40	Spherical	0.0	0.014563	68.106	0.0	0.1271
41	Exponential	0.0014637	0.0013429	42.431	0.52170	0.1443
42	Exponential	0.0	0.00076561	45.085	0.0	0.0662

Table 1. (*continued*)

43	Exponential	0.013585	0.0072033	68.106	0.65349	0.2256
44	Exponential	0.025536	0.0149	68.106	0.63156	0.2836
45	Exponential	0.0	0.0020793	68.106	0.0	0.0354
46	Exponential	0.14481	0.066573	68.106	0.68505	0.8175
47	Exponential	0.0004472	0.027884	58.578	0.01578	0.2094
48	Exponential	0.0	0.00065703	3.4653	0.0	0.0317
49	Exponential	0.010057	0.01046	68.106	0.49017	0.1462
50	Exponential	0.000497	0.00039249	68.106	0.55874	0.2657
51	Gaussian	0.0008611	0.048674	68.106	0.01738	0.1748

4 Conclusion

This paper study the spatial data mining method based on geostatistics analysis model and design, develop and establish the spatial data mining module. The results of module proved the method is available.

Acknowledgment

This study is financially supported by the National Natural Science Foundation of China (No: 60774096) and Key Projects in the National Science & Technology Pillar Program Nation (No: 2008BAK49B05).

References

1. Reghunath, R., Sreedhara Murthy, T.R., Raghavan, B.R.: Time series analysis to monitor and assess water resources: A Moving average approach. Environmental Monitoring and Assessment 109, 65–72 (2005)
2. Kumar, D., Ahmed, S.: Seasonal behaviour of spatial variability of groundwater level in a granitic aquifer in monsoon climate. Current Science 84, 188–198 (2005)
3. Theodossiou, N., Latinopoulos, P.: Evaluation and optimization of groundwater observation networks using the kriging methodology. Environmental Modelling and Software 21, 991–1000 (2006)
4. Desbarats, A.J., Logan, C.E., Hinton, M.L., Sharpe, D.R.: On the kriging of water elevations using collateral information from a digital elevation model. Journal of Hydrology 225, 25–38 (2002)
5. Triantafilis, J., Odeh, I.O.A., Warr, B., Ahmed, M.F.: Mapping of salinity risk in the lower Namoi valley using non-linear kriging methods. Agricultural Water Management 69, 203–231 (2004)

6. Christakos, G.: Modern Spatiotemporal Geostatistics. Oxford university Press, New York (2000)
7. Olea, R., Davis, J.: Optimizing the High Plains aquifer water-level observation network, K.G. S. Open File Report 1999-15 (1999)
8. Olea, R., Davis, J.: 1999b. Sampling analysis and mapping of water levels in the High Plains aquifer of Kansas, K.G.S. Open File Report 1999-11 (1999)
9. Deb, K., Pratap, A., Agarwal, S., Meyarivan, T.: A Fast and Elitist Multi-objective Genetic Algorithm: NSGA-II. IEEE Transactions on Evolutionary Computation, 182–197 (2002)
10. Goovaerts, P.: Geostatistics for Natural Resources Evaluation. Oxford University Press, New York (1997)
11. Isaaks, E., Srivastava, R.M.: An Introduction To Applied Geostatistics. Oxford University Press, New York (1989)
12. Kitanidis, P.K.: Introduction to Geostatistics: Application to Hydrogeology. Cambridge University Press, Cambridge (1997)

Nondestructive Examination of VC Content of Intact Shatangju with Near Infrared (NIR) Spectroscopy Based on Wavelet De-noising

Fen Dai, Tiansheng Hong, Xuejun Yue, Ya Hong, and Yan Li

Key Laboratory of Key Technology on Agricultural Machine and Equipment
(South China Agricultural University), Ministry of Education
College of Engineering, South China Agricultural University
Guangzhou, China

Abstract. The objective of this research was to determine how NIR measurements of VC content in Shatangju (Citrus reticulate Blanco) was affected by wavelet de-noising (WD) method. Firstly, outlier samples (NO.3, 17, 76) were removed based on sample residuals. Then the spectra of 85 samples within 500-2500nm were decomposed in level 2,3 and 4 using the orthogonal wavelet functions DB n(n=2,3,4,5,6,7,8). Lastly the precision and stability of PLS model with different pretreatments were compared. WD was examined to be the optimal spectrum preprocessing method. The PLS model with DB2 wavelet de-noise (in decomposition level 4) produced best result (RMSEC=6.006, RMSECV=8.080, r_c =0.896 and r_v=0.808). The results showed that the NIR model treated by WD is feasible to detect VC content of Shatangju rapidly and nondestructively.

Keywords: near infrared (NIR) spectroscopy, wavelet transformation, VC content, Shatangju (Citrus reticulate Blanco).

1 Introduction

Citrus fruit is popular allover the world, which has the world's biggest planting area [1]. The Shatangju (Citrus reticulate Blanco) is one of the varieties, which is deeply loved by the people. Vitamin C (VC) content is a major characteristic used for assessing Shatangju quality. Nowadays, most of methods to detect the VC content are destructive and time-consuming. An efficient and effective VC content detection system is urgently needed for the fruit industry. Near-infrared (NIR) measurement is a rapid and nondestructive technique. Current applications of NIR spectroscopy in agriculture product and food processing include the quantitative determinations in a wide range of products. Lu (2001) evaluated the potential of NIR reflectance (800-1700nm) for measurement of the firmness(r=0.80, SEP=0.55-0.44) and sugar content (r=0.89-0.97, SEP=0.71-0.65) of sweet cherries. Lu et al. (2002) investigated a NIR sensing technique for rapid acquisition of spectral information in the spectral region

D. Zeng (Ed.): Future Intelligent Information Systems, LNEE 86, pp. 467–474.
springerlink.com © Springer-Verlag Berlin Heidelberg 2011

between 900 nm and 1500 nm to predict the sugar content of two apple cultivars. The correlations of prediction for sugar content were equal to, or greater than, 0.81 and prediction errors were between 0.5% and 0.7% for the two cultivars. D.C. Slaughter et al. (2003) investigated a nondestructive optical method based upon near infrared spectrophotometric techniques for determining the soluble solid content (SSC) of fresh whole prune. The results of SSC prediction were: R2 =0.96, SEP=1.02brix. LIU Yande (2006) investigated methods for eliminating noise signal in visible adsorption spectra of fruit juice sample using wavelet and wavelet packet. The results demonstrated that the wavelet and wavelet packet analysis had advantage in de-noise signal process of spectra and could be used well in the fruit juice quality measurement. Ma Lan (2009) studied Nondestructive examination of total sugar in tomatoes with near infrared spectroscopy based on wavelet transform. The results showed that PLS model with Wavelet De-noise spectrum gave a correlation coefficient between prediction and actual of 0．930，a root mean square error of cross validation (RMSEC of 0.466%，and a standard error of calibration (RMSEC) of 0.469%，as well as a standard error of prediction (RMSEP)of 0.260%.

However, little work has been done on analyses of intact Shatangju. In this research, the basic theory and algorithm of wavelet were introduced. The FieldSpec 3 spectrometer (Analytical Spectral Device, ASD Co., USA) was used to measure the reflectance spectra of 88 samples. Usually the VC content in the Shatangju is low, so it is important to eliminate the noise and improve signal noise ratio (SNR) of spectral data. 9 kinds of spectra correction algorithms were used and evaluated in this work. The wavelet de-noise (WD) produced the best noise removing capability. The results demonstrated This PLS model with WD could produced the low root mean square error of calibration (RMSEC=6.006), low root mean square error of prediction (RMSEP=8.080) and the high correlation coefficient (rc =0.896and rv =0.808) between the predicted and measured parameter values.

2 Materials and Methods

2.1 Materials

A box of 88 samples from Si Hui city, Guangdong province were used in this experiment. All the 88 oranges were used to build and validate the model, which established the relationships between the spectrum measurements and VC contents. The full cross validation method was adopted to validate the model.

2.2 Spectrometer Equipment

FieldSpec 3 spectrometer (analytical spectral device, ASD Co., USA) was used in this experiment (Fig 2.). Its parameters are showed in table1. Spectrum data was exported in ASCII text. Commercial software ASD View Spec Pro， unscrambler9.8 and Matlab7.0 was used to analyzed the Spectrum data.

Fig. 1. FieldSpec 3 spectrometer

Table 1. Specifications of FieldSpec 3 spectrometer

NO	Preferences	Value
1	Spectral range(nm)	350-2500nm， 350-1050nm
2	Sampling interval(nm)	1.4nm@350-1000nm, 2nm@1000-2500nm
3	Resolution (nm)	3nm@350-1000nm, 7nm@1000-2500nm
4	Sampling velocity(ms)	100

2.3 Spectrum Acquisition

The 350nm-2500nm reflectance spectra were measured at three locations of each sample equator. These locations were at a distance of120o in sequence. These locations were marked for sugar VC content measurements. Every location was scanned 30 times, and then the 30 spectra were averaged as the reflectance spectrum of the location. Three location spectra of a sample were averaged as the sample reflectance spectrum. A white board was used as a reference for reflectance measurements. A reference spectrum was collected and stored every 15-30 minutes when samples were measured.

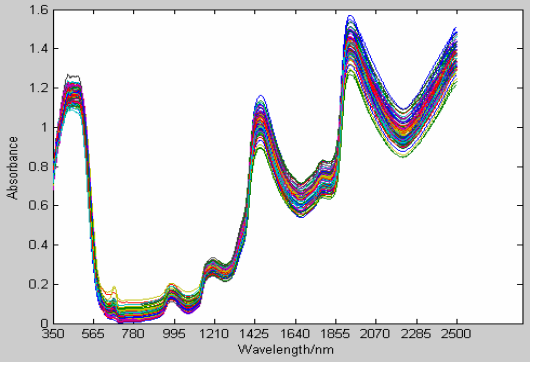

Fig. 2. Raw near infrared spectra of the 88 samples

2.4 LAB VC Content Measurement

According to national standard of China: Determination of Vitamin C in vegetables and fruits (GB/T 6195-86), 2,6-dichloro-indophenol titration method was used to measure VC content of samples. 10g flesh (with pericarp) of a sample was knifed from one location where spectra were collected. Then the 10g flesh (with pericarp) and oxalic acid were triturated, diluted, filtrated and titrated. The value of VC content was calculated according to the amount of 2,6-dichloro-indophenol that was consumed. the VC content of each sample was obtained by averaging from the VC contents at the three different locations of one sample. Summary distributional statistics for VC content of calibration and validation data set is showed in table2. The VC content measurements (n=88) were fairly normally distributed around the mean. The determination values of samples cover a large enough range, which is helpful to develop models.

Table 2. VC Content of Samples

Samples	Min(mg/100g)	Max(mg/100g)	Mean(mg/100g)	S.D (%)
88	20.528	90.068	53.734	13.657

2.5 The Principle of Eliminating Noise with Wavelet Method

Suppose a signal has a discrete approximation f(n) in level 2^L together with noise w(n). Observation data is x(n) = f(n) + w(n). We decompose x(n) under the following orthonormal basis:

$$B = [\{\Phi_{J,m}(n)\}_{m\in Z}, \{\Psi_{j,m}(n)\}_{L<j\le J, m\in Z}]$$

where the families of functions $\{\Phi_{J,m}(n)\}_{m\in Z}$ and $\{\Psi_{j,m}(n)\}_{L<j\le J,m\in Z}$ are obtained by dilating and translating the scaling function $\Phi(n)$ and orthogonal wavelet function $\Psi(n)$ respectively. Eliminating noise with wavelet method is to reconstruct f by thresholding the decomposition coefficients, that is f can be estimated by

$$\tilde{F} = \sum_{j=L+1}^{J}\sum_{m}\rho_T\left(\langle x,\Psi_{j,m}\rangle\right)\Psi_{j,m} + \sum_{m}\rho_T\left(\langle x,\Phi_{J,m}\rangle\right)\Phi_{J,m}$$

Where ρ_T are the coefficients after hard or soft thresholding. For a general signal, the energy of the signal is mainly concentrated on the low frequency part, so we should keep the approximate coefficients and take the thresholded wavelet coefficients since the energy of the noise is focused on the high frequency part. So noise is reduced in a large sense by setting those wavelet coefficients lower than the threshold to zero. The signal's sharp region will generate the wavelet coefficients whose magnitude is very large. Keeping these wavelet coefficients can avoid smoothing the sharp region. Therefore, the signal's details which have important characteristic are saved. That's the essential difference between the wavelet method and the frequency filtering method based on Fourier transform. The usual wavelets are Mexican hat wavelet, DOG wavelet , Daubechies wavelets and so on. Among these, Daubechies（dbn）wavelets

are compactly supported orthogonal wavelets, which have many effective applications in spectral analysis.

2.6 Data Analysis

The spectra were transferred into the notebook pc through wireless network. The commercial software package ASD View Spec Pro (ASD Co., USA), unscrambler9.7 (CAMO Co., USA) and MATLAB7.0 were used for processing the data and developing determination models for the sample set. In this study, the quality of calibration model was quantified by the root mean square error of calibration (RMSEC), the root mean square error of prediction (RMSEP) and the correlation coefficient (r_c and r_v) between the predicted and measured parameter values. A good model should have a low RMSEC, a low RMSEP and a high r value. The RMSEC and RMSEP are calculated as follows:

$$RMSEC = \sqrt{\frac{1}{I_c - 1}\sum_{i=1}^{I_c}(\hat{y}_i - y_i)^2}$$

$$RMSECV = \sqrt{\frac{1}{I_p - 1}\sum_{i=1}^{I_p}(\hat{y}_i - y_i - bias)^2}$$

$$bias = \frac{1}{I_p}\sum_{i=1}^{I_p}(\hat{y}_i - y_i)$$

Where:

$\hat{y}_i$ = predicted value of the i-th observation.

y_i = measured value of the i-th observation.

I_c = number of observations in calibration set.

I_p = number of observations in prediction set.

3 Results and Discussion

3.1 Samples Outliers Removing

An outlier is a sample which looks so different from the others that it either is not well described by the model or influences the model too much. Outliers should be investigated: there may have been errors in data collection or transcription, or those samples may have to be removed if they do not belong to the population of interest. Outliers can be detected by PCA Score plots, Leverages measurement or sample Residuals. Residuals measure how well samples fit the model determined by the components. In this article, the selection of outliers was based on the residual sample variance. A PLS model was developed with all the 88 samples as the calibration set and the validation set. NO. 3, 17 and 76samples had much larger residual variance than other samples. It demonstrated that NO. 3, 17 and 76Samples were poorly described by the model, which nevertheless fitted the other samples quite well. Such

samples were strangers to the family of samples well described by the model, i.e. outliers. So NO.3, 17 and 76 samples were removed from the sample set.

3.2 Wavelet De-noising

Program for eliminating noise signal in NIR spectra using wavelet transformation was made by MATLAB7.0. The Birgé–Massart strategy was applied to calculate level-dependent thresholds, thresholding mode is soft thresholding. The spectra of 85 samples within 500-2500nm were decomposed in level 2,3,4 and 5 using the orthogonal wavelet functions DBn(n=1,2,3,4,5,6,7,8). Then PLS models were developed with the reconstructed NIR spectra. All the models were validated by full cross validation. The result was showed in the table 3.

Models based on different wavelet de-noising spectra were compared in table3. All the DBn wavelet transformation can Eliminating Noise at different degree. The models based on the WD spectra produced lower root mean square error and higher

Table 3. Comparison of Wavelet De-noising with Different Wavelet Functions and Different Decomposition Levels

No.	*Function*	*Level*	*calibration*		validation	
			RMSEC	**r_c**	**RMSECV**	**r_v**
1	DB1	5	7.544	0.830	11.172	**0.598**
2	DB1	4	5.054	0.927	8.865	**0.781**
3	DB1	3	6.888	0.860	9.575	**0.721**
4	DB1	2	7.412	0.836	9.727	**0.708**
5	DB2	5	7.022	0.855	9.492	**0.724**
6	DB2	4	6.006	0.896	8.080	**0.808**
7	DB2	3	7.299	0.842	9.198	**0.740**
8	DB2	2	7.608	0.827	9.398	**0.727**
9	DB3	5	6.340	0.883	8.925	**0.760**
10	DB3	4	6.528	0.876	8.615	**0.777**
11	DB3	3	7.580	0.828	9.355	**0.730**
12	DB3	2	7.621	0.826	9.398	**0.727**
13	DB4	5	7.577	0.828	9.880	**0.692**
14	DB4	4	6.593	0.873	8.558	**0.779**
15	DB4	3	7.600	0.827	9.374	**0.728**
16	DB4	2	7.622	0.826	9.399	**0.726**
17	DB5	5	6.535	0.875	8.906	**0.759**
18	DB5	4	6.630	0.871	8.715	**0.771**
19	DB5	3	7.612	0.826	9.385	**0.727**
20	DB5	2	7.622	0.826	9.398	**0.726**
21	DB6	5	6.854	0.862	9.562	**0.720**
22	DB6	4	6.669	0.870	8.735	**0.769**
23	DB6	3	7.605	0.828	9.381	**0.728**
24	DB6	2	7.621	0.826	9.398	**0.727**
25	DB7	5	6.618	0.872	9.696	**0.713**
26	DB7	4	6.754	0.866	8.834	**0.763**
27	DB7	3	7.602	0.827	9.377	**0.728**
28	DB7	2	7.620	0.826	9.398	**0.727**
29	DB8	5	5.932	0.899	9.201	**0.749**
30	DB8	4	6.778	0.865	8.941	**0.757**
31	DB8	3	7.563	0.829	9.345	**0.730**
32	DB8	2	7.621	0.826	9.398	**0.727**
33	NON		7.619	0.826	9.605	**0.715**

correlation coefficient than the model based on original spectra. It was demonstrated that the wavelet de-noising is an effective pretreatment method in spectra analysis. Different wavelet transformation resulted in different model precision and stability. It is obvious that in the same decomposition Level, DB2 wavelet transformation produced the lowest root mean square error and the highest correlation coefficient.

Also, different decomposition Level affected the result significantly, Even if the same wavelet function was applied. For example, the DB2 wavelet de-noising spectra in different decomposition levels resulted different model quality. The de-noising spectra in level 5 decomposed the spectrum data too much and eliminated the noise and useful information. It was distorted and looked so different from the original spectroscopy. Nevertheless the de-noise spectra in level 2 and 3 did not eliminate the noise adequately and effectively. The decomposition in level 4 was more useful to improve the quality of models than other decomposition levels.

Among them, the decomposition in level 4 of DB2 wavelet function produced best noise removing capability and obtained optimal calibration model.

3.3 Comparison of Different Pretreatment Method

In the work, other 8 types of pretreatment methods were used. The results for VC content calibration models of PLS regression methods using different spectral correction is presented in Table 4.

Table 4. The results for VC content calibration models of PLS regression methods

No	Pretreatment	calibration		Validation	
		RMSEC	$\mathbf{r_c}$	**RMSECV**	$\mathbf{r_v}$
1	non	7.619	0.826	9.605	0.715
2	First derivative	4.851	0.933	11.011	0.633
3	Second derivative	12.023	0.457	14.410	0.025
4	Normalize	7.730	0.820	9.568	0.718
5	MSC	7.818	0.816	9.267	0.735
6	Baseline	7.825	0.815	9.638	0.713
7	SNV	7.837	0.815	9.473	0.720
8	Smooth(3)	7.630	0.825	9.398	0.726
9	De-trending	7.690	0.822	9.431	0.722
10	DB2 wavelet(4 level)	6.006	0.896	8.080	**0.808**

Most of the pretreatment method listed in table 4 are not useful in these spectra data analysis. Among them, first derivative produced the rc of 0.933 and RMSEC of 4.851, but the r_v of 0.633 and RMSECV of 11.011 were far from the r_c and RMSEC. It demonstrates the model with First derivative pretreatment is very unstable. So first derivative is not suitable for these spectra data analysis. It is obvious that wavelet de-noising produces best noise removing capability and is useful to improve the quality of models.

4 Conclusion

Near infrared reflectance with wavelet de-noise was used to estimate the VC content in Citrus reticulate Blanco from 500 nm to 2500 nm. Methods for eliminating noise

signal in Near infrared spectra using different pretreatment were investigated. Wavelet de-noise produces better noise removing capability than other pretreatment and is useful to improve the quality of models. Among them, the PLS model with DB2 wavelet de-noise (in decomposition level 4) produced best result (RMSEC=6.006, RMSECV=8.080, rc =0.896and rv =0.808). This research has established a new de-noise technique for non-destructively estimating VC content of intact citrus.

Acknowledgments. The authors gratefully acknowledge the financial support provided by South China Agriculture University President Foundation (2009K005), Modern Agriculture Industry Technology System Construction Foundation of China ([2007] No.14).

References

1. Hong, T.-s., Qiao, J., Wang, N., et al.: Non-destructive inspection of Chinese pear quality based on hyperspectral imaging technique. J. Transactions of the CSAE 23(2), 151–155 (2007)
2. Hong, T.-s., Li, Z., Wu, C.-y., et al.: Review of hyperspectral mage technology for non – destructive inspection of fruit quality. Transactions of the CSAE 23(11), 280–285 (2007)
3. Lu, H.-s., Ying, Y.-b., Fu, X.-p., et al.: Estimation of Soluble Solids Content of Apple Fresh Juice by FTNIR Spectroscopy. J. Spectroscopy and Spectral Analysis 27(3), 494–498 (2007)
4. Slaughter, D.C., Thompson, J.F., Tan, E.S.: Nondestructive determination of total and soluble solids in fresh prune using near infrared spectroscopy. J. Postharvest Biology and Technology 28, 437–444 (2003)
5. Liu, Y., Ying, Y., Chen, Z., Fu, X.: Application of near infrared spectroscopy with fiber optics for detecting interior quality in peaches. In: Proceedings of SPIE The International Society for Optical Engineering, Monitoring Food Safety, Agriculture, and Plant Health, vol. 5271, pp. 347–355 (2004)
6. Liu, Y.-d., Chen, X.-m., Sun, X.-d., et al.: Nondestructive Measurement of Vitamin C in Nanfeng Tangerine by Visible/Near-Infrared Diffuse Reflectance Spectroscopy. J. Spectroscopy and Spectral Analysis 28(10), 2318–2320 (2008)
7. Xia, J.-f., Liu, X.-y., Li, P.-w., Wang, W., Ding, X.-x., et al.: Approach to nondestructive measurement of Vitamin C content of orange with near-infrared spectroscopy treated by wavelet transform. Transactions of the CSAE 23(6), 170–174 (2007)
8. Ma, L., Xia, J.-f., Zhang, Z.-f.: Effects of Spectral Pretreatment on Nondestructive Evaluation of Soluble Solids Content of Tomatoes with near Infrared Spectroscopy. Journal of Huazhong Agricultural University 27(5), 672–675 (2008)
9. Xia, J.-f., Li, X.-y., Li, P.-w., Wang, W., Ding, X.-x., et al.: An Approach to Measure Inner Quality of Orange with Near-infrared Spectroscopy Treated by Wavelet Do-noised. Journal of Huazhong Agricultural University 26(1), 120–123 (2007)
10. Ma, L., Xia, J.-f., Zhang, Z.-f., Wang, Z.-s., et al.: Nondestructive Determination of Total Sugar Content in Tomatoes by Near Infrared Spectroscopy. J. Food Science and Technology (2009)
11. Xia, J.-f., Li, X.-y., et al.: Wavelet Optimization for Near-infrared Spectra Denoising of Vitamin C Content of Umbilical Orange. J. Transactions of the Chinese Society for Agricultural Machinery 40(4), 143–146 (2009)

Applying PD Online Measurement Technique to Assess Stator Insulation State of Hydro-generators

Gong Chuanli[1], Wan Yuan[1,2], Yang Yeping[1], and Chi Hailong[1]

[1] Automation Department of China Institute of Water Resources and Hydropower Research, Beijing, 100038, China
[2] Wuling Power Corporation, Changsha, Hunan, 410004, China
hubeigcl@163.com

Abstract. Partial discharge (PD) online measurement is considered as one of the most effective means to assess stator insulation state and prevent sudden accidents of hydro-generator. However, the existence of external interferences has greatly reduced the credibility of PD online measurement technology of hydro-generators. In this paper, a set of high reliable hydro-generator PD on-site measurement system was developed, which made use of PDA technique to obtain PD pulses, and in order to eliminate the external interferences and ensure the reliability of PD pulses acquisition, the combination of directional double sensors and pulse time-delay technique are adopted, which can effectively suppress the external pulse shaped interferences (PSI) from power network. At present, the system has been applied to several hydro-generators in a huge-size hydropower plant to assess the stator insulation state, and a lot of on-site measurement results were achieved and explained. An actual failure of the stator insulation was checked out by the system and a great deal of economic loss was avoided, which greatly increases the credibility of the PD online monitoring technology.

Keywords: Partial discharge (PD), External interferences, Online measurement, Hydro-generator, Stator insulation state, Pulse shaped interferences (PSI).

1 Introduction

Partial discharges (PDs) turns out to be a very important symptom of the most common stator insulation failure processes (although rarely a cause) of the large-size hydro-generators, including [1]:

- poor impregnation with epoxy;
- poorly made semi-conductive coatings;
- insufficient spacing between coils in the end winding area;
- loose coils in the slot;
- overheating (long-term thermal deterioration);
- winding contamination by moisture, oil, dirt, etc.;
- load cycling problems;
- poor electrical connections (although this is not strictly an insulation problem).

D. Zeng (Ed.): Future Intelligent Information Systems, LNEE 86, pp. 475–482.
springerlink.com © Springer-Verlag Berlin Heidelberg 2011

Various methods have been developed to measure the PD activity in a stator winding. The most popular methods are those that can be implemented during normal operation of the machine to online assess stator insulation state, since costly outages can be avoided [2].

In this paper, a set of PD online measurement system for large-size hydro-generators (HPDMS) has been developed by The system was developed by professor Li Zhaohui (who is a professor in School of Hydropower and Information Engineering of Huazhong University of Science and Technology (HUST)) and his assistants, to on-site assess the stator insulation state [7]. In order to eliminate the external interferences and ensure the reliability of PD pulses acquisition, the combination of directional double sensors and pulse time-delay technique are adopted, which can effectively suppress the external pulse shaped interferences (PSI) from power network. At present, HPDMS the system has been applied to several hydro-generators in a huge-size hydropower plant to assess the stator insulation state and a lot of on-site measurement results were achieved and explained. An actual failure of the stator insulation was checked out by HPDMS and a great deal of economic loss is avoided, which greatly increases the credibility of the PD online monitoring technology [7].

2 PD Online Measurement System for Hydro-generators

The PDA method, which is the most common method for hydro-generator PD monitoring in the world and invented by G.C. Stone [1], [2], is used for HPDMS. According to PDA method, two sensors per phase are mounted on the hydro-generator outlet terminals to obtain PD pulses. Each sensor comprises of a high-voltage capacitor C (300pF) and a detection impedance R (100Ω). Total of 6 sensors are needed for a hydro-generator. When frequency of the signal is *f*, the impedance value *Z* of the high-voltage capacitor C for the signal can be described as (1)

$$Z = \frac{1}{2\pi fC} \tag{1}$$

Therefore, when f =50Hz , Z = 10.6MΩ; when f =10MHz , Z = 10.6MΩ, Z = 53 Ω. The high-voltage capacitor C behaves as quite large impedance for low frequency signal but low impedance for high frequency signal. As most of PD pulses are high frequency signal, the sensors of PDA method can detect PD pulses with good sensitivity.

The PC-Card construction in hardware was adopted by HPDMS. In addition to 6 sensors, HPDMS consists of a hardware signal processing device (HSPD), a high-speed data acquisition (DAQ) card, an industrial control computer (IPC) (shown in Fig.1.). The system software is run on IPC. PD pulses detected by the sensors were sent into HSPD as the original data after hardware processing including amplification, attenuation, and interferences suppression, and then transmitted to DAQ card. In HPDMS, the voltage synchronous signal that helps PD analysis and discharge pattern recognition was also connected to DAQ card to trigger the PD pulses sampling. In order to improve the accuracy of PD pulses analysis, the sample rate of DAQ card is 100M/s.

The system software was run on IPC for interferences suppression, discharge pattern recognition, PD distribution analysis and historical data records, etc. The final analysis results were feedback to the user to assess the stator of stator insulation and diagnosis the insulation fault.

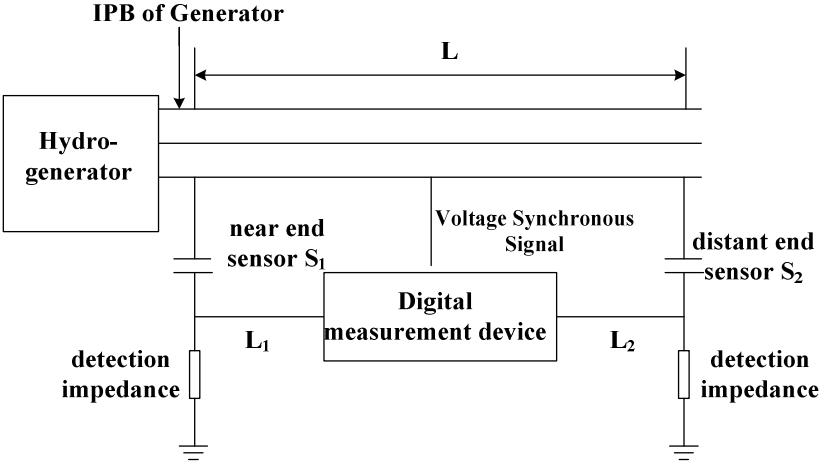

Fig. 1. System structure

3 Interferences Suppression

Unfortunately, there were usually many types of electrical interferences to contend with in PD on-site monitoring which greatly reduced the credibility of PD online measurement technique [3], hereinto, the discrete spectrum interferences (DSI) and pulse shape interferences (PSI) were two type interferences which are most difficult to be eliminated. In order to reduce the two type interferences (DSI, PSI) and ensure the reliability of PD pulses acquisition, the following two techniques are adopted.

3.1 DSI Suppression

For hydro-generator PD online measurement, DSI is usually generated by carrier communication signal, power-frequency signal and its harmonic, etc. Experimental results show that the frequency of most DSI is lower than 2MHz while the frequency of PD pulses is much higher than 5MHz [3]. Each sensor of HPDMS comprises of a high-voltage capacitor C(300pF)and a detection impedance R(100Ω), which can be considered as a high-pass filter. The low limit frequency F_c of the high-pass filter is described as (2)

$$F_C = \frac{1}{2\pi RC} \approx 5MHz \tag{2}$$

So the impedance of each sensor is very large impedance for low frequency signal but very small impedance for high frequency signals, and DSI and some low frequency PSI can be suppressed because of their frequency characteristics.

In addition, the system makes use of the digital high-pass filter named IIR filter by software to suppress DSI, the low frequency limit of the IIR high-pass filter is 5MHz.

3.2 PSI Suppression

The pulse shape and frequency characteristics of PSI are very similar to PD pulses, so PSI, most of which comes from the power network, is specifically difficult to suppress.

In order to depress PSI from the power network, the combination of directional double sensors and pulse time-delay technique [3] are adopted in HPDMS, and both hardware and software are used, the detailed processing are as follows:

(a) Two sensors per phase called near end sensor S_1 and distant end sensor S_2, which are separated by L(>2m), are mounted on the machine terminals. The signal from the S_1 is transferred to the HSPD through a coaxial cable with length L_1, correspondingly S_2 is connected with the HSPD through a coaxial cable with length L_2. The method of PD sensors installation is shown in Figure 1.

(b) The proper length L_1 and L_2 is chose to meet (3), which can make sure PSI from the network coupled by S_1 and S_2 arrive at the HSPD at the same time Contrarily, the PD pulses generated inside the generator arrive the S_I first and then coupled by S_2. Let us assume that pulses generated inside the generator coupled by S_I will arrive HSPD earlier than the signal coupled by S_2 with the time delay Δt, if the propagation velocity along the line of the pulses generated inside the generator is v_p, the value of Δt can be calculated by (4).

$$L_2 = L + L_1 \tag{3}$$

$$\Delta t = \frac{L + L_2 - L_1}{v_p} = \frac{2L}{v_p} \tag{4}$$

(c) A criterion time delay Δt_0 can be set. When $\Delta t > \Delta t_0$, the signal will be considered as PD pulses, or it will be considered as PSI.

(d) The choice of the value of Δt_0 must take full account of the max propagation velocity along the line of PD pulses generated inside the generator. To obtain the max propagation velocity of PD pulses is very difficult, and needs a large number of theoretical calculations and simulation experiments. If the max propagation velocity of PD pulses is v_m, the value of Δt_0 can be calculated by (5).

$$\Delta t_0 = \frac{2L}{v_m} \tag{5}$$

4 Data Analysis and Stator Insulation Assessment

At present, HPDMS has been applied to several large-size hydro-generators in a huge-size hydropower plant to assess stator insulation state, and achieved good effects in the industrial applications. The online measurement results were shown in the following and have proved the effectiveness and reliability of HPDMS [7].

4.1 On-Site PSI Elimination

Fig.2. shows the effect of on-site PSI elimination of HPDMS, by making use of the combination of directional double sensors and pulse time-delay technique, all of pulse shape signal (shown in Fig.2(a).) which mixed PD pulses and external interferences from power network could be divided into two types because of their time delay of arrival in HPDMS through two paths respectively called near end sensor S_1 and distant end sensor S_2 in a phase. The pulses, which arrived HPDMS in the different time though two paths, was regarded as PD pulses (shown in Fig.2(b).), The pulses, which arrived HPDMS at almost the same time though two paths, was considered as PSI from power network (shown in Fig.2(c).).

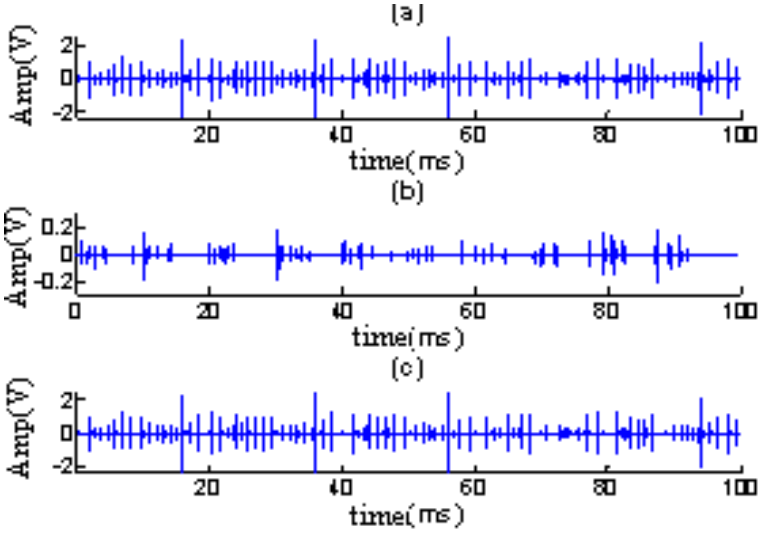

Fig. 2. Effects of PSI suppression method. (a) pulses composed by external interferences pulses from power network and PD pulses; (b) PD pulses; (c) external interferences pulses from power network.

4.2 PD Pattern Analysis

Fig.3. is the PD distribution for a certain hydro-generator (including two-dimensional PD distributions: $H_{qmax}(\varphi)$, $H_n(q)$) and three-dimensional PD distributions $H_n(q, \varphi)$) which can be calculated by statistics of PD pulses in 50 power cycles[4],[5]. Two characteristics of PD pulses distribution can be described From PD distributions: (a) PD pulses were focused in the phase angle segments of [0, 90] and [180, 270] degree; (b) the magnitude and repetition rate of PD pulses in positive and negative half power cycle were very symmetrical. Both of the distribution characteristics can be regarded as “fingerprint” for PD pattern recognition, By recognition of PD distributions, the discharge pattern was regarded as the internal discharges, which was caused by the internal air gap in stator insulation of the hydro-generator [4], [5].

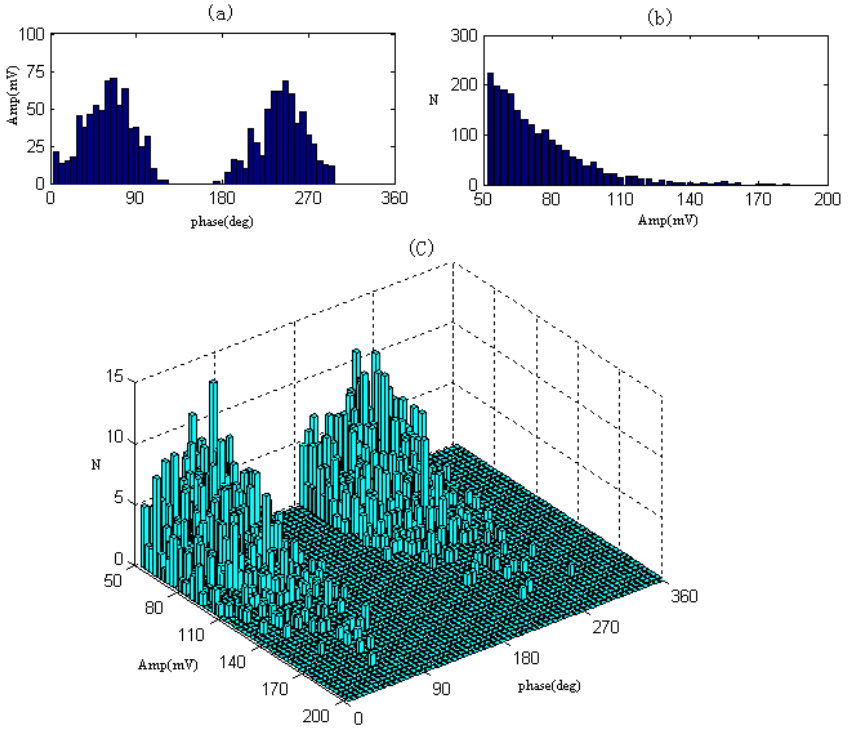

Fig. 3. PD distributions. (a) Hqmax(φ); (b)Hn(q)); (c)Hn(q, φ)).

4.3 PD Trend and Assessment of Stator Insulation State

HPDMS has successfully checked out stator insulation problem of a hydro-generator in a huge-size hydroelectric plant by PD trend analysis and stator insulation state assessment, and avoided huge economic losses. The trends of NQN with respect to time when the stator insulation is in failure are shown in the following Fig.4 [7].

From the point of G.C. Stone [6], NQN stands for the sum of all PD's amplitude in valid windows, it has positive correlation with the stator insulation state and analysis of NQN tendency can diagnosis the failure of the stator insulation. So the trends of NQN with respect to time plays a key role in stator insulation state assessment.

From Fig.4, we can find that the NQN of positive and negative discharges of phase A, B, C all increased rapidly, they are all more than normal level from April 6 to April 18. In G.C. Stone's opinion [6], If the there was obvious increasing shown in the tendency, it indicates that stators winding insulation is deteriorating quickly. So from the trend of NQN with respect to time above, the stator insulation state of the hydro-generator is apparently deteriorating since April 6;

After checking the hydro-generator sets in April 18th, a metallic tube with length of 1m, diameter of 20mm was found in the stator windings between phase A and B near to the high voltage end [7]. Therefore, during normal operation of the generator, PD occurred in the position of the defect (metallic tube), which was considered as end

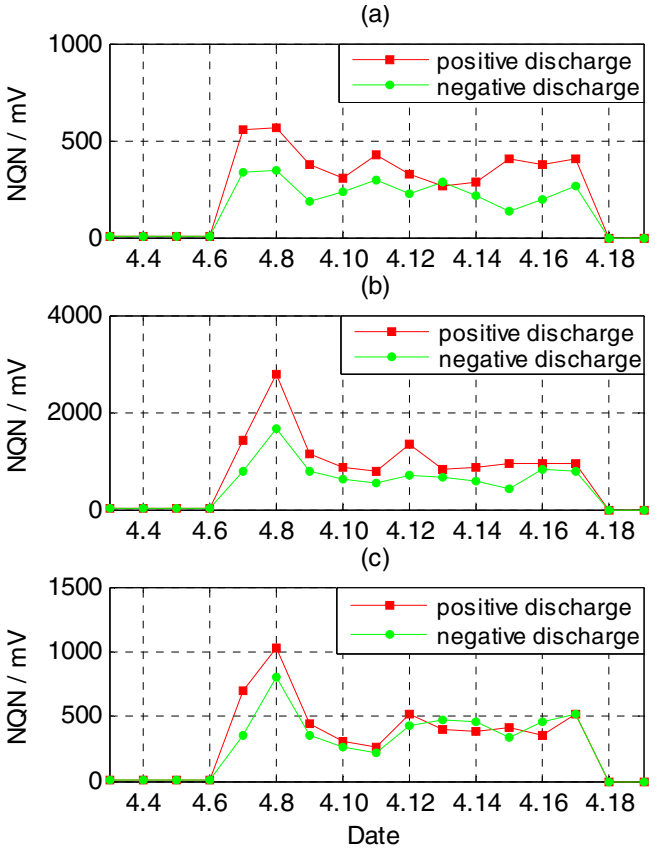

Fig. 4. The trend of NQN of positive and negative discharge with respect to time when the stator insulation is in failure. (a) NQN of phase A;(b) NQN of phase B; (c) NQN of phase C.

surface discharge, and winding insulation of the hydro-generator was being degradation [7]. The online monitoring result was essentially consistent with the actual stator insulation fault, which proved the effectiveness of HPDMS.

5 Conclusion

This paper applied on-site PD measurement technique to assess stator insulation state of hydro-generators and has developed a set of high reliability PD online measurement system for hydro-generators. At present, the system has been applied into several hydro-generators in a huge-sige hydropower plant, and achieved good effect in the industrial field. The following conclusion can be obtained by the application of the system.

(1) PDA method for hydro-generators PD online measurement can obtain wonderful performance in the the industrial field. Therefore, the PDA method is very

effective to be applied in PD online measurement for hydro-generators and quite useful to assess stator insulation state of hydro-generators.

(2) The high-voltage capacitor C of PDA method behaves as quite large impedance for low frequency signal but low impedance for high frequency signal. As most of PD pulses are high frequency signal, the sensors of PDA method can detect PD pulses with good sensitivity.

(3) The combination of directional double sensors and pulse time-delay technique can perfectly distinguish PD pulses and external interferences from power network and ensure the reliability of PD pulses acquisition.

(4) PD distributions analysis is beneficial to identify discharge pattern and determine discharge reason. Moreover, the trend of NQN with respect to time has positive correlation with the stator insulation state and analysis of NQN tendency can diagnosis the failure of the stator insulation. Therefore, the trend of NQN with respect to time plays a key role in stator insulation state assessment.

References

1. Stone, G.C., Warren, V.: Objective Methods to Interpret Partial-Discharge Data on Rotating-Machine Stator Windings. IEEE Transaction on Industry Applications 42, 195–200 (2006)
2. Stone, G.C.: Why Calibration of Partial Discharge Measurements for Motor and Generator Windings with pC Can't Be Done. IEEE Electrical Insulation Magazine 14, 19–32 (1998)
3. Yang, X., Zang, Z., et al.: The Study of Noise-rejection by Using Pulse Time-delay Identification Method and the Analysis of PD Data Obtained in the Field. In: 4th International Conference on Solid Dielectrics, pp. 236–240. Xi'an (2007)
4. Tanaka, T.: Partial discharge pulse distribution pattern analysis. IEE Proc. Sci. Meas. Techno. 142, 46–50 (1995)
5. Gulski, E.: Digital Analysis of Partial Discharges. IEEE Trans. on Dielectrics and Electrical Insulation 2, 822–837 (1995)
6. Stone, G.C.: Partial Discharge Diagnostics and Electrical Equipment Insulation Condition Assessment. IEEE Transactions on Dielectrics and Electrical Insulation 12, 891–902 (2005)
7. Hong, W., Yuan, W., Li, Z.: Monitoring and analysis of partial discharge of the large-size hydro-generator. In: Proceeding of 1st International Conference on Hydropower Technology & Key Equipment, Beijing, pp. 463–466 (2006)

Applying UHF PD On-site Monitoring to Large-Size Power Transformer and Pulses Analysis

Gong Chuanli[1], Wan Yuan[1,2], Yang Yeping[1], and Chi Hailong[1]

[1] Automation Department of China Institute of Water Resources and Hydropower Research, Beijing, 100038, China
[2] Wuling Power Corporation, Changsha, Hunan, 410004, China
hubeigcl@163.com

Abstract. The use of partial discharge (PD) on-site monitoring as an indicator of HV equipments insulation condition is well known. However, the existence of external interferences has greatly reduced the credibility of PD on-site measurement technology of HV equipments. This paper describes practical application of the UHF PD detection method on a new oil-immersed power transformer and to suppress interference, an internal UHF sensor (antenna) was designed and successfully installed to power transformers for its insulation condition assessment which can effectively avoid the frequency band of the external interferences. As the frequency band of this UHF sensor was 300~1500MHz, envelope detection technique was used to extract UHF signals excited from PD sources inside the transformer. The results of MATLAB simulations have shown that UHF PD signals can be effectively extracted by this method. Using the monitoring system established in this paper, plenty of external interferences pulses and UHF PD pulses were recorded and investigated, PD pulses with small amplitude can be effectively detected, which reveal that UHF PD measurements can effectively measure small level of discharges with good sensitivity.

Keywords: Partial discharge (PD); On-site monitoring; External interferences; Envelope detection; Power transformers; UHF sensor.

1 Introduction

Partial discharges (PDs) in oil-immersed power transformers are often predecessors of serious insulation faults. For this reason, PD measurements are an important diagnostic tool to monitor the insulation condition of large-size power transformers. It is widely accepted that the UHF technique can be used to detect and identify PD defects in power transformers, and it has made tremendous achievements in this regard [1].

Previous research has also demonstrated that PDs inside power transformer show impulse-shaped signals with a front time less than 1 ns [2], [3]. The electromagnetic (EM) waves radiated by the discharge sources in transformer oil with a frequency range of 300 to 3000 MHz, which propagate at the speed of light as TEM-, TE- and TM-waves [4]. Because oil and paper, which act as central insulation in transformers,

D. Zeng (Ed.): Future Intelligent Information Systems, LNEE 86, pp. 483–490.
springerlink.com © Springer-Verlag Berlin Heidelberg 2011

have almost the same dielectric parameters in particular permittivity, the propagation of EM waves is scarcely influenced by oil-paper combination. However, reflection and refraction take place when they meet electric conductive obstacles such as cores, windings, angular modules, flanges, etc., which increase the difficulty of UHF PD detection [4].

To couple these EM waves emitted by PD sources, the UHF sensor [5] is to be mounted inside the transformer tank in this paper, which can prevent mostly external interferences, e.g. corona in air, light strikes. One great advantage of UHF technique described in this paper is the high signal-to-noise ratio (SNR), and another is the higher sensitivity to detect PD signals emanating from discharges buried inside the insulation.

In the long-term continuous monitoring process, plenty of external interferences pulses and UHF PD pulses were recorded and studied, PD pulses with small amplitude can be effectively detected, which reveal that UHF PD measurements can detect small level of discharges with good sensitivity.

2 UHF PD Detection Technique

UHF PD detection is based on the detection of UHF signals generated in the event of partial discharges. However, power transformer is totally encapsulated metal tank and scarcely any EM waves can radiate out of it. Therefore, in order to couple the UHF PD signals radiated inside the transformer, an internal UHF sensor was designed to be mounted into the tank in this paper.

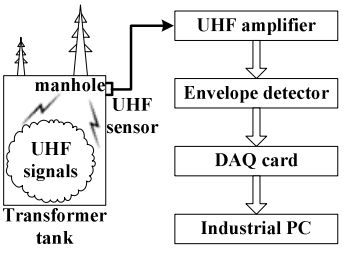

Fig. 1. Diagram of UHF PD on-site detection system for transformer

Based on this internal UHF sensor which was fixed on the transformer tank, a UHF PD on-line monitoring system was established as shown in Fig. 1. The system was developed by professor Li Zhaohui (who is a professor in School of Hydropower and Information Engineering of Huazhong University of Science and Technology (HUST)) and his assistants [8], Original UHF signals were pre-amplified using an amplifier and transmitted by coaxial cables to the envelope detector for lowering frequency, and then sampled in an industrial computer for pulse extraction and identification.

2.1 UHF Sensor

It is well known that the operation environment of the sensor used for internal fitting is very bad and adverse. Firstly, it has to work in the mineral oil which is causticity and has high temperature (perhaps > 120℃). Secondly, it is required to operate in 50 Hz EM fields of significant magnitude. And thirdly, it should be immune from the effects of external interferences including lightning, switching surges, etc. Furthermore, it is difficult to remove the internally mounted sensor when the transformer is running, so the sensor must have high reliability and run in the tank for a long time [5].

It is regrettable that there is no commercial sensor meeting these requirements, so it was necessary to develop special one in-house. In this paper, a two-wire Archimedean planar spiral antenna, illustrated in Fig. 2, was selected as the UHF coupler [2], [5], [7]. The broadband antenna was designed with bandwidth from 300MHz to 1500MHz, and the center frequency was ~800MHz.

For the sake of improving installation feasibility in the field, the antenna was encapsulated by epoxy resins, which played roles as insulation, anti-corrosion, anti-oxidation and tolerance high temperature. Before left factory, a very rigorous test was carried out to the UHF sensor, which revealed that it could work in transformer tank [8].

Fig. 2. A two-wire Archimedean planar spiral antenna

Compared to the traditional monitoring methods, UHF PD monitoring method for large-size power transformers has several advantages as follows:

(1) The detection band of UHF PD monitoring method is 300MHz~15000MHz, and the band of most local external interferences is under 100MHz [2], [4], [6], so the UHF method can avoid most local interferences and detect PD with high sensitivity.
(2) The UHF PD sensor is usually buried inside the transformer and the transformer enclosure has a good shielding effect, so most of the external high frequency signals can not enter inside the tank, which shows that the UHF method has a strong immunity to external noise. Serious experiments show that because the transformer enclosure can prevent electromagnetic wave intrusion, the UHF method is almost undetectable to the corona discharge in air outside the transformer [2], [6].
(3) Because there is no electrical connection between the UHF detection sensor and the power transformer's high voltage side completely, the UHF detection method is more safe and reliable for the power secondary system and the operator than the other PD monitoring methods.

2.2 UHF Envelope Detector

In PD measurements, it is often attaching importance to the following two aspects: 1) maximum and mean discharge amplitude, and 2) the phase positions at which PD signals occur. Therefore, a special signal pretreatment method is needed to reduce the frequency of original PD signals, which can be sampled by common data acquisition (DAQ) cards. To preserve the amplitude and phase information of PDs, envelope detection technique is used to preprocess the UHF signals. In the lab, a MATLAB model as shown in Fig. 3 was designed to simulate the envelope detection process.

In the simulation circuit, the charging capacitance, C, will determine the performance of the envelope detection. Let diode internal resistance R_d=100Ω, charging capacitance C=1pF, load resistance R=10^5 Ω, thus, charging time constant τ_c=R_dC=0.1ns<<1ns, discharging time constant τ_d=RC=100ns.

It has been proven that PD signals captured from onsite detection are oscillatory signals with a mass of attenuation, which can be illustrated using the following exponential equations:

$$f_1(t) = A\exp(-t/\tau)\sin(2\pi f_c t) \tag{1}$$

$$f_2(t) = A\left(\exp(-1.3t/\tau) - \exp(-2.2t/\tau)\right)\sin(2\pi f_c t) \tag{2}$$

Where A, τ and f_c represents signal amplitude, attenuation coefficient and oscillation frequency, respectively [8].

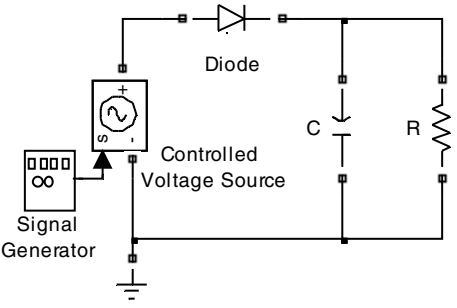

Fig. 3. The MATLAB simulation circuit of envelope detection

The PD pulses determined by (1) and (2) make up of the input of "signal generator" in Fig. 3, which controls the voltage source. Using the circuit and simulation parameters mentioned above, the envelope detection experiments were taken place in a computer with MATLAB 7.0. The blue solid line "in" in Fig. 4 represents the original UHF PD signals, and the red dotted line "out" is the output signals after envelope detection. Compared with original input signals, the outputs retain the amplitude and have almost no phase shift, specifically, the signals envelope was extracted veraciously [7].

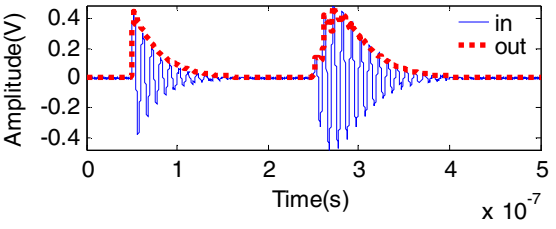

Fig. 4. The envelope results of simulation circuit

3 External Interference Pulses Analysis

It has been proven the external interferences including lightning strikes and switching operations play important roles in the impact effect of transformer turn-to-turn insulation [7]. On one hand, these over-voltage strike pulses are interferences in UHF PD detection, and on the other they act as impacts to transformer insulation [7]. Therefore, it is vital to record these over-voltage strike pulses automatically. As the strikes intensity is very sharp, a lot of external interferences were captured by the online monitoring system.

3.1 Analysis of Lightning Strike Pulses

Fig. 5(a) shows a single lightning pulse from onsite. The lightning pulse has a mild rising edge, and its duration is more than 1ms. In a sampling period (100ms), about 1~3 lightning pulses were obtained by the UHF PD on-site monitoring system [8].

The three-dimensional distribution of lightning strikes pulses was presented in Fig. 5(b). It can be seen that these distributions are nearly irrelevant with power cycle and the maximum pulse magnitude is much higher than 0.1mv [8].

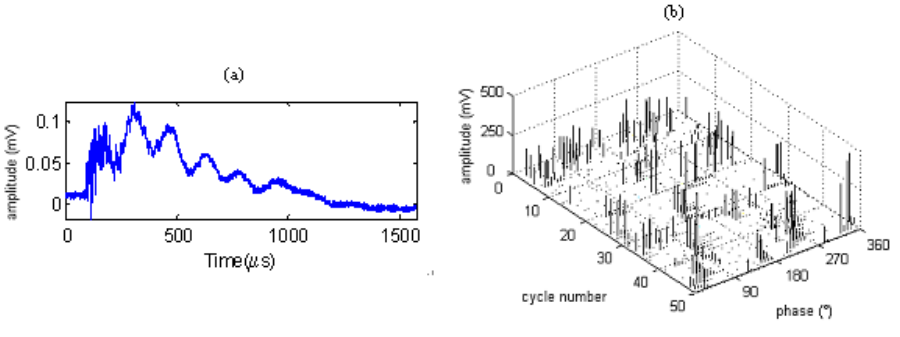

Fig. 5. Single pulse of lightning strikes and their distribution (a) Single pulse shape; (b) distribution

3.2 Analysis of Switching Operations Pulses

To evaluate the influence of the HV equipments adjacent the transformer, the records of switching operations in the switching station were studied. Fig. 6 shows two single

pulses of switching operation. The rising edge of positive pulse is in the forefront and its duration is ~1μs; while negative pulse appears a falling edge in first, and its duration is almost the same with positive one. Frequency spectrum has shown that there dominating energy concentrated in the following two frequency bands: 0.3~1.0 MHz and 2.5~3.0 MHz.

Moreover, the detected signals from switching operations are analyzed in three-dimensional phase resolved form, see in Fig. 6(c). Note that these signals were not recorded at a continual time, raw data files were logged when the signals generated by the switching operation. The characteristic of these time-domain signals shows that the pulses are concentrated in the peak value vicinity of positive and negative half cycle respectively (45°~135° and 90°~315°). Generally, the signal amplitude varies with the distance of the HV equipments. If the distance is more recent, the signal amplitude will be greater [8].

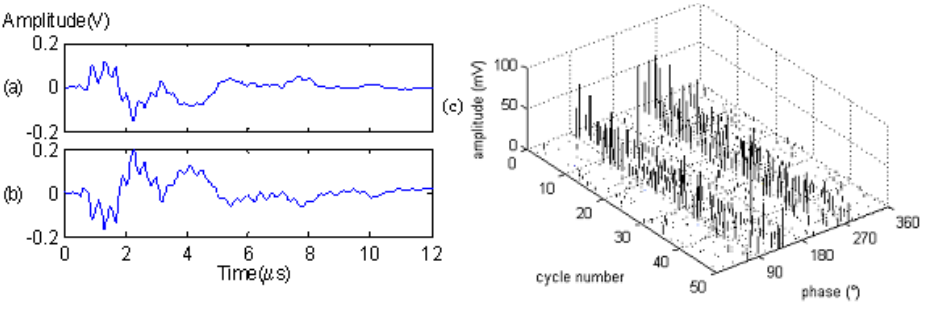

Fig. 6. Single pulse of switching operation: pulses and their distribution: (a) Positive pulse; (b) Negative pulse; (c) three-dimensional distribution

4 PD Pulses Analysis

The UHF PD online monitoring system has been applied into several power transformers, it has obtained very good online monitoring effect in the industrial application and achieved plent of UHF PD pulses from different transformers [8]. In this paper, UHF PD pulses during power transformer in stable operating state were recorded and analyzed, the relationship between PD activities and voltage is investigated and PD distribution and pattern reorganization were studied.

4.1 UHF PD Pulses Under Transformer in Stable Operating State

Generally, PD pulses have the property of periodic distribution in power cycle during transformer in stable operating state [6], [7]. Fig. 7 shows the PD pulses distribution in a power cycle and a single PD pulse waveform when the transformer was under stable condition., the PD pulses distribution is with obvious discipline and a single PD pulse is with steep rising edge ,less than 500ms duration time. PD pulse waveform achieved by UHF method is much different from that by pulse current method because of the refraction and reflection effect of the electromagnetic wave internal transformer box. The hatox of PD pulse decays seriously and pulse peak appears after the pulse rising edge.

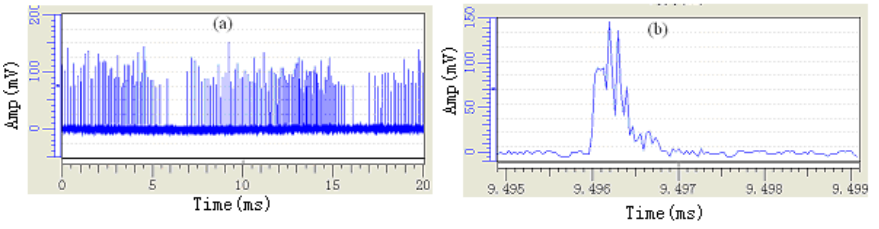

Fig. 7. UHF PD pulse. (a) PD pulses distribution in a power cycle;(b) single PD pulse waveform.

4.2 Relationship between PD Activities and Voltage

Fig. 8 shows PD activities with respect to voltage in the step-up test of transformer. We can conclude that as the voltage increased, the PD pulses repetition increased but the pulses interval gradually reduced, and the initial discharge phase was more and more closed to 0 degree, all of those are consistent with the theoretical results [7], which greatly increase the credibility of the UHF PD online monitoring technique.

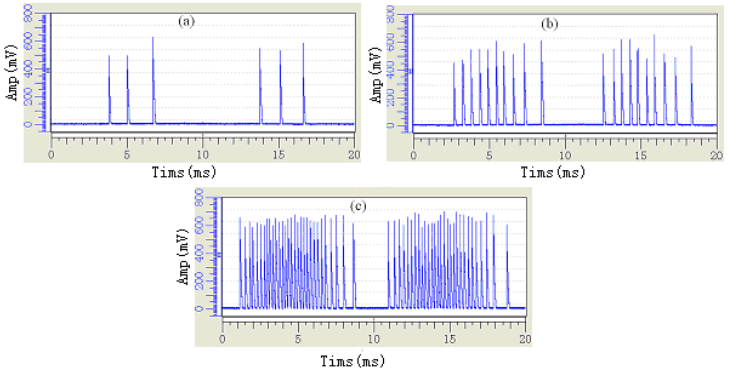

Fig. 8. PDs with respect to voltage in the step-up test. (a) PDs under low voltage; (b) PDs under middle voltage;(c) PDs under high voltage.

5 Conclusion

In this paper a practical application of the UHF technique was described to detect PDs inside the power transformer. An internal UHF sensor has been successfully installed into large-size oil-immersed power transformer. Experimental results suggest that this internal UHF sensor and envelope detector can effectively extract UHF PD signals excited from discharge sources.

Onsite monitoring results have confirmed that PD detection using UHF method results in higher or at least the same sensitivity as IEC 60270 recommendations. Moreover, External disturbances including lightning strikes and adjacent HV equipments operation can never be effectively detected. Due to continuous online data

collection when the transformer is under operation, a lot of UHF PD pulses and external interferences were obtained and studied, it can be concluded that UHF PD patterns of internal discharges differ from external disturbances significantly. Furthermore, time-domain characteristics of the signals such as rising edge, pulses interval, and duration are very different as well.

In summary, UHF technique has the potential to give all required inputs for transformer insulation assessment and is effective to determine whether any discharge activity appears, which could provide an early warning of a developing defect of power transformers.

References

1. Judd, M.D., Cleary, G.P., Bennoch, C.J.: Applying UHF partial discharge detection to power transformers. IEEE Power Eng. Rev. 22, 57–59 (2002)
2. Pearson, J.S., Farish, O., et al.: Partial discharge diagnostics for gas insulated substations. IEEE Trans. Dielect. Elect. Insul. 2, 893–905 (1995)
3. Judd, M.D., Farish, O., Pearson, J.S., Hampton, B.F.: Dielectric windows for UHF partial discharge detection. IEEE Trans. Dielect. Elect. Insul. 8, 953–958 (2001)
4. Raja, K., Devaux, F., Lelaidier, S.: Recognition of discharge sources using UHF PD signatures. IEEE Elect. Insul. Mag. 18, 8–14 (2002)
5. Wang, G.L., Hao, Y.P., Li, Y.M.: Study on the ultra-high-frequency sensors for PD detection in power transformer. In: Proc. of 2001 Int. Symp. on Elect. Insul. Mater., Himeji, pp. 793–796 (2001)
6. Gulski, E.: Digital Analysis of Partial Discharges. IEEE Trans. Dielec. Elect. Insul. 2, 822–837 (1995)
7. Judd, M.D., Yang, L., Hunter, I.B.B.: Partial discharge monitoring for power transformers using UHF sensors Part 1: Sensors and signal interpretation. IEEE Elect. Insul. Mag. 21, 5–13 (2005)
8. Liu, M., Li, Z.: An Online UHF PD Monitoring System for Power Transformer and Its Applications. In: 2010 Asia-Pacific Power and Energy Engineering Conference (APPEEC), Cheng Du, pp. 373–376 (2010)

Probe-Fed Stacked Plate Antenna with Low VSWR for Digital Television Terrestrial Broadcasting Applications

Zhongbao Wang, Shaojun Fang, and Shiqiang Fu

School of Information Science and Technology, Dalian Maritime University, Liaoning, 116026, China
{wangzb,fangshj,fushq}@dlmu.edu.cn

Abstract. A probe-fed stacked plate antenna with low VSWR is proposed for digital television terrestrial broadcasting applications. Based on standard rules for designing conventional microstrip antennas, the radiating plates are designed. To obtain 50 Ohm impedance matching, a rectangular stub is attached to one of the radiating edges of the main plate and is coplanar with the main plate. By tuning the stub, the input resistance and reactance can be easily determined. The method is used to design a probe-fed stacked rectangular plate antenna. Experimental results show that this design is capable of achieving an impedance bandwidth of about 7.6% with respect to the centre frequency of the antenna for VSWR<1.1 and a gain level of about 10dBi. The low VSWR and high gain make this element suitable for digital television terrestrial broadcasting applications.

Keywords: Stacked plate antenna, rectangular stub, probe-fed, low VSWR, digital terrestrial television broadcasting.

1 Introduction

Digital Television (DTV) has been a very exciting topic in the television broadcasting world for years. DTV as well as high definition television (HDTV) services empowered by advanced digital broadcasting technologies have indeed successfully brought millions of viewers the excellent watching experience never realized before from watching analog TV. DTV services can be delivered by terrestrial, satellite, cable broadcasting, or over the internet, and therefore, several transmission standards have been proposed to build the nationwide DTV network and provide the possibility of implementing the Single Frequency Network (SFN) for the better utilization of the spectrum [1], [2], [3]. Among them, digital television terrestrial broadcasting (DTTB) standard which defines the air-interface of the DTV signals is considered to be of the most importance and usually the adoption is mandatory. It is a tendency in the world because of the technology to realize better efficiency of frequency resources, multi channel, high quality and high functional system. And the authorized carrier frequency is UHF band, therefore acceleration of reconstruction of the equipment at the existing TV station is expected [4].

D. Zeng (Ed.): Future Intelligent Information Systems, LNEE 86, pp. 491–497.
springerlink.com © Springer-Verlag Berlin Heidelberg 2011

Usually, the analog TV terrestrial broadcasting uses multiple channels in common. Therefore, antennas of the TV transmitting station are required properties of broad bandwidth and high gain. Owing to wideband and high gain, the slotted cylinder antenna, and 2 or 4-dipoles panel antenna had mainly been used at the UHF band until now, and batwing antenna used at the VHF band [5]. However, the structure of the antennas is complex. It is difficulty in manufacture and makes high cost.

Currently, plate antennas are widely used in satellite communication and mobile communication due to their low profile, low cost and ease of manufacture [6]. However, their intrinsic weakness is narrow impedance bandwidth. Some excellent techniques have been proposed to broaden the impedance bandwidth, including the use of different shape plates [7], [8] and ground [9], [10], addition of parasitic plates [11], [12]. Unfortunately, the impedance bandwidth of the available plate antennas is still narrow when applying the VSWR<1.1 requirement. As we known, the VSWR of the antennas of the TV transmitting station is less than 1.1 [5]. Therefore, plate antennas have not been used in the TV transmitting station up to now.

With the development of DTTB technology, antennas of the DTTB transmitting station are required properties of low cost but not broad bandwidth, especially in the Single Frequency Network. Therefore, plate antennas may be used in DTTB systems. To achieve the goal, a probe-fed stacked rectangular plate antenna with low VSWR is proposed in this paper for DTTB applications. By using the rectangular stub impedance matching technique and the stacked plate configuration, the impedance bandwidth for VSWR<1.1 is enhanced to 7.6% with respect to the centre frequency of the antenna. Furthermore, the antenna has a gain level of about 10dBi across the operating bandwidth.

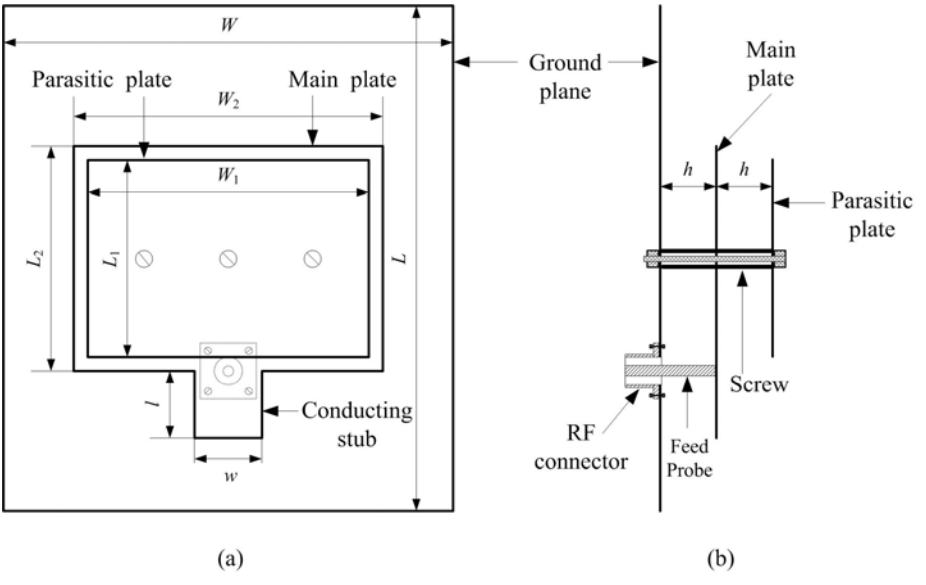

Fig. 1. Geometry of the proposed antenna. (a) Top view. (b) Side view.

2 Antenna Structure

The geometry of the proposed probe-fed stacked rectangular plate antenna with a rectangular stub is shown in Figure 1. The antenna is composed of two suspended radiating plates, a rectangular stub, a feed probe, a ground plane, a RF connector and three screws. The parasitic and main suspended radiating plates are rectangle in shape and have dimensions of $L_1 \times W_1$ and $L_2 \times W_2$, respectively. The radiating plates, which act as typical radiators, are designed based on standard rules for designing conventional microstrip antennas. The main radiating plate is suspended above the ground plane at a height of h. To enhance the bandwidth, a parasitic radiating plate is positioned above the main plate. The chosen spacing between the main and parasitic radiating plate also is h. The antenna has a ground plane with dimensions of $L \times W$, and the suspended radiating plates are positioned at the center of the ground plane. Air substrate is used in this configuration to achieve broader bandwidth, higher gain, and lower cost. Owing to the large spacing between the main plate and ground plane, a coaxial probe is used to excite the main plate instead of the microstrip line often employed on an electrically thin dielectric substrate. To compensate the large input inductance aroused from the long probe and obtain 50 Ohm impedance matching, a conducting stub is used as a broadband impedance matching network. The stub is attached to one of the radiating edges of the main plate and is coplanar with the main plate. By properly selecting the stub dimensions of $l \times w$, the input resistance and reactance can be easily determined.

3 Procedures of Antenna Design

The procedure described here is aimed at introducing a method to achieve a plate antenna design with a wide impedance bandwidth. The procedures are as follows:

1. Choose a spacing $h \approx 0.052\lambda_0$ between the main radiating plate and the ground (between the main and parasitic radiating plate).
2. Calculate the resonant length of the plates L_1 and L_2 with $L_1 \approx 0.37\lambda_0$ and $L_2 \approx 0.40\lambda_0$.
3. Determine the value of l for which the input resistance at the center frequency f_0 is 50 Ohm.
4. Tune the value of w for which the input reactance is near zero.

4 Experimental Result and Analysis

To verify feasibility of the proposed antenna, a probe-fed stacked rectangular plate antenna is designed and simulated by using HFSS 3-D EM simulator. The centre frequency of the designed antenna is chosen at 790MHz. Then it is fabricated and measured with an Anritsu MS2026A network analyzer. Figure 2 gives a photograph of the antenna prototype. The experimental results show that the antenna displays good input impedance matching, high gain and hemispherical radiation pattern. In

addition, the geometrical parameters found to achieve good performance are as follows: L_1=141 mm, W_1=214 mm, L_2=150 mm, W_2=222 mm, l=60 mm, w=41 mm, L=400 mm, W=350 mm, and h=20 mm.

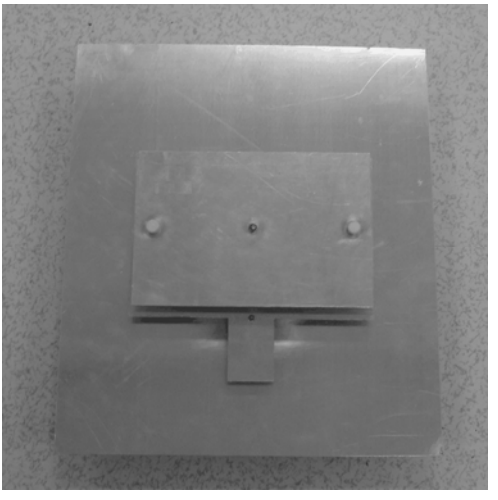

Fig. 2. Photograph of the proposed antenna prototype

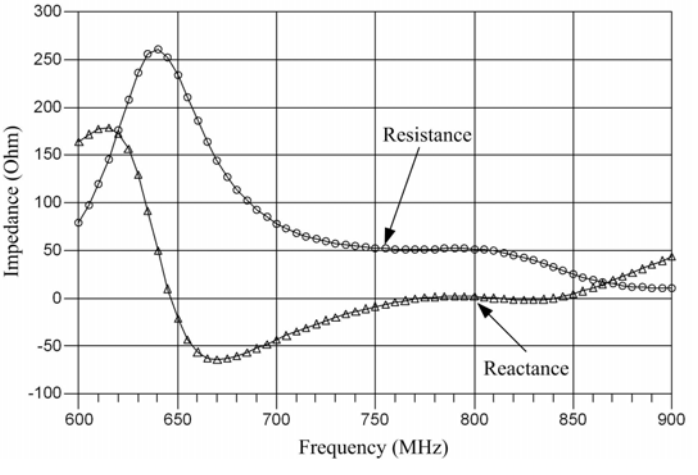

Fig. 3. Input impedance of the proposed antenna

The input impedance against the frequency is shown in Figure 3. It is clearly observed that input resistance varies around 50 Ω ranging from 740 to 820 MHz and the input reactance keeps small ranging from 760 to 850 MHz. The large reactance usually resulted from the large air spacing can effectively be cancelled out with the help of the conducting stub.

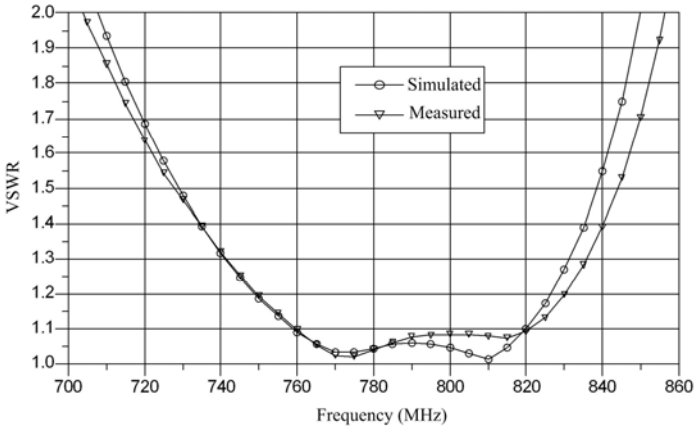

Fig. 4. Simulated and measured VSWR of the proposed antenna

A comparison between the simulated and measured VSWR shows good agreement, as displayed in Figure 4. The impedance bandwidth of the proposed antenna can reach up to 7.6%, ranging from 760 to 820 MHz for VSWR<1.1, which attributes to the stacked plate configuration and the stub impedance matching technique.

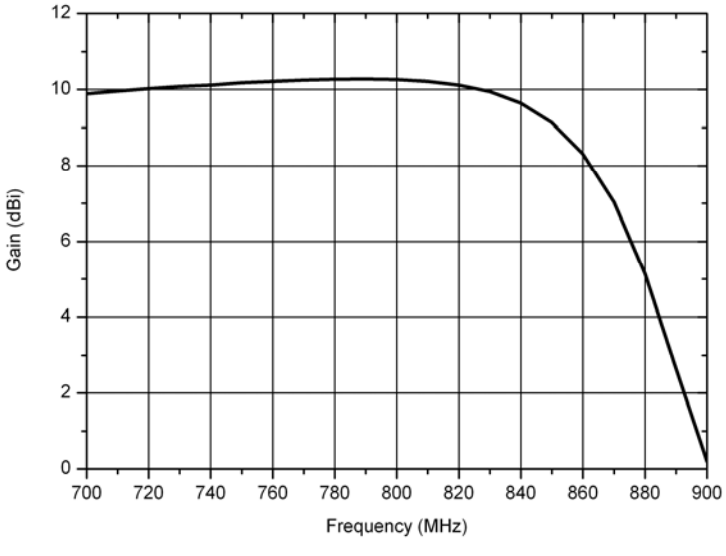

Fig. 5. Simulated gain of the proposed antenna

Figure 5 shows the antenna gain. It is clearly observed that the antenna gain is about 10dBi in the VSWR<1.1 impedance bandwidth.

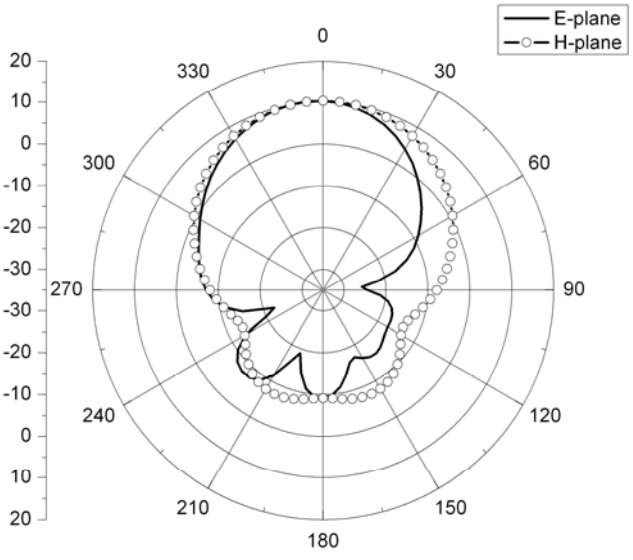

Fig. 6. Simulated radiation patterns of the proposed antenna

Figure 6 show the simulated radiation patterns of the proposed antenna in E-plane and H-plane at 790MHz. It is observed that the radiation patterns in H-plane are symmetrical and the back-lobe radiation levels are below -19 dB. The half power beam widths are about 50° in the E-plane and 60° in the H-plane. It is also observed that the asymmetrical radiation patterns in E-plane. The distortion of the radiation pattern has also been observed in other kinds of the suspended plate antennas, for example, in [11] and [12]. This may be mainly due to the excitation of the higher order modes and the feed probe, at which the distribution of the co-polarized currents is asymmetrical with respect to the x-axis in the E plane. This deficiency needs a further improvement.

5 Conclusion

A novel probe-fed stacked rectangular plate antenna is presented. By using the stub impedance matching technique and the stacked plate configuration, the impedance bandwidth for VSWR<1.1 is enhanced to 7.6% with respect to the centre frequency of the antenna. The VSWR of the antenna is much lower than other available wideband plate antennas. In addition, the antenna has a gain level of about 10dBi across the operating bandwidth. More importantly, the antenna configuration is simple and easy for fabrication, which makes it suitable for digital television terrestrial broadcasting applications.

Acknowledgments. This work was partly supported by the National Natural Science Foundation of China (Grant No. 60771032), the Traffic Applied Basic Research Project of the Ministry of Transport of China (Grant No. 2010-329-225-030) and the Fundamental Research Funds for the Central Universities.

References

1. Song, J., Yang, Z.X., Yang, L., Gong, K., Pan, C.Y., Wang, J., Wu, Y.S.: Technical Review on Chinese Digital Terrestrial Television Broadcasting Standard and Measurements on Some Working Modes. IEEE Transactions on Broadcasting 53, 1–7 (2007)
2. Zhang, W.J., Guan, Y.F., Liang, W.Q., He, D.Z., Ju, F., Sun, J.: An Introduction of the Chinese DTTB Standard and Analysis of the PN595 Working Modes. IEEE Transactions on Broadcasting 53, 8–13 (2007)
3. Zhou, J.H., Ou, Z.H., Rautiainen, M., Koskela, T., Ylianttila, M.: Digital Television for Mobile Devices. IEEE Multimedia 16, 60–71 (2009)
4. Kondo, M., Sumihiro, S., Sato, G.: Two-Stacked Circular Loop Antenna for Digital Terrestrial TV Broadcasting. In: International Conference on Computational Electromagnetics and Its Applications, pp. 577–580. IEEE Press, New York (1999)
5. Guan, Y.F.: Application of Radio and Television Transmitting Antenna Technology. Value Engineering 11, 128–131 (2010) (in Chinese)
6. Low, X.N., Toh, W.K., Chen, Z.N.: Broadband Suspended Plate Antenna for WiFi/WiMAX Applications. In: 6th International Conference on Information, Communications and Signal Processing, pp. 1–5. IEEE Press, New York (2007)
7. Chen, Z.N.: Broadband Suspended Plate Antenna with Concaved Center Portion. IEEE Transactions on Antennas and Propagation 53, 1550–1551 (2005)
8. Ge, Y.H., Esselle, K.P., Bird, T.S.: A Compact E-shaped Patch Antenna with Corrugated Wings. IEEE Transactions on Antennas and Propagation 54, 2411–2413 (2006)
9. Hsu, W.H., Wong, K.L.: Broad-band Probe-fed Patch Antenna with a U-shaped Ground Plane for Cross- Polarization Reduction. IEEE Transactions on Antennas and Propagation 50, 352–355 (2002)
10. Wong, K.L., Tang, C.L., Chiou, J.Y.: Broad-band Probe-fed Patch Antenna with a W-shaped Ground Plane. IEEE Transactions on Antennas and Propagation 50, 827–831 (2002)
11. Chen, Z.N., Chia, M.Y.W., Lim, C.L.: A Stacked Suspended Plate Antenna. Microwave and Optical Technology Letters 37, 337–339 (2003)
12. Matin, M.A., Sharif, B.S., Tsimenidis, C.C.: Probe Fed Stacked Patch Antenna for Wideband Applications. IEEE Transactions on Antennas and Propagation 55, 2385–2388 (2007)

An Approach of Error Compensation on Sensors Based on Recursive Least Squares Algorithm

Musheng Deng[1], Zhezhao Zeng[2], and Lan Li[1]

[1] Electrical Engineering Department, Hunan Railway Professional Technology College, Zhuzhou 412001, China
dsjing@sina.com, LiLan680808@126.com
[2] College of Electrical and Information Engineering, Changsha University of Science & Technology, Changsha 410076, China
hncs6699@yahoo.com.cn

Abstract. In order to improve the error compensation precision of sensors, an approach of the error compensation of sensors based on the recursive least squares (RLS) algorithm was proposed. To validate the validity of the method, the simulation example of the error compensation of sensor was given. The result showed that the approach of the error compensation of sensors using the recursive least squares algorithm has a very high accuracy. Thus, the method proposed is effective.

Keywords: Neural network, recursive least squares, sensor, error compensation.

1 Introduction

It is well known that sensors are usually sensitive to temperature, and also have nonlinear errors. Therefore, to produce high-precision sensor, its error must be compensated. There are many methods of error compensations [1-4], such as optimal linear fitting method [2,4], polynomial curve fitting approach based on least square method [6], compensation method of nonlinear inverse function [5], and nonlinear compensation method based on neural network algorithm [7], etc. Usually, linear fitting method and nonlinear compensation method of inverse function have larger compensation error, and lower compensation accuracy, hence, are seldom adopted. Polynomial curve fitting approach based on least square method has a higher compensation precision. But when there are many data, it is easy to appear the oscillatory, and is unable to obtain the coefficients of polynomial, thus its application is restricted. The document [7] introduced a nonlinear compensation method based on neural network algorithm, and obtained better error compensation, but because activation functions of hidden layer neurons are non-orthogonal functions, convergence is very slow using the BP algorithms to train neural network, and it is necessary to update weights of the two-layer neurons. It is very obvious to need large computation with bad real-time performance. In order to improve the error compensation accuracy and the real-time performance of sensors, an error compensation method of sensors using the neural network algorithm with orthogonal basis functions is proposed.

D. Zeng (Ed.): Future Intelligent Information Systems, LNEE 86, pp. 499–504.
springerlink.com © Springer-Verlag Berlin Heidelberg 2011

2 Neural Network Model

The neural network model is showed in figure1. Where, the activation functions of hidden layer neurons are as follows:

$$c_0(x_k) = 1,\ c_1(x_k) = \cos\left[\frac{\pi}{b-a}(x_k - a)\right],\ldots\ldots,$$

$$c_N(x_k) = \cos\left[N\frac{\pi}{b-a}(x_k - a)\right] \tag{1}$$

Weights from the input layer to the hidden layer are identically equal to 1, and weights from hidden layer to the output layer are $w_n (n = 0,1,\cdots N)$. The $y(x_k)$ is the neural network output, and training samples set is:

$$\left\{x_k,\quad y_d(x_k)\,|_{k=0,1,\cdots,m}\right\}.$$

2.1 The Algorithm Description

According to figure 1, the neural network algorithm is as follows:

Given an arbitrary weight vector $\mathbf{W} = [w_0, w_1, \cdots, w_N]^T$, then the output of neural network is as

$$y(x_k) = \sum_{n=0}^{N} w_n c_n(x_k) \tag{2}$$

Or

$$y(x_k) = \mathbf{C}(x_k)\mathbf{W} \tag{3}$$

where $\mathbf{C}(x_k) = [c_0(x_k), c_1(x_k), \cdots, c_N(x_k)]$.

And an error function can be obtained:

$$e(k) = y_d(x_k) - y(x_k) \tag{4}$$

Define an objective function J as follows:

$$J = \frac{1}{2}e^2(k) \tag{5}$$

To minimize the objective function J, let $\frac{\partial J}{\partial \mathbf{W}} = 0$, Available recursive least square algorithm:

$$\mathbf{W}^{k+1} = \mathbf{W}^k + \mathbf{Q}^k[y_d(x_k) - \mathbf{C}(x_k)\mathbf{W}^k] \tag{6}$$

$$\mathbf{Q}^k = \frac{\mathbf{P}^k \mathbf{C}^T(x_k)}{1 + \mathbf{C}(x_k)\mathbf{P}^k \mathbf{C}^T(x_k)} \tag{7}$$

$$\mathbf{P}^{k+1} = [\mathbf{I} - \mathbf{Q}^k \mathbf{C}(x_k)]\mathbf{P}^k \tag{8}$$

($k = 0,1,\cdots,M$)

Given an arbitrary initial weight vector $\mathbf{W}^0$, and let $\mathbf{P}^0 = \alpha\mathbf{I} \in \mathbf{R}^{(N+1)\times(N+1)}$, α is a large enough positive(Generally take $\alpha = 10^6 \sim 10^{10}$). $\mathbf{I} \in \mathbf{R}^{(N+1)\times(N+1)}$ is a unit matrix.

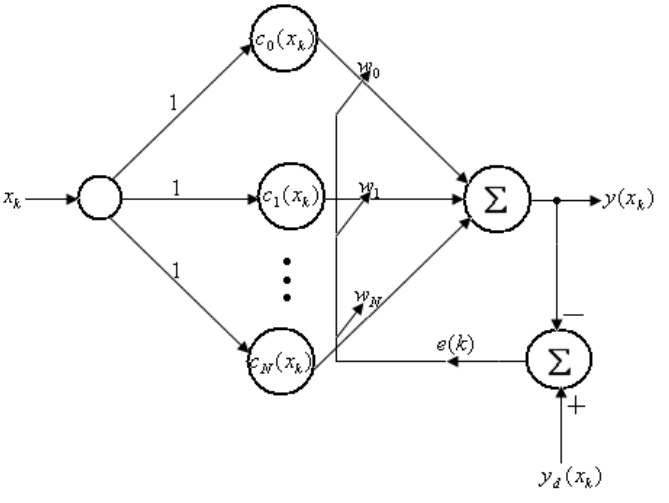

Fig. 1. The model of neural network based on cosine basis functions

2.2 Algorithm Steps

INPUT: initial weights: $w_n^0 (n = 0,1,\cdots N)$; training sample set: $\{x_k, \quad y_d(x_k)\}$; tolerance *Tol*; Max iterations N; let k=0;

OUTPUT: The weights: $w_n^k (n = 0,1,\cdots N)$

Step 1: While k<=N do Steps 2-5

Step 2: computing the output of neural network: $y(x_k) = \sum_{n=0}^{N} w_n c_n(x_k)$

Let $e(k) = y_d(x_k) - y(x_k)$, and $J = \frac{1}{2} e^2(k)$

Step 3: Update the weights: $\mathbf{W}^{k+1} = \mathbf{W}^k + \mathbf{Q}^k [y_d(x_k) - \mathbf{C}(x_k)\mathbf{W}^k]$

Where, $\mathbf{Q}^k = \dfrac{\mathbf{P}^k \mathbf{C}^T(x_k)}{1+\mathbf{C}(x_k)\mathbf{P}^k\mathbf{C}^T(x_k)}$, $\mathbf{P}^{k+1} = [\mathbf{I} - \mathbf{Q}^k \mathbf{C}(x_k)]\mathbf{P}^k$

Step 4: If J<=Tol then

OUTPUT $w_n^k (n = 0,1,\cdots N)$; (The procedure was successful.)

STOP

Step 5: Set k=k+1

Go back to step 2

Step 6: **OUTPUT** ('the method failed after N iterations);

(The procedure was unsuccessful.)

STOP

3 Simulation Examples

3.1 The Error Compensation of Magnetic Sensor

As the Hall element is not only the magnetic sensitive element, but also the temperature sensitive element, therefore, both nonlinear error compensation and temperature error compensation of magnetic sensors should be considered. In order to validate the validity of the proposed algorithm, the nonlinear and temperature characteristic of magnetic sensor were compensated using the algorithm proposed. The data used in the algorithm were selected from the reference [4] and was shown as Table1.

Table 1. [4]

Nonlinear characteristic		Temperature characteristic standard magnetic field given: 100mT	
The standard magnetic field: Bn/mT	The measured value of magnetic field Vx/mT	Temperature values T/℃	The measured value of magnetic field Yt/mT
50.00	50.11	1.6	103.42
100.00	100.08	10.0	102.09
150.00	149.91	20.0	100.68
200.00	199.63	30.2	99.46
		39.9	98.49

3.2 Nonlinear Characteristic Results Using Neural Network Algorithm

In the algorithm proposed, let a=50, and b=200. Take measured value of magnetic field as the input of neural network, and standard value of magnetic field as the training samples of neural network. Give $Tol=10^{-6}$, and produce random initial weights vector: $\mathbf{W} = rand(4,1)$. After two iterations, neural network weights are as follows:

$$\mathbf{W} = [125.0046507, -66.7367389, -0.0027297, -8.2655549]$$

3.3 Temperature Characteristic Results Using Neural Network Algorithm

Let a=1.6, and b=39.9. Use temperature as the input of neural network, and measured values of magnetic field as the training sample set of neural network. Give $Tol=10^{-6}$, and produce random initial weights vector: **W**=*rand*(5,1). After two iterations, neural network weights were as:

$$\mathbf{W} = [100.7119865,\ 2.0770096, 0.1652038, 0.3879908, 0.0778040]$$

3.4 The Compensation Results of the Magnetic Sensor

After the neural network trainings, the compensation results of nonlinear and temperature characteristic of magnetic sensors were showed in table 2.

Table 2. The compensation results of magnetic sensor

Nonlinear characteristic		Temperature characteristic standard magnetic field: 100mT	
The standard magnetic field: Bn/mT	The compensation values of magnetic field: Vx/mT	Temperature values: T/℃	The compensation values of magnetic field: Yt/mT
50.00	50.000003	1.6	103. 4199895
100.00	99.999978	10.0	102.0899750
150.00	149.999939	20.0	100.6799730
200.00	199.999955	30.2	99.4599742
		39.9	98.4899878

4 Conclusions

We know from table2 that the nonlinear characteristic and temperature characteristic of the magnetic sensor were compensated very well using the neural network algorithm with cosine basis functions. The compensation accuracy is very high, such as, the compensation accuracy of the nonlinear characteristic reaches to $4.07155\times10^{-5}\%$, and the compensation accuracy of the temperature characteristic reaches to $2.6663\times10^{-5}\%$. Compared with reference [4], it has significant advantages. Therefore, it is an effective method of sensor error compensation.

Acknowledgments

This work is supported by the plan project (2009GK3186) of science and technology of Hunan, the key projects (08A006) of the Education Department of Hunan, and the plan project (K0904040-11) of science and technology of Changsha, Hunan, China.

References

1. Tandeske, D.: Pressure Sensors. Marcel Dekker, INC (1991)
2. Sun, H., Guo, Z.: Pressure sensor and its error compensation. Chinese Sensor world (3), 14–16 (2002)

3. Xu, J.: Using single-chip processor software to achieve the sensor's temperature error compensation. Chinese Modern Electronic Technology (10), 97–99 (2002)
4. Sun, H., Guo, Z.: Technology of error compensation on sensors. Chinese Journal of Sensors and Actuators (1), 90–92 (2004)
5. Li, D., Zhao, X.: An inverse function correction methods of sensor nonlinear characteristic. Chinese Journal of Scientific Instrument 12(2), 215–218 (1991)
6. Sun, Y.: Normalizing the polynomial-match for a nonlinear function in sensors and solid electronics. Chinese Journal of Electronic Devices 27(1), 1–7 (2004)
7. Su, Y., Sun, Y.: Comparing the different arithmetic methods for the offset drift compensation of pressure sensor. Chinese Journal of Sensors and Actuators (3), 375–378 (2004)
8. Chen, M., Ma, L.: Fitting way of sensor characteristic. Chinese Journal of Transducer Technology 2(1), 38–40 (2003)

A Fitting Approach of the Temperature Characteristic Curve of Sensor Based on the Recursive Least Squares Algorithm

Musheng Deng[1], Zhezhao Zeng[2], and Yi Xiong[1]

[1] Electrical Engineering Department, Hunan Railway Professional Technology College, Zhuzhou 412001, China
dsjing@sina.com, xy2310@163.com
[2] College of Electrical and Information Engineering, Changsha University of Science & Technology, Changsha 410076, China
hncs6699@yahoo.com.cn

Abstract. To improve effectively temperature compensation characteristic of sensor, a method fitting the temperature characteristic curve was proposed. The simulating example of the sensitivity-temperature characteristic curve of sensor was given. The result shows that the temperature characteristic fitting curve of sensor using the neural network algorithm is very both smooth and accurate. The fitting precision is up to 10^{-6}. Therefore, the method of curve fitting based on the neural network algorithm is effective.

Keywords: Neural networks, Sensor, Curve fitting, Temperature characteristic.

1 Introduction

It is well known that sensor has features of rapid responsibility, high sensitivity , perfect stability, high measurement precision, preferable parameter of lag error and resolution and so on [1],[2]. But sensitivity in sensors was strongly influenced by temperature. Consequently, the sensitive and its measurement system simulation have become an important parameter in the research of sensor. As the sensor's characteristic curve there is a certain nonlinear, but the linear methods were applied in many engineering calculation which may lead to greater nonlinear error [3-6]. In order to eliminate or compensate for the nonlinear errors of sensor or apply the sensor nonlinear characteristics, It is proposed by references [2-7] that mathematical model and algorithm of cubic spline functions, fitting method of the best straight line, least squares polynomial curve fitting and nonlinear compensation method of the nonlinear inverse function compensation, etc. which have achieved a certain degree of nonlinear compensation effects. Fitting accuracy of cubic spline function's mathematical model is not high enough (10^{-3}). Linear fitting method and nonlinear inverse function compensation method have bigger compensation errors and lower compensation accuracy, hence, they should not be used. Least squares polynomial curve fitting has higher compensation accuracy, but the oscillatory easily occurrences while data are

D. Zeng (Ed.): Future Intelligent Information Systems, LNEE 86, pp. 505–510.
springerlink.com © Springer-Verlag Berlin Heidelberg 2011

increased, and it is very difficult to obtain polynomial coefficients, hence its application is limited. To further enhance the curve fitting accuracy, the model fitting sensor characteristic curve based on the neural network algorithm was proposed in this paper. To test the neural network algorithm effectiveness, the simulating example of the sensitivity-temperature characteristic curve of sensor was introduced.

2 The Neural Network Model and Algorithm with Fourier Basis Functions

2.1 Continuous-Time Fourier Series of Periodic Signal

As everyone knows, the signal $f_p(t)$ with periodic T can be expressed as a continuous-time Fourier series, namely:

$$f_p(t) = a_0 + \sum_{n=1}^{\infty} a_n \cos(n\omega_0 t) + \sum_{n=1}^{\infty} b_n \sin(n\omega_0 t) \tag{1}$$

Where $\omega_0 = \frac{2\pi}{T}$ is the fundamental angular frequency, a_0 is the DC component, a_n and b_n are Fourier series coefficients, which are:

$$a_0 = \frac{1}{T}\int_0^T f(t)dt\ ,\quad a_n = \frac{2}{T}\int_0^T f(t)\cos(n\omega_0 t)dt\ ,$$

$$b_n = \frac{2}{T}\int_0^T f(t)\sin(n\omega_0 t)dt \tag{2}$$

Where $f(t)$ ($0 \le t \le T$) is time-limited non-periodic signal. If let $f(t)$ be extended to periodic signal $f_p(t)$ according to the period T , we have:

$$f_p(t) = \sum_{m=-\infty}^{\infty} f(t - mT) \tag{3}$$

Where m is an integer. Obviously, when $0 \le t \le T$, $f_p(t) = f(t)$ .As a result continuous-time Fourier series of periodic signal $f_p(t)$ can be also expressed as form (1) in the main cycle $0 \le t \le T$. If $f(t)$ （ $0 \le \omega \le N\omega_0$ ） is frequency band-limited, formula (1) can rewrite:

$$f(t) = a_0 + \sum_{n=1}^{N} a_n \cos(n\omega_0 t) + \sum_{n=1}^{N} b_n \sin(n\omega_0 t) \tag{4}$$

In order to facilitate numerical calculation, formula (4) is discrete by the following form:

$$f(k) = a_0 + \sum_{n=1}^{N} a_n \cos(n\omega_0 k T_s) + \sum_{n=1}^{N} b_n \sin(n\omega_0 k T_s) \tag{5}$$

Where T_s is sampling period, and $T_s \le \frac{\pi}{N\omega_0} = \frac{T}{2N}$, if $T_s = \frac{T}{2N}$, formula (5) is :

$$f(k) = a_0 + \sum_{n=1}^{N} a_n \cos(\frac{\pi}{N} nk) + \sum_{n=1}^{N} b_n \sin(\frac{\pi}{N} nk) \tag{6}$$

$k = 0,1,\cdots,M$, $M \ge 2N-1$.

2.2 The Neural Network Model Based on Fourier Basis Functions

We know form the formula (6), if $f(k)$ is the output of the neural network , $f_d(k)$ is neural network training sample, a_n and b_n are the training weights of the neural network, $\cos(\frac{\pi}{N} nk)$ and $\sin(\frac{\pi}{N} nk)$ are neural network activation functions, then Figure 1 shows the neural network model with Fourier basis functions.

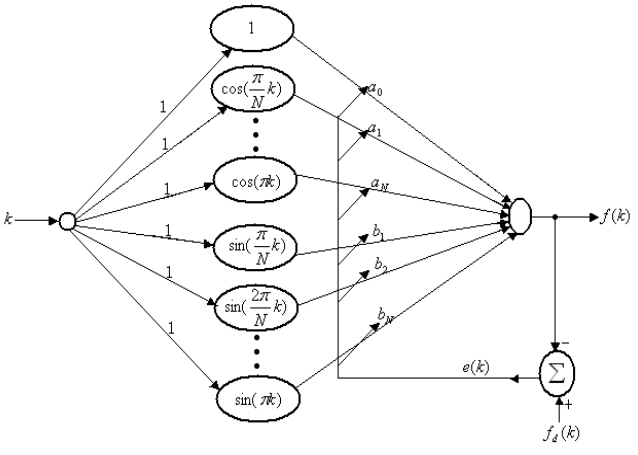

Fig. 1. The neural network model with Fourier basis functions

2.3 The Neural Network Algorithm

The output of the neural network:

$$f(k) = a_0 + \sum_{n=1}^{N} a_n \cos(\frac{\pi}{N} nk) + \sum_{n=1}^{N} b_n \sin(\frac{\pi}{N} nk) \tag{7}$$

Let $\mathbf{W} = [a_0, a_1, \cdots, a_N, b_1, \cdots, b_N]^T$, $c_n(k) = \cos(\frac{\pi}{N} nk)$, $n = 0,1,\cdots,N$, and $s_n(k) = \sin(\frac{\pi}{N} nk)$, $n = 1,\cdots,N$.

Defined $\mathbf{C}(k) = [c_0(k), \cdots, c_N(k), s_1(k), \cdots, s_N(k)]$, then, formula (7) can be rewritten into the following form

$$f(k) = \mathbf{C}(k)\mathbf{W} \tag{8}$$

Computing error:

$$e(k) = f_d(k) - f(k) \tag{9}$$

Defined Objective function:

$$J = \frac{1}{2}\sum_{k=0}^{M} e^2(k) \tag{10}$$

To minimize the objective function J , let $\frac{\partial J}{\partial \mathbf{W}} = 0$, Available recursive least square algorithm:

$$\mathbf{W}^{k+1} = \mathbf{W}^k + \mathbf{Q}^k[f_d(k) - \mathbf{C}(k)\mathbf{W}^k] \tag{11}$$

$$\mathbf{Q}^k = \frac{\mathbf{P}^k\mathbf{C}^T(k)}{1 + \mathbf{C}(k)\mathbf{P}^k\mathbf{C}^T(k)} \tag{12}$$

$$\mathbf{P}^{k+1} = [\mathbf{I} - \mathbf{Q}^k\mathbf{C}(k)]\mathbf{P}^k \tag{13}$$

($k = 0,1,\cdots,M$).

Given an arbitrary initial weight vector $\mathbf{W}^0 \in \mathbf{R}^{(2N+1)}$, and let $\mathbf{P}^0 = \alpha\mathbf{I} \in \mathbf{R}^{(2N+1)\times(2N+1)}$, α is a large enough positive (Generally take $\alpha = 10^6 \sim 10^{10}$). $\mathbf{I} \in \mathbf{R}^{(2N+1)\times(2N+1)}$ is an unit matrix.

3 Curve Fitting of Sensor

In order to validate the effectiveness of the above mentioned algorithm, the sensitivity-temperature curve [2] of Nano-sensor is taken as a fitting example, which the experimental data are shown in table 1. We can see from table 1 that the period was equal to $T = 480 - 180 = 300(s)$, hence, the fundamental angular frequency is $\omega_0 = \frac{2\pi}{T} = \frac{\pi}{150}(rad/s)$, let sampling period $T_s = 10(s)$. If $T_s = \frac{T}{2N}$, $N = 15$, and the number of neurons of hidden layers is $2N + 1 = 31$, then, network

topological structure is $1\times31\times1$. Let $t=190+kT_s$, for each $k=0,1,\cdots,29$. Given an arbitrary initial weight vector $\mathbf{W}^0$, and defined an arbitrary small real positive $Tol=10^{-6}$, the data of table 1 are taken as neural network training samples. After 2 iterations, the fitting curve was shown in figure 2, in which the Black Points indicated testing data given (sample data), and the solid lines indicated neural network's fitting results. From figure 2 we can see the fitting curve of sensitivity-temperature of sensor is very smooth using the neural network algorithm.

Table 1. Sensitivity-temperature measurement data

temperature/℃ /sensitivity /mV	temperature/℃ /sensitivity /mV	temperature/℃ /sensitivity /mV
190 /1.44	290/3.40	390/5.64
200/1.41	300/3.76	400/5.74
210/1.40	310/4.09	410/5.83
220/1.44	320/4.39	420/5.90
230/1.53	330/4.65	430/5.95
240 /1.71	340/4.88	440/5.92
250/1.97	350/5.07	450/5.75
260/2.30	360/5.24	460/5.38
270/2.67	370/5.39	470/4.88
280/3.04	380/5.52	480/4.27

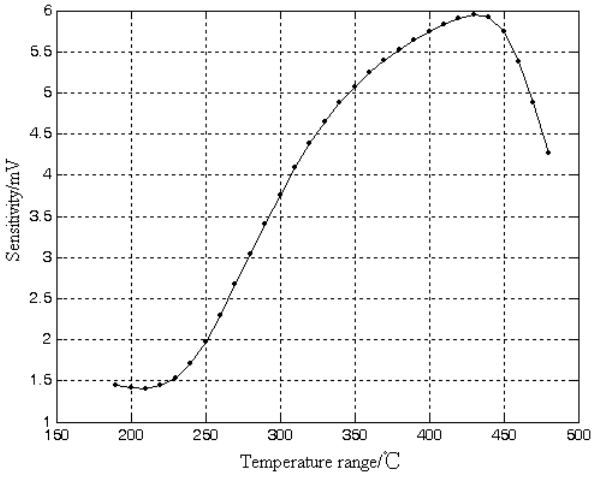

Fig. 2. Fitting Curve using neural network algorithm

4 Conclusions

The results show that the fitting curve of sensitivity-temperature characteristic of sensor is very smooth using the neural network algorithm. The absolute accuracy is

up to 4.369868×10^{-7}, and the relative accuracy of the fitting curve is up to $3.0346\times10^{-5}\%$. The fitting accuracy is a thousand times of the reference [2]. Therefore, it is an effective method of curve fitting.

Acknowledgments

This work is supported by the plan project (2009GK3186) of science and technology of Hunan, the key projects (08A006) of the Education Department of Hunan, and the plan project (K0904040-11) of science and technology of Changsha, Hunan, China.

References

1. Gu, N., Fu, D., Zhang, H., et al.: Nano technology and application. People's Posts & Telecommunications Publishing House, Beijing (2002)
2. Jian, Q., Liu, H.: Study on SnO_2 Nano-sensor sensitivity-temperature characteristic curve fitting. Chinese Journal of Sensors and Actuators 18(1), 50–52 (2005)
3. Sun, H., Guo, Z.: Pressure sensors and error compensation. Sensor World (China) (3), 14–16 (2002)
4. Li, D., Zhao, X.: An inverse function correction methods of sensor nonlinear characteristic. Chinese Journal of Scientific Instrument 12(2), 215–218 (1991)
5. Sun, Y.: Normalizing the polynomial-match for a nonlinear function in sensors and solid electronics. Chinese Journal of Electronic Devices 27(1), 1–7 (2004)
6. Sun, D., Zhang, L., Wang, Y., et al.: Based on the product type least squares fitting characteristics of the sensor. Chinese Journal of Sensors and Actuators 15(4), 293–298 (2002)
7. Chen, M., Ma, L.: Fitting way of sensor characteristic. Chinese Journal of Transducer Technology 2(1), 38–40 (2003)

An Optimum Design Method of High-Order Digital Differentiator

Aiguo Meng[1], Yuxiang Tu[2], and Zhezhao Zeng[1]

[1] College of Electrical and Information Engineering,
Changsha University of Science & Technology, Changsha 410076, China
Tuyuxiang2009@126.com, hncs6699@yahoo.com.cn
[2] College of Computer and Communication Engineering,
Hunan University, Changsha 410086, China
meng_ai_guo@163.com

Abstract. The paper introduces in detail the optimal design approach of high-order digital differentiator based on the recursive least squares algorithm. The main idea is to minimize the sum of the square errors between the amplitude response of the ideal differentiator and that of the designed by training the weight vector of neural networks, then obtaining the impulse response of digital differentiator. The optimal design approach is introduced by examples of high-order digital differentiator. The results showed that the high-order digital differentiator designed has very high precision and very fast convergence speed. Therefore, the presented optimum design method of high-order digital differentiator is significantly effective.

Keywords: Neural networks, optimal design, digital differentiator, recursive least squares algorithm.

1 Introduction

It has been well known that differentiators play an important role in optical and biological signal processing. However, the design of high-order differentiators is always a difficult issue. McClellan, et al. [1] proposed a computer program used for the design of the first-order differentiators, i.e. McClellan-Parks algorithm. Others [2] modified such an algorithm and used it in the design of high-order differentiators. The method of eigenfilter was proposed in literature [3]. However, all results above approaches were significantly different from the ideal ones.

The design of high-order digital differentiators is essentially an issue of multi-variable optimization. However, there exist many local minima on the corresponding optimization surfaces, and it is difficult to describe the distribution of the minimum solutions. Recently, the genetic algorithm (GA) has been applied in this field [4]. The literature [5] proposed a method for the design of high-order digital differentiators based on simulated annealing (SA). Compared with other methods, its design result has been improved significantly. However, the errors in such a design were still large up to 10^{-3}. This paper proposed an optimal design method of high-order digital differentiators based on neural network algorithms (NNA). The main idea is to

D. Zeng (Ed.): Future Intelligent Information Systems, LNEE 86, pp. 511–516.
springerlink.com © Springer-Verlag Berlin Heidelberg 2011

minimize the sum of error squares of the amplitude-frequency response between the ideal differentiator and that of the designed by training the weight vector of neural networks, then obtaining the impulse response of digital differentiator.

2 Amplitude–Frequency Response of Digital Differentiator

For a (N-1)th order digital differentiator, it is expressed as

$$H(z) = \sum_{n=0}^{N-1} h(n) z^{-n} \tag{1}$$

where $H(z)$ is a transfer function of the differentiator, $h(n)$ is its impulse response, and N is its length. If N is an even number, and that

$$h(n) = -h(N-1-n) \tag{2}$$

then the amplitude-frequency response of differentiator can be expressed as

$$\hat{H}(\Omega) = \sum_{n=1}^{\frac{N}{2}} d_n \sin\left[\Omega\left(n - \frac{1}{2}\right)\right] \tag{3}$$

where $\hat{H}(\Omega)$ is the amplitude-frequency response of differentiator with a linear phase, and that

$$d_n = 2h(\tfrac{N}{2} - n), \text{ and } n = 1,2,...,\tfrac{N}{2} \tag{4}$$

It is well known that formula (3) is the expression of type-four FIR differentiator with a linear phase. We see from Eq. (3) that the amplitude-frequency response of differentiator is a Fourier series, and d_n is the Fourier coefficients. Once achieved d_n, we can acquire $h(n)$ via Eq. (4), i.e. $h(\frac{N}{2} - n) = \frac{d_n}{2}$, where $n = 1,2,...,\frac{N}{2}$. Considering the odd symmetry condition of formula (2), then we can get a digital differentiator with a linear phase, i.e. $h(n)$, where $n = 0,1,2,...,N-1$. Apparently, in order to design a digital differentiator, we must first obtain d_n. Now we discuss the neural network algorithm based on the activation matrix S^T produced by sine basis functions so that we can acquire d_n.

3 Algorithm Description

Suppose that

$$\mathbf{W} = [d_1, \cdots, d_{N/2}]^T, \mathbf{S}_n(\Omega_k) = \sin[(n - \tfrac{1}{2})\Omega_k], (n = 1,2,\cdots,N/2),$$

and

$$\mathbf{S}(\Omega_k) = [s_1(\Omega_k), \cdots s_{\frac{N}{2}}(\Omega_k)] \tag{5}$$

where $\Omega_k = \dfrac{2\pi}{N-1}k$, $k = 0,1,\cdots,\frac{N-1}{2}$,then the formula (3) can be expressed as

$$\hat{H}(\Omega_k) = \mathbf{S}(\Omega_k)\mathbf{W} \tag{6}$$

Fig.1 shows the model of neural network based on sine basis functions.

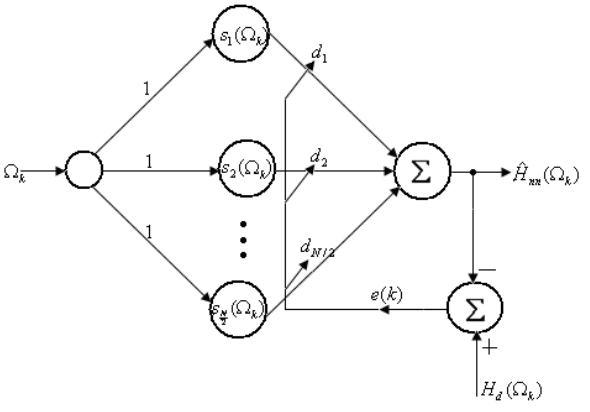

Fig. 1. The model of neural network

The output of neural network is expressed by

$$\hat{H}_{nn}(\Omega_k) = \mathbf{S}(\Omega_k)\mathbf{W}^k \tag{7}$$

Where $\hat{H}_{nn}(\Omega_k)$ is the output of the neural network, $H_d(\Omega_k)$ is the amplitude response of the ideal digital differentiator, $\mathbf{W}^k$ is the weight vector of the neural network, $\mathbf{S}(\Omega_k)$ is the activation vector of the hidden units of neural network, and $\left\{\Omega_k, \quad H_d(\Omega_k) \middle| k = 0,\cdots(N-1)/2\right\}$ is the training samples of the neural network.

We define an objective function J as follows:

$$J = \frac{1}{2}\sum_{k=0}^{N/2-1} e^2(k) \tag{8}$$

Here, $e(k) = H_d(\Omega_k) - \hat{H}_{nn}(\Omega_k)$.

To minimize the objective function J, let

$$\frac{\partial J}{\partial \mathbf{W}} = 0$$

Available recursive least square algorithm:

$$\mathbf{W}^{k+1} = \mathbf{W}^k + \mathbf{Q}^k[H_d(\Omega_k) - \mathbf{S}(\Omega_k)\mathbf{W}^k] \tag{9}$$

$$\mathbf{Q}^k = \frac{\mathbf{P}^k\mathbf{S}^T(\Omega_k)}{1+\mathbf{S}(\Omega_k)\mathbf{P}^k\mathbf{S}^T(\Omega_k)} \tag{10}$$

$$\mathbf{P}^{k+1} = [\mathbf{I} - \mathbf{Q}^k\mathbf{S}(\Omega_k)]\mathbf{P}^k \tag{11}$$

$k = 0,1,\cdots,(N-1)/2$.

Given an arbitrary initial weight vector $\mathbf{W}^0$, and let $\mathbf{P}^0 = \alpha\mathbf{I} \in \mathbf{R}^{N/2\times N/2}$, α is a large enough positive(Generally take $\alpha = 10^6 \sim 10^{10}$). $\mathbf{I} \in \mathbf{R}^{N/2\times N/2}$ is a unit matrix.

By comparing formula(6) and formula(7), we can find distinctly that the amplitude-frequency response $\hat{H}(\Omega_k)$ of digital differentiator is the same as the output $\hat{H}_{nn}(\Omega_k)$ of neural network k. Therefore, Fourier coefficient d_n in formula (6) is the weight d_n of neural network in formula (7). We can design a digital differentiator as long as we train an ideal amplitude-frequency response $H_d(\Omega_k)$ of a digital differentiator to obtain the weight d_n of neural network, i.e. Fourier coefficient d_n of digital differentiator. Formula (9)-formula (11) can now be used in a computer program to calculate the weight d_n of the neural network and the whole algorithm is summarized as follows.

Step1. Sample equably the desired amplitude-frequency response $|H_d(e^{j\Omega})|$ to obtain the training sample set of the neural network, i.e. $\{\Omega_k,\ H_d(\Omega_k) | k = 0,\cdots(N-1)/2\}$, where $\Omega_k = \frac{2\pi}{N-1}k$, $k = 0,1,\cdots,\frac{N-1}{2}$. Produce the random weight d_n, and define an arbitrary small positive real number Tol . computing the activation vector $\mathbf{S}(\Omega_k) = [s_1(\Omega_k),\cdots s_{\frac{N}{2}}(\Omega_k)]$ of the hidden units of neural network, take $\alpha = 10^6$;

Step2. Computing gain vector $\mathbf{Q}^k$ using formula (10), and produce new predicted output $\hat{H}_{nn}(\Omega_k)$ of neural network using formula (9) ;

Step3. Calculating error function and object function:

$$e(k) = H_d(\Omega_k) - \hat{H}_{nn}(\Omega_k),\ J = \frac{1}{2}\sum_{k=0}^{(N-1)/2} e^2(k)$$

Step4. Update the weight vector

$$\mathbf{W}^{k+1} = \mathbf{W}^k + \mathbf{Q}^k[H_d(\Omega_k) - \mathbf{S}(\Omega_k)\mathbf{W}^k]$$

and

$$\mathbf{P}^{k+1} = [\mathbf{I} - \mathbf{Q}^k\mathbf{S}(\Omega_k)]\mathbf{P}^k$$

Step5. If $J > Tol$, go to Step2, otherwise, stop the training of the neural network

4 Optimum Design Example

In this section, one simulation example will be given. The purpose is to verify the theorem of the convergence theorem of the neural network algorithm presented above and supports the optimal design approach of digital differentiator with a linear phase based on the neural network algorithm.

Simulation1: Design a 201-order digital differentiator. Suppose that its ideal amplitude-frequency property is as

$$| H_d(e^{j\Omega}) | = \begin{cases} +\Omega & ,0 \le \Omega < \pi \\ -\Omega & ,-\pi < \Omega < 0 \end{cases}$$

Initial conditions are as follows.

Let $N = 202$, sample $\left|H_d(e^{j\Omega})\right|$ equably to obtain training sample vector $\mathbf{H}_d$ in range of $\Omega \in [0,\pi]$, i.e. $\Omega_k = \dfrac{\pi}{100}k$, ($k = 0,1,2,\ldots,100$). Produce the random weight vector $\mathbf{W}^0$, and define $Tol = 10^{-10}$. Actual training sample vector is as follows

$$\mathbf{H}_d = [linspace(0, \quad \pi, \quad 101)]$$

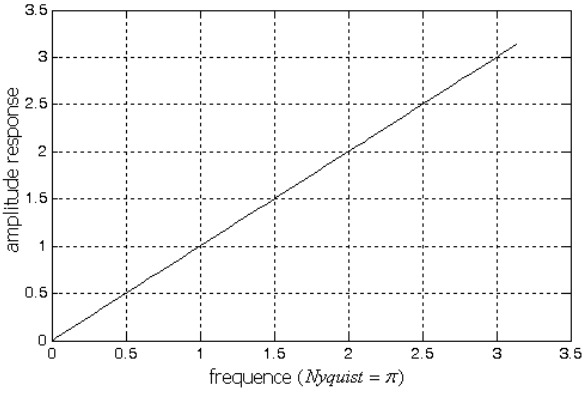

Fig. 2. Amplitude-frequency response of the simulation 1

Where *linspace* is linearly spaced vector function in MATLAB. After two iterations of neural network, we can obtain the accumulative square error $J = 3.6551 \times 10^{-13}$. The amplitude-frequency response of the 201-order digital differentiator with the linear phase is shown in Figure 2.

5 Conclusions

This paper presents an optimal design method about high-order digital differentiator with the linear phase based on the algorithm of neural network whose activation vector is $\mathbf{S}$ produced by formula (5). The main idea of the approach is to obtain the impulse response of digital differentiator by training the weight vector $\mathbf{W}$ of neural network. Since the method is not involved in operation of inverse matrix, it solves the difficult problem effectively on designing high order digital differentiator. The algorithm is not only suitable for designing high order digital differentiator, but also for designing low order digital differentiator. We can see from the amplitude frequency response of ***simulation 1*** that this approach features such characteristics as fast convergence, high precision, and random initial conditions. Therefore, it is a significantly effective optimal design approach.

Acknowledgments

This work is supported by the plan project (2009GK3186) of science and technology of Hunan, the key projects (08A006) of the Education Department of Hunan, and the plan project (K0904040-11) of science and technology of Changsha, Hunan, China.

References

1. McClellan, J.H., Parks, T.W., Rabiner, L.R.: A Computer Program for Designing Optimum FIR Linear Phase Digital Filters. IEEE Trans. On Audio Electroacoust 21, 506–526 (1973)
2. Rahenkamp, C.A., Kumar, B.V.: Modifications to the McClellan-Parks and Rabiner Computer Program for Designing Higher Order Differentiating FIR Filters. IEEE Trans. On Acoust Speech Signal Process 34, 1671–1674 (1986)
3. Pei, S.C., Shyu, J.J.: Eigenfilter Design of Higher-Order Digital Differentiating. IEEE Trans. On Acoust Speech Signal Process 37, 505–511 (1989)
4. Zeng, S.T., Lu, H.C.: Genetic Algorithm Approach for Designing Higher-order Digital Differentiators. Signal Processing 79(2), 175–186 (1999)
5. Wang, L., Li, W.-f., Zheng, D.-z.: Simulated Annealing for Designing Higher-Order Digital Differentiator. Systems Engineering and Electronics, china 23(12), 1–3 (2001)

Time-Dependent Entropy for Studying Time-Varying Visual ERP Series

Lisha Sun, Zhi Xiong, and Zhangceng Li

College of Engineering, Shantou University, Guangdong 515063, China
lssun@stu.edu.cn

Abstract. The Tsallis-like time-dependent entropy (TDE), called nonextensive entropy, is developed to study the event-related potential signals (ERPs) in a cue, "E"-orientation discrimination task. The statistical characteristics of the TDE for different signal distributions are studied. The TDE analytic results indicate that with the appearance of P2 and N2, a significant decrease of TDE was correlated with the responses to small size cue which support the theoretic analysis. This method provides a novel quantitative measurement for ERPs actives and may be useful in developing a monitoring tool.

Keywords: time-dependent entropy, nonextensive entropy, event-related potential signals.

1 Introduction

The EEG can be regarded as a reflection of ensembles of generators producing oscillations in several frequency ranges, which are active in a very complex manner. Under stimulation they begin to act together in a coherent way. Thus, this transition from a disordered to an ordered state is accompanied by a resonance phenomenon and results in frequency stabilization, synchronization, and enhancement of the ongoing EEG activity, which produces event-related brain potentials [1], [2].

Recently, information measures, including the traditional Shannon entropy, have been shown to be effective in dealing with complex signals [3]. The concept of entropy has been extensively used in statistical mechanics and thermodynamics. Particularly, Shannon entropy is based on the Boltzmann-Gibbs (BG) statistical mechanics and standard thermodynamics and get large success, but unfortunately the BG statistical mechanics, also called extensive statistical mechanics, only address those extensive systems involving short-ranged effective microscopic interactions. Now it has been discovered that there exist long-range spatial interactions and long-term interactions in a lot of physical systems [4], [5]. BG statistical mechanics has difficulty in resolving these systems. To overcome this limitation, Tsallis postulated the non-extensive statistic mechanism and defined the non-extensive entropy, now called Tsallis entropy [6].

Within this framework, the major objective of the present work was to characterize in a quantitative way that would exploit the precise temporal relation of changes in the ongoing EEG to certain tasks. But entropy itself is a description of average uncertainly

D. Zeng (Ed.): Future Intelligent Information Systems, LNEE 86, pp. 517–524.
springerlink.com © Springer-Verlag Berlin Heidelberg 2011

in the signal duration recorded and it is not useful for analyzing nonstationarity. To get a temporal evolution of entropy, an alternative time dependent entropy (TDE) measure based on sliding temporal window technique is applied. The TDE is a relatively new method of quantitative analysis that proved to have several advantages over previous methods.

2 Method

2.1 Nonextensive Entropy

The entropy is a thermodynamic quantity describing the amount of disorder in the system. It is often obtained from the probabilities distribution p=$\{p_i\}$, where p_i is the probability of finding the system in the i th microstate with $0 \le p_i \le 1$ and $\sum_{i=1}^{M} p_i = 1$. M is the total number of microstates. Allowing for $0\ln 0 = 0$, the classical Shannon entropy [7] is expressed as follows:

$$SE = -\sum_{i=1}^{M} p_i \ln(p_i) \ . \tag{1}$$

The unit of entropy is bit, nat and kit, the corresponding choice of the logarithm's base is 2, e, 10 respectively. The Shannon entropy is based on framework of BG statistic, which is based on the hypothesis that the researched system has additivity, also named extensivity. Namely one composite system $(A \cup B)$, if A and B are two independent systems or their interaction is so small that it can be neglect, the Shannon entropy has extensivity:

$$S(A \cup B) = S(A) + S(B) \ . \tag{2}$$

When long-rang spatial relation and long-term relation exist, the systems are regarded as non-extensive. Nonextensive entropy should be used.

Theorem 1. Let Δ_M be an n-dimensional simplex defined by $\Delta_M := \left\{(p_1, \cdots p_M) \mid p_i \ge 0, \sum_{i=1}^{M} p_i = 1\right\}$. The following axioms [GSK1]~[GSK4] determine the function $S_q : \Delta_M \to R^+$ such that

$$S_q(p_1, \cdots p_n) = (1 - \sum_{i=1}^{M} p_i^q) / \phi(q) \ . \tag{3}$$

where $q \in R^+$ and $\phi(q)$ satisfies properties i)-iv)

i). $\phi(q)$ is continuous and has the same sign as $q-1$, i.e.

$$\phi(q)(q-1)>0 \quad (q\neq 1) \ . \tag{4}$$

ii). $$\lim_{q\to 1}\phi(q)=\phi(1)=0, \quad \phi(q)\neq 0 \ (q\neq 1) \ . \tag{5}$$

iii). there exists an interval $(a,b)\subset R^{+}$ such that $a<1<b$ and $\phi(q)$ is differentiable on the interval

$$(a,1)\cup(1,b) \ . \tag{6}$$

iv). there exists a constant $k>0$ such that

$$\lim_{q\to 1}(d\phi(q)/dq)=1/k \ . \tag{7}$$

[GSK1] continuity: S_q is continuous in Δ_M and $q\in R^{+}$;

[GSK2] maximality: for any $q\in R^{+}$, any $M\in N$ and any $(p_1,\cdots,p_M)\in\Delta_M$

$$S_q(p_1,\cdots,p_M)\leq S_q\left(1/M,\cdots,1/M\right) \ . \tag{8}$$

[GSK3] generalized Shannon additivity: under the constraints: $p_{ij}\geq 0, p_i=\sum_{i=1}^{m_i}p_{ij}\ \forall i=1,\cdots,M,\forall j=1,\cdots,m_i$ and $\sum_{i=1}^{M}p_i=1$, the following equality holds:

$$S_q(p_{11},\cdots,p_{Mm})=S_q(p_1,\cdots,p_M)+\sum_{i=1}^{M}p_i^q S_q\left(p_{i1}/p_i,\cdots,p_{im_i}/p_i\right) \ . \tag{9}$$

[GSK4] expandability:

$$S_q(p_1,\cdots,p_M,0)=S_q(p_1,\cdots,p_M) \ . \tag{10}$$

The proof of the above theorem is given in [8].

When choose $\phi(q)=q-1$, we have the Tsallis entropy[5]:

$$TE=(1-\sum_{i=1}^{M}p_i^q)/(q-1) \ . \tag{11}$$

Considering $0\leq p\leq 1$ in Eq. (11), $p_i^q\leq p_i$ for $q>1$ and $p_i^q\geq p_i$ for $q<1$, hence $q>1$ and $q<1$ will respectively correspond to the frequent and rare events.

When q approaches 1,

$$\begin{aligned}\lim_{q\to 1} TE &= \lim_{q\to 1}(1-\sum_{i=1}^{M} p_i^q)/(q-1)\\ &= \lim_{q\to 1}(-\sum_{i=1}^{M} p_i^q \ln p_i) \\ &= -\sum_{i=1}^{M} p_i \ln p_i\end{aligned} \quad . \tag{12}$$

Eq. (11) recovers to the usual Shannon entropy in Eq. (1) .TE is non-extensive such that:

$$TE(A \cup B) = TE(A) + TE(B) + (1-q)TE(A)TE(B) \quad . \tag{13}$$

In this pseudo-additive formalism of Eq. (13), and considering $TE \geq 0$, the cases $q<1$, $q=1$ and $q>1$, respectively, correspond to superextensive $TE(A\cup B) > TE(A)+TE(B)$, extensive $TE(A\cup B) = TE(A)+TE(B)$, and subextensive $TE(A\cup B) < TE(A)+TE(B)$ statistics. Thus, q is a measure of the nonextensivity of the system and is regarded as the nonextensive degree.

2.2 Time-Dependent Entropy

Entropy itself is a description of average uncertainty in the signal duration recorded. It lacks sensitivity to the signal's nonstationary. To overcome this limitation, we used an alternative time dependent entropy measure based on sliding temporal window technique which can capture instantaneous changes of the signal [3], [9].

We suppose the processed signal is $\{s(k): k=1,\cdots,N\}$, then we define a sliding temporal window $W(n;w;\Delta)=\{s(i), i=1+n\Delta,\cdots,w+n\Delta\}, n=1,2,\cdots,[N/\Delta]-w+1,$ where [x] denotes the integer part of x, where Δ denotes the sliding step, usually the window's width $W \leq N$. Within each window $W(n;w;\Delta)$, we introduce the set $\{I_i : i=1,\cdots,M\}$ of disjoint amplitude intervals such that

$$W(n;w;\Delta) = \bigcup_{i-1}^{M} I_i \quad . \tag{14}$$

Where M is the number of partitions of the EEG amplitude in the window W. We defined $p^n(I_i)$ denoting the probability that the signal $s(i)\in W(n;w;\Delta)$ belongs to the interval I_i. This probability is the ratio between the number of $s(i)$ -values of $W(n;w;\Delta)$ found within the interval I_i and the total number of $s(i)$ -values in $W(n;w;\Delta)$. Then the Tsallis entropy of the n th sliding window is:

$$TDE(n) = (1-\sum_{i=1}^{M}(p^n(I_i))^q)/(q-1) \quad . \tag{15}$$

2.3 Subjects and Stimuli

We obtained experimental EEG recording from several voluntary without any medication known to affect the EEG. Participants were between 20 and 25 years of age, right-handed, and had normal or corrected to normal vision. They reported no history of neurological illness. The cue was a black circle varied in three different sizes randomly. The foci of the circles were always at the center of the screen. There were 11 capital English letters in the circle where one of them was "E" or "Ǝ" and the others were "ɯ". "E" or "Ǝ" was designed as the target stimulus. When the cue was large, the capital maybe appeared within the three circles. When the cue was medium, the capital maybe appeared within the medium and small circles. When the cue was small, the capital maybe appeared only within the small circle. The task of the subjects was to search the target within the cue circle and discriminate its orientation. EEG was recorded with the 32 Channel Geodesic EEG/ERP system. Sampling frequency was set to 250Hz.

3 Results

One of the important advantages of the non-extensive TDE is it can capture the local irregularity changes [10]. If bursts are added to a stationary signal, when the bursts go into the sliding window, the amplitude distribution of the signal in the window will be change and then the illustration of the signal probability distribution function will become more acutely.

We explored the experiment EEG recording, due to the involvement of the visual system, interest was focused on anterosuperior (Fz) and inferoposterior (Pz) of the brain. In each visual evoked potential (VEP) experiment, there were 100 samples before the stimulus and we only chose 400ms data after stimulation to analyze. The results of the VEP experiment are show in the Fig.1. In both cases, two major positive deflections (P1 and P2) and two major negative deflections (N1 and N2) are observed after stimulation, with different topographic maxima. The P1 and N1 components were caused by visual attention and P2 and N2 component were caused by cue.

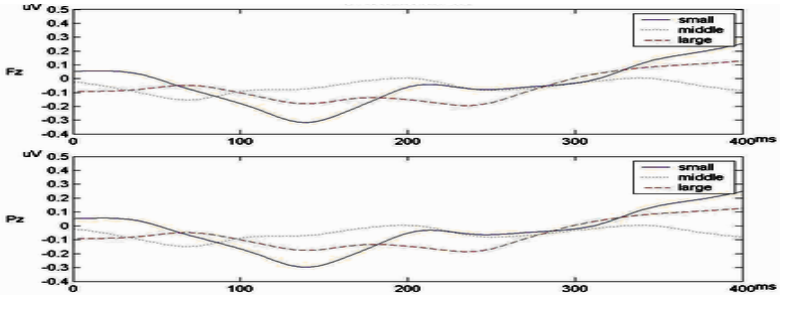

Fig. 1. The results of the VEP experiments

4 Discussion

In this work, we applied the nonextensive time-dependent entropy to analyze the ERPs. The experimental results agreed with the previous findings(overview in [11][12]). The TDE of the P1 component under stimulation enlarged but the TDE of the inferoposterior N1 decreased when the attentive region size enlarged. So we could say that the P1 and N1 components under visual attention were related to the spatial location processes mainly because that the larger the TDE was, the more disorder the brain was and when the brain was in the stage of information process the degree of disorder became larger. Cue-evoked P2 and N2 components were related to the size of attentive region. When the cue size enlarged the reaction time (RT) to the targets in anterosuperior P2 became longer, while the amplitudes of the inferoposterior and anterosuperior N2 decreased (show in Fig.1). With the appearance of P2 and N2, a significant decrease of TDE was correlated with the responses to small size cue (show in Fig.2). That was because it was easier in small cue size than in the large cue size when searching the target within the cue circle and the corresponding processing time of brain was shortened. The entropy is a measure of degree of disorder in the system. In the processing stage of brain the degree of disorder was larger so the entropy was larger. The processes of spatial location information were earlier than the other information, which supported the theory that spatial selection is a prerequisite for correct processes of visual object information. In other VEP experiments, focusing on F3, Cz, P3 and 01 components, according to the analyses of the time series and the TDE of each component, we also could find that 1). Cz component is not very sensitive to visual stimulus; 2). when the brain was in the stage of information process, the sequence of appearance of order point after visual stimulus is F3→Cz→P3→01. That is to say: for the visual stimulus, the reaction time is different for different area (maybe we can say the reaction time exists delay from the front area to the back); 3). For F3, Cz and P3 areas, the minimum TDE appears after stimulus of rare events, means that these areas are more sensitive to rare events, quite the opposite, the 01 area is more sensitive to frequent events.

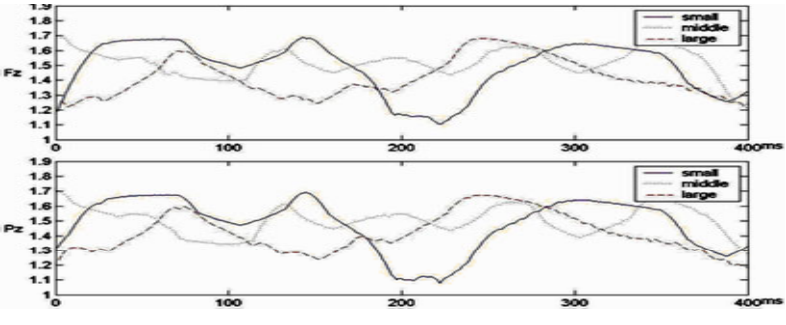

Fig. 2. Shows the TDE analytic results, using the sliding window with w=64, q=1.5 and n=100

In this work, we find the monitoring capability is intensified with the improvement of the nonextensive parameter "q", correspondingly, the descriptive capability of the stationary "background" signal is decreased. There is a case shown in Fig.3. In Fig.3 shows the relation between the choice of "q" and the monitoring capability of the nonextensive TDE.

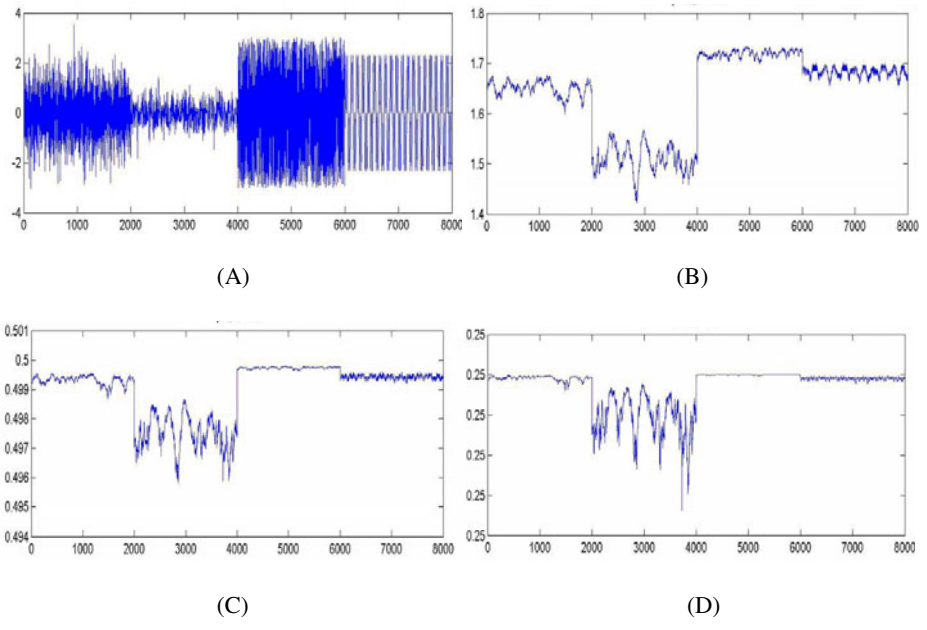

Fig. 3. Illustration of the relation between the value of "q" and the monitoring capability of the nonextensive TDE. Fig. 3(A) Series composed of 4 segments distributed differently, each segment has 2000 points respectively. (I) normal distribution with mean value 0 and standard deviation 0.8; (II): the I signal went thought a low-pass filter (III) uniform distribution in [-3, 3]; (IV): third harmonic generation; Fig. 3(B) (C) (D) are the TDE analytic result with w=128, n=100, but the "q" value in (B) is 1.5, in (C) is 3 and in (D) is 5.

5 Conclusion

The nonextensive entropy provided a novel statistical description of the EEG and ERPs. The TDE based on sliding temporal window approach is shown to be useful for tracking diversity of EEG signals with local irregularity. We demonstrate the performances of the statistical characteristics of nonextensive TDE in quantifying the irregularity of EEG time series.

Acknowlegements. This work is supported by the Natural Science Foundation of China (61072037) and the Natural Science Foundation of Guangdong (10151503101000011), respectively.

References

1. Basar, E.: Brain Function and Oscillation. I. Brain Oscillations. Principles and Approaches. Springer, New York (1998)
2. Basar, E.: Brain Function and Oscillations. II. Integrative Brain Function. Neurophysiology and Cognitive Processes. Springer, New York (1999)

3. Martin, M.T., Plastino, A.R., Plastino, A.: Tsallis-like information measures and the analysis of complex signals. Physica A 275, 262–271 (2000)
4. Tsallis, C.: Generalized entropy-based criterion for consistent testing. Phys. Rev. 58, 1442–1445 (1998)
5. Tsallis, C.: Nonextensive statistics: Theoretical, experimental and computational evidences and connections. Braz. J. Phys. 29, 1 (1999)
6. Tsallis, C., de Albuquerque, M.P.: Are citations of scientific papers a case of nonextensivity? Eur. Phys. J. B 13, 777–780 (2000)
7. Shannon, C.E.: A mathematical theory of communication. Bell Sys. Tech. J. 27, 379–423, 623-656 (1948)
8. Suyari, H.: Generalization of Shannon–Khinchin Axioms to Nonextensive Systems and the Uniqueness Theorem for the Nonextensive Entropy. IEEE Transacitions on Infromation Theory 50, 1783–1787 (2004)
9. Capurro, A., Diambra, L., Lorenzo, D., et al.: Tsallis entropy and cortical dynamics: the analysis of EEG signals. Physica A 257, 149 (1998)
10. Gamero, L.G., Plastino, A., Torres, M.E.: Wavelet analysis and nonlinear dynamics in a nonextensive setting. Physica A 246, 487–509 (1997)
11. Mangun, G.R., Hillyard, S.A.: Mechanisms and models of selective attention. In: Rugg, M.D., Coles, M.G.H. (eds.) Eletrophysiology of Mind, pp. 40–78. Oxford University Press, Oxford (1995)
12. Hawkins, H.L., Hillyard, S.A., Luck, S.J., Mouloua, M., Downing, C.J.: Visual attention modulates signal detectability. J. Exp. Psychol. Hum. Percept. Perform. 16, 802–811 (1990)

Experimental Study on Anti-rust Oil Atomization in the Electrostatic Oiler

Wang Zhaohui, Gao Quanjie, Wang Jiaqing, and Wang Jijun

College of Machinery and Automation, Wuhan University of Science and Technology,
Heping road 947, 430081 Wuhan, P.R. China
wzhuiboy@yahoo.com.cn, gaoquanjie@wust.edu.cn,
chenglewan@163.com, wangjj13@sany.com.cn

Abstract. The anti-rust oil can be evenly sprayed on the surface of metal plate by high-voltage electrostatic effect in the electrostatic oiler, it is widely used in production line of steel, non-ferrous metal plate, and other processes which need high-quality oiled. The anti-rust oil atomization experimental study in the electrostatic oiler shows: when the voltage is stronger, the oil jet length become smaller generally. The atomizing angle increases as the voltage is increased, when the voltage arrives at a certain value, the atomizing angle reaches the maximum. The oil particle size decreases as the increased voltage, and its distribution is different at different voltage.

Keywords: electrostatic oiler; atomization; jet length; atomizing angle; particle size.

1 Introduction

The oil atomization can be carried out effectively by using electrostatic atomization technology. With the development of our society, using raw materials efficiently and decreasing environmental pollution become more and more important. Applying an electrostatic field to improve the effect of atomization has been used extensively in electrostatic spray-painting, electrostatic spray-dusting, electrostatic ink-spray printing and electrostatic pesticide spraying of surface engineering applications and micro manufacturing equipment [1-4]. So it was a new overlapping task needed research, which had very important theoretical significance and practical value.

The pre-studies have showed: the electrostatic field played a significant role on the oil atomization for uniforming and thinning droplets. The oil atomization in the electrostatic field was the process that the oil was broken into charged droplets with the action of the static electricity, compared with other atomization technology, such electrostatic atomization process involved the electricity had its own characteristics [5-7]. Because the track of charged droplets was theoretically determined by the electric field strength, so different voltages could be applied to control the track and produce the scattered droplets for various scales. These advantages had made electrostatic atomization technology be widely studied in theoretical research and application area.

D. Zeng (Ed.): Future Intelligent Information Systems, LNEE 86, pp. 525–531.
springerlink.com © Springer-Verlag Berlin Heidelberg 2011

The electrostatic oiler is a high-tech product combing with the electrohydraulic technology. With the high voltage electrostatic effect, the anti-rust oil is evenly sprayed on the surface of metal plate. It can be widely used in the production line of steel, nonferrous metal plate and other process which need high-quality spraying oil technology [8-10]. Through the high voltage electrostatic field, the oil droplets after atomization is more evenly; the oil particle size can be greatly decreased, and the uniformity and deposition efficiency of the oil droplets spectrums are improved.

2 The Electrostatic Oiler

The electrostatic oiler is mainly composed of four parts which are the oiled room, supplying oil and circulating heating system, the high voltage power system and the electric control system. The spraying blade, the guide plate, the supported and hanged car are fixed in the oiled room; Oil supply pump station, umlaufheizung pump station and the recycling tank are included in the supplying oil and circulating heating system; The high voltage control cabinet and the transformer are main components of the high voltage power supply system; The electric control system is composed of the programmable logic controller, the AC control system, the DC control system, the digital temperature control system and oil level monitor and control system. The basic principle of charged oil atomization in the electrostatic oiler is shown in Fig. 1.

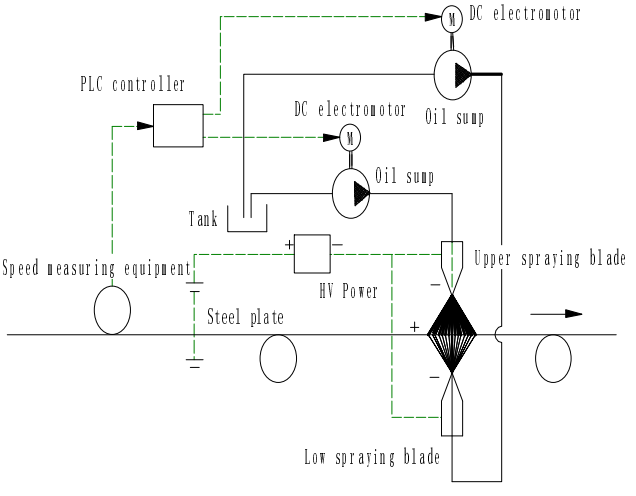

Fig. 1. Working principle diagram of the electrostatic oiler

The spraying blade is usually connected to the negative electrode of the high voltage DC power supply, which the working voltage is 20-70kV, and the moving steel plate is touched down, so the high voltage electrostatic field is generated [11-12]. In the electric field, the positive and negative ions in the air move fast along the power lines, the positive ions tend to the blade, and the negative ions move to the

steel plate. So the ions will collide the neutral molecules on the way, which loosing electron in the process become into the new positive ions, the electron pushed out attach to a number of the neutral molecules to become into the new anions. Because of being in the strong electric field generated by the high voltage power, this ionization effect is very intensity, and so the number of ions between the blade and the steel plate rapid increase. At the same time, the edge of the blade is very sharp, so it is easier to form so-called "corona discharge" to accelerate the air ionization in the electric field. The oil droplets outflowing from the edge of the blade are attracted easily by the grounded steel plate after adsorbing by the plasmas, so that it can move fast to the steel plate, and ultimately the oil droplets are evenly sprayed on the steel plate. Usually in theory, the charged oil passes through the jet area, the transient area and the atomization area.

3 Experimental

3.1 Experimental Instrument and Method

The electrostatic oiler experimental platform, a SONY DSC-F717 advanced digital camera, an adjustable tripod, the ATEST-212 laser particle size analyzer, a graduated scale, a note and a support needed to prepare.

In this experiment, the key factors for selecting the anti-rust oil were as follows: the oil temperature was 45℃, the surface tension of oil was 25×10-3N/m, the viscosity of oil was 11.8mm2/s, the conductivity of oil was 3s/m. In addition, spraying requirement for coating oil to the single-sided steel plate was 2.5g/ml, the distance between the blade and the steel plate was 195mm, and the rated speed of the DC motor of oil supply pump station was 1000rpm.

The pictures of charged oil atomization were obtained by the high-speed camera method and the diameter of the oil droplets after spraying could be got by the laser particle size analyzer in the electrostatic oiler. The advantage of the high-speed camera method was that it could make us record the process of the oil jet for continuous breaking up in a very short time, so it was suitable to study the atomization of oil jet from the macroscopic view, which the jet length and the atomizing angle could be observed and calculated. At the same time, the charged oil droplets particle size and its distribution could be analyzed from the microcosmic view.

3.2 Experimental Process

① The advanced digital camera fixed to the adjustable tripod should be in front of the blade by its tip side. At the same time, the receiver and transmitter of the laser particle size analyzer should be adjusted to make sure that theirs' axes were the same straight line.

② Started atomization devices and set the oil flow to a certain level. When the working station was stable at a later time, the camera and the laser particle size analyzer could be opened.

③ Fixed the distance between the blade and the steel plate, the working voltage was adjusted to the minimum and the oil outflow from the blade to be shot. Gradually increased the voltage, the oil spraying pictures would be taken and the experimental data of oil particle size would be obtained by the laser particle size analyzer.
④ Similarly fixed the digital camera to the adjustable tripod in front of the blade by its length side at an appropriate distance, repeat the steps ②,③.
⑤ After the experiment, the photos in the digital camera were imported to the computer and the software of image processing was used to deal with the photographs, then the jet length and the atomizing angle would be analyzed with the changed voltage. The data of the oil particle size and its distribution could be obtained by the laser particle size analyzer. Thus it could be more comprehensive to analyze the effect of oil atomization in the electrostatic oiler.

3.3 Experimental Phenomena

Fig.2 and Fig.3 showed the experimental phenomena. Seeing from the tip direction of the blade, when the voltage was 0-20kV, the oil dropped down, and with the voltage increased gradually, it turned into jet-like shape. When the voltage arrived at 20-30kV, the oil jet was gradually transformed into a fork-like shape and this bifurcation was not obvious, oil was the vertical-down screen like a square. When the voltage became to 30-50kV, there would be a clear bifurcation phenomenon of the oil jet, at the same time the oil was sprayed with the cone-shaped, and the atomizing angle was larger. Then oil droplets distribution was very uneven, and more oil particles were on both sides of the jet, only a small number of the particles were on middle of the oil jet. However, when the voltage turned into 50-60kV, the atomizing angle decreased gradually, and the droplets distribution was uniform than before. When the voltage achieved above 60kV, the atomizing angle was almost unchanged and it was to be stable. Seeing from the length direction of the blade, increasing the voltage, the dripping oil would become into the jet and the oil line spacing became smaller, and then the charged oil atomization occurred at a certain distance away from the edge of the blade.

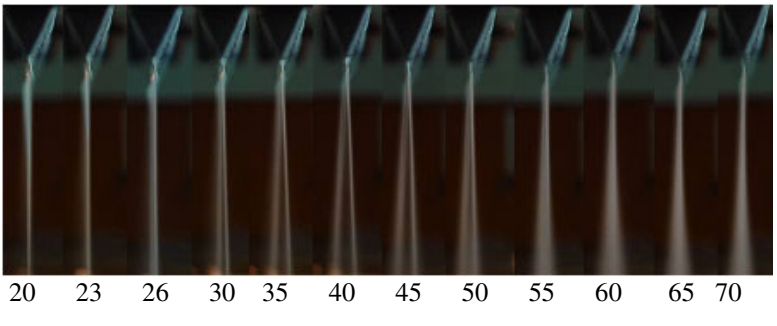

Fig. 2. Spraying shapes of charged oil under different voltages in the face of the tip of the blade in the electrostatic oiler

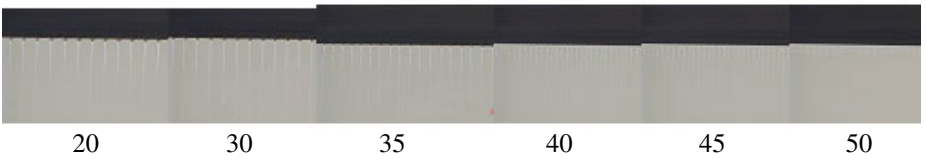

Fig. 3. Distribution of oil line spacing under different voltages in the face of the length of the blade the electrostatic oiler

4 Results and Analysis

4.1 The Change of the Jet Length with the Voltage

When the voltage was 0-23kV, the dripping oil became into the jet. During this process, the velocity of the jet was increased by the electric field with the increased voltage, so the jet state would be steady. When the voltage arrived at 23-26kV, the jet length was shortened. This was the reason that with the voltage was raised, breaking frequency of droplets increased by the rapid increasing of the surface wave's frequency of oil jet. When the voltage reached 26-32kV, the oil jet length decreased as the voltage increased. The slope of absolute value for the ratio of the jet length to the voltage was gradually decreased, and its relation curve between the jet length and the voltage became from the convex into the concave.

When the voltage came to 32-60kV, the jet length decreased as the increasing voltage slowly, and the phenomenon of corona discharge occurred step by step at this stage, which changed the space electric field. Because the ratio of the charges on the oil surface to the voltage increased, so the ratio of the electrostatic force affecting the jet to the voltage increased. As the jet length decreased, the electric field strength was large enough, so the impact of the gravity to the jet began to be negligible. When the applied voltage was high enough, it could duce the charge as many as possible, which the deformation of the jet surface would increase significantly at this time. Then it would produce more oil droplets at the breaking moment.

4.2 The Change of the Atomizing Angle with the Voltage

When the voltage was below 26kV, as the voltage increased, the state of the dripping oil would turned into a jet-like shape. Because at that time the oil jet was not still broken, so the atomizing angle was zero. When the voltage changed from 26kV to 35kV, the atomizing angle increased continuously, that is because the Coulomb force among the droplets promoted them mutually exclusive. When the voltage was 35-45kV, the oil atomization became uneven for increasing the voltage. Then the primary droplets and satellite droplets became to produce, and at that time the influence of Coulomb force began to decrease. So the number of the particles was larger on both sides of the spraying oil jet and smaller in middle, thus the atomizing angle would be increased somewhat at this time due to the unevenness of the oil droplets.

As the voltage continued to increase, the primary droplets and satellite droplets were more obvious. When the voltage was 45kV, it would reach a stable limitation producing the primary droplets and satellite droplets. Based on the theories of

electrostatics and fluid dynamics, when the ratio of the primary droplets size to the satellite droplets size reached a certain value, the radius of the primary droplets would be decreased while the radius of the satellite droplets would be increased after continuing to increase the voltage, so when the voltage was 45-50kV, the atomizing angle was stable in general. But when the voltage attained at 50-62kV, the primary droplets and satellite droplets began to degrade. When the voltage was above 62kV, as the jet length tended to be zero gradually, the atomizing angle would be stable and not to be changed, so the effect of oil atomization would be best for spraying.

4.3 The Change of the Droplets Size and Its Distribution with the Voltage

In this study, the ATEST-212 laser particle size analyzer was utilized to discuss the droplets size and its distribution. Usually, the working voltage was 20-70kV in the electrostatic oiler, and the rpm of the servo motor was controlled at 90-150r/min. During the experiment, the spraying capacity should not be set too big since the special structure of the oil balde. The study showed that: When the rpm was 90r/min and the woking voltage was 30kV, the droplets size was big and its distribution became bimodal-shaped; when the voltage reached at 50kV, the droplets size was a good normal distribution; when the voltage arrived at 65kV, the particle size continued to decrease and its distribution was more uniform; while when the voltage was up to 75kV, although the particle size decreased all the same, the uniformity of the droplets size distribution reduced. Therefore, it was found that: charged oil atomization could be get the best effect when the working voltage was 65kV in the electrostatic oiler.

5 Summary

(1) As the voltage increases, the oil jet length decreases, and the velocity of the jet increases, the disturbance waves on the jet surface develop fasterly, so the jet easily breakes, which lead the jet length is shorter. However, the effect of the voltage on the jet length is different in every area.
(2) When the voltage is lower, the atomizing angle increases as the increasing voltage. When the voltage reaches to a certain value, the atomizing angle gets the maximum. While the atomizing angle will begin to decrease if the voltage continue increases, finally it is to be stable.
(3) The oil droplets size decreases as the voltage increases, and the distribution of the particle size is different at different voltages. Charged oil atomization could be getting the best effect when the working voltage is 65kV in the electrostatic oiler.

Because of limited experimental resources, only the jet length, the atomizing angle and the oil particle size were analyzed under different voltages in the electrostatic oiler during this experiment. For future research, other parameters, such as the flow, the temperature and different electrode shape, should also be studied. Some major factors, such as thickness, homogeneous properties and depositional efficiency of oil droplets, should be tested. Such studies can offer insights for electrostatic atomization in large-scale industrial applications.

Acknowledgements

This project was supported by the National New Products Program, China (No.2006GRD10004) and Natural Science Foundation of Hubei Province, China (No.2009CDB314).

References

1. Colbert, S.A., Cairncross, R.A.: A discrete drop let transport model for predicting spray coating patterns of an electrostatic rotary atomizer. Journal of Electrostatics 64(3), 234–246 (2006)
2. Zhao, S., Castle, G.S.P., Adamiak, K.: The effect of space charge on the performance of an electrostatic induction charging spray nozzle. Journal of Electrostatics 63(3-4), 261–272 (2005)
3. Li, F., Yin, X.Y., Yin, X.Z.: Instability analysis of an inner-driving coaxial jet inside a coaxial electrode for the non-equipotential case. Journal of Electrostatics 66(1), 58–70 (2008)
4. Priol, L., Baudel, P., Louste, C., et al.: Theoretical and experimental study (linear stability and Malvern granulometry) on electrified jets of diesel oil in atomization regime. Journal of Electrostatics 64(7-9), 591–596 (2006)
5. Lintanf, A., Neagu, R., Djurado, E.: Nanocrystalline Pt thin films prepared by electrostatic spray deposition for automotive exhaust gas treatment. Solid State Ionics 177(39-40), 3491–3499 (2007)
6. Paine, M.D., Alexander, M.S., Smith, K.L., et al.: Controlled electrospray pulsation for deposition of femtoliter fluid droplets onto surfaces. Journal of Aerosol Science 38(3), 315–324 (2007)
7. Hyungho, P., Kyoungtae, K., Sangsoo, K.: Effects of a guard plate on the characteristics of an electrospray in the cone-jet mode. Journal of Aerosol Science 35(11), 1295–1312 (2004)
8. Gao, Q.J.: Research on charged atomization in electrostatic oiler. China Mechanical Engineering 13(7), 552–554 (2002)
9. Wang, Z.H., Liao, Z.F., Gao, Q.J., et al.: Research on experiment and simulation of oil atomization in electrostatic oiler. Mechanical Science and Technology for Aerospace Engineering 27(5), 662–666 (2008)
10. Wang, Z.H., Liao, Z.F., Gao, Q.J., et al.: Experimental study on properties of oil jet in a high voltage electrostatic field. Journal of Experiments in Fluid Mechanics 23(2), 36–39 (2009)
11. Wang, Z.H., Liao, Z.F., Gao, Q.J., et al.: Study on oil corona discharge and atomization experiment with electrostatic spray. High Voltage Engineering 35(3), 636–640 (2009)
12. Zhou, H.S., Xian, F.S., Gao, L.G.: Research into charged jet atomization. Journal of Jiangsu University: Natural Science Edition 16(4), 7–10 (1995)

Study on Magnesium Alloy Auto Body Based on Front Impact*

Hongtu Sun, Guozhe Shen, and Ping Hu

School of Automotive Engineering
Dalian University of Technology
Dalian, Liaoning Province, China
sunhongtu@sohu.com

Abstract. Magnesium alloy is a lightweight material which is potential to decrease the weight of auto body for lightweight. Experiments were performed to study the mechanics characterization of AZ61 magnesium alloy at normal temperature. The steel structure of an auto body was improved with AZ61 magnesium alloy as a case study. The weight of the magnesium alloy auto body parts decreases dramatically. The finite element method and multi-body dynamic method were applied to simulate the front impact of the magnesium alloy auto body and the occupant restraint system. The results of the magnesium alloy auto body were compared to the results of the original auto body according to the China New Car Assessment Program (C-NCAP) test. The results show the feasibility of the application of magnesium alloy on auto body based on the performance of stiffness, modal and safety of front impact.

Index Terms: Magnesium alloy, Auto body, Lightweight, Front impact.

1 Introduction

Lightweight of structures is an effective method to increase fuel efficiency of vehicle on the development of vehicles. Multiple candidates for replacing mild steel in automotive structures have been proposed, such as advanced high strength steels aluminum [1] or magnesium alloys [2], and composite materials [3].

Magnesium alloy which is a typical lightweight material has been applied on auto body. He et al. studied the characterization of magnesium alloy and the application on auto industry [4]. Song et al. introduced the development of magnesium alloy in the lightweight of vehicle [5]. Gao et al. redesigned the roof of a car by magnesium alloy to replace the steel structure. The mechanics characterization of magnesium alloy structure is compared to the original structure with finite element method [6]. Zhang et al. studied the effect of deformation condition on the mechanics of AZ61 magnesium alloy [7]. Yang et al. studied the effect of heat treatment on the deformation of AZ61 magnesium alloy [8].

* This work is partially supported by NSF Grant #19832020 to P. Hu and NSFOU Grant #10125208 to P. Hu.

D. Zeng (Ed.): Future Intelligent Information Systems, LNEE 86, pp. 533–541.
springerlink.com © Springer-Verlag Berlin Heidelberg 2011

The purpose of this research is to study the material characterization and the application of magnesium alloy on auto body. The material experiments are carried out to study the mechanics characterization of magnesium alloy. The finite element and multi-body dynamic method are applied to simulate the front impact of a car as a case study according to China New Car Assessment Program (C-NCAP) [9] crash tests. The kinematic and dynamic responses of the auto body and occupant are analyzed in the front impact. The results from the simulation analyses of magnesium alloy car body are compared against the original steel auto body to verify the feasibility of the application of magnesium alloy on auto body.

2 Magnesium Alloy Auto Body

A. Mechanics Characterization of Magnesium Alloy

Magnesium-Aluminum alloys and Magnesium-Zinc-Aluminum alloys are general magnesium alloy used for deformation. The typical Magnesium-Aluminum alloy includes AZ31, AZ61 and AZ80. AZ61 which is a kind of general and cheap magnesium alloy has high strength, plasticity and anti-corrosion characteristic. AZ61 is applied on this research according to the mechanics requirement of auto body and feasibility of manufacture. The magnesium alloy parts on the auto body are manufactured by the die-casting method. The contents of AZ61 are listed in the Table 1.

Table 1. Main Contents of AZ61

Contents	Mg	Al	Zn	Mn	Si
Percents (%)	91.9	6.5	1	0.3	0.3

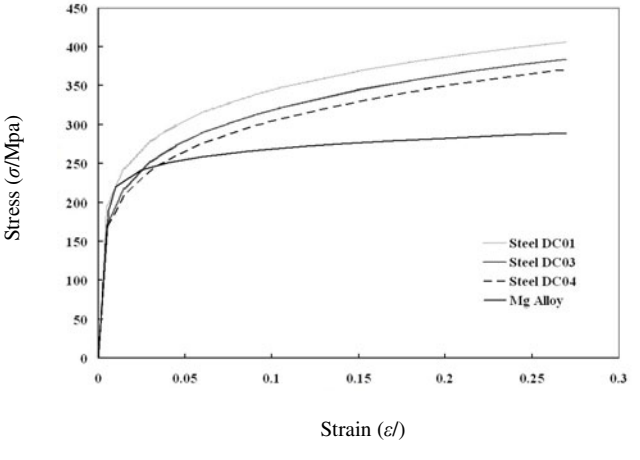

Fig. 1. Stress and strain curves

Mechanics experiments are performed to the samples of AZ61 magnesium alloy. The mechanics characterization of stress and strain on different strain rate is obtained by the press experiments on AZ61 samples with different press rate in normal temperature. The mechanics characterization of AZ61 magnesium alloy is different with steels. Figure 1 shows the strain and stress curves of AZ61 and steels which are generally applied on auto body.

Modulus of elasticity of AZ61 magnesium alloy is 42.2Gpa, yield strength is 241.2Mpa, tensile strength is 270.1Mpa, and Poisson ratio is 0.35. The modulus of elasticity of magnesium alloy which is lower than steel shows that magnesium alloy can absorb more energy in impact by more deformation at the same crash condition. At the same time, magnesium alloy can bear high vibration load of impact to be appropriate for auto body. However, the stiffness, strength and plasticity need to be improved to be applied on auto body by the modification of thickness and shape of parts section.

The press experiment data in normal temperature were analyzed. The constitutive relation of Johnson-Cook is given by:

$$\sigma_i = (218.2 + 396.3\varepsilon_p^{0.1219})(1 + 0.023\ln \dot{\varepsilon}/\dot{\varepsilon}_0)\,. \tag{1}$$

Where σ_i is effective stress, ε_p is effective strain, and $\dot{\varepsilon}/\dot{\varepsilon}_0$ is rate of strain.

The density of AZ61 magnesium alloy is 1800kg/m^3, which is 23% of steel. It shows that the application of magnesium alloy can dramatically decrease weight of auto body with the same structure.

B. Magnesium Alloy Auto Body

The design of magnesium alloy auto body is required to match the parts around the magnesium alloy parts for the manufacture, installation, and the mechanics requirement of auto body. The magnesium alloy parts which replace the original steel parts are main structure to absorb the energy in impact. The stiffness and modal of auto body are important mechanics characterization in design. Figure 2 shows the original steel structure of an auto body. There are 58 steel parts which are welded on the auto body. The materials of these steel parts are 3 kinds of steel which are shown in Figure 1. The thicknesses of the steel parts are from 0.8mm to 2.5mm.

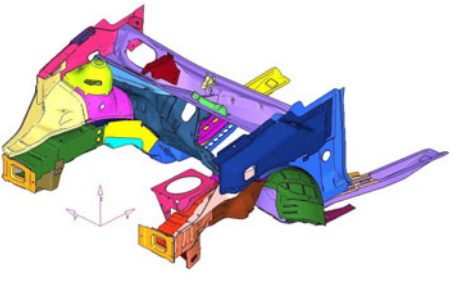

Fig. 2. Original steel parts structure

The magnesium alloy auto body is designed according to the original steel structure. The structure of magnesium alloy auto body has the same shape characterization as the original steel structure for the installation and reliability. Some of parts are designed to one magnesium alloy part for the simplification of the installation process, the less parts and the cost of manufacture. The reinforcement ribs are added on the magnesium alloy parts to improve the stiffness of the structure. There are 9 magnesium alloy parts which are designed to replace original steel parts of the auto body.

Figure 3 shows the all magnesium alloy parts structure which has the similar shape of the original steel structure. Welding can not be applied on the linkage of the magnesium alloy parts which has low melting point, high linear expansivity and heat conductivity. The magnesium alloy parts are then riveted together with the others of the auto body.

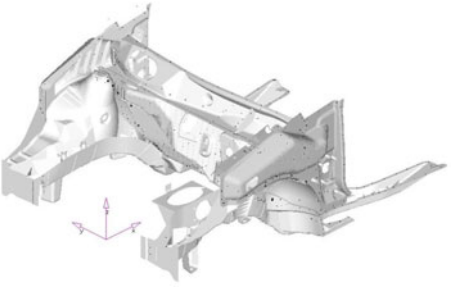

Fig. 3. Magnesium alloy parts structure

The thicknesses of the magnesium alloy parts are 3mm which are for the same mechanics characterization as the original steel structure. The lightweight mass of magnesium alloy auto body is 35.85kg, which is 10.3% of the weight of the auto body, 56.1% lighter than the original steel structure. The weight of auto body decreases dramatically due to the application of magnesium alloy.

3 Analysis of Mechanics Characterization

Stiffness and modal of bend and torsion are important mechanic characterization which is verified to satisfy the requirement of auto body. Finite element method is applied to simulate the stiffness and modal of auto body for magnesium alloy and steel auto body. Figure 4 shows the finite element model of the auto body for the mechanic characterization.

The bend stiffness, torsion stiffness, first bend and torsion modal of auto body are calculated in MSC/NASTRAN. Table 2 lists the stiffness and modal of auto body.

The bend stiffness of magnesium alloy auto body is 4.9% lower than steel auto body. However, the Torsion stiffness of magnesium alloy auto body is 1% higher than steel auto body. The similar result is concluded on the bend modal and torsion modal. It shows that the magnesium alloy auto body satisfies the mechanics requirement of auto body.

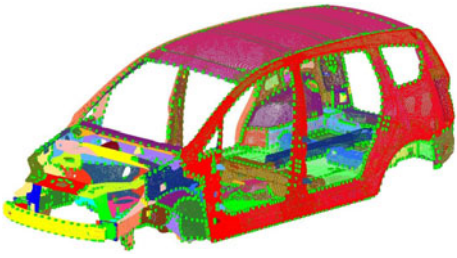

Fig. 4. Finite element model of auto body

Table 2. Stiffness and Modal Auto Body

Auto body	Bend stiffness (k_b/Nmrad^{-1})	Torsion stiffness (k_b/Nmrad^{-1})	Bend modal (k_b/Nmrad^{-1})	Torsion modal (k_b/Nmrad^{-1})
Steel	9560	686000	380.0	29.4
Magnesium alloy	9090	69200	36.1	30.8

4 Analysis of Front Impact

A. Analysis of Auto Body

The finite element model for front impact includes the auto body, chassis and seats which have 1582534 points and 1589805 elements. The finite element model for the front impact is shown in Figure 5.

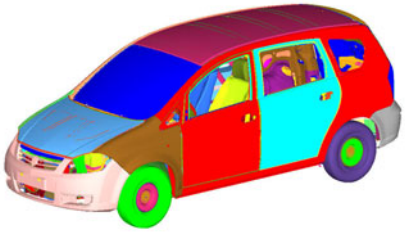

Fig. 5. Finite element model for front impact

The finite element models are simulated in LS-DYNA for front impact at 50km/h velocity according to the C-NCAP test. The deformations of the steel auto body and magnesium alloy auto body are shown in Figure 6.

It shows from the Figure 6 that the deformations of the magnesium alloy auto body are less than the deformations of steel auto body on the front parts. The maximum intrusion displacements on the auto body parts are listed in Table 3.

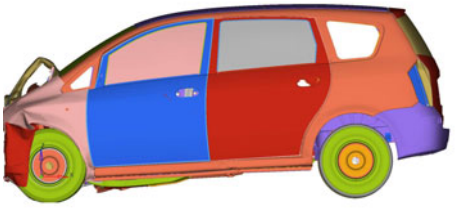

(a) Original steel

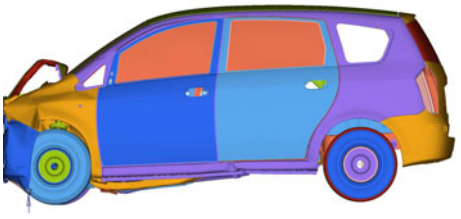

(b) Magnesium alloy

Fig. 6. Deformations of auto body

Table 3. Maximum Intrusion Displacements of Auto Body

Auto body	Front frame (i_f/mm)	Fire wall (i_w/mm)	B pillar (i_p/mm)
Steel	16.8	187	633
Magnesium alloy	18.5	166	568

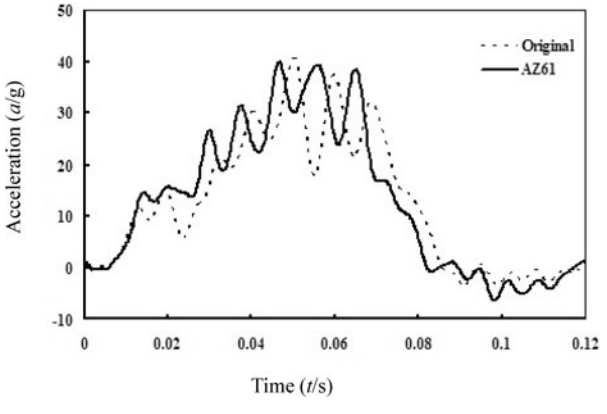

Fig. 7. Accelerations of auto bodies

The maximum intrusion of B pillar on magnesium alloy car body is 10.3% less than steel auto body; fire wall on magnesium alloy is 11.2% less than steel auto body. The reason is that the deformations of magnesium alloy parts decrease due to the higher thicknesses which mean the less absorbed energy in impact. However, the

maximum intrusion of front frame of magnesium alloy is higher than steel auto body due to the more absorbed energy on the front frame parts of auto body. The X accelerations of auto body are shown in Figure 7.

The acceleration curve of magnesium alloy auto body is similar to the steel auto body. The maximum acceleration of original auto body is 40.68g at 50ms. The maximum acceleration of magnesium alloy auto body is 42.64g at 47ms. The less deformations of magnesium alloy auto body in impact result in the less absorbed energy which is the reason for the higher and earlier maximum acceleration.

B. Analysis of Occupant Restraint System

Injuries of occupant are important criterion for the safety in crash. The occupant restraint system is simulated by multi-body dynamic method to calculate the injury of occupant in impact. The model of occupant restraint system is shown in Figure 8.

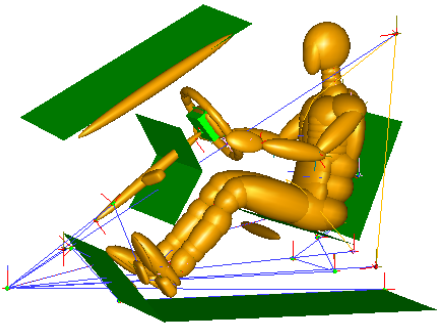

Fig. 8. Multi-body model of occupant restraint system

The occupant restraint system model includes seat, steering system, instrument panel, wind shield, pedals, floor and dummy. The Hybrid III 50 percentiles is applied in the model. The results from finite element method on auto body are inputted into the model of the occupant restraint system in MADYMO. The response of the occupant restraint system is shown in Figure 9.

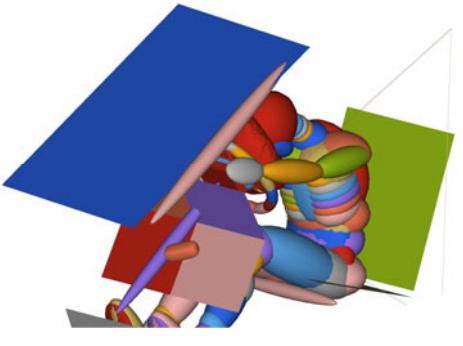

Fig. 9. Response of occupant restraint system

The injuries of occupant are calculated according to the criterion of C-NCAP. The X accelerations of occupant's head are shown in Figure 10.

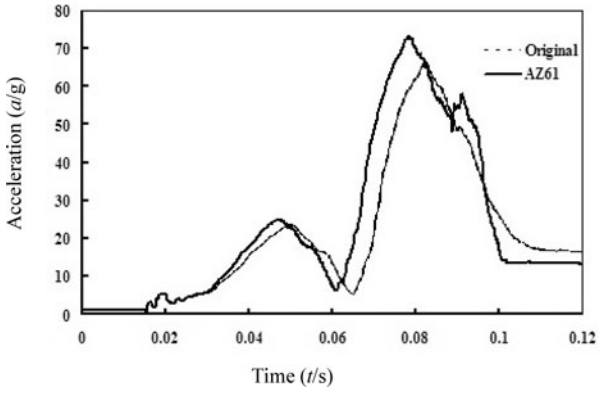

Fig. 10. Accelerations of occupant's head

The maximum acceleration of occupant's head in the impact of the original steel auto body is 50.55g at 81ms. The maximum acceleration of occupant's head in the impact of the magnesium alloy auto body is 52.46g at 79ms. The different maximum acceleration is from the results of auto body in impact. The occupant's head injury of HIC36 in the impact of the magnesium alloy auto body is 367.2 which are 4.72% higher than the steel auto body. The results show that the safety of magnesium alloy auto body is similar to the original steel body which are both satisfies the safety requirement of C-NCAP.

5 Conclusions

The mechanic experiments of magnesium alloy AZ61 are performed to study the constitutive relation of magnesium alloy. The original steel auto body is improved by the magnesium alloy auto body for lightweight. The weight of magnesium alloy auto body which has less parts and manufacture process is 56.1% lighter than original steel auto body. The finite element and multi-body dynamic methods are applied to simulate the front impact of auto body. The safety of the magnesium alloy auto body is verified by the comparison to the results of original steel body in front impact according to C-NCAP.

Acknowledgment

This project is supported by National Natural Science Foundation of China (Grant No. 19832020), National Science Fund of Outstanding Youths of China (Grant No. 10125208), Chongqing Municipal Programs for Science and Technology Development of China (Grant No. CSTC, 2007AA4008), and National Key Technology R&D Program of China (Grant No. 2006BA104B04-2).

References

[1] Hanssen, A., Langseth, M., Hopperstand, O.: Static and dynamic crushing of square aluminum extrusions with aluminum foam filler. International Journal of Impact Engineering 24(4), 347–383 (2000)
[2] Oliveria, A., Worswick, M., Grantab, R., et al.: Effect of forming process variables on the crashworthiness of aluminum alloy tubes. International Journal of Impact Engineering 32(5), 826–846 (2006)
[3] Langstedt, G., Asnafi, N.: A new lightweight metal-composite metal panel for applications in the automotive and other industries. Thin Walled Structures 36(4), 289–310 (2000)
[4] He, Y., Yang, C.: Application of Magnesium Alloy in Automotive Industry. Automotive Technology & Material 6, 25–27 (2002) (in Chinese)
[5] Song, K.: The development and application of magnesium alloys in automotive industry. Mechanical Research & Application 20(2), 14–16 (2007) (in Chinese)
[6] Gao, Y., Cheng, J., Yu, H.: Structure Design and Analysis of Magnesium-Alloy Car Roof Members. Automotive Technology 4, 9–12 (2008) (in Chinese)
[7] Zhang, X., Zhang, Z.: The effect of distortion condition on mechanical behavior of AZ61 magnesium alloy. Journal of Plasticity Engineering 15(1), 76–78 (2008) (in Chinese)
[8] Yang, L., Yao, Y., Yao, J., et al.: Effect of heat treatment on mechanical properties of extruded AZ61 magnesium alloy. Journal of Shenyang University of Technology 28(4), 662–665 (2006) (in Chinese)
[9] Chinese Automotive Technology & Research Center, C-NCAP(2006), http://www.c-ncap.org

Overlay Routing Middleware for Multimedia Communications

Zheng He, Xiaohong Huang, and Yan Ma

Institute of Networking Technology,
Beijing University of Posts and Telecommunications

Abstract. As multimedia communications are developing rapidly in Internet, in order to improve the end-to-end (E2E) performance, we propose an overlay routing layer middleware (ORLM) aiming to overcome the limit inherent in the Internet's IP-layer routing service with the aid of a cross-layer design, based on the ALTO service and the NGI QoS support. In this paper, we mainly show the design principles and details of our routing middleware, including the general architecture and function modules, the proposed flow label definition and its related usage in the overlay network scenario, and the TE (Traffic Engineering) –awareness feature.

Keywords: overlay routing; flow label; ALTO service.

1 Introduction

In recent years, multimedia applications have been widely used to provide users with racy and lifelike experiences while they are interactively communicating on the Internet. However, the Internets current architecture (IPv4) almost remains the same as its original design based on the principles fitting data transmission applications. Therefore, despite the increase of backbone and access bandwidth, it is still stringent for the current Internet infrastructure to support high-quality multimedia communications. Moreover, much work has revealed that the current IP-layer routing service was far from ideal to generate optimal E2E paths [1-3].

Motivated by the above introduction, we propose a routing layer middleware to complement the current IP-layer routing service to better support the E2E performance requirement of multimedia communications. The most important idea of this middleware is to provide enhanced transport-layer mechanism by efficiently discovering, measuring, constructing, utilizing and maintaining a number of application-layer paths that are comprised of proper relays in the overlay network, without occupying too much link bandwidth and deteriorating the network condition. To achieve the goal, depending on NGI QoS support, flow label in IPv6 [4], and ALTO service [5], an overlay network is established, in which every participant endhost that starts a session of multimedia communications is able to ask another suitable participant end-hosts to construct application-layer paths. Thereafter, the multimedia data can also be simultaneously transmitted through one or multiple application-layer paths adaptively according to the corresponding QoS requirements.

D. Zeng (Ed.): Future Intelligent Information Systems, LNEE 86, pp. 543–550.
springerlink.com © Springer-Verlag Berlin Heidelberg 2011

This paper presents the structure design, and the rest is organized as follows. Section 2 presents some existing overlay routing schemes. Section 3 elaborates the architecture of routing layer middleware and its design principles, and finally, section 4 concludes the paper.

2 Related Work

In this section, we briefly review some related QoS overlay architectures.

Resilient Overlay Networks (RONs) are proposed to detect and recover from Internet path failures by actively monitoring the quality of overlay links and routing packets based on application-specific metrics.

The Spine architecture applies TCP-like loss recovery and congestion control on each overlay link to reduce the latency and jitter of reliable connections [6]. Though highly flexible, end-user overlays usually cannot provide end-to-end QoS guarantees, since they normally cross many uncontrolled intermediate domains. Moreover, it is difficult to design an effective economic model for ISPs to adopt end-user overlays.

ORLM differs from RON and Spines on several aspects. First, both RON and Spines made use of overlay routing techniques to improve the E2E path reliability and performance for all types of Internet applications, but ORLM is particularly suitable for interactive multimedia communications. Specifically, ORLM supports to differentiate the QoS class of multimedia data flows and accordingly transmit them through different paths, but RON and Spines did not. Finally, ORLM constructs flexible hot count application-layer paths proactively; it not only leverages the large scale of overlay networks to achieve path diversity, but also can coordinate multiple paths to overcome the limit of IP-layers single path routing service.

3 ORLM Design Principles

3.1 ORLM Architecture

Conceptually, ORLM locates between the application software and the current Internet's transport-layer service. Fig.1 shows the structure of a typical application of multimedia communications utilizing ORLM to enhance its data transmission.

- **ALTO Service Module:** This module is used to send ALTO queries, just as ALTO client. In this paper, it is embedded in the ORLM.
- **Neighbor Maintainer:** The maintainer contains a list of online neighbors, which is obtained from another end hosts (Peer Exchange), Distributed Hash Table (DHT) or application servers.
- **Path Selector:** This module obtains the relay candidates based on the ALTO guidance and performs active measurements, using flow label, to determine which relay candidates are able to compose application-layer paths that can offer capable E2E performance.
- **Path Manager:** This module administers the paths chosen by Path Selector and dispatch packets to each of them, which is including Path Quality Monitor, Path Quality Controller and Forwarding Table.

- **Path Quality Monitor:** This module frequently checks quality of application-layer paths, using a special type of flow label.
- **Path Quality Controller:** This module is used to adjust and control the state of each path. When congestion happens, the corresponding control mechanism starts.
- **Forwarding Table:** The table records the application-layer paths.

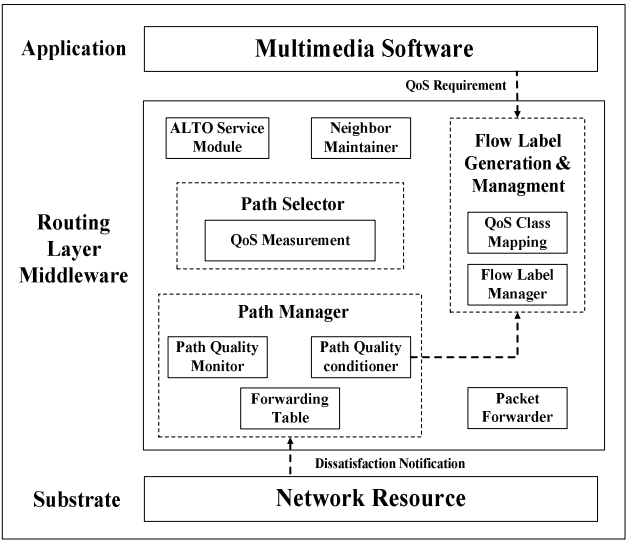

Fig. 1. Overlay Routing Layer Middleware Architecture

- **Packet Forwarding:** The module is used to forward multimedia data, according to the Forwarding Table.
- **Flow-Label Generation & Management:** This module is for flow label management, which includes Flow Label Manager and QoS Class Mapping Module.
  - **Flow Label Manager:** This module is responsible for label generation, label distribution, label elimination and related label management.
  - **QoS Class Mapping Module:** This module is to map different QoS requirement to different QoS Class Code (QCC), in order to classify different types of data.

The multimedia software specifies and delivers the data and their corresponding QoS requirement to the ORLM. Invoked by the application, the sender ORLM passes the inputs, from multimedia software, to the Path Manager module, which then transmits the multimedia data with a proper combination of a number of application-layer paths according to the data's specified requirements.

Every relay along an application-layer path has to run a packet forwarder module as a daemon process to forward packets on application-layer for the sessions using this path. Finally, all packets successfully arriving will be received by the receiver's

Path Manager module, which will store the data in a jitter buffer and hand in the reconstructed data to the receiver's multimedia software through the ORLM. The transmission procedure is shown in Fig.2.

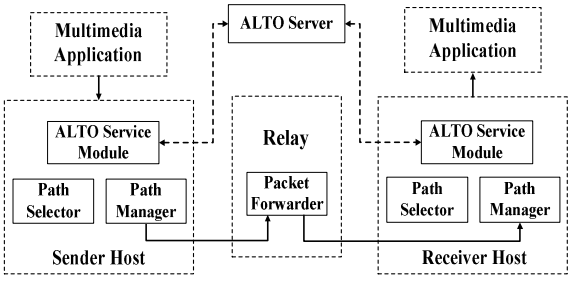

Fig. 2. Data Transmission Procedure Utilizing ORLM

As a whole functional distributed system, ORLM depends on another control plane component. The Neighbor Maintainer contains a list of online neighbors, which are candidates for multimedia data relay. The ALTO Service module is used to choose the suitable relay nodes, according to the ALTO guidance from the ALTO server. The Path Selector is used to efficiently find out high quality application-layer paths.

Next, we elaborate the design principles of ORLM.

3.2 Flow Label Definition and Usage

IPv6, the next-generation Internet Protocol, implements new features which have added two new fields, in the IPv6 main header, that can be used to support quality of service. These two fields are 8 bits Class of Service (CoS) and a 20bit flow identification field.

In this paper, we are trying to discovery a number of application-layer paths with different performance properties by using flow label to carry QoS requirement, as a carrier, when measuring the E2E performance of application-layer paths. And we also propose flow label as an explicit congestion notification (ECN) to inform the sender to decrease data rate with the congestion level information, in order to adjust the path state adaptively, when congestion happens. To realize the objective, a modified IPv6 Flow Label specification is presented in Fig.3.

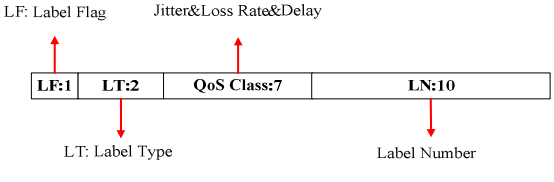

Fig. 3. The modified Flow Label format

According to the investigation of different QoS class definition of ITU-T [7], ATM [8], IntServ [9], DiffServ [10], MPLS [11], 802.1d [12] and 802.11e [12], a table of QoS requirement for different multimedia applications is obtained, shown in Table.1, which concludes the preferred bounds of Delay, Jitter and Loss Rate for current typical multimedia applications with the summation from [7][8][13]. Therefore, based on the table and due to the limited length of FL, Jitter has 2-bit, Loss Rate has 2 and Delay has 3, which represent the QoS requirement. The rest of 10-bit Label Number (LN) is randomly generated by source for flowidentification. The detailed flow label field is presented in Fig.4.

Label Flag	1	QoS Requirement – related draft
	0	No QoS Requirement - Default
Label Type	00	Probe – By source
	01	ECN – By relay or destination
	10	For future
	11	For future
QoS Class	Jitter	Three kinds – By source
	Delay	Eight kinds – By source
	Loss Rate	Four kinds – By source
Label Number	Random Generation	Flow Identification - By source

Fig. 4. The proposed Flow Label field

Table 1. QoS Requirement of Different Multimedia Applications

Applications	Delay	Jitter	Loss Rate
Conversional voice	100ms	1ms	10^{-2}~10^{-4}
Voice message(playback)	1s	1ms	10^{-2}~10^{-4}
Voice message(record)	2s	1ms	10^{-2}~10^{-4}
Video phone	150ms	130ms	10^{-4}
Video Conference	5ms	1ms	10^{-4}
High Quality streaming audio	10s	N/A	10^{-4}
Interactive Games	200ms	N/A	0

During the network measurement process, in the broadcast mode, the overlay nodes have to maintain forwarding tables, shown in Fig.5 and Fig.6, in order to record and make use of related routing state information for data transmission.

Neighbor ID X is the neighbor sequence number in the Neighbor Maintainer. In the forwarding table of relay, the combination of source address and flow label specifies one data flow uniquely.

Destination Address	Next Hop	Flow Label	
DA_1	Neighbor_ID_1	Class I	Flow Identity_1
DA_1	Neighbor_ID_2	Class I	Flow Identity_1
DA_2	Neighbor_ID_3	Class II	Flow Identity_2

Fig. 5. The proposed Flow Label field

Previous Hop	Source Address	Flow Label		Next Hop
Neighbor_ID_1	SA_1	Class I	Flow Identity_1	Neighbor_ID_2
Neighbor_ID_3	SA_1	Class I	Flow Identity_2	Neighbor_ID_4
Neighbor_ID_5	SA_2	Class I	Flow Identity_1	Neighbor_ID_6

Fig. 6. Forwarding Table in Relay

Moreover, depending on this two-tuple, ORLM is able to obtain a number of node-disjoined application-layer paths. Besides that, in the scenario of smallscale overlay network, ORLM can distinguish a unique data flow just depending on the label number, which represents the flow identity.

In this way, we could use flow label (20bit) to route data instead of the traditional IP address (128bit), which means the lookup time could be decreased by that kind of label switching mechanism, just like MPLS. In order to improve that, we conducted some simulations by OPNET Modeler Education Version.

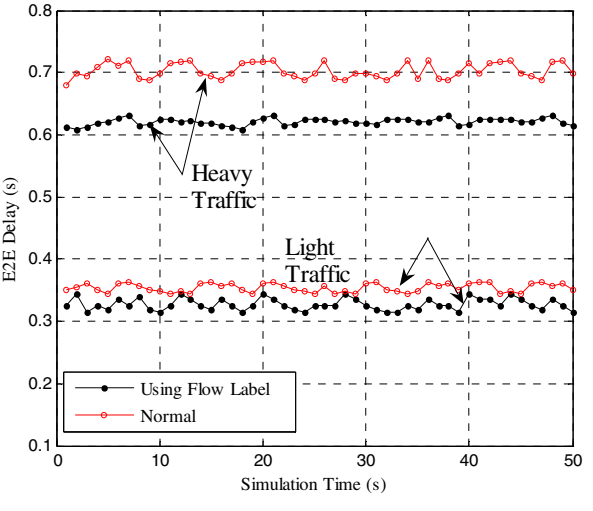

Fig. 7. Transmission Performance Using Flow Label

Fig.7 is the performance comparison between normal solution and our flow label solution. We can see that using flow label is able to decrease the E2E delay, since the lookup time could be reduced by means of flow label switching mechanism. Moreover, with the traffic becoming bigger, the performance improvement is bigger.

4 Conclusion and Future Work

As more and more applications of multimedia software are emerging and developing rapidly on the Internet, this paper proposes an overlay routing layer middleware named ORLM. Essentially, ORLM aims to provide a flexible multi-path transmission service for multimedia applications by means of application-layer transmission.

In this paper, we mainly show the general architecture of the routing middleware and our application-layer transmission mechanism that is to help make good use of available relays and a diversity of application-layer paths. Besides, the proposed flow label definition and its related usage in the overlay network scenario and the TE-awareness overlay routing design rationale are also detailed introduced.

In future work, our goal is to develop ORLM as a prototype on PlanetLab and obtain corresponding experiment results to verify the feasibility and effectiveness of ORLM on improving the transmission reliability and quality of multimedia communications.

Acknowledgments. The authors would like to thank...This paper is supported by the Fundamental Research Funds for the Central Universities (No.2009RC0501), Project 60772111 supported by National Natural Science Foundation of China, International Scientific and Technological Cooperation Program (S2010GR0902) and China 973 Programme (No. 2007CB310701).

References

1. Paxson, V.: End-to-end routing behavior in the internet. IEEE/ACM Transactions on Networking 5(5), 601–615 (1997)
2. Neil, S., Ratul, M., Thomas, A.: Quantifying the causes of path inflation. In: Proceedings of ACM SIGCOMM Conference, Karlsruhe, Germany (2003)
3. Labovitz, C., Ahuja, A., Bose, A., et al.: Delayed internet routing convergence. IEEE/ACM Transactions on Networking 9(3), 293–306 (2001)
4. Conta, A., Deering, S.: IPv6 Flow Label Specification IETF). RFC 3697, 1-9 (2004)
5. Peterson, J., Gurbani, V., Marocco, E., et al.: ALTO Working Group Charter (IETF 2009), `http://www.ietf.org/html.charters/alto-charter.html`
6. Spines. Johns Hopkins University, Baltimore (2003), `http://www.spines.org`
7. ITU-T Recommendation Y.1541
8. McDysan, D., Spohn, D.: ATM. McGraw-Hill, New York (1999)
9. Braden, R., Clark, D., Shenker, S.: Integrated Services in the Internet Architecture: an Overview. RFC 1633 (June 1994)
10. Blake, S., Black, D., Carlson, M., et al.: An Architecture for Differentiated Services. RFC 2475 (December 1998)

11. Rosen, E., Callon, R.: Multiprotocol Label Switching Architecture. RFC3031 (January 2001)
12. Park, S.Y.: Collaborative QoS Architecture between DiffServ and 802.11e Wireless LAN. In: Proc. IEEE VTC 2003-Spring, Jeju, Korea (April 2003)
13. Marchese, M.: QoS Over Heterogeneous Networks, pp. 235–246. John Wiley and Sons, Ltd, Chichester (2007)

Whisper Communication: Power Control Based Distributed Transmit Beamforming*

An Li, Li Zhang, Hui-lin Zhou, and Yu-hao Wang

Department of Electronic Information Engineering, Nanchang University,
Nanchang 330031, China
promisewind.an@gmail.com

Abstract. Distributed beamforming has been recently introduced to enable low-power long-range communication. A whisper communication employing distributed beamforming with power control to increase security is proposed. We discuss and compare several optimizing problems of the beamforming schemes at various scenarios, in order to determine the best transmission scheme obtained to minimize the transmit power under the constraint of given certain SINR set. Furthermore, we present a power and beamformer updating algorithm to implement distributed beamforming. Simulation results show that TDMA_AF outperforms other transmit fashion for single beamforming and RA_AF may be preferable for multibeamforming.

Keywords: whisper communication, distributed beamforming, power control.

1 Introduction

Covert communication is of great significance to military affairs, intelligence and national safety, which has been attached great importance to and paid close attention to all countries over the world. Especially in modern high-tech information warfare, the rapid development of military anti- reconnaissance technology has led to an increasing demand for higher confidential and secure communications. One such application is for various Quick Response Units: every solider is armed with a hand-held wireless set, and it is required to transmit the detected data over long distances without being heard by the enemy. In this scenario, directional transmitting is a preferred means to achieve spatial diversity gain, avoid interference and increase security, since more power is directed in the desired direction, less is scattered in undesired directions. Simultaneously, minimizing the transmission power while satisfying given signal-to-interference-and-noise-ratio (SINR) is also beneficial to further lower the probability of being detected, since, outside the transmission range and desired direction, the transmitted power is reduced as low as possible.

In general, this can be achieved by distributed transmit beamforming with power control. All hand-held wireless sets act collaboratively as a virtual antenna array and

* This work is supported by the National Natural Science Foundation of China (No. 60762005, 61062009), the Science and Technology Foundation of Department of Education in Jiangxi Province (No. GJJ10070, GJJ08011).

D. Zeng (Ed.): Future Intelligent Information Systems, LNEE 86, pp. 551–559.
springerlink.com © Springer-Verlag Berlin Heidelberg 2011

adjust their transmission weights to form a beam to cooperatively transmit a common signal [1]. Certainly, considering the mobile of Quick Response Unit, the implement of distributed transmit beamforming also can employ the fixed wireless sensor network (WSN) [2]. Several researchers have looked at joint beamforming and power control problem from different points of view. The works [3] presented an extended algorithm including cooperative transmission from all the base stations to each mobile in CDMA networks. In [4], the cooperative beamforming concept and power efficiency issues in fading channels have been treated. In [5], the authors discussed the optimal system design for distributed multi-beam beamforming, which goals is to maximize the minimal received SINR at destination under a maximal transmit power constraint and minimal received power constraints for unintended destinations. In [6], the optimal problem of various metrics of the received SNR is addressed by choosing different transmit powers.

In this paper, a whisper communication making use of distributed beamforming and power control to increase security is presented, in which transmission power is optimized to make the message to be right heard at destination. We analyze and compare several optimal beamforming schemes at various scenarios, which are obtained to minimize the transmit power under a given set of SINR. Furthermore, we propose a cooperative transmission algorithm to update the power and optimal beamformers. Monte Carlo simulations validate the performance of the proposed analysis and further provides helpful guidelines for determine the best transmission scheme for given certain scenarios.

2 System Model

Consider a K-member Quick Response Unit, there are K low-power single-antenna hand-held wireless sets carried by soldiers (source). Due to the mobility of source node, a WSN of low-power single-antenna nodes is terrestrially deployed for implementing cooperative beamforming. For simplicity, let us assume WSN is divided into multiple clusters, and all sources are in the cluster of interest there are a set of N sensor nodes, designated as collaborating nodes $c_1,\cdots, c_N$. All nodes are uniformly located inside a disk of radius R. A node is designated as the cluster Head (CH). At slot n, the source H_k wishes to communicate with a faraway destination D_j. The packet transmitted by H_k consists of L PSK symbols, denoted by $\mathbf{s}_k(n)$, each having the unit power. Assume that a slotted packet system is considered and the transmission of each message is split into two steps. The first step is the message sending by the source node, namely, local broadcasting; the second one is the transmission of message by all nodes, namely, cooperative beamforming. Let the channel response between H_k and c_i be denoted by $a_{ki}(n)$ and follow a iid circularly symmetric complex Gaussian random variables with zero-mean and varianceσ_a^2. The gain stays the same during the slot duration, but can change between slots. For any sufficiently faraway destination D_j, consider large scale fading (path loss and shadowing) playing the dominant role so that the complex basedband-equivalent channel gain between c_i and D_j is $b_j e^{j(2\pi/\lambda)d_{ij}}$, where b_j is the path loss,$\lambda$is the wavelength, and d_{ij} is the distance between n_i and the destination D_j.

3 Single Beam Transmission with Power Control

In this section, single beam formed at each time and all sources having a common destination D_0 is considered under our system model. We derive the mathematical formulation of the minimal transmit powers and optimal beamformers under a given SINR set on several transmission strategy.

A. TDMA_DF

If a time-division multiple-access (TDMA) scheme and *decode-and-forward* (DF) scheme were to be employed, each source node transmits their signals one by one. Thus, when H_m transmits, the received signal at c_i is

$$\mathbf{x}_i(n) = a_{mi}\sqrt{P_{m0}}\mathbf{s}_m(n) + \boldsymbol{\mu}_i(n), \quad 1 \le i \le N, i \ne m, \tag{1}$$

where P_{m0} is the transmit power of source H_m, which is chosen so that N collaborating nodes can correctly decode the transmitted symbol. $\boldsymbol{\mu}_i(n) \sim \mathcal{CN}(\mathbf{0}, \sigma_\mu^2 \mathbf{I}_L)$ denotes the AWGN at c_i, where $\mathbf{I}_L$ is an $L*L$ identity matrix. Then in slot $n+m$, $m=1,2,\cdots, N$, to beamforming signal $\mathbf{s}_m(n)$, N cooperative nodes collaborating transmit a weighted version of signal $\mathbf{s}_m(n)$, i.e. $\bar{\mathbf{x}}_i(n+m) = \mathbf{s}_m(n)\omega_i^m(n) \quad 0 \le i \le N$, where ω_i^m is the weight of c_i when beamforming s_m. So the signal received at location D_0 in slot $n+m$ is

$$\mathbf{y}(n+m) = \sum_{i=1}^{K} \sqrt{P_m} b_i \mathbf{s}_i(n)\omega_i^m(n) + \mathbf{v}(n+m), \tag{2}$$

where P_m is the transmit power of c_i when cooperative beamforming. Without loss of generality, we assume that the transmit power budgets for each node are the same. $\boldsymbol{v}(n+m)$ is the noise at destination D_0, which is assumed to be iid as a zero-mean complex white Gaussian random variable with variance $\sigma_v^2 \mathbf{I}_L$.

Denote $\boldsymbol{\omega}^m(n) = [\omega_1^m(n), \cdots, \omega_N^m(n)]^{\mathrm{H}}$, $\mathbf{b} = [b_0 e^{j(2\pi/\lambda)d_{10}}, \cdots, b_0 e^{j(2\pi/\lambda)d_{N0}}]^{\mathrm{T}}$, then $\mathbf{y}(n+m)$ can be written as

$$\mathbf{y}(n+m) = \sqrt{P_m}\boldsymbol{\omega}_m^{\mathrm{H}}\mathbf{b}\mathbf{s}_m(n) + \mathbf{v}(n+m). \tag{3}$$

For the given vectors $\mathbf{b}$, the receive SINR at destination D_0 can be expressed as

$$\gamma_m = \frac{P_m(\boldsymbol{\omega}^m)^{\mathrm{H}}\mathbf{b}\mathbf{b}^H\boldsymbol{\omega}^m}{\sigma_v^2}. \tag{4}$$

Under a given target SINR set $\{\gamma_m^*, 1 \le m \le \mathrm{K}\}$, the single destination whisper communication problem is to find the optimal beamforming matrix to minimize the transmit power of the collaborating nodes.

$$\text{(C1)} \quad \begin{array}{l} C(\boldsymbol{\omega}^*) = \min\limits_{\boldsymbol{\omega}} \max\limits_{1 \le m \le K} P_m(\gamma_m, \boldsymbol{\omega}) \\ \text{subject to} \left\{\gamma_m(\mathbf{P}, \boldsymbol{\omega}) = \gamma_m^*\right\} \cup \left\{(\boldsymbol{\omega}^m)^{\mathrm{H}}\boldsymbol{\omega}^m = 1\right\} \end{array}. \tag{5}$$

Substituting the constraint into the objective function in Eq. (5), the optimization problem of Eq. (5) can be rewritten as

$$C\left(\boldsymbol{\omega}^*\right)=\min_{\boldsymbol{\omega}}\max_{1\le m\le K}\frac{\gamma_m^*\sigma_v^2(\boldsymbol{\omega}^m)^{\mathrm{H}}\boldsymbol{\omega}_m}{(\boldsymbol{\omega}^m)^{\mathrm{H}}\mathbf{b}\mathbf{b}^{\mathrm{H}}\boldsymbol{\omega}_m}\ . \tag{6}$$

Taking the derivative of $P_m(\gamma_m^*,\boldsymbol{\omega}^m)$ in Eq. (6) with respect to$\boldsymbol{\omega}$and setting it to be zeros, we obtain the optimal weights that minimize the transmit power and the corresponding transmit power are

$$\begin{aligned}\boldsymbol{\omega}^m&=\beta\mathbf{b}\\ \beta&=\sqrt{1/\left(\mathbf{b}^{\mathrm{H}}\mathbf{b}\right)}\ .\end{aligned} \tag{7}$$

$$P_m=\gamma_m^*\sigma_v^2/\left(\mathbf{b}^{\mathrm{H}}\mathbf{b}\right). \tag{8}$$

B. TDMA_AF

If each cooperative node does not attempt to decode but directly forward the received symbol one by one (namely *amplify-and-forward* (AF)), then the received signal at c_i of Eq. (1) is first normalized by$\xi_i=(\mathrm{E}\{|\mathbf{x}_i(n)|^2\})^{1/2}$, that is,

$$\mathbf{x}_i(n)=\frac{a_{mi}\sqrt{P_{m0}}\mathbf{s}_m(n)}{\sqrt{|a_{mi}|^2P_{m0}+\sigma_\mu^2}}+\frac{1}{\sqrt{|a_{mi}|^2P_{m0}+\sigma_\mu^2}}\boldsymbol{\mu}_i(n)\quad 1\le i\le N, i\ne m\ . \tag{9}$$

Then in slot $n+m$, m=1,2, ⋯, N, each node transmits the signal $\mathbf{x}_i(n+m)=\omega_i^m(n)\mathbf{x}_i(n)$ to beamforming $\mathbf{s}_m(n)$, where $\mathbf{x}_m(\mathrm{n})=\mathbf{s}_m(n)$. Thus, the received signal at destination D_0 in slot $n+m$ is

$$\mathbf{y}(n+m)=\sum_{i=1}^{K}\sqrt{P_m}b_i\omega_i^m(n)\mathbf{x}_i(n)+\mathbf{v}(n+m)\ . \tag{10}$$

Denote$\boldsymbol{\omega}^m(n)$= $[\omega_1^m(n),\cdots,\ \omega_N^m(n)]^{\mathrm{H}}$, $\mathbf{h}^m=[b_0P_{m0}^{1/2}\ a_{m1}e^{j(2\pi/\lambda)d_{10}}/\xi_1,\ \cdots,\ b_0P_{m0}^{1/2}\ a_{mN}e^{j(2\pi/\lambda)d_{N0}}/\xi_N]^{\mathrm{H}}$, $\mathbf{u}(n)=[b_0e^{j(2\pi/\lambda)d_{10}}\mathbf{u}_1(n)/\ \xi_1;\ \cdots;\ b_0e^{j(2\pi/\lambda)d_{N0}}\mathbf{u}_N(n)/\xi_N]$. Then $\mathbf{y}(n+m)$ can be written as

$$\mathbf{y}\left(n+m\right)=\sqrt{P_m}(\boldsymbol{\omega}^m)^{\mathrm{H}}\mathbf{h}\mathbf{s}_m\left(n\right)+\sqrt{P_m}(\boldsymbol{\omega}^m)^{\mathrm{H}}\boldsymbol{\mu}(n)+\mathbf{v}(n+m)\ . \tag{11}$$

Further define matrices $\mathbf{R}^m=\mathbf{h}^m(\mathbf{h}^m)^{\mathrm{H}}$, $\mathbf{Q}$=diag{[$|b_0|^2\sigma_\mu^2/\xi_1^2$, ⋯, $|b_0|^2\sigma_\mu^2/\xi_N^2$]}. For the given vectors $\mathbf{h}$, the received SINR at destination D_0 can be expressed as

$$\gamma_m=\frac{P_m(\boldsymbol{\omega}^m)^{\mathrm{H}}\mathbf{R}^m\boldsymbol{\omega}^m}{P_m(\boldsymbol{\omega}^m)^{\mathrm{H}}\mathbf{Q}\boldsymbol{\omega}^m+\sigma_v^2}\ . \tag{12}$$

The problem of single destination whisper communication of minimizing the transmit power P_m given target SINR set $\{\gamma_m^*,\ 1\le m\le\mathrm{K}\}$ can be formulated as

$$\text{(C2)}\quad C\left(\boldsymbol{\omega}^*\right)=\min_{\boldsymbol{\omega}}\max_{1\le m\le K}\frac{\gamma_m^*\sigma_v^2(\boldsymbol{\omega}^m)^{\mathrm{H}}\boldsymbol{\omega}^m}{(\boldsymbol{\omega}^m)^{\mathrm{H}}\left(\mathbf{R}^m-\gamma_m^*\mathbf{Q}\right)\boldsymbol{\omega}^m}\ , \tag{13}$$

which is an eigenvalue problem [7]. The minimum of P_m is in inverse proportion to the maximum eigenvalue of the symmetric matrix ($\mathbf{R}^m$-$\gamma_m^*\mathbf{Q}$)**,** and the corresponding eigenvector is the optimal weight-coefficient vector $\boldsymbol{\omega}^m$.

C. RA_AF

In this subsection, consider the broadcast nature of wireless channel, in slot n, all sources simultaneously transmit their packets to make the cooperative nodes share the information in a *random access* (RA) fashion, the received signal at node c_i is

$$\mathbf{x}_i(n) = \sum_{k=1}^{K} a_{ki}\sqrt{P_{k0}}\mathbf{s}_k(n) + \boldsymbol{\mu}_i(n), \quad 1 \le i \le N . \tag{14}$$

Then in slot $n+m$, m=1,2, ⋯, K, each node c_i employs AF schemes and transmits the signal $\bar{\mathbf{x}}_i(n+m) = \mathbf{x}_i(n)\omega_i^m(n)$, so the signal received at location D_0 in slot $n+m$ is

$$\mathbf{y}(n+m) = \sum_{i=1}^{N} b_i \mathbf{x}_i(n)\omega_i^m(n) + \mathbf{v}(n+m) . \tag{15}$$

Using vector notation $\mathbf{y}(n+m)$ can be written as

$$\mathbf{y}(n+m) = (\boldsymbol{\omega}^m)^{\mathrm{H}}\mathbf{h}_m\mathbf{s}_m(n) + \sum_{k=1,k\neq m}^{K} (\boldsymbol{\omega}^m)^{\mathrm{H}}\mathbf{h}_k\mathbf{s}_k(n) + (\boldsymbol{\omega}^m)^{\mathrm{H}}\boldsymbol{\mu}(n) + \mathbf{v}(n+m), \tag{16}$$

where $\mathbf{h}^m=[b_0P_{m0}^{1/2}\ a_{m1}e^{j(2\pi/\lambda)d_{10}},\cdots,\ b_0P_{m0}^{1/2}\ a_{mN}\ e^{j(2\pi/\lambda)d_{N0}}]^{\mathrm{H}}$, $\mathbf{u}(n)=[b_0e^{j(2\pi/\lambda)d_{10}}\mathbf{u}_1(n);\ \ldots;\ b_0e^{j(2\pi/\lambda)d_{N0}}\mathbf{u}_N(n)]$. Redefine $\mathbf{Q}^m=\sum_{k=1,k\neq m}^{K}\mathbf{h}^k(\mathbf{h}^k)^{\mathrm{H}} + b_0^2\sigma_\mu^2\mathbf{I}_N$, $\mathbf{O} = diag\{\sum_{k=1}^{K}P_{k0}|a_{k1}|^2 \cdots, \sum_{k=1}^{K}P_{k0}|a_{kN}|^2 + \sigma_\mu^2\}$. For the given vectors $\mathbf{h}^m$, m=1, 2, ⋯,K, the received SINR at destination D_0 can be expressed as

$$\gamma_m = \frac{(\boldsymbol{\omega}^m)^{\mathrm{H}}\mathbf{R}^m\boldsymbol{\omega}^m}{(\boldsymbol{\omega}^m)^{\mathrm{H}}\mathbf{Q}^m\boldsymbol{\omega}^m + \sigma_v^2} . \tag{17}$$

Under a given target SINR set $\{\gamma_m^*,\ 1\le m\le K\}$, the single destination whisper communication problem is to find the optimal beamforming matrix to minimize the transmit power of the collaborating nodes.

$$\text{(C3)}\quad \begin{array}{l} C(\boldsymbol{\omega}^*) = \min\limits_{\boldsymbol{\omega}} \max\limits_{1\le m\le K} P_m(\gamma_m, \boldsymbol{\omega}) \\ \text{subject to}\ \{\gamma_m(\mathbf{P},\boldsymbol{\omega}) = \gamma_m^*\} \cup \{(\boldsymbol{\omega}^m)^{\mathrm{H}}\mathbf{O}\boldsymbol{\omega}^m = P_m\} \end{array} . \tag{18}$$

Substituting the constraint into the objective function in Eq. (18), the optimization problem of Eq. (18) can be rewritten as

$$C(\boldsymbol{\omega}^*) = \min_{\boldsymbol{\omega}} \max_{1\le m\le K} \frac{\gamma_m^*\sigma_v^2(\boldsymbol{\omega}^m)^{\mathrm{H}}\mathbf{O}\boldsymbol{\omega}^m}{(\boldsymbol{\omega}^m)^{\mathrm{H}}(\mathbf{R}^m - \gamma_m^*\mathbf{Q}^m)\boldsymbol{\omega}^m} . \tag{19}$$

Taking the derivative of $P_m(\gamma_m^*,\boldsymbol{\omega}_m)$ in Eq. (19) with respect to$\boldsymbol{\omega}$and setting it to be zeros, we obtain

$$\mathbf{O}^{-1}(\mathbf{R}^m - \gamma_m^*\mathbf{Q}^m)\boldsymbol{\omega}^m = \frac{\gamma_m^*\sigma_v^2}{P_m}\boldsymbol{\omega}^m , \tag{20}$$

which is a generalized eigenvalue problem. The minimum of P_m is the scaled maximum eigenvalue of the symmetric matrix $\mathbf{O}^{-1}(\mathbf{R}^m-\gamma_m^*\mathbf{Q}^m)$, and the corresponding eigenvector is the optimal weight-coefficient vector$\boldsymbol{\omega}^m$, which are not difficult to be solved by some of the most widely numerical methods, the QZ algorithm and the C-RISE algorithm as well as Krylov subspace methods.

If first normalizing signal of Eq. (14) by$\xi_i=(\mathrm{E}\{|\mathbf{x}_i(n)|^2\})^{1/2}$, the problem of single destination whisper communication can be formulated as Eq. (13), which solution is a simple eigenvalue problem, just the matrix $\mathbf{Q}$ is replaced by a new matrix $\mathbf{Q}^m$, denoted by $\mathbf{Q}^m=\sum_{\substack{k=1\\k\neq m}}^{K}\mathbf{h}^k(\mathbf{h}^k)^{\mathrm{H}}+b_0^2\sigma_\mu^2\mathbf{I}_N$.

4 Multiple Simultaneous Beams Transmit with Power Control

In this section, we discuss the scenario of different source packets having distinct destination. From Eq. (2) and Eq. (9), we can see that when employing TDMA multiple beams just can be formed in K time slot. In one slot, no inter-beam interference occurs, but from Eq. (14), we know that for the RA_AF fashion, multiple beams can be formed in one slot, each beam formed on one direction. In this paper, we consider a suboptimal weight design for minimizing the transmit power to completely null out the inter-beam.

To form K beams, Eq. (14) should be rewritten as

$$\bar{\mathbf{x}}_i(n+1)=\sum_{m=1}^{K}\mathbf{x}_i(n)\omega_i^m(n)\quad 1\le i\le N\,, \tag{21}$$

which means for different beam, the optimal weights are the same, so denote $\boldsymbol{\omega}(n)=[\omega_1(n),\cdots,\ \omega_N(n)]^{\mathrm{H}}$, $\mathbf{h}_i^m=[b_iP_{m0}^{1/2}a_1^m e^{j(2\pi/\lambda)d_{1i}},\ \cdots,\ b_iP_{m0}^{1/2}a_N^m e^{j(2\pi/\lambda)d_{Ni}}]^{\mathrm{H}}$, $\mathbf{U}_m(n)=[b_me^{j(2\pi/\lambda)d_{1m}}\mathbf{u}_1(n);\ \cdots;\ b_me^{j(2\pi/\lambda)d_{Nm}}\mathbf{u}_N(n)]$, then $\mathbf{y}(m;n+1)$ can be rewritten as

$$\mathbf{y}(m;n+1)=\boldsymbol{\omega}^{\mathrm{H}}\mathbf{h}_m^m\mathbf{s}_m(n)+\sum_{k=1,k\neq m}^{K}\boldsymbol{\omega}^{\mathrm{H}}\mathbf{h}_k^m\mathbf{s}_k(n)+\boldsymbol{\omega}^{\mathrm{H}}\mathbf{U}_m(n)+\mathbf{v}(m;n+1)\,. \tag{22}$$

Similarly as single beam transmission, the received SINR at destination D_m can be expressed as

$$\gamma_m=\frac{\boldsymbol{\omega}^{\mathrm{H}}\mathbf{R}_m^m\boldsymbol{\omega}}{\boldsymbol{\omega}^{\mathrm{H}}\mathbf{Q}_m^m\boldsymbol{\omega}+\sigma_v^2}\,, \tag{23}$$

where $\mathbf{R}_m^m=\mathbf{h}_m^m(\mathbf{h}_m^m)^{\mathrm{H}}$, $\mathbf{Q}_m^m=\sum_{\substack{k=1\\k\neq m}}^{K}\mathbf{h}_k^m(\mathbf{h}_k^m)^{\mathrm{H}}+b_m^2\sigma_\mu^2\mathbf{I}_N$. Given target SINR set $\{\gamma_m^*,\ 1\le m\le K\}$, the multiple destination whisper communication problem is to find the optimal beamforming matrix to minimize the transmit power of the collaborating nodes and minimize the inter-beam interference.

$$C\left(\boldsymbol{\omega}^*\right) = \min_{\boldsymbol{\omega}} \max_{1\le m\le K} P_m\left(\gamma_m, \boldsymbol{\omega}\right)$$

$$\text{(C4)} \quad \text{subject to} \begin{cases} \gamma_m\left(\mathbf{P}, \boldsymbol{\omega}\right) = \gamma_m^* \\ \boldsymbol{\omega}^{\mathrm{H}}\mathbf{O}\boldsymbol{\omega} = P_m \\ \boldsymbol{\omega}^{\mathrm{H}}\mathbf{h}_i^m (h_i^m)^{\mathrm{H}}\boldsymbol{\omega} \le P_{\min},\ i \ne m \end{cases} . \tag{24}$$

where $P_{\min}$ is the assigned minimize interference power. In this paper, we assume the interference could be completely nulled out, i.e., $\boldsymbol{\omega}^{\mathrm{H}}\ \mathbf{h}_i^m = 0$, $i \neq m$. Substituting the constraint into the objective function in Eq. (24), the optimization problem (C4) can be formulated as

$$C\left(\boldsymbol{\omega}^*\right) = \min_{\boldsymbol{\omega}} \frac{\gamma_m^* \sigma_v^2 \boldsymbol{\omega}^{\mathrm{H}}\mathbf{O}\boldsymbol{\omega}}{\boldsymbol{\omega}^{\mathrm{H}}\left(\mathbf{R}_m^m - \gamma_m^* \sigma_\mu^2 \mathbf{I}_N\right)\boldsymbol{\omega}} . \tag{25}$$

The solution of this Rayleigh quotient problem is can be solved as Eq.(20). We can obtain the minimum of P_m is the scaled maximum eigenvalue of the symmetric matrix $\mathbf{O}^{-1}(\mathbf{R}_m^m - \gamma_m^* \sigma_\mu^2 \mathbf{I}_N)$, and the corresponding eigenvector is the optimal beam vector $\boldsymbol{\omega}$.

5 Cooperative Transmission Algorithm

From Eq. (9), (13), (20), and Eq.(24), we can see that the global CSI (i.e. a_{ki}, b_j, and d_{ij}) is needed for the calculation of optimal beamformer and transmit power. We assume the global CSI is available, but considering the periodic change of environment, optimal beamformer and transmit power are involved in the updating process. The following are a simple one-bit feedback closed-loop updating algortihm.

1. An initial value for the optimal beamformer $\boldsymbol{\omega}^{(0)}$ and transmit power $P^{(0)}$ is chosen given certain $\gamma^{(0)}$.
2. When the global CSI is reestimated, calculatingγ* using Eq. (4), (12), or (23). If $|\gamma^* - \gamma^{(0)}|$ is smaller than a predefined threshold, then stop and wait for a period.
3. When γ is updated, calculating $\boldsymbol{\omega}^{(*)}$, $P^{(*)}$ using Eq. (7), (8), (13), (20) or Eq.(25).
4. Waiting for a period, go to step (2).

6 Simulations

In all experiments, we share the following common parameters. SINR budgets for all destinations are the same. The noise power $\sigma_\mu^2 = \sigma_v^2 = -50$dBm. All channel responses are simulated based on the assumptions given in our system model, and assumed to be perfectly estimated. We ran each case with 100 independent Monte Carlo runs.

NOR_RA_AF denotes the fashion of first normalizing signal of Eq. (14). DT denotes the fashion of direction transmit without any weights. The transmit power can be expressed as $P_m = \gamma_m^* \sigma_v^2 / b_0^2$, which is independent of K and N.

Fig. 1 shows the average minimal transmit power versus path loss, where we fix the number of source at K=4, and number of cooperative nodes at N=10. As observed,

for single beamforming, TDMA_AF outperforms other transmit fashion, while the performance of DT is the worse. Performance of RA_AF and NOR_RA_AF is almost identical, but RA_AF outperforms NOR_RA_AF in multibeamforming case. The average minimal transmit power versus number of cooperative nodes is shown in Fig. 2, where the path loss b_0 is -30dB and number of sources is also chosen at K=4. As expected, the increasing of N improves the performance of TDMA_DF, TDMA_AF, RA_AF, and NOR_RA_AF, but does not affect DT.

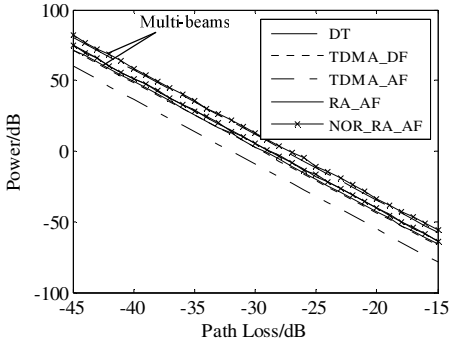

Fig. 1. Transmit Power vs. Path Loss

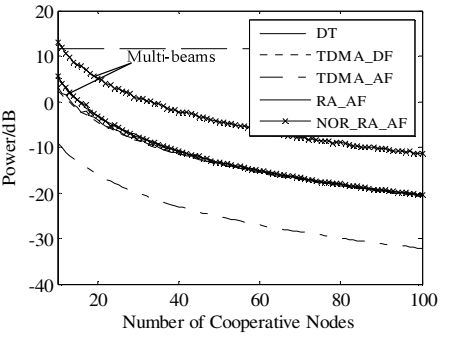

Fig. 2. Power vs. Number of Cooperative Nodes

Fig. 3 shows the average minimal transmit power versus number of sources at N=10, b_0=-30dB. It can be seen from Figure 3 that performance of RA_AF and NOR_RA_AF significantly degrades when number of sources is large as K increases, more power would be allocated to multi-user interferences. In addition, the increasing of K does almost not affect NOR_RA_AF for multibeamforming. Fig. 4 shows the average minimum transmit power versus given SNR/SINR set. As expected, larger SNR/SINR is given, more transmit power is needed as there exist noise and interference in wireless channel.

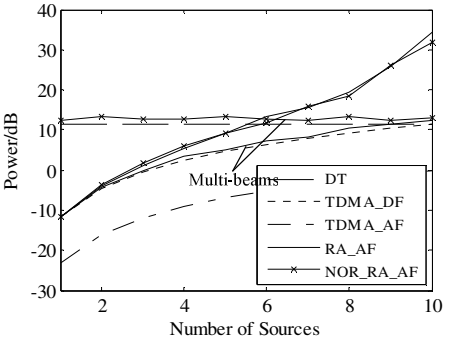

Fig. 3. Transmit Power vs. Number of Sources

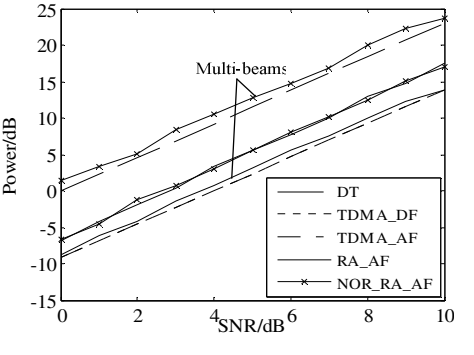

Fig. 4. Transmit Power vs. Given SNR

7 Conclusion

We have analyzed the problem of both single-beam whisper communication case, in which multiple sources communicate with a common destination, and multi-beam whisper communication, in which multiple sources transmit to different destinations. We analyze and compare several optimal weight designs for single-beam whisper communication to minimize transmit power given certain SINR set at various scenarios. Then we developed the joint power control and minimal inter-beam interference algorithm to solve the multi-beam whisper communication problem. Furthermore, we proposed a power and optimal beamformers updating algorithm. Simulation results are provided to verify the performances of the proposed algorithms.

References

1. Ochiai, H., Mitran, P., Poor, H.V., Tarokh, V.: Collaborative beamforming for distributed wireless Ad Hoc sensor networks. IEEE Trans. Signal Processing 53(11), 4110–4124 (2005)
2. Ahmed, M.F.A., Vorobyov, S.A.: Performance characteristics of collaborative beamforming for wireless sensor networks with Gaussian distributed sensor nodes. In: ICASSP 2008, pp. 3249–3252. IEEE Press, New York (2008)
3. Gema, P., Carmen, B.: Cooperative transmission for wireless networks using power control and beamforming. In: EUSIPCO 2004, pp. 177–180. Academic Press, Salt Lake City (2004)
4. Madan, R., Mehta, N.B.: Energy-efficient cooperative relaying over fading channels with simple relay selection. In: Globecom 2006, pp. 1–6. IEEE Press, New York (2008)
5. Li, C., Wang, X.: Cooperative multibeamforming in Ad Hoc networks. EURASIP Journal on Advances in Signal Processing, 1–11 (2008)
6. Betz, S.M., Vicent Poor, H., Petropulu, A.P.: Cooperative Beamforming and Power Control. In: ACSSC 2007, pp. 2117–2123. IEEE Press, New York (2007)
7. Hasu, V.: Eigenvalue Approach to Joint Power Control and Beamforming for CDMA Systems. In: ISSSTA 2002, pp. 561–565. IEEE Press, New York (2002)

A High-Accuracy Current Sensing Circuit with Clamping Current Compensation for Current-Mode DC-DC Buck Converter

Miao Yang, Weifeng Sun, Shen Xu, Mu Li, and Shengli Lu

National ASIC System Engineering Research Center, Southeast University, Nanjing 210096, China
yangmiao8623@163.com

Abstract. In this paper, a detailed analysis method of eliminating clamping current error is first proposed. A high accuracy on chip current sensing circuit with clamping current compensation technique for current-mode DC-DC buck converter is presented. When the aspect ratios of the switch transistor and the sensing transistor meet certain proportion, the clamping current error can be eliminated. At the same time, the current sensing circuit has no operation amplifier so that it wouldn't reduce the power efficiency. The simulated results show that the accuracy of proposed current censing circuit is higher than 94% and up to 99.7% for load current from 50mA to 500mA.

Keywords: Current sensing Clamping current Series transistors Accuracy.

1 Introduction

In recent years, switching power supply has widely applied in portable electronic systems' market by its high efficiency, stability and dynamic characteristics. Portable systems require high-efficiency low-voltage supply from a single battery source for maximizing the system run time. Buck (step-down) converters become the first choice in portable systems. Both voltage-mode and current-mode controls are widely used in buck converter designs. The voltage mode buck converter is easy to design, but has slower transient response. Especially, current-mode control shows additional advantages of automatic over-current protection, better closed-loop stability and faster dynamic responses.

A simplified structure of current-mode buck converter is illustrated in Fig. 1. The current-mode buck converter contains two loops: an inner current loop and an outer voltage loop, which can provide much better closed-loop stability and faster dynamic responses compared with the voltage-mode buck converter. However, there are many difficulties and problems on circuit realization of current-sensing module and slope compensation module, especially the high current sensing circuit's accuracy design. Many different current-sensing circuits have been developed and implemented to sense the inductor current. A simple method for sensing the output current is that uses an external resistor in series with the inductor or power transistor [1]. But this

D. Zeng (Ed.): Future Intelligent Information Systems, LNEE 86, pp. 561–568.
springerlink.com © Springer-Verlag Berlin Heidelberg 2011

approach not only reduces power efficiency but also requires an off-chip resistor, which will increase the size of the power module. This way is not suitable to design high integrated or efficiency switching power converter. Based on an American patent in 1998 [2], nearly a decade the mainstream current sensing techniques have adopted similar structure from the patent. There are two derivational structures in emergent papers: one uses operational amplifier to clamp the voltage of VA and VB and make them equal [3-6]; the other employs current mirror make the voltage of VA and VB equal [7-9]. Both of these schematics neglect the affection of the clamping current I_{clamp}, which will introduce a term in the current sensing expression and result in inaccurate sensing current.

In this paper, technique to compensate the error by the clamping current I_{clamp} is successfully developed and thoroughly discussed. The purpose of this paper is to provide a method of eliminating clamping current. The clamping current error can be eliminated when the aspect ratios of the switch transistor and the sensing transistor meet certain proportion. The second section first introduces the proposed design and its advantages. Then results and discussions are shown in the third section. Finally, the fourth section gives the conclusion.

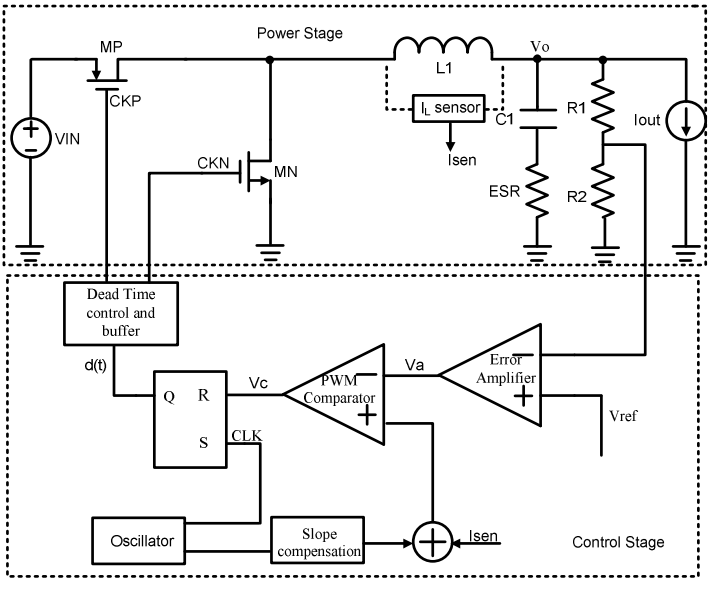

Fig. 1. Simplified current-mode buck converter block diagram

2 Proposed On-chip Current-Sensing Circuit

The appropriate aspect ratio of the transistor MSW and several series MOSFET are used to solve the problem of clamping current error in the proposed current sensing circuit, which can be seen in Fig.2. The principle of operation will be described in detail as follows.

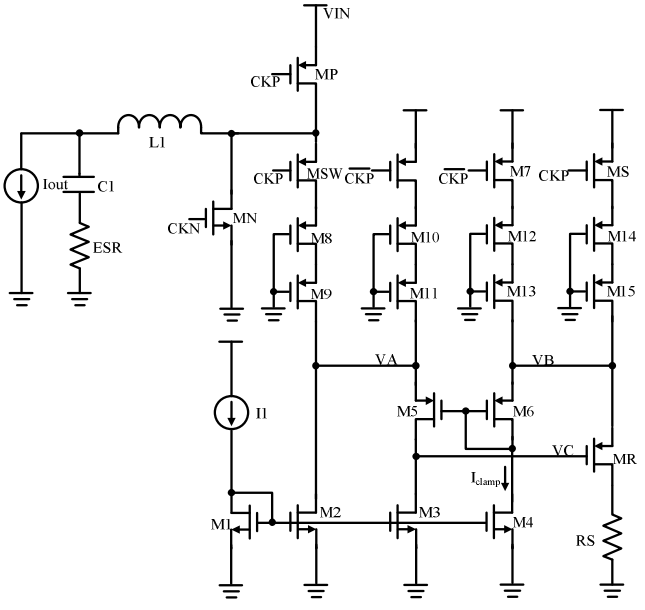

Fig. 2. Proposed current sensing circuit

Since the power PMOS MP is operated in the triode region, the drain current can be obtained as:

$$I_P = \frac{1}{2}\mu_P C_{ox}\frac{W_{MP}}{L_{MP}}(2(V_{SG}-|V_{TP}|)V_{SD\_MP}-V_{SD\_MP}^2) \tag{1}$$

Where u_p, C_{ox}, W_{MP}, L_{MP}, V_{SG}, V_{TP}, and V_{SD_MP} stand for effective channel mobility, gate oxide capacitance per unit area, channel width and length of MP transistor, source-gate voltage, threshold voltage, and source-drain voltage, respectively. The source-gate voltage and threshold voltage of the power PMOS MP are equal to that of the sensing PMOS MS. Since the sensing PMOS MS is also operated in the triode region, the actual sensing current can be obtained as:

$$I_{sense} = \frac{1}{2}\mu_P C_{ox}\frac{W_{MS}}{L_{MS}}(2(V_{SG}-|V_{TP}|)V_{SD\_MS}-V_{SD\_MS}^2)-I_{clamp} \tag{2}$$

where W_{MS}, L_{MS}, V_{SD_MS} stand for channel width and length of MS transistor, source-drain voltage of MS transistor, respectively. If the relationship of the aspect ratio between the sensing PMOS MS and the power PMOS MP is designed as 1:K. In order to make the sensing current proportional copy the inductor current precisely. The relationship between the actual sensing current and the drain of the power PMOS MP should be as follows:

$$K = \frac{I_P}{I_{MS}} = \frac{\frac{W_{MP}}{L_{MP}}}{\frac{W_{MS}}{L_{MS}}} \tag{3}$$

Therefore, a necessary and sufficient condition of Eq.(3) is that:

$$\frac{(2(V_{SG} - |V_{TP}|)V_{SD\_MP} - V_{SD\_MP}^2)}{(2(V_{SG} - |V_{TP}|)V_{SD\_MS} - V_{SD\_MS}^2) - \frac{I_{clamp}}{\frac{1}{2}\mu_p C_{ox}\frac{W_{MS}}{L_{MS}}}} = 1 \tag{4}$$

Neglecting the highest order term of Eq.(4), the drain current of MP becomes

$$V_{SD\_MP} = V_{SD\_MS} - \frac{I_{clamp}}{\mu_p C_{ox}(V_{SG} - |V_{TP}|)\frac{W_{MS}}{L_{MS}}} \tag{5}$$

The transistors of M3, M4, M5 and M6 compose a current mirror. The current mirror and the feedback transistor MR make the potential of VA equal to the potential of VB. Besides, M2, M3 and M4 have equivalent aspect ratios. Therefore, the drain current of M2 and M3 are equal to the clamping current Iclamp. Then Eq.(6) becomes:

$$\frac{2I_{clamp}}{\mu_p C_{ox}(V_{SG} - |V_{TP}|)_{MSW}\frac{W_{MSW}}{L_{MSW}}} = \frac{I_{clamp}}{\mu_p C_{ox}(V_{SG} - |V_{TP}|)\frac{W_{MS}}{L_{MS}}} \tag{6}$$

The source of the switch MSW is connected to the drain of the power MOS MP, not the power VIN. The source-gate voltage of the switch MSW is less than the source-gate voltage of the sensing transistor MS. When the aspect ratios of the switch MSW is adopted less than and close to two times of the aspect ratios of the sensing transistor MS, the clamping current error can be eliminated.

From Fig.4, when the clock signal CKP is low, the transistor MS is on. The MOS MS, M14 and M15 compose a pair of composite transistors. The series association of three transistors has a transconductance-to-output conductance ratio as high as that of a long-channel transistor but a shorter “physical channel length.” Hence, the composite transistors have a cutoff frequency higher than the cutoff frequency of its dc equivalent long-channel transistor [10]. The other advantage is that the equivalent gate length of the sensing transistor MS and the switch MSW get triple length of signal transistor. The match of the two transistors will become better, so the sensing error by clamping current can be eliminated better.

3 Simulation Results and Discussion

We use the SMIC 0.13um 1P8M 3.3V CMOS process to design and simulate the proposed on chip current sensing circuit for the current-mode control DC-DC buck converter.

The buck converter operates at 2MHz switching frequency, which provides maximum load current 500mA and adjustable output voltage from 1V to 1.8V. The peak efficiency of the converter is up to 96%. The proposed current sensing circuit can sense the load current from 50mA to 500mA very precisely. The formula of calculating sensing accuracy can be represented as:

$$accuracy = 1 - \frac{\left| \frac{(W/L)_P}{(W/L)_{MS}} \cdot I_{CS} - I_P \right|}{I_P} \tag{7}$$

Fig.3 shows that the accuracy of the proposed sensing circuit for inductor peak current from 50 to 600mA at VIN=3.3V. From the result, we can know that this sensing circuit has a wide current sensing range with high accuracy. The minimum accuracy and the maximal accuracy are 94.8% and 99.7% for load current from 50mA from 500mA, respectively. The accuracy of the proposed sensing circuit for power VIN is from 2.7 to 3.5V at load current of 200mA, which can be seen in Fig.4. Fig.5 shows that the accuracy of the proposed sensing circuit for temperature from -20 to 80 ℃ at VIN=3.3V and load current of 200mA. The accuracy is always above 96% when power supply varies from 2.7V to 3.5V. The accuracy variation of the proposed current sensing circuit is only 0.35% for temperature from -20 to 80℃. The two figures have proved that the proposed sensing circuit is insensitive to the power supply and temperature. Fig.6 shows the simulated power-conversion efficiency at VIN=3.3V and output voltage Vo=1.6V with different load currents. From the results, the efficiency is always high than 93.5% and the peak efficiency is close to 96%. This proves the effectiveness of the designs of the other analog and digital building blocks, as well as the proposed current-sensing circuit. Comparisons and results with previous papers are summarized in Table 1. The proposed circuit has the highest sensing accuracy and the widest sensing range. Besides, the power conversion efficiency is the highest. Fig.7 shows the layout of the current mode buck converter with the current sensing circuit. The whole chip size is 1.65 mm^2 and the proposed current sensing circuit size is only 0.002 mm^2. Now the chip is being fabricated in SMIC.

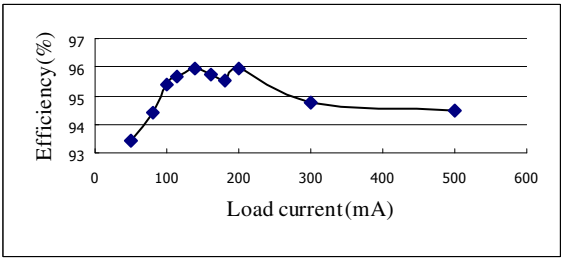

Fig. 3. The accuracy of the proposed sensing circuit for load current from 50 to 500mA

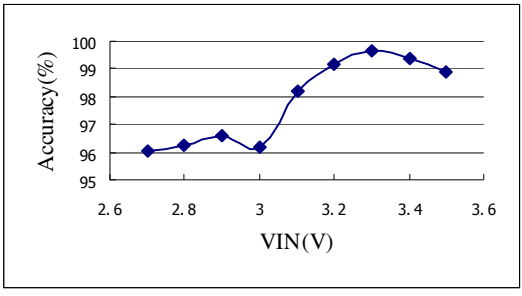

Fig. 4. The accuracy of the proposed sensing circuit for power supply from 2.7 to 3.5V

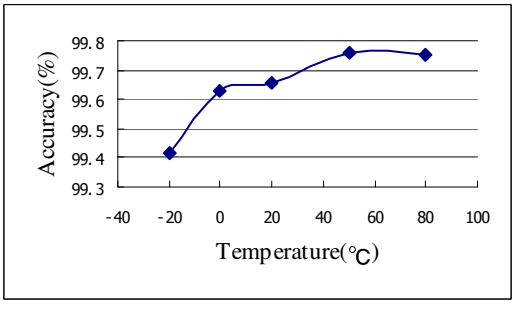

Fig. 5. The accuracy of the proposed sensing circuit for temperature from -20 to 80℃

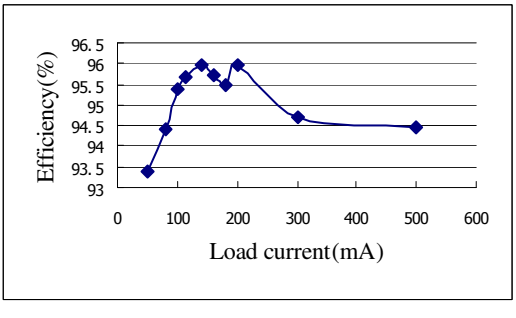

Fig. 6. Simulated conversion efficiency of the buck converter

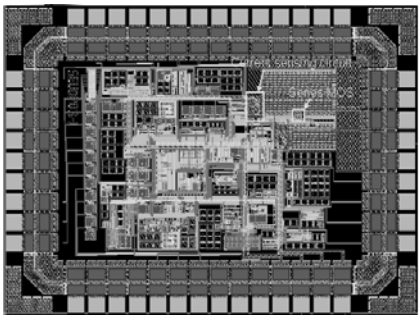

Fig. 7. The layout of whole buck converter chip

Table 1. Comparison of the current-sensing circuits for current-mode control DC-DC buck converter

paper	[4]	[5]	[7]	[8]	[9]	This work
Year	2005	2004	2005	2008	2007	2010
frequency(MHz)	0.5	1	0.5	1.4	2.5	2
Maximum accuracy	99%	N/A	98.2%	99%	97%	99.7%
Maximum power efficiency	89%	89.5%	N/A	91.2%	N/A	96%
Range of sensing current (mA)	50-120	50-450	N/A	50-500	N/A	50-500
process	0.6um	0.6um	0.35um	0.18um	0.35um	0.13um

4 Conclusion

In this paper, the design of current sensing circuit with clamping current compensation is presented, including analysis, circuit implementations and simulation results. The main innovations of this paper are twofold: 1) the detailed analysis of the method of eliminating clamping current error; 2) adopting series MOS substitute to single MOS as sensing MOS MS and the switch MOS MSW to reach better performance. Simulation results show that the proposed circuit has better performance than previous designs. The test chip is being fabricated with SMIC 0.13um 1P8M 3.3V CMOS process.

References

1. Forghani-zadeh, H.P., Rincón-Mora, G.A.: Current-sensing techniques for DC-DC converters. In: IEEE Midwest Symp. on Circuits and Systems, pp. 577–580 (2002)
2. Ki, W-H.: Current Sensing Technique using MOS Transistors Scaling with Matched Bipolm Current Sources, U.S. Patent 5757174 (1998)

3. Park, J., Choi, J., Jeong, W., Yu, S., Jang, K., Choi, Y., Choi, J.: Current-sensing technique for current-mode DC-DC buck converter with offset-voltage compensation. In: IEEE Asia Pacific Conference on Circuits and Systems, APCCAS 2008, pp. 1704–1707 (2008)
4. Leung, C.Y., Mok, P.K.T., Leung, K.N.: An integrated CMOS current-sensing circuit for low-voltage current-mode buck regulator. IEEE Tran. Circuits SystII. 52(7), 394–397 (2005)
5. Lee, C.F., Mok, P.K.T.: A monolithic current-mode CMOS DC-DC Converter with On-Chip Current Sensing Technique. IEEE J. Solid-State Circuits 39, 3–14 (2004)
6. Man, T.Y., Mok, P.K.T., Chan, M.: Design of fast-response on-chip current sensor for current-mode controlled buck converters with MHz switching frequency. In: IEEE Conference on Electron Devices and Solid-State Circuits, EDSSC 2007, pp. 382–392 (2007)
7. Chang, C.H., Chang, R.C.: A novel current sensing circuit for a current-mode control CMOS DC-DC buck converter. VLSI Design, Automation and Test, 120–123 (2005)
8. Cheng, K.-H., Su, C.-W., Ko, H.-H.: A high-accuracy and high-efficiency on-chip current sensing for current-mode control CMOS DC-DC buck converter. In: IEEE 15th International Electronics, Circuits and Systems Conference, pp. 458–461 (2008)
9. Du, M., Lee, H.: A 2.5MHz, 97%-accuracy on-chip current sensor with dynamically-biased shunt feedback for current-mode switching DC-DC converters. In: Proc. IEEE Int. Symp. on Circuits and Systems, pp. 3274–3277 (2008)
10. Galup-Montoro, C., Schneider, M.C., Loss, I.J.B.: Series-parallel association of FET's for high gain and high frequency applications. IEEE J. Solid-State Circuits 29(9), 1094–1101 (1994)

Digital Controlled Frequency Modulation Microwave Signal for CPT Atomic Clock

Jian Xu[1], Zhiyin Gan[1], Xiong Shi[2], and Sheng Liu[1]

[1] School of Mechanical Science and Engineering, Huazhong University of Science and Technology, Luoyu Road 1037, 430074, Wuhan, China
[2] Department of Electrical and Information Engineering, Wuhan Polytechnic University, Wuhan, China, 430023

Abstract. This paper proposed a new circuitry to make frequency modulation (FM) microwave signal for coherent population trapping (CPT) atomic clock application. This circuitry employed one phase lock loop (PLL) chip and one direct digital synthesis (DDS) chip to complete the FM for the microwave signal used in CPT atomic clock. The FM frequency and depth could be controlled by DDS. Test results showed this circuitry could well make the FM signal for CPT atomic application.

Keywords: FM, PLL, DDS, CPT, Atomic Clock.

1 Introduction

Atomic clock could provide the most stable frequency references. In the past 50 years, atomic clocks have provided the most stable frequency references in many fields such as communication, satellite navigation system or science measurement [1-3]. As without microwave cavity, the CPT atomic clock is the primary clock for miniaturization. Furthermore, with the vertical cavity surface emitting laser (VCSEL), the physics system of the CPT atomic clock was miniaturized very much [4-5].

Due to the CPT atomic clock based on the CPT phenomenon which needs two coherent lights between which the frequency difference is equal to the ground-state hyperfine splitting of the alkali metal [4, 6-8] and employed the VCSEL as its light source [4, 7], there must be a microwave signal used to modulate its current to introduce these two coherent lights. Therefore, the stability of the microwave signal would affect the light frequency stability of the two coherent lights and then affect the stability of the output frequency of atomic clock.

In order to detect the error between the frequency of microwave signal and the half of the ground-state hyperfine splitting of the alkali metal, lock-in amplifier (LIA) technology was employed [4, 7-10] which needs the microwave signal to be frequency modulated. Furthermore, the frequency modulation (FM) frequency and depth would affect the error detection quality [5, 6]. However, in the past of development of the atomic clock, there rarely was reported about a simple, versatile for controlling the frequency and depth of FM circuitry for atomic clock [4, 6].

D. Zeng (Ed.): Future Intelligent Information Systems, LNEE 86, pp. 569–575.
springerlink.com © Springer-Verlag Berlin Heidelberg 2011

Based on the development of IC and communication technology, this paper proposed a circuitry to realize the FM microwave signal for atomic clock. This circuitry employed one phase lock loop (PLL) IC chip to generate the demand microwave signal and with special design, the FM could be applied to this microwave signal. Moreover, the direct digital synthesizer (DDS) was used to generate the FM signal and control the modulating frequency and depth. Frequency spectrum analysis showed that this circuitry could well done the FM for the microwave signal for atomic clock.

2 Circuitry Design

2.1 Microwave Oscillator Design

Because the CPT atomic clock based on the CPT phenomenon and employed one VCSEL as its light source, the microwave signal must be used to modulate the injection current of the VCSEL to introduce the two coherent lights which the CPT phenomenon required. Moreover, the frequency of the microwave signal should be equal to half of the ground-state hyperfine splitting of the alkali metal used in CPT atomic clock. Therefore, the microwave signal should be generated first.

In the past years, the discrete components such as BJTs, resistors, capacitors and inductors etc were used to design and architect the microwave oscillator for CPT atomic clock [4, 6]. However this circuit design was not only difficult but also hard to be fabricated.

As the development of the communication and IC technology, there are many chips could be used to make the microwave oscillator [11] in the frequency range of the CPT atomic clock.

Taking ^{87}Rb CPT atomic clock as example, the microwave signal it required is 3.4 GHz. For this frequency, there are many PLL chips could be used. Considering the miniaturization of the CPT atomic clock, the PLL chip TRF1221 was employed because of the integrated VCOs which could further minimize the design difficulty.

2.2 FM for the Microwave Signal

With the standard circuit configuration, we could obtain the 3.4 GHz without difficulty. However, as presented above, LIA was employed in CPT atomic clock to detect the error between the frequency of microwave signal and the half of the ground-state hyperfine splitting of the alkali metal to stabilize the output frequency as a reference. As well-known, the LIA requires the detected signal should be amplitude modulated (AM) by a certain signal. And in atomic clock, there was FM to AM transformation because of the VCSEL employed for frequency discrimination and the photodiode for the detection. Therefore, the microwave signal should be frequency modulated.

Therefore, in our design, we employed the one-point frequency modulation theory to eliminate the difficulty which would be introduced by inputting the FM reference signal to make FM microwave signal. First, the PLL loop filter output was buffered and then added a sinuous wave whose frequency could be controlled to output to the VCOs

input pins of the PLL chip TRF1221. Fig. 1 showed this configuration. The buffer was used to stabilize the loop filter output signal and the sinuous wave was used to make the FM. The digital control part was used to control the carrier frequency and the gain control part was used to control the output signal power. The reference signal was CLK_Ref which was shown in Fig. 1.

In order to make this FM versatile for changing the frequency and depth of FM, a DDS chip AD9850 was used as it could be controlled with TRF1221 by one microcontroller. The sinuous wave would be given by this DDS chip with frequency and amplitude controlled. That would lead the frequency and the depth of FM controlled. In the Fig. 1, the VCSELSCAN port was the input port of the DDS modulating signal.

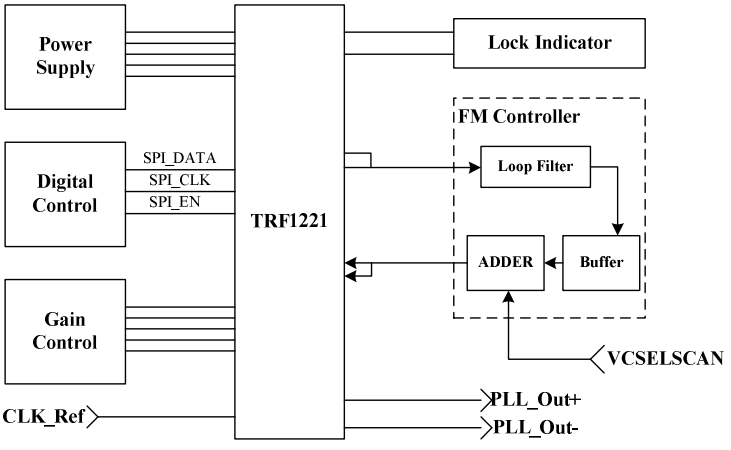

Fig. 1. Configuration for the FM microwave oscillator

3 Experiments and Results

With the circuitry designed above, we made the PCBs to realize the design. In order to demonstrate our design, we used the spectrum analyzer Agilent N1996A to detect the signal output from the oscillator. And with the function of FM demodulation, we also made the demodulation for the detected signal and compared with the signal we used for modulating.

Fig. 2 showed the output of microwave oscillator without FM in which the marker indicates the peak is 3.4 GHz which is equal to the half of the ground-state superfine energy level splitting.

Fig. 3 showed the FM signal and the demodulated signal after we use the 1 kHz 600 mV modulation signal. And Fig. 4 and Fig. 5 showed the corresponding signals with 500 Hz 600 mV and 300 Hz 600 mV modulating signal inputs respectively. As we see, in the right of the Fig. 3, the frequency of the detected demodulated signal was equal to the difference of the peaks in the left of the figures which was the same in the Fig. 4 and Fig. 5. Therefore, we could conclude that the FM was successful by the circuitry we designed.

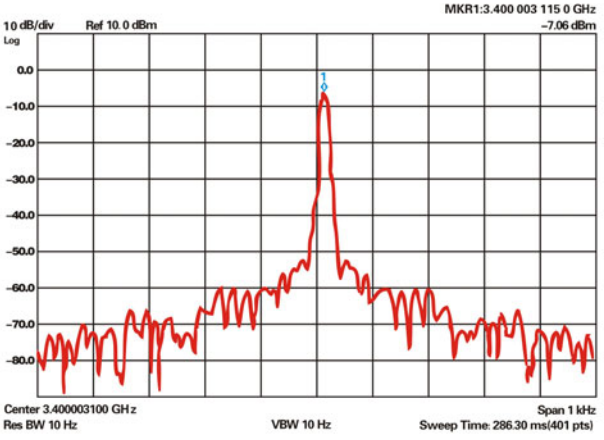

Fig. 2. Output of microwave oscillator without FM, marker indicates 3.4 GHz

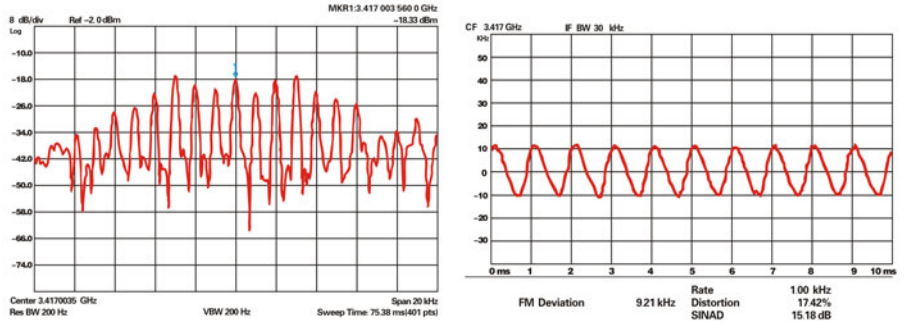

Fig. 3. 3.4 GHz FM signal with 1 kHz modulation (left) and signal demodulated by Agilent N1996A

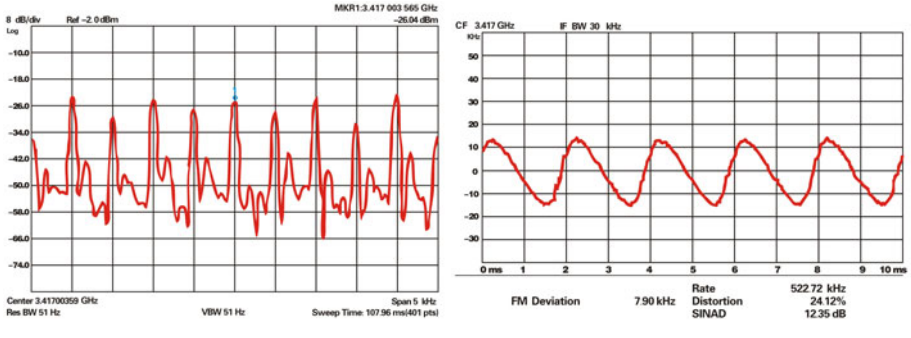

Fig. 4. 3.4 GHz FM signal with 500 Hz modulation (left) and signal demodulated by Agilent N1996A

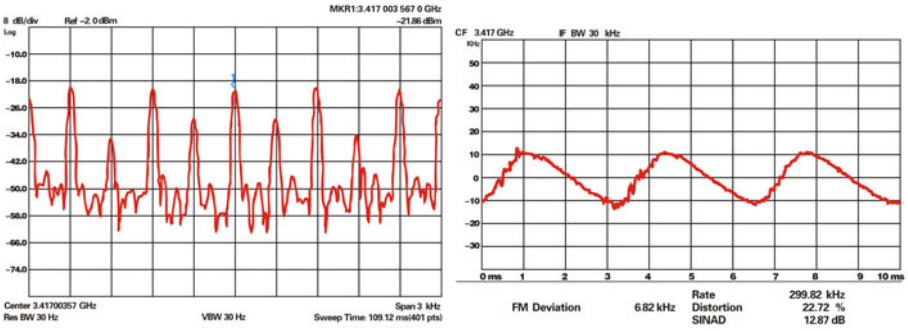

Fig. 5. 3.4 GHz FM signal with 300 Hz modulation (left) and signal demodulated by Agilent N1996A

However we could observe from the figures, the quality of the demodulated signal in Fig. 3 is better than the signal in Fig. 4 and Fig. 5. And with other frequencies for experiments, we also found that if the modulating frequency lower, the demodulated signal would be worse. Moreover, when the modulating frequency was low to 100 Hz, the demodulated signal was too noisy which is shown in Fig. 6. That means the FM microwave signal could not operate normally. That because the signal was inputted into the PLL chip without well filtered. And due to the interrupt from the power line, the signal would not be as better as our demand.

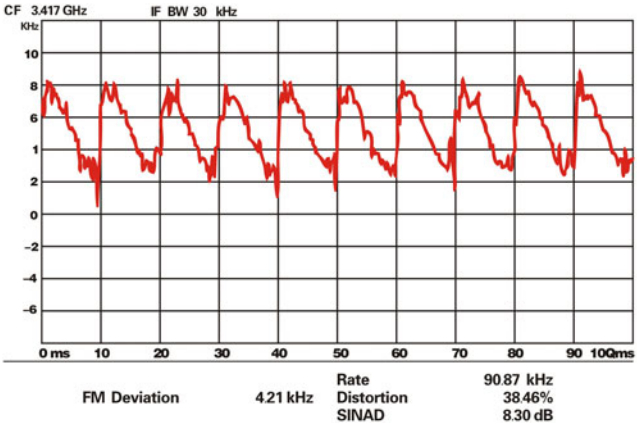

Fig. 6. Demodulated signal for 100 Hz FM with 3.4 GHz carrier

On the other hand, from these figures, it could be observed that with the different frequency but the same amplitude modulation, the amplitude of the sidebands of the FM microwave signal were not equal to the carrier frequency and with different difference.

It means that the modulation indexes in these figures were not the same and indicates that the modulation index could be controlled by changing the modulating frequency which corresponds with the FM theory. Furthermore, we could also found that the change of the amplitude of the modulating signal would also affect the modulation index. As the modulating signal outputted from the DDS chip, the modulating frequency and the modulation depth could be controlled by the program in the microcontroller.

4 Conclusions

With special configuration for the PLL chip, we proposed and realized a new circuitry for the FM microwave signal of 3.4 GHz for the ^{87}Rb CPT atomic clock. Experiment results showed that the circuit could well output the FM microwave signal with frequency and modulation depth controlled by the DDS synthesizer with changing frequency and amplitude of the modulating signal. For atomic clock application, the modulating frequency should be not close to 100 Hz and the modulating frequency and amplitude should be carefully chosen to make the optimal modulation index for the CPT phenomenon. Last but not least, the signal should be carefully filtered.

Acknowledgement

This work is supported by the National High-tech R&D Program (863 Program) under Gran No. 2006AA04Z346. The authors would like to appreciate Mr. Yang You for the helpful discussion in the circuit design and experiment, and also appreciate Dr. Tingkai Zhang for useful discussion on CPT atomic clock.

References

1. Lyons, H.: The Atomic Clock – A Universal Standard for Frequency and Time. Am. Scholar 19, 159–168 (1950)
2. Townes, C.H.: Atomic Clocks and Frequency Stabilization on Microwave Spectral Lines. J. App. Phys. 22, 1365–1372 (1951)
3. Quinn, T.: Fifty Years of Atomic Time Keeping: 1995 to 2005. Metrologia 42 (2005)
4. Vanier, J.: Atomic Clock Based on Coherent Population Trapping: A Review. Appl. Phys. B 81, 421–442 (2005)
5. Kitching, J., Knappe, S., Liew, L., et al.: Microfabricated Atomic Clock. In: 18th IEEE International Conference on Micro Electro Mechanical Systems, pp. 1–7. IEEE Press, Miami (2005)
6. Brannon, A., Jankovic, M., Breithbarth, J., et al.: A Local Oscillator for Chip-scale Atomic Clock at NIST. In: 2006 IEEE International Frequency Control Symposium and Exposition, pp. 443–447. IEEE Press, Miami (2007)
7. Serkland, D.K., Peake, G.M., Beib, K.M., et al.: VCSELs for Atomic Clock. In: Proc. of SPIE, vol. 6132, pp. 6132081–61320811 (2006)

8. Kitching, J., Knappe, S., Vukicevic, N., et al.: A Microwave Frequency Reference Based on VCSEL-Driven Dark Line Resonances in Cs Vapor. IEEE Tran. Instr. Meas. 49(6), 1313–1317 (2000)
9. Weel, M., Kumarakrishnan, A.: Laser-frequency Stabilization Using a Lock-in Amplifier. Can. J. Phys. 80, 1449–1458 (2002)
10. Sowka, K., Weel, M., Cauchi, S., et al.: A home-built Lock-in Amplifier for Laser Frequency Stabilization. Can. J. Phys. 83, 907–918 (2005)
11. PLL Chips and DDS Chips Information, http://www.ti.com, http://www.analog.com

Application of Ground Electric Field Information in Lightning Forecast

Wei He[1], Hong Jian Liu[1], Ba Lin Xu[2], Xiao Chong Liang[1], and You Ju Liu[3]

[1] Institute of Physics and Electronic Information, Yunnan Normal University, Kunming, China, 650092
[2] Yunnan Province Meteorological Bureau, Kunming, China, 650065
[3] Baosan College
He99wei@yahoo.com.cn

Abstract. Based on the atmospheric electric field monitoring data and lightning location data, the principle, method and process of lightning warning and forecasting is analyzed. The results show that lightning location and the distance between lightning location and atmospheric electric field instrument are major factors in warning and forecasting. It may be adjust the electric field threshold according to the specific terrain environment. The combination method of electric threshold warning and differential electric threshold warning is more effectively in lightning warning and forecasting, which minimize the loss to people's lives and socio-economic.

Keyword: atmospheric electric field, lightning location, lightning forecasting, threshold.

1 Introduction

Lightning occurring with various effects such as audio, light, heat, electromagnetic field etc. is a very complicated natural phenomenon, which provides effective information for the monitoring and warning of lightning. Directly or indirectly monitoring devices, such as meteorological satellite, lightning locator, SAFIR system, global lightning monitoring system and atmospheric electric field instrument, are based on the effects that lightning cause on [1]. Some of these effects are temporary, only in a phase of a moment. Lightning monitoring system is based on the Schumann Resonance, which can not been detected until it occurs. So it is difficult to forecast in advance of the lightning strike. Satellite Images, SAFIR system and global lightning monitoring system are suitable for monitoring the global large-scale regions, but it is difficult to accurately tell the difference in small-scale regions. So only the electric effect occurs throughout all stages before and after lightning (including thunder clouds forming, developing, and dissipating, etc.). That is to say, atmospheric electric field on the ground changes according to charged cloud, and atmosphere electric field instrument can detect these changes. So we can understand the charge accumulation of thundercloud and judge the possibility of lightning occurring in the region.

D. Zeng (Ed.): Future Intelligent Information Systems, LNEE 86, pp. 577–583.
springerlink.com © Springer-Verlag Berlin Heidelberg 2011

2 Lightning Activity and Electric Field Variation

As for the distribution of thundercloud charge, positive charge center is in the upper, equivalent negative charge center in the lower, and a small amount of positive charge in the bottom of thunderstorm cloud. When striking, lightning current generated electrostatic field, induced field and radiation field, and electrostatic field focus on closer area away from the lightning point. There are mainly electrostatic field on the ground before lightning, and superimpose electric field of lightning. As the ground is approximately ideal conductor, electric field nearby is considered perpendicular to the ground [3] [4]. Radiation field may not been taken into account because atmospheric electric field instrument work on electrostatic field, as shown in figure 1.

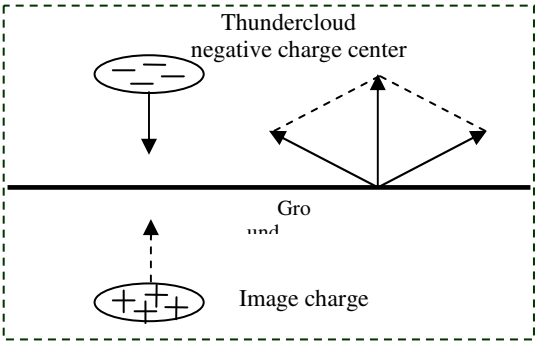

Fig. 1. Vertical electric field generated by thundercloud and lightning current on the ideal ground

Generally, ground electric field would appear abnormally when there are thunderstorms clouds or moving clouds within 40km. When conditions are ripe, it just takes 20 minutes form the beginning to accumulating charge to lightning [2]. Surface electric field will produce pulse changes because of the sudden variations of the thunderstorm cloud charge in instantaneous.

When there is no lightning around, the ground electric field curve changes smoothly, as shown in figure2. But there is cloud-to-cloud or cloud-to-ground lightning flashes, the atmosphere electric field will be a significant change. So the activity status of charged cloud can be detected through the electric field change curve. Figure3 shows the atmospheric electric field change curve in a lightning flash process occurring at 17 July 2006, in Kunming city, Yunnan province, China, recorded by Meteorological Administration atmospheric electric field instrument. From the lightning curve, the formation of lightning includes several stages [2]. 1) Ground electric field curve changes gradually from smoothly to fast positive and negative jitter, and electric field range increases gradually. So, it can be judged that there are thunderclouds forming in the vicinity of the electric field instrument, or there is small energy cloud-to-cloud lightning flashes occurring in the distance. 2) The electric field near the ground strengthens unceasingly at the negative direction, so it can be judged that negative charge, accumulated at the bottom of a cloud, is increasing. The curve moves integrally

to the negative direction with fast jitter curve superimposed. It can be judged that unstable thunderstorm clouds, cloud-to-cloud lightning flashes and negative charge accumulated contributes to the superposition of results. When cloud-to-ground electric field reachs to the atmospheric breakdown threshold, lightning leader occurs, leading to the ground field revering instantaneously, and forming a fast changing peak upward. After discharge, the clouds will re-assembled charge immediately, and continue to the next lightning process. 3)As conditions are ripe, thunderstorm clouds electrifier is very quickly [2]. Electric field on the ground increases exponentially, appearing to stronger fast changing peaks upward. Other times it is at a steady negative electric field, and thunderstorm cloud is low potential relative to the ground. 4) Ground electric field is gradually approaching zero, so it can be judged that cloud is no charged, drift or disappear.

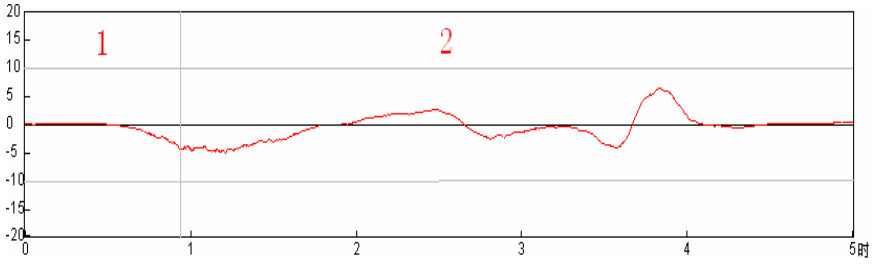

Fig. 2. Electric field probing results that did not develop into thunderstorms

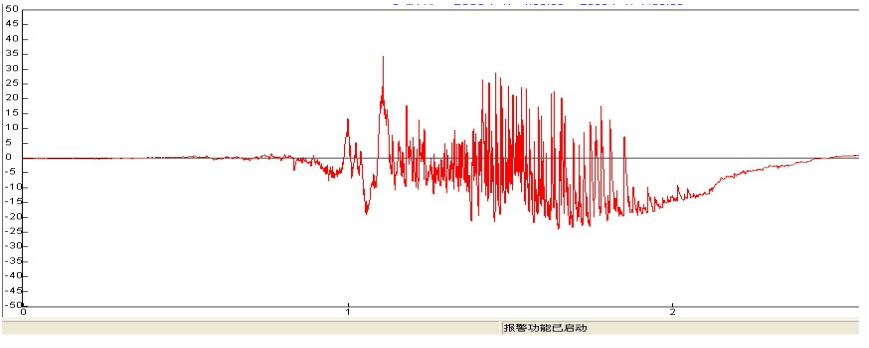

Fig. 3. Ground electric field change curve recorded at a lightning process occurred in 17 July 2006, at Kunming city

3 Method of Lightning Warning

3.1 Atmospheric Electric Field Instrument

Atmospheric electric field instrument is the equipment that are used to measure the intensity, change and polarity of atmospheric electric field, and it measures the electric

field based on the principle that conductor in the electric field induced charge. When the cloud charge separates, the ground electric field will change accordingly. As the intensity of it relates to the accumulation and distribution of cloud charge, by measuring the variation of electric field on the ground, charge variation of high-altitude clouds can be reflected, which some prediction can be made for the risk of occurrence of lightning. Atmospheric electric field instrument is suitable for some small range of lightning detection such as riot control stations, airports, depot, ammunition depots etc., and their main specifications is shown in table 1. To expand the range of measurement and improve measurement accuracy, atmospheric electric field instrument network must be built.

Table 1. Mainly technical index of atmospheric electric field instrument

name of performance	Indicators parameters
Detection range of electric field	0～±50kv/m
Sensitivity	10V/m
measuring error	<10%
detection range	0~20km
power source	220ACV±10%
power consumption	<10W
Working temperature	-25 ℃～+55 ℃
Working humidity	Relative humidity 99%

The above analysis shows that electric alarm should be based on the standard whether. It is fast jittering initially and the electric field intensity reaching some level of electric threshold. Electric threshold is generally divided into 5 alarms such as 2kV/m, 5kV/m, 8kV/m, 12kV/m and 15kV/m. Different duration time of warning can be got by setting the electric threshold.

3.2 Electric Field Instrument and Lightning Location System

In domestic and foreign, lightning monitoring and warning technology are mainly lightning location detecting system and atmospheric electric field instrument having introduced above. The former can record the time and location of lightning occurring, a statistical behavior after happening. The latter can not only record the thundercloud charge changes before lightning, but also record the lightning process during thunderstorms. By combining the two methods, so as to better understand the activities of charged clouds, and effectively monitor and early warn the thunder and lightning.

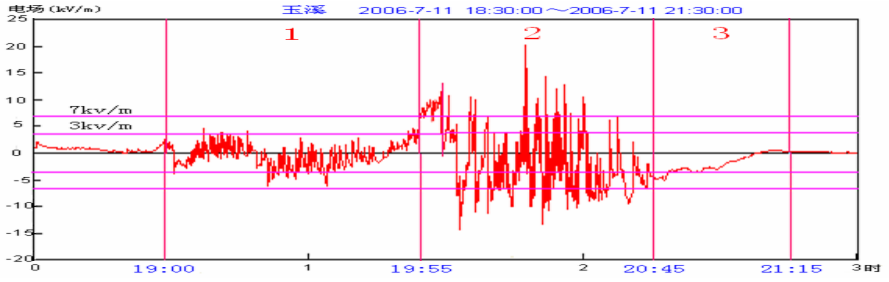

Fig. 4. Electric field variation curve recorded at Yuxi city

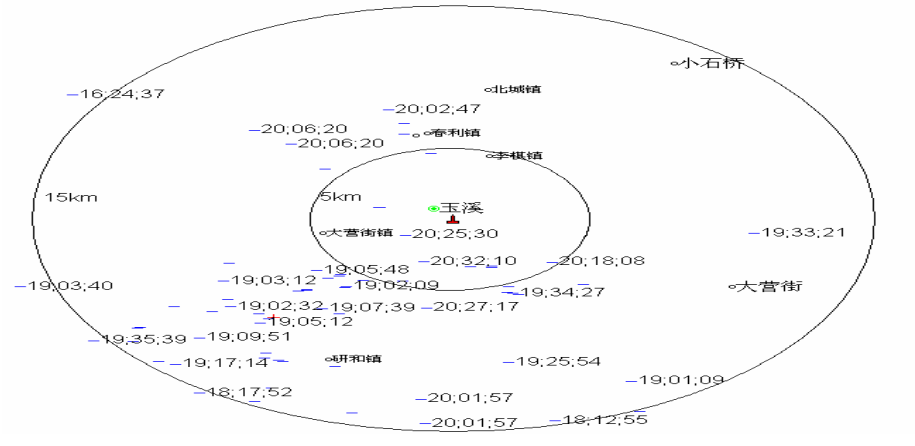

Fig. 5. detection data recorded in a thunderstorm process at Yuxi city

As can be seen from Figure 4, electric field curve starts to change and jitter rapidly at 19: 00, when cloud-to-cloud or cloud-to-ground lightning flashes occur mainly at 15km outside the electric field instrument. At 19: 00-19: 55, the electric field intensity increased, lightning occurred at 5-15km away from the field instrument; Then at 20:30, electric field intensity reaches 20kv/m or so, and lightning occurred at less than 5km away from the electric field instrument; So It can be inferred that the size of the electric field intensity related to the distance between lightning point and the electric field instrument, the greater the distance the smaller the field intensity. The field instrument is stipulated as center, drawing four laps whose radius is 5km, 10km, 20km and 50km [3]. The closer the lightning location away from the electric field instrument, the higher the lightning alarm level is. So the lightning has a total of 4 levels alarm, integrated lightning location and electric field, receiving a maximum of 9 levels alarm. In general, depending on the different applications, 30 minutes early warning can be got when the integrated alarm level up to five. When the integrated alarm level reached to 6 or 7, it shows that lightning will be likely to occur within 5km in 10 minutes. Table 2 shows the alarm levels and alarm (lightning occur within 10km) success rate. Combining with

manual or electric field instrument networks, so as to determining the trend of thunderstorm clouds moving and changing, the success rate of alarm can dramatically been improved.

Table 2. Classification of electric field instrument alarm [5]

Comprehensive alarm level	4	5	6	**7**
Success rate of alarm	>60 %	>70 %	>80 %	>90 %
Alarm time ahead(min)	40	30	20	10

4 Conclusions

Lightning location and the distance between electric field instruments are taken as the reference in lightning warning and forecasting. Atmospheric electric field intensity changes before lightning occurring, and lightning time, location, intensity, direction of movement can be warned in advance by monitoring the polarity of the charge, intensity, distribution and evolution of thunderstorm cloud with electric field instrument and lightning location system. Combined with the installation position of electric field instrument and the local conditions such as terrain, varied the alarm level appropriately, more accurate and short time lightning warning can be got.

It must combinate the method of electric threshold warning and differential electric threshold warning, so as to improve the efficiency of lightning warning. When the atmospheric electric field exceeds alarm threshold, by combining with fast jitter in the initial phase of the electric field, false alarm rate can be reduced effectively. At the same time, it may be better if it is combined with the differential threshold warning technologies. Time difference of atmospheric electric field represents the change rate of time. The results show that, by using differential electric threshold warning, it not only can absent forecast rate be reduced but also accurately records the time when thunderstorms occur.

As atmospheric electric field instrument are very sensitive to the changes of electric field caused by local thunderstorms, using alone the data detected by atmospheric electric field instrument in lightning warning and forecast often results in more false prediction [7]. So combined with ground electric field instrument monitoring network and lightning location system, together with monitoring and warning equipment such as meteorological satellites, weather radar equipment, the location and movement direction of thunderstorms can be determined effectively, which play a role of network monitoring, early warning local thunderstorms.

Acknowledgements. This project was suppored by National Natural Science program (50367001) and Yunnan Province Science and Technology bureau program (2009ZC055M).

References

[1] He, W., Li, S.-c., Gao, Y.g.: EMC design in lightning protection of computer network. In: Asia-Pacific Conference on Environmental Electromagnetics CEEM 2006 (2006)
[2] Wu, J., Chen, Y.-F., Zeng, Z.-C.: Means of using ground electric field instrument and lightning location information in short lightning warning. Meteorology and Environmental Sciences 32(1), 47–50 (2009)
[3] He, W., Gao, Y.-G.: Surface impedance method to calculate the horizontal field of lightning. Beijing University of Posts and Telecommunications 14(1), 13–18 (1999)
[4] Chen, W.-m.: Lightning Principles, 2nd edn., pp. 266–276. Meteorological Press, Beijing (2003)
[5] He, W., Li, S.-c., Xu, B.-l.: Electromagnetic Field of Straight Lightning in the Building. In: Proceedings of the XVI International Conference on Gas Discharges and their Applications GD 2006(2006)
[6] Qiang, W., Wang, J.-C.: Effectiveness analysis of electric field timing difference in early warning of lightning. Meteorological science 29(5), 657–663 (2009)
[7] Wu, M.-J.: Atmospheric electric field characteristics and technology of lightning warning. Meteorology and Hydrology Marine Instrument 1, 10–14 (2010)

Research on Shielding Failure Rate for Transmission Lines Considering Working Voltage

Hong Jian Liu[1], Wei He[1,*], Ba Lin Xu[2], Xiao Chong Liang[1], and Kai Hong Zhou[1]

[1] Institute of Physics and Electronic Information, Yunnan Normal University, Kunming, China, 650092
[2] Yunnan Province Meteorological Bureau, Kunming, China, 650065
He99wei@yahoo.com.cn

Abstract. In order to analyze and improve the lightning shielding performance of transmission lines, working voltage is considered as an influence factor to the striking distance. The relationship between maximum striking distance and lightning polarity, or the size and polarity of working voltage is obtained. It is demonstrated with example that lightning shielding performance can be effectively improved through balancing the values of inclination angle θ, tower height h and shielding angle α.

Keywords: Improved EGM; maximum striking distance; lightning shielding failure; lightning shielding performance.

1 Introduction

At present, the main research methods of shielding failure rate of transmission lines are: standard method, leader progression model (LPM) [1] [2], electrogeometric model (EGM) [3]. Standard method is an approximate calculation based on statistical results, which often does not reflect the specific circumstances of lightning shielding failure. Classic EGM also has its shortcomings [3]: do not consider, 1) the randomness of lightning; 2) the actual terrain of transmission lines; 3) the differences when lightning strikes the Earth, shield wire and transmission lines. Then, experts and scholars have proposed some improvement methods: striking distance is relevant not only to the lightning current amplitude but also to the height of object [4] [5]; Literature [6] considers the impact of working voltage on the striking distance and proposes a correction method and so on. The article uses the voltage correction coefficient to further discuss the model of EGM, deduces the calculation method of maximum striking distance, and obtains a better analysis and evaluation of lightning shielding performance.

2 Influencing Factors of Striking Distance

Table 1 shows the expressions of striking distance.

* Corresponding author.

D. Zeng (Ed.): Future Intelligent Information Systems, LNEE 86, pp. 585–590.
springerlink.com © Springer-Verlag Berlin Heidelberg 2011

Table 1. Expressions of striking distance

	striking distance	constants
IEEE working group	$r = aI_m{}^b$	a=10, b=0.65
Eriksson, Rizk	$r = aI_m{}^b h^c$	a=0.67, b=0.74, c=0.6

None of the above considering the influence of working voltage, leading to some deviation compared with the actual observation data when analyzing the lightning shield failure rate of transmission lines with extra-high voltage. Literature [6] points out that striking distance is relevant not only to the lightning current amplitude and height of object but also to the size of working voltage. The striking distance of shield wire is

$$r_{\mathrm{b}} = aI_m{}^b h^c \tag{1}$$

So the striking distance of transmission lines is

$$r_v = r_{\mathrm{b}} e^{dV} = aI_m{}^b h^c e^{dV} \tag{2}$$

Where e^{dV} is voltage correction coefficient, V is working voltage of transmission lines including positive and negative values. For positive lightning leader, d=-0.0003, and for negative lightning leader, d=0.0003.

The selectivity of lightning leader to the shield wire and ground is different. Striking distance coefficient k_g can be used to characterize this distinction

$$r_g = k_g r_{\mathrm{b}} \tag{3}$$

Table 2 shows the relationship between k_g and average height of shield wire h. The article selects the values k_g recommended by IEEE working group.

Table 2. The relationship between k_g and h [5]

	striking distance coefficient k_g
Shadow Width	$k_g = 22/h$
Eriksson	$k_g = 1.08 - h/59$
Rizk	$k_g = 1.05 - h/87$
IEEE working group	$k_g = \begin{cases} 0.36 + 0.17\ln(43-h) & h < 40m \\ 0.55 & h > 40m \end{cases}$

3 Model Analyzing

As is showed in fig. 1, O is the intersection point of the tower center line and the ground (see fig.1), O_b and O_l are shield wire and transmission lines respectively, B_i is the intersection point of the two circles, whose centre and radius are O_b , r_b and O_l , r_l respectively. Straight line C_iD_i and arc B_iC_i intersect at point C_i . A_iB_i , B_iC_i and C_iD_i together form a lightning locating surface along the radial direction of lines.

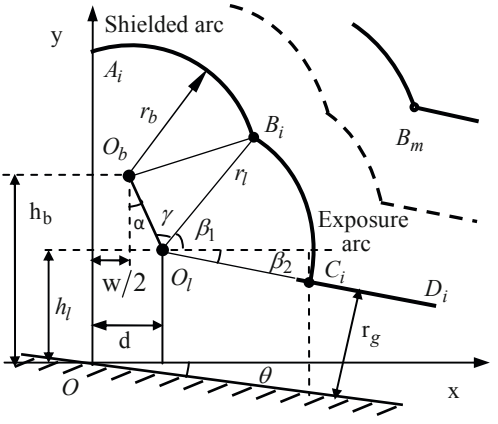

Fig. 1. EGM of considering working voltage

h_l —average height of transmission lines, h_b —average height of shield wire, d— distance between tower center and transmission lines, w—distance between the two shield wire, θ —inclination angle, α —shielding angle

If lightning leader falls on A_iB_i , transmission lines can be effectively protected, where A_iB_i is called shielded arc. If leader falls on B_iC_i , it wound hit the transmission lines, where B_iC_i is called exposure arc. If leader falls on C_iD_i , it would hit on the ground. Different lightning currents correspond to different striking distance, so a series of locating surfaces can be drawn. When B_iC_i shorten to a point B_m , transmission lines is no longer affected by greater lightning currents, striking distance reaches the maximum value r_m .

4 Deducing Method of Maximum Striking Distance

Striking distance that is determined by lightning withstand level $I_{\min}$ is called the critical striking distance r_c

$$r_c = 0.67 I_{\min}{}^{0.74} h^{0.6} e^{dV}\ ,\ I_{\min} = 2 \times U_{50\%} / Z \tag{4}$$

Where $U_{50\%}$ (kV) is the 50% impulse discharge voltage of insulator string, and Z is the impedance of transmission lines.

Angle α , θ , β_1 and β_2 have positive and negative values, whose final edge sweep clockwise as "-", counterclockwise as "+". By geometric relations

$$\begin{aligned} &r_v \sin(-\beta_1) = h_l - \\ &\left\{ r_g / \cos(-\theta) - \left[d + r_v \cos(-\beta_1) \right] \tan(-\theta) \right\} \end{aligned} \tag{5}$$

In $\Delta O_b O_l B_i$, let $\angle O_b O_l B_i = \gamma$, using cosine law

$$r_b{}^2 = \left(\frac{h_b - h_l}{\cos\alpha}\right)^2 + r_v{}^2 - 2\frac{h_b - h_l}{\cos\alpha} r_v \cos\gamma \tag{6}$$

Angle relationship

$$\beta_2 = 90^0 + \alpha - \gamma \tag{7}$$

From equations (5) ~ (7)

$$\beta_1 = \theta + \arcsin\left(\frac{d\sin\theta - h_l\cos\theta}{r_v} + \frac{k_g}{k_v}\right) \tag{8}$$

$$\begin{aligned} &\beta_2 = \alpha + \arcsin \\ &\left[\frac{h_b - h_l}{2 r_v \cos\alpha} + \frac{\cos\alpha}{2(h_b - h_l)} \cdot \frac{k_v{}^2 - 1}{k_v{}^2} \cdot r_v \right] \end{aligned} \tag{9}$$

$\beta_2 - \beta_1$ is central angle corresponding to the exposure arc (fig. 1). When $\beta_2 - \beta_1 > 0$, striking distance does not exist. So maximum striking distance can be solved when

$$\beta_2 - \beta_1 = 0 \tag{10}$$

From equations (8) ~ (10), maximum striking distance r_m can be solved.

The relationship between r_m and dc working voltage V is shown in fig. 2. For negative lightning leader (fig. 2a), r_m will increase with the increase of V. When voltage V up to a certain value, the r_m does not exist, than lightning with any current values can strike on the transmission lines, so shield wire lose its shielding performance. Maximum striking distance of positive polarity transmission lines is greater than that of negative, meaning that positive polarity transmission lines can attract stronger lightning currents. In other words, lightning protection performance of positive polarity transmission lines is poorer than that of negative, which is consistent with the actual observation data. On the contrary, the situation of positive lightning leader is shown in fig. 2b.

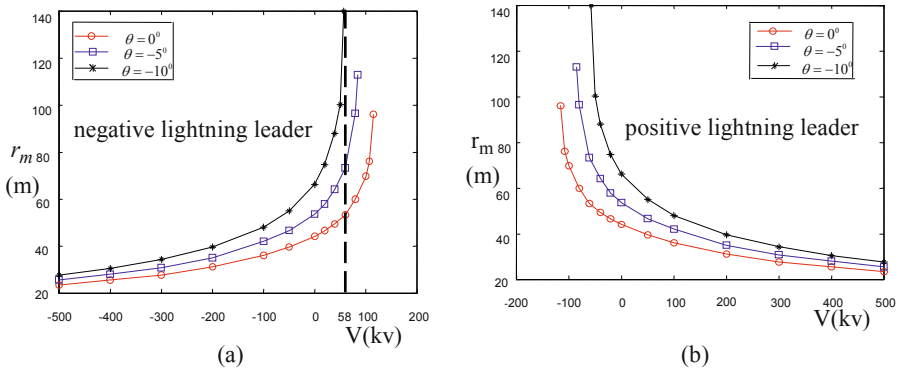

Fig. 2. The relationship between maximum striking distance and DC working voltage

The size of the striking distance coefficient can affect the maximum striking distance r_m. For a given voltage value, r_m will decrease with the increase of coefficient (see Fig. 3). So, lightning shielding failure rate can be reduced by increasing the value of coefficient, such as reducing the height of tower, changing the earth resistivity.

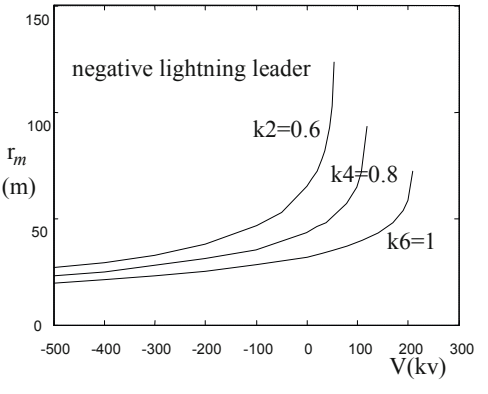

Fig. 3. The relationship between maximum striking distance and striking distance coefficient

5 Example Analysis of Lightning Shielding Performance

A transmission lines with 500kV dc voltage, let $h_b = 31m$, $h_l = 21m$, $w = 24m$, $d = 14m$, $\alpha = \arctan(\frac{d - w/2}{h_b - h_l}) = 11.3^0$, $\theta = -10^0$, $k_g = 0.36 + 0.17\ln(43 - 31) = 0.7824$.

Assuming that the lightning withstand level of transmission lines is 15.8kA, from (4), one obtains $r_c = 34.89m$. Discussions: (1) the voltage of transmission lines. When neglecting the working voltage, that is V=0, obtaining $r_m = 66.3m > r_c = 34.89m$, the lines are only shielded partly; When considering the working voltage, let $V = -500kv$, for negative lightning leader d=0.0003, obtaining $r_m = 27.62m < r_c = 34.89m$, the lines are shielded effectively; When $V = 500kv$, r_m do not exist. Thus it can be seen that the size and polarity of the voltage can impact the shielding effect. (2) Striking distance coefficient. Let $\theta = 0^0$, V=0, when k=0.5, obtains $r_m = 86.13m$, when k=1, obtains $r_m = 31.87m$. So, striking distance coefficient can affect the lightning shielding performance apparently.

6 Conclusions

(1) Because negative lightning accounts for most in nature, lightning protection performance of negative polarity transmission lines is stronger than that of positive, which is consistent with the actual observation data; (2) When $r_c < r < r_m$, lightning shielding failure exists; when $r_c \geq r_m$, the transmission lines can be shielded effectively. So, it is very important to design appropriate shielding angle and tower height; (3) comprehensive consideration of inclination angle θ, tower height h and shielding angle α is instructive in designing and reforming of transmission lines.

Acknowledgements

This project was suppored by National Natural Science program (50367001) and Yunnan Province Science and Technology bureau program (2009ZC055M).

References

[1] Brown, G.W., Whitehead, E.R.: Field and analytical studies of transmission line shielding: Part II. IEEE Trans. PAS 88(5), 617–625 (1969)
[2] Dellera, L., Garbagnati, E.: Lightning stroke simulation by means of the leader Propagation model parts I and II. IEEE Trans. on Power Delivery 5(4), 2009–2029 (1990)
[3] Zhu, S.-y., Deng, Y.-r.: Research on shielding lightning performance of electric transmission line with the improved EGM. High Voltage Apparatus 44(1), 56–58 (2008)
[4] Eriksson: An Improved Electro-geometric Model For Transmission Line Shielding Analysis. IEEE Transactions on Power Delivery 2(3), 871–886 (1987)
[5] Young, F., Clayton, J.M., Hileman, A.R.: Shielding of Transmission Lines. IEEE Transactions on Power Apparatus and Systems (82), 132–154 (1963)
[6] He, W., Li, S.-c., Gao, Y.: EMC design in lightning protection of computer network. In: Asia-Pacific Conference on Environmental Electromagnetics CEEM 2006 (2006)

Research on Printing Video Shot Boundary Detection

Fu-Cheng You and Yu-Jie Chen

Information & Mechanical Engineering School
Beijing Institute of Graphic Communication
Beijing, China
youfucheng@bigc.edu.cn, chenyujie0311@163.com

Abstract. This paper mainly analysis features of printing video. This kind of video almost has the common features that uneven illumination and camera with shake and so on. According to this features, hue histogram based-on HSV color model is used for detecting the cut shots of printing machinery video. And, an improved double-threshold comparison method based-on hue histogram based-on HSV color model is proposed and used for detecting gradual shots. This new method improves the accuracy by detecting the false start position of gradual shot. At the end of this paper, the results of experiments are given out, which indicate that the shot boundary detection algorithms proposed in this paper are efficient and with higher accuracy when it used for detecting the shot boundaries of printing video.

Keywords: Printing video; Shot detection; Cut shot; Gradual shot; False start position of gradual shot.

1 Introduction

With the rapid development of science and technology, multimedia technology and internet technology are becoming increasingly popular, and its application fields are more and more widely. Multimedia information technology has provided us with comprehensive and intuitive information, and it affects our lives and thinking ways. Our studies and lives depend on multimedia more and more. The same is true in the printing industry.

Nowadays, the internet is filled with various videos related to printing publish and printing machinery, that provide great convenience for the people who engaged in printing industry. But, at the same time of getting convenience, the vast amounts of video information also bring many troubles. Facing to the massive video data on the internet, how can we quickly and accurately find the video clips which we need? This requires effective video retrieval technology supported. Conventional text-based video retrieval methods have been unable to meet the needs of the people, then, content-based video retrieval that using video features directly is a high efficient method of video retrieval which combines with image understanding, artificial intelligence and other techniques. Shot detection is the first step and also the most important step of the content-based video retrieval.

D. Zeng (Ed.): Future Intelligent Information Systems, LNEE 86, pp. 591–598.
springerlink.com © Springer-Verlag Berlin Heidelberg 2011

2 Printing Video Features and Printing Video Shot Types

2.1 Printing Video Features

Printing video from coarse to fine can be divided into printing video stream, scene, shot and frame. And the structure diagram of the printing video is given out in Fig. 1.

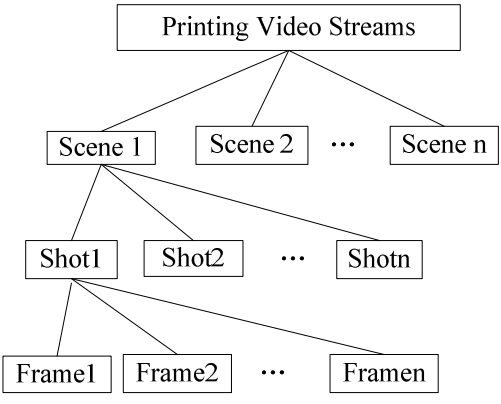

Fig. 1. The structure of diagram of printing video

Video stream is at the top level of video structure, it mainly composed by a series of scenes, then scenes of video can be further divided into some shots [1], and each shot is a continuous content shot that shot by a camera, each shot is composed by lots of frames, which is the smallest unit of video data, and a frame is a static picture.

There are many types of video programs, such as news, sports, movies, and so on, each kind of video has its own unique feathers. Taking news for examples, its mainly contents are composed by a series news story units, each story unit is a relatively independent events in content, and anchor shots always exist at the beginning of a story unit [2]. In the field of printing, printing video has its own unique feathers, too. Generally, the scenes of printing video are relatively single, and video contents are relatively simple, and no complicated explosion scenes of movies. The content of printing video is almost introducing the machine running and operation and other relatively simple scenes. But, there are some videos which shot by non-professional people, this kind of video always have some phenomenon, such as uneven illumination and camera with shake and so on which require that the shot detection algorithms used in this kind of videos must have certain tolerance with movement and light.

2.2 Printing Video Shot Types

There are two types of printing video shot: cut shot and gradual shot.

Cut shot is a shot change into another shot directly, there is no any video editing effects, and no time delay in the processing of conversion. The boundary of this kind of

shot is very obvious, and can be detected easily. Relative to cut shot detection, the boundary detection of gradual shot is more complicated. Gradual shot is described as follows: in the process of shot change from one to another, it added some video editing effects. Generally, the types of gradual shot are fade, dissolve, wipe, etc.

3 Detection Algorithms of Cut Shot

Generally, the detection algorithms are divided into two types: based on compressed domain and based on non-compressed domain. The detection algorithms based on compressed domain detect boundary by parsing the encode information of compressed domain. Based on DCT coefficients, based on DC coefficients and based on motion vectors are its basic methods. The shot detection algorithms based on non-compressed domain detect boundary by calculating the feature difference between images, pixel difference method, histogram comparison method and based on contour edge method are the mainly methods.

There is no transition delay between cut shots, the difference between last frame of the first shot and first frame of the second shot is very big, the shot boundary is very obvious, so, cut shot can be detected easily. At present, the cut shot detection technology has developed quite mature, the following lists some commonly used cut shot detection algorithms.

3.1 Conventional Cut Shot Detection Algorithms

3.1.1 Pixel Difference Method

Pixel difference method is the easiest and most easy understood method in shot detection algorithms. Pixel difference method is calculating the pixel gray difference that on the corresponding position of two adjacent frames. Supposed $g_{n-1}(x, y)$ and $g_n(x, y)$ represent the gray of two adjacent frames, and (x, y) is pixel of different positions, then pixel difference method can be described by:

$$T = \sum | g_n(x, y) - g_{n-1}(x, y) | \tag{1}$$

If the finally result is bigger than a threshold that pre-set, we can believe that cut shot is exist here.

Although the calculation of pixel difference method is very easy and can be understood easily, but it can be affected by shot moment easily, therefore, the applications of it are not widely.

3.1.2 Histogram Comparison

Histogram is one of the used most features in image processing. Gray histogram [3] and color histogram [4] of image are used most in shot detection, and histogram comparison is the most used method in shot detection. Supposing that $H_{n-1}(x, y)$ and

$H_n(x, y)$ represent the histograms of two adjacent frames, then gray histogram comparison can be described by:

$$T = \sum | H_n(x, y) - H_{n-1}(x, y) | \tag{2}$$

Color histogram comparison can be described by:

$$T = \sum (|H_n^R(x,y) - H_{n-1}^R(x,y)| + |H_n^G(x,y) - H_{n-1}^G(x,y)| + |H_n^B(x,y) - H_{n-1}^B(x,y)|) \tag{3}$$

The same as pixel difference method, if the finally result is bigger than a pre-set threshold, then, we can believe that cut shot is exist here.

3.1.3 Method Based-on Contour

The method of based-on contour mainly depends on contours of objects of adjacent two frames or edge information. If the adjacent two frames belong to two shots, the contents of frames have many differences. Correspondingly, the contours of objects in scene have changed. Generally, the contours of two frames in one shot are not differ too far, and the contours of two frames in two shots are not overlap completely, so we can detect cut shot by calculating the distances of pixels of two adjacent frames. But, the experiment of based-on contour of Zabhi [5] is not ideal, and, large amount of computations are limiting its application.

In the methods above, the choice of thresholds is very important, and it is also a difficult in shot detection, constant threshold will cause different levels of false detection and missed detection. Thus, Hanjialic proposes an algorithm based-on probability and statistics [6], which uses a non-constant threshold. Pan Lei proposed a method of histogram combined with pixel in Ref. [7], this method is effective to avoid false detection caused by pixel difference method and missed detection caused by histogram comparison. In addition, there are many methods of adaptive threshold of cut detection have been proposed, such as average frame difference method, etc. For the cut shot detection algorithms, the current development is already quite mature.

3.2 Hue Histogram Comparison Based-on HSV Color Model

The same as news video and sports video, printing video has its own features. Because of this features, it is very important to choose right shot detection method. This type of video is very sensitive to light, therefore, this paper gives up RGB color model when detect cut shot, but choose HSV color model. In this paper, H component or S component of HSV color model can be used to detect shot of printing video, and V component is given up because it can be affected by light.

3.2.1 Introduction of HSV Color Model

HSV color model is a color model for visual perception, the three color components are hue (H), saturation (S) and value (V). Hue refers to the color, saturation is the degree of

color, value refers to the human eye can feel the degree of light [8]. And the value information of image is unrelated to the color information. Therefore, in order to avoid false detection caused by uneven illumination, in this paper, only hue histogram is used to detect printing video cut shot.

3.2.2 Cut Shot Detection of Printing Video

The form of cut shot is very single. Correspondingly, the detection is very simple too. In this paper, hue histogram is used and the procedure is described as follows:

Firstly, color image is changed from RGB color model to HSV color model. The equation is given by:

$$\mathrm{H} = \begin{cases} \theta & \mathrm{G} \geq \mathrm{B} \\ 2\pi - \theta & \mathrm{G} < \mathrm{B} \end{cases} \tag{4}$$

In the equation (4),

$$\theta = \cos^{-1}\left[\frac{\frac{1}{2}\left[(R-G)+(R-B)\right]}{\sqrt{(R-G)^2+(R-B)(G-B)}} \right] \tag{5}$$

$$V = \frac{1}{\sqrt{3}}\left[R+G+B\right], \qquad R,G,B \in [0,1] \tag{6}$$

$$S = 1 - \frac{\sqrt{3}}{V}\min(R,G,B) \tag{7}$$

Then, the hue histogram is calculated.

And then, the adjacent frame difference $\mathrm{T_i}$ is calculated by the following equation.

$$\mathrm{T_i} = H_n^H(x,y) - H_{n-1}^H(x,y) \tag{8}$$

Finally, determine the difference between adjacent frames $\mathrm{T_i}$ whether is bigger than the pre-set threshold T, if $\mathrm{T_i} \geq T$, we can think that cut shot takes place here, otherwise, shot is not change.

The following images are extracted shot boundary frames from a printing video according to the algorithm described above. In these images, Frame 39 and Frame 40, Frame 118 and Frame 119, Frame 170 and Frame 171 belong to one shot, and Frame 40 and Frame 118, Frame 119 and Frame 170 are beginning frames and ending frames of one shot. Experiment results show that the method used to detect the printing video cut shot is very effective.

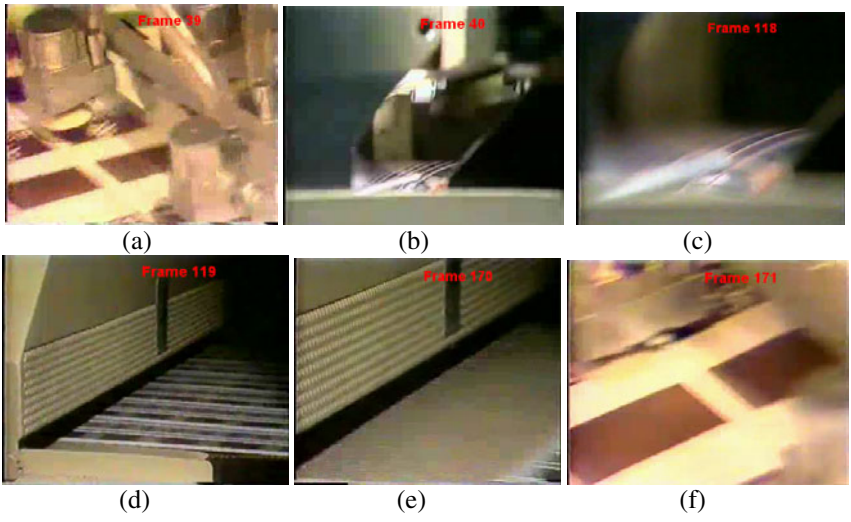

Fig. 2. Detected shot boundary frames

4 Detection Algorithm of Gradual Shot

Because of gradual shot has various types and complicated process, therefore, the detection algorithm is not as simple as cut shot. So, although the detection algorithms of cut shot have already mature, but the gradual shot detection algorithms is not mature, and it is a hard and focus of research in the field of shot detection.

4.1 Conventional Detection Algorithms of Gradual shot

4.1.1 Double-Threshold Comparison

Generally, double-threshold will set two thresholds T_L and T_H, and $T_L < T_H$, if frame difference of two adjacent images is bigger than T_L and smaller than T_H, then, the current frame is marked as gradual start position, from this position, we start to calculate interval frame difference, if frame difference of interval L is bigger than T_H, gradual shot is over [9].

4.1.2 Method Based-on Model

Method based-on model is using prior knowledge of editor of gradual shot to building model, and detection is complemented by the model. In fact, it is anti-process of video editing [10].

4.2 Improved Double-Threshold Comparison Based-on HSV Color Model

This method is based-on HSV color model using improved double-threshold comparison of hue histogram. About HSV color model, its content is already introduced in Section 2.1.

A large number experiments show that, no matter what type of gradual shot, the frame differences of hue histogram almost have the common feature as shown in Fig.3. False start position of gradual shot is caused by camera jitter and other reasons.

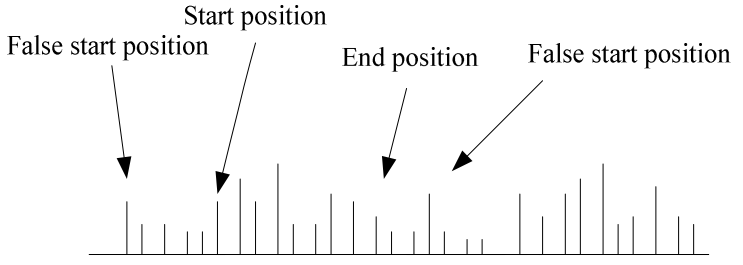

Fig. 3. Simulation diagram of frame difference features of gradual shot

We can know from Fig.3, because of false start position, there must be some false detections and missed detections of gradual shot. For that, this paper proposes an improved double-threshold comparison, specifically described as follows:

Pre-set two thresholds T_L and T_H, and $T_L < T_H$, if frame difference of adjacent two frames is bigger than T_L and smaller than T_H, the current frame can be marked as impossible start position, if the following three or four (it is an experience value) frame difference are also smaller than T_L, then, the marked frame is not the real start position of gradual shot, it is false start position and should be given up, then re-looking for the real start position. After finding the real start position, from current frame beginning, the following frame differences are added, unit the sum is bigger than T_H that meaning the gradient is over, the following frame is belong to another shot. And if one frame difference is bigger than T_H, it is meaning that it is cut shot.

The experiments show that the above method is effective not only for the gradual shots but also for some special shots.

5 Conclusion

This paper analyzes the unique features of printing video, to avoid the impact of uneven illumination in the video capture process choosing hue histogram as the detection feature, and this method also has a certain tolerance with a slight movement of camera. In the boundary detection of gradual shot, because of identification of false start position, the boundary detection accuracy is improved greatly.

Acknowledgments. This paper is support by Beijing Higher Institute Research Center of Printing Equipment and the Funding Project for Academic Human Resources Development in Institutions of Higher Learning under the Jurisdiction of Beijing Municipality.

References

1. Feng, D.D., Siu, W.-C., Zhang, H.-J., Liu, X.-D.: Multimedia Information Retrieval and Management, pp. 26–39. Tsinghua University Press, Beijing (2009)
2. Zhang, Y.-J.: Image Engineering () Image Understanding, 2nd edn., pp. 383–396. Tsinghua University Press, Beijing (2008)
3. Tonomura, Y., Abe, S.: Content Oriented Visual Interface Using Video Icons for Visual Database Systems. Journal of Visual Languages and Computing, 183–198 (1990)
4. Nagasaka, A., Tanaka, Y.: Automatic Video Indexing and Full-video Search for Object Appearances. In: IFIP Working Conference on Visual Database Systems, Budapest, Hungary, pp. 113–127 (1991)
5. Zabhi, R., Miller, J., Mai, K.: A Feature-based Algorithm for Detecting and Classing Scene Breaks. In: Proc. ACM Multimedia, pp. 189–200 (1995)
6. Hanjialic, A.: Shot-boundary Detection: Unraveled and Resolved? IEEE Circuits and Systems for Video Technology, 90–105 (2002)
7. Lei, P., Xin, S.: An Improved Algorithm for Detecting Video Abrupt Chang. Digital TV and Digital Video (266), 14–16 (2004)
8. Sun, J.-D., Shan, Z.: Underlying Image Features Extraction and Retrieval Technology, pp. 49–53. Publishing House of Electronics Industry, Beijing (2009)
9. Zhu, A.-H., Lian, L.: The Technology of Shot Segmentation Content-based Video Retrieval. Journal of Information (3), 66–68 (2004)
10. Li, Z.-M., Yu, G.-B., Liu, Y.-J.: An Overview of Content-based Video Retrieval. Information Technology 22(7), 850–852 (2004)

Optical Flow Detection Algorithm and Application Based on Accelerated Function

Fu-Cheng You and Ying-Jie Liu

Information & Mechanical Engineering School, Beijing Institute of Graphic Communication, Beijing, 102600, China
youfucheng@bigc.edu.cn, liuyingjiea@hotmail.com

Abstract. A novel approach that integrates multigrid computation and Harris corner extraction is proposed for solving the problems of high complexity and low speed in conventional optical flow computation. Firstly, Harris corners are extracted from grabbed frame images of real-time video. Then corner images are generated on the basis of corner coordinates. Secondly, an efficient computational technique based on multigrid is adopted to optimize the optical flow estimation on the consecutive corner images. Therefore, real-time movement can be detected by optical flow vector field. After many experiments on videos with moving objects in different backgrounds and rates of frame grabbing, experimental results demonstrate the higher computational speed. This approach is applied to detect moving objects in real-time videos and the results are very encouraging. The approach aims at accelerating optical flow computation, also being robust to disturbance of complex background due to only adopting corner images.

Keywords: optical flow; multigrid computation; Harris corner; moving objects real-time detection.

1 Introduction

The efficient computation of optical flow is a prerequisite for a large number of applications, such as moving objects detection, real-time tracking and so on [1]. The key point to estimate optical flow is to solve linear or nonlinear equation systems. However, conventional solutions for optical flow estimation are often considered to be too slow for real-time applications. In particular, the computational costs for solving linear and nonlinear equation systems are regarded as too high.

Under this background, an approach that integrates multigrid computation and Harris corner extraction is proposed in the paper for solving the problems of high complexity and low speed in conventional optical flow computation. It is seen that the optical flow computed using multigrid algorithm enables faster computation of 2-D velocity field in image sequence. After many experiments with the proposed algorithm, optical flow computation on Harris corner image sequence via multigrid method displays higher speed and can meet with the real-time detecting applications. Moreover, the approach is robust to disturbance of complex background of the video

D. Zeng (Ed.): Future Intelligent Information Systems, LNEE 86, pp. 599–606.
springerlink.com © Springer-Verlag Berlin Heidelberg 2011

because Harris corner images reduce the computation during the solution of optical flow. Experimental results are provided to demonstrate the effectiveness and efficiency of the proposed approach.

2 Work Flow of Accelerated Optical Flow Detection

Work flow of optical flow detection based on accelerated function is shown in Fig. 1. Acquire image sequence from real-time video firstly. Then image sequence is transferred from frame grabber into computer memory. Secondly, color space of image sequence needs to be transferred to gray level. Then detect and extract Harris corners from image sequence. Therefore corner image sequence is generated. Thirdly, compute optical flow via multigrid method. Then optical flow vector field can detect moving objects in real-time videos.

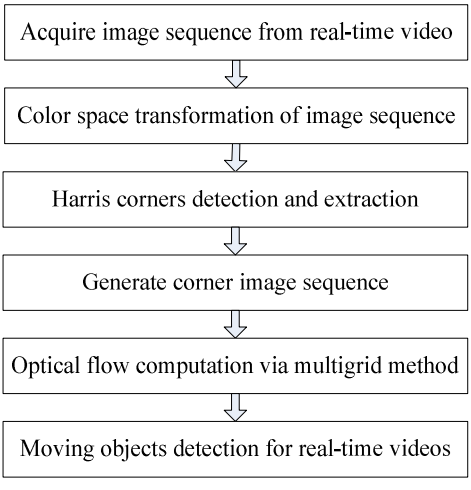

Fig. 1. Work Flow of Accelerated Optical Flow Detection

3 Harris Corner Extraction

Interest point extraction is significant. Corner pixels are typical interest points in image. One of the most commonly used interest point detectors is the Harris corner detector in computer vision applications. Harris corner has the advantages of simple computation and easy implementation.

3.1 Pre-process on Image Sequence

Color space of image sequence needs to be transferred to gray level for the purpose of Harris corner extraction and further optical flow estimation. The transformation is implemented by (1), where Y stands for the main gray information of an image [2].

$$Y = 0.299 \times R + 0.587 \times G + 0.114 \times B \tag{1}$$

3.2 Harris Corner Extraction

Harris corner extraction is based on the autocorrelation matrix of image gradients [3]. Harris corner detector is based upon the smoothed matrix, $M(x, y)$, shown by (**2**), where $I_{x,c}$ and $I_{y,c}$ are the first derivatives of an image, which denote the gradients in horizontal and vertical directions, and G stands for a Gaussian smoothing function.

$$M(x, y) = G * \begin{bmatrix} \sum_{c=1}^{n} I_{x,c}{}^2 & \sum_{c=1}^{n} I_{x,c} I_{y,c} \\ \sum_{c=1}^{n} I_{x,c} I_{y,c} & \sum_{c=1}^{n} I_{y,c}{}^2 \end{bmatrix} \tag{2}$$

Then corner response function of Harris corner detector is based on the determinant and trace of the autocorrelation matrix as shown in (3), where α is a positive constant controlling corner sensitivity of detector.

$$R_{harris}(x, y) = \det(M) - \alpha \cdot [trace(M)]^2 \tag{3}$$

After calculating the corner response for all pixels in an image, non-maxima suppression is used to get the corner points, whose coordinates are as output.

3.3 Corner Image Generation

Corner image sequence is then generated based on above corner points in order to reduce the computation of optical flow.

4 Optical Flow Estimation Based on Multigrid Computation

To ensure that the nonlinear equation systems can be solved efficiently, the bidirectional multigrid method can be used [4]. The multigrid idea is based on two principles: error smoothing and coarse grid correction. They form a multigrid algorithm to solve linear Euler-Lagrange equation, which is changed from constraint equation of optical flow. Accelerated function is implemented by multigrid solver to ensure an efficient solution of partial differential equations with the advantage of fast convergence. The usual Gauss-Seidel iteration has a remarkable smoothing effect on the error [5].

When discretized, the corresponding Euler-Lagrange equations form a linear system of equations [6]. The algorithm is based on the minimization of an energy function (4) that contains gradient constancy assumption, which has the advantage of being invariant to additive global illumination changes [7].

$$E(v) = \int_{\Omega} \psi(|I(x+v,t+1) - I(x,t)|^2 + \alpha |\nabla I(x+v,t+1) - \nabla I(x,t)|^2) dx \tag{4}$$

For purpose of clarity, reformulate the linear equation systems as shown in (5) [8]. Here A^k denotes equation matrix and x^k stands for the accurate result.

$$A^k x^k = f^k \tag{5}$$

Step 1. Compute the defect. Multigrid method starts with a basic iterative solver by performing several iterations, where high frequencies of the error are removed. If the result after these iterations is denoted by $\tilde{x}^k$, the error e^k is given by (6).

$$e^k = x^k - \tilde{x}^k \tag{6}$$

Step 2. Restrict the defect (Fine-to-coarse transfer). Evidently, find e^k in order to correct the approximation $\tilde{x}^k$. Although e^k cannot be computed directly, the linearity of A^k allows its computation via (7), where r^k is called the residual.

$$A^k e^k = A^k (x^k - \tilde{x}^k) = A^k x^k - A^k \tilde{x}^k = f^k - A^k \tilde{x}^k = r^k \tag{7}$$

Since high frequencies of the error have already been removed, computation can be accelerated by solving equation system at a coarser resolution with grid size K in (8).

$$A^k x^k = f^k \rightarrow A^K e^K = r^K \tag{8}$$

Step 3. Interpolate the correction (Coarse-to-fine transfer) and compute new approximation. After solving the residual on the coarse grid, the solution is transferred back to the fine grid. Then approximation is corrected by the computed error, as shown in (9).

$$\tilde{x}_{new}^{\ k} = e^k + \tilde{x}^k \tag{9}$$

Multigrid computation has good approximated accuracy and fast convergence for function and gratitude. It can overcome iterative errors on different scales and reduce iterative times to a great extent. Therefore the iterative process is converged faster than other approaches.

5 Experiments and Results Analysis

Two videos are selected from experiments in the paper as shown in Fig. 2, which are acquired from real-time surveillance system, displaying the effectiveness of accelerated optical flow detection. As shown in Fig. 2, simple background of video (a) has less disturbances, while complex background of video (b) has more disturbances.

The numbers at the top-left in below figures denote grabbed frame number in image sequence. Size of the two video images is 320×240 pixels and the sample rate is 5 and 10 frames per second respectively.

(a) Simple Background (b) Complex Background

Fig. 2. Real-time Videos with Moving Objects

5.1 Harris Corner Extraction

According to the size of 320×240 pixels for two videos, the region of 10×10 pixels is confirmed to generate corner image sequence. Thus less information of gray scale and higher speed of optical flow detection can be achieved. After gray image transformation, Harris corners are extracted from every image from sequence respectively, and then corner image sequence is generated as shown in Fig. 3.

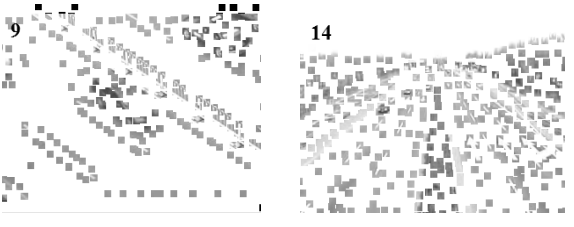

(a) Simple Background (b) Complex Background

Fig. 3. Corner Images Generated from Real-timeVideos

5.2 Optical Flow Estimation Based on Accelerated Algorithm

Experiments are implemented in different rates of frame grabbing on real-time videos and different backgrounds respectively. Different frames are grabbed from real-time videos, and results of optical flow fields are also displayed below. Regions of moving objects are detected and marked by rectangle in the frames.

Detect moving objects for video (a) with simple background in grabbing rate of 5 frames per second (5 f/s). Output is shown in Fig. 4.

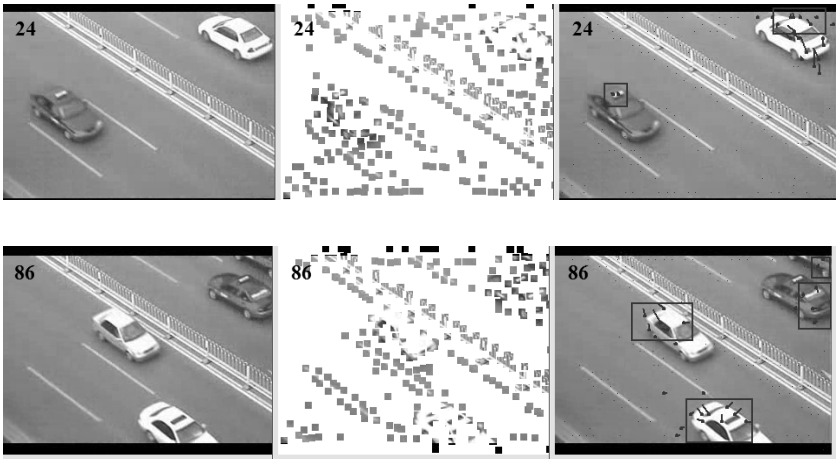

(a) Original gray image (b) Corner image (c) Detected results

Fig. 4. Output of Moving Objects in Video with Simple Background (5 f/s)

Detect moving objects for video (a) with simple background in grabbing rate of 10 frames per second (10 f/s). Output is shown in Fig. 5.

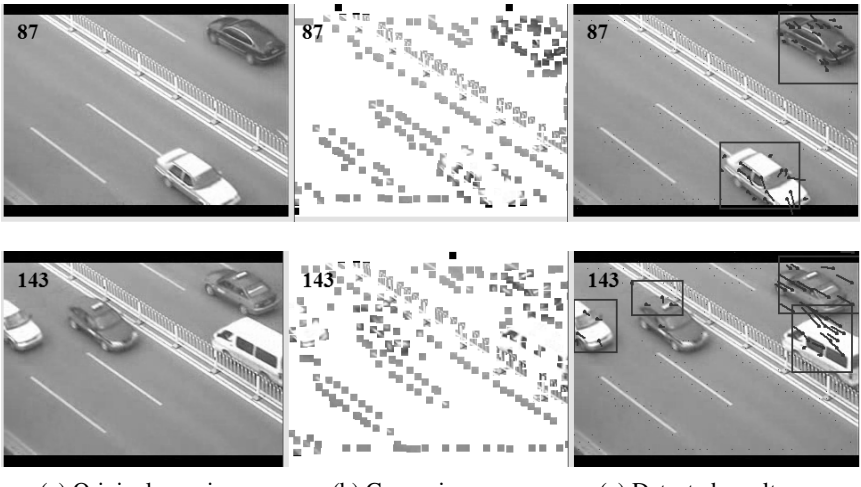

(a) Original gray image (b) Corner image (c) Detected results

Fig. 5. Output of Moving Objects in Video with Simple Background (10 f/s)

It is obvious that video (b) of Fig. 2 exhibits highly dynamic background, illumination change and low contrast. Detect moving objects for video (b) with complex background in grabbing rate of 5 frames per second (5 f/s). Output is shown in Fig. 6.

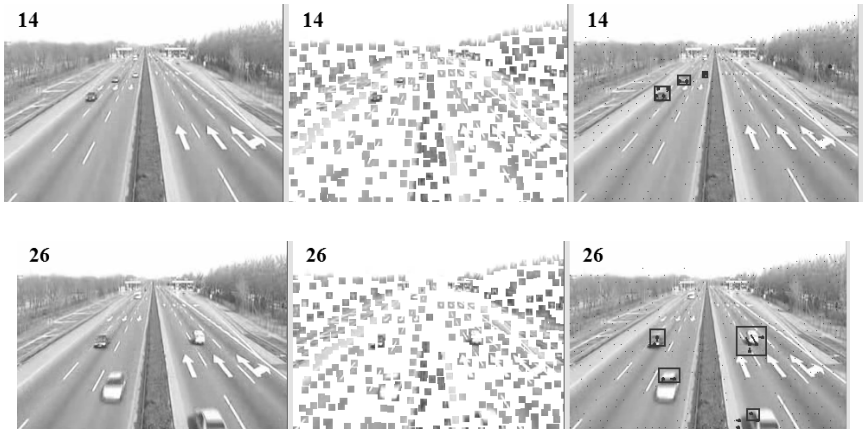

(a) Original gray image (b) Corner image (c) Detected results

Fig. 6. Output of Moving Objects in Video with Complex Background (5 f/s)

Detect moving objects for video (b) with complex background in grabbing rate of 10 frames per second (10 f/s). Output is shown in Fig. 7.

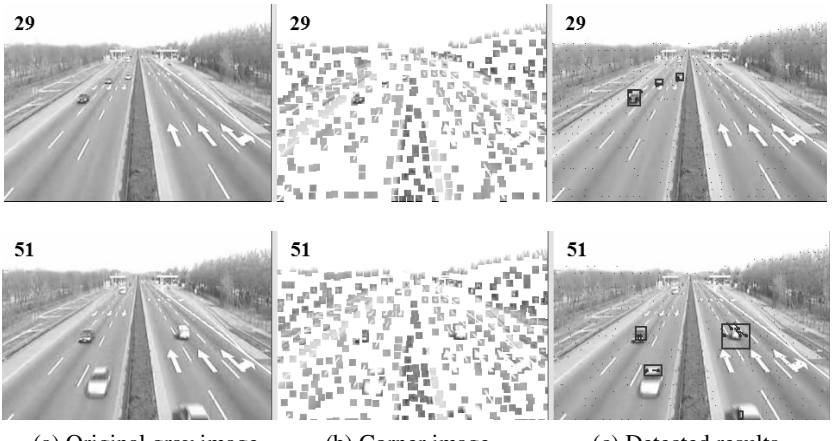

(a) Original gray image (b) Corner image (c) Detected results

Fig. 7. Output of Moving Objects in Video with Complex Background (10 f/s)

Relative experimental data for video sequence processing are shown in Table 1.

Table 1. Experimental data for different video sequence (Unit: frames per second)

Video background	(a) Simple		(b) Complex	
Rate of real-time frame grabbing	5	10	5	10
Rate of frame processing with acceleration	9.34	9.12	9.93	10.18

From experimental data, it can be concluded that the proposed accelerated algorithm of optical flow computation in the paper can meet with the needs of real-time motion detection. Therefore the advantages of optical flow detection can be applied in real-time detection of moving objects.

6 Conclusion

In this paper, an accelerated algorithm that integrates multigrid computation and Harris corner extraction is proposed. The effectiveness of the proposed algorithm for real-time motion detection is also demonstrated. Due to the desirable features of accelerated optical flow computation, the proposed approach is efficient and suitable for moving objects detection in real-time video surveillance.

Acknowledgement

This paper is supported by Beijing Higher Institute Research Centre of Printing Equipment and the Funding Project for Academic Human Resources Development in Institutions of Higher Learning under the Jurisdiction of Beijing Municipality.

References

1. Frey, D., Ulrich, M., Hinz, S.: Evaluation of Efficient Methods for Optical Flow Computation. Photogrammetrie Fernerkundung Geoinformation 1, 5–16 (2010)
2. Jia, Y.: Machine Vision, pp. 151–155. Scientific Press, Beijing (2000)
3. Harris, C., Stephens, M.: A combined corner and edge detector. In: Proceedings of the 4th Alvey Vision Conference, pp. 147–151 (1988)
4. Bruhn, A., Weickert, J., Feddern, C., Kohlberger, T., Schnörr, C.: Variational Optical Flow Computation in Real Time. IEEE Transactions on Image Processing 14(5), 608–615 (2005)
5. Trottenberg, U., Oosterlee, C., Schüller, A.: Multigrid, pp. 28–40. Academic Press, Inc., San Diego (2000)
6. Mitiche, A., Mansouri, A.R.: On convergence of the Horn and Schunck optical-flow estimation method. IEEE Trans. Image Process 13(6), 848–852 (2002)
7. Brox, T., Bruhn, A., Papenberg, N., Weickert, J.: High Accuracy Optical Flow Estimation Based on a Theory for Warping. In: Pajdla, T., Matas, J. (eds.) ECCV 2004. LNCS, vol. 3024, pp. 25–36. Springer, Heidelberg (2004)
8. Bruhn, A., Weickert, J., Kohlberger, T., Schnörr, C.: A Multigrid Platform for Real-Time Motion Computation with Discontinuity-Preserving Variational Methods. International Journal of Computer Vision 70(3), 257–277 (2006)

A 'Frequency Blind' Method for Symbol Rate Estimation

Saurav Zaman Khan[1], Ahmed Mostayed[2], and Md. Ekramul Kabir[3]

[1] Department of Biomedical Engineering, Kyung Hee University, Suwon, Republic of Korea
saurav.zaman@khu.ac.kr
[2] Department of Mechanical Engineering, University of Western Australia, Perth, WA, Australia
mostayed@mech.uwa.edu.au
[3] Department of Applied Physics, Electronic and Communication Engineering, University of Dhaka, Dhaka, Bangladesh

Abstract. Estimation of the symbol rate has important applications in receiver synchronization for symbol time recovery. In this paper the problem is investigated using Smoothen Non-Linear Energy Operator (SNEO). Unlike wavelet based methods in [2], [3], [4] the proposed algorithm is completely blind because it does not require any priory information regarding the modulation type or carrier frequency. Moreover, the proposed algorithm is computationally efficient. Simulation results also proof the effectiveness of the proposed algorithm.

Keywords: Digital Modulation, Symbol Rate, Non-linear Energy Operator, SNEO.

1 Introduction

Blind estimation of unknown channel parameters is an open problem to the engineers and scientist in non-cooperative communication systems. In modern electronic warfare it is important to monitor the hostile signals [1] which are required to decode before jamming. Therefore, to demodulate the unknown received signals two priory information is required: the unknown modulation type which refers to the Automatic Modulation Identification problem and estimation of the symbol duration/rate for receiver synchronization.

In [2], [3] a Wavelet based symbol rate estimation method is proposed utilizing the fact that Haar wavelet can detect phase changes for M-ary PSK signals. Xu et al. [4] showed that methods proposed in [2] and [3] have major drawbacks strongly depending on the carrier frequency and therefore worked on base-band signals only. Moreover, they extended their method for other modulation types. Gao et al. [5] proposed an algorithm called 'MORAL', which is based on Morlet wavelet transform and autocorrelation. They have reported higher estimation precision approaching more closely to Cramer-Rao lower bound. In [6] a cyclic autocorrelation based method was proposed to estimate symbol rate for M-ary PSK signals by maximizing the autocorrelation function. In [7] another autocorrelation based algorithm is proposed which works on base-band signals and the symbol rate estimated by method of least squares. However, they have shown simulation results only for ASK signals. A Direct Frequency Estimation (DFM) based algorithm is proposed in [8] for PSK and QAM signal.

D. Zeng (Ed.): Future Intelligent Information Systems, LNEE 86, pp. 607–614.
springerlink.com © Springer-Verlag Berlin Heidelberg 2011

This paper proposes an algorithm based on Non-Linear Energy Operator (NEO) for symbol rate estimation. The main attraction of NEO is its simple structure and low computational complexity. The proposed method is 'Frequency Blind' as it does not require any carrier frequency removal [4]. The idea of the proposed method is to track down the energy of the modulated signal. Since discontinuity occurs at the vicinity of the symbol transition, a delta like spike is generated which is further processed to estimate the symbol duration.

The paper is organized as follows: In section II preliminaries on non-linear energy operator is presented. Signal model along with the algorithm and smoothing operation for reduction of the interfering terms is described in section III. Finally performance analysis and conclusion is presented in the section IV and V respectively.

2 Preliminaries

The non-linear energy operator (NEO) for a continuous real valued signal, $x(t)$, which tracks down the energy of the signal is defined as [9],

$$\psi(x) = (\dot{x})^2 - x\ddot{x} \quad . \tag{1}$$

According to [10] for complex valued signal this definition can be extended to

$$\psi_c(x) = \dot{x}\dot{x}^* - \frac{1}{2}(x^*\ddot{x} + x\ddot{x}^*) \quad . \tag{2}$$

This can be further simplified to,

$$\psi_c(x) = \psi_c(x_r) + \psi_c(x_i) \tag{3}$$

where x_r and x_i are the real and complex components of the signal respectively.

NEO possesses many important properties [11]. Among these properties the multiplication and differentiation property is used in this paper to derive the algorithm.

The Discrete NEO is defined by approximating the differentiation with finite difference

$$\psi_d[x(n)] = x^2(n) - x(n-1)x(n+1) \quad . \tag{4}$$

2.1 Multiplication Property

$$\psi(gh) = h^2\psi(g) + g^2\psi(h) \quad . \tag{5}$$

2.2 Differentiation Property

$$\dot{\psi}(x) = \psi(x\dot{x}) = \dot{x}\ddot{x} - x\dddot{x} \quad . \tag{6}$$

3 Proposed Algorithm

3.1 Signal Model

In this article the signals are modelled as follows,

$$s(t) = x(t) + \mu(t) \quad . \tag{7}$$

where $x(t)$ is assumed to be the analytic form (obtained from Hilbert transform) of receiver signal. Therefore,

$$x(t) = a(t)\exp(j\theta(t)) \tag{8}$$

And $\mu(t)$ is zero mean White Gaussian noise with variance σ_μ .

3.2 Derivation of the Algorithm

Using the simplified definition of equation 3 and applying the multiplication property of equation 5, for the analytical signal $x(t)$ (in equation 8) we can prove,

$$\psi[x(t)] = 2[a(t)\dot{\theta}(t)]^2 + \psi[a(t)] \quad . \tag{9}$$

Now taking the derivative of the equation 9 and using the differentiation property of equation 6,

$$\psi(x\dot{x}) = 4a(t)\dot{\theta}(t)[\dot{a}(t)\dot{\theta}(t) + a(t)\ddot{\theta}(t)] + \psi(a\dot{a})] \tag{10}$$

For an M-PSK signal with phase angle

$$\theta_{PSK} = \omega_c t + \frac{2\pi k}{M}[u(t,n) - u(t,n-1)] \qquad k = 0,1,2,\cdots\cdots, M-1$$

$$\psi_{PSK}(x\dot{x}) = \frac{8\pi^2 Ak}{M}[\delta'(t,n) - \delta'(t,n-1)] \times [\omega_c + \frac{2\pi k}{M}\{\delta(t,n) - \delta(t,n-1)\}] . \tag{11}$$

For an M-FSK signal with phase angle

$$\theta_{FSK} = \omega_c t + \Delta\omega_k[u(t,n) - u(t,n-1)]t + \alpha \qquad k = \pm 1, \pm 2, \pm 3, \cdots\cdots, \pm(\frac{M}{2} - 1)$$

$$\begin{aligned}\psi_{FSK}(x\dot{x}) = {} & 4A^2\Delta\omega_k\omega_c[\delta(t,n) - \delta(t,n-1) + nT_s\delta'(t,n) - (n-1)T_s\delta'(t,n-1)] \\ & + 4A^2\Delta\omega_k^2[u(t,n) - u(t,n-1) + nT_s\delta(t,n) - (n-1)T_s\delta(t,n-1)] \\ & \times[\delta(t,n) - \delta(t,n-1) + nT_s\delta'(t,n) - (n-1)T_s\delta'(t,n-1)]\end{aligned} . \tag{12}$$

For an M-ASK signal with amplitude

$$a_{ASK} = A_k[u(t,n) - u(t,n-1)] \qquad A_k = \pm 1, \pm 2, \pm 3, \cdots\cdots, \pm(M-1)$$

$$\psi_{ASK}(x\dot{x}) = 2A_k^2\omega_c^2\delta(t,n-1) + A_k^2\{\delta(t,n)-\delta(t,n-1)\}\{\delta'(t,n)-\delta'(t,n-1)\} - A_k^2\{u(t,n)-u(t,n-1)\}\{\delta''(t,n)-\delta''(t,n-1)\}] \quad . \quad (13)$$

For an M-QAM signal with amplitude $a_{QAM} = A_k[u(t,n)-u(t,n-1)]$ and phase $\theta_{QAM} = \omega_c t + \varphi_k[u(t,n)-u(t,n-1)]$

$$\begin{aligned}\psi_{QAM}(x\dot{x}) = 2A_k^2[&\omega_c\{u(t,n)-u(t,n-1)\}+\frac{1}{2}\varphi_k\delta(t,n-1)] \\ &\times[\omega_c\{\delta(t,n)-\delta(t,n-1)\}+\frac{1}{2}\varphi_k\delta'(t,n-1)]+ \\ &A_k^2\{\delta(t,n)-\delta(t,n-1)\}\{\delta'(t,n)-\delta'(t,n-1)\} \\ &-\{u(t,n)-u(t,n-1)\}\{\delta''(t,n)-\delta''(t,n-1)\}]\end{aligned} \quad (14)$$

For all four cases described above, $u(t,n) := u(t-nT_s)$, $\delta(t,n) := \delta(t-nT_s)$, $u(.)$ s the Heaviside Step Function and $\delta(.)$ id Dirac-Delta function. From equation 11-14 it is clear that during the transition of the symbol a spike like signal is generated and within the symbol duration the energy is constant. To estimate the symbol duration magnitude square of the Fast Fourier Transform (FFT) is taken. Symbol rate is estimated either from the difference of two consecutive peak locations or from the location of the first peak.

3.3 Signals with Noise

From the previous section it is clear that the accuracy of symbol rate estimation is mainly depends on the efficient spike detection. It was shown in [12] that to enhance the spike from the background signal it is required to compute $E[\psi(s)]$. To estimate $E[\psi(s)]$ a time domain windowing method was proposed in [12] which is known as smoothen non-linear energy operator (SNEO). Mathematically,

$$\psi_s(s\dot{s}) = \psi(s\dot{s}) \otimes w(t) \quad . \quad (15)$$

To compute the symbol duration FFT of $|\psi_s[s\dot{s}]|$ is calculated. The symbol duration T_s can be estimated from the location of the highest peak. The time domain windowing is equivalent to low pass FIR filtering. To emphasize the peak position at the frequency domain; a narrow band low pass filter is desirable which in turns increase the window length in time domain, hence reduce the time resolution. Therefore, the window type and width of the window are required to optimize to achieve sufficient reduction of interference without losing much of its time resolution. In this article all simulation results are obtained using a 15 point Gaussian window as it provides the best estimation results for all modulation cases.

Fig. 2 shows the results for a random bit stream of QPSK signal at SNR = 15dB. A 15 point long Gaussian window is used for smoothing purpose. The highest peak is located at the inverse of the symbol duration.

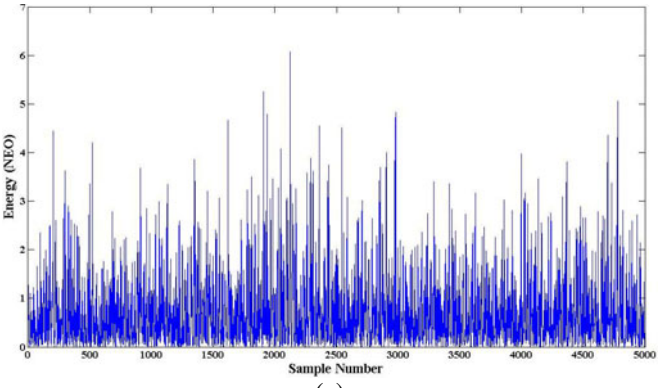

(a)

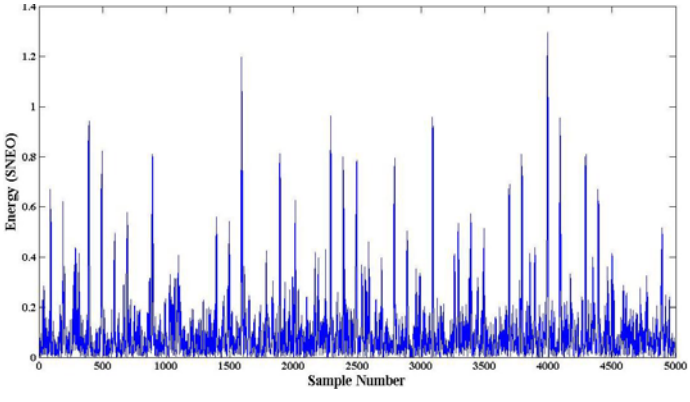

(b)

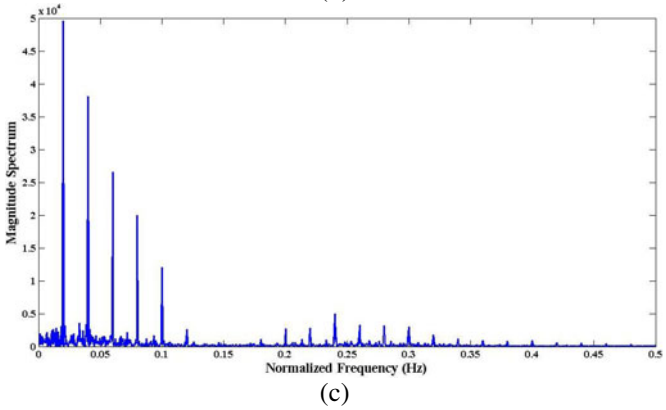

(c)

Fig. 1. (a) $\psi(s\dot{s})$ (b) $\psi_s(s\dot{s})$ and (c) $\left|FFT\right|^2$

4 Performance

To evaluate the performance of the proposed method percentage of correct estimation rate for different modulation type and different values of SNR is plotted in figure 3(a) and 3(b). In this experiment modulated parameter is set at f_c / f_s whereas, f_c, f_s are the sampling and carrier frequency respectively. Moreover, to reduce the interference of noise 15 point long Gaussian window is used. Percentage of correct estimation is calculated from 100 experiments for each type of modulated signals. If the estimation error is within 1% of the true values, then it is called a correct estimation. It can be found that for modulation types QPSK and 4-ASK the proposed method is valid for $SNR \geq 7dB$. For the 8-FSK signals this threshold is at $SNR \geq 4dB$ but for the 4-QAM signal this algorithm is valid at $SNR \geq 9dB$. For 4-FSK and BPSK the proposed system performed well at around $SNR \geq 3dB$ Table 1 shows the comparison of the proposed method with other major algorithms.

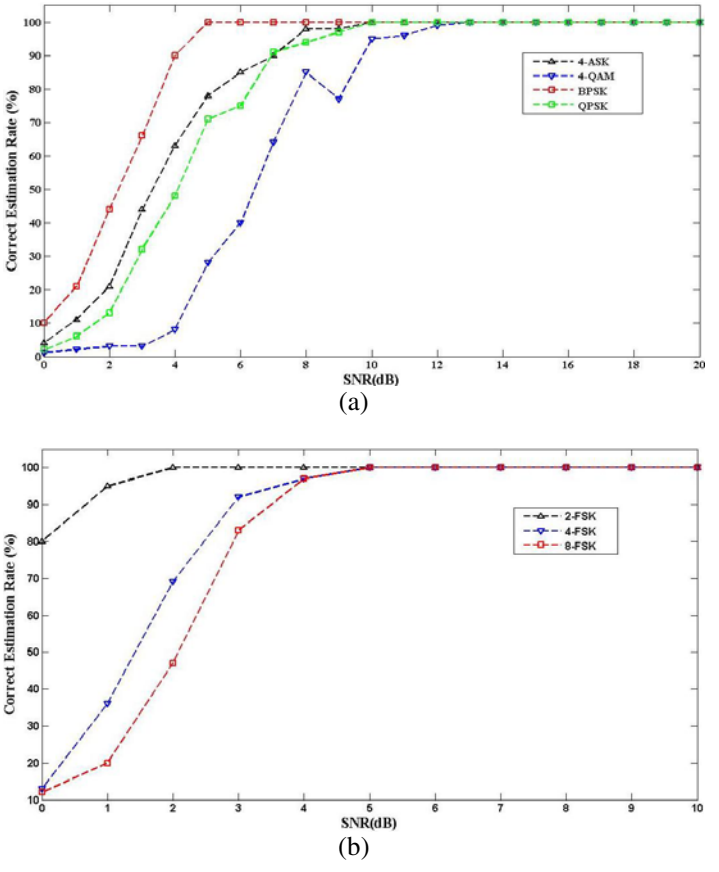

Fig. 2. Performance of the proposed method in noise. (a) ASK, PSK and QAM. (b) FSK

Table 1. Comparison of the proposed algorithm with other algorithms

Algorithm	Method	Modulation Type	Carrier frequency removal	SNR
Ho et al. [2]	Single-scale Haar Wavelet	M-ary PSK	N	-
Chan et al. [3]	Multi-scale Haar Wavelet	M-ary PSK	N	> 7 db
Jun et al. [4]	Multi-scale Haar Wavelet	PAM, QAM, FSK, PSK	Y	>4 db
MORAL [5]	Morlet Wavelet + Autocorrela -tion	M-ary PSK	Estimation of carrier frequency required to determine scale	>2 db
Yin et al. [6]	Autocorrela -tion	M-ary PSK	N	-
Chan et al. [7]	Autocorrela -tion	ASK	Y	Error less than 3% between 0-10 db
Barnes et al. [8]	DFE	M-ary PSK, QAM	N	>8 db
Proposed	SNEO	M-ary PAM, QAM, FSK, PSK	N	FSK: >4 db PSK,QAM: > 10 db

5 Conclusion

A blind symbol rate estimation method is proposed. A smoothen non-linear energy operator is used instead of non-liner energy operator directly, because of its weak anti noise ability. Finally, symbol rate is estimated from the FFT of the output spectra of smoothen non-linear energy operator. Experiment result shows that the algorithm is valid at SNR 10 dB within 1% error limit.

References

1. Dobre, O.A., Abdi, A., Bar-Ness, Y., Su, W.: Blind modulation classification: a concept whose time has come. In: Proc. IEEE Sarnoff Symposium, Princeton, US, pp. 223–228 (2005)
2. Ho, K.C., Prokopiw, W., Chan, Y.T.: Modulation Identification of Digital Signals by the Wavelet Transform. IEE Proceedings – Radar, Sonar and Navigation 147(4), 169–176 (2000)

3. Chan, Y.T., Plews, J.W., Ho, K.C.: Symbol Rate Estimation by the Wavelet Transform. In: IEEE International Symposium on Circuits and Systems, pp. 177–180 (1997)
4. Xu, J., Wang, F.-P., Wang, Z.-J.: The Improvement of Symbol Rate Estimation by the Wavelet Transform. In: ICCCS 2005 (2005)
5. Gao, Y., Li, M., Huang, Z., Lu, J.: A symbol rate estimation algorithm based on Morlet wavelet transform and autocorrelation. In: YC-ICT 2009, Beijing, pp. 239–242 (2009)
6. Yin, W., Wang, K.: A new method to symbol rate estimation of MPSK signals. In: Congress on Image and Signal Processing (CISP 2008), China, pp. 394–398 (2008)
7. Chan, Y.T., Lee, B.H., Inkol, R., Chan, F.: Estimation of symbol rate from the autocorrelation function. In: Canadian Conference on Electrical and Computer Engineering (CCECE 2009), pp. 547–550 (2009)
8. Barnes, W.J., LaSorte, N., Rafai, H., Yeary, M.B.: Symbol rate classification of PSK/QAM signals using direct frequency estimators. In: Instrumentation and Measurement Technology Conference (I2MTC 2009), Singapore, pp. 943–946 (2009)
9. Kaiser, J.F.: On a Simple Algorithm to Calculate the Energy of a Signal. In: Proc. IEE International Conference Acoustic Speech and Signal Processing, Albuquerque, NM, pp. 381–384 (1990)
10. Hamila, R., Astola, J., Cheikh, F.A., Gabbouj, M., Renfors, M.: Teager Energy and Ambiguity Function. IEEE Transaction on Signal Processing 47(1), 260–262 (1999)
11. Kaiser, J.F.: Some Useful Properties of Teager's Energy Operators. In: Proc. IEEE International Conference Acoustic Speech and Signal Processing, Minneapolis, MN, vol. 3, pp. 149–152 (1993)
12. Mukhopadhyay, S., Ray, G.C.: A New Interpretation of Non-Linear Energy Operator and Its Efficiency in Spike Detection. IEEE Trans. on Biomedical Engineering 45(2), 180–187 (1998)

Determination of Fuse Characteristic for a Larger Coordinated Area between Fuse and Recloser Due to Distributed Generation

A. Mosaddegh and A. Kazemi

Department of Electrical Engineering, Iran University of Science and Technology,
Alqadir, Square, Narmak, Tehran, Iran
Abolfazl_mosaddegh@elec.iust.ac.ir,
Kazemi@iust.ac.ir

Abstract. Nowadays distributed generation (DG) plays an important role in power networks such as reducing line losses, increasing the reliability of systems and so on. Because of the miscoordination between fuse and recloser due to presence of DG, it is more important to determine the fuse characteristic properly. This paper proposes a new method to determine fuse characteristic to have a wider coordinated area between fuse-recloser. The test system RBTS bus 2 is chosen as a distributed test system. The results show that the proposed method is efficient enough to make a larger coordinated area between fuse and recloser and the coordination in presence of DG for higher fault currents is maintained.

Keywords: Distributed Generation (DG), distribution system, fuse, recloser, miscoordination.

1 Introduction

One of the most important and effective methods for feeder protection in distribution systems is the traditional protection methods like fuse-recloser protection [1]-[3]. Although the technology improvements have caused to use microprocessor relays in transmission networks, fuse still has not lost its creditability. The importance of fuse presence is more when it can be seen that the issue of fuse reliability, not only eliminates the fuses, but also it emphasizes to remain the fuses in lateral feeders. The fuse saving schedule can be done in the presence of recloser and by using recloser fast-mode operation, fuse can be protected before its operation. The fast -mode recloser can prevent permanent interruption in the desired lateral feeders.

On the other hand, nowadays, presence of distributed generation (DG) in electrical networks is essential and not only it enhances the power quality in networks [4], but also it is the main source of electricity in remote areas. Interrupting in a part of feeder, DG can generate required electricity and prevent any interruption in that isolated area. For example, in sensitive areas, DG can be as a backup generation and it increases reliability in the supported district [5]. In a system whose lateral feeders are protected by fuses and backup protection is done by recloser, if the presence of DG because of

D. Zeng (Ed.): Future Intelligent Information Systems, LNEE 86, pp. 615–622.
springerlink.com © Springer-Verlag Berlin Heidelberg 2011

some reasons like a need for backup generation or an increase the electricity generation is felt, the miscoordination between fuse and recloser may be occurred. In such situation, because the current flowing through the fuse is derived fro m the DG - in addition to the network -, it increases in amount (in comparison with no DG presence) and the fuse that should operate after fast-mode recloser, loses its coordination with recloser and operates sooner than recloser operation. If fuse operates, there is no electricity in lateral feeders and because the fuse is the protection device which its operation is equal to its loss, replacement is necessary. Therefore as the time will be need for fuse replacement, the lateral feeder must remain without electricity. This problem reduces the reliability indices in mentioned distribution network [6]. Albeit, sometimes the fuse operation before fast-mode recloser operation is justified such as whenever there is no sensitivity to power outage for users (such as residential users) or while power outage is important for the security of consumptions. One of these proposed methods in this case is to make recoordination between fuse and recloser and in this case, the settings of the entire network's fuses and reclosers in presence of DG have to be changed. Another group of researchers had believed in the determination of a threshold for DG [7]. By this threshold, the fuse-recloser remains coordinated. The other ones had proposed a schedule of DG outage fro m the network in the fault situation to maintain the coordinated area [8]. Due to possibility of no disconnection of DG in the desired time and hence instability in the network, usually experts refuse to do that. This problem is mo re considerable when the DG penetration is high and disconnecting of the DG is undesirable.

In this paper, considering all mentioned cases, it has been tried that in the case of presence of no DG, fuses should be chosen so that in the wider range of current, the coordination between fuse and recloser is kept. Even in the presence of DG, this will cause a better coordination and fuse and recloser encounter with the problem of miscoordination with less intensity.

To begin with, the section 2, in brief, discusses about the miscoordination between fuse and recloser. The modeling of protection equipments and the problem of miscoordination between those devices are discussed. The fuse setting with a numerical example is shown in section 3. Finally, the conclusion is drawn in section 4.

2 Miscoordination between Fuse and Recloser

2.1 Modeling Protection Devices

Fig. 1 illustrates a typical feeder in a distribution networks with protection devices to protect the feeder [4]. Fig. 2 indicates that how the protection devices operate in time domain and how they coordinate with each other is indicated typically [4], [9].

As can be seen in Fig. 2, the available protective devices are circuit breaker (CB), recloser and lateral fuses that are in the downstream side of recloser. The main function of recloser is to prevent lateral fuses from blowing up and to operate when the temporary faults occurred. Fuse should operate when permanent faults occurred and meanwhile the temporary faults should not affect its performance and operation.

So, based on these equipments duties, the protection of fuse is concerned as an important and a serious issue. Because of the fuses that are located downstream the recloser must be protected, the recloser can be as a backup protection for those fuses.

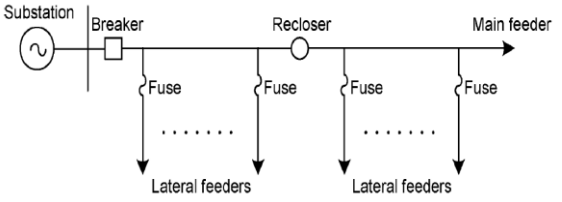

Fig. 1. Typical radial distribution feeder

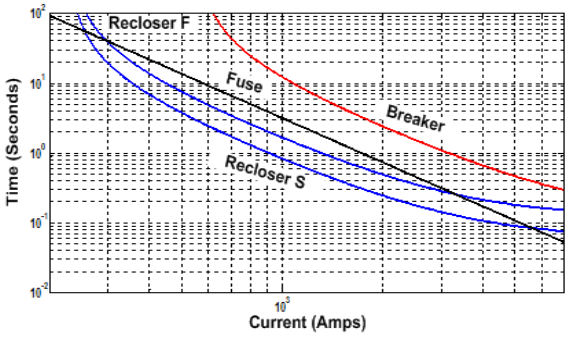

Fig. 2. Operating curves of the breaker, recloser, and fuse

The circuit breaker duty is to operate when the faults occurred in front of the recloser. The mathematical equations for modeling of equipments operation have been used. For circuit breaker and recloser, it can be said that the current inversely related to the time and therefore, the following equation can be applied for them [9]:

$$t(I) = TD\left[\frac{A}{M^{p} - 1} + B\right]. \quad (1)$$

where

t operating time of device;
I fault current seen by the device;
TD time dials etting;
M ratio of I / Ipi ckup (I_{pickup} is the re lay current s et point);
A, B, p Cons trains for particular curve characteristics.
I_{pickup} is also derived from the below equation:

$$I_{pi\ ckup} = OLF \times I_{nom}. \quad (2)$$

where
I_{nom} the nominal current;
OLF the overload factor that depends on the loads and the equipments which are protected.

In log-log space, it can be assumed a linear relationship between the current and the time for fuse. This equation can simplify the calculations and describes as follows [9]:

$$\log(t) = a \log(I) + b. \quad (3)$$

which a and b are obtained from curve fitting.

2.2 Problem of Miscoordination between Fuse and Recloser

One of the important problems in distribution lines is the line protection and the coordination between equipments in lines. Since most distribution lines have a longer lifetime than DG presence in power networks and the subject of DG presence and its effectiveness is undeniable, it should be thought any remedies to solve the protection problem of DG presence. As it was mentioned in part 2.1, according to Fig. 3, if only one DG installed in the network, the DG and the fuse totally can have four cases that can be compared with each other in the networks.

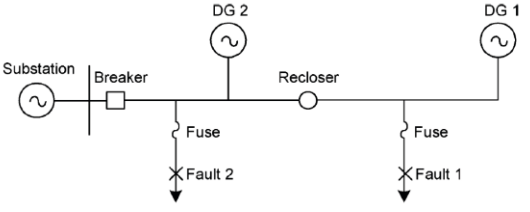

Fig. 3. Sample typical distribution system

In Table 1, the cases are counted briefly [4]. According to [4] and Table 1, only in cases 1 and 3, the coordination between fuse and recloser could be in trouble. Moreover, fuse can be selected so that it has the highest rate o f coordination with recloser for a larger current. In the next section, with a numerical example, the protection setting for fuses is implemented.

Table 1. Description of fault current seen by recloser and fuse

Case	DG source	Fault location	Description
1	DG 1	Fault 1	$I_{recloser} = I_{substation}$ and $I_{fuse} = I_{substation} + I_{DG}$
2	DG 1	Fault 2	$I_{recloser} = I_{DG}$ and $I_{fuse} = I_{substation} + I_{DG}$
3	DG 2	Fault 1	$I_{recloser} = I_{fuse} = I_{substation} + I_{DG}$
4	DG 2	Fault 2	No $I_{recloser}$ and $I_{fuse} = I_{substation} + I_{DG}$

3 Numerical Example for Fuse Seting

Based on the miscoordination in case 1) and case 3) between fuse and recloser in section 2, this coordination must be mentioned more carefully. The test system is RBTS bus 2 which is shown in Fig. 4. In this case, based on the mathematical equation discussed in section 2, the protection setting for fuse, recloser and breaker is carried out. The DG source has the subtransient reactance of 20% and the value of the power factor is set to be 0.875 leading [9]. The parameters of A, B and p of (1) are

28.2, 0.1217 and 2 respectively. For circuit breaker and slow-mode recloser, the TD parameter is set to 1 while it is set to 0.5 for fast-mode recloser [9]. The values of the nominal and pickup current for breaker and recloser are presented in Table 2.

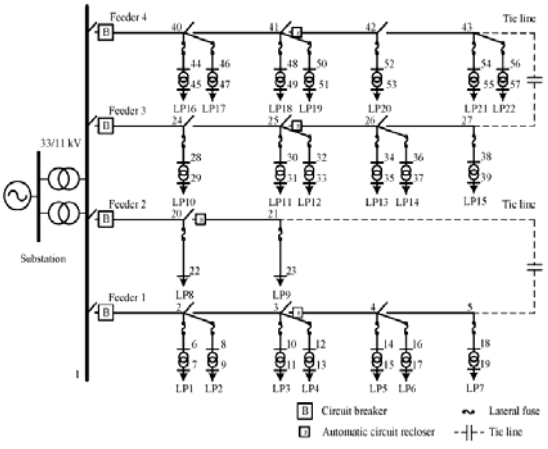

Fig. 4. Test system RBTS bus 2

Table 2. Nominal and pickup current of CBs and reclosers

Current (A)	Feeder 1	Feeder 2	Feeder 3	Feeder 4
Inom, breaker	365.72	253.53	310.77	341.45
Inom, recloser	151.87	136.45	161.23	163.26
Ipickup, breaker	548.58	380.30	466.15	512.1
Ipickup, recloser	227.80	204.68	241.84	244.89

To determine fuse characteristic, the fault calculation must be carried out. By the bus impedance from matrix Zbus, the three-phase fault is calculated. Because the three-phase fault usually is the severe fault in systems, only this kind of fault is mentioned for fuse characteristic determination. The coefficient of a in (3) which is the slope of the straight line of fuse curve is selected -1.8 [4], [10]. By calculating the fault current fro m the fault calculation, the b coefficient is determined in equation (3). Hence, the aim is to find the coefficient b in (3) so that the highest rate of coordination between fuse and recloser is achieved.

3.1 Conventional Model

In this model, the b coefficient in (3) achieved when there is no DG installed in the system. After the calculation of fault current, by means of operating time of recloser in fast and slow-mode, the operating time of fuse is obtained from the below equation [4]:

$$t_{fuse} = \frac{t_{recloser\ ,slow} + t_{recloser\ ,fast}}{2}. \quad (4)$$

Because the operating time of fuse must be faster than operating time of slow-mode recloser and also slower than operating time of fast-mode recloser, the setting for operating time of fuse is the average of these two operating times. With a one operating point in the log -log plot (fault current and operating time) and as lope of-1.8, the coefficient b is determined.

For instance Fig. 5 shows the operating curves of breaker and recloser in feeder 1 and fuse in line 5-18 while no DG is installed in the end of feeders i.e. the points 5, 21, 27 and 43 or to be installed near the reclosers i.e. the points 3, 20, 25 and 41. b is calculated 5.4872 for this situation.

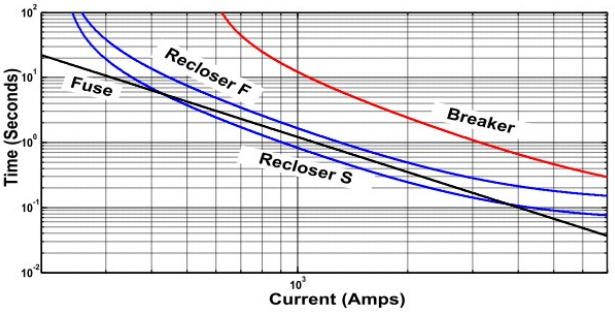

Fig. 5. Operating curves of the breaker, recloser, and fuse 5-18 in conventional model

As it can be seen in Fig. 5, the fuse operates correctly in the current range of about 420 to 3765 A, i.e. fuse operates faster than slow-mode recloser and slower than fast-mode recloser in this range. In other words, if the faults will occur in this current range, the fuse will not blow up and the schedule for fuse saving is carried out truly. The three-phase fault current occurred in point 18 and the maximum fault current passed from the fuse in line 5-18 is 1440 A. Therefore the fuse in line 5-18 does not operate before fast-mode recloser and the schedule operates correctly.

After the DG installation, because the lateral lines are also fed fro m another source (i.e. DG), the fault current usually increases in a large magnitude. For instance, if DG is installed in point 5, the fault current will be 4100 A for fuse 5-18. Hence, it can be seen that the miscoordination between fuse and recloser may be occurred in some cases. This considerable problem should be solved or improved by a better model for fuse which is exhibited in part 3.2.

3.2 Improved Model

In this model, instead of taking the average of two time values of fast and slow -mode recloser and fault current (without DG installation) as an operation point, after considering a margin with slow-mode recloser curve, the fuse characteristic curve is determined specifically. This margin is used as an interval between recloser and fuse in time domain for operating sequence and the fuse has to operate at least after that time margin of fast-mode recloser operation. Nearer the fuse curve to the slow-mode recloser, farther from fast-mode recloser and larger the coordination area of fuse -recloser. The margin of 100 ms from the operation point in the situation of no DG

installation is chosen to make a larger coordination area. In this method, the coefficient b is achieved which it means that fuse characteristic is determined. For instance for fuse 5-18, according to (1) and Table 1, the 100 ms (0.1 sec.) margin from slow-mode recloser curve is derived from (5):

$$t_{margin}\ (I) + 0.1 = \frac{28.2}{(\frac{I}{227.7988})^2 - 1} + 0.1217\ . \tag{5}$$

If t_{margin}= t_{fuse}, so with the operating point of fuse (three-phase fault current) and (3), b is obtained. b for the fuse 5-18 will be 5.5575. Fig. 6 shows the protection equipment characteristic for feeder 1 and fuse 5-18 with imp roved model for fuse curve characteristic.

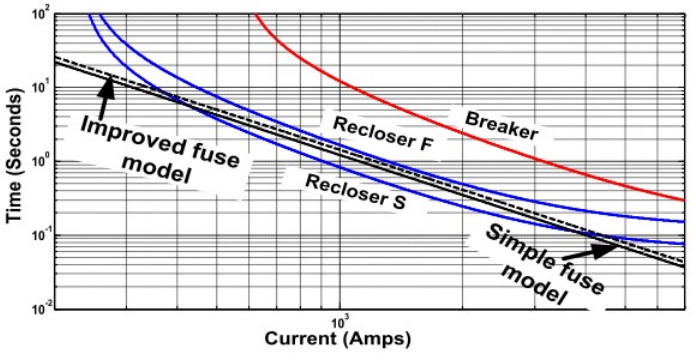

Fig. 6. Operating curves of the breaker, recloser, and fuse 5-18 in an imp roved model

Table 3 indicated the improved model for all fuses characteristic curves. As it can be seen in Table 3, the improved model in all fuse characteristic curves gives better results.

Table 3. Fuse characteristic in simp le and imp roved models

Fuse number	Simple model for fuse		Improved model for fuse	
	b	Current margin [A]	b	Current margin [A]
14	5.4922	425 – 3790	5.5473	380 - 4280
15	5.4875	425 – 3735	5.5564	370 - 4375
16	5.4930	425 – 3740	5.5463	375 - 4235
17	5.4878	425 – 3800	5.5555	370 - 4385
18	5.4872	420 – 3765	5.5575	370 - 4410
19	5.4866	420 – 3745	5.5665	365 - 4510
23	5.4449	350 – 3740	5.4527	350 - 3810
34	5.5381	450 – 4015	5.5952	400 - 4610
35	5.5338	455 – 3995	5.6051	395 - 4710
36	5.5375	445 – 4060	5.5961	405 - 4630
37	5.5337	450 – 4025	5.6060	395 - 4645
38	5.5337	395 – 4025	5.6061	390 - 4690
39	5.5336	450 – 4000	5.6156	390 - 4775
52	5.5451	455 – 4065	5.6101	400 - 4705
53	5.5431	455 – 4075	5.6201	395 - 4845
54	5.5431	455 – 4075	5.6210	395 - 4855
55	5.5445	455 – 4080	5.6307	385 - 4925
56	5.5431	455 – 4070	5.6218	395 – 4790
57	5.5447	450 – 4030	5.6315	395 - 4935

4 Conclusion

As several advantages of DG for distribution systems, it has also some disadvantages. The protection problem and the coordination between these equipments, is one of these disadvantages. The most important problem for fuse in relation with recloser is the miscoordination between them due to presence of DG. The method of this paper for eliminating or degrading of this maloperation is to determine the best characteristic of fuse curve for the larger coordination between those ones. Using mathematical equations, the fuse characteristic is determined. This characteristic can be used to install the best fuses in the new distribution networks or to modify or change the fuses in the available distribution systems.

References

1. Santoso, S., Short, T.A.: Identification of Fuse and Recloser Op erations in a Radial Distribution System. IEEE Transaction on Power Delivery 22(4), 2370–2377 (2007)
2. Brahma, S.M., Girgis, A.A.: Imp act of Distributed Generation on Fuse and Relay Coordination: Analysis and Remedies. In: Proceeding International Association Science and Technology, FL, pp. 384–389 (2001)
3. Chaitusaney, S., Yokoyama, A.: Conflict between Backup Generation and Recloser-Fuse M is coordination in Reliability Aspect from Distributed Generation. In: Proceeding IASTED International Conference Energy Power Systems, pp. 205–210 (2006)
4. Dugan, R.C., McGranaghan, M.F., Santoso, S., Beaty, H.W.: Electrical Power Systems Quality. McGraw-Hill, New York (2002)
5. Chaitusaney, S., Yokoyama, A.: Prevention of Reliability Degradation from Recloser-Fuse M iscoordination Due to Distributed Generation. IEEE Transaction on Power Delivery 23(4), 2545–2554 (2008)
6. McDermott, T.E., Dugen, R.C.: Distributed Generation Imp act on Reliability and Power Quality Indices. In: Proceeding IEEE Rural Electric Power Conference, pp. D3–D3_7 (2002)
7. Bhowmik, A., Maitra, A., Halpin, S.M., Schatz, J.E.: Determination of Allowable Penetration Levels of Distribution Resources Based on Harmonic Limit Considerations. IEEE Transaction on Power Delivery 18(2), 619–624 (2003)
8. IEEE Standard for Interconnectin g Distributed Resources with Electric Power Systems, IEEE Std. 1547-2003 (2003)
9. IEEE Standard Inverse-Time Characteristic Equations for Overcurrent Relays, IEEE Std. C37.112-1996 (1997)
10. Allan, R.N., Billinton, R., Sjarief, I., Goel, L., So, K.S.: A Reliability Test System for Educational Purp oses – Basic Distribution System Data and Results. IEEE Transaction on Power Systems 6(2), 813–820 (1991)

The IIC Bus Configuration of the Video Decoder Chip TVP5154 Based on FPGA*

Yu-lin Zhang[1], Tang-qing Yuan[1], and You-yi Wang[2]

[1] School of Information Science and Engineering University of Jinan, Jinan, China
[2] School of computer Science and technology Shandong University, Jinan, China
{Yu-lin Zhang,Tang-qing Yuan,You-yi Wang,ytqcom}@163.com

Abstract. Aiming at multi-channel video capturing of the system of video acquisition, this paper proposed a simple configuration scheme of the decoder chip TVP5154. It introduces the protocol of IIC and the setting methods of registers of the decoder chip TVP5154. It uses the hardware description language veriglog to control IIC bus. This process can initialize the decoder TVP5154 after power up or reset. The results show that the configuration of TVP5154 can capture video data of four channels at the same time in the same manner and finish video decoding.

Keywords: IIC bus, TVP5154 decoder, four channels, FPGA.

1 Introduction

IIC is developed by Philips. It is a simple bi-direction 2-wire bus for efficient inter-IC control. This protocol benefits both systems designers and equipment manufacture. It simplifies the circuit and improves the efficiency of hardware. [1] It is widely used in many fields and it has been an industrial standard. The design is a part of video capture system. It uses the decoder chip TVP5154 which has four separate video decoder channels. It can receive four separate video data and output four separate video data. Before it works, we must configure its registers. We use IIC bus to configure it. After it has been set up, the four separate channels can do the same thing at the same time.

2 IIC Bus

IIC (inter - IC) is a bus standard made by PHILIP company in order to control and communicate between IC (Integrated Circuit). It has two wires and it is SCL (serial clock) and SDA (serial data). The two wires can carry information between the devices which are connected to the bus. On the bus, each device has a unique address and it can operate as a transmitter or a receiver. Whether it is a transmitter or not that depends on the devices' function. Each device can be transmitter or receiver, but it

* Project supported by Shandong Doctor Fund (03BS005) and NSF of Shandong (Y2007G46).

D. Zeng (Ed.): Future Intelligent Information Systems, LNEE 86, pp. 623–629.
springerlink.com © Springer-Verlag Berlin Heidelberg 2011

can only be either a transmitter or a receiver at the same time. The devices can also be considered as masters or slaves when the data transfers. The device which initiates a data transfer on the bus it will be the master and the device which is addressed is considered as the slave.

2.1 Transferring Data

The transferring data set one byte as a unit. Each byte placed on the SDA line must be eight bits long and each bit occupies one clock pulse. Each byte must be followed an acknowledge bit. The acknowledge-related clock pulse is generated by the IIC master. [2] When the data is transferring, each bit will sample during the high period of the SCL. So SDA line must be stable when the SCL is high, except for start and stop condition. The state of SDA can be changed only when the SCL is low.

2.2 Data Validity

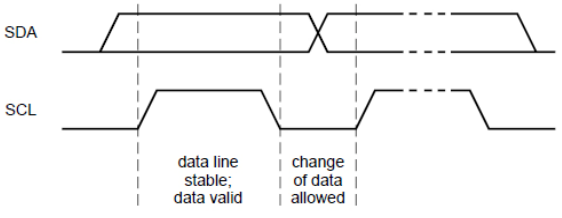

Fig. 1. Bit transfer on the IIC-bus. The data on the SDA line must be stable during the high period of the SCL, except for start and stop conditions. The high or low state of the data line will be changed only when the clock signal on the SCL line is in the low condition.

2.3 Start and Stop Signals

The IIC-bus will be free while no master requests to send data and in the same time the SDA line and SCL line is high.[3] If there is a mater which tries to control the data transition on the IIC-bus, it must generate a START signal. The master can also generate a stop signal to end the data transition. So the START and STOP conditions are always generated by the master.

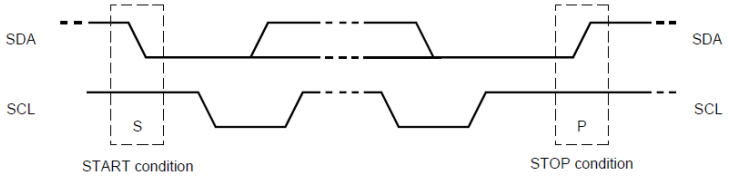

Fig. 2. START and STOP conditions: START condition is defined that a high to low transition on the SDA line while SCL is high. It is one unique case. While this situation occurs it indicates a START condition. STOP condition is defined that a low to high transition on the SDA line while SCL is high.

Acknowledge

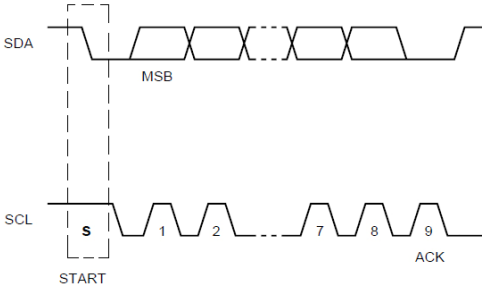

Fig. 3. Acknowledge after a byte. Acknowledge is signal that it must follow each transferred byte. The acknowledge-related clock pulse is generated by the master. During the acknowledge clock pulse, the transmitter releases the SDA line, while the receiver pulls down the SDA line.

3 TVP5154 Decoder

The TVP5154 device is a 4-channel, low-power, NTSC/PAL/SECAM video decoder. All four channels of the TVP5154 are controlled independently. The decoders share one crystal for all channels and all supported standards. The TVP5154 can be programmed using a single inter-integrated circuit (IIC) serial interface. IIC commands can be sent to one or more decoder cores simultaneously, reducing the amount of IIC activity necessary to configure each core. A register controls which decoder core receives IIC commands, and it can be configured such that all four decoders receive commands at the same time.

The TVP5154 decoder is initialized and controlled by sets of internal registers that set all device operating parameters. Communication between the external controller and the TVP5154 decoder is through the IIC. To initialize the registers of the TVP5154 decoder, we use FPGA chip to control IIC bus by programming. We will control the four channels of the TVP5154, so to simplify programming of each of the four decoder channels, a single IIC writing transaction can be transmitted to any one or more of the four cores in parallel. This reduces the time required to download firmware or configure the device when all channels are configured in the same manner. It also enables the address for all registers to be common across all decoders.

4 IIC Configure

4.1 Frequency Division Module

The data transfer rate on the bus is up to 400 kbit /s, but the FPGA chip is 50MHZ. So the FPGA's frequency must be divided. We can use a frequency division module to solve this problem.

Table 1. Part of the registers of the TVP5154

REGISTER FUNCTION	ADDRESS	DEFAULT	R/W(1)
Video input source selection #1	00h	00h	R/W
Analog channel controls	01h	15h	R/W
Operation mode controls	02h	00h	R/W
Miscellaneous controls	03h	01h	R/W
Autoswitch mask	04h	DCh	R/W
Clock control	05h	08h	R/W
Color killer threshold control	06h	10h	R/W
Luminance processing control #1	07h	60h	R/W
Luminance processing control #2	08h	00h	R/W
Brightness control	09h	80h	R/W
Color saturation control	0Ah	80h	R/W
Hue control	0Bh	00h	R/W
Contrast control	0Ch	80h	R/W
Outputs and data rates select	0Dh	47h	R/W
Luminance processing control #3	0Eh	00h	R/W
Configuration shared pins	0Fh	08h	R/W
Reserved	10h		
Active video cropping start MSB for unscaled data	11h	00h	R/W
Active video cropping start LSB for unscaled data	12h	00h	R/W
Active video cropping stop MSB for unscaled data	13h	00h	R/W
Active video cropping stop LSB for unscaled data	14h	00h	R/W
Genlock/RTC	15h	01h	R/W
Horizontal sync start	16h	00h	R/W

(1) R = Read only, W = Write only, R/W = Read and write

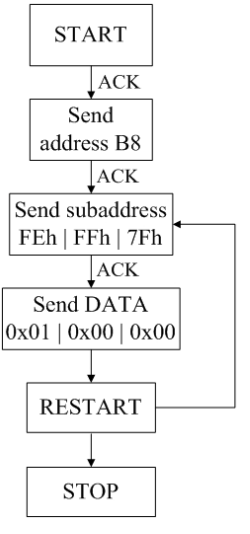

Fig. 4. The procedure of setting the register 0xFE and 0xFF is on the IIC bus. As is show in fig.4, it generates a start signal first and then sends the IIC sub-address 0xFE. After this, it sends the initial data 0x0F of the register of sub-address 0xFE. After sending data, it will restart. This repeat will not stop until it finishes configuring the three registers. Of course, after every byte an acknowledge signal will be followed.

4.2 The Writing Operation of the Registers

According to the TVP5154's data sheet, IIC sub-address 0xFE contains four bits with each bit corresponding to one of the decoder cores. If this bit is set, IIC writing transactions are sent to the corresponding decoder core. If the bit is 0, the corresponding decoder will not receive the IIC write transactions. So we must write 0x0F to the register 0xFE first. After this setting, the four channels can be configured in the same manner. Meanwhile, the register 0xFF must be set to 0x00. IIC register 0xFE controls which of the four decoders receives IIC commands. IIC register 0xFF controls which decoder core responds to IIC reads. According to the data sheet, we know after power up or the hardware reset, each decoder must be started by writing 0x00 to register 7Fh for all four decoders. So we know the procedure via the data sheet.

4.3 Use LUT to Set the Value of the Registers

TVP5154 has more than one hundred control registers. We must configure them before the system start to work to achieve specific function. To simplify programming, we use LUT(Look Up Table) to configure the initial data of the registers.[4] The data of the registers is as shown in table.1.

Part program of using LUT is followed:

```
always @(posedge clk or negedge rst_n)
begin
           if(!rst_n)
            begin
                NS    <= WR_IDLE;
              sda_r <= 1'b1;
              num   <= 4'd0;
              reg_lut <= 1'b0;
              LUT_INDEX <= 7'd0;
              int_end <= 1'b0;
              lut_end <= 1'b0;
            end
else begin
      if(LUT_INDEX <= LUT_SIZE)
         case( NS )
            001: begin
```

```
                I2C_LUT_DATA <= {8'hB8, LUT_DATA};
                I2C_START <= 1'b1;
                NS <= 2'd010;
                end
              010: begin
                if(I2C_END)
                  begin
                     if(!I2C_ACK)
                        NS <= 2'd100;
                     else begin
                        NS <= 2'd001;
                        I2C_START <= 1'b0;
                        end
                  end
                end
              100: begin
                LUT_INDEX <= LUT_INDEX + 1'b1;
                NS <= 2'd001;
                end
              endcase
       end
always @(LUT_INDEX)
               begin
         case(LUT_INDEX)
               0:   LUT_DATA <= 16'h0000;
               1:   LUT_DATA <= 16'h0115;
               2:   LUT_DATA <= 16'h0200;
               3:   LUT_DATA <= 16'h0301;
               4:   LUT_DATA <= 16'h04DC;
                  ……
            default: ;
                endcase
             end
```

5 Conclusion

This design realizes the configuration of the decoder TVP5154 with the hardware description language verilog. It simplifies programming of the system. The design makes it possible to control all channels in the same manner. It uses FPGA chip to control IIC bus. It improves the system's integration level and stability. Meanwhile, it decreases the development cost and improves its design efficiency. The design has a good potential in its extended function. It will have a good prospect.

References

1. The I2C-Bus Specification Version 2.1 (January 2000)
2. Tvp5154 4-Channel Low-Power Pal/Ntsc/Secam Video Decoder With Independent Scalers And Fast Lock, Texas Instruments Incorporated (2006)
3. Yuan, H.: Design of I2C configuration interface of ADV7181 on SOPC. Journal of Hubei Institute for Nationalities (Natural Science Edition) (2007)
4. Han, H.: The I2C Bus Configuration of the Video Decoder Chip Based on FPGA. Control & Automation (2009)

Performance Analysis of Continuous-Time Non-persistent CSMA with Monitoring in Internet of Things

Hongwei Ding, Dongfeng Zhao, and Yifan Zhao

Department of Communication Engineering, Yunnan University, No. 2 North Green Lake, 650091, Kunming, Yunnan, China
dhw1964@yahoo.cn

Abstract. With the communication network and more rapid business growth, more and more users want to be rich, more high-quality information services, and the original service business than a single control strategy can not meet the QoS multi-service quality of service. This article uses the continuous-time non-persistent CSMA random access mode to realize "automation" and "intelligent" basic features in the Internet of Things. And we get to the throughput of the continuous-time non-persistent CSMA with monitoring using the average cycle analysis method, through computer simulations to verify the correctness of the analysis.

Keywords: continuous-time, non-persistent CSMA, intelligent, information packet, throughput.

1 Introduction

Internet of Things is the basis of the Internet in the computer, using RFID, wireless data communications technology, to construct a covered everything in the world. In Internet of Things, the commodities to each other to "exchange" without human intervention. The essence is to use radio frequency identification (RFID) technology, the Internet through the computer realized products of the automatic identification and interconnection and sharing of information [1].

Internet of things to make full use of next-generation IT technologies among the industries, specifically, is to embed sensors and equipment to the power grid, railways, bridges, tunnels, highways, buildings, water systems, dams, oil and gas pipelines, etc. kinds of objects, then the "Internet of things" to integrate with the existing Internet to achieve social and physical human system integration, network integration among this, there is a strong central ability to super-computer cluster, able to integrate the personnel network , machinery, equipment and basic facilities, management and control in real time, on this basis, Human beings can be more precise management of production and life to achieve "intelligent" status, increase resource utilization and productivity levels to improve human and the relationship between nature [2].

D. Zeng (Ed.): Future Intelligent Information Systems, LNEE 86, pp. 631–636.
springerlink.com © Springer-Verlag Berlin Heidelberg 2011

The essence of the Internet of things is mainly reflected in three aspects: First, the Internet features, that require the physical network must be able to achieve interoperability of the Internet; Second, identification and communication features, which include the Internet of Things "thing" must To have the automatic identification and material objects communication (M2M) functions; third, intelligent features, the network should have the automatic, self-feedback and the characteristics of intelligent control.

Internet of Things in the persons and things, things and things as the platform for the access way into polling multiple access methods and random multiple access method. Among them, the random access method is divided into discrete time random multiple access methods and continuous-time random multiple access system access methods. This paper will uses the continuous-time non-persistent CSMA with monitoring function random multiple access system to achieve "automation" and "intelligent" feature, first asked that the system has the availability of a client feedback to the sender of information, monitoring functions. Enabling intelligent identification, positioning, remote monitoring, network status tracking, fault alarm, automatic measurement and control functions.

2 System Model Description

Consider the time axis and let t be the time of arrival of a packet which senses the channel idle and such that no other packet is in the process of transmission. Any other packet arriving between t and $t+a$ will sense the channel as unused, will transmit, and hence will cause a conflict. If no other terminal transmits a packet during these a seconds, then the first packet will be successful [3].

In continuous-time non-persistent CSMA with monitoring function random multiple access system, when the terminal sends information packet, there must be three states appear that the information packet is successfully transmitted, the information packet collision, and idle channel situation. We use monitoring the channel mode in continuous-time non-persistent CSMA random multiple access system. The first, we need to monitor the information packet was successfully transmitted the case. When the information packet is successfully received, on the receiving end, transmitting a feedback confirmation message to inform the sender that the information packet has been successfully received, the sender will receive a confirmation message after the delay a, and Supposing that the time length of confirmation message a; when the information packet collision, the receiver will feedback a collision feedback message to inform the sender, the same, the sender will receive a collision feedback information after the delay a, the length of the collision feedback information also a. Therefore, the successful transmission of information packet and simultaneous confirmation message, expressed by U_τ; information packet collision, Information packet collisions and collision feedback information is also emerging, expressed by B_τ.

Therefore, in this continuous-time random multiple access system will have three kinds of incidents. (1) The information packet is successfully sent, the random variables indicated with U, successful transmission of information packet and

simultaneous confirmation message, expressing with U_τ. (2) The information packet collision, expressing with B, the information packet collisions and simultaneous the collision feedback also, expressing with the B_τ. (3) in the slots no information packet arrival, expressing with I. The first event and the second event combined together as the channel busy event, there is busy and free events must alternate in the channel, so that we see on the time axis two kinds of events that alternating random process, shown in Fig. 1.

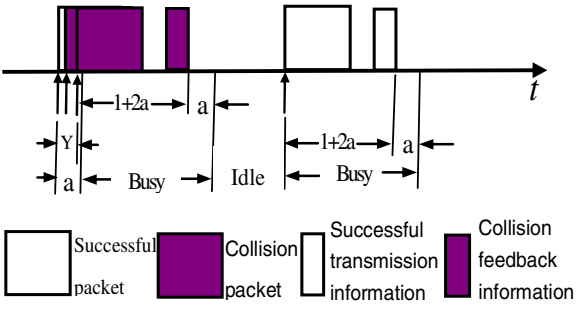

Fig. 1. The continuous-time non-persistent CSMA random access system with monitoring function.

3 Analysis of Continuous-Time Non-persistent CSMA with Monitoring

If probability distribution of Arriving k information packets in the time interval a. We can get

$$\frac{(Ga)^k e^{-Ga}}{k!} \quad (k = 0,1,2,...)$$

Where G is the average arrival rate of information packet. Then it is said to obey Poisson distribution.

Next, we will think of such the continuous-time non-persistent with monitoring function random access system using the method of analysis of the average cycle.

Let $t+Y$ be the time of occurrence of the last packet arriving between t and $t+a$. The transmission of all packets arriving in $(t,t+Y)$ will be completed at $t+Y+1+2a$. Only a seconds later will the channel be sensed unused. Now, any terminal becoming ready between $t+a$ and $t+Y+1+3a$ will sense the channel busy and hence will reschedule its packet. The interval between t and t+Y+1+3a is called a transmission period (TP). Note that there can be at most one successful transmission during a TP. Define an idle period to be the period of time between two consecutive TP's (also called busy periods in this simple case). A busy period plus the

following idle period constitute a cycle [3]. Let BU be the expected duration of the busy period, I the expected duration of the idle period, and BU+I the expected length of a cycle [4,5]. Let U denote the time during a cycle that the channel is used without conflicts. Using renewal theory arguments, the average channel utilization is simply given by

$$S = \frac{\overline{U}}{\overline{BU} + \overline{I}}. \tag{1}$$

The probability that a TP is successful is simply the probability that no terminal transmits during the first a seconds of the period and is equal to e^{-aG}. Therefore, the length of successful transmission of information packet and simultaneous confirmation message is

$$\overline{U}_{\tau} = (1+2a)e^{-aG}. \tag{2}$$

Among them, the success of the length of time to send the information packet for

$$\overline{U} = e^{-aG}. \tag{3}$$

In the literature[6], a cycle within the channel is idle, the average time for

$$P(I > t) = \mathrm{e}^{-Gt}. \tag{4}$$

So, we can get

$$P(I \le t) = 1 - \mathrm{e}^{-Gt}. \tag{5}$$

Therefore, we can get the probability density function of the idle events

$$p(t) = G\mathrm{e}^{-Gt}. \tag{6}$$

So, we can get

$$\overline{I} = \frac{1}{G}. \tag{7}$$

The average duration of a busy interval is $\overline{BU} = 1 + \overline{Y} + 3a$, $\overline{Y}$ is the expected value of Y.

In the literature [3], the distribution function for Y is given

$$P(Y \le y) = P(\text{no information packet arriving in a} - \text{Y}) = \mathrm{e}^{-G(a-y)}$$

Therefore, we can get the probability density function

$$p(y) = G\mathrm{e}^{-G(a-y)}. \tag{8}$$

$$\overline{Y} = \int_0^a yp(y)dy = a - \frac{1}{G}(1 - e^{-aG}) \ . \tag{9}$$

$$S = \frac{\overline{U}}{\overline{BU} + \overline{I}} = \frac{Ge^{-aG}}{G(1+4a) + e^{-aG}} \ . \tag{10}$$

4 Simulation

In the continuous-time non-persistent CSMA with monitoring function random multiple access system based on the analysis, we conducted a computer simulation [7,8], theoretical calculation and computer simulation using the same parameter values were the result of taking a = 0.1, as Fig.2. shown.

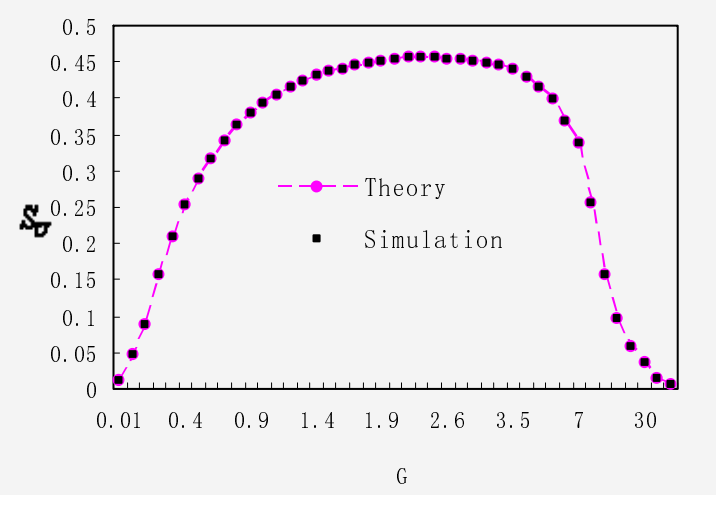

Fig. 2. The relationship between throughput and arrival rate

5 Conclusions

Figure 2. illustrate that the simulation results have been verified to agree well with the theoretical results.

We Analysis the throughput of the continuous-time non-persistent CSMA with monitoring function random multiple access system in favor of finding solutions for system optimization

We can send to the sender the confirmation information and feedback collision information to collect the system state information. So we can monitor, test and analysis the system.

References

1. Wanhua, Y.: Concept of and Basic Content of the Internet of Things. China Information Times 5, 1–3 (2010)
2. Yi, L., Huofeng, C.: Pondering on Internet of Things. Value Engineering (08), 126–127 (2010)
3. Kleinrock, L., Tobagi, F.A.: Packet Switching in Radio Channels: Part 1 – Carrier Sense Multiple-Access Modand Their Throughput-Delay Characteristics. IEEE Transactions on Communications 23(12), 1400–1416 (1975)
4. Bicheng, L.: The Softswitch-based Personal Monitoring Communications. Zte Communications (04), 47–50 (2006)
5. Hu, X., Zhou, L.: Research on Signaling Monitor System of Switch Soft Networks. Telecommunications Science (01), 34–37 (2007)
6. Zhao, D.: Study on a New Analyzing Method for Random Access Channel. In: Second International Conference and Exhibition on Information Infrastructure, Beijing, pp. 16–29 (April 1998)
7. Zhao, D.: Study on Analyzing Method for Random Access Protocol. Journal of Electronics 16(1), 44–49 (1999)
8. Zhou, N., Zhao, D., Ding, H.: Analysis of Multi-Channel and Random Multi-Access Ad hoc Networks Protocol with Two-dimensional Probability. In: Proceedings of ISCIIA 2006 Computational Intelligence and Industrial Applications Conference, November 22-25, pp. 26–32 (2006)

Application of WSN of Continuous-Time Polling System with Vacations and Using M-Gated Services

Hongwei Ding, Dongfeng Zhao, and Yifan Zhao

Department of Communication Engineering, Yunnan University, No. 2 North Green Lake, 650091, Kunming, Yunnan, China
dhw1964@yahoo.cn

Abstract. In this paper, we propose the model of applying for WSN of continuous time polling system with vacations and using M-Gated services. By the imbedded Markov chain theory, the generating functions of queue length of arrival information packets at the sensor node is obtained. Also, the Laplace-Stieltjes transform (LST) of packet delay distribution function is derived. Mean waiting time of information packet at the sensor node is obtained. Especially we can obtain some corresponding results under some especial cases. The results reveal that our system model can guarantee better QoS and system stability, and it has better efficiency than that of traditional gated service.

Keywords: WSN, continuous-time polling system, M-Gated services, mean waiting time, bulk arrival.

1 Introduction

Wireless sensor network consists of integrated sensors, data processing unit and communication module tiny nodes, these nodes form by way of self-organization network, by means of the built-in sensor nodes where the environmental temperature, humidity, noise, light intensity, pressure, soil composition, the size of moving objects, speed, direction, and many other physical phenomena of interest [1]. Because of its practicality, and is widely used as domestic and international research focus in recent years. Access methods for wireless sensor network is divided into polling methods and random multiple access Multiple Access Method. Among them, the Polling method is divided into discrete time polling multiple access methods and time continuous polling multiple access system access. For a long time, researchers struggle to improve the performance of the polling systems by the studying polling order, service disciplines and servicing order in the terminals. The choice of service disciplines decides the servicing time and proficiency of each terminal, it is necessary to focus on both priority of service demand and fairness. Therefore, study of polling servicing disciplines is a focus these years. The original analysis and research mostly concentrated on the symmetric polling system and if having a deeper understanding of polling system we need the study change from the originally single service strategy to mixed service strategy and from a single-level system development to a multi-level

D. Zeng (Ed.): Future Intelligent Information Systems, LNEE 86, pp. 637–644.
springerlink.com © Springer-Verlag Berlin Heidelberg 2011

polling system [2]. Only in this way, the control of polling system will become more flexible and effective and can become more powerful utility in the application of more fields [3].

M-Gated Services obtained by choosing different M different levels of service. We consider the polling system with multiple vacations an bulk arrival using M-gated services in continuous time [10]. We suppose that the station of the system can access the channel through a M-gated access policy in continuous time. And we assume s time of packets, the station is vacation. When the station is idle to *(S+1)*th time of packets, the station is permitted to transmit the definite of packets stored in its buffer, and then transmit the other definite packets during the transmission. If the packets still remain in the buffer of the station, the third, the fourth or even the *M*th data transmission will be arranged in which upon receiving polling messages during the service time. Otherwise, the times of data transmission are no more than *M*. With the help of embedded Markov chain theory and a generation function method [4-6], we study the controlling mechanism as well as the effects of different parameter value of *M* for the system, and then compare the results through computer simulated experiments. The results show that the proposed model is more efficient than the traditional polling system with gated access policy.

2 System Model

Analysis of polling systems with other the same way as in the analysis before we make the following assumptions.

2.1 System Operating Conditions

1) We assume the station is vacation before *(S+1)*th time of packets. The station is vacation to *(S+1)*th time of packets, the station can transmit a bulk arrival packets in probability *p*. During the continuous time period, the arrivals of the message packets waiting for transmission follow an independent distribution with generation function $\tilde{A}_i(z)$, mean value $p(1-p)^s\lambda_i = \tilde{A}_i'(1)$, and variance $\sigma_\lambda^2 = \tilde{A}_i''(1) + p(1-p)^s\lambda_i - p^2(1-p)^{2s}\lambda_i^2$ for the station.

2) The timing variables for each station to transmit message packets are independent of each other in the probability distribution which has a generation function $\tilde{B}_i(z)$, mean value $\beta_i = \tilde{B}_i'(1)$, variance $\sigma_\beta^2 = \tilde{B}_i''(1) + \beta_i - \beta_i^2$.

3) The variable walking time between common station and hub station are independent of each other in the probability distribution which has a generation function $\tilde{R}(z)$, mean value $\gamma = \tilde{R}'(1)$ and variance $\sigma_\gamma^2 = \tilde{R}''(1) + \gamma - \gamma^2$.

4) Each station has enough storage so that no message packets are lost under the First Come and First Service (FCFS) rule, and the system work in the condition of continuous time state, the system is stability, service intensity $N\rho < 1$.

2.2 System Generation Function

In the literature [8] and [9], the following formula is given

$$\begin{aligned}
&\tilde{G}_{(i+1)1}\left(z_1,z_2,...,z_i,...,z_N\right)=\lim_{n\to\infty}E\left[\prod_{j=1}^{N}z_j^{\xi_j(n+1)}\right]=\tilde{R}_i\left(\sum_{j=1}^{N}p(1-p)^s\lambda_j\left(1-z_j\right)\right)\\
&\tilde{G}_{im}\left(z_1,z_2,...,z_{i-1},\tilde{B}_i\left(\sum_{j=1}^{N}p(1-p)^s\lambda_j\left(1-z_j\right)\right),z_{i+1},...,z_N\right)\\
&\tilde{G}_{im}\left(z_1,z_2,...,z_i,...,z_N\right)\\
&=\tilde{G}_{i(m-1)}\left(z_1,z_2,...,z_{i-1},\tilde{B}_i\left(\sum_{j=1}^{N}p(1-p)^s\lambda_j\left(1-z_j\right)\right),z_{i+1},...,z_N\right)\\
&\qquad\qquad\cdots\cdots\\
&\tilde{G}_{i3}\left(z_1,z_2,...,z_i,...,z_N\right)\\
&=\tilde{G}_{i2}\left(z_1,z_2,...,z_{i-1},\tilde{B}_i\left(\sum_{j=1}^{N}p(1-p)^s\lambda_j\left(1-z_j\right)\right),z_{i+1},...,z_N\right)\\
&\tilde{G}_{i2}\left(z_1,z_2,...,z_i,...,z_N\right)\\
&=\tilde{G}_{i1}\left(z_1,z_2,...,z_{i-1},\tilde{B}_i\left(\sum_{j=1}^{N}p(1-p)^s\lambda_j\left(1-z_j\right)\right),z_{i+1},...,z_N\right)\\
&\qquad i=1,2,\cdots,N\ .
\end{aligned}\tag{1}$$

3 Analysis of System Performance

The performance of the system, including the Mean queue length and mean delay of the information packet, this paper analyzes mean delay of the information packet.

3.1 Mean Queue Length

Let the average number of message packets at station j at t_n be defined as $\tilde{g}_{ix}\left(j\right)$ in reference [8] and [9], then

$$\tilde{g}_{ix}\left(i\right)=\frac{N\gamma p(1-p)^s\lambda\left(1-\rho\right)\rho^{x-1}}{\left(1-\rho^m\right)\left(1-N\rho\right)}\tag{2}$$

$$i=1,2,\cdots,N;\ x=1,2,\cdots,m\ .$$

3.2 Calculating $\tilde{g}_i\left(i,i\right)$

Reference methods of analysis used in [10], we can get $\tilde{g}_i\left(i,i\right)$. Let

$$\tilde{g}_i(j,k) = \lim_{z_1,z_2,\cdots,z_N \to 1} \frac{\partial^2 \tilde{G}_{(i+1)x}(z_1, z_2 \cdots, z_N)}{\partial z_j \partial z_k}. \tag{3}$$

$$i = 1,2,\cdots,N \ ; \ j = 1,2,\cdots,N \ ; k = 1,2,\cdots,N \ .$$

System of service intensity $N\rho < 1$ and gives

$$\begin{aligned}\tilde{g}_{(i+1)1}(j,k) &= p^2(1-p)^{2s}\lambda^2\tilde{R}_i''(0) + \gamma p(1-p)^s\lambda[\tilde{g}_{im}(j) + \tilde{g}_{im}(k)] + 2\gamma p p(1-p)^s\lambda\tilde{g}_{im}(i) \\ &+ p^2(1-p)^{2s}\lambda^2 B''(0)\sum_{x=1}^{m}\tilde{g}_{ix}(i) + \tilde{g}_{i1}(j,k) + \rho\sum_{x=1}^{m}\left[\tilde{g}_{ix}(j,i) + \tilde{g}_{ix}(i,k)\right] \\ &+ \rho^2\sum_{x=1}^{m}\tilde{g}_{ix}(i,i)\end{aligned} \tag{4}$$

$$i \neq j, i \neq k, j \neq k \ .$$

$$\begin{aligned}\tilde{g}_{(i+1)1}(j,i) &= p^2(1-p)^{2s}\lambda^2\tilde{R}_i''(0) + \gamma p(1-p)^s\lambda\tilde{g}_{im}(j) + 2\gamma p p(1-p)^s\lambda\tilde{g}_{im}(i) \\ &+ p^2(1-p)^{2s}\lambda^2 B''(0)\sum_{x=1}^{m}\tilde{g}_{ix}(i) + \tilde{g}_{i1}(j,i) + (\rho-1)\sum_{x=1}^{m}\tilde{g}_{ix}(j,i) + \rho^2\sum_{x=1}^{m}\tilde{g}_{ix}(i,i)\end{aligned} \tag{5}$$

$$i \neq j \ .$$

$$\begin{aligned}\tilde{g}_{(i+1)1}(j,j) &= p^2(1-p)^{2s}\lambda^2\tilde{R}_i''(0) + 2\gamma p(1-p)^s\lambda\tilde{g}_{im}(j) + 2\gamma p p(1-p)^s\lambda\tilde{g}_{im}(i) \\ &+ p^2(1-p)^{2s}\lambda^2 B''(0)\sum_{x=1}^{m}\tilde{g}_{ix}(i) + \tilde{g}_{i1}(j,j) + 2\rho\sum_{x=1}^{m}\tilde{g}_{ix}(j,i) + \rho^2\sum_{x=1}^{m}\tilde{g}_{ix}(i,i)\end{aligned} \tag{6}$$

$$i \neq j \ .$$

$$\begin{aligned}\tilde{g}_{(i+1)1}(i,i) &= p^2(1-p)^{2s}\lambda^2\tilde{R}_i''(0) + 2\gamma p p(1-p)^s\lambda\tilde{g}_{im}(i) + p^2(1-p)^{2s}\lambda^2 B''(0)\sum_{x=1}^{m}\tilde{g}_{ix}(i) + \tilde{g}_{i1}(i,i) \\ &- \sum_{x=1}^{m}\tilde{g}_{ix}(i,i) + \rho^2\sum_{x=1}^{m}\tilde{g}_{ix}(i,i)\end{aligned} \tag{7}$$

Calculation of (5) and (6), we can get,

$$\begin{aligned}&\sum_{k=1}^{N}\sum_{\substack{j=1 \\ \neq k}}^{N}\tilde{g}_j(j,k) \\ &= \rho\sum_{k=1}^{N}\sum_{\substack{j=1 \\ \neq k}}^{N}\left[\sum_{\substack{i=1 \\ \neq j}}^{N}\tilde{g}_i(j,i) + \frac{\rho}{2}\left(\frac{1-\rho^m}{1-\rho}\right)\sum_{\substack{i=1 \\ \neq j \\ \neq k}}^{N}\tilde{g}_i(i,i) + \rho^m\tilde{g}_j(j,j)\right] + \tilde{C}_1\end{aligned} \tag{8}$$

$\tilde{C}_1$ is the amount of remaining for the purpose of calculating. Calculation of (7) and (8), we can get

$$\sum_{j=1}^{N} \tilde{g}_j(j,j) = \frac{\rho}{(1-\rho)(1+\rho^m)} \sum_{j=1}^{N} \sum_{\substack{i=1 \\ \neq j}}^{N} \left[2\tilde{g}_i(j,i) + \rho\left(\frac{1-\rho^m}{1-\rho}\right)\tilde{g}_i(i,i) \right] + \tilde{C}_2 \tag{9}$$

$\tilde{C}_2$ is the amount of remaining for the purpose of calculating. After the result of (9) substitution (10), and simplification, we can get,

$$\tilde{g}_i(i,i) = \frac{N\gamma p^2 (1-p)^{2s} \lambda^2 (1-\rho)}{(1-\rho^{2m})(1-N\rho)} \left\{ \frac{\tilde{R}''(0)}{\gamma} + \frac{1}{(1-\rho)(1-N\rho)} \left[\left(N-1+\rho^{m-1}(1-N\rho)\right) p(1-p)^s \lambda \tilde{B}''(0) + (N-1)\gamma(1-\rho) + \frac{2N\gamma(1-\rho)^2 \rho^m}{1-\rho^m} \right] \right\} \tag{10}$$

3.3 Mean Waiting Time

Reference methods of analysis used in [10], we can get the mean waiting time of the system. The mean waiting time of information packet $\tilde{w}_i$, denotes the time from when a packet enters into the queue at station i ($i = 1, 2, \cdots, N$) to when it is transmitted [7-9].

According to the controlling mechanism of the system, the average time delay of message packet, $E[\tilde{w}_i]$, can be derived as follows.

Server polling service ith station, the status of information packet is $\tilde{\xi}_{ix\alpha}(n)$ at the xth time, and has the following relation,

$$\tilde{\xi}_{ix\alpha}(n) = \tilde{\xi}_{ix}(n) - \alpha + \tilde{\eta}_i\left(\tilde{v}_{ix\alpha}\right)$$

$$x = 1, 2, \cdots, m; \alpha = 1, 2, \cdots, \tilde{\xi}_{ix}(n)$$

$\tilde{v}_{ix\alpha}(n)$ is the server in the xth time service, a total service time of α packets, then $\tilde{\eta}_i(\tilde{v}_{ix\alpha})$ is the information packets that entry ith station in the service time. After the server completes an information packet service, the generation function of the ith station for the probability distribution is,

$$\tilde{Q}_i(z_i)=\lim_{n\to\infty}E\left[\frac{1}{K_i}\sum_{x=1}^{m}\sum_{\alpha=1}^{\psi}z_i^{\tilde{\xi}_{ix\alpha}(n)}\right]$$
$$=\frac{\tilde{B}_i\left(p(1-p)^s\lambda_i(1-z_i)\right)}{K_i\left[z_i-\tilde{B}_i\left(p(1-p)^s\lambda_i(1-z_i)\right)\right]}\left[\tilde{G}_i(1,...,z_i,1,...,1)\right. \tag{11}$$
$$\left.-\tilde{G}_i\left(1,...,\tilde{B}_i\left(p(1-p)^s\lambda_i\left(1-\tilde{H}_{im}\left(0,\cdots,p(1-p)^s\lambda_i(1-z_i),0,\cdots,0\right)\right)\right),1,\cdots,1\right)\right]$$

In fact, $K_i=\tilde{g}_i(i)$, $\psi=\tilde{\xi}_{ix}(n)$, the delay of information packet LST relation,

$$\tilde{W}_i(s_i)\tilde{B}_i(s_i)=\tilde{Q}_i\left(1-\frac{s_i}{p(1-p)^s\lambda_i}\right) \tag{12}$$

$i=1,2,\cdots,N$.

The mean delay of the packet in system,

$$E(\tilde{w}_{mG})=-\tilde{W}_i'(0)=\frac{1}{2}\left[\frac{\left(1+\rho^m\right)\tilde{g}_i(i,i)}{p(1-p)^s\lambda\tilde{g}_i(i)}+\frac{\left(1-\rho^{m-1}\right)p(1-p)^s\lambda\tilde{B}''(0)}{1-\rho}\right]$$
$$=\frac{1}{2}\left\{\frac{\tilde{R}''(0)}{\gamma}+\frac{1}{1-N\rho}\left[Np(1-p)^s\lambda\tilde{B}''(0)+(N-1)\gamma+\frac{2N\gamma(1-\rho)\rho^m}{1-\rho^m}\right]\right\} \tag{13}$$

$$i=1,2,\cdots,N \quad .$$

When the station has not been vacation, $s=0, p=1$, we can obtain Equations 14. We have obtained Equations 14 In reference [10].

$$E(\tilde{w}_{mG})=-\tilde{W}_i'(0)=\frac{1}{2}\left[\frac{\left(1+\rho^m\right)\tilde{g}_i(i,i)}{\lambda\tilde{g}_i(i)}+\frac{\left(1-\rho^{m-1}\right)\lambda\tilde{B}''(0)}{1-\rho}\right]$$
$$=\frac{1}{2}\left\{\frac{\tilde{R}''(0)}{\gamma}+\frac{1}{1-N\rho}\left[N\lambda\tilde{B}''(0)+(N-1)\gamma+\frac{2N\gamma(1-\rho)\rho^m}{1-\rho^m}\right]\right\} \tag{14}$$

$$i=1,2,\cdots,N \quad .$$

4 Theoretical and Simulated Results

Assume the wireless sensor network consists of 5 stations, m=3, γ= 1,β=10 or 10, and we assume the station has not been vacation, That is $s=0, p=1$. The theoretical

mean information packet waiting time has been calculated for the stations, and Matlab tool are used to give the comparison results of the system. The theoretical and simulated results of mean message packet waiting time are shown in Figs. 1.

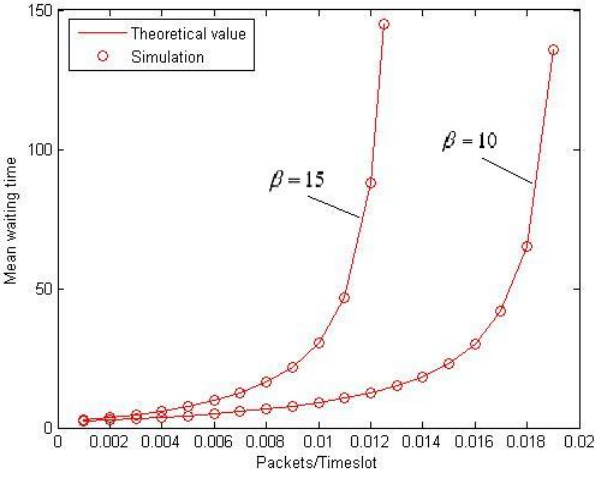

Fig. 1. Mean waiting time with m=3, N=5, β=10, γ=1

The symbols represent the simulation results for different arrival rate of message packets using 3-Gated service with 5 stations. The four figures show that the mean queue length, the mean cyclic period, and the mean waiting time have close relation to the number of stations, arrival rate of packets, and the control value of M-gated service on the condition of keeping service time and walking time in specific values.

With increasing of the arrival rate of packets, for a specific number of stations, the mean waiting time increases.

Simulation results have been verified to agree well with the theoretical results.

The fact demonstrates that our model is well distinguished in the current scheme with the lower waiting time and performs a little better than the traditional gated polling mechanism for the same number of stations. Thus, this model can efficiently guarantee the QoS of the WLAN system.

5 Conclusions

Information packet mean waiting delay results. By studying a M-Gated service polling system control mechanism, analyzed the m control parameter value of effective control. M-gated service polling system, a combination of two basic polling systems, system control more effective. The results reveal that our system model can guarantee better QoS and system stability, and it has better efficiency than that of traditional gated service.

References

1. Elson, J., Romer, K.: Wireless Sensor Networks: A New Regime for Time Synchronization. In: Proceedings of the First Workshop on Hot Topics in Net-works (HotNets-I), October 28-29, Princeton, New Jersey (2002)
2. Yang, Z.-j., Zhao, D.-f., Ding, H.-w., Zhao, Y.-f.: Research on Two-class Priority Based Polling System. Electronica Sinica 37(7), 1452–1456 (2009) (in Chinese)
3. Zhao, D., Zheng, S.: Analysis of a Polling Model with Exhaustive Service. Acta. Electronica Sinica 22(5), 102–107 (1994) (in Chinese)
4. Zhao, D., Zheng, S.: Message Waiting Time Analysis for a Polling System with Gated Service. Journal of China Institute of Communications 15(2), 18–23 (1994) (in Chinese)
5. Zhao, D.: Performance Analysis of Polling Systems with Limited Service. Journal of Electronics 15(1), 43–49 (1998)
6. Zhang, Y.-m., Zhang, X., Yang, D.-c., Zhao, D.-f.: Polling Multiple Access Protocol Based on the Waiting Time and Channel State. Journal of Beijing University of Posts and Telecommunications 31(4), 126–139 (2008) (in Chinese)
7. Liu, q., Zhang, Z., Zhang, N.: Mean cyclic time f queuing priority station polling system. Journal of China Institute of Communications 20(2), 86–91 (1999) (in Chinese)
8. Ding, H., Zhao, D., Zhao, Y.: Queue-length nalysis of continuous-time polling system with vacations using M-gated services. Applied Mechanics and Materials 20-23, 427–431 (2010)
9. Ding, H., Zhao, D., Zhao, Y.: Modeling and analysis of polling system with M-gated services. In: 2009 2nd International Conference on Future Information Technology and Management Engineering, FITME 2009, pp. 317–319 (2009)
10. Ding, H., Zhao, D., Zhao, Y., Ma, X.: Packet delay analysis of continuous-time polling system with M-gated services. In: CCTAE 2010 International Conference on Computer and Communication Technologies in Agriculture Engineering, vol. 3, pp. 408–411 (2010)

A PSO-Based Algorithm for Gateway Placement in Wireless Mesh Networks*

Lan Yao[1] and Feng Zeng[2]

[1] College of Mathematics and Econometric
Hunan University
Changsha, China
yao@hnu.edu.cn
[2] Department of Computer Science and Technology
Hunan International Economics University
Changsha, China
fengzeng@mail.csu.edu.cn

Abstract. In a wireless mesh network (WMN), the optimal placement of gateways is important to the network performance. In this paper, we propose a particle swarm optimization (PSO) algorithm PSO-LBPG to get the optimal solution. In the algorithm PSO-LBPG, a greedy algorithm is used to partition the network into load-balance clusters, and each cluster satisfies QoS requirements. Simulation results show that the number of gateways generated by PSO-LBPG is nearly equal to the results from other gateway placement algorithms, and as far as the load balancing on the gateways is concerned, PSO-LBPG performs much better than the others.

Keywords: wireless mesh network, gateway placement, load balance, particle swarm optimization, greedy algorithm.

1 Introduction

A key technology, wireless mesh networks (WMNs), has emerged recently for future broadband wireless access. In WMNs, there are two types of node, mesh routers and mesh clients. Some mesh routers, called gateway nodes, are directly connected with the Internet, and the most traffic in WMNs is exchanged with the Internet through the gateways. The architecture of WMNs can be classified into three main groups: Infrastructure/Backbone, Client WMNs and Hybrid WMNs [1, 2]. In this paper, we focus our discussion on the design of the backbone in the WMNs.

The traffic distribution in a WMN is typically skewed, as most of the user traffic is directed to/from a wired network [3]. Hence, especially when the traffic is heavy, the gateways become the bottlenecks of the network. For optimal performance, the WMN should be divided into disjoint clusters, covering all nodes in the network. Within each cluster, the cluster head would serve as the gateway, connected to the wired network.

* This work was supported by the High School Science Research Project of Hunan (08C510).

D. Zeng (Ed.): Future Intelligent Information Systems, LNEE 86, pp. 645–652.
springerlink.com © Springer-Verlag Berlin Heidelberg 2011

In a WMN, the more gateways placed, the better performance will be gained. But, the higher cost will be charged. The problem of gateway placement in a WMN is to place a minimum number of gateways for the sake of cost, while ensuring the QoS requirements. Different from previous work, in this paper, we take into account the balance of the load on the gateways.

In the past several years, a lot of work has been done on the problem of gateway placement in WMNs. In [4], Wong identified two main technical problems: gateway placement for minimizing communication delay and for minimum communication cost. For both objectives, they had developed a series of techniques and novel negative selection statistically-tuned heuristic algorithms, using the same strategy: at each step they decide which of the candidate gateways will be eliminated from further consideration. In [5], Chandra explored the placement problem under three wireless link models. For each model, they developed algorithms to efficiently place gateways in the network, aiming to minimize the number of required gateways while guaranteeing users' bandwidth requirements. In [6], Bejerano presented polynomial time approximation algorithm for partitioning the network nodes into minimal number of disjoint clusters that satisfy multiple constraints and used a spanning tree rooted at each cluster head (i.e. gateway) for message delivery. In [7], Aoun proposed a polynomial time near-optimal algorithm which recursively computes minimum weighted dominating sets, while consistently preserving QoS requirements across iterations. In [8], He formulated the gateway placement problem as a linear program (LP) issue, then developed two heuristic algorithms for the purpose of cost-efficient gateway placement. In [9], Li addressed gateway place problem in WMN for throughput optimization, and proposed a gateway deployment method using a cross-layer throughput optimization.

The above algorithms try to place minimum gateways in a WMN, while ensuring QoS requirements. But, they put little emphasis on the balance of load on the gateways. In this paper, we address the problem of gateway load balancing placement in a WMN, aim to achieve load balancing on the gateways in the WMNs, using minimum number of gateway and ensuring the QoS requirements.

2 System Description

2.1 Network Model

We consider a WMN represented by an undirected graph $G(V, E)$, $n=|V|$ is the number of nodes in the graph. Each node $v \in V$ represents a mesh router or gateway. The neighborhood of v, denoted by $N(v)$, is the set of nodes residing in it's transmission range. A bidirectional wireless link exists between v and every neighbor $u \in N(v)$ and is represented by an edge $(u, v) \in E$.

Let $G = \{g_1, g_2, \ldots, g_k\}$ be the set of $\boldsymbol{k}$ gateway nodes, where g_i is actually node v_{n-k+i}, for $1 \le i \le k$. All other wireless nodes v_i (for $1 \le i \le n-k$) $\in \overline{G} = V - G$ are ordinary mesh nodes. Each ordinary mesh node u will aggregate the traffic from all its users and then route them to the Internet through some gateway nodes. For simplicity, we denote the cumulated traffic on mesh node u as $W(u)$.

2.2 Problem Description

We assume the WMN is divided into k clusters, and each cluster has only one gateway (cluster head) serving the nodes inside the cluster. Consequently, there are k gateways in the network. Let C_i be the set of nodes in the cluster i ($1 \le i \le k$), and the sum of all C_i ($1 \le i \le k$) is equal to the set of all nodes V. For $1 \le i \le k$, $g_i \in C_i$ is the only gateway node in the cluster C_i. Assumed each gateway g_i can direct all the traffic from other nodes inside the cluster to the Internet, the load of gateway, denoted by $L(g_i)$, is the sum of traffic on all nodes inside the cluster.

In each cluster C_i, we should ensure the QoS requirements. The distance (minimum number of hops) between gateway g_i and the node u ($u \in C_i$) is denoted by $D(g_i, u)$. To satisfy the delay constraint, $D(g_i, u)$ has the upper bound value of R. Generally, the more nodes in a cluster, the worse the performance in the cluster is. Hence, an upper bound S is given to the size of a cluster. The degree of a node u ($u \in C_i$) in the cluster, denoted by $\delta(u)$, also has important impact on the interference around the node. Therefore, an upper bound D should be given to guarantee the transmission ability on the node.

To formulate the gateway placement problem, we define a binary variable x_{ij}. If the gateway g_i and the mesh node v_j are belong to the same cluster, x_{ij} will take the value of 1 (g_i is called to be the assigned gateway of v_j), otherwise, x_{ij} is 0. Then, we can formulate load balancing gateway placement problem to linear programming problem as follows.

$$\min\ k = |G|,\ VAR = \sqrt{\frac{1}{|G|-1}\sum_{g_i \in G}(L(g_i)-\overline{L})^2}$$

s.t.

(a) $C_i \bigcap C_j = \Phi\ (1 \le i, j \le k, i \ne j)$

(b) $C_i \bigcap G = \{g_i\}\ (1 \le i \le k)$

(c) $\forall\ \mathrm{v_j} \in V,\ \sum_{g_i \in G} \mathrm{x_{ij}} = 1$

(d) $\forall\ \mathrm{v_j} \in V,\ \sum_{g_i \in G} (\mathrm{d_{ij}} \times \mathrm{x_{ij}}) \le R$

(e) $\forall\ \mathrm{v_j} \in V,\ \delta(v_j) \le D$

(f) $\forall\ \mathrm{g_i} \in G,\ \sum_{v_j \in V} \mathrm{x_{ij}} \le S$

(g) $\forall\ \mathrm{g_i} \in G,\ \mathrm{L(g_i)} = \sum_{v_j \in V} (\mathrm{x_{ij}} \times W(v_j))$

We have two goals: minimum value of k and VAR, VAR is the sample standard deviation of load on the gateways.

As described above, the gateway placement problem is converted to a linear programming (LP) problem, which is NP hard [7]. In this paper, we propose a greedy algorithm GREEDY-LBC to partition a WMN into load-balance and disjointed

clusters, and present a near-optimal algorithm PSO-LBPG based on particle swarm optimization algorithm to solve the gateway placement problem. In PSO-LBPG, GREEDY-LBC is used to improve the performance.

3 Algorithm for Network Clustering

We propose a greedy algorithm for load balancing clustering (GREEDY-LBC) in a WMN. GREEDY-LBC is described as follows.

Input: the original network and the set of gateway nodes GW ;

Output: the completed set of gateway nodes and clustering result $\{C_1, C_2, \ldots, C_k\}$;

Steps:

(a) For each $g_i \in GW$, let $L(g_i)=W(g_i)$, $C_i=\{g_i\}$ $(1 \le i \le k, k=|GW|)$; $r=1$;

(b) For each $g_i \in GW$, width first QoS constraining search to max distance r;

(c) For each node v searched in step (b), if v is searched only by g_i, then $C_i= C_i+\{v\}$, $L(g_i)= L(g_i)+W(v)$;

(d) For each node u searched more than one times in step (b), u should joint into the cluster with less load ;

(e) $r=r+1$, if $r<R$, go to step (b) ;

(f) If each node in V is covered by one of sets in $\{C_1, C_2, \ldots, C_k\}$, then **algorithm end**; else go to step (g) ;

(g) In the uncovered nodes, randomly select a node g as the gateway node ;

(h) $GW=GW+\{g\}$, $k=k+1$, $C_k=\{g\}$, $L(g)=W(g)$ and width first QoS constraining search in all uncovered nodes from g to the max distance R, then the searched and uncovered nodes join into the cluster C_k, update $L(g)$ and C_k, go to step (f).

From the steps, if the input provides enough gateway nodes to build the clusters covering all nodes and satisfying the QoS constraints, GREEDY-LBC will end in step (f). Otherwise, GREEDY-LBC will randomly select some of uncovered nodes as gateway nodes to build more clusters in order to cover all uncovered nodes, as described in step (g) and (h). The output of GREEDY-LBC is an updated string implying the gateway nodes and clustering result $\{C_1, C_2, \ldots, C_k\}$.

4 PSO-Based Algorithm for Gateway Placement

The greedy algorithm GREEDY-LBC is difficult to get the two goals (minimum number of gateways and load balancing on the gateways) at the same time. However, the technology of particle swarm optimization (PSO) does well in multiple goal optimization searching. Compared with genetic algorithm, PSO is easier to realized, and has less complexity in parameters setting [10]. Consequently, we present a PSO based algorithm for load balancing placement of gateways (**PSO-LBPG**).

Based on particle swarm optimization theories [11-13], PSO-LBPG can be described as follows.

4.1 Particle Encoding and Some Representations

We use a binary string with the length n ($n=|V|$ is the number of nodes in a WMN) as a particle to denote a potential solution of gateway placement. $X_i=(x_{i1}, x_{i2}, \ldots, x_{in})$ is used to denote a particle, and also represented for its location. Here, $x_{ij} \in \{0,1\}$ ($1 \le j \le n$, $1 \le i \le N$) is the j^{th} bit of the i^{th} particle in the population, and N is the size of the population. If the value of x_{ij} is 1, the node v_j is a gateway node in the solution of X_i.

However, because the bits with the value 1 in the strings are not enough, many binary strings with the length n could not be valid particles. Also, they are not the solutions to the gateway placement problem, because the clustering based on the gateways is not able to cover all nodes in the network. To these strings, we can use the greedy algorithm GREEDY-LBC to update them to be valid particles.

Each particle, also called a potential solution, flies in the n-dimensional problem space with a velocity, which is dynamically adjusted according to its and its colleagues flying experiences. The best previous location (which giving the best fitness value) of the i^{th} particle is represented as $P_i = (p_{i1}, p_{i2}, \ldots, p_{in})$, also called pbest. The best location among all the particles is represented by the symbol *gbest*. The velocity for the i^{th} particle is represented as $V_i = (v_{i1}, v_{i2}, \ldots, v_{in})$.

4.2 Fitness Function

The fitness value of the i^{th} particle X_i is defined as follows.

$$f(X_i) = \lambda_1 \frac{n - c(X_i)}{n} + \lambda_2 \frac{Q - VAR(X_i)}{Q} \tag{1}$$

In (1), λ_1 and λ_2 are accommodation coefficients used to adjust the optimization extent of gateway number k and gateway load deviation VAR, $c(X_i)$ is the gateway number in the solution X_i, $VAR(X_i)$ is the sample standard deviation of load on the gateways in the solution X_i, and Q is the max value of $VAR(X_i)$ for $1 \le i \le N$.

4.3 Location and Velocity Updating Equations

The particle swarm optimization concept consists of, at each time step, changing the velocity and location of each particle toward its pbest and gbest locations according to the equation (2) and (3), respectively. The value of x_{ij} is limited to 0 or 1 through sigmoid function shown in equation (4).

$$v_{ij} = w v_{ij} + c_1 r_1 (p_{ij} - x_{ij}) + c_2 r_2 (gbest_j - x_{ij}) \tag{2}$$

$$x_{ij} = \begin{cases} 1 & r < Sig(v_{ij}) \\ 0 & \text{others} \end{cases} \tag{3}$$

$$Sig(x) = \frac{1}{1+e^{-x}} \tag{4}$$

In the above equations, w is inertia weight, c_1 and c_2 are acceleration constants, and r, r_1 and r_2 are random float variables in the range [0, 1]. For equation (2), the first part represents the inertia of pervious velocity; the second part represents the private thinking by itself; the third part represents the cooperation among the particles. The velocity v_{ij} is limited by v_{max}, and in the context, we set v_{max} =4 [14].

4.4 Algorithm Description

The pseudocode of PSO-LBPG can be shown as follows.

```
1    Particle  PSO-LBPG(n, N, GEN, … )
2    {
3       InitialGroup(N); //randomly generate N particles
4       for(iter=0; iter<GEN; iter++){
5               GetPbest(X, N);
6               GetGbest(X, N);
7               UpdateVelocity(V, N);
8               UpdateLocation(X, N);
9               for(i=1; i<=N; i++)
10                ValidateByGreedy_LBC(X, i);
11      }
12      return  GetGbest(X, N);
13   }
```

The algorithm firstly uses GREEDY-LBC to generate initial particle group (line 3). Then the algorithm runs GEN iterations to get the optimal particle. In each step, line 5 gets the previous best location of each particle, line 6 gets the global best particle, line 7 and 8 get the updated velocity and location respectively, particle validation is done to each particle. At last, the algorithm outputs the optimal particle, which represents the solution to the load balancing gateway placement problem.

5 Simulation

In the simulation, we generate *100* random topologies, and execute GREEDY-LBC, PSO-LBPG and Recursive_DS [7] algorithms in these topologies. Each topology consists of *150* nodes placed in an area of *15×15*. The communication radius is set to 1. The parameters in PSO-LBPG are set: λ_1*=0.95*, λ_2*=0.05*, *N=20*, *GEN=50* (maximum iteration number).

From the experiment data, we get the standard deviation (*VAR*) of the load on the gateways. In Fig.5, Fig.6, and Fig.7, the *VAR* value is shown under various constraints of R, D and S. Compared with other two algorithms, PSO-LBPG has obvious advantage in load balancing placement of gateways.

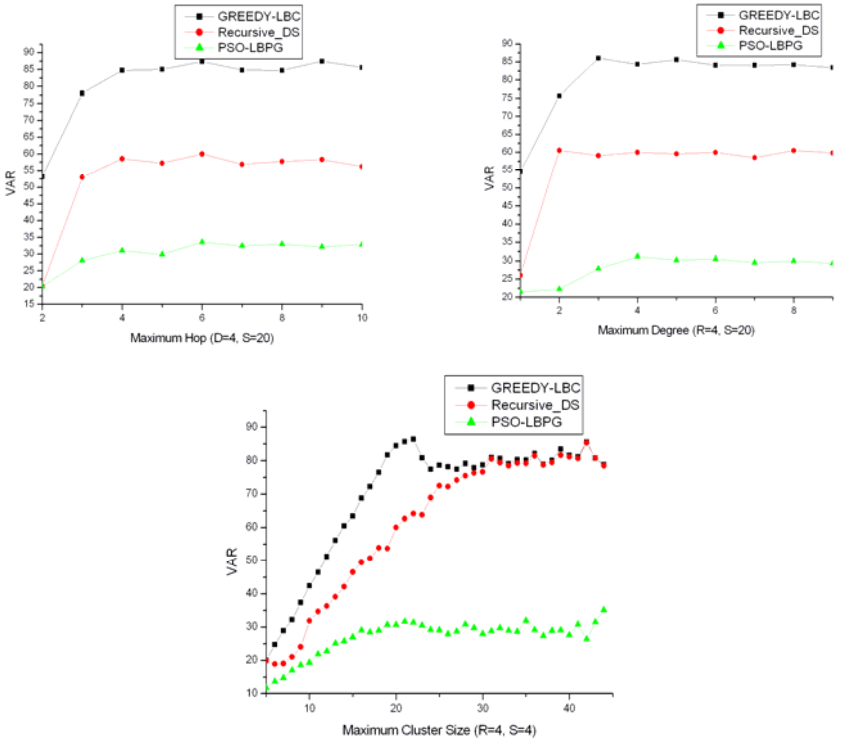

Fig. 1. comparison of load balancing on gateways

6 Conclusion

Based on previous work, we address the gateway placement problem and put emphasis on the load balancing of gateways. A PSO based algorithm PSO-LBPG has been proposed for load balancing gateway placement in wireless mesh networks. In PSO-LBPG, a greedy algorithm GREEDY-LBC is used to partition a WMN into load balancing clusters. Experiment results show that PSO-LBPG can achieve load balancing gateway placement, meanwhile optimizing the number of gateways and ensuring QoS constraints in the network.

References

1. Akyildiz, I.F., Wang, X.: A survey on wireless mesh networks. IEEE Communications Magazine 43(9), 23–30 (2005)
2. Bruno, R., Conti, M., Gregori, E.: Mesh networks: commodity multihop ad hoc networks. IEEE Communications Magazine 43(3), 123–131 (2005)
3. Raniwala, A., Chiueh, T.-c.: Architecture and algorithms for an ieee 802.11-based multi-channel wireless mesh network. In: Infocom 2005 (2005)

4. Wong, J.L., Jafari, R., Potkonjak, M.: Gateway Placement for Latency and Energy Efficient Data Aggregation. In: 29th Annual IEEE International Conference on Local Computer Networks, pp. 490–497 (2004)
5. Chandra, R., Qiu, L., Jain, K., et al.: Optimizing the Placement of Integration Points in Multi-hop Wireless Networks. In: Proceedings of IEEE ICNP, Berlin (2004)
6. Bejerano, Y.: Efficient integration of multihop wireless and wired networks with QoS constraints. IEEE/ACM Transactions on Networking 12(6), 1064–1078 (2004)
7. Aoun, B., Boutaba, R., Iraqi, Y., et al.: Gateway Placement Optimization in Wireless Mesh Networks With QoS Constraints. IEEE Journal on Selected Areas in Communications 24(11), 2127–2136 (2006)
8. He, B., Xie, B., Agrawal, D.P.: Optimizing the Internet Gateway Deployment in a Wireless Mesh Network. Mobile Adhoc and Sensor Systems, 1–9 (2007)
9. Li, F., Wang, Y., Li, X.-Y.: Gateway Placement for Throughput Optimization in Wireless Mesh Networks. In: ICC (2007)
10. Angeline, P.J.: Evolutionary Optimization Versus Particle Swarm Optimization: Philosophy and Performance Differences. In: Porto, V.W., Waagen, D. (eds.) EP 1998. LNCS, vol. 1447, pp. 601–610. Springer, Heidelberg (1998)
11. Kennedy, J., Eberhart, R.C.: A discrete binary version of the particle swarm algorithm. In: Proceedings of the 1997 Conference on Systems, Man and Cybernetics, pp. 4104–4109 (1997)
12. Kennedy, J., Eberhart, R.C.: Particle swarm optimization. In: Proceedings of IEEE International Conference on Neural Networks, pp. 1942–1948 (1995)
13. Eberhart, R.C., Kennedy, J.: A new optimizer using particle swarm theory. In: Proceedings of the Sixth International Symposium on Micro Machine and Human Science, pp. 39–43 (1995)
14. Eberhart, R.C., Kennedy, J.: Swarm Intelligence. Morgan Kaufmann, San Francisco (2001)

An Accurate Voltage Measurement System Based on DSP and Optical Fiber Transmission

Qiufeng Shang and Hao Li

Department of Electronic and Telecommunication Engineering
North China Electric Power University
Baoding, China
lindashqf@126.com, lightmanlee@gmail.com

Abstract. Accurate voltage measurement is very important for power energy measurement. To reduce the total error of power energy measurement, a novel voltage measurement system is designed in this paper. The system uses Digital Signal Processor (DSP) to accomplish signal acquisition and processing, and uses optical fiber to realize zero voltage drops in long distance transmission. The results of expriment show that amplitude error of the voltage measurement system is less than 0.03% and phase error is less than 0.3', and the error analysis proved for a class 0.2 voltage transformer (VT), system errors can be ignored. This voltage measurement system can satisfy the demand of high accuracy power energy measurement.

Keywords: voltage measurement, DSP, optical fiber transmission.

1 Introduction

With the development of digital power system and smart grid, accurate measurement of power energy became more and more important. An accurate power energy measurement needs voltage data and current data as accurately as possible. But, because long distance transmission from voltage transformer (VT) secondary side to power energy meter, voltage drops was introduced in VT secondary loop. The error introduce by VT secondary loop voltage drops is the biggest cause of total error in the power energy measurement [1]. Many solutions were proposed for eliminated VT secondary loop voltage drops [2]. But those solutions can not radically work this problem out. This paper proposes a novel voltage measurement system based on Digital Signal Processor (DSP) and optical fiber transmission. It makes full use of the DSP's excellent capability to calculate, and use optical fiber to avoid voltage drops and improve system performance of anti-electromagnetic interference. The system is composed of two parts: transmitter and receiver. Transmitter can finish voltage data acquisition, and send data to receiver through optical fiber transmission. Receiver can realize calculation, storage, alarm and signal switching functions. The voltage measurement system can measure voltage data accurately and speedily, minimize the economic losses caused of measurement error.

D. Zeng (Ed.): Future Intelligent Information Systems, LNEE 86, pp. 653–659.
springerlink.com © Springer-Verlag Berlin Heidelberg 2011

2 The Hardware Structure of System

The hardware structure of voltage measurement system is shown as Fig.1. The transmitter is located nearby secondary winding terminal outdoor and the receiver is in the main control room. The optical fiber is used to transport data between transmitter and receiver. The analog voltage signal is converted to digital optical pulse by transmitter. After O/E conversion and power amplification, receiver supplies the analog and digital signals which include VT secondary voltage information to the secondary equipment (such as power energy meter).

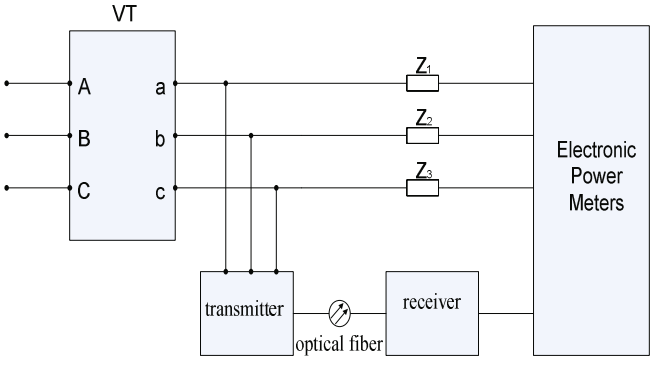

Fig. 1. The Hardware Structure of System

2.1 Transmitter

The hardware structure of transmitter is shown as Fig.2. Voltage regulator module adopt high accuracy voltage converter to enable the VT secondary voltage fit for input scope of the measurement system. Signal modulation module includes an instrumentation amplifier and a low-pass filter. A/D conversion module adopts ADS8342. Main control module use TI Company's TMS320VC5509A to control ADS8342 and store data. E/O conversion module adopts Agilent Company's HFBR-1414. Because of using active electronic circuit, transmitter needs external power supply. Transmitter uses VT secondary voltage as power source by means of rectifier, filter and DC/DC converter.

Transmitter collected data by hardware synchronous sampling (phase-locked loop) which improves computational efficiency compared with Quasi-synchronous algorithm. According to Nyquist's sampling theorem, to rebuild the characteristics of original signal, the sampling frequency must be twice than the highest frequency which in the original spectrum. As usual, sampling frequency is 5~10 times faster than the highest frequency of original signal. Taking into account the design of future system expansion requirements, the system needs to measure 2~21 times or higher harmonic parameters. So the sampling frequency must be higher than $50 \times 21 \times 5 = 5.25$ KHz. Considering enough time left to data processing, sampling frequency is selected as 12.8 KHz, which means 256 samples per signal cycle.

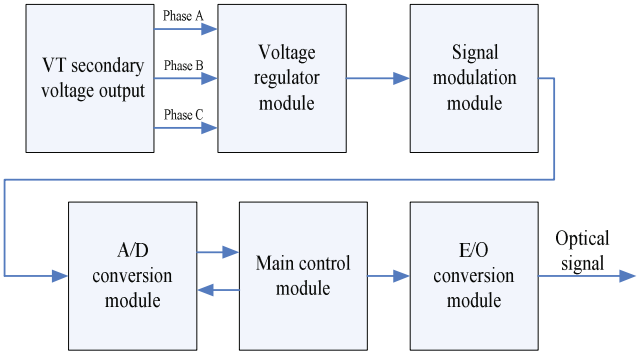

Fig. 2. The Hardware Structure of Transmitter

2.2 Receiver

The hardware structure of receiver is shown as Fig.3. O/E conversion module adopts Agilent Company's HFBR-2412, then sends signal to data processing and communication module which main control chip is TMS320VC5509A too. Aided by Current signal acquisition device, receiver can use as an electronic power energy meter; it also can be connected with traditional power energy meter through D/A conversion module and power amplifier module. Receiver can use 220V power supply in the main control room after AC/DC converter, also can use DC panel as power source when emergency.

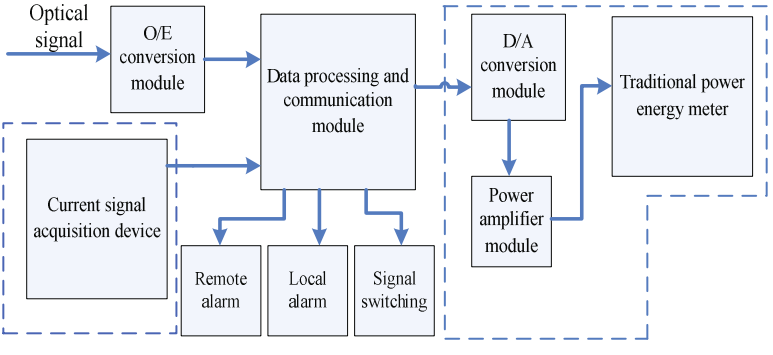

Fig. 3. The Hardware Structure of Receiver

For improving the reliability of the system, receiver also has signal switching and alarm functions. In the event of a fault, the system can alarm and switch signal to traditional VT secondary voltage automatically and switch back when system recovery, make sure no loss of power energy measurement.

3 The Description of System Software

Programs are debugged by Code Composer Studio (CCS) and loaded into the FLASH chips of transmitter and receiver, which can be booted by BootLoader. CCS is an

integrated software development environment which TI developed for TMS320 series DSP software design. Based on the structure of system hardware, the system software is composed of 2 parts: the software on transmitter, and the software on receiver.

3.1 The Software on Transmitter

The flow chart of transmitter main program is shown as Fig.4 (a). The task of main program is system initialization and data transmitting. System initialization includes: peripherals and variables initialization, and enable the needed interrupts. After initialization, the main program starts measurement and chooses which signal channel as phase-locked loop input. Data are collected by interrupt service routine and transmitted by data transmitting sub program.

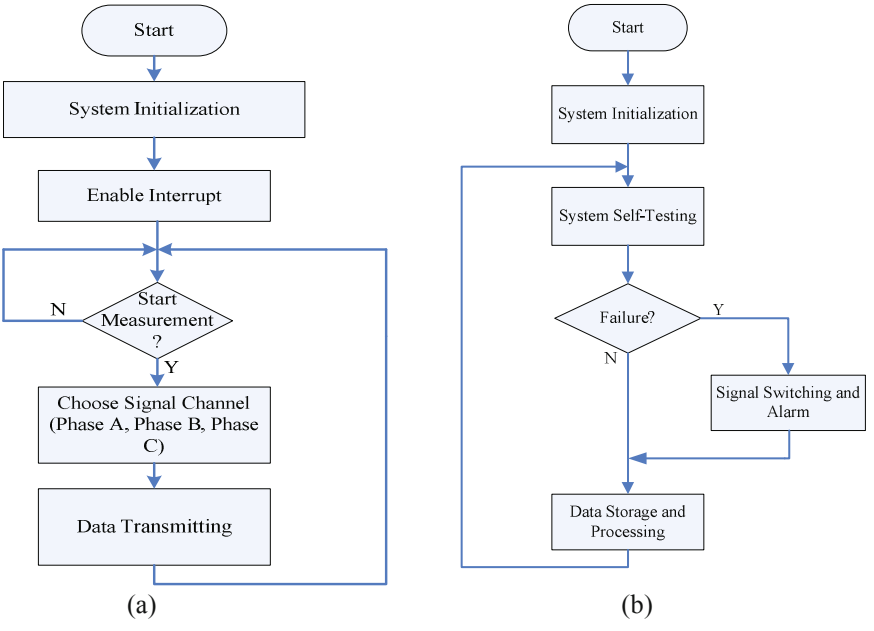

Fig. 4. The Flow Chart of the Transmitter and Receiver main program

3.2 The Software on Receiver

The flow chart of receiver main program is shown as Fig.4 (b). Receiver system initialization is similar as the transmitter. Then the main program starts system self-testing. When failure (such as open-phase, data acquisition failure and so on) was found, signal switching and alarm sub program started working to make sure measurement system work properly. All data is processed and stored by data storage and processing sub program.

4 Experiment and Error Analysis

4.1 Experiment Results

The experiment schematic is shown as Fig.5. For testing the performance of voltage measurement system error, signal generator send 50Hz sine signal to voltage measurement system and standard voltage transformer at same time. NI Company's PIC-4474 sampled the both outputs of measurement system and standard transformer channels. PIC-4474 is a 24-bit resolution, 4 simultaneously sampled analog inputs at up to 102.4kS/s dynamic signal acquisition card. Fast Fourier Transformation (FFT) program is used to calculate system error. The results are shown in Table1.

4.2 Error Analysis

The accuracy of voltage measurement system must satisfy the principle of minimal errors. This means errors introduced by voltage measurement system can be ignored compare with entire error of voltage data acquisition equipment. Let E_1 for VT relative error (suppose voltage measurement system error can be ignored), E_2 for error introduced by voltage measurement system. Follow the law of error propagation, entire equipment error is:

$$\xi = \sqrt{E_1+E_2} \tag{1}$$

ξ' means equipment error when ignored E_2, so

$$\xi \approx \xi' \tag{2}$$

If that error with one significant figure, approximate expression (2) must be satisfy the condition:

$$\xi - \xi' < 0.05\xi \tag{3}$$

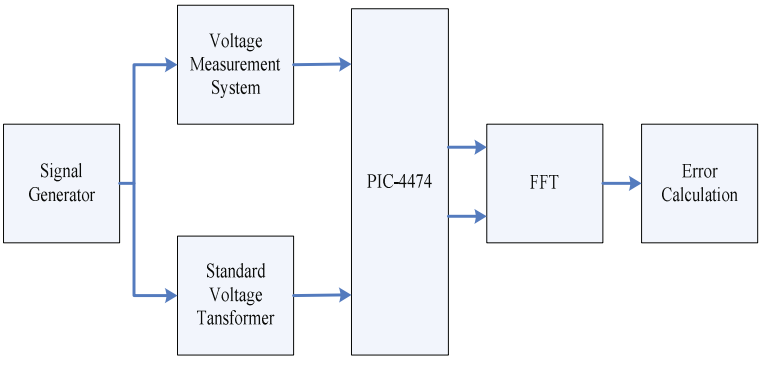

Fig. 5. The Experiment schematic

Table 1. Experiment results

EXP NO.	Standard signal amplitude($\times 10^6$)	Test signal amplitude($\times 10^6$)	Amplitude error ($\times 10^{-4}$)	Standard signal phase(rad)	Test signal phase (rad)	Phase error(')
1	1.1573	1.1574	0.86	-0.502198	-0.502165	0.11
2	1.1548	1.1546	1.73	-0.502351	-0.502282	0.24
3	1.1460	1.1458	1.74	0.308111	0.308147	0.12
4	1.1537	1.1540	2.60	0.502433	0.502489	0.22
5	1.1530	1.1528	1.73	0.401587	0.401637	0.29
6	1.1422	1.1423	0.88	-0.457181	-0.457134	0.16
7	1.1437	1.1435	1.74	0.503281	0.503349	0.23
8	1.1500	1.1499	0.87	0.298011	0.298066	0.19
9	1.1468	1.1471	2.61	-0.468382	-0.468333	0.17
10	1.1438	1.1440	1.75	0.306123	0.306161	0.13

Expression (3) means:

$$(0.95\xi)^2 < \xi^2 - E_2^2 \tag{4}$$

So,

$$E_2 \le \frac{1}{3}\xi \tag{5}$$

Expression (5) proves that the errors introduced by voltage measurement system can be ignored if it not more than one-third of entire voltage data acquisition equipment error. According to the experimental results, maximum amplitude error less than 0.03%, maximum phase error less than 0.3'. When using a class 0.2 VT, voltage measurement system errors can be ignored.

5 Conclusion

This paper proposed an accurate voltage measurement system based on DSP and optical fiber transmission. The system combines the DSP's strong capability of calculation and optical fiber's capability of anti-electromagnetic interference, effectively improves the accuracy of power energy. The results of experiment show that: the amplitude error less than 0.03%, phase error less than 0.3'. Error analysis shows that the voltage measurement system errors can be ignored when using class 0.2 VT.

References

[1] Peng, S.: Test calculations and improved technologies of power energy measurement error introduced by VT secondary loop voltage drops. Water Resources and Electric Power Press (1987)
[2] Chen, X.: Power energy measurement system PT secondary loop voltage drops causes and solutions. Electrical Measurement and Instrumentation 390(35), 33–35 (1998)
[3] Texas Instruments, TMS320VC5509 User's Manual (2004)
[4] Texas Instruments, Code Composer Studio Development Tools v3.3 Getting Started Guide (2008)
[5] Texas Instruments, ADS8342 datasheet (2003)
[6] Shang, Q., Yang, Y., Gao, H.: Development and Calibration of an Active Optical Current Transformer With High Accuracy. Transactions of China Electro technical Society 20(3), 105–110 (2005)
[7] Shang, Q., Du, C.: A Novel Measurement System of Electric Power Parameters Based on DSP and ARM. In: 2009 International Conference on Measuring Technology and Mechatronics Automation, vol. 3, pp. 353–356 (2009

Study on Coating Properties Measurement System Based on FEF Sensor

Yunzhi Huang[1] and Li Feng[2]

[1] School of Electrical Engineering and Automation, Hefei University of Technology, Hefei, Anhui, China
[2] GE Healthcare, Beijing, China
hqyz@hfut.edu.cn

Abstract. Fringing electric field (FEF) sensors are widely used for nondestructive measurement of material properties, with the advantages of one-side access, controllability of signal strength, image capability, etc. This paper presents the application of fringing electric field (FEF) sensors in coating properties measurement. The distribution of the electrical field and the measurement response was simulated off-line with Ansoft Maxwell. In addition, one of the equivalent circuits for FEF sensors was analyzed and the coating properties testing system was developed based on Labview. The primed and painted Aluminum sample was measured. The results lend valuable insights into the sensitivity of the measurement and provide the experimental data for the parameter estimation to the inverse problem of coating properties.

Keywords: Fringing Electric Field Sensor, Coating Properties, Finite Element Method, Labview.

1 Introduction

Many types of surface coatings are widely used in the manufacturing industry. The properties of the layer of paint and primer or any other functional coating impacts its efficacy. In certain applications the thickness of these layers has significant impact on the operating cost of the system. This can be seen in aerospace applications as decreased fuel efficiency due to dead load, and in automobile applications as increased kiln time for drying parts. There are many traditional measurements for surface coating inspections, such as magnetic induction, eddy-current and ultrasonic. However, current trends to substitute metal structures with composite materials seriously influences coating methods, as well as their properties, making it sometimes more difficult to use traditional measurements. A non-destructive testing technology based on Fringing Electric Field (FEF) sensors is suggested in this paper. The Finite element method is typically used to simulate the theoretical sensor response. The measurement system is developed and the experiment for a metal substrate that has been partially coated with primer and paint is presented.

D. Zeng (Ed.): Future Intelligent Information Systems, LNEE 86, pp. 661–667.
springerlink.com © Springer-Verlag Berlin Heidelberg 2011

2 Fringing Electric Field Sensor

Fringing Electric Field sensors are widely used in nondestructive testing, moisture imaging, chemical sensing, biological sensing, and micro-scale mechanical sensing [1]. However, there are quite a few different characteristics between the traditional parallel plate capacitor sensors and FEF. This differences include the non-homogenous electric field distribution, the electric energy gathering around electrodes edges, the different sensitivities of different parts of the sample, the nonlinear relationship between the output of the sensor, and the dielectric or physical properties of the sample. One main advantage of such devices is that fringing electric fields associated with interdigital electrodes can provide one-side penetration of material under testing. By varying the penetration depth, interdigital devices can be used for three-dimensional imaging. A sinusoidal 'drive' voltage is applied to one set of the electrodes, and a 'sensed signal' is measured on the other set of electrodes. The imposed drive and sense voltages create a nearly periodic voltage on the sensor surface. The basic structure and the excitation pattern of the FEF sensor is shown in Fig.1. The equivalent circuit of the sensor of a half-wavelength cell is shown in Fig.2.

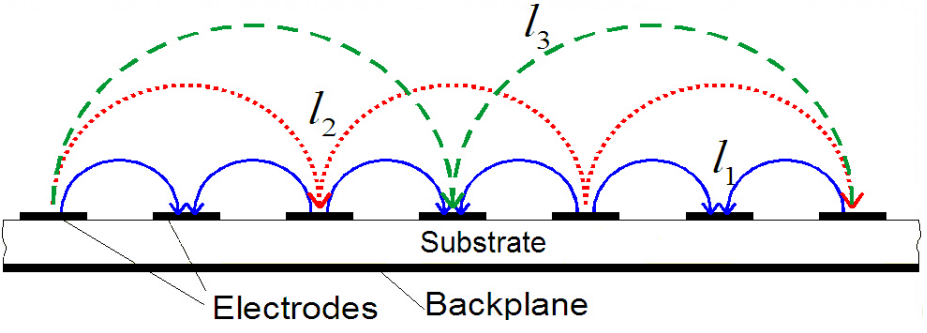

Fig. 1. This figure demonstrates the basic structure of the sensor, and the behavior of the equipotential electric field lines)

For each wavelength, a follower amplifier drives the guard plane at the substrate bottom at the voltage $V_G = V_s$,thus eliminating any current between the sensing electrode and the guard electrode [2-3]. The complex voltage gain of the sensor is the ratio of the phasor voltage of the sensing electrode and the phasor voltage of the driven electrode.

$$\hat{G} = \frac{\hat{V}_s}{\hat{V}_D} = \frac{G_{12} + j\omega C_{12}}{G_{12} + j\omega(C_{12} + C_L + C_s)} \tag{1}$$

Where, C_L is the load capacitance, C_s is the combined effects of the stray capacitance of the sensor leads, gate of the operational amplitude, and fringing fields to the surrounding objects [1].

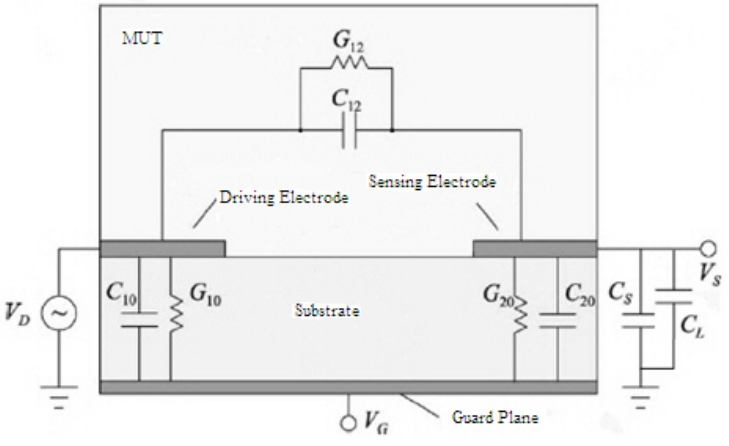

Fig. 2. This figure describes the floating voltage equivalent circuit for a FEF sensor

Suppose the magnitude of the complex voltage gain is A and the phase between $\hat{V}_s$ and $\hat{V}_D$ is φ; then the complex gain is given by

$$\hat{G} = A\cos\varphi + jA\sin\varphi = Ae^{j\varphi} \tag{2}$$

Combining (1) and (2) gives the capacitance C_{12} and the conductance G_{12},

$$C_{12} = \frac{A^2(C_L + C_s) - A\cos\varphi(C_L + C_s)}{2A\cos\varphi - 1 - A^2} \tag{3}$$

$$G_{12} = \frac{\omega A(C_L + C_s)\sin\varphi}{2A\cos\varphi - 1 - A^2} \tag{4}$$

3 Simulation

The Ansoft Maxwell has been used extensively for calculation of capacitance and conductance matrices [4,5]. Fig.3 shows the electric field distribution for samples with different permittivity in one-half wavelength cross section. The measurement response is simulated with the parameter analysis tool [6], the constraint for the distance between the sample and the electrode is added. The capacitance between the driven and sensing electrodes is calculated by changing the distance. Fig.4 shows the changes of the capacitance as a result of a increasing distance.

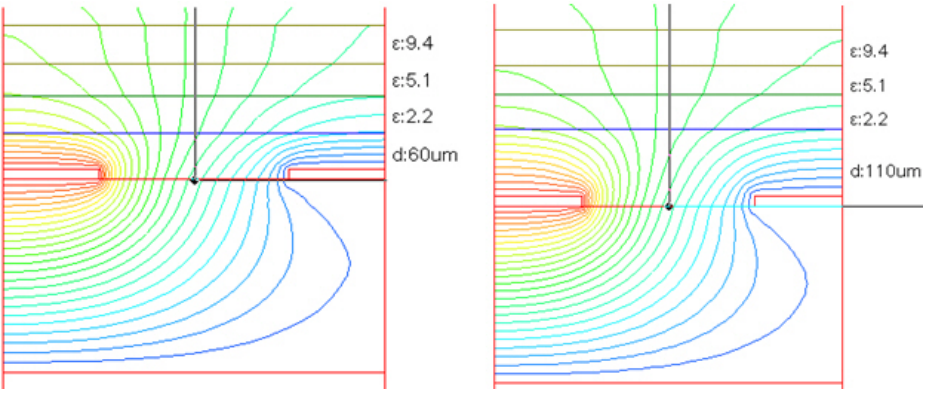

Fig. 3. The electric field with the 3 lays sample with the different permittivity in different distance between the sample and the electrodes. (The left figure is for 60um distance, and the right figure is for 110um distance)

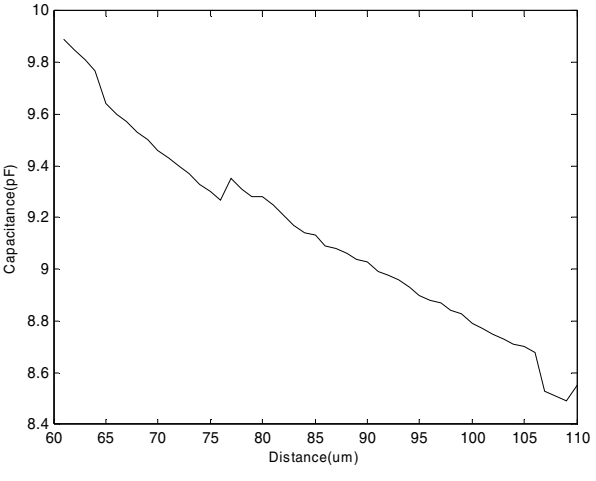

Fig. 4. The transcapacitance changes by a increasing distance. (The sample has three layers and each layer has the different permittivity)

4 The Measurement System

4.1 Overall

The measurement system integrates the testing circuit, the FEF sensor and the 3D axis motor controller (Newport MFN25CC). The testing circuit can be used with a stand alone function generator and power supply unit to control the FEF sensor and acquire measurements. The 3D axis motor controller can form a three dimensional movement

base and move the stage installed on the motor controller. The FEF sensor is attached on the stage and measurements are acquired after each movement. The system works by receiving user input on where the motors should move and in what increments. It then moves the motors through all the positions defined, taking and recording measurements after each step. Fig.5 shows the schematic diagram of the system.

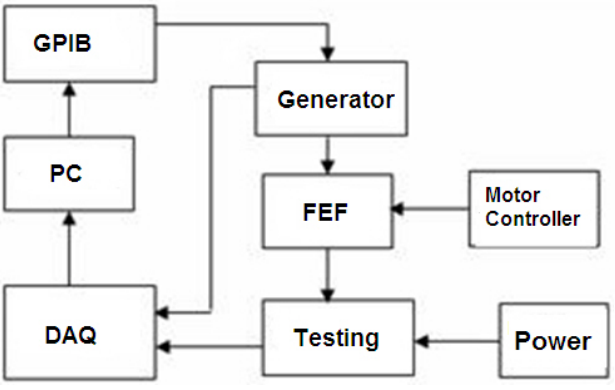

Fig. 5. The schematic diagram of measurement system based on Labview

4.2 Measurement Principles

The FEF sensor with 1mm wavelength is positioned above the sample and attached to a movable platform. The platform was mounted on the motor controller and can be moved with a micro-positioning stage. The sensor was placed in contact with the sample and then moved upwards in steps of 10 μm. At each elevation relative to the sample, the impedance values were measured over a range of excitation frequencies varying from 5Hz to 10 kHz.

The measurements are taken in a three dimensional motor movement space and then plotted onto 3D graphs and also saved into data files, both of which show various aspects of the measured data at each point. Data acquisition software was developed in LabView.

The software was divided into three main sections - the motor control, the measuring system and the 3D graphing system.

4.3 Experimental Results

Measurements were made on a metal substrate that had been partially coated with primer and paint. The metal substrate was made of Aluminum Alloy2024T-3. The thickness of the Aluminum substrate, the primer, and the paint layer were 1.285mm, 0.072mm and 0.063mm respectively. The capacitance of the Z-oriented sweep of two coating layers and one coating layer at low and high frequencies is shown in Fig.6 and in Fig.7. separately. The wavelength of the fringing electric field sensor, which was mounted on the motion controller, is 1mm. The sweep range is (0,2.5mm].

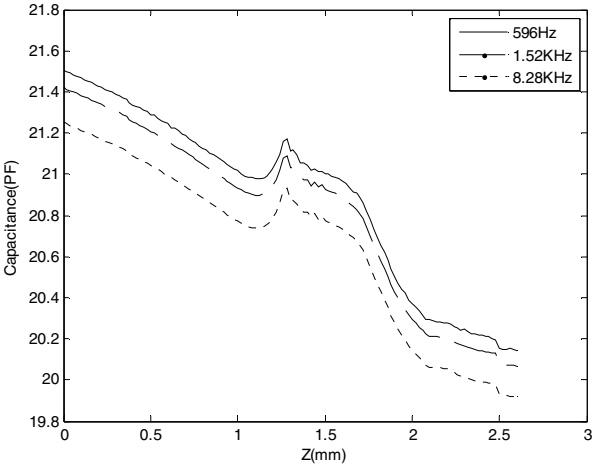

Fig. 6. The capacitance between the driven and the sensing electrodes of Z-oriented sweep with one layer coating

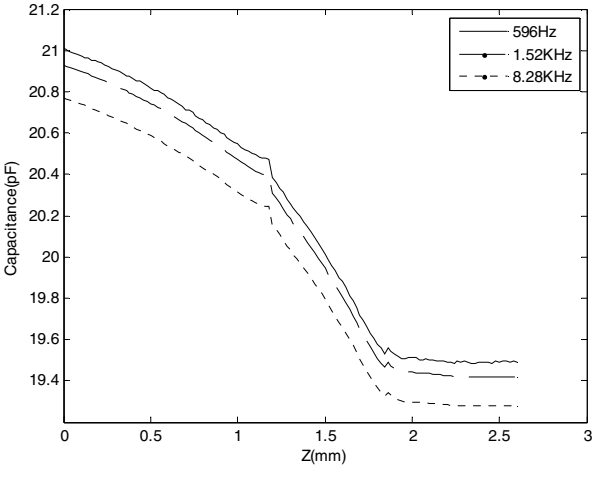

Fig. 7. The capacitance between the driven and the sensing electrodes of Z-oriented sweep with two layer coating

5 Conclusion

This paper proposes a coating properties measurement system capable of in-process, non-contact measurement of the properties of multi-layer coatings. Preliminary results show the FEF sensor can detect and distinguish between the uncoated, primed, and painted parts of the sample. This provides the experimental data for the advanced research on the properties evaluation algorithm.

Acknowledgements

This work is supported by a Specialized Research Fund for the Doctoral Program of Higher Education (New Teachers) No. 200803591019. The authors would like to extend special thanks to Prof. Mamishev, whose help, advice and supervision was invaluable. Our deep thanks go to K. Sundara-rajan Marko Oviir and Anthnoy Simon for help with the system development.

References

1. Mamishev, A.V., Sundara-Rajan, K., Yang, F., Du, Y., Zahn, M.: Interdigital Sensors and Transducers. Processing of the IEEE 92(5) (May 2004)
2. Mamishev, A.V., Du, Y., Lesieutre, B.C., Zahn, M.: Development and application of Fringing Electric Field Sensors and parameter estimation algorithms. Journal of Electrostatic 46, 109–123 (1999)
3. Lesieutre, B.C., Mamishev, A.V., Du, Y., Keskiner, E., Zahn, M., Verghese, G.C.: Forward and inverse parameter estimation algorithm of interdigital dielectrometry sensors. IEEE Trans. Dielect. Elect. Insulation 8(4), 577–588 (2001)
4. Mamishev, A.V., Zahn, M., Lesieutre, B.C., Berdnikov, B.A.: Influence of geometric parameters on characteristic of an interdigital sensor. In: IEEE Conf. Electrical Insulation and Dielectric Phenomena, pp. 550–553 (1996)
5. Mamishev, A.V., Lesieutre, B.C., Zahn, M.: Optimization of multi-wavelength interdigital dielectrometry instrumentation and algorithms. IEEE Trans. Dielect. Elect. Insulation, 408–420 (June 1998)
6. Liu, G., Zhao, L., Jiang, J.: Ansoft Engineering Electromagnetic Finite Element Analysis, pp. 159–170. Publishing House of Electronics Industry, Beijing (2005)

Author Index